GeoPlanet: Earth and Planetary Sciences

Valerio de Rubeis
Zbigniew Czechowski
Roman Teisseyre
Editors

Synchronization and Triggering: from Fracture to Earthquake Processes

Springer

GeoPlanet: Earth and Planetary Sciences

For further volumes:
http://www.springer.com/series/8821

Valerio de Rubeis • Zbigniew Czechowski • Roman Teisseyre
Editors

Synchronization and Triggering: from Fracture to Earthquake Processes

Laboratory, Field Analysis and Theories

Springer

Editors
Valerio de Rubeis
Istituto Nazionale di Geofisica e
Vulcanologia (INGV)
Via Vigna Murata 605
00143 Roma
Italy
derubeis@ingv.it

Zbigniew Czechowski
Institute of Geophysics
Polish Academy of Sciences
Ks. Janusza 64
01-452 Warsaw
Poland
zczech@igf.edu.pl

Roman Teisseyre
Institute of Geophysics
Polish Academy of Sciences
Ks. Janusza 64
01-452 Warsaw
Poland
rt@igf.edu.pl

The GeoPlanet: Earth and Planetary Sciences Book Series is in part a continuation of Monographic Volumes of Publications of the Institute of Geophysics, Polish Academy of Sciences, the journal published since 1962 (http://pub.igf.edu.pl/index.php).

ISSN 2190-5193
ISBN 978-3-642-12299-6 e-ISBN 978-3-642-12300-9
DOI 10.1007/978-3-642-12300-9
Springer Heidelberg Dordrecht London New York

Library of Congress Control Number: 2010937646

Cover design: deblik, Berlin

Printed on acid-free paper

Springer is part of Springer Science+Business Media (www.springer.com)

Series Editors

Managing Editor

Advisory Board

Tilman SPOHN
Institut für Planetenforschung
Deutsches Zentrum für Luft- und Raumfahrt
in der Helmholtz Gemeinschaft
Berlin, Germany

Krzysztof STASIEWICZ
Swedish Institute of Space Physics
Uppsala, Sweden

Roman TEISSEYRE
Earth's Interior Dynamics Lab.
Institute of Geophysics,
Polish Academy of Sciences
Warszawa, Poland

Jacek TRONCZYNSKI
Laboratory of Biogeochemistry
of Organic Contaminants,
IFREMER DCN_BE
Nantes, France

Steve WALLIS
School of the Built Environment,
Heriot-Watt University, Riccarton,
Edinburgh, Scotland, UK

Wacław M. ZUBEREK
Department of Applied Geology
University of Silesia
Sosnowiec, Poland

Contents

Introduction

Processes of synchronization and interaction play a very special role in different physical problems concerning the dynamics of the Earth's interior; they are of particular importance in the study of seismic phenomena, and their complexity is strongly affected by the variety of geological structures and inhomogeneities of the medium that hamper the course of these processes and their intensity. The attempt to tackle these problems is a great challenge from experimental, observational and theoretical point of view.

We present in this Monograph the theoretical and experimental results achieved in the frame of the European Project **"Triggering and synchronization of seismic/acoustic events by weak external forcing as a sign of approaching the critical point" (INTAS Ref. Nr 05-1000008-7889);** in this Project, which was inspired by Professor Tamaz Chelidze, our aim was to give grounds for better understanding and interpretation of dynamical interactive processes of physical fields, both found in the laboratory experiments as well as in field observations. One of the leading problems – related to synchronization and interaction of different physical fields in fracture processes – concerns triggering and initiation of rupture and displacements within the Earth interior. From this point of view, the results from laboratory studies on synchronization and interaction and those found and involved in field observations, helped to improve the theoretical background. Reversely, some of the presented new theoretical approaches have served to stimulate laboratory and field studies.

The **theoretical part** of the Monograph deals with the synchronization and interaction processes among the physical fields. Starting with a consideration on complex nonlinear systems, as observed in the geophysical time series and in laboratory experiments, like the study of frictional instabilities, we pass to the theoretical background of triggering and synchronization processes.

In Chapter 1, the **nonlinear dynamics** is considered **as a tool for revealing synchronization and ordering in geophysical time series**. The authors investigate the case of Caucasus seismicity, where the analysis reveals highly nonlinear structures in temporal, energy and space domains of seismic time series.

In Chapter 2, **Models of stick-slip motion: impact of periodic forcing,** the authors review the modern concept of seismic process relaying mainly on the frictional instabilities which develop on preexisting tectonic faults; additional external forcing provokes triggering and synchronization during stick-slip process described by the nonlinear interaction of objects.

The interaction and synchronization processes are considered in Chapter 3, **Shear oscillations, rotations and interactions in an asymmetric continuum.** In this study the author focuses on his recently developed Asymmetric Continuum Theory, in which synchronization may also take place between the fields shifted in phase by $\pi/2$, e.g., between strains and rotations, as it occurs in the release and rebound seismic processes.

In Chapter 4, **processes in micro-fracture continuum** are described as the extended micro-fragmentation processes based on the double transport process. The generalization of the Navier-Stokes transport approach, the derived nonlinear equations and solitons are discussed.

Chapter 5, **On a simple 1-D stochastic cellular automaton with avalanches – simulation and analytical results,** presents a very simple automaton for which evolution equations may be derived and solved analytically. Next, the model is used for the analytical derivation of the adequate Ito equation.

In Chapter 6, **Ito equations as macroscopic stochastic models of geophysical phenomena: construction of the models on the basis of time series,** the authors show that the Ito equations can be useful macroscopic models of phenomena in which microscopic interactions are averaged in an adequate way. They arrive at this result using the method of constructing Ito models from geophysical time series and time series generated by cellular automata.

In Chapter 7, **The importance of the privilege for appearance of long-tail distributions,** a unified description, by the privilege concept, is proposed for origins of a wide range of observational long-tail distributions and patterns revealing a fractal form.

We trace the **triggering and synchronization phenomena** in the part related to **laboratory experiments:** this is especially important when dealing with earthquake activity and the related experiments.

Based on the laboratory experiments on triggering and synchronization of mechanical instabilities (slip events) by weak electromagnetic or mechanical forcing, **triggering and synchronization of stick-slip: experiments on a spring-slider system** (Chapter 8) are considered as connected with nonlinear interactions close to the critical state. These instabilities were registered by the acoustic emission (bursts) generated by slips in the spring-slider system. Using the tools of nonlinear dynamics the dependence of strength of synchronization on the intensity and frequency of forcing (Arnold's tongue) was established. New effect of high order synchronization of slip events, with various winding numbers has been revealed in spring-slider system experiments.

In Chapter 9, **Oscillating load-induced acoustic emission in laboratory experiment,** the authors analyze the characteristics of acoustic emissions in Westerly granite samples (pre-fractured cores) under confining pressure of 160 MPa.

Correlation between the acoustic response and sine load has been observed. The acoustic activity, synchronized with the applied oscillating load, is probably due to high strain-sensitivity in transient, unstable mode, while it almost disappears after the "stick-slip" event.

Acoustic emission dynamics initiated by fluid infusion on laboratory scale (Chapter 10) has been studied in heterogeneous laboratory samples subjected to an axial load, lasting several months, and due to the repeatedly injected fluid. The acoustic emission has drastically increased as a result of penetration of a small volume of fluid. In the case of mechanical upload, the dynamics of relaxation processes of acoustic emission differs significantly from that when the process runs due to the injection of liquid. In the former case it complies with the Omori law, while in the latter the intensity of acoustic emission passes through a strongly marked maximum, similar to swarm seismicity.

In Chapter 11, **Acoustic emission spectra classification from rock samples of Etna basalt in deformation-decompression laboratory experiments,** the authors arrive at the cluster identification of acoustic emissions belonging to the same experimental stage; this made it possible to discriminate the high and low frequency events belonging to the two phases and to discover a new type of event, called 'hybrid', characterized by an intermediate distribution of frequencies.

In Chapter 12, **Phase shifted fields: some experimental evidence,** the authors present examples of synchronization processes between the deformation and electric fields and between the acoustic waves and electric oscillations: these synchronizations proceed with a phase shift of $\pi/2$ as expected due to the theoretical studies.

The final part of the Monograph presents the **field observations** related to some synchronization mechanisms revealed.

In Chapter 13, **Periodical oscillations of microseisms before the Sumatra earthquake of December 26, 2004,** the seismic broadband records were analyzed, with the help of various methods, to detect the hidden periodicities, multiple coherence effects and asymmetric low-frequency impulses. The main feature of the synchronization between the microseismic oscillations on different seismic stations was starting 53 hours before the Sumatra earthquake. It was found that the main synchronizing period increases with time from values of the order of minutes toward few tens minutes, i.e., it was detected that the period of collective effect within the observed data has been gradually increasing.

In Chapter 14, **Synchronizations of microseismic oscillations as the indicators of the instability of a seismically active region** the results are presented showing **t**hat synchronization of microseismic oscillations at different stations was detected starting several days before the Kronotskoe 05.12.1997 ($M = 7.8$) and Hokkaido 25.09.2003 ($M = 8.3$) earthquakes; the synchronization intervals are indicators of the unstable state of a seismically active region and could be regarded as earthquake precursors.

In Chapter 15, **Multifractal Parameters of Low-Frequency Microseisms,** the effects found are interpreted as an increase in the degree of synchronization of microseismic noise on Japan's islands after the September 25, 2003 Hokkaido event. It could be a foreshock of an even stronger future earthquake, as follows

from the well-known statement that synchronization is one of the signs of an approaching catastrophe.

In Chapter 16, **changes in dynamics of seismic processes around Enguri high dam reservoir induced by periodic variation of water level** were investigated using nonlinear dynamics methods. The evidence is presented showing that an increase of the order in dynamics of daily occurrence, as well as temporal and energy distributions of earthquakes took place around Enguri high dam water reservoir (Western Georgia) during the periodic variation of the water level in the lake.

The dynamical complexity of water level variations in wells has been analyzed in order to find strong earthquakes signatures (Chapter 17). Dependence of dynamics on the presence of periodic components in the data records (time series) was investigated. Modern tools of time series analysis (Lempel-Ziv complexity measure and singular value decomposition technique) confirmed that these variations are a response to different periodic, as well as non-periodic influences, including earthquake-related strain generation in the earth crust.

In Chapter 18, **Detecting quasi-harmonic factors synchronizing relaxation processes: application to seismology,** the solutions of equations corresponding to relaxation oscillator discharge moments for stress processes reveal the "gaps", i.e., time intervals when discharge processes are forbidden. The discharges inside the period of external forcing show that strong and long-time growing earthquakes are related to wider gaps, while fast growth of stress gives birth to narrow gaps.

Chapter 19, **Stacked analysis of earthquake sequences: statistical space-time definition of clustering and Omori law behavior** brings an analysis of the aftershocks sequences. An extension of the definition of a sequence is proposed by introducing space-time constrains for the analysis of decay rate and clustering. The related catalogues have been analyzed even under their fractal dimension aspect, correlated with the space and time clustering.

The final Chapter 20, **Dynamical changes induced by strong electromagnetic discharges in earthquakes' waiting time distribution at the Bishkek test area (Central Asia),** describes the effect of releases of strong current pulses on the local seismic regime, revealed by nonlinear dynamics approach; such experiments influenced the dynamics of seismic process and increased the regularity in the waiting times' series.

We can conclude that the contributions included in this monograph deal with a wide variety of topics, with emphasis on the synchronization and interactive processes which reveal co-action or influence the dynamics of seismicity; the laboratory experiments and theoretical new approaches presented help to understand and tackle these problems.

Part I
Theoretical Studies

Chapter 1
Nonlinear Dynamics as a Tool for Revealing Synchronization and Ordering in Geophysical Time Series: Application to Caucasus Seismicity

Teimuraz Matcharashvili and Tamaz Chelidze

1.1 Introduction

It is a common statement in scientific literature that the complexity of nature has always been an inevitable problem in our efforts towards understanding spatial forms of natural objects and temporal evolution of natural processes. "Complex" and "complexity" are now quite popular scientific terms, though there is little consensus on their official definitions and they still have a variety of meanings depending on the context [Arecci, 1996; Shiner, 1999]. This is so because the study of complexity in both dynamical and structural sense is in its infancy, being at the same time a rapidly developing field in the forefront of many areas of science, including mathematics, physics, geophysics, economics, biology, etc.

Natural systems and/or processes are complex mainly due to their nonlinearity, an intrinsic property of the underlying laws conditioning the absence of determinism of the Universe. The presence of this property is revealed in the specificity of systems whose temporal behavior and spatial structures were named "complex" [Kantz, 1997; Matcharashvili, 2000]. In order to avoid misunderstanding caused by the tradition associating the term nonlinearity exclusively with dynamics, it should be stressed that at present the terms nonlinearity and complexity are commonly regarded as synonyms. This is convenient in order to address both complex nonlinear temporal evolution and complex non-Euclidean spatial forms of natural systems. As an inherent property, nonlinearity or complexity is revealed in the absence of deterministic cause-effect relation observed on different spatial and temporal scales. This property incorporates phenomena with a very broad diversity

T. Matcharashvili (✉)
Georgian Technical University, 77 Kostava ave., 0171 Tbilisi, Georgia
M. Nodia Institute of Geophysics, 1 Alexidze str., 0171 Tbilisi, Georgia
e-mail: matcharashvili@gtu.ge

T. Chelidze
M. Nodia Institute of Geophysics, 1 Alexidze str., 0171 Tbilisi, Georgia
e-mail: tamaz.chelidze@gmail.com

V. de Rubeis et al. (eds.), *Synchronization and Triggering: from Fracture to Earthquake Processes*, GeoPlanet: Earth and Planetary Sciences 1,
DOI 10.1007/978-3-642-12300-9_1,

of dynamical features. Generally speaking, this diversity manifests itself in a certain kind of hierarchy of dynamical behavior, ranging from strict determinism to total randomness. The most important is the fact that between these extremes there are many intermediate states that reveal different degree of orderliness, such as, e.g., periodicity, quasiperiodicity, deterministic chaos, low and high dimensional dynamics, hyperchaos, etc. [Theiler, 1997; Kantz, 1997].

Until recently, neither a qualitative detection nor a quantitative evaluation of these intermediate states has been possible because of the absence of a corresponding mathematical formalism and appropriate data analysis methods. At present, the time series nonlinear analysis universal technique has been elaborated [Packard et al, 1980; Berge et al, 1984; Eckmann et al, 1987; Abarbanel et al, 1993; Rapp et al, 1993; Kantz, Shreiber 1997], which often (but not always) enables us to achieve correct qualitative and quantitative assessment of complex processes by their dynamical characteristics.

It is necessary to mention that traditional linear methods are mostly not suitable for complex processes of interest. This is why in different fields of science and practice there has been an explosion of papers searching for methods aiming at detection of peculiarities of complex systems evolution in order to achieve reliable identification of processes by their dynamics. As the complex systems are characterized by different transitions between regular, laminar, and chaotic behaviors, the knowledge of these transitions is necessary for understanding the process. In this respect, one of the fundamental problems is how to measure the complexity of both local and global dynamical behaviors from the observed time series.

There are several main approaches to quantify the complexity of processes by analyzing the measured time series [Boffetta, 2001]. Some of them have roots in dynamical systems and fractal theory and include Lyapunov exponents, Kolmogorov-Sinai entropy, and fractal dimensions [Eckmann et al. 1987]. These methods are based on reconstruction and testing of phase space objects equivalent to the unknown dynamics. The other methods stem from the information theory including Shannon entropy [Shannon, 1948], algorithmic complexity [Shiner, 1999; Yao, 2004] etc., and are mostly based on symbolic dynamics.

For different complex systems, various approaches to complexity measurements can be used. The common problem of many methods is the requirement of long, high quality stationary data sets, which is not always easy to fulfill in analyses of real natural or laboratory systems. To overcome these difficulties, new tests have been proposed, such as recurrence plots (RP) and recurrence quantitative analysis (RQA). These methods equip us for gaining new understanding on the complex natural dynamics.

1.2 Overview of nonlinear data analysis methods

Most nonlinear data analysis methods are based on reconstruction and inspection of the state or phase space of the investigated process. When the system of interest is nonrandom, it has a property known as recurrence [Ruelle, 1994]. This means that

after some transients, the system comes back close to the same points in phase space again and again. The character of time evolution of trajectory forms a phase space structure or attractor of the system. The shape of attractor provides essential information on dynamical features of the investigated process. Generally, a point in a phase space is associated with a single state of the system which is fully defined by a set of m dynamical variables. It is clear that to have a complete description of the state of the dynamic system, these m physical quantities should all be measured, at least in principle. Unfortunately, in most of experimental situations, not all (and often only a single) physical quantities of state variable can be measured; all what we have is an one-dimensional time series and from this series we have to learn as much as possible about the system that generated the signal. According to Takens' theorem it is possible to catch the essential dynamical properties of a system by a reconstruction of its phase space by only one variable. Two- and three-dimensional phase portraits encapsulating essential dynamical properties of the analyzed complex process are used as qualitative tests of the process dynamics. They enable to accomplish first qualitative visual inspection of unknown dynamics and uncover general properties of the analyzed process. Qualitative analysis allows us to reveal possible existence of specific attractors, e.g., strange ones which point to the deterministic chaotic behavior.

Further, the phase space can be analyzed using quantitative methods.

For both qualitative and quantitative approaches, the phase space should be reconstructed from measured (or simulated) data sets. Generally, the measurements commonly result in discrete time series $g_i(t)$, where $t = i\Delta t$, and Δt is the sampling rate. As a rule, the sampling rate is constant, forming equidistant time series but this is not always the case. The time series taken at time intervals of different length, the so-called unevenly sampled time series, are also quite common [Schreiber, 1999]. As far as system variables are coupled, a single component contains essential information about the dynamics of the whole system [Rapp et al., 1993; Castro, 1997; Kantz, 1997]. Therefore, the trajectory reconstructed from this scalar time series is expected to have the same properties as the trajectory embedded in the original phase space, formed by all m state variables. Packard et al. (1980) and Takens (1981) independently proposed the idea of using single sequence of measurements to transform process dynamics into the phase space structure to gain information on the unknown underlying dynamics from this structure. According to the embedding theorem, there exists a one-to-one image of attractor in the embedding space, if the embedding dimension is sufficiently high [Hegger, 1999]. The idea was successfully realized after Takens proved that it is possible to reconstruct from a single scalar time series a new attractor which is diffeomorphically equivalent to the attractor in the original state space of the system under study. Essentially two methods of reconstructions are available: delay coordinates and derivative coordinates. Derivative coordinates were originally proposed by Packard et al. (1980) and consist of using the higher order derivatives of the measured time series as the independent coordinates. Since derivatives are more susceptible to noise, this is usually not very practical for real data which are very noisy themselves. Therefore, the method of delay coordinates was recognized as a more practical tool. Delaying data by T helps to exclude distortions of analysed dynamics caused by

temporal closeness of observations. The T value should be large enough to avoid insubstantial functional dependence between data and not so large to make them completely independent statistically. If these conditions are fulfilled, a set of d-dimensional vectors in d-dimensional space can be reconstructed:

$$\bar{X}(i) = [x(i), x(i+T),\ x(i+2T), \ldots., x(n+(d-1)T)]. \tag{1.1}$$

According to Takens' theorem, the reconstructed dynamics is equivalent to the dynamics of the real underlying system [Packard, 1980; Takens, 1981]. Equivalence of two dynamics means that their dynamical invariants (e.g., generalized dimensions, the Lyapunov spectrum, recurrence characteristics, etc., to be shortly described below) are identical. The delay time, T, for the reconstructions can be calculated from the autocorrelation function or mutual information (MI) first minimum. The averaged mutual information evaluates the amount of bits of information shared between two data sets over a range of time delays is defined as [Abarbanel,1993; Kantz, 1997; Cover, 1991; Kraskov, 2004]:

$$I(X,Y) = \sum_{ij}^{N} p(i,j) \log_2 \frac{p(i,j)}{p_x(i) p_y(j)}, \tag{1.2}$$

where $p_x(i)$ and $p_y(j)$ are the probabilities of finding $x(i)$ and $x(i+T)$ measurements in time series, respectively, $p(i,j)$ is a joint probability of finding measurements $x(i)$ and $x(i+T)$ in time series, and T is the time lag. It is important to mention that in contrast to the linear correlation coefficient (which also can be used for delay time calculation), MI is sensitive also to dependences which are not linear, i.e., do not manifest themselves in the covariance. MI is zero if and only if the two random variables are strictly independent. The MI calculation is also important as a tool to provide information on phase space points probability distribution.

In order to define the correct value of embedding dimension $d_e \geq 2d_a + 1$ (where d_e is the dimension of embedding space and d_a is attractor's dimension) one may use the so-called false nearest neighbor method [Kennel, 1992; Hegger, 1999]. The percentage of false nearest neighbors (phase points projected into neighborhoods of points to which they would not belong in higher dimensions) approaches zero as the dimension of the phase space increases.

Since phase space structure attractor or image of dynamics is formed, the two most popular ways for the quantitative evaluation of complexity of analyzed dynamics are: quantification of the average evolution patterns of neighboring trajectories in the state space, and/or quantification of the geometric patterns of the state space object.

Evolution of phase space trajectories could be analyzed by calculation of spectrum of Lyapunov exponents or, as it is often done, by calculation of maximal Lyapunov exponent $\lambda_{\max}$. Generally, Lyapunov exponents quantify the average exponential rate of divergence of neighbouring trajectories in the state space, and thus provide a measure of the system's response to local perturbations [Rosenstein, 1993; Kantz, 1997]. For measured data sets, the maximum Lyapunov exponent $\lambda_{\max}$ for a

dynamical system can be determined from the equation: $d(t) = d_0 e^{\lambda_{\max} t}$, where $d(t)$ is the mean divergence between neighboring trajectories in the state space at time t and d_0 is the initial separation between neighboring points. There are several methods [Wolf, 1985; Sato, 1987; Rosenstein, 1993] for estimating $\lambda_{\max}$ which often suffer from drawbacks that are serious for practical use, namely, the estimates of $\lambda_{\max}$ are unreliable for small data sets and need essential computational resources. Generally, if $\lambda<0$, phase trajectories are drawing together and the considered dynamical system has an attractor in the form of a fixed point. When $\lambda=0$, the system tends to a stable limit cycle. $\lambda>0$ means that phase trajectories are moving away and such a system may be chaotic or random (Rosenstein, 1993).

In order to characterize the unknown dynamics by the geometry of their reconstructed phase structures, an algorithm for calculation of fractal dimensions of phase space point sets should be used. It is known that the fractal dimension of an attractor roughly characterizes the complexity and gives a lower bound for the number of equations or variables needed for modeling the underlying dynamical process. There are several such measures based on quantification of self-similar properties of phase space objects. These measures are: the information dimension (d_i), the Hausdorf dimension d_H, etc. [Abarbanel, 1993; Kantz, 1997]. We shortly describe here only the GPA method of computing correlation dimension or fractal dimension as proposed by Grassberger and Procaccia [1983]. In spite of difficulties in using it for real data sets, GPA remains to be the most popular and often used method for quantifying geometrical features of phase space objects. This is probably due to the simplicity of the algorithm [Bhattacharya, 1999] and the fact that the same intermediate calculations are used to estimate both dimension and entropy. The correlation sum, $C(r, N)$, quantifies the way in which the density of points in the state space scales with the size of the volume containing those points. This approach is based on the idea of correlation sum. Correlation sum $C(r)$ of set of points in the vector space is defined as the fraction of all possible pairs of points which are closer than a given distance r. The basic formula useful for practical application is

$$C(r,N) = \frac{2}{(N-w)(N-w+1)} \sum_{i=1}^{N} \sum_{j=i+w}^{N} \Theta(r - \|x_i - x_j\|), \tag{1.3}$$

where $\Theta(x)$ is the Heaviside step function, $\Theta(x)=0$ if $x \leq 0$ and $\Theta(x)=1$ if $x \geq 0$. $\|x_i - x_j\|$ is the Euclidian norm. Points with $i = j$ are excluded. w is the Theiler's window for fractal systems for time series that are long enough. For small r, $C(r) \propto r^{\nu}$ relationship is correct. Commonly, such a dependence is correct only for the restricted range of r values, the so-called scaling region. Correlation dimension ν or d_2 is defined as

$$\nu = d_2 = \lim_{r \to 0} \frac{\log C(r)}{\log(r)}. \tag{1.4}$$

In practice, the d_2 value is found from the slopes of $\log C(r,N)$ versus $\log r$ curves for different phase space dimensions. In order to achieve appropriate linearity of the relationship between $\log[C(r, N)]$ and $\log r$, one has to determine local slopes, or the so-called ''local scaling exponents''[Kantz, 1997]. The true correlation dimension of an unknown process is the saturation value of d_2, which does not change by increasing phase space dimension. If saturation does not take place, the correlation dimension is infinitely large which is typical for random processes.

For a correct analysis it is necessary to have data sequences that are long enough, at least $N \geq 10^{d/2}$, where N is a length of time series and d is the dimension of attractor [Abarbanel, 1993]. The three dimensions mentioned above are related by $d_2 < d_i < d_H$, with equality when the points in the state space are distributed uniformly over the attractor. In spite of popularity of d_2 calculation method, findings by GPA must be interpreted with great care as it is well known that linear stochastic processes can also mimic low-dimensional dynamics [Theiler et al. 1992; Rapp et al., 1993]. In other words, the saturation of a correlation dimension and the existence of positive Lyapunov exponents cannot always be considered as a proof of deterministic chaos, predictable in sense of patterns, which is closest to quasi-periodic dynamical regime [Rapp et al. 1993; Kantz and Shreiber, 1997]. Since linear correlations lead to many spurious conclusions in nonlinear time series analyses, it is important that the obtained results be verified using the so-called surrogate data approach. This is a method to test the null hypothesis that the analyzed time series are generated by a specific process with the known linear properties [Theiler et al., 1992]. It should be stressed again that the above phase space measures have strict restrictions in the sense of time series length and are mostly relevant for low dimensional or deterministically chaotic systems. When the dynamics of the investigated process is more complex or when dimension of underlying attractor is moderately large, say $d_2 > 5$, all the results of dimensional analysis on finite amount of real data series are not grounded well enough [Schreiber, 1999]. Moreover the real data series are often very noisy, containing measurement noise as well as dynamical noise (noise interacting with dynamics), and then the conventional estimates fail as well. Therefore, when we deal with complex dynamics, a less ambitious and more realistic goal commonly applied is to search for the inherent nonlinearity of the processes, or to rank them by the extent of nonlinearity. The practical importance of this statement becomes clear in the light of known facts that in most cases the dynamical behavior of natural scale-invariant processes is non random, revealing nonlinear structure, while valid evidences of deterministic chaotic type of dynamics are very seldom [Theiler, 1997; Marzocchi et al., 1997; Goltz, 1997].

The above-mentioned method of surrogate data equips us for testing the nonlinear structure of complex dynamics (Theiler, 1992). The surrogate data is inherently a stochastic signal which mimics certain statistical properties, such as temporal autocorrelation or Fourier power spectra of the original signal. The surrogates can be constructed from the original time series on the basis of different null hypotheses. The three types of most often used surrogates address the three main hypotheses: temporally independent noise, linearly filtered noise, and

nonlinear transformation of linear filtered noise. So whenever we try to quantify the degree of nonlinearity, the results of calculation of the above measures should be compared with the similar quantities for surrogate data sets. Phase randomized surrogate sets (obtained by destroying the nonlinear structure through randomization of the phases of a Fourier transform of the original time series and following invert transformation) are often used to test the null hypothesis that the time series are linearly correlated with Gaussian noise [Theiler et al., 1992]. Also a Gaussian scaled random phase (GSRP) surrogate set can be generated to address the null hypothesis that the original time series is a linearly correlated noise that has been transformed by a static, monotone nonlinearity [Rapp et al., 1993, 1994]. The GSRP surrogates are generated in a three-step procedure. At first, a Gaussian set of random numbers is generated, which has the same rank structure as the original time series. After this, the phase randomized surrogates of these Gaussian sets are constructed. Finally, the rank structure of original time series must be reordered according to the rank structure of the phase randomized Gaussian set [Theiler, 1992].

Generally, these two methods of generation of surrogates are based on shuffling of the original data set but, in the case of Gaussian scaled random phase surrogates, the controlled shuffles [Rapp et al., 1994] can give more precise and reliable results than the unstructured shuffles of the random phase surrogates.

Commonly, for testing the null hypothesis, d_2 is used as the discriminating metric. There are several ways to measure the difference between the discriminating metric measure of the original (given by M_{orig}) and the surrogate (given by M_{surr}) time series.

The most commonly used measure of the significance of the difference between the original time series and the surrogate data is given by the criterion: $S = |\langle M_{surr}\rangle - M_{orig}|/\sigma_{surr}$, where σ_{surr} denotes standard deviation of M_{surr}. The details of the procedure, as well as an analytic expression for ΔS, the uncertainty in S, are described in Theiler et al. [1992].

Alternatively, the Monte Carlo probability can be used, defined as:

$$P_M = (\text{number of cases } M \leq M_{orig})/(\text{number of cases})$$

where P_M is an empirical measure of the probability that a value of M_{surr} will be less than M_{orig}. It is particularly appropriate when the number of surrogates is small, or when the distribution of values of M obtained with surrogates is non-Gaussian (Rapp et al. 1994).

For rejecting the null hypothesis, the Barnard and Hope nonparametric test can be used (Rapp et al. 1994). With this criterion, the null hypothesis is rejected at a confidence level $p_c = 1/(N_{surr}+1)$, if $M_{orig} < M_{surr}$ for all the surrogates.

One of the serious problems in real data analyses is the influence of noises. It is preferable to use the so-called nonlinear noise reduction (which in fact is phase space nonlinear filtering) instead of common linear filtering procedures. The latter, as it is well known, may destroy the original nonlinear structure of analyzed complex processes [Hegger and Kantz 1999; Schreiber, 2000]. Nonlinear noise reduction relies on the exploration of reconstructed phase space of the considered

dynamical process instead of frequency information of linear filters [Hegger and Kantz, 1999; Schreiber, 1993; Kantz and Schreiber, 1997].

As it was many times pointed out above, most methods of analysis need rather long and stationary data sets, which is commonly not typical of the measured time series. This was a strong impetus for a further development of new techniques to get an insight into the complex processes, having not very long and rather noisy observable time series. For this purpose, several measures of complexity, mostly based on a symbolic dynamics approach, have been proposed, such as Renyi entropies, the effective measure complexity, the ε and Lempel-Ziv complexity (LZC) measure, etc. [Lempel, 1976; Wackerbauer, 1994; Rapp, 2001]. The LZC is especially suitable for relatively short real data sets because is not so demanding as to the time series length as other methods [Zhang, 1999; Matcharashvili, 2001].

It is necessary to mention the approach based on the study of attractor's organization, or testing of topology of phase space images of unknown dynamics. This technique, oriented on exploration of phase space structure or image of dynamics, is the method of recurrence plots (RP) [Eckmann et al., 1987]. Let us recall here that if the dynamical system has any deterministic structure, an attractor appears in the state space. As it was already mentioned, the attractor is a set of points in phase space, towards which a dynamical path will converge. Again, the recurrence is a fundamental property of nonrandom dynamical systems, the state of which, although exponentially diverges under small disturbances, but after some time the system will come back to a state that is arbitrarily close to a former state. Recurrence plots visualize such a recurrent behavior of dynamical system. Real processes are usually characterized by complex dynamics to be embedded in high-dimensional phase spaces. RP enables to investigate structure in these high-dimensional phase spaces through a two-dimensional representation of its recurrences. It is most important to say that the recurrence plot method is effective for nonstationary and rather short time series [Gilmore, 1993, 1998].

Generally speaking, the recurrence plots are designed to locate hidden recurring patterns and structure in time series and are defined as $N \times N$ symmetric matrix:

$$R_{i,j} = \Theta(\varepsilon_i - \left\|\bar{x}_i - \bar{x}_j\right\|),\ i,j = 1,...,N, \tag{1.5}$$

where $\vec{x}_{i,j}$ are phase space vectors reconstructed using Takens' time delay method. Insofar, as the RP is based on Takens' delay-coordinate embedding, when this procedure is correctly carried out, the dynamical invariants of the true and reconstructed dynamics are identical. Therefore, it is natural to assume that the RP of a correctly reconstructed trajectory bears similarity to RP of the true dynamics. In fact, $\vec{x}_i$ stands for the point in phase space at which the system is situated at time i, ε_i is a predefined cut-off distance, $\Theta(x)$ is the Heaviside function. The cut-off distance defines a sphere centered at $\vec{x}_i$. As far as recurrence of the phase space trajectory to a certain state is a fundamental property of deterministic dynamical system [Argyris, 1994; Ott, 1993; Marwan, 2002], the trajectory in the reconstructed phase space returns at time i into the ε-neighborhood of where it was at

time j (i.e. if $\vec{x}_i$ is closer to $\vec{x}_j$ than the cut-off distance) $R_{i,j} = 1$ and these two vectors are considered to be recurrent. Otherwise $R_{i,j} = 0$. According to Eckman et al. [1987], the $R_{i,j}$ values can be visualized by black and white dots, but often the recurrence plot relates $R_{i,j}$ distances to a color, e.g., the longer the distance, the "cooler" the color. Thus, the recurrence plot is a solid rectangular plot consisting of pixels whose colors correspond to the magnitude of data values in a two-dimensional array and whose coordinates correspond to the locations of the data values in the array.

The black points indicate the recurrences of the investigated dynamical system revealing their hidden regular and clustering properties. By definition, RP is symmetric and has black main diagonal (the line of identity) formed by distances in matrix. In order to understand RP it should be stressed that it visualizes the distance matrix which represents autocorrelation in the series at all possible time (distance) scales. As far as distances are computed for all possible pairs, on the RP plots the elements near the diagonal correspond to short range correlation, whereas the long range correlations are revealed by the points distant from the diagonal. Hence if the analyzed dynamics (time series) is deterministic (ordered, regular), then the recurrence plot shows short line segments parallel to the main upward diagonal. At the same time, if dynamics is purely random, the RP will not present any structure at all. One of the crucial points in RP analysis is the selection of cutoff distance ε or radius. If ε is selected too low no recurrent point will be found. At the same time, it cannot be set too high as then every point will be assumed as recurrent. Exhaustive overview on this subject can be found in Zbilut [1998], Marwan [2003].

The primordial aim of RP testing was the visual inspection of structures located in high dimensional phase spaces where the above-mentioned methods are useless, especially when we deal with real data sets. The view of recurrence plots provides a unique possibility to observe time evolution patterns of phase space trajectories, both at large and short scales. According to Eckmann et al. [1987], by analysing the large scale patterns or typology, recurrence plots can be characterized as homogeneous (dynamics with uniformly distributed characteristics), periodic (dynamics with distinct periodic components), drift (dynamics with slowly varying parameters) and/or disrupted (dynamics characterized by abrupt changes). By small scale inspection, patterns (or texture) of recurrence plots can be characterized as single dots, diagonal lines, vertical lines and horizontal lines. The exact recurrent dynamics causes long diagonal lines separated by a fixed distance. A large amount of single isolated scattered dots and the vanishing amount of lines is typical for heavily fluctuating dynamics under the influence of non correlated noises (by the way, in this case insufficient dimension of embedding space is not excluded). The non regular occurrence of short as well as long diagonal lines is characteristic for low-dimensional chaotic processes, and the non regular occurrence of extended uniform areas corresponds to irregular high-dimensional dynamics. In a more general sense, the line structures in RP exhibit local time relationship between the current phase space trajectory segments. The stationarity of the whole time series requires that the density of line segments be uniform.

As far as RP was developed for single data sets, Zbilut et al. [1998] have expanded it by considering two different time series. The cross-recurrence between two series, x_i and y_i, is defined as $CR_{i,j} = \Theta(\varepsilon_i - \|\bar{x}_i - \bar{x}_j\|)$. Here, the two time series are embedded in the same phase space. The representation is analogous to RP, and it is called a cross-recurrence plot (CRP) [Marwan, 2003].

Qualitative patterns of unknown dynamics presented as fine structure of RP or CRP are often too difficult to be considered in detail. Zbilut and Webber [Zbilut, 1992] have developed a tool which quantifies the structures in RPs, namely, the Recurrence Quantitative Analysis (RQA). They define measures using the recurrence point density, the length of diagonal, and vertical structures in the recurrence plot, the recurrence rate, the entropy of recurrent points' distribution, etc. Presently at least 8 different statistical RQA values are known [Zbilut, 1992; Ivanski, 1998; Marwan, 2003], practical meaning of which is not always quite clear. Computation of these measures in small windows moving along the main diagonal of the RP reveal the time dependent behavior of these variables making it possible to identify the unknown dynamical patterns in time series [Zbilut, 1992; Marwan, 2002].

Here we will briefly touch only main RQA statistical values. The first of these statistics, termed % recurrence (%REC), is simply the percentage of points on the RP that are darkened or in other words those pairs of points whose spacing is below the predefined cut-off distance ε_i. It quantifies the number of time instants characterized by a recurrence in the signals' interaction: the more periodic the signal dynamics, the higherthe (%REC) value. Stochastic behavior causes very short diagonals, whereas deterministic behavior causes longer diagonals.

The second RQA statistic is called % determinism (%DET); it measures the percentage of recurrent points in a RP that are contained in lines parallel to the main diagonal. The main diagonal itself is excluded from these calculations because points there are trivially recurrent. Intuitively, %DET measures how ''organized'' the RP is. This variable discriminates between the isolated recurrent points and those forming diagonals. Since a diagonal represents points close to each other, successively forward in time, DET also contains the information about the duration of a stable interaction: the longer the interactions, the higher the DET value. Stochastic and heavily fluctuating data cause none or only short diagonals, whereas deterministic systems cause longer diagonals.

The third often used RQA statistics, called entropy (ENT), is closely related to %DET. ENT is Shannon information entropy of line distribution measured in bits and is calculated by binning the diagonal lines according to their lengths and using the following formula:

$$\mathrm{ENT} = -\sum_{k=1}^{N} P_k \log_2 P_k$$

where N is the number of bins and P_k is the percentage of all lines that fall into bin k. In other words, P_k is defined as the ratio between the number of k-point long diagonals, and the total number of diagonals. ENT is measured in bits of information, because of the base-2 logarithm. Thus, whereas DET accounts for the number of the diagonals, ENT quantifies the distribution of the diagonal line lengths.

The more different the lengths of the diagonals, the more complex the deterministic structure of the RP. A more complex dynamics will require a larger number of bits (ENT) to be represented.

The fourth RQA statistics, termed TREND, measures how quickly a RP goes away from the main diagonal. As the name suggests, TREND is intended to detect nonstationarity in the data. The fifth RQA statistics is called length of the maximal deterministic line (MAXLINE) and is equal to the reciprocal of the longest line length found in the computation of DET, or $1/line_{\max}$. Eckmann, Kamphorst, and Ruelle claim that line lengths on RPs are directly related to the inverse of the largest positive Lyapunov exponent [Eckmann et al., 1987]. Relatively small $line_{\max}$ values are therefore indicative of chaotic behavior. In a purely periodic signal, there is an opposite extreme, lines tend to be very long, so MAXLINE is very small.

The RQA technique gives a local view of the studied time series, based on the single distance pairs in phase space and is suited for the detection of changes of analyzed dynamics. This method is the most comfortable for qualitative discrimination between signals and random noise.

1.3 Investigation of dynamics of complex natural process: Caucasus seismicity

The significant variability exhibited both in time and in space makes the problem of identification and quantification of geophysical phenomena extremely complicated. Therefore, the best way to understand dynamical features of complex geophysical processes is to analyse the measured data sets using modern nonlinear methods.

Earthquakes are expression of the continuing evolution of the planet Earth and of the deformation of its crust. Dynamics of seismic processes is viewed as extremely complicated, so that the level of "turbulence" of the lithosphere exceeds that of the atmosphere [Kagan, 1992, 1994, 1997].

During more than one hundred years of instrumental observations, several important characteristics of spatial, temporal and energetic distributions of earthquakes have been revealed [Scholz, 1990; Keilis-Borok, 1990; Turcotte, 1992; Goltz, 1997; Matcharashvili, 2000; Rundle, 2000]. Nevertheless, the question of dynamics of seismic processes remains the subject of intense discussions because it is directly tied with the problem of earthquake prediction. Opponents of earthquake prediction [Kagan, 1992, 1994, 1997; Kanamori, 2001; Geller, 1999; Ben-Zion, 2008 etc.] regard seismic processes as completely random while proponents assume them as complex and high-dimensional though not random [Main, 1997; Wyss, 1997; Chelidze, 1997; Knopoff, 1999]. Indeed, completely random processes are unpredictable on any spatial and temporal scales. On the other hand, in processes with nonrandom dynamical structure there always exist specific spatial and temporal scales for which the system is close to deterministic, i.e., it is predictable at least for a not very far future. From this point of view, if seismic process has a nonrandom structure it could not be regarded as unpredictable. Of course, it is

clear that predictability in this sense does not necessarily mean "real" forecast of every hazardous event in practically meaningful time scales. At present, evidence of nonrandom structure of seismicity has mainly scientific importance because it gives ground to efforts aimed at finding predictive markers. This is also important for modern ideas on possible control of practically unpredictable seismic processes. To bring some light into this problem, we consider dynamic structure of seismic process in Caucasus.

As mentioned above, one of the most popular approaches to the problem of identification of patterns of complex dynamics, including seismicity, is based on the evaluation of nonlinear structures (or, just the same, of nonlinear structures of appropriate time series) [Theiler et al., 1992; Rapp et al., 1993]. In this way, it is possible to achieve reliable detection of dynamical regime(s) of seismic process by calculating their measurable characteristics. These characteristics can be calculated for a general seismic process as well as prior to and after strong earthquakes. This is important in search of possible earthquake predictive dynamical markers. It is known that from both, qualitative and quantitative points of view, seismological data bases are as a rule not sufficient for proper nonlinear evaluation of lithospheric dynamics, even for relatively low-dimensional processes. Therefore, similar to other fields, evaluation of nonlinear structure of geophysical data seems to be a more appropriate approach.

In order to answer the above question on the dynamical characteristics and nonlinear structure of earthquake generation it is necessary to investigate dynamical properties of seismic processes in all three domains: energetic, spatial and temporal. For this purpose, "time series" of inter-event time intervals (waiting times), magnitude sequences and inter-event distances, have been analyzed for earthquakes in Caucasian region. Analyzed were also similar time series of smaller regions of Greater Caucasus and Javakheti in1962–1993. All these time series were taken from the earthquake catalogue for the Caucasus and the adjacent territories of Northern Turkey and Northern Iran for the 1962–1993 time period (Seismological Data Base of Institute of Geophysics, Tbilisi, Georgia).

It was shown that despite the fact that the size and temporal distributions of earthquakes obey a power law, they are dynamically quite different. The magnitude distribution of earthquakes in the Caucasian region is undoubtedly high-dimensional, d_2 as a rule is larger than 8 ($d_2 > 5$ is assumed as a high dimensionality threshold) [Sprott, 1997]. According to our results as well as reports of other authors [Sadovsky, Pisarenko, 1991; Korvin, 1992] the fractal dimension for the distribution of inter-earthquake distances is low ($d_2 < 2$). Most interesting is that the waiting times distribution reveals an obviously low dimensional nonlinear structure (d_2 of the order of 1.6–2.5 and λ_{max} of the order of 0.2–0.7), although it can not be recognized as a deterministic chaos [Matcharashvili, 2000] (see Fig. 1.1). The low dimensionality of earthquakes temporal distribution is in complete agreement with earlier results for other parts of the globe [Goltz, 1998].

The next main goal of investigation was a qualitative evaluation of earthquakes′ time and size distribution peculiarities, taking place before and after strongest regional events as well as quantitative discrimination of dynamical characteristics preceding and following largest regional earthquakes.

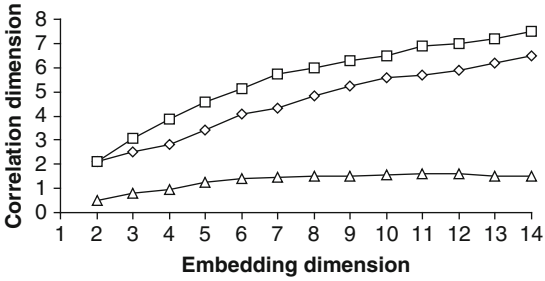

Fig. 1.1 Typical plot of correlation dimension d_2 versus embedding dimension p for the Caucasus, the Greater Caucasus, and the Javakheti region, magnitude (middle curve) and waiting times (lower curve) sequences. The upper curve represents the random numbers set

So as a next step on the way to a better understanding of the underlying dynamics of earthquake generation, we have undertaken comparison of the properties of waiting time distribution before and after large events. For this purpose we have considered waiting time sequences of a seismic catalogue, separately before and after the largest events, using the above-mentioned tests such as correlation dimension, Lyapunov exponent calculation as a measure of non-linearity.

We investigated dynamical characteristics of seismic processes before and after four earthquakes of the Caucasian region (Daghestan, Paravani, Spitak and Racha) that were the strongest in the considered period.

According to the results of our analysis, the general properties of dynamics of earthquakes temporal distribution before and after the largest regional events do not indicate a qualitative difference from the integral dynamics obtained by consideration of time series from the whole original catalogues [Matcharashvili, 2002, 2007]. Indeed, correlation dimensions of all the considered waiting time sequences from the original catalogue (containing all independent events and aftershocks above the threshold magnitude), both preceding and following the largest events in the Caucasus, converge to a limit value. At the same time it is important that these values are not coinciding. Consequently, as long as all the investigated time series have correlation dimension lower than the low dimensional threshold ($d_2 < 5$) [see also Goltz, 1998], it can be deduced that the temporal distribution of earthquakes is characterized by a low-dimensional dynamics before, as well as after the largest regional events. At the same time, in the energetic domain earthquakes' magnitude distribution remains high-dimensional before and after strong events. As it was stressed above, the results of dimensional calculations, especially when a low-dimensional process is detected, should be verified using special methods.

While testing low-dimensional interevent time sequences, we have typical problems, always encountered in testing real, usually short and noisy time series. As it was already mentioned, in order to overcome discriminating problems, as in the case of high-dimensional processes, one has to test time series for the evidence of nonlinearity [Theiler and Prichard, 1997]. One additional reason why this approach becomes popular, is that from the practical point of view the goal of detecting nonlinearity in low dimensional data is easier than a confident identification of chaotic dynamics [Theiler, 1992].

It was found that in all cases the time interval sequences obtained from the original catalogue above the threshold magnitudes before and after the largest events reveal evidence of a nonlinear structure. In other words, the null hypothesis that these sequences are generated by linearly correlated noise or by static monotone nonlinearity should be rejected. The significance of differences of **S**-measure of natural sequences before and after the earthquakes considered from the appropriate phase randomized ($\mathbf{S}_{PR}$) and Gaussian scaled random phases ($\mathbf{S}_{GSRP}$) surrogates are significant at $p < 0.005$ confidence level; thus the significance of differences for waiting time sequences before and after Dagestan (M = 6.6) earthquake are $\mathbf{S}_{PR} = 55.6 \pm 0.27$, $\mathbf{S}_{GSRP} = 15.9 \pm 0.20$ and $\mathbf{S}_{PR} = 50.5 \pm 0.15$, $\mathbf{S}_{GSRP} = 17.1 \pm 0.13$; for Paravani (M = 5.6) earthquake $\mathbf{S}_{RP} = 51.1 \pm 0.21$, $\mathbf{S}_{GSRP} = 16.2 \pm 0.13$ and $\mathbf{S}_{PR} = 64.2 \pm 0.27$, $\mathbf{S}_{GSRP} = 11.5 \pm 0.17$; for Spitak (M = 6.9) earthquake $\mathbf{S}_{PR} = 49.2 \pm 0.12$, $\mathbf{S}_{GSRP} = 11.4 \pm 0.12$ and $\mathbf{S}_{PR} = 52.2 \pm 0.27$, $\mathbf{S}_{GSRP} = 15.2 \pm 0.19$; for Racha (M = 6.9) earthquake $\mathbf{S}_{PR} = 57.6 \pm 0.23$, $\mathbf{S}_{GSRP} = 16.3 \pm 0.23$ and $\mathbf{S}_{PR} = 51.5 \pm 0.17$, $\mathbf{S}_{GSRP} = 18.4 \pm 0.11$.

Besides, for a nonlinear structure testing, the RQA method is suitable for short seismic data sets. As shown in Figs. 1.2 and 1.3, the extent of the order in magnitude distribution of Caucasian earthquakes before and after M6.9 Racha earthquake has been noticeably changed. Strictly speaking, the energetic distribution becomes more regular while the temporal distribution becomes essentially irregular. It is

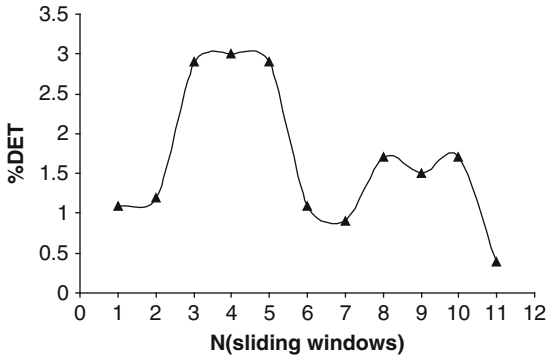

Fig. 1.2 RQA measure, %DET, for Racha (M6.9) earthquake magnitude sequences. Consecutive non overlapping 500 data width sliding windows (M6.9 event occurred in 5-th window, and M6.2 in 8-th window)

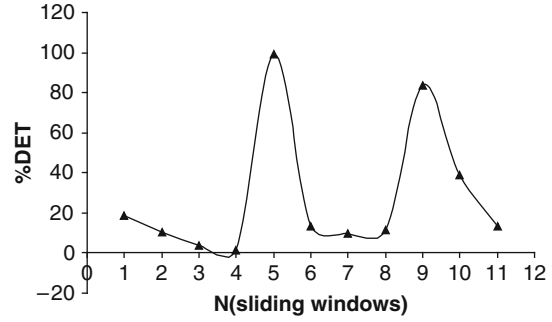

Fig. 1.3 RQA measure, %DET, for Racha (M6.9) earthquake inter-event time intervals sequences. Consecutive non-overlapping 500 data width sliding windows (M6.9 event occurred in 5-th window, and M6.2 in 8-th window)

worth to mention that a decrease of the order in earthquake temporal distribution is distinctive for both strong Racha earthquakes, M6.9 and its aftershock M6.2. At the same time, an increase of the order in energetic distribution is not so clear.

To understand the above-mentioned differences in the correlation dimension values before and after largest earthquakes, we used a sliding windows technique. We considered a sequence of 6695 events of Paravani earthquakes inter-event time intervals. Here No = 5300 is the ordinal number of the time interval which directly precedes the largest earthquake. We have calculated d_2 for 1000 event sliding windows with a step of 50 events starting with event No = 3200 up to event No = 5800. Hence, the first window consists of time interval sequences between earthquakes in the range of ordinal numbers 3200–4200. As shown in Fig. 1.4, values of d_2 decrease for the windows following the largest event. The decrease begins when a sliding window contains about 20 inter-event time intervals after the largest event, and becomes significant when 40–50 such events are included in the sequence. Note that the window 4310–5310, like the window 4300–5300, reveals the background value of a correlation dimension for waiting time sequences before the largest earthquake. It seems doubtful to expect that such an essential change in the dynamical properties of the considered sequence could have been caused by the addition of so few new data, unless there is a hidden regularity in the sufficiently long waiting time sequence containing data preceding the largest event.

Next we used RQA approach to further quantify dynamical changes in earthquakes energetic and temporal distributions in Javakheti region. As shown in Figs. 1.5 and 1.6, dynamical changes in earthquakes energetic and spatial distributions detected before and after Paravani earthquake are very similar to those found before and after the Racha strong earthquake.

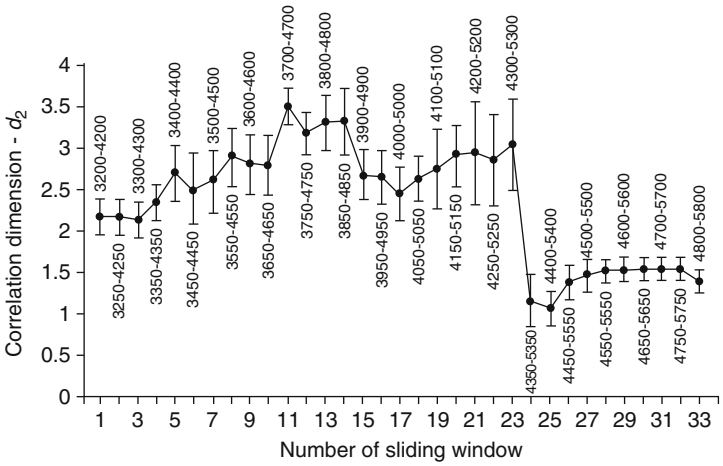

Fig. 1.4 Variation of correlation dimension d_2 of waiting time sequences calculated for sliding windows containing 1000 consecutive time intervals at 50 events step (Paravani earthquake epicentral area)

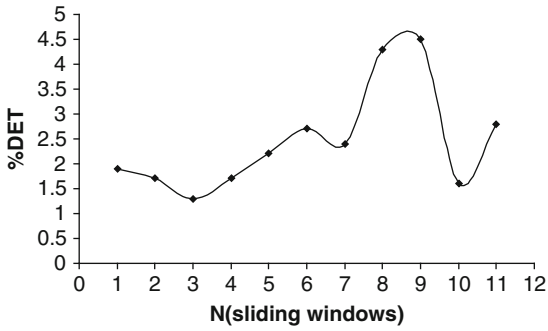

Fig. 1.5 RQA measure, %DET, for Paravani (M5.6) earthquake magnitude sequences. Consecutive non overlapping 600 data width sliding windows (M5.3 event occurred in 6-th window, M5.6 in 9-th window, and M5.1 in 11-th window)

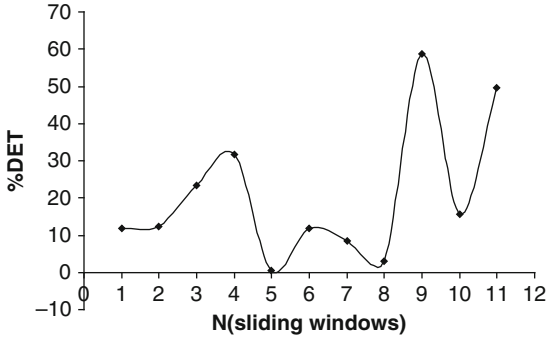

Fig. 1.6 RQA measure, %DET, for Paravani (M5.6) interevent time intervals sequences. Consecutive non overlapping 600 data width sliding windows (M5.3 event occurred in 6-th window, M5.6 in 9-th window, and M5.1 in 11-th window)

Indeed, magnitude distribution before the M5.6 earthquake becomes more regular while temporal distribution becomes noticeably irregular. Also, similar to the Racha earthquake, changes were observed before the M5.1 earthquake which may be regarded as an aftershock; namely a decrease in the order of temporal distribution, while an increase of the order in magnitude distribution is not clear. It is interesting to mention that the same situation was observed for M5.3 earthquake preceding the main M5.6 event.

These results indicate that measuring of dynamical characteristics of seismic time series may provide markers having in future a precursory value which may help in developing modern earthquake prediction approaches [Matcharashvili et al. 2002].

Thus it is clear that seismicity in two domains (temporal and spatial) out of three (energetic, temporal and spatial) reveals low-dimensional nonlinear structure. This and similar results lead to understanding that in spite of extreme complexity, the processes related to the earthquake generation are characterized by some internal dynamic structure and thus are not completely random [Smirnov, 1995; Goltz, 1998; Rundle et al. 2000; Matcharashvili et al. 2002]. Despite the proofs that seismic activity is a non-random process, the physics of internal or external factors involved is still poorly understood, but it can be asserted that the general problem of

earthquake prediction and/or earthquake triggering, one of the most challenging targets of nowadays science, should not be further considered as an "alchemy of present time" [Geller, 1999]. In other words, the quest for earthquake predictive markers or triggering factors should be recognized as obviously difficult, though scientifically well grounded task related to the search for determinism in the complex seismic process.

References

Abarbanel, H. D. I., Brown, R., Sidorowich Tsimring, L. S., Rev. Mod. Phys., 65, 4, 1331–1392, 1993.

Antani, J.A., Wayne, H.H., Kuzman, W.J., Am. J. Cardiol. 43, 2, 239–247, 1979.

Arecchi, F.T., Fariny, Lexicon of Complexity, A., ABS. Sest. F. Firenze, 1996.

Argyris, J. H., Faust, G., Haase, M., An Exploration of Chaos, North-Holland, Amsterdam, 1994.

Bak, P., Tang, C., Wiesenfeld, K. Phys.Rev. A., 38, 364–374. 1988.

Beeler, N.M., Lockner, D.A., J. Geophys. Res., 108: ESE 8,1–17. 2003.

Bennett, C. H., in *Complexity, Entropy and the Physics of Information*, edited by W. H. Zurek, Addison-Wesley, Reading, MA, 1990.

Ben-Zion, Y. Collective Behavior of Earthquakes and Faults. Rev. of Geophysics, 46, doi: 10.1029/2008RG000260

Berge, P., Pomeau, Y., Vidal, C., Order within chaos. J. Wiley, NY, 1984

Bhattacharya, J., In Search of Regularity in Irregular and Complex Signals, PhD Thesis, 1999.

Boffetta, G., Cencini, M., Falcioni, M., Vulpiani, A., Phys. Rep. 356, 367, 2001.

Bowman D., Ouillon G., Sammis C., Sornette A., Sornette, D., J. Geophys. Res. 103: 24359–24372. 1998.

Casdagli, M.C. Physica D 108, 12–44, 1997.

Castro, R., Sauer, T., Phys. Rev. E 55, No 1, 287–290, 1997.

Chelidze, T., Matcharashvili, T., Computers and Geosciences, 2003, 29. 5. 587–593.

Chelidze, T., Matcharashvili, T., Gogiashvili, J., Lursmanashvili, O., Devidze, M., Nonlinear Processes in Geophysics, 2005, 12, 1–8.

Cover T. M., J. A. Thomas, *Elements of Information Theory* (Wiley, New York, 1991).

Eckman, J.P., Kamphorst, S.O., Ruelle, D., Recurrence Plots of Dynamical Systems, *Europhys. Lett.*, **4**, 973–977, 1987.

Elbert, T., Ray, W.J., Kowalik, Z.J., Skinner, J.E., Graf, E. K., Birnbauer, N., Physiol Rev. v 74. 1-49, 1994.

Garfinkel, A., Chen, P., Walter, D.O., Karaguezian, H., Kogan, B., Evans, S.J., Karpoukhin, M., Hwang, C., Uchida, T., Gotoh, M., Weiss, J.N., J. Clin. Invest. 99, 2, 305–314, 1997.

Gavrilenko, P., G, Melikadze., Chelidze, T., Gibert, D., Kumsiashvili, G., Geophys. J. Int., 2000,143, 83–98.

Geller, R.J., Earthquake prediction: is this debate necessary? Nature, Macmillan Publishers Ltd 1999 Registered No. 785998 (http://helix.nature.com/debates).

Gilmore, R., J. Econ. Behav. Organization, 22, 1993, 209–237.

Gilmore, R., Rev. Mod. Phys. 70, 1455–1529, 1998.

Goltz C, Fractal and chaotic properties of earthquakes, Springer, Berlin, 1998.

Govindan, R.B., Narayanan, K., Gopinathan, M.S., Chaos, 8, 2, 495–502, 1998.

Grassberger, P., Procaccia, I., Rev. A. 28, 4, 2591–2593, 1983.

Hegger, R., Kantz, H., Schreiber, T. Chaos **9**, 413–440, 1999.

Hodgson, Geoffrey M.. Economics and Evolution: Bringing Life Back into Economics. Ann Arbor: University of Michigan Press. 1993

Ivanski, J., E. Bradley, Chaos **8**, 861 1998
Johansen, A., Sornette, D., Phys. Rev. Lett. 82: 5152–5155. 1999.
Jones, N., New Scientist. June 30, 34–37. 2001.
Kagan, Y.Y., Physica D77, 160–192, 1994.
Kagan, Y.Y., Geophys. J. Int., 131, 505–525, 1997.
Kanamori, H., Brodsky, E.E., Physics Today, 2001, 6, 34–40.
Kantz, H., Schreiber, T., Nonlinear time series analysis, Cambridge, University Press, 1997.
Keilis-Borok, V.I., Physica D, 77, 193–199, 1994.
Kennel, MB, Brown R and Abarbanel, HDI, Phys. Rev. A 45, 3403–3411, 1992
King, C. Y., Azuma, S., Igarashi, G., Ohno, M., Saito, H., Wakita, H., J. Geoph. Res. 104, B6, 13073–13082, 1999
Knopof, L., Earthquake prediction is difficult but not impossible, Nature, Macmillan Publishers Ltd 1999 Registered No. 785998
Korvin, G., Fractal models in the earth sciences, Elsevier, NY, 1992.
Kraskov, A., Stögbauer, H., Grassberger, P., Phys. Rev. E, 69, 066138, 2004.
Kumpel, H., Evidence for self-similarity in the harmonic development of earth tides, in: Kruhl, J.H. (Ed), Fractals and dynamic systems in geoscience, Springer, Berlin,, 213–220. 1994.
Lefebvre, J.H., Goodings, D.A., Kamath., Fallen, E.L., Chaos, 3. 2. 267–276. 1993.
Main, I., Nature, 1997, 385, 19–20.
McCauley, Joseph L. 2004. *Dynamics of Markets:* Econophysics and Finance. Cambridge, UK: Cambridge University Press.
Mason, D. T., Spenn, J.F., Zelis, R., Am. J. Cardiol. 26. 3. 248–257. 1970.
Marzochi, W., Physica D, 90, 31–39, 1996.
Marwan, M., Wessel, N., Meyerfeldt, U., Schirdewan, A., Kurths, J., Phys. Rev. E., 66, 026702, 2002.
Marwan, M., Encounters with neighborhood, PhD Thesis, 2003.
Matcharashvili, T., Chelidze, T., Javakhishvili, Z., Nonlinear Processes in Geophysics, 7, 9–19. 2000.
Matcharashvili, T., Janiashvili, M., Sulis, W., Trofimova, I., (Eds), Nonlinear dynamics in life and social sciences. IOS Press, Amsterdam, 2001, 204–214.
Matcharashvili, T., Chelidze, T., Javakhishvili Z., Ghlonti, E. Computers & Geosciences 2002, 28. 5. 693–700.
Ott, E., Chaos in Dynamical Systems, Cambridge University,Press, Cambridge, 1993.
Packard, N.H., Crutchfield, J.P., Farmer, J.D., Shaw, R.S., Phys. Rev. Lett. 45, 712–716, 1980.
Peinke, J., Matcharashvili, T., Chelidze, T., Gogiashvili, J., Nawroth, A., Lursmanashvili, O., Javakhishvili, Z.,Influence of Periodic Variations in Water Level on Regional Seismic Activity Around a Large Reservoir: Field and Laboratory Model Phys. Earth. Planet. Int. 2006, (1–2), 130–142
Pikkujamsa, S., Makikallio, T., Sourander, L., Raiha, I., Puukka, P., Skytta, J., Peng, C. K., Goldberger, A., Huikuri, H., Circulation, 100, 4, 393–399, 1999.
Rapp, P.E., Albano, A.M., Schmah, T.I, Farwell, L. A., Phys. Rev. E., 47, 4, 2289–2297, 1993.
Rapp, P.E., Albano, A.M., Zimmerman, I. D., Jumenez-Montero, M.A., Phys. Lett. A., 192, 1, 27-33, 1994.
Rapp, P. E., Cellucci, C. J., Korslund, K. E., Watanabe, T. A., Jimenez-Montano, M. A., Phys. Rev. E **64**, 016209, 2001.
Ruelle, D., Physics Today, 47, 7, 24–32, 1994
Rombouts S.A., Keunen, R.W., Stam, C.J., 1995. Phys.Lett. A. 202.5,6.352–358.
Rosenstein, M. T., Collins, J. J., DeLuca, C. J., Physica D, **65**, 117–134,1993.
Rundle, J., Turcotte, D., Klein, W., (Editors), 2000. GeoComplexity and the physics of earthquakes, American Geophysical Union, Washington.
Sato, S., Sano, M., Sawada, Y., Prog. Theor. Phys. 77, 1–5, 1987.
Schreiber, T., Phys. Rep. 308,1–64, 1999
Schreiber, T., Schmitz, A., Phys. Rev. E 59, 044, 1999.

Schreiber, T., Phys. Rev. E, 1993, 47, 4, 2401–2404.
Shannon, C. E., Bell Syst. Tech. J. **27**, 379 (1948); **27**, 623, 1948.
Shannon, C. E., *The Mathematical Theory of Communication*, University of Illinois, Urbana, IL, 1964.
Shiner, J. S., Davison, M., Landsberg, P. T., Phys. Rev. E, 59, 2, 1459–1464, 1999.
Scholz C.H., Nature, 1990, 348, 197–198.
Sibson, R., 1994. Crustal stress, faulting and fluid flow, in Parnell J. (Ed), Geofluids: Origin, Migration and Evolution of Fluids in sedimentary Basins. The Geological Society, London, 69-84.
Simpson, D.W., Leith, W. S., Scholz, C., 1988. Bull. Seism. Soc. Am. 78: 2025–2040.
Smirnov, V.B., J. of Earthq. Prediction Res., 1995, 4, 31–45.
Sivakumar B, Berndtsson R, Olsson J, Jinno K. Hydrol. Sci. J. 47, 1, 149–58, 2002
Sprott, J. C., Rowlands, G., Chaos data analyzer; the professional version. AIP, NY, 1995.
Takens, F., ''Detecting strange attractors in fluid turbulence,'' in *Dynamical Systems and Turbulence*, edited by D. Rand and L.-S. Young, Springer, Berlin, 1981, pp. 366–381
Talwani, P., Pure and appl. geophys, 150: 473–492. 1997.
Tarasov, N.T. Transactions (Doklady) of the Russian Academy of Sciences, 353A (3), 445–448, 1997.
Theiler, J., Eubank, S., Longtin, A., Galdrikian, B., Farmer, J.D., Physica, D58,77–94, 1992.
Theiler, J., Prichard, D., Using "Surrogate-surrogate data" to calibrate the actual rate of false positives in tests for nonlinearity in time seies. in "Nonlinear dynamics and Time Series" eds. Cutler, D., Kaplan, D.T., 11, 99–113, Fields Institute Communications, 1997.
Turcotte, D., Fractals and chaos in geology and geophysics. University Press, Cambridge, 1992.
Vidale, J. E., D. C. Agnew, M. J. S. Johnston, and D. H. Oppenheimer, J. Geophys. Res., 103, 24,567–24,572. 1998.
Volykhin, A.M., Bragin, V.D., Zubovich, A.P., Geodynamic Processes in Geophysical Fields, Moscow: Nauka, 1993.
Wackerbauer, R., Witt, A., Atmanspacher, H., Kurths, J., Scheingraber, H., Chaos, Solitons Fractals **4**, 133,1994.
Weiss, J.N., Garfinkel, A., Karaguezian, H., Zhilin, Q., Chen, P., Circulation, 99(21), 2819–2826, 1999.
Wolf, A., Swift, J., Swinney, H., Vastano, J., Physica D, 16, 285–317, 1985.
Wyss, M., Science, 278, 487–488. 1997
Yang, P., Brasseur, G. P., Gille, J. C., Madronich, S., Physica D76, 3310343, 1994.
Yao, W., C, Essex., Yu, P., Davison, M., Phys. Rev. E. 69, 110–123, 2004
Zbilut, J.P., Weber, C, L., Phys. Lett. A 171, 199–203, 1992
Zbilut, J.P., A. Giuliani, C.L. Webber Jr., Phys. Lett. A 246 (1998) 122–128.
Zhang, X., Thakor, N.V., IEEE Trans. on Biomed. Eng. 46, 5. 548–555. 1999
Zokhowski, M., Winkowska-Nowak, K., Nowak, A., Phys. Rev. E. 56, 3, 3725–3727, 1997.

Chapter 2
Models of Stick-Slip Motion: Impact of Periodic Forcing

T. Chelidze and N. Varamashvili

Abstract The modern concept of seismic processes relays mainly on the model of frictional instability, which develops on the preexisting tectonic fault, in contrast to the earlier assumptions on the brittle fracture of the crust material attaining the critical stress.

The Ditrich-Ruina equation for shear stress describes almost all main features of slip, obtained in numerous experiments: it shows that the frictional force is not a constant, but is time-dependent and undergoes complex evolution during the slip event. The equation is nonlinear, and consequently the slip process should manifest such properties as high sensitivity to weak external forcing, hysteresis effect, etc. It is quite natural that the instabilities of friction excite vibrations, including acoustic emission (AE). The AE is expected to occur during slips and be absent during stick phase. We presume that acoustic measurements may reveal the fine details of friction mechanism, which are beyond the reach of direct displacement-measuring techniques.

The additional forcing, which can be much smaller than the main driving force, may provoke triggering and synchronization during stick-slip process, which means that these phenomena are invoked by nonlinear interaction of objects. An attempt to compile and analyze the rate- and state slip equation taking into account the periodic forcing is made.

2.1 Introduction

It is well known from the surface physics that the friction (adhesion) force *Ff* is a result of intermolecular and intersurface forces of mainly electromagnetic origin: (i) purely electrostatic (Coulomb) forces, (ii) polarization due to the induced dipole moments, and (iii) quantum-mechanical forces. Friction results in transmission and

T. Chelidze (✉) and N. Varamashvili
M. Nodia Institute of Geophysics, 1 Alexidze str., 0171 Tbilisi, Georgia
e-mail: tamaz.chelidze@gmail.com

V. de Rubeis et al. (eds.), *Synchronization and Triggering: from Fracture to Earthquake Processes*, GeoPlanet: Earth and Planetary Sciences 1,
DOI 10.1007/978-3-642-12300-9_2,

Table 2.1. A capsule story of friction models:

Time Arrow ↓	Amonton, 1699	$\tau = \sigma_n \mu$
	Coulomb, 1773	$\tau = c + \sigma_n \mu$
	Hubbert and Rubbey, 1959	$\tau = c + \mu(\sigma_n - P_p) = c + \sigma \mu_{eff}$
	Brace and Byerlee, 1966	$\tau = \sigma_0(\mu_0 + a\, ln(V/V_o) + bln(V\Theta/D_0))$
	Burridge-Knopoff, 1967	$d\Theta/dt = 1 - (V\Theta/D_0)$
	Dietrich, 1972,	
	Ruina, 1983	

dissipation of energy. Kinetic energy of motion is converted into thermal energy mostly by acoustic processes. Instability in sliding occurs when the friction pumps to the system more energy than can be dissipated by the stationary process.

The modern concept of seismic process relays mainly on the model of frictional instability, which develops on the preexisting tectonic fault, in contrast to the earlier assumptions on the brittle fracture of the crust material at attaining the critical stress. The first simple friction models suggested by Amonton and Coulomb were refined by Hubert and Rubbey (1979), Brace and Byerlee (1966), Burridge and Knopoff (1967), Dieterich (1979) and Ruina (1983): the capsule story of friction models, showing main stages of development in this area, is presented in Table 2.1.

Here τ and σ_n are shear and normal stresses, respectively, μ is the friction coefficient, c is the adhesion term, P_p is the pore pressure, V and V_0 are current and initial velocities of drag, Θ is the state variable, D_0 is the critical slip distance, and a and b are constants.

The last expression for shear stress describes almost all main features of slip, obtained in numerous experiments: it shows that the frictional force is not a constant, but is time-dependent and undergoes complex evolution during slip event. The equation is nonlinear, and consequently the slip process should manifest such properties as high sensitivity to weak external forcing, hysteresis effect, etc.

2.2 Main details of experimental stick-slip results

Depending on conditions (spring stiffness k, velocity of drag V, normal stress σ_n, slip surface state θ), three main types of friction are observed by displacement recording: stick-slip, inertial regime, and stable regime. Figure 2.1 shows spring deflection δx, top plate position x and its instantaneous velocity V during stick-slip motion.

The stick-slip regime is observed at relatively low velocities V and low stiffness. At higher V, the transition to inertial periodic oscillations occurs; at still higher V we have the stable sliding with fluctuations.

The single slip events were investigated in detail by Nasuno et al (1997): after application of tangential force, the velocity of slip drastically increases and then decreases (Fig. 2.2).

The instantaneous frictional force $\mu(t) = F_f / Mg$ during the slip event experiences hysteresis (Fig. 2.3): during the stick stage, μ increases until the static

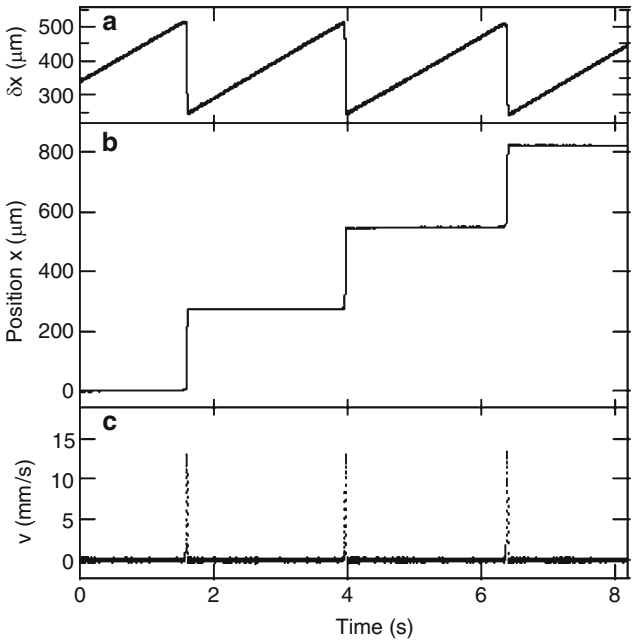

Fig. 2.1 Spring deflection δx top plate position x and its instantaneous velocity V during stick-slip motion (Nasuno et al. 1997)

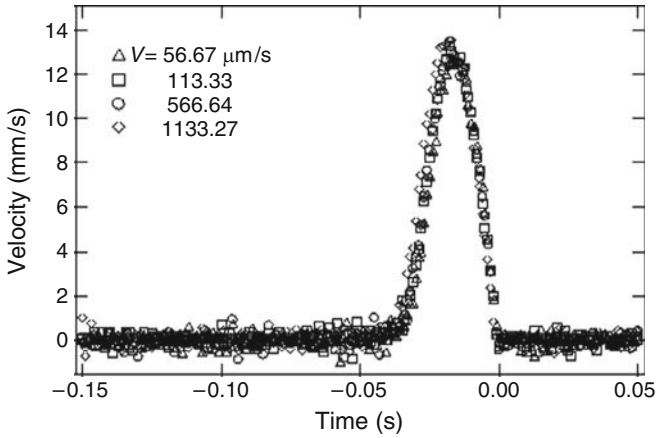

Fig. 2.2 The slip velocity evolution during single slip event for various driving velocities V = 56.67; 113.33; 566.64 and 1133.27 mm/s (Nasuno et al. 1997)

threshold $\mu_s = F_s/Mg$ is attained, and the slip begins. During slip, μ decreases to its kinetic value; after this, at the deceleration stage it drops to the initial value μ_0 (Nasuno et al. 1998).

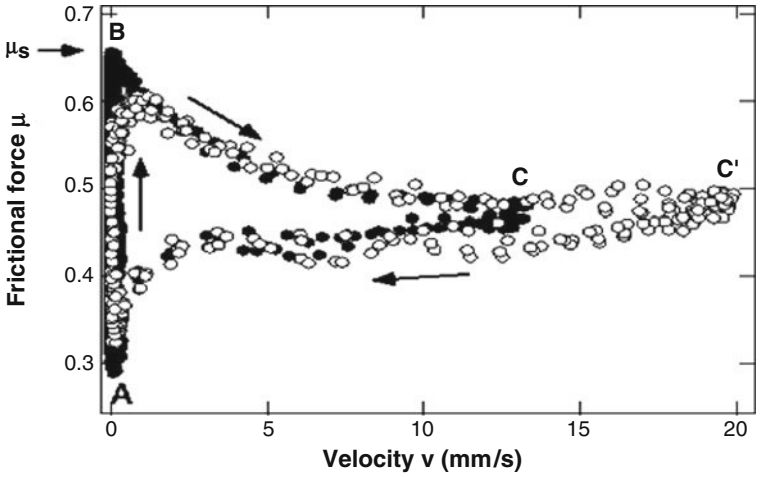

Fig. 2.3 Frictional force μ versus slip velocity during a slip event (Nasuno et al. 1998)

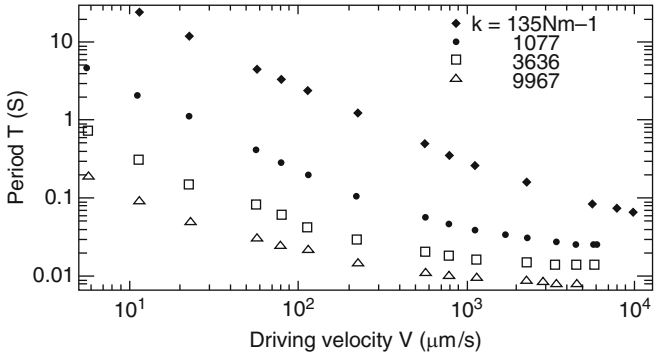

Fig. 2.4 Dependence of slip recurrence period T on velocity V and stiffness k (Nasuno et al. 1998)

Mean period of stick-slip motion T depends on the drive velocity V and spring stiffness k; $T \sim 1/V$ at low V and T decreases with increase of k (Fig. 2.4; Nasuno et al. 1998).

For understanding the physics of stick-slip motion it is very interesting to note that each slip is connected with relatively slow vertical displacement of D_v of the (top) sliding plate relative to the fixed lower plate; it is evident that the maximum of D_v precedes the maximum of tangential velocity V_t. This means that before the slip in horizontal direction, the top plate is rising up; evidently, the plate is ascending and the large asperities, which prevent slip and the slip displacement, occur at reaching the critical number of contact points (threshold). This suggestion is confirmed by the above-mentioned experimental evidence of small vertical displacement preceding the slip event (Fig. 2.5), which means that the number of contact points n decreases to some threshold value n_c making possible the

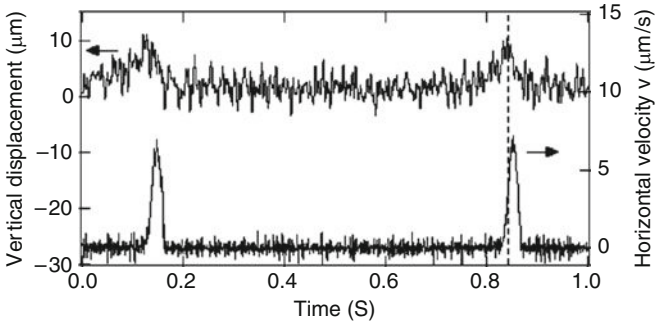

Fig. 2.5 Vertical displacement D_v and tangential velocity V_t of the top plate versus time (Nasuno et al. 1998)

macroscopic tangential displacement. The mathematical formalism, similar to that of percolation model of fracture, could be developed for the slip process (Chelidze, 1986). It seems that the percolation theory, namely, the model of percolation for tangential shift of contacting fractal surfaces, may explain the transition of friction coefficient from the static to kineticvalue at attaining some critical value of contact points of shearing fractal surfaces. In Chelidze (1986) the guess is given about a possibility of applying the percolation model of fracture to tectonic fault dynamics.

It is quite natural that the instabilities of friction excite vibrations, including acoustic emission (AE). The reverse effects are also observed, namely, vibrations affect the friction (Akay, 2002; Chelidze, Varamashvili et al., 2002; Chelidze and Lursmanashvili, 2003; Chelidze, Gvelesiani et al., 2004; Chelidze, Matcharashvili et al., 2005; Chelidze and Matcharashvili, 2007; Chelidze, Lursmanashvili et al., 2006). We presume that acoustic measurements may reveal the fine details of friction mechanism, which are beyond the reach of direct displacement-measuring techniques. The situation is similar to brittle fracture studies, where AE is much more sensitive to micro-fracturing than traditional stress-strain experiments.

In this connection, we presume that the so-called stable sliding is not stable at all, but involves fast micro-events that can not be registered by (slow) displacement sensors.

2.3 Mathematical models of friction

The mathematical expressions for the shear stress τ, formulated by Dietrich and Ruina (Table 2.1) are in agreement with the majority of observed data on stick-slip. It is shown that for some critical stiffness k_c the system undergoes Hopf bifurcation, leading finally to instability. The solution of the system in this case demonstrates all details, characteristic for (chaotic) nonlinear dynamics (Becker, 2000).

An analysis of the experimental data obtained by investigating of spring-slider system motion has led to empirical law, named rate- and state-dependent friction

law (Dieterich, 1979; Ruina, 1983). When the sliding velocity is changed in laboratory friction experiments, two effects are seen to occur to the dynamic coefficient of friction (Bureau et al, 2000; Kanamori and Brodsky, 2004; Boettcher and Marone, 2004). First, there is a "direct" effect that opposes the change in velocity. Hence, if the velocity is increased, the dynamic friction coefficient will correspondingly rise (Fig. 2.2). If the sliding velocity is reduced, the dynamic friction coefficient will drop. This can be described as "rate-dependent friction". The second effect refers to the fact that, after abrupt changes in velocity, the frictional resistance evolves to a new steady state over a characteristic slip distance D_0; this is termed "evolution effect".

The rate and state dependent friction can be quantified as follows (Dieterich, 1979; Ruina, 1983; Kanamori and Brodsky, 2004; Scholz, 1998).

$$\tau = \sigma_o\left(\mu_o + a\ ln\left(\frac{V}{V_o}\right) + b\ ln\left(\frac{V_o\theta}{D_o}\right)\right), \tag{2.1}$$

where μ_0 is the initial coefficient of friction, V is the new sliding velocity, V_0 is the initial sliding velocity, θ is the state variable, D_0 is the critical slip distance, and a and b are two experimentally determined constants.

The state variable varies according to:

$$\frac{d\theta}{dt} = 1 - \frac{V\theta}{D_o} \tag{2.2}$$

In the spring-slider model, dependence of upper sliding plate velocity on time can be graphically presented as shown in Fig. 2.6:

For qualitative analysis of processes, in the transient area between stages 1 and 2 (near stage 2), the equation of motion for this system, under the assumption of $\left|\frac{\theta V}{D_0}\right| \gg 1$, can be written as (Kanamori and Brodsky, 2004):

$$\sigma_o\left(\mu_o + a\ ln\ \dot{x} + b\ ln\ \theta_o - \frac{b}{D_o}x\right) = -kx + kx_o, \tag{2.3}$$

where $\dot{x}$ represents displacement, x_0 the spring elongation, and k the spring stiffness.

By integration of (2.3) for the initial conditions $x = 0$ and $\dot{x} = \dot{x}_0$ for t = 0, we obtain:

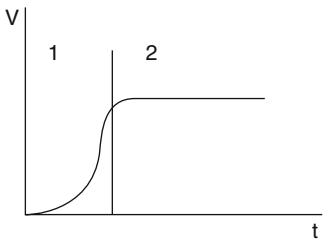

Fig. 2.6 Velocity vs. time during a stick-slip motion

$$\dot{x} = \left[\frac{1}{\dot{x}_o} - \frac{Ht}{a}\right]^{-1} \quad \text{where } H = -\frac{k}{\sigma_o} + \frac{b}{D_o} \tag{2.4}$$

From (2.4) it follows that the sliding velocity spontaneously increases at the time $t_f = \frac{a}{H}(1/\dot{x}_0)$. That is system's destabilizing (relaxation) time. We can say that t_f is a period of stick-slip for our system.

In the case of addition of periodical normal forcing to the main driving force, we can write the equation of motion for our system in the following way (Bureau et al. 2000; Varamashvili and Simonishvili, 2005; Varamashvili, 2006; Putelat et al., 2007):

$$m\frac{d^2x}{dt^2} = k(Vt - X) - W\left(\mu_o + a_o \ln\left(\frac{V}{V_o}\right) + b_o \ln\left(\frac{\theta V_o}{D_o}\right)\right) \tag{2.5}$$

$$\frac{d\theta}{dt} = 1 - \frac{\theta V}{D_o} - \frac{aW}{bW}\theta \tag{2.6}$$

where $W = W_o(1 + \varepsilon\cos(\omega t))$, $W_0\varepsilon$ is the amplitude of forcing, ω is the frequency of forcing, and $T = \frac{2\pi}{\omega}$ is the period of forcing.

In the received system we will solve equation (2.6) to obtain T and we will insert the obtained solution into equation (2.5). For definite parameters from equation (2.5) we obtain the following equation:

$$\ddot{x} + 0.1t\dot{x} + 100t\dot{x} + 100x - 45 - 2\ln\left[1 + \sec\left(\frac{t}{4}\right)^2\right] = 0 \tag{2.7}$$

We solved equation (2.7) using numerical method and the solution is presented in graphic form in Fig. 2.7.

In Fig. 2.7, on the X axis is the current time, and on the Y axis the displacement. From this figure it is evident that for the given parameters the displacement is periodic and decreasing. In fact, experiments show that the stick-slip process has a quasi-periodic character. To simulate the quasi-periodic process we enter periodic normal pressure into equation (2.6) with one-order larger period than the period of

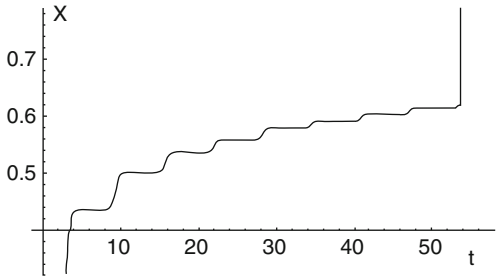

Fig. 2.7. Periodic and decreasing displacement of sliding plate

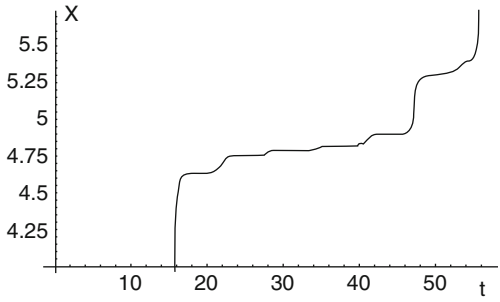

Fig. 2.8 Quasiperiodic displacement of sliding plate according to equation (2.8)

natural stick-slip at corresponding parameters. The idea is to simulate roughness of adjoining surfaces by large period normal loading (we presume that the roughness of surfaces leads to quasi-periodicity of stick-slip process). By means of change of parameters we can try to simulate sliding surfaces of blocks. For definite parameters in equation (2.5) we receive the following equation:

$$\ddot{x} + 6\log(\dot{x}) + 1.7t\dot{x} + 6.8x - 10.9\log\left[\sec\left(\frac{t}{2}\right)^2\right] + 3\cos(0.0999t)\log(\dot{x}) + 3\cos(0.0999t)t\dot{x} + 3\cos(0.0999t)\log\left[\sec\left(\frac{t}{2}\right)^2\right] = 0 \tag{2.8}$$

By solving this equation numerically and presenting the solution graphically, we get Fig. 2.8.

From Fig. 2.8 it is evident that for given parameters the stick-slip process has a quasiperiodic character that reflects experimental data.

For further processing of the method we should try to go from the qualitative agreement of theoretical data with experimental ones to their quantitative conformity.

For solving this system of differential equations (eqs. 2.5 and 2.6), we should make it dimensionless. We introduce dimensionless variables in the following way: dimensionless coordinate is $x = \frac{X}{x_s}$, where x_s is coordinate center of mass of the upper plate in the steady state, dimensionless time is $\tau = \frac{t}{T}$, where T is the period of forcing, dimensionless velocity is $v = \frac{V}{v_s}$, where v_s is the velocity of the steady state, dimensionless state variable is $\vartheta = \frac{\theta}{\theta_s}$, where $\theta = \frac{D_0}{v_s}$ is the state variable at the steady state, characteristic length is $l = v_s T$. After making equations (2.5) and (2.6) dimensionless we obtain:

$$\frac{d^2x}{dt^2} = \beta_1\left(\tau\frac{dx}{d\tau} - x\right) - \beta_2(1 + \varepsilon\cos(2\pi\tau))\left[1 + a\ ln\left(\frac{v}{v_o}\right) + b\ ln\left(\beta_3\frac{\vartheta v_o}{d_o}\right)\right] \tag{2.9}$$

$$\frac{d\vartheta}{d\tau} = \frac{T}{\theta_s} - \frac{\vartheta v}{d_o} - \frac{a\omega}{b\omega}\vartheta, \tag{2.10}$$

with the dimensionless parameters

$$v_o = \frac{v_o}{v_s}, \quad a = \frac{a_o}{\mu_o}, \quad b = \frac{b_o}{\mu_o}, \quad d_o = \frac{D_o}{\imath},$$

$$\beta_1 = \frac{kT^2}{m}, \quad \beta_2 = \frac{W_o \mu_o T^2}{m x^5}, \quad \beta_3 = \frac{\theta_s v_s}{\imath},$$

If the forcing amplitude is small as compared to the constant component ($\varepsilon \ll 1$), we can use perturbation theory and write the coordinate, velocity center of mass of the upper plate, and the state variable as:

$$x = 1 + \delta x, \quad v = 1 + \delta v, \quad \vartheta = 1 + \delta\vartheta$$

where δx, δv, $\delta\vartheta$ are small additions.

After simple transformation, equation of the upper plate center mass motion in first order of perturbation theory comes to the equation for harmonic oscillator with variable external force and friction:

$$\delta\ddot{x} + \gamma_1(\tau)\delta\dot{x} + \gamma_2(\tau)\delta x = f(\tau) \tag{2.11}$$

where

$$\gamma_1 = [\beta_1\tau - a\beta_2(1 + \varepsilon\cos(2\pi\tau))],$$

$$\gamma_2 = \frac{b}{d_0}\beta_2(1 + \frac{d_o}{b} + \varepsilon\cos(2\pi\tau)),$$

$$f(\tau) = \beta_1 + \beta_2(1 + \varepsilon\cos(2\pi\tau))\left[1 - a\ ln\ v_o + b\ ln\frac{\beta_3 v_o}{d_o} + \frac{b}{d_o^2}e^{\frac{1}{d_o}\tau}\right.$$
$$\left. \times \int_o^\tau \delta x e^{\frac{1}{d_o}t}dt + \frac{2\pi\varepsilon\alpha}{b}e^{\frac{-1}{d_o}}\int_o^\tau e^{\frac{1}{d_o}t}\frac{\sin(2\pi t)}{1 + \varepsilon\cos(2\pi t)}dt\right] \tag{2.12}$$

If the variable external forcing is zero, then one of the solutions of homogeneous equation for harmonic oscillators presents Hermitian polynomial.

The general solution of inhomogeneous equation of second order is:

$$\ddot{z} + P(\tau)\dot{z} + Q(\tau)z = F(\tau) \tag{2.13}$$

The general solution for homogeneous equation of harmonic oscillator is:

$$z^0(\tau) = Az_1^0(\tau) + Bz_2^0(\tau)$$

where $Z_1^0(\tau)$ presents Hermitian polynomial, and $Z_2^0(\tau)$ can be expressed through $Z_1^0(\tau)$ using the known relation:

$$z_2^o(\tau) = z_1^o(\tau)W(0)\int_o^\tau \frac{e^{-\int_o^{\tau'} Pd\tau''}}{z_1(\tau')^2}d\tau'$$

where W is Wronskian.

The general solution of inhomogeneous equation (2.13) is the sum of partial solution of inhomogeneous equation $z^1(\tau)$ and general solution of homogeneous equation $z^0(\tau)$:

$$z(\tau) = z'(\tau) + z^o(\tau)$$

where

$$z'(\tau) = \int_0^\tau \frac{z_2^0(\tau)z_1^0(\tau') - z_1^0(\tau)z_2^0(\tau')}{W}F(\tau')d\tau'$$

The solution of eq. (2.13) is quite complicated, but it can give new insights in the dynamics of stick-slip motion.

Acknowledgments Dr. Guram Samsonidze made essential and constructive review of this paper. We acknowledgefunding of the Georgian National Foundation (Grant No. GNSF/ST06/5-028) and INTAS foundation (Ref. No.05-100008-7889).

References

Akay, A. 2002, Acoustics of Friction. J. Acoust. Soc. Am., **111**, 1525-1548.

Burridge R. and Knopoff L. 1967. Model and theoretical seismicity. Bulletin of the Seismological Society of America, 57(3): 341-371

Boettcher M. S., Marone C. 2004, Effects of normal stress variation on the strength and stability of creeping faults. Journal of Geophysical Research, 109, B03406

Brace W. E., and Byerlee I. D. 1966. Stick slip as a mechanism for earthquakes. Science, v.153, pp. 990-992

Bureau, L., Baumberger, T., and Caroli, C. 2000. Shear response of a frictional influence to anormal load modulation. Phys. Rev. E, 62, pp. 6810-6820

Chelidze T., 1986. Percolation Theory as a Tool for Imitation of Fracture Process in Rocks. Pageoph., 124, 731–748.

Chelidze T., Varamashvili N., Devidze M., Chelidze Z., Chikhladze V., and Matcharashvili T. 2002. Laboratory study of electromagnetic initiation of slip. Annals of Geophysics, 45, 587-599

Chelidze T. and Lursmanashvili O. 2003. Electromagnetic and mechanical control of slip: laboratory experiments with slider system. Nonlinear processes in Geophysics, 20, 1-8

Chelidze T., Gvelesiani A., Varamashvili N., Devidze M., Chikchladze V., Chelidze Z., and Elashvili M. 2004. Electrmagnetic initiation of slip: laboratory model. Acta Geophysica Polonica, 52, 49-62

Chelidze T., Matcharashvili T., Gogiashvili J., Lursmanashvili O., and Devidze M. 2005. Phase synchronization of slip in laboratory slider system. Nonlinear Processes in Geophysics, 12, 163–170.

Chelidze T., Matcharashvili T. 2007. Complexity of seismic process, measuring and applications – A review, Tectonophysics, 431, 49-61

Chelidze T., Lursmanashvili O., Matcharashvili T., Devidze M. 2006. Triggering and synchronization of stick slip: waiting times and frequency-energy distribution. Tectonophysics, 424, 139-155

Dieterich, J.H. Modeling of rock friction 1. 1979. Experimental results and constitutive equations. Journal of Geophysical Research, 84B, 2161-2168

Hubbert M. King and Rubey W. W., 1979. Role of Fluid Pressure in Mechanics of Overthrust Faulting, Bulletin of Geological Society of America, 70, 155-166

Kanamori H., and Brodsky E. 2004. The physics of earthquakes. Rep. Prog. Phys. 67, pp. 1429-1496

Nasuno S., Kudrolli A., Bak A., and Gollub J. P. 1998, Time-resolved studies of stick-slip friction in sheared granular layers. Phys. Rev. E 58, 2161–2171

Nasuno S., Kudrolli A., and Gollub J. P. 1997. Friction in Granular Layers: Hysteresis and Precursors. Phys. Rev. Lett. 79, 949–952

Putelat T., Dawes J.H.P., Willis J.R. 2007. Sliding modes of two interacting frictional interfaces. Journal of the Mechanics and Physics of Solids, 55, 2073-2105

Ruina A. 1983. Slip instability and state variable friction laws. Journal of Geophysical Research, 88, 10359-10370

Scholz C. H. Earthquakes and friction laws. Nature, 1998, 391, 37-42

Varamashvili N., Simonishvili T. 2005. Calculation of stick-slip parameters at periodical normal forcing. Journal of the Geophysical Society, Issue (A), Physics of Solid Earth, 10A, 86-90

Varamashvili N. 2006, Stick-slip and periodical normal forcing. Journal of the Geophysical Society, Issue(A), Physics ofSolid Earth, 11, 10-14

Chapter 3
Shear Oscillations, Rotations and Interactions in Asymmetric Continuum

Roman Teisseyre

Abstract A concise asymmetric continuum theory including the relations between stresses, strains, interaction fields and defects is presented. In the presented theory, the motion equations for antisymmetric part of stresses replace the balance of angular momentum. Considering the symmetric stresses, we present a new form of the motion equations for the deviatoric part of strains, arriving at the definition of shear-twist motion as the oscillation of the axes of shears and their amplitudes. With the help of Dirac tensors we present an invariant form of these motions. The motions – displacement and rotations – generated in source processes, e.g., in an earthquake source, may be generated independently or with some phase shift due to the rebound processes; therefore, in the presented asymmetric continuum theory we introduce the phase shift index between the strains and rotations. The presented invariant system of motion equations makes it possible to obtain solutions with the simultaneous strains and rotation motion or those with the $\pi/2$ phase shift between them.

Further, we include in this asymmetric theory, besides the mechanical system, some interaction fields, e.g., thermal and electric interaction.terms. The presented interaction theory is equivalent to that given by Kröner, but it is practically much simpler and includes new solutions with the simultaneous strains and rotation motions or those with the phase shift between them.

3.1 Introduction

We present some elements of the asymmetric continuum theory with some important applications; our consideration on the asymmetric continuum theory includes:

R. Teisseyre
Institute of Geophysics, Polish Academy of Sciences, ul. Ksiecia Janusza 64, 01-452 Warszawa, Poland
e-mail: rt@igf.edu.pl

V. de Rubeis et al. (eds.), *Synchronization and Triggering: from Fracture to Earthquake Processes*, GeoPlanet: Earth and Planetary Sciences 1,
DOI 10.1007/978-3-642-12300-9_3,

– balance laws for the symmetric and antisymmetric stresses and related wave fields
– fundamental relations between the asymmetric stresses and dislocation fields
– hypothesis of a synchronization process based on the rebound processes and the wave
– solution with the phase shift between strains and rotations
– interaction of physical fields with a mechanical system; our consideration is limited to the thermal and electric interaction.terms.

The presented theoretical study generalizes those presented by Teisseyre (2008), Teisseyre (2009), and Teisseyre and Gorski (2009).

3.2 Asymmetric Continuum

Our asymmetric theory differs essentially from the other approaches; e.g., the theory of asymmetric elasticity founded by Nowacki (1986); it includes the couple-stresses introduced in a similar way as in the micropolar and micromorphic theories (see: Eringen, 1999).

A search to improve the classic continuum theory is based on the numerous defaults of the classic theory. We can add here one more example of such defaults, as pointed out by Roux and Guyon (1985). Those authors compared various numerical simulations with the experimental data related to electric and mechanical coupling; some especially poor results concern the cases in which the momentum effects play an essential role. The authors suggest that the angular elasticity should be taken into account. Making the reference to the publication by Crandall et al (1978), they suggest that the elastic energies related to normal and shear forces should be supplemented by the terms including the flexion torque and torsion torque when constructing a more general definition of the Hamiltonian.

Our version of the asymmetric theory includes the asymmetric stresses, symmetric strains and rotations; it permits to include the phase shift between the displacement and rotation motions. As regards the constitutive laws joining the antisymmetric stresses and rotations we follow some ideas introduced by Shimbo (1975; 1995) and related consideration on the friction processes and rotation of grains.

We have constructed our theory (Teisseyre, 2009) as based on the asymmetric stresses, S_{kl}, and deformations: symmetric strains, E_{kl}, and antisymmetric rotations, ω_{kl}:

$$S_{kl} = S_{(kl)} + S_{[kl]}, \quad E_{kl} = E_{(kl)}, \quad \omega_{kl} = \omega_{[kl]} \tag{3.1}$$

We underline that the deformation energy becomes related also to rotation motions:

$$E = \frac{1}{2} S_{kl}(E_{kl} + \omega_{kl}) = \frac{1}{2} S_{(kl)} E_{kl} + \frac{1}{2} S_{[kl]} \omega_{kl}$$

Instead of the Kröner method (Kröner, 1981) based on the self-fields, we introduce the material structure indexes, $e^0$and χ^0, which may help us to join the deformation fields, strains and rotations, with the observed displacement motions:

$$\begin{aligned} E_{kl} &= e^0 E^0_{kl} = e^0 \frac{1}{2}\left(\frac{\partial}{\partial x_k}u_l + \frac{\partial}{\partial x_l}u_k\right), \\ \omega_{kl} &= \chi^0 \omega^0_{kl} = \chi^0\left[\frac{\partial}{\partial x_k}u_l - \frac{\partial}{\partial x_l}u_k\right] \end{aligned} \tag{3.2}$$

For $e^0 = 1$and $\chi^0 = 0$, we return to classic elasticity, while for $e^0 = 0$ and $\chi^0 = 1$ we will have a continuum with rigid, densely packed spheres with friction sensitive to an external moment load. The independent fields (E_{kl}, ω_{kl}) lead us to defects and extreme deformations.

In our theory, for solid elastic bodies we put:

$$e^0 = 1, \qquad E_{kl} = E^0_{kl}, \qquad \omega_{kl} = \chi^0 \omega^0_{kl} \tag{3.3}$$

where the phase index χ^0 may vary from 0 to ± 1 or $\pm$i.

The Shimbo (1975) consideration helps us to present the constitutive relations:

$$S_{(kl)} = \lambda \delta_{kl} E_{ss} + 2\mu E_{lk}, \quad S_{[kl]} = 2\mu\omega_{kl}, \quad S^D_{(kl)} = 2\mu E^D_{kl}, \tag{3.4}$$

where symbols $S^D_{(kl)}$ and E^D_{kl} mean the respective deviatoric tensors, e.g., $S^D_{(kl)} = S_{(kl)} - \frac{1}{3}\delta_{kl}S_{ss}$.

Now, we can consider the motion equations for asymmetric stresses (Teisseyre, 2009). The motion equation for the symmetric part of stresses, $\partial S_{(kl)}/\partial x_k = \rho\partial^2 u_l/\partial t^2 + F_l - \partial p/\partial x_l$, leads to the relation:

$$\frac{\partial^2}{\partial x_n \partial x_l}\lambda E_{ss} + \mu\left(\frac{\partial^2}{\partial x_k \partial x_k}E_{nl} + \frac{\partial^2}{\partial x_l \partial x_n}E_{ss}\right) = \rho\frac{\partial^2}{\partial t^2}E_{nl} + \frac{1}{2}\left(\frac{\partial F_n}{\partial x_l} + \frac{\partial F_l}{\partial x_n}\right) - \frac{\partial^2}{\partial x_n \partial x_l}p \tag{3.5}$$

This expression can be divided into the wave equations for the axial and deviatoric strains:

$$(\lambda + 2\mu)\frac{\partial^2}{\partial x_k \partial x_k}E_{ss} - \rho\frac{\partial^2}{\partial t^2}E_{ss} = -\frac{\partial^2}{\partial x_k \partial x_k}p \quad \text{at} \quad \frac{\partial}{\partial x_s}F_s = 0 \tag{3.6}$$

$$\begin{aligned} \mu\frac{\partial^2 E^D_{nl}}{\partial x_k \partial x_k} - \rho\frac{\partial^2 E^D_{nl}}{\partial t^2} &= -(\lambda+\mu)\left(\frac{\partial^2 E_{ss}}{\partial x_n \partial x_l} - \frac{\delta_{nl}\partial^2 E_{ss}}{3\partial x_k \partial x_k}\right) + \frac{1}{2}\left(\frac{\partial F_n}{\partial x_l} + \frac{\partial F_l}{\partial x_n}\right) \\ &\quad - \left(\frac{\partial^2 p}{\partial x_n \partial x_l} - \frac{\delta_{nl}\partial^2 p}{3\partial x_k \partial x_k}\right) \end{aligned} \tag{3.7}$$

We shall note that in Teisseyre (2008 and 2009) the last relation was presented with some mistakes.

The balance relation for the antisymmetric stresses $S_{[ni]}$ can be deduced from the balance of the stress moment (Teisseyre, 2009):

$$\frac{1}{l^2}\frac{\partial M_{lk}}{\partial x_k} = \varepsilon_{lki}\frac{\partial^2}{\partial x_k \partial x_n} S_{[ni]} = \rho \varepsilon_{lki}\ddot{\omega}_{ki} + \varepsilon_{lki} K_{[ki]} = \rho \varepsilon_{lki}\ddot{\omega}_{ki} + \frac{1}{2}\left(\frac{\partial F_i}{\partial x_k} - \frac{\partial F_k}{\partial x_i}\right) \quad (3.8)$$

where l is the characteristic Cosserat length, $K_{[ki]}$ is a couple of external forces and an angular moment, M_{lk}, is defined as the gradient of the antisymmetric stresses, $M_{lk} = \varepsilon_{lki}\frac{\partial}{\partial x_n} S_{[ni]}$.

For the balance law we can write now:

$$\frac{\partial}{l^2 \partial x_k} M_{lk} = \frac{\varepsilon_{lki}\partial^2}{\partial x_k \partial x_n} S_{[ni]} = \frac{\varepsilon_{lki}\partial^2}{\partial x_n \partial x_n} S_{[ki]} = \rho \varepsilon_{lki}\ddot{\omega}_{ki} + \varepsilon_{lki} K_{[ki]},$$

or

$$\mu\, \Delta \omega_{ki} - \rho \ddot{\omega}_{ki} = K_{[ki]} \quad (3.9)$$

where the transformation we made, $\frac{\varepsilon_{lki}\partial^2 \omega_{ni}}{\partial x_k \partial x_n} \rightarrow \frac{\varepsilon_{lki}\partial^2 \omega_{ki}}{\partial x_n \partial x_n}$, is valid for any antisymmetric non-source fields, $\partial \omega_s / \partial x_s = 0$ (where $\omega_l = {}^1/_2 \varepsilon_{lki}\omega_{ki}$) and at the compatibility condition $\varepsilon_{imk}\varepsilon_{jns}\frac{\partial^2}{\partial x_m \partial x_n}\omega_{ks} = 0$.

The final relation (3.9) replaces that for the stress moment.

Experimental evidences for the appearance of rotation and shear oscillation (sometimes called the shear-twist) in a seismic field is based on the records of seismic rotation fields (see: Teisseyre at al.(eds), 2006; Teisseyre, 2009, Teisseyre K.P., 2007).

3.3 Rotation and shear-twist motions

The rotation motion is governed by equations (3.9), while relation (3.7) for the shear deviatoric strain, E^D_{ik}, transformed to its off-diagonal form, achieved in a special coordinate system, may be replaced by the shear-twist pseudo-vector, $\tilde{E}_s$:

$$\{\tilde{E}_s\} = \{E^D_{23},\ \ E^D_{31},\ \ E^D_{12}\} \quad (3.10)$$

However, we can maintain this definition as an invariant form for any system with the help of the Dirac tensors; the 4D invariant tensor, $\tilde{E}_{\lambda\kappa}$, built initially in the special system (3.10), may now be defined as:

$$\tilde{E}_{\lambda\kappa} = \mathrm{i}\tilde{E}_1\gamma^1 + \mathrm{i}\tilde{E}_2\gamma^2 + \tilde{E}_3\gamma^3 = \begin{bmatrix} 0 & \tilde{E}_3 & -\tilde{E}_2 & -\tilde{E}_1 \\ -\tilde{E}_3 & 0 & \tilde{E}_1 & -\tilde{E}_2 \\ \tilde{E}_2 & -\tilde{E}_1 & 0 & -\tilde{E}_3 \\ \tilde{E}_1 & \tilde{E}_2 & \tilde{E}_3 & 0 \end{bmatrix} \tag{3.11}$$

where the values $\{\tilde{E}_s\}$ are treated as the scalars found in the off-diagonal form (3.10); the Dirac tensors of the antisymmetric type, as used here, are given as follows:

$$\gamma^1 = \mathrm{i}\begin{bmatrix} 0 & 0 & 0 & 1 \\ 0 & 0 & -1 & 0 \\ 0 & 1 & 0 & 0 \\ -1 & 0 & 0 & 0 \end{bmatrix}, \quad \gamma^2 = \mathrm{i}\begin{bmatrix} 0 & 0 & 1 & 0 \\ 0 & 0 & 0 & 1 \\ -1 & 0 & 0 & 0 \\ 0 & -1 & 0 & 0 \end{bmatrix}, \quad \gamma^3 = \begin{bmatrix} 0 & 1 & 0 & 0 \\ -1 & 0 & 0 & 0 \\ 0 & 0 & 0 & -1 \\ 0 & 0 & 1 & 0 \end{bmatrix}$$

We have chosen the antisymmetric Dirac tensors to enable a comparison with the rotation field ω. Using these definitions we can write for the antisymmetric tensor $\tilde{E}_{\lambda\kappa}$ the relations equivalent to eq. 3.7 (Teisseyre, 2009):

$$\mu\Delta\tilde{E}_{\lambda\kappa} - \rho\frac{\partial^2}{\partial t^2}\tilde{E}_{\lambda\kappa} = Y_{\lambda\kappa} \tag{3.12}$$

where according to (3.7) we will have

$$Y_{\lambda\kappa} = \mathrm{i}Y_{23}\gamma^1 + \mathrm{i}Y_{31}\gamma^2 + Y_{12}\gamma^3 = \begin{bmatrix} 0 & Y_{12} & -Y_{31} & -Y_{23} \\ -Y_{12} & 0 & Y_{23} & -Y_{31} \\ Y_{31} & -Y_{23} & 0 & -Y_{12} \\ Y_{23} & Y_{31} & Y_{12} & 0 \end{bmatrix}$$

and

$$Y_{lq} = -(\lambda{+}\mu)\left(\frac{\partial^2 E_{ss}}{\partial x_l \partial x_q} - \frac{\delta_{lq}\partial^2 E_{ss}}{3\partial x_k \partial x_k}\right) + \frac{1}{2}\left(\frac{\partial F_n}{\partial x_l} + \frac{\partial F_l}{\partial x_q}\right) - \left(\frac{\partial^2 p}{\partial x_l \partial x_q}\right)$$

Note that there remains an influence of the axial stresses on the deviatoric field. The shear-twist, $\tilde{E}_s$, means the off-diagonal oscillation of shear axes and its amplitude as caused by internal processes. In the special coordinate system, in which we have simplified the deviatoric strains to the off-diagonal form, $\tilde{E}_s$, we have now defined the shear-twist invariant vector form.

The rotation and twist motions form the complex rotation tensor; the related relations joining these fields follow from the standard conservation law in 4D:

$$\tilde{\omega}_{\lambda\kappa} = \omega_{\lambda\kappa} + \mathrm{i}\tilde{E}_{\lambda\kappa}; \quad \frac{\partial}{\partial x^\kappa}\tilde{\omega}_{\lambda\kappa} = \frac{4\pi}{V}J_\lambda; \quad x^\lambda = \{x^1, x^2, x^3, x^4\},\ x^4 = \mathrm{i}Vt \tag{3.13}$$

or

$$\frac{\partial}{\partial x^{\kappa}}\omega_{\lambda\kappa}=\frac{4\pi}{V}J_{\lambda};\quad \frac{\partial}{\partial x^{\kappa}}\tilde{E}_{\lambda\kappa}=0;\ x^{\lambda}=\{x^1,x^2,x^3,x^4\},\ x^4=\mathrm{i}Vt \tag{3.13a}$$

where we introduced the defect-related current field, J_k, and velocity, V, under the condition that this velocity will be transformed according to the relativistic rules for a sum of velocities.

This system of equations can be split into the twist and rotation Maxwell-like equations:

$$\text{rot}\ \omega-\frac{\mathrm{d}\tilde{\omega}}{V\mathrm{d}t}=4\pi\mathrm{J};\quad \text{rot}\ \tilde{\omega}+\frac{\mathrm{d}\omega}{V\mathrm{d}t}=0 \tag{3.14}$$

where the related velocity depends on the interaction between the rotations and the shear-twist pseudo-vector oscillations of the compression-dilatation axes (or the shear axes shifted by π/4). Note that both fields, rotation and shear, have the azimuth dependent amplitudes.

For the wave equations we obtain:

$$\Delta\omega-\frac{\partial^2}{V^2\partial t^2}\omega=-\frac{4\pi}{V}\in_{npq}\frac{\partial}{\partial x_p}J_q;\quad \Delta\tilde{\omega}-\frac{\partial^2}{V^2\partial t^2}\tilde{\omega}=\frac{4\pi}{V^2}\dot{J}_n+4\pi\frac{\partial}{\partial x_n}\rho \tag{3.15}$$

where $\tilde{\omega}_s\equiv\tilde{E}_s$ and ω_s present the shear-twist and rotation vectors, respectively, the current relates to defect flow, e.g., dislocations, and ρ relates to defect density.

The idea that the rotation-related amplitudes may differ from the P or S waves arises after experimental study on the velocity of rotation waves (K.P. Teisseyre, private communication, 2009). The relations (3.14) indicate that the rotation wave velocity, V_0, appears as an effect of the mutual interaction between the rotations and shear-twist rotational oscillations.

After Teisseyre et al. (2008) we may write the local solution of the system (3.14) for the twist and spin waves shifted mutually in phases:

$$\omega_s=\pm\mathrm{i}\tilde{\omega}_s,\quad \omega_s=\omega_s^0 exp[\mathrm{i}(k_i x_i-\bar{\omega}t),\quad \tilde{\omega}_s=\tilde{\omega}_s^0 exp[\mathrm{i}(k_i x_i-\bar{\omega}t)] \tag{3.16}$$

where $\omega_s^0=\pm\mathrm{i}\tilde{\omega}_s^0$.

The related waves, ω_s and $\tilde{\omega}_s$ help us to explain the synchronization of the micro-fracture phenomena; these conjunct solutions show that one of these motions will be delayed in phase by $\pi/2$. Figure 3.1 gives an example of such a synchronization (K.P. Teisseyre, 2007).

Finally, let us note that when comparing our theoretical approach with the experimental measurements obtained, e.g., from the strain-meter or rotation-seismograph systems (strain determination on one plane requires a set of 3 instruments), we should transform these experimental data to the off-diagonal shear values.

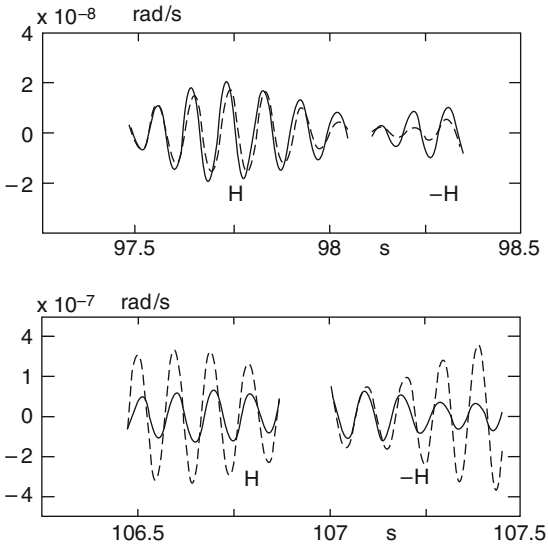

Fig. 3.1 An example of synchronization between the rotations and shear-twist oscillations obtained by applying the Hilbert transform (H)

3.4 Dislocations and disclinations: fragmentation and cracks

In our former papers (Teisseyre 2001, Teisseyre, 2008, Teisseyre and Boratyński 2003) we have introduced the definition of the twist-bend tensor, χ_{mq}:

$$\chi_{mq} = \varepsilon_{ksq} \frac{\partial \omega_{mk}}{\partial x_s} \tag{3.17}$$

which differs from that introduced by Kossecka and DeWitt (1977); according to their definition, the Burgers and Frank vectors would vanish when defining the defects from the twist-bend tensor.

Our definitions, describing the dislocation nuclei, help to obtain the Burgers and Frank vectors and dislocation and disclination densities directly from (3.17):

$$B_l = \oint [E_{kl} + \omega_{kl}] \mathrm{d}l_k \text{ and } \Omega_q = \oint \chi_{pq} \mathrm{d}l_p = \int\int \theta_{pq} \mathrm{d}s_p \tag{3.18}$$

and with the definition

$$B_l = \int\int \left(\alpha_{pl} - \frac{1}{2} \delta_{pl} \alpha_{ss} \right) \mathrm{d}s_p \tag{3.19}$$

we obtain the expressions for the defect densities (cf., eq. 3.2):

$$\alpha_{pl} - \frac{1}{2}\delta_{pl}\alpha_{ss} = \varepsilon_{pmk}\frac{\partial}{\partial x_m}\left(E_{kl} + \omega_{kl}\right) = \varepsilon_{pmk}\frac{\partial}{\partial x_m}\left(e^0 E^0_{kl} + \chi^0\,\omega^0_{kl}\right),\ \theta_{pq} = 0 \tag{3.20}$$

and relation with stresses (Teisseyre, 2008),

$$\alpha_{pl} - \frac{1}{2}\delta_{pl}\alpha_{ss} = \frac{\varepsilon_{pmk}}{2\mu}\frac{\partial}{\partial x_m}\left(S_{(kl)} - \frac{\nu}{1+\nu}\delta_{kl}S_{ii} + S_{[kl]}\right) \tag{3.21}$$

Another definition of the defect nuclei for the twist-bend tensor can introduce the vortex defects with the specific dislocations and disclinations; when defining:

$$\chi_{mq} = \frac{1}{l}\,\omega_{mq} \tag{3.22}$$

we obtain the same expression for dislocation field, but different for disclinations (cf., eq. 3.20):

$$\theta_{pq} = \varepsilon_{pmk}\frac{\partial \chi_{kq}}{\partial x_m} = \frac{1}{l}\varepsilon_{pmk}\frac{\partial \omega_{kq}}{\partial x_m} = \frac{1}{l}\varepsilon_{pmk}\varepsilon_{kqs}\frac{\partial \omega_s}{\partial x_m} = -\frac{1}{l}\frac{\partial \omega_p}{\partial x_q} \tag{3.23}$$

Disclinations related to gradient of rotation become the vortex-defects. An array of the vortex-defects can help us to approximate the fragmentation/cracks (similarly as an array of dislocations approximates a crack).

Finally, we obtain the relation for disclinations and antisymmetric stresses as follows

$$\theta_{pq} = \frac{1}{l}\varepsilon_{pmk}\frac{\partial \omega_{kq}}{\partial x_m} = \frac{1}{2\mu}\varepsilon_{pmk}\frac{\partial S_{[kq]}}{\partial x_m} \tag{3.24}$$

3.5 Interaction fields

First, we recall that the two independent fields, E_{lk} and ω_{kl}, or equivalently, $\tilde{E}_{\lambda\kappa}$ and $\omega_{\lambda\kappa}$, subjected together to the equations of motions (eqs. 3.6, 3.7, 3.9 or 3.13), can be directly coupled by the phase-delayed solution as written in special off-diagonal coordinate system (3.16):

$$E^D_{kl} = \pm \mathrm{i}\omega_{kl} \tag{3.25}$$

Presenting the theory of interaction processes we can write a very general form of the constitutive laws (Teisseyre, 2008):

$$S_{(kl)} = 2\mu\left(e^0 E^0_{kl} + e'\delta_{kl}H + e''H_{(kl)}\right), \quad S_{[kl]} = 2\mu\left[\chi^0\omega^0_{kl} + \chi'\varepsilon_{kls}G_s + \chi''G_{[kl]}\right] \tag{3.26}$$

where $E^0_{kl} = \left(\frac{\partial u_l}{\partial x_k} + \frac{\partial u_k}{\partial x_l}\right)$, $\omega^0_{kl} = \left[\frac{\partial u_l}{\partial x_k} - \frac{\partial u_k}{\partial x_l}\right]$ and $H, H_{(kl)}, G_s, G_{[kl]}$ are the non-mechanical stress-influencing fields; the constants we introduced, e^0, e', e'' and χ^0, χ', χ'', are the phase constants which may vary from 0 to ± 1or $\pm$ i. According to standard asymmetric theory, we relate the strain and rotation with displacements according to eq. 3.2.

However, considering the specific cases separately we can assume that an influence of the mechanical fields, E^0_{kl} or ω^0_{kl}, on the other physical fields (e.g., electric ones) is direct; therefore, it will be enough to assume that the phase shift constants are equal: $e^0 = e' = e''$ and $\chi^0 = \chi' = \chi''$. This assumption means that the interaction between the deformations and non-mechanical fields proceeds without a delay (no phase shift), while the coupling between the mechanical fields themselves may occur with the phase delay, as given in relation (3.25) describing the release-rebound process.

Therefore, further on, instead of (3.26), we write:

$$\begin{aligned} S_{(kl)} &= 2\mu E_{kl} = 2\mu e^0\left(E^0_{kl} + \delta_{kl}H + H_{(kl)}\right), \\ S_{[kl]} &= 2\mu\omega_{kl} = 2\mu\chi^0\left(\omega^0_{kl} + \varepsilon_{kls}G_s + G_{[kl]}\right) \end{aligned} \tag{3.27}$$

Thus, in our approach the elastic deformation fields can be defined as follows:

$$E_{kl} = e^0\left(E^0_{kl} + \delta_{kl}H + H_{(kl)}\right), \quad \omega_{kl} = \chi^0\left[\omega^0_{kl} + \varepsilon_{kls}G_s + G_{[kl]}\right] \tag{3.28}$$

The symmetric and antysimmetric stresses remain to be given, in an elastic regime, by relations (3.4).

We should keep in mind that, in the Kröner metod, the physically significant elastic fields, S_{ks}, E_{ks}, ω_{ks}, are given by the differences between the total fields, S^0_{ks}, E^0_{ks}, ω^0_{ks} (related directly to the displacement differentials), and the self fields, S^S_{ks}, E^S_{ks}, ω^S_{ks} (related to internal interaction nuclei): $S_{ks} = S^0_{ks} - S^S_{ks}$, $E_{ks} = E^0_{ks} - E^S_{ks}$, $\omega_{ks} = \omega^0_{ks} - \omega^S_{ks}$.

It is only the total field that preserves the usual symmetry properties: elastic and self fields may be asymmetric. A comparison of our approach and that used used in the Kröner method was given by Teissyere (2008); we recall here only that the interaction fields in the Kröner theory enter through the self-nuclei whose fields appear in the self- stress, self-strain and self-rotation fields; the relation between the total, elastic and self fields is the following:

$$S^T_{ks} = S^E_{ks} + S^S_{ks}, \quad E^T_{ks} = E^E_{ks} + E^S_{ks}, \quad \omega^T_{ks} = \omega^E_{ks} + \omega^S_{ks}$$

In the Kröner theory, the elastic fields represent the physical fields; the total field preserves the usual symmetry properties, while the elastic and self fields may be asymmetric.

In our approach the stresses are asymmetric, as explained at the beginning.

3.6 Direct relations between defect and electric fields

Returning to the derived relations (3.21) and (3.24) we rewrite them, by virtue of (3.27), as:

$$e^0\varepsilon_{pmk}\frac{\partial}{\partial x_m}\left(\left(E^0_{kl}+\delta_{kl}H+H_{(kl)}\right)-\frac{\nu}{1+\nu}\delta_{kl}e^0\left(E^0_{ii}+3H+H_{(ii)}\right)\right)+$$
$$\chi^0\varepsilon_{pmk}\frac{\partial}{\partial x_m}\left(\omega^0_{kl}+\varepsilon_{kls}G_s+G_{[kl]}\right)=\alpha_{pl}-\frac{1}{2}\delta_{pl}\alpha_{ss} \tag{3.29}$$

and

$$\chi^0\varepsilon_{pmk}\frac{\partial}{\partial x_m}\left(\omega^0_{kl}+\varepsilon_{kls}G_s+G_{[kl]}\right)=\theta_{pq} \tag{3.30}$$

These relations could be used as the differential equations for a chosen non-mechanical field (selected from the set: $H, H_{(kl)}, \ G_s, G_{[kl]}$) to estimate directly its influence on the defect fields (given dislocation and disclination densities); or to find an influence of defects on the non-mechanical fields.

3.7 Interaction examples

3.7.1 Thermal interaction

For a thermal field, we write a more generalized relation than that in the classic elastic theory:

$$S_{(kl)}=2\mu e^0\left(E^0_{kl}-\delta_{kl}\alpha^{\text{th}}(T-T_0)\right), \quad S_{[kl]}=2\mu\chi^0\omega^0_{kl} \tag{3.31a}$$

Comparing with (3.27) we put

$$S_{(kl)}=2\mu e^0\left(E^0_{kl}+\delta_{kl}H\right), \qquad S_{[kl]}=2\mu\chi^0\omega^0_{kl} \tag{3.31b}$$

where $H=-\alpha^{\text{th}}(T-T_0)$ and where for $e^0=1$ and $\chi^0=0$ we return to the classic case.

The equivalent relation between this thermal field and the dislocations becomes:

$$\varepsilon_{pml}\frac{\partial}{\partial x_m}\left(E^0_{kl}-e^0\alpha^{\text{th}}\frac{1-2\nu}{1+\nu}(T-T_0)\right)=\alpha^{\text{edge}}_{pl} \tag{3.32}$$

and there is no contribution from screw dislocations.

3.7.2 Piezoelectric effects

The classical piezoelectric effect appears in anisotropic crystals, piezoelectric dielectrics; after Toupin (1956; see: Mindlin, 1972, Teisseyre, 2001a) we write the constitutive law as:

$$S_{ij} = 2\mu E_{kl} - e_{kij}E_k \tag{3.33a}$$

where E_k is the electric field, e_{kij} are the piezoelectric stress constants.

We can rewrite this relation as follows:

$$S_{(ij)} = \lambda\delta_{ij}E_{ss} + 2\mu E_{kl} - e_{k(ij)}E_k,\ S_{[ij]} = 2\mu\omega_{kl} - e_{k[ij]}E_k \tag{3.33b}$$

According to our approach (3.28) we obtain:

$$E_{kl} = e^0\left(E^0_{kl} + h_s\delta_{kl}E_s + \varepsilon_{s(kl)}gE_s\right),\quad \omega_{kl} = \chi^0\left(\omega^0_{kl} + \varepsilon_{s[kl]}gE_s\right) \tag{3.33c}$$

where we have separated the piezoelectric constant into its symmetric and antisymmetric parts and introduced other definitions:

$$e_{kij} = -2\mu\left(h_k\delta_{ij} + \varepsilon_{kij}g\right)\quad \text{and}\quad H\delta_{ij} = h_k\delta_{ij}E_k,\ G_{[ij]} = \varepsilon_{kij}gE_k \tag{3.34}$$

The equivalent relation between this piezoelectric field and the defect densities becomes:

$$e^0\varepsilon_{pmk}\frac{\partial}{\partial x_m}\left(\left(E^0_{kl} + h_s\delta_{kl}E_s\right) - \frac{v}{1+v}\delta_{kl}\left(E^0_{ss} + 3h_sE_s\right)\right) + \chi^0\varepsilon_{pmk}\frac{\partial}{\partial x_m}\left(\omega^0_{kl} + \varepsilon_{skl}gE_s\right) = \alpha_{pl} - \frac{1}{2}\delta_{pl}\alpha_{ss} \tag{3.35a}$$

$$\varepsilon_{pmk}\frac{\partial\chi_{kq}}{\partial x_m} = \frac{1}{l}\chi^0\varepsilon_{pmk}\frac{\partial}{\partial x_m}\left(\omega^0_{kq} + \varepsilon_{skq}gE_s\right) = \theta_{pq} \tag{3.35b}$$

We note that the piezoelectric constants for various crystallographic classes have been discussed by Nowacki (1983).

3.7.3 Polarization gradient theory

According to Mindlin (1972), the internal energy depends also on the polarization gradient; we can write:

$$\Pi_{ij} = \frac{\partial \Pi_i}{\partial x_j} \tag{3.36}$$

where polarization, $\Pi_i = D_i - \varepsilon E_i$, is defined by difference of electric displacement, D, and electric field, E, with ε being the permittivity of vacuum. The gradient theory, related to electric polarization, makes use of the fact that, under the applied load, the displacements of a moving dislocation core (electrically charged) influence the surrounding defect cloud (such a cloud shall have the opposite charge, compensating that of a dislocation core).

The constitutive relations (Mindlin, 1972; Nowacki,1983) with the respective material constants can be written as follows:

$$S_{ij} = 2\mu E_{ij} + f_{kij}\Pi_k + d_{klij}\Pi_{kl} \tag{3.37}$$

and, according to relations (1-3), can be generalized for the asymmetric stresses to the following form (cf., Teisseyre, 2001):

$$S_{(ij)} = \lambda\delta_{ij}E_{ss} + 2\mu E_{ij} + f_{k(ij)}\Pi_k + d_{kl(ij)}\Pi_{kl}, \quad S_{[ij]} = 2\mu\omega_{ij} + f_{k[ij]}\Pi_k + d_{kl[ij]}\Pi_{kl} \tag{3.38}$$

Now, we can present the contributions to the asymmetric strains and rotations caused by the electric polarization coupling:

$$E_{ij} = e^0\left(E^0_{ij} + \frac{1}{2\mu}f_{k(ij)}\Pi_k + \frac{1}{2\mu}d_{kl(ij)}\Pi_{kl}\right) \tag{3.39a}$$

$$\omega_{ij} = \chi^0\left(\omega^0_{ij} + \frac{1}{2\mu}f_{k[ij]}\Pi_k + \frac{1}{2\mu}d_{kl[ij]}\Pi_{kl}\right) \tag{3.39b}$$

For the direct relation with defects we write according to (3.29) and (3.30):

$$\begin{aligned} &e^0\varepsilon_{pmk}\frac{\partial}{\partial x_m}\left(\left(E^0_{kl} + \frac{1}{2\mu}f_{k(ij)}\Pi_k + \frac{1}{2\mu}d_{kl(ij)}\Pi_{kl}\right)\right. \\ &\left. - \frac{v}{1+v}\delta_{kl}e^0\left(\frac{1}{2\mu}f_{k(ss)}\Pi_k + \frac{1}{2\mu}d_{kl(ss)}\Pi_{kl}\right)\right) \\ &+ \chi^0\varepsilon_{pmk}\frac{\partial}{\partial x_m}\left(\omega^0_{kl} + \varepsilon_{kls}G_s + G_{[kl]}\right) = \alpha_{pl} - \frac{1}{2}\delta_{pl}\alpha_{ss} \end{aligned} \tag{3.40a}$$

$$\chi^0\varepsilon_{pmk}\frac{\partial}{\partial x_m}\left(\omega^0_{kl} + \varepsilon_{kls}G_s + G_{[kl]}\right) = \theta_{pq} \tag{3.40b}$$

Moreover, note that some experiments (see: e.g., Hadijcondis and Mavromatou, 1994, 1995) indicate that the anomalous piezoelectric effects, observed in the laboratory experiments, correspond to the time rate of the applied load.

The problem of magnetostrictive effects can be treated in a similar way.

3.7.4 *Interaction chains: electric and acoustic effects*

Finally, we can note that the shear and axial stresses influence (cf., eq. 3.7) the solution for the deviatoric stresses, E^D_{nl}, and, further on, these strains can influence the rotation field (cf., eq. 3.14); we can express this coupling also by one of possible solutions of the system (3.16):

$$\omega_{\lambda\kappa} = \pm \mathrm{i}\tilde{E}_{\lambda\kappa} \tag{3.41}$$

It seems reasonable to believe that the coupling between the mechanical and electric (or electric polarization) field proceeds in an instantaneous manner, because such effects follow from the displacement of the ions. However, as shown in (3.29), the interaction.between the mechanical fields can proceed with a phase delay due to the release-rebound sequence. Hence, we can have different interaction chains (cf., eqs 3.7 and 3.12) like, e.g., the following ones:

$$E^D_{nl} \rightarrow \mathrm{i}\omega_{nl} \rightarrow \mathrm{i}\Pi_s \tag{3.42a}$$

where the shears coupled to the phase-delayed rotations lead to polarization effects,

$$p \rightarrow E^D_{nl} \rightarrow \mathrm{i}\omega_{nl} \rightarrow \mathrm{i}\Pi_s \tag{3.42b}$$

where a pressure variation (mechanical forcing) initiates a similar chain,

$$E_s \rightarrow \omega_{nl} \rightarrow \mathrm{i}E_{nl} \tag{3.42c}$$

where the electric field variations force rotation effects and the micro-strain releases revealed by the acoustic bursts occurring with the phase delay.

3.8 Conclusions

- We have presented the asymmetric continuum theory including different types of material states: from elastic continuum to granulated/crushed material.
- We have assumed the balance relation for the antisymmetric stresses as equivalent to that for the stress couple. We have defined the 4D invariant form of the shear-twist field.
- The spin and the shear-twist oscillation of the off-diagonal shear axes led us to the relations for the rotation and rotational shear-twist waves.
- We have presented a new definition for dislocation and disclination density field permitting to derive the relations between the asymmetric stresses and linear defect densities.

- We have presented a new relation for the interaction between the strains and rotations and other physical fields; these relations are more general than those between the stresses and some physical fields as, in this new approach, we consider the asymmetric fields and also we may include a phase shift when a rebound process provoked by some energy release shall be considered.
- The direct relations are given between the defect densities and the non-mechanical fields.
- Some examples are given for the interaction between the strains or rotations on the one side, and the electric and electric polarization fields on the other.
- The experimental evidence for the appearance of spin and twist motion in a seismic field is based on the records of the seismic rotation fields (see: Teisseyre at al., 2006; Teisseyre K.P, 2007). Comparison between the experimental data (e.g., strain variation in time as can be obtained from the strain-meter or rotation-seismograph systems) and theoretical consideration on twist field (shears in the off-diagonal system) require transformation of the obtained theoretical twist motion values to the diagonal shear ones.
- The asymmetric continuum theory includes description of the states close to micro-fracture processes; the hypothesis on the local synchronization, related to the special complex solution for the rotation and twist fields, is confirmed by some correlations observed between the recorded twist and spin seismic wave groups.

References

Boratyński W., Teisseyre R., 2006, Continuum with rotation nuclei and defects: dislocations and disclination fields, pp 57-66. In: Teisseyre R., Takeo M. and Majewski E. (eds) "Earthquake Source Asymmetry, Structural Media and Rotation Effects", Springer, pp 582.

Crandall S.H., Dahl N.C., Lardner T.J. 1978, An Introduction to the mechanics of solids, McGraw Hill

DeWitt, R., 1971, Relation between dislocations and disclinations, J. Appl. Phys., 3304-3308.

Eringen A.C., 1999, Microcontinuum Field Theories, Springer, Berlin.

Feng S., Sen P.N., 1984, Percolation on elastic networks: new exponent and threshold, Phys. Rev. Lett. 52 p 216-219

Feng S., Sen P.N., Halperin B.I., Lobb C.J., 1984, Percolation on two dimensional elastic networks with rationally invariant bound-bending forces, Phys. Rev. B 30 p 5386-5389

Feng S., 1985, Percolation properties of granular elastic networks in two dimensions,on Elastic Networks: New Exponent and Threshold, Phys. Rev. B 32 p 510-513

Kossecka E., and DeWitt R., 1977, Disclination kinematic, Arch. Mech., 633-651.

Kröner E., 1981, Continuum Theory of Defects. In: Balian R, Kleman M, Poirer JP (eds) Physique des Defauts / Physics of Defects (Les Houches, Session XXXV, 1980), North Holland Publ Com, Dordrecht.

Mindlin R.D., 1972, Elasticity, piezoelectricity and crystal lattice dynamics, J. Elast., 4, 217-282.

Nowacki W., 1986 Theory of Asymmetric Elasticity, PWN, Warszawa and Pergamon Press, Oxford, New York, Toronto, Sydney, Paris, Frankfurt, pp. 383.

Nowacki W., 1986, Thermoelasticity, Pergamon Press - PWN, Warszawa, pp. 566.

Roux S., Guyon E., 1985, Mechanical percolation: a small beam lattice study, J. Physique Lett. 46, L-999-L-1004

Shimbo M., 1975, A geometrical formulation of asymmetric features in plasticity, Bull.Fac. Eng., Hokkaido Univ., Vol 77, pp 155-159.

Shimbo M., 1995, Non-Riemannian geometrical approach to deformation and friction. In: R. Teisseyre (ed.), Theory of Earthquake Premonitory and Fracture Processes, PWN (Polish Scientific Publishers), Warszawa, pp 520-528.

Teisseyre K.P., 2007, Analysis of a group of seismic events using rotational components, Acta Geophysica, Vol 55, pp 535-553.

Teisseyre R, 2001, Deformation Dynamics: Continuum with Self-Deformation Nuclei. In "Earthquake Thermodynamics and Phase Transformations in the Earth Interior" Eds. R. Teisseyre, H. Nagahama and E. Majewski, Academic Press, pp 143-16509

Teisseyre R, 2008, Asymmetric Continuum: Standard Theory. In "Physics of Asymmetric Continua : Extreme and Fracture Processes" Eds. R. Teisseyre, H. Nagahama and E. Majewski, Springer, pp 95-109

Teisseyre R, 2009, Tutorial on New Development in Physics of Rotation Motions, Bull. Seismol. Soc. Am., vol. 99, 2B, pp 1028-1039

Teisseyre R., Boratyński W., 2003, Continua with self-rotation nuclei: evolution of asymmetric fields. Mech. Res. Commun., Vol 30, pp 235-240.

Teisseyre R, Górski M, 2008, Introduction to Asymmetric Continuum: Fundamental Point Deformations. In "Physics of Asymmetric Continua : Extreme and Fracture Processes" Eds. R. Teisseyre, H. Nagahama and E. Majewski, Springer, pp 3-15

Teisseyre R, Górski M, Teisseyre K.P, 2008, Fracture Processes: Spin and Twist-Shear Coincidence, In "Physics of Asymmetric Continua : Extreme and Fracture Processes" Eds. R. Teisseyre, H. Nagahama and E. Majewski, Springer, pp 111-122

Teisseyre R and Górski M, 2009, Fundamental Deformations in Asymmetric Continuum: Motions and Fracturing, Bull. Seismol. Soc. Am., vol. 99, 2B, pp 1132-1136

Teisseyre R., Takeo M. and Majewski E., (eds), 2006 Earthquake Source Asymmetry, Structural Media and Rotation Effects, Springer, pp. 582.

Teisseyre R, Nagahama T, Majewski E (eds), (2008) Physics of Asymmetric Continuum: Extreme and Fracture Processes, Springer, pp 293

Toupin R.A., 1956, The elastic dielectrics, J. Rat. Mech. Anal., 849-915.

Chapter 4
Processes in Micro-Fracture Continuum

Roman Teisseyre and Zbigniew Czechowski

Abstract In the frame of the asymmetric continuum theory we present some aspects of the micro-fracture processes. An extension of this theory, accommodating for a significant increase of external load, can describe some features of a progressively granulated and fractured material. According to our theory, two kinds of motions – displacements and rotations – in some source processes, e.g., in an earthquake source, may be generated independently or with some phase shift due to the rebound release processes. The asymmetric theory includes a possible phase shift between the simultaneous solutions for the displacement and rotation motions. Equivalently, we present the solutions with the simultaneous strain and rotation motions or those with the $\pi/2$ phase shift between them. Such specific solutions can explain the synchronization action in fracture processes.

Further, we describe on this basis some properties of the slip motion along a fracture zone and micro-fragmentation appearing in the flattened vortex process. Our approach relates to the processes under a very high confining load. The derived nonlinear equations are discussed.

4.1 Introduction

We present some elements of the asymmetric continuum theory with important applications; our consideration on the asymmetric continuum theory includes:

- balance laws for the symmetric and antisymmetric stresses and related wave fields,
- hypothesis of a synchronization process based on the rebound processes and the wave solution with the phase shift between the strains and rotations,
- formation of a granulated (mylonite) zone during fracture processes.

R. Teisseyre (✉) and Z. Czechowski
Institute of Geophysics, Polish Academy of Sciences, ul. Ksiecia Janusza 64, 01-452 Warszawa, Poland
e-mail: rt@igf.edu.pl

V. de Rubeis et al. (eds.), *Synchronization and Triggering: from Fracture to Earthquake Processes*, GeoPlanet: Earth and Planetary Sciences 1,
DOI 10.1007/978-3-642-12300-9_4,

4.2 Asymmetric Continuum

One version of the asymmetric theories of elasticity has been founded by Nowacki (1986); this theory includes the couple-stresses introduced similarly as in the micropolar and micromorphic theories (see: Eringen, 1999). Our version of the asymmetric theory includes the asymmetric stresses, symmetric strains and antisymmetric rotations and permits for a possible phase shift between the displacement and rotation motions. For the constitutive laws joining the antisymmetric stresses and rotations we follow some ideas introduced by Shimbo (1975; 1995) and related considerations on the friction processes and rotation of grains.

Experimental evidences for the appearance of rotation and shear oscillation (twist) in a seismic field are based on the records of seismic rotation fields (see: Teisseyre et al.(eds), 2006; Teisseyre K.P., 2007).

4.2.1 Standard asymmetric continuum

We follow the asymmetric theory with the asymmetric stresses, S_{kl}, and deformations, symmetric strains - E_{kl} and rotations - ω_{kl} (Teisseyre, 2009; Teisseyre, Chapter 3, this issue):

$$S_{kl} = S_{(kl)} + S_{[kl]}, \quad E_{kl} = E_{(kl)}, \quad \omega_{kl} = \omega_{[kl]} \tag{4.1}$$

Let us underline that the energy stored, E, becomes related also to rotational deformation:

$$E = \frac{1}{2} S_{kl}(E_{kl} + \omega_{kl}) = \frac{1}{2} S_{(kl)} E_{kl} + \frac{1}{2} S_{[kl]} \omega_{kl}$$

Instead of the Kröner method (Kröner, 1981) based on the self-fields we introduce the material structure indexes, e^0 and χ^0, joining the deformation fields, strains and rotations, with the displacement motions:

$$\begin{aligned} E_{kl} &= e^0 E^0_{kl} = e^0 \frac{1}{2}\left(\frac{\partial}{\partial x_k} u_l + \frac{\partial}{\partial x_l} u_k\right), \\ \omega_{kl} &= \chi^0 \omega^0_{kl} = \chi^0 \left[\frac{\partial}{\partial x_k} u_l - \frac{\partial}{\partial x_l} u_k\right]. \end{aligned} \tag{4.2a}$$

For $\chi^0 = 0$, $e^0 = 1$ we return to classic elasticity, while for $e^0 = 0$, $\chi^0 = 1$, we would have a continuum with the rigid, densely packed spheres with friction subjected to an external moment load.

The independent fields (E_{kl}, ω_{kl}) lead us to defects and extreme deformations (Teisseyre and Gorski, 2009).

For solid elastic bodies we will put simply:

$$e^0 = 1, \chi^0 ; \qquad E_{kl} = E^0_{kl} , \qquad \omega_{kl} = \chi^0 \omega^0_{kl} , \tag{4.2b}$$

where the phase index χ^0 may vary from 0 to $\chi^0 = \{\pm 1, \pm \mathrm{i}\}$

The Shimbo consideration (1975) supplements the classical constitutive relation:

$$S_{(kl)} = \lambda \delta_{kl} E_{ss} + 2\mu E_{kl} , \qquad S_{[kl]} = 2\mu \omega_{kl} \tag{4.3}$$

We will consider the simplified system of motion equations at a constant density (Teisseyre, 2009);

$$(\lambda + 2\mu) \frac{\partial^2}{\partial x_k \partial x_k} E_{ss} = \rho \frac{\partial^2}{\partial t^2} E_{ss} - \frac{\partial^2}{\partial x_s \partial x_s} p \tag{4.4a}$$

$$\mu \frac{\partial^2 E^D_{nl}}{\partial x_k \partial x_k} - \rho \frac{\partial^2 E^D_{nl}}{\partial t^2} = -(\lambda + \mu) \left(\frac{\partial^2 E_{ss}}{\partial x_l \partial x_n} - \frac{\delta_{nl}}{3} \frac{\partial^2 E_{ss}}{\partial x_k \partial x_k} \right) + Y_{nl} \tag{4.4b}$$

where

$$Y_{nl} = \frac{1}{2} \left(\frac{\partial F_n}{\partial x_l} + \frac{\partial F_l}{\partial x_n} - \frac{\partial^2 p}{\partial x_n \partial x_l} + \frac{1}{3} \frac{\partial^2}{\partial x_n \partial x_l} p \right) \quad \text{at} \quad \frac{\partial F_n}{\partial x_n} = 0 \ \text{ and } \ \partial u_k / \partial x_k = 0$$

The field, E^D_{nl}, can be used to define the shear-twist vector meaning the rotational oscillations of the shear axes and its amplitude (cf., Teisseyre, 2009).

For the independent rotation we write, instead of the balance of the angular moments

$$\mu \Delta \omega_{ki} = \rho \frac{\partial^2 \omega_{ki}}{\partial t^2} + K_{[ki]} \tag{4.5a}$$

where the balance of stress moments is replaced with that for the antisymmetric stresses:

$$\frac{\partial}{\partial x_k} M_{pk} = \varepsilon_{pki} l^2 \frac{\partial^2}{\partial x_k \partial x_n} S_{[ni]} = 2\mu \varepsilon_{pki} l^2 \frac{\partial^2 \omega_{ki}}{\partial x_n \partial x_n} = 2\mu \varepsilon_{pki} l^2 \frac{\partial^2 \omega_{ki}}{\partial x_n \partial x_n} \tag{4.5b}$$

Here, we shall also note the important equivalence

$$\varepsilon_{pki} \frac{\partial^2 \omega_{ni}}{\partial x_k \partial x_n} = \varepsilon_{pki} \frac{\partial^2 \omega_{ki}}{\partial x_n \partial x_n} \ \text{ at the condition } \ \varepsilon_{pki} \frac{\partial \omega_{ki}}{\partial x_p} = 0, \quad \text{or} \quad \frac{\partial \omega_p}{\partial x_p} = 0 \tag{4.5c}$$

We can write that the force moment relates to the angular moment; this statement leads to a definition employing an effective rotation motion, Ω:

$$\frac{\partial}{\partial x_k} M_{pk} = 2\mu\varepsilon_{pki} l^2 \frac{\partial^2 \omega_{ni}}{\partial x_k \partial x_n} \rightarrow M_{pk} = 2\mu\varepsilon_{pki} l^2 \frac{\partial \omega_{ni}}{\partial x_n} = 2\mu\varepsilon_{pki} l \Omega_i, \quad \Omega_i = l \frac{\partial \omega_{ni}}{\partial x_n} \tag{4.6a}$$

including the neighboring rotating elements with the adequately defined characteristic Cosserat length. Instead of (4.5a) we write :

$$\mu \frac{\partial^2 \Omega_i}{\partial x_n \partial x_n} = \rho \frac{\partial^2 \Omega_i}{\partial t^2} + K_i \tag{4.6b}$$

4.3 Slip and fragmentation transport in fracture micro-continuum

In a solid continuum, the advanced deformations - slip and fragmentation processes - could be described with the help of the Navier-Stokes transport idea; we may explain such processes with the help of the slip-transport, υ, and fragmentation-transport $\tilde{\upsilon}$.

Considering a simple case with a constant density, we can transform the displacement motion equation exchanging the partial time derivatives to the total ones:

$$\begin{aligned} \frac{\partial}{\partial t} u_i \rightarrow \frac{\mathrm{d}}{\mathrm{d}t} u_i &= \frac{\partial}{\partial t} u_i + \upsilon_s \frac{\partial}{\partial x_s} u_i \quad \text{and} \\ \frac{\partial^2}{\partial t^2} u_i \rightarrow \frac{\mathrm{d}^2}{\mathrm{d}t^2} u_i &= \left(\frac{\partial}{\partial t} + \upsilon_s \frac{\partial}{\partial x_s} \right) \left(\frac{\partial}{\partial t} u_i + \upsilon_s \frac{\partial}{\partial x_s} u_i \right) \end{aligned} \tag{4.7}$$

and we arrive at a type of the Navier-Stokes transport equation related to slip in solids:

$$\rho \frac{\mathrm{d}^2}{\mathrm{d}t^2} u_i = \rho \frac{\mathrm{d}}{\mathrm{d}t} \upsilon_i = \tilde{\eta} \frac{\partial^2}{\partial x_k \partial x_k} \upsilon_i - F_i$$

or

$$\frac{\partial^2 u_i}{\partial t^2} + \frac{\partial \upsilon_k}{\partial t} \frac{\partial u_i}{\partial x_k} + 2\upsilon_k \frac{\partial \upsilon_i}{\partial x_k} + \upsilon_k \frac{\partial \upsilon_s}{\partial x_k} \frac{\partial u_i}{\partial x_s} + \upsilon_k \upsilon_s \frac{\partial^2}{\partial x_k \partial x_s} u_i = \frac{\mu}{\rho} \frac{\partial^2 u_i}{\partial x_k \partial x_k} - \frac{F_i}{\rho}, \tag{4.8}$$

where in the particular case we may put $\upsilon_i = \frac{\partial}{\partial t} u_i$.

The obtained relation (4.8) describes transport process related to a slip micro-fracture process.

For the fragmentation phenomena and fragmentation/transport we can introduce the arcuate transport process. Thus, when in equation (4.6b) we consider the rotation transport with a related characteristic length, l, serving as a rotation arm:

$$\tilde{\upsilon}_k = \varepsilon_{ksn} l_s \frac{\partial \Omega_n}{\partial t}, \quad \frac{\mathrm{d}}{\mathrm{d}t} \to \frac{\partial}{\partial t} + \tilde{\upsilon}_s \frac{\partial}{\partial x_s}, \tag{4.9}$$

then we obtain (in a constant density case):

$$\frac{\partial^2 \Omega_{ni}}{\partial t^2} + \frac{\partial \tilde{\upsilon}_k}{\partial t}\frac{\partial \Omega_{ni}}{\partial x_k} + 2\tilde{\upsilon}_k \frac{\partial \Omega_{ni}}{\partial x_k} + \tilde{\upsilon}_k \frac{\partial \tilde{\upsilon}_s}{\partial x_k}\frac{\partial \Omega_{ni}}{\partial x_s} + \tilde{\upsilon}_k \tilde{\upsilon}_s \frac{\partial^2 \Omega_{ni}}{\partial x_k \partial x_s} = \frac{\mu}{\rho}\Delta\Omega_{ni} - \frac{K_{[ni]}}{\rho}. \tag{4.10}$$

Further, we focus on the vortex motions with the vortices oriented along the z-axis. On the plane $z = \text{const}$ we may have some variable characteristic length, L, related to a possible vorticity, while along the z-axis the characteristic length will remain very small:

$$l_k = \{L, L, l\}; \quad L \gg l \tag{4.11}$$

We pass to the cylindrical coordinate system; the transport (4.9) becomes as follows:

$$\tilde{\upsilon}_r \approx L\frac{\partial \Omega_z}{\partial t}, \quad \tilde{\upsilon}_\varphi \approx -L\frac{\partial \Omega_z}{\partial t}, \quad \tilde{\upsilon}_z \approx L\left(\frac{\partial \Omega_\varphi}{\partial t} - \frac{\partial \Omega_r}{\partial t}\right) \tag{4.12}$$

Accordingly, the total time derivative becomes

$$\frac{\mathrm{d}}{\mathrm{d}t} = \frac{\partial}{\partial t} + L\left\{\frac{\partial \Omega_z}{\partial t}\left(\frac{\partial}{\partial r} - \frac{\partial}{r\partial\varphi}\right) + \left(\frac{\partial \Omega_\varphi}{\partial t} - \frac{\partial \Omega_r}{\partial t}\right)\frac{\partial}{\partial z}\right\} \tag{4.13a}$$

and for $\Omega_r \ll \Omega_z$, $\Omega_\varphi \ll \Omega_z$ and $L(r, \varphi, z)$

$$\begin{aligned}\frac{\mathrm{d}^2}{\mathrm{d}t^2} &= \left\{\frac{\partial}{\partial t} + L\frac{\partial \Omega_z}{\partial t}\left(\frac{\partial}{\partial r} - \frac{\partial}{r\partial\varphi}\right)\right\}\left\{\frac{\partial}{\partial t} + L\frac{\partial \Omega_z}{\partial t}\left(\frac{\partial}{\partial r} - \frac{\partial}{r\partial\varphi}\right)\right\} \\ &= \frac{\partial^2}{\partial t^2} + L^2\left(\frac{\partial \Omega_z}{\partial t}\right)^2\left(\frac{\partial^2}{\partial r^2} + \frac{\partial^2}{r^2\partial\varphi^2} - 2\frac{\partial^2}{r\partial r\partial\varphi}\right) + 2L\frac{\partial \Omega_z}{\partial t}\left(\frac{\partial^2}{r\partial t\partial\varphi} - \frac{\partial^2}{\partial t\partial r}\right) \\ &\quad + L\frac{\partial^2 \Omega_z}{\partial t^2}\left(\frac{\partial}{\partial r} - \frac{\partial}{r\partial\varphi}\right) + L^2\left(\frac{\partial \Omega_z}{\partial t}\right)^2\left(\frac{\partial \Omega_z}{\partial r} - \frac{\partial \Omega_z}{r\partial\varphi}\right)\left(\frac{\partial}{\partial r} - \frac{\partial}{r\partial\varphi}\right)\end{aligned} \tag{4.13b}$$

Thus, for the macroscopic rotation field (4.6b) (external forces omitted) we obtain:

$$\frac{\tilde{\mu}}{\tilde{\rho}}\Delta\Omega_z - \frac{\partial^2\Omega_z}{\partial t^2} - M_z = 0 \tag{4.14a}$$

where the constants $\tilde{\mu}$ and $\tilde{\rho}$ relate to a medium with the advanced micro-fracture, and we have put the transport term:

$$\begin{aligned} M_z = 2L^2\left(\frac{\partial\Omega_z}{\partial t}\right)^2\left(\frac{\partial^2\Omega_z}{\partial r^2}+\frac{\partial^2\Omega_z}{r^2\partial\varphi^2}-2\frac{\partial^2\Omega_z}{r\partial r\partial\varphi}\right)+2L\frac{\partial\Omega_z}{\partial t}\left(\frac{\partial^2\Omega_z}{\partial t\partial r}-\frac{\partial^2\Omega_z}{r\partial t\partial\varphi}\right) \\ +L\frac{\partial^2\Omega_z}{\partial t^2}\left(\frac{\partial\Omega_z}{\partial r}-\frac{\partial\Omega_z}{r\partial\varphi}\right) \end{aligned} \tag{4.14b}$$

The obtained relation describes the overall transport processes in the micro-fracture medium.

4.4 Local transport in sources of asymmetric elastic continuum

Maintaining the motion equations (4.4) and (4.6) we introduce into the source definition the transport term, M, as defined in (4.14b); this form of a local transport is based on hidden micro-transport elements related to a local slip or fragmentation. Here, we will consider a problem in which the micro-fracture processes concentrated in a source concern a fragmentation (rotation effects) and can be expressed by a source rotation moment introduced into equation (4.6); we put

$$M_z(\Omega_z, L) \to K_z, \quad \text{and} \quad K_z = K\exp(-\alpha t); \quad K = M = \text{constant} \tag{4.15a}$$

where Ω_z follows from the solution (4.6) and the condition that K remains constant.

As mentioned above, the condition for K (to be constant), includes also some material degradation effects and we have assumed that these local degradation processes can be related to the transport phenomena concentrated in a source.

According to (4.15a) we put

$$M_z = M\exp(-\alpha t), \quad \Omega_z = \Omega\exp(-\alpha t), \tag{4.15b}$$

and for the variable vortex radius $L(r, z)$, using (4.14b), we obtain the condition:

$$2L^2\alpha^2\Omega^2\frac{\partial^2\Omega}{\partial r^2} + 3\alpha^2 L\Omega\frac{\partial\Omega}{\partial r} - \alpha^2\Omega = M \tag{4.15c}$$

The solution for Ω shall be found from (4.6) or (4.14a) for M constant; under a plane shear load rotation field, in solids, it shall depend on φ, however, we can

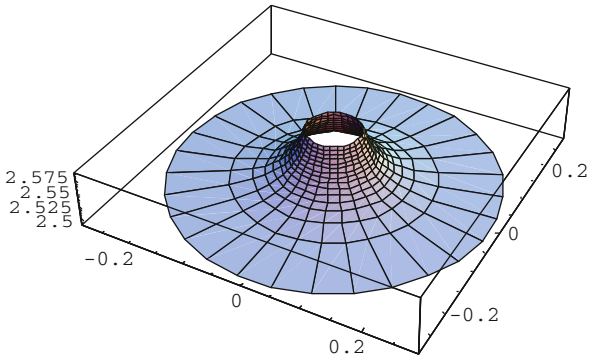

Fig. 4.1 Vortex structure concentrated in the vicinity of the source fragmentation plane

express this dependance through the function $\sin 2\varphi$ as follows from the consecutive angular changes of the shears along a plane. We obtain from (4.15b):

$$\frac{\partial^2\Omega}{\partial r^2}+\frac{\partial\Omega}{r\partial r}+\frac{\partial^2\Omega}{r^2\partial\varphi^2}+\frac{\partial^2\Omega}{\partial z^2}-\alpha^2\tilde{\rho}\Omega=\frac{\partial^2\Omega}{\partial r^2}+\frac{\partial\Omega}{r\partial r}-\frac{4\Omega}{r^2}+\frac{\partial^2\Omega}{\partial z^2}-\alpha^2\tilde{\rho}\Omega=\frac{1}{\tilde{\mu}}M \tag{4.16}$$

The respective numerical solution of this equation may be used to compute from (4.15c) the fragmentation arm changes, L, which enables us to present this fragmentation similarly to a vortex structure (Fig. 4.1). The presented changes of this vortex arm can be revealed when computing L from (4.15c) with the initial condition $L = r_0$. As presented in this figure, this numerical solution is given with a change of the scales along the vortex plane in comparison to the z-axis; we expressed this by a change of the rigidity parameter μ to $\tilde{\mu}$, as presented in eq. (4.6). In this way, we take into account the fact that, due to fragmentation, the material parameters along this plane undergo essential changes due to these micro-fracture processes.

We shall underline that the vortex process starts due to a point source, that is, reversely than it is usually considered in the vortex problems. The vortex arm increases up from a point source $r = 0$, and the vortex is concentrated near the fragmentation plane (this is quite different in comparison to vortices in fluids). This follows from our assumption that the material properties in a fragmentation plane have become changed, in comparison to those along the direction perpendicular to it, while the material properties remain almost unchanged.

4.5 Shear and confining loads

In the local micro-fracture zones, the shear and confining loads lead to the transport processes related to the displacement and rotation motions.

The transport relations for the displacement motions are especially important for the slip processes under a shear load; in that case, the rotational transport can sometimes be neglected (Fig. 4.2).

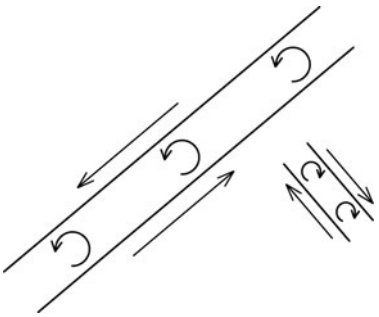

Fig. 4.2 Shear load: sketch of slip elements and the opposite rotations as appear along the main slip and a double couple partner

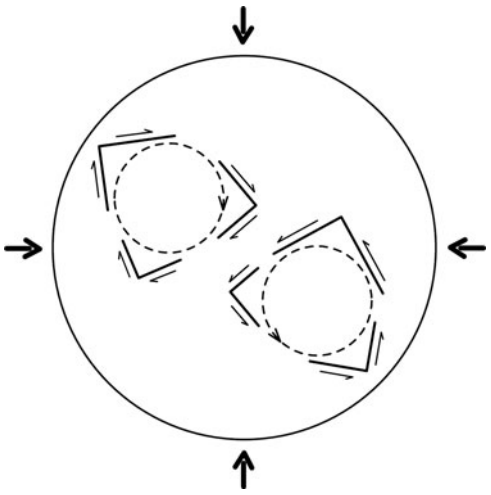

Fig. 4.3 Confining load: the induced opposite shears inside the fragmentation elements; the opposite shear couples result in a rotation of fragmented elements

Under a confining load, the fragmentation processes may be described by a helical transport incorporated into the rotation field equations. The induced shear micro-fractures appear in this case along the perpendicular slip fragments; the related induced shears would be mutually compensated inside some micro-region in which a common rotation sense will produce a micro-fragmentation circular structure (Fig. 4.3). At the neighboring fragments, the rotation sense might be opposite. However, the induced consecutive shears inside a particular fragmentation element will be manifested by the perpendicular micro-displacement couples; these rotation couples, contrary to shear couples, result in a rotational micro-fragment, while the resulting shear field will become compensated almost to null. Thus, a fracture running according to this scenario, due to induced rotation couples, leads to the material fragmentation and rotation; the directions of rotations can be opposite inside the material under an applied confining load. This is an opposite case to that of shear process, which leads to the shear nuclei, described by the double couples in the conventional meaning.

However, we shall notice that variable inner shear fields, caused by the inner micro-fractures and related stress releases at the neighboring sites, may cause the rotational oscillations of the main axes of these double couples; this kind of rotation motion is called shear-twist (Teisseyre, 2009).

However, to get a better understanding of the fracture processes we may consider jointly the micro-slip and micro-fragmentation processes. When approaching the micro-fracture and fracture states we should consider also the consecutive substantial changes in the material properties and in the governing equations. The material properties undergo changes, e.g., from the elastic to plastic and, further on, to crushed, granulated and even partly melted mylonite.

Moreover, an influence of the rotation processes of various nature and scale may be of great importance when some vortex micro-structures will appear. To outline such an approach we may follow the asymmetric continuum theory; we start with the relations presented above (Eqs. 4.1–4.5) as concerns the perfect elasticity. During a further deterioration, related to plastic flow and micro-fracture processes, we assume that the compressibility relation, expressed by means of the axial part of stresses and strains, remains practically unchanged (however, some changes in the value of compressibility can be easily included).

Under a shear load, the micro-fracture processes can proceed as follows: shear stresses and related strains cause some changes in the angular molecule orientations, then the slip motion and break of the molecular bonds start with an immediate drop of shears, and then there appears the rebound rotation retarded in phase. Under a compression load, the induced defects cause an appearance of the opposite shear centers, then some micro-breaks lead to the rotations and fragmentation process, and then there appear the rebound slip motions retarded in phase. In the first case, the shears create the dynamic angular deformations leading to the bond breaks and slip propagation followed by the rebound rotations retarded in phase. In the second case, the micro-fractures under compression lead to the opposite sense of the induced shear motions: the twist motions and the related fragmentation and granulation processes precede the slip rebounds retarded in phase.

4.6 Conclusions

The considered rotational (helical) transport processes are expected to occur in the granulated structures or those undergoing the micro-fragmentation processes; the presented new development in solid theory with the micro-fracture and fragmentation processes describes the independent rebound release processes occurring with a possible phase shift between the rotation and shear-twist oscillations. Any torque moment caused by the independent transport and micro-fracture may generate the spin and shear-twist motions.

The slip-fracture and fragmentation processes caused by a joint action of shear and confining loads may run with a mutual interaction. The equations for the joint

slip-shear and fragmentation-pressure processes take into account a possible shift between the related oscillations and the rebound release dynamics.

The obtained relations for the helical transport differ essentially from those for fluids; here, we deal with the square time rates of the transport contributions; this is related to the transition: $\partial^2/\partial t^2 \rightarrow \mathrm{d}^2/\mathrm{d}t^2$ and to the material changes due to fragmentation process.

Acknowledgement The authors would like to express their thanks to Dr M. Gorski and W. Boratynski for their help in the numerical computations and preparation of figures.

References

Boratyński W., Teisseyre R., 2006, Continuum with rotation nuclei and defects: dislocations and disclination fields, pp 57-66. In: Teisseyre R., Takeo M. and Majewski E. (eds) "Earthquake Source Asymmetry, Structural Media and Rotation Effects", Springer, pp 582.

Eringen A.C., 1999, Microcontinuum Field Theories, Springer, Berlin.

Kossecka E., DeWitt R., 1977, Disclination kinematic, Arch. Mech. Vol 29, 633-651.

Kröner E., 1981, Continuum Theory of Defects. In: Balian R, Kleman M, Poirer JP (eds) Physique des Defauts / Physics of Defects (Les Houches, Session XXXV, 1980), North Holland Publ Com, Dordrecht.

Nowacki W., 1986 Theory of Asymmetric Elasticity, PWN, Warszawa and Pergamon Press, Oxford, New York, Toronto, Sydney, Paris, Frankfurt, pp. 383.

Shimbo M., 1975, A geometrical formulation of asymmetric features in plasticity, Bull.Fac. Eng., Hokkaido Univ., Vol 77, pp 155-159.

Shimbo M., 1995, Non-Riemannian geometrical approach to deformation and friction. In: R. Teisseyre (ed.), Theory of Earthquake Premonitory and Fracture Processes, PWN (Polish Scientific Publishers), Warszawa, pp 520-528.

Teisseyre K.P., 2007, Analysis of a group of seismic events using rotational components, Acta Geophysica, Vol 55, pp 535-553.

Teisseyre R., 2001, Evolution, propagation and diffusion of dislocation fields, pp 167-198. In: Teisseyre R, Majewski E, (eds) Earthquake thermodynamics and phase transformations in the Earth's interior, Academic Press, San Diego, pp 670.

Teisseyre R., Boratyński W., 2003, Continua with self-rotation nuclei: evolution of asymmetric fields. Mech. Res. Commun., Vol 30, pp 235-240.

Teisseyre R., Takeo M. and Majewski E., (eds), 2006, Earthquake Source Asymmetry, Structural Media and Rotation Effects, Springer, pp. 582.

Teisseyre R, Takeo M, Majewski E (eds), 2006, Earthquake Source Asymmetry, Structural Media and Rotation Effects, Springer, pp 582.

Teisseyre R, Nagahama T, Majewski E (eds), 2008, Physics of Asymmetric Continuum: Extreme and Fracture Processes, Springer, pp 293.

Teisseyre R, 2009, Tutorial on New Development in Physics of Rotation Motions, Bull. Seismol. Soc. Am., vol. 99, 2B, pp 1028–1039.

Teisseyre R and Górski M, 2009, Fundamental Deformations in Asymmetric Continuum: Motions and Fracturing, Bull. Seismol. Soc. Am., vol. 99, 2B, pp 1132–1136.

Teisseyre R, Górski M, 2008, Introduction to Asymmetric Continuum: Fundamental Point Deformations. In "Physics of Asymmetric Continua : Extreme and Fracture Processes" Eds. R. Teisseyre, H. Nagahama and E. Majewski, Springer, pp 3–15.

Teisseyre R, 2008, Asymmetric Continuum: Standard Theory, In "Physics of Asymmetric Continua: Extreme and Fracture Processes" Eds. R. Teisseyre, H. Nagahama and E. Majewski, Springer, pp 95–109.

Teisseyre R, Górski M, Teisseyre K.P, 2008, Fracture Processes: Spin and Twist-Shear Coincidence, In "Physics of Asymmetric Continua : Extreme and Fracture Processes" Eds. R. Teisseyre, H. Nagahama and E. Majewski, Springer, pp 111–122.

Chapter 5
On a Simple Stochastic Cellular Automaton with Avalanches: Simulation and Analytical Results

Mariusz Białecki and Zbigniew Czechowski

5.1 Introduction

Cellular automata (CA) models are widely used in many natural and human sciences. The rule that defines CA, which may be very simple, can lead to a very complicated evolution of a system and rich structure of produced patterns. It often comes from nonlinearity present in the system. The rule of the model encodes the crucial features of the phenomenon under investigation. It contains the information about the behaviour of the automaton and usually is suggestive (convincing) reference point for explanations of its properties. Instead of equations, the rule often plays a central role in description of automata. CA are also convenient and hence attractive tools for making computer simulations; being completely discrete, in principle, CA do not require any approximation procedure for machine implementation.

There is also a complementary approach to CA models. The key idea is very classical: write down equations and analyse them. In spite of a nonlinearity of the equations that often makes the task complicated, it focuses attention of many researches (see, for example, Chopard and Droz., 2005). An interesting example of this approach in the domain of integrable systems is the soliton cellular automaton (see Tokihiro, 2004). This elegant automaton is a completely discrete version of a soliton equation, hence it is very special even among deterministic automata. It is also to be noted that equations for automata can serve as natural basis for applying both sophisticated mathematics and quite "exotic" mathematical structures to the subject (see Białecki and Doliwa, 2005, and also Białecki, 2009, where an attempt to present a deterministic evolution of some system over finite fields is presented in a way allowing for direct comparison with possible experiments). Our aim is to

M. Białecki (✉) and Z. Czechowski
Institute of Geophysics, Polish Academy of Sciences, ul. Ks. Janusza 64, Warszawa, Poland
e-mail: bialecki@igf.edu.pl; zczech@igf.edu.pl

V. de Rubeis et al. (eds.), *Synchronization and Triggering: from Fracture to Earthquake Processes*, GeoPlanet: Earth and Planetary Sciences 1,
DOI 10.1007/978-3-642-12300-9_5,

extend this approach to the *stochastic* automat; in this chapter we are dealing with the 1-dimensional domino automaton inspired by earthquakes. We point out that studying properties of the system may be neater with equations than with numerical experiments. It is also useful for finding theoretical explanations and providing exact quantitative presentation of different features of a system. Still, to find a system which can be satisfactorily described in this way is a challenge.

Earthquakes are extremely complex phenomena and thus it is very difficult to fully reflect their properties by theoretical models. Such geophysical phenomena are usually subjected to simplifications in order to retain some control on the proposed physical/mathematical framework. However, even significant simplifications do not protect us from leaving the elegant domain of transparent formulas and exact solutions. An interesting example of considerations of simple cellular automaton in the context of earthquakes is given by Tejedor et al. (2008), where the Gutenberg-Richter law is observed. The appearance of inverse-power distributions is an interesting topic itself and was investigated in the broader context of a privilege (see Czechowski, 2003) and also with connection to Ito equation (see Czechowski and Rozmarynowska, 2008). The ideas presented here deliver a method to advance the studies (see the next chapter in this monograph).

Here we propose and discuss stochastic domino automaton - another extremely simple model inspired by earthquakes. The domino automaton inherits only two of its characteristic features. One is the "pumping" of energy at a constant rate, which reflects uniform stress increase as an effect of tectonic plates' motion with constant relative velocity. The second is the presence of relaxations, when the stress increases above a threshold in some place, and the energy is released in a very short period of time. The simplicity of the model leads, however, to the avalanche distribution different from the Gutenberg-Richter law. These two effects are represented as follows. Each of the cells (discrete places on a line) can be empty or contain one standing domino block (later called also a particle). In one time step, one cell from all is randomly chosen. If the cell is empty, the domino block takes the position. If the cell is occupied, the domino gives an impulse which falls down the domino blocks in the cell and in all its adjacent neighbours if occupied (in both directions). Fallen blocks are removed and that means an avalanche occurs. Then the procedure repeats in the next time step. The precise definition of the domino automaton is given in the next section.

Our aim in this chapter is twofold. The first is to present a new simple *stochastic* cellular automaton model and the second is to apply the direct analytic approach to this stochastic automaton. We prefer here an elementary approach to the description of the automaton and we make no use of applicable Markov processes terminology. In this context the domino automaton is discussed in the next chapter.

The structure of the paper is as follows. In Section 5.2 the definition of the automaton is given and basic properties from the numerical experiment are presented. Next we derive the set of equations for the average values of the parameters of the model in Section 5.3. Finally, in Section 5.4 we discuss the obtained results and point out directions for future work.

5.2 The random domino automaton

Consider one dimensional (line) model with N discrete number of places. In a single time step, a particle (representing a portion of energy) is added to the system at the randomly chosen place (called also cell). In our model every place is equally likely. If the chosen cell is empty, it becomes occupied. If the chosen place is already occupied, the incoming energy plays a role of a trigger and a relaxation takes place. By a relaxation we mean an immediate removal of the particle from the chosen cell and all its adjacent occupied cells. It produces an avalanche of a size equal to the number of cells changing their state. An example of relaxation of the size **four** is presented in the diagram below.

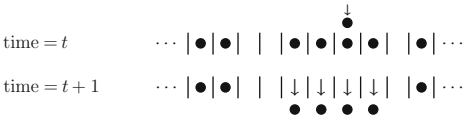

To study the evolution of the automaton, numerical experiments were performed. In simulations we investigate the one-dimensional lattice of size $N = 500$ cells. After an initial stage, in which the lattice is saturated, a stationary quasi-equilibrium stage takes place. The first parameter to be monitored is the density $\rho(t)$, defined as the number of occupied cells in the instant t divided by the lattice size N. As the model is invented in the context of earthquakes, it is interesting to trace the avalanche sizes $w(t)$. To skip the dull process of gradual increase of density between avalanches, we present these quantities after each avalanche only, as functions $w(k)$ and $\rho(k)$, where k is the number of avalanches.

Examples for $w(k)$ and $\rho(k)$ from numerical experiment is presented in Fig. 5.1. The distribution of fluctuations for density $\rho(k)$ resembles the Gaussian distribution (see Fig. 5.2) with average $<\rho> = 0.3075$ and variance $\sigma^2 = 0.000598$. These parameters are equal to parameters estimated from the time series. The primary aim and the main motivation of the next section is to derive the value of $<\rho>$ analytically.

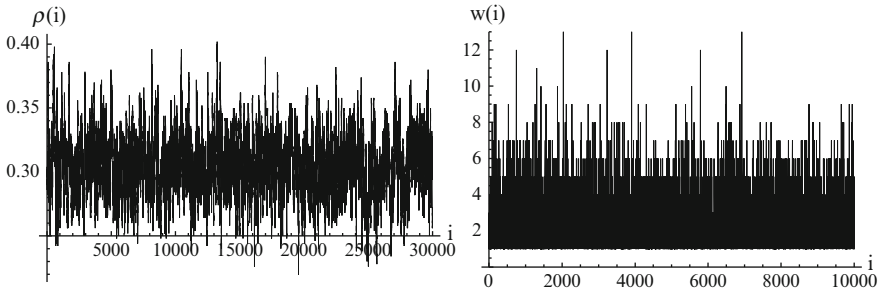

Fig. 5.1 Simulation results for time series of system density $\rho(k)$ and avalanche sizes $w(k)$ of the 1D domino automaton with lattice size $N = 500$. The parameter k means the number of avalanches

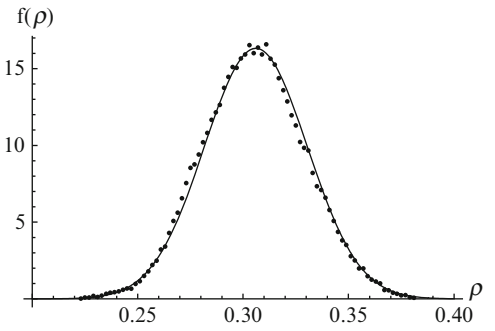

Fig. 5.2 The distribution of fluctuations $f(\rho)$ for the density ρ from the simulation (dots) and fitted Gaussian distribution (line). The average density is $<\rho> = 0.3075$ and the variance is $\sigma^2 = 5.98*10^{-4}$

5.3 Quasi-equilibrium equations

One of the evident properties of the domino automaton is its stochasticity, stipulated in its definition. Thus, we are interested in its mean properties rather then exact evolution. The numerical experiments suggest that the density of a system oscillates in a random way around an average value. Note, the density is also a probability of avalanche, hence the variations of density are subject to "u-shape" potential. For high densities, the probability of their decrease by relaxation is also high; for small densities their growth is more likely. Thus, we will describe the behaviour of the automaton under the assumption that it reaches a quasi-equilibrium and the parameters of the system, like density and others (defined below), do not depend of time. The variables are treated as physical variables in a sense of statistical physics.

Fix the size of the lattice N and assume periodic boundary conditions (regard the first cell as adjacent to the last one). In the system, alter sequences of occupied and empty cells. Such a sequence of i subsequent occupied cells are called the cluster of the length i (shortly i-cluster); the sequence of i subsequent empty cells are called empty cluster of the length i. The values of i can be 1, 2, . . ., and are bounded, at least by the size N. Define by n_i the number of i-clusters and by n_i^0 the number of empty i-clusters. Denote the total number of clusters by n, then

$$n = \sum_{i \geq 1} n_i = \sum_{i \geq 1} n_i^0 \tag{5.1}$$

because of the periodic boundary conditions. It is also straightforward from the definitions that

$$\rho = \frac{1}{N} \sum_{i \geq 1} i n_i, \tag{5.2}$$

and also

$$\frac{1}{N}\sum_{i\geq 1}(n_i + n_i^0)i = 1, \tag{5.3}$$

which tells that any cell is either occupied or empty. The variables ρ and n_i are our basic objects.

In a single time step, the number of occupied cells may increase by one or decrease by i in a case of an avalanche of size i. If the value of ρ on average does not depend of time, there must be a balance between expected values of loses and gains in the number of occupied cells. In other words, the stationarity condition requires that flow in is equal to flow out. The expected value of increasing density is equal to the probability of choosing an empty space, namely $(1-\rho)$. The probability of relaxation of any size i is $\frac{in_i}{N}$, and since the avalanche of any possible size i can contribute, then the stationarity condition gives

$$(1-\rho) = \frac{1}{N}\sum_{i\geq 1} n_i i^2. \tag{5.4}$$

Using equation (5.2), it may be written as

$$N = \sum_{i\geq 1} n_i i(i+1). \tag{5.5}$$

The obtained equation gives a restriction for n_is in a case of asymptotic behaviour, where $N \to \infty$.

To be solved, equation (5.2) requires extra relations. As a first rough step consider the percolation approximation (see Stauffer and Aharony, 1992)

$$n_i = c(1-\rho)^2\rho^2. \tag{5.6}$$

From equation (5.2) it follows

$$\frac{1}{(1-\rho)^2}\frac{N}{c} = \sum_{i\geq 1}\rho^{i-1}i = \frac{d}{d\rho}\sum_{i\geq 1}\rho^i = \frac{d}{d\rho}\frac{\rho}{1-\rho} = \frac{d}{d\rho}\frac{1}{1-\rho}$$

so $c = N$ and ρ is the only parameter of the family of distributions. The use of (5.6) in condition (5.5) gives

$$1 = \sum_{i=1}^{N_0}(1-\rho)^2\rho^i i(i+1),$$

where N_0 is a upper size limit for clusters, hence (after manipulation like above) one has

$$\frac{1}{(1-\rho)^2} = \rho \frac{d^2}{d\rho^2} \frac{\rho^2(1-\rho^{N_0})}{1-\rho}.$$

Finally, neglecting terms with N_0 (if $N_0 \approx 100$ the accuracy is better than 10^{-25}) one can obtain

$$1 = \frac{2\rho}{(1-\rho)} \quad \text{or} \quad \rho = \frac{1}{3}.$$

The automaton rule says that there is a "coupling" between the adjacent cells, since the rule of relaxations takes out the whole cluster, so treating cells as independent, like in (5.6), is erroneous. Thus, the percolation approximation gives the value of ρ different by several percent from a value $<\rho> \sim 0.3075$ from numerical simulation of the automaton. Better estimation of ρ needs an extra reasoning.

For the computations below we use a weaker assumption, namely *clusters are distributed independently*, by which we mean that the length of the "next" cluster does not depend on the length of the "previous" one. In other words, our investigations are done up to the order of clusters.

To write down equations for the numbers of clusters of length i, i.e., for n_i s, we consider all possibilities of losses of such clusters as well as their creation, and next we claim that on average the gains and losses compensate each other.

Losses. There are two ways to destroy an i-cluster: by enlarging and by provoking the avalanche depending on where an incoming particle is thrown.

$$\cdots | \quad | \underbrace{\bullet | \bullet | \cdots | \bullet}_{i} | \quad | \cdots$$

(a) Enlarging. For any cluster there are two cells adjacent to its ends, so the probability is

$$\sim 2\frac{n_i}{N}.$$

Here we just count the number of such empty cells. If a single empty cell is between two clusters of length i it is counted twice, as it should be. Hit of such a cell reduces the number of i-clusters by two.

(b) Relaxation. In this case it is enough to hit any of the occupied cells of the cluster, so the probability is

$$\sim \frac{in_i}{N}.$$

Gains. There are in general two possibilities to create i-cluster: enlarging $(i-1)$-cluster and joining two smaller clusters.

(a) Enlarging. We need to consider cases $i = 1$ and $i \geq 2$ separately.

Case $i = 1$. There is only one way to form a solitary occupied cell: an incoming ball must hit the empty place with two empty places on the both sides.

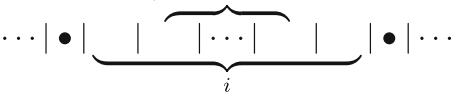

The probability is proportional to the number of interior cells in empty clusters of the length three and bigger

$$\sim \sum_{i\geq 3} \frac{(i-2)}{i} \frac{in_i^0}{N}.$$

But the expression above can be simplified as follows

$$\sum_{i\geq 3} n_i^o (i-2) = \sum_{i\geq 1} n_i^0 (i-2) + n_1^0 = (1-\rho)N - 2n + n_1^0,$$

where we used equation (5.3). Finally the probability is

$$\sim (1-\rho) - 2\frac{n}{N} + \frac{n_1^0}{N}.$$

Case $i \geq 2$. An enlarging a $(i-1)$-cluster to the size i is possible if the adjacent empty cluster is of the size bigger than one

$$\sim 2\frac{n_{i-1}}{N} \frac{\sum\limits_{i\geq 2} n_i^0}{n^0} = 2\frac{n_{i-1}}{N} \frac{(n^0 - n_1^0)}{n^0} = 2\frac{n_{i-1}}{N}(1 - \frac{n_1^0}{n}),$$

where the multiplier 2 counts left and right cases.

(b) Joining two clusters. To create i-cluster from two smaller ones, a cluster of size $k \in \{1, 2, ..., (i-2)\}$ and the other of the size $(i-1)-k$ are necessary.

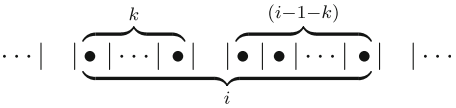

The probability is proportional to the number of empty *1*-clusters between k-cluster and *(i−1−k)*-cluster, hence

$$\sim \frac{n_1^0}{N} \sum_{k=1}^{i-2} \frac{n_k}{n} \cdot \frac{n_{i-1-k}}{n}.$$

The dot in the multiplication above underlines the independence assumption for the order of clusters. The last equation introduces also an extra quadratic nonlinearity into the system, so far nonlinearity was present via n.

The balance between gains and losses for clusters gives the following set of equations for n_i

$$n_1 = \frac{1}{3}(1-\rho)N - \frac{2}{3}n + \frac{1}{3}n_1^0, \tag{5.7}$$

$$n_2 = \frac{1}{2}(1-\frac{n_1^0}{n})n_1, \tag{5.8}$$

$$n_i = \frac{1}{i+2}\left(2n_{i-1}(1-\frac{n_1^0}{n}) + n_1^0\sum_{k=1}^{i-2}\frac{n_k n_{i-1-k}}{n^2}\right) \quad \text{for} \quad i \geq 3, \tag{5.9}$$

where $n = \sum_{i\geq 1} n_i$ and $\rho = \frac{1}{N}\sum_{i\geq 1} i n_i$.

In the above set of equations there is one extra variable n_1^0. But the system is closed for variables $\{n_1^0, n_1, n_2, n_3, \ldots\}$ since we derived the balance equation for ρ, which can be written in the form of equation (5.5)

$$N = \sum_{i\geq 1} n_i i(i+1).$$

Thus we derive the set of nonlinear equations exactly describing our model. It is also possible to write down an analogous set of equation for empty clusters (see Białecki and Czechowski, 2010). The numerical values of the density ρ, the average size of cluster $<i>$ and the average size of the avalanche $<w>$ are compared in Table 5.1 with percolation approximation results and with simulation results. The agreement of the values in quasi-equilibrium description with numerical experiment is striking.

From the set of equations, multiplying n_i by *(i+2)* for $i = 2, 3, \ldots$ and summing them up we obtain

$$\sum_{i\geq 2} n_i(i+2) = 2(1-\frac{n_1^0}{n})\sum_{i\geq 2} n_{i-1} + \frac{n_1^0}{n^2}\sum_{i\geq 3}\sum_{k=1}^{i-2} n_k n_{i-1-k}.$$

Table 5.1 The average density $<\rho>$, the average size of a cluster $<i>$, and the average size of an avalanche $<w>$ for simulation results, quasi-equilibrium model and percolation model

	Simulation results	Q-Equilibrium model	Percolation model
$<\rho>$	0.3075	0.308	1/3
$<i>$	1.5974	1.597	3/2
$<w>$	2.2487	2.252	2

Using the identity

$$\sum_{i\geq 3}\sum_{k=1}^{i-2} n_k n_{i-1-k} = (n_1 + n_2 + \ldots)^2 = n^2$$

the above formula reduces to

$$N\sum_{i\geq 1} i n_i = 3n_1 - n_1^0 \quad \text{or} \quad n_1 = \frac{1}{3}(N\rho + n_1^0).$$

Comparing with the equation for n_1 we obtain the following constraint

$$2n = N(1-2\rho). \tag{5.10}$$

Note that from equations (5.1), (5.2) and (5.4) it follows that n/N, ρ, and $\rho\langle w\rangle$ can be interpreted as the zeroth ($m_0 = \frac{1}{N}\sum n_i$), the first ($m_1 = \frac{1}{N}\sum i n_i$) and the second ($m_2 = \frac{1}{N}\sum i^2 n_i$) moment of the distribution of n_i respectively. The balance equation (5.5) is a relation between the first and the second moment. Equation (5.10) relates the zero and the first moment. Thus, relations between moments can be written as

$$m_1 = \frac{1}{2} - m_0, \tag{5.11}$$

$$m_2 = \frac{1}{2} + m_0. \tag{5.12}$$

An average size of the cluster $<i>$ is given by the relation $<i> = \frac{N\rho}{n}$, and from equation (5.10) we get

$$<i> = \frac{2\rho}{(1-2\rho)}. \tag{5.13}$$

An average size of the avalanche $<w>$ is given by

$$<w> = \frac{1}{\rho N}\sum_{i\geq 1} n_i i^2 = \frac{1-\rho}{\rho}. \tag{5.14}$$

These formulas are well consistent with the numerical data as presented in Table 5.1.

In the set of equations, the variables n_1 and n_2 are treated in a slightly different way from the others n_i, i.e., where $i \geq 3$. This fact and the form of equation (5.9) suggest using the following formula

$$n_i = ke^{-i\gamma} \quad \text{for} \quad i = 3, 4, \ldots, \tag{5.15}$$

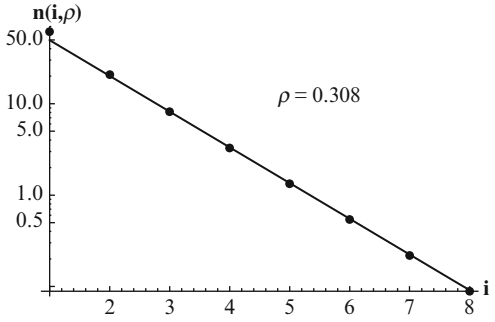

Fig. 5.3 Values of n_i from the equilibrium model (dots) compared to the approximation $ke^{-i\gamma}$

where k and γ are some constants. After substitution to equation (5.9), for $i \geq 6$ one gets

$$e^{-\gamma} = \frac{1}{i+2}\left(2c + \frac{1-c}{n}(2n_1 e^{-\gamma} + 2n_2 e^{-2\gamma} + k(i-6))\right),$$

where $c = (1 - \frac{n_1^0}{n})$. (For $3 \leq i \leq 5$ there are different coefficients at n_1 and n_2.) For a big n one obtains

$$e^{-\gamma} \approx \frac{k}{n}(1-c) = \frac{kn_1^0}{n^2},$$

or simply

$$n_i \approx k(\frac{kn_1^0}{n^2})^i. \tag{5.16}$$

It strongly resembles percolation dependence for n_i. The value of k can be found from equation (5.1)

$$n = n_1 + n_2 + k\sum_{i\geq 3} e^{-i\gamma} = n_1 + n_2 + k\frac{e^{-3\gamma}}{1-e^{-\gamma}}.$$

In our case *N=500*, which gives $k \approx 122$. The approximation is surprisingly good even for n_2, as shown in Figure 5.3.

5.4 Summary and discussion

The proposed random domino cellular automaton exhibits a nice mathematical structure. As presented above, it is possible to derive from first principles (elementary combinatorics) the set of equations (5.3) and (5.7)–(5.9) exactly describing

the average values of the parameters of the model. These equations are highly nonlinear, but without neglecting any terms, we derive formulas for an average cluster size (5.13) and average avalanche size (5.14) in the model. Moreover, we find an approximation formula (5.16), which displays intimate relation to the percolation. Thus, our approach may be a substantial improvement of the other percolation models as it proved to be here.

Another remarkable property of our system are relations between moments of the distribution of n_i. Equations (5.11) and (5.12) are of very simple and symmetric form. They suggest it is possible to classify models according to the number of moments (of successive orders) related to each other. For example, the domino automaton has three moments related by two equations. In case of models with generating function, it corresponds to the order of differential equation satisfied by the generating function. Also, it is interesting to study relevance of a generating function in our model.

The agreement with numerical data is evident, as already shown in Table 5.1. Moreover, the theoretical formulas derived for the quasi-equilibrium state (and thus characterized by the fixed value of density) look also valid when considered as a function of density even quite far from the average value. To display this property, we perform the following simulations. After each avalanche, apart from calculation of density $\rho(k)$, we calculate the number of clusters of succeeding sizes. Then, after the cycle of $n = 60\,000$ avalanches, we group the clusters in classes with the same ρ and in each class we find average of succeeding cluster sizes. In this way we obtain values of function $n(i, \rho)$, where cluster sizes $i = 1, 2, \ldots, 13$ and $\rho \in (0.2, 0.4)$. Three graphs of function $n(i)$ for three chosen values of ρ (i.e., equilibrium density $\rho = 0.308$, and two quite extreme values: $\rho = 0.256$ and $\rho = 0.398$) are presented in Figure 5.4. Simulation data (points) and analytical formulas (continuous line) are in a very good agreement even for extreme values of ρ. A scattering for bigger values of i may be a result of smaller number of data for these values of ρ (see Fig. 5.1). Geometric size distribution $n(i) = (1-\rho)^2\rho^i$- resulting from 1-D percolation model and represented by dashed line - differs more significantly from simulation data. The fourth plot in Figure 5.4 shows that the cumulative value of $n_i = \sum_{\rho} n(i, \rho)$ does not differ much from $n(i, \rho)$ selected for the average value of ρ.

The above reasoning leads to the following argument related to possible experimental verification of the model. Notice the equations of the model use the fixed average values, defined for quasi-equilibrium state. To apply these relations to observed data, one should restrict to the data from the region in which the actual density is equal, or at least close to, the value of the average density. Hence to select proper data one needs to know the actual microscopic state of the automaton. Such a procedure is possible in simulation, but not in an experiment. Thus, the very small differences $|d(i)|$ between cumulative and equilibrium values of n_i suggest that variables in obtained equations can be approximated by cumulative values, which can be collected without bothering of which density they are related to. Therefore, unselected experimental data can be used for a test to find out if they obey relations of the model or not.

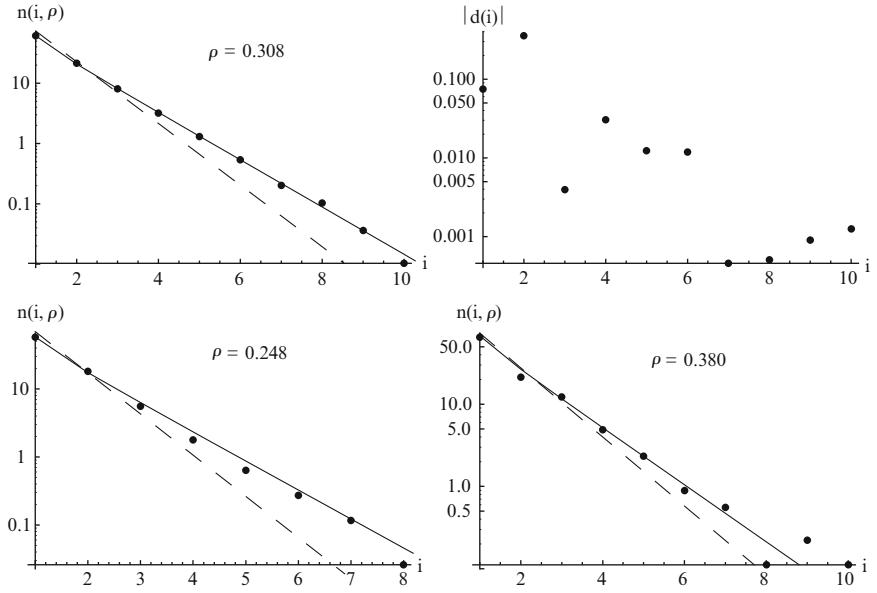

Fig. 5.4 The numbers of clusters $n(i, \rho)$ for size i for three chosen densities ρ: the equilibrium $\rho = 0.308$ and two quite extreme values $\rho = 0.248$ and $\rho = 0.380$. The top right panel shows difference $|d(i)|$ between $n(i,\rho)$ in equilibrium case and cumulative n_i for all densities. Dots represent simulation data (selected for the given density), solid line - formulas for the equilibrium model and dashed line - percolation model

The proposed random domino cellular automaton is an extremely simplified model of earthquakes and there is no surprise it does not give deep insight into them. However, the presented method of analysis may lead to substantial improvement in constructing and understanding models of various natural phenomena. The advantage of the model is its transparent description without neglecting higher terms and other approximations. The exact formulas can serve as a basis for testing more complicated ideas like some application of the Ito equation to geophysics (see the next chapter in this monograph).

Last but not least, we enumerate few straightforward generalizations. Each element of the presented automaton - including the incidence rule - can be subjected to various modifications. To be more specific, one can consider different geometry of the array (for example, a tree shaped like Bethe lattice or any in bigger dimension), different capacities of cells and different kinds of blocks (particles) can be distributed to the system. Also there are many kinds of dependence of energy release threshold (on space position, on states of cells in a neighbourhood etc.) just to mention few ideas. We leave these possibilities for further investigations.

Acknowledgement This work is supported by the project INTAS 05-1000008-7889.

References

Białecki M. and A. Doliwa, 2005, *Algebro-geometric solution of the dKP equation over a finite field out of a hyperelliptic curve*. Commun. Math. Phys., 253:157-170.

Białecki M., *On discrete Sato-like theory with some specializations for finite fields (Recent Trends in Integrable Systems)*, 2009, RIMS Kokyuroku, 1650:154-161.

Białecki M. and Z. Czechowski. In preparation, 2010.

Chopard B. and M.Droz, 2005, *Cellular Automata Modeling of Physical Systems*. Cambridge University Press.

Czechowski Z., 2003, *The privilege as the cause of power distributions in geophysics*. Geophys. J. Int., 154:754-766.

Czechowski Z. and A. Rozmarynowska, 2008, *The importance of the privilege for appearance of inverse-power solutions in Ito equations*. Physica A, 387:5403-5416.

Stauffer D. and A. Aharony, 1992, *Introduction to Percolation Theory*. Taylor & Francis.

Tejedor A., S. Ambroj, J. B. Gomez, and A. F. Pacheco, 2008, *Predictability of the large relaxations in a cellular automaton model*. J. Phys. A: Math. Theor, 41:375102 (16pp).

Tokihiro T., *Ultradiscrete Systems (Cellular Automata),* 2004, In B.Grammaticos, T.Kosmann-Schwarzbach and T.Tamizhmani, editors, *Discrete integrable systems*, volume 644 of Lecture Notes in Physics, pages 383-424. Springer-Verlag.

Chapter 6
Ito Equations as Macroscopic Stochastic Models of Geophysical Phenomena – Construction of the Models on the Basis of Time Series

Z. Czechowski and M. Białecki

6.1 Introduction

Stochastic processes are commonly used to build macroscopic phenomenological models of physical, geophysical, biological or economical systems. Earthquakes are particularly predestinated to be described by stochastic processes. Occurring in the crust, mechanisms which generate events are very complex and inaccessible for a direct observation. We can register only some external phenomena such as seismic waves, surface deformations or other indirect effects. However, the construction of adequate macroscopic models (stochastic processes) describing observable phenomena may help in understanding the intrinsic processes on the microscopic level (i.e., the physical model of seismic source) and then in analysing of such effects as synchronization or triggering.

Ordinarily, the microscopic description of the phenomenon can be given by a system of nonlinear differential equations or, in computer simulations, by some rules which govern the microscopic evolution of the model. Some simple stochastic input may be included in both approaches.

The microscopic model may be a system of many degrees of freedom; however, in many cases its macroscopic behaviour is characterized by one or two dominative modes. Such a macroscopic variable (variables) can be given, for example, by an average of some function of microscopic variables or even by a predominant (or that which can be observed in practice) microscopic variable itself.

Therefore, a behaviour of the macroscopic variable may be governed by the mixed stochastic process with additive/multiplicative fluctuations. Starting from a microscopic description, these fluctuations arise from the elimination of the irrelevant degrees of freedom in favor of a small number of macroscopic variables.

Z. Czechowski (✉) and M. Białecki
Institute of Geophysics, Polish Academy of Sciences, Księcia Janusza 64, 01-452, Warsaw, Poland
e-mail: zczech@igf.edu.pl; mbiałecki@igf.edu.pl

V. de Rubeis et al. (eds.), *Synchronization and Triggering: from Fracture to Earthquake Processes*, GeoPlanet: Earth and Planetary Sciences 1,
DOI 10.1007/978-3-642-12300-9_6,

The form and parameters of the macroscopic stochastic equation are determined by the complex action of intrinsic degrees of freedom on the evolution of the macroscopic variable.

The modeling of phenomena which have stochastic features can be performed by using:

- linear stochastic models, e.g., ARMA, etc. . ., (Markov of order m),
- nonlinear deterministic models which lead to a deterministic chaos,
- nonlinear stochastic models, e.g., Ito, Fokker-Planck (Markov of order 1).

Physical systems (isolated) may be described by the Markov process, then all microscopic variables comprise the vector y. Moreover, for some systems the reduction in dimensionality can be performed and then the process is approximately Markovian (on the macroscopic level).

Here, we consider only scalar stochastic processes and we assume that they can be approximated by diffusive Markov processes.

One-dimensional diffusive Markov process $Y(t)$ is governed by the Ito stochastic differential equation [e.g. Oksendal 1998]

$$dy = a(y)dt + \sqrt{b(y)dW(t)}, \tag{6.1}$$

where $a(y)$ and $b(y)$ are known to be the drift and diffusion coefficients, respectively, and $W(t)$ is the Wiener process. The transition probability density of $Y(t)$, denoted by $p(y,t) = P(y, t|y_{t\text{-}dt}, t\text{-}dt)$, is governed by the Fokker-Planck equation [e.g. Risken 1996]

$$\frac{\partial}{\partial t}p(y,t) = -\frac{\partial}{\partial y}[a(y)p(y,t)] + \frac{1}{2}\frac{\partial^2}{\partial y^2}[b(y)p(y,t)]. \tag{6.2}$$

Physical interpretation of the Ito equation is simple: it is the modified diffusion in the potential niche. Classical diffusion described by the term $\sqrt{b}dW(t)$ (additive fluctuation) can be modified by the dependence on the current value of y, i.e., $\sqrt{b(y)}dW(t)$ (multiplicative fluctuation). The potential $V(y)$ is given by the drift term, $V'(y) = -a(y)$. The shape and slope of the potential niche $V(y)$ and the strength of the stochastic force $\sqrt{b(y)}dW(t)$ are an average effect of intrinsic interactions in the microscopic level and of boundary conditions.

The histogram method [Siegert et al. 1998] of reconstruction of the Ito equation from the time series data was tested successfully by their authors in cases of time series generated by Ito equations only. However, for real, geophysical time series the question arises whether the resulting Ito equation (in which both terms have simple physical interpretations) is physically adequate to the phenomenon under investigation [Czechowski and Rozmarynowska 2008, Rozmarynowska 2009].

The aim of the paper is to show that Ito equations may constitute quite good macroscopic models of phenomena (where y is the variable which is measured) in

which microscopic interactions are averaged in an adequate way. Then, the three important questions arise:

1. How does the microscopic working of a model determine forms of functions *a(y)* and *b(y)* in the related Ito equation?
2. Can we extract from the form of the Ito equation any conclusions concerning microscopic aspects of the phenomena?
3. Can an unknown process be reliably described by 1-D Ito model?

In order to answer the first question we investigate (in Section 6.2) simple microscopic toy models, whose full evolution is observed during computer simulation. We choose some quantity in the model, which may be interesting for an outer observer and we register its fluctuation as a time series. By using the histogram method of reconstruction of the Ito equation on the basis of time series we obtain adequate drift and diffusion terms.

Section 6.3 includes some answer to the second question. For the case of geophysical time series we construct the Ito equation. An analysis of functions *a(y)* and *b(y)* leads to some interesting conclusions concerning some microscopic features of the phenomena.

In order to answer the third question, a simpler problem (in Section 6.4) is considered: a geophysical phenomenon is replaced (modeled) by a simple cellular automaton. The evolution of the model leads to the time series of some variable, which is interesting for the observer. The aim is to derive **analytically**, on the basis of automaton rules, the stochastic Ito equation for the variable and to compare the equation with that reconstructed by the histogram method from time series generated by the cellular automaton.

In Section 6.5 two examples of the stochastic control are analyzed.

6.2 What do *a(y)* and *b(y)* consist of?

We are going to check how the microscopic working of a model determines forms of functions *a(y)* and *b(y)* in the related Ito equation. In order to do it we construct toy models whose working is simple and stationary. Then we choose some quantity *y* which may be considered as a macroscopic observable. The toy model generates the time series for this quantity. Next we use the histogram method to construct functions *a(y)* and *b(y)* in the Ito equation. Because we can follow the microscopic working of the model in detail, we may try to link it to the macroscopic behaviour of drift and diffusion terms.

1. Random replacing of black and white cells on 2-D array

The model (we follow our paper, Czechowski and Rozmarynowska 2008) aims at demonstration how the potential arises during the purely random process. We start from a state of a square array (*LxL* cells) in which black (occupied) and

white (empty) cells are randomly distributed. Then we fix an integer value k, which is smaller than number L^2 of all cells in the array. At each step of time evolution, two integers n_1 and n_2 are randomly drawn from the interval $[0, k]$. Next, we define the state replacing procedure. Two individuals jump by turns randomly on the array. The first changes black cells on white (but white leaves white), the second white on black (but black leaves black). The first jumps n_1 times, the second n_2 times. After the step of the procedure we count the number of black cells on the grid (see Fig. 6.1) – this is the first x_1 in our time series. We repeat the procedure N times to complete the time series $x_1, x_2, \ldots, x_N$. The transformed time series (see Fig. 6.1)

$$y_i = \frac{x_i}{L^2} - \frac{1}{2} \tag{6.3}$$

is analyzed. The histogram procedure calculates histograms of joint and stationary distribution functions (Fig. 6.2) and leads to drift and diffusion functions in the form of

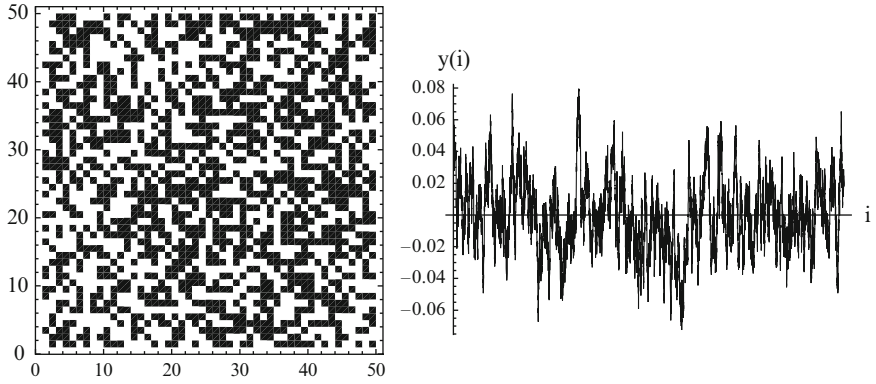

Fig. 6.1 The toy model 1: an example of the array state (left), time series resulting from the evolution of the model, $N = 10000$

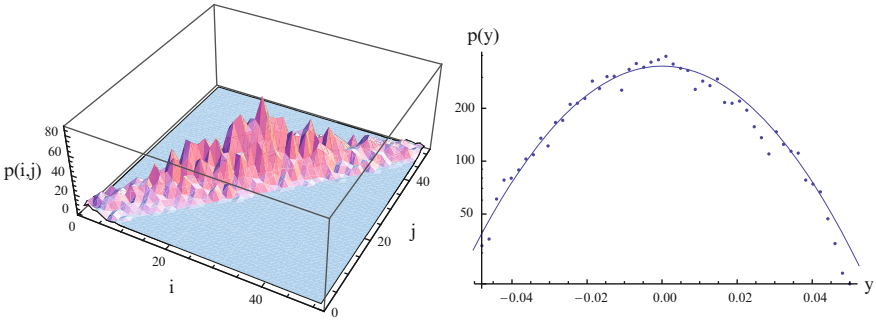

Fig. 6.2 Histograms *p(i,j)* (left) and *p(i)* (right) constructed from the time series (Fig. 6.1), line – Gaussian fit

clouds of points (resulting from these histograms). We can see from Fig. 6.3 that *a(y)* may be approximated by the decreasing linear function $a(y) = -2.8423y$ and *b(y)* by the constant $b = 0.0019$.

It can be shown that the drift *a(y)* (or the potential $V(y) = 1.4217y^2$) does not result from any external forces in the model but rather from the limitation of size of the array. This resembles the Ehrenfest urn model [e.g. Feller 1966]. Fig. 6.4 shows that when the size of the array is increasing, $L = 50$, 100, 150, then the drift force diminishes and the niche of potential is shallowing. Of course, the same effect may be obtained for the fixed array ($L = 50$) and decreasing parameter k, $k = 2500$, 1000, 500, 200 and 50 (see Fig. 6.4). Fig. 6.5 explains this behaviour: for a small array ($L = 50$) and for $k = 50$ random variables do not diffuse too far from the average value and the process resembles the Rayleigh particle walk. However, for a big array ($L = 150$) distant excursions are possible, because then there is a greater probability of creation of new areas with the same cell states, in comparison with the previous step of the evolution procedure. Then the process resembles the random walk (see Fig. 6.5c) but it is stationary. With $L \to \infty$ the process tends to the non-stationary random walk.

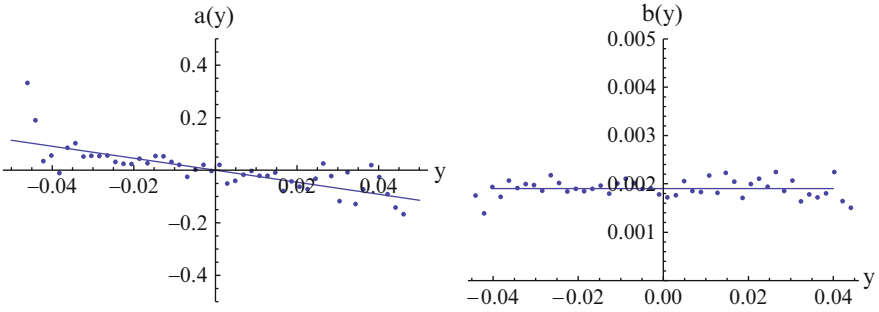

Fig. 6.3 Illustration of coefficients *a(y)* and *b(y)* calculated (points) by the histogram method from the time series (Fig. 6.1). Lines present fitted functions: $a(y) = -2.8423y$ and $b(y) = 0.0019$

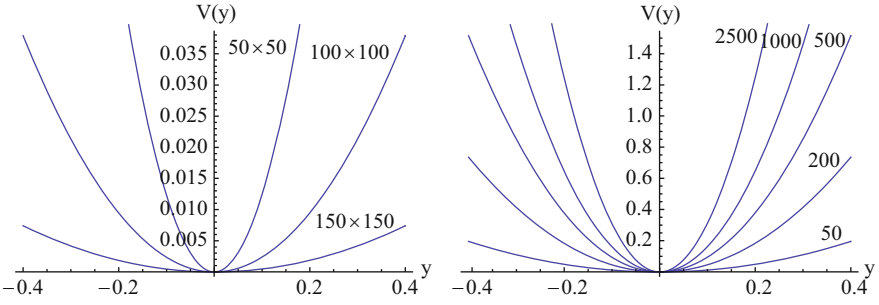

Fig. 6.4 Potential niches: left - for increasing array size: *50x50*, *100x100* and *150x150* with assumed parameter $k = 50$ for each case, right - for increasing parameter $k = 50$, 200, 500, 1000, and 2500 for the fixed array size *50x50*

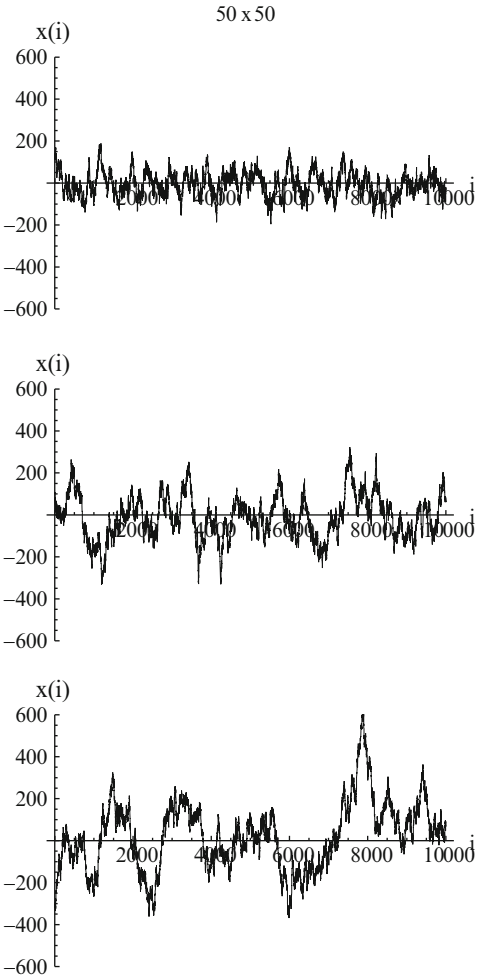

Fig. 6.5 Comparison of three time series for three array sizes (*50x50*, *100x100* and *150x150*) with assumed parameter $k = 50$ for each case

2. Evolution of "forests"

The second, more complex model described the evolution of "forests". We constructed the model in such a way in order to demonstrate how multiplicative fluctuations may be generated [see Czechowski and Rozmarynowska 2008].

We put the initial state of the array in the form of large primaeval forest (see Fig. 6.6). Next we assume the two competitive processes:

– a random number $r_1 \in$ [0, current perimeter size] of new trees (black cells) grows only on the perimeter of forests,
– a random number $r_2 \in$ [0, current number of trees] of trees disappears in random places in forests.

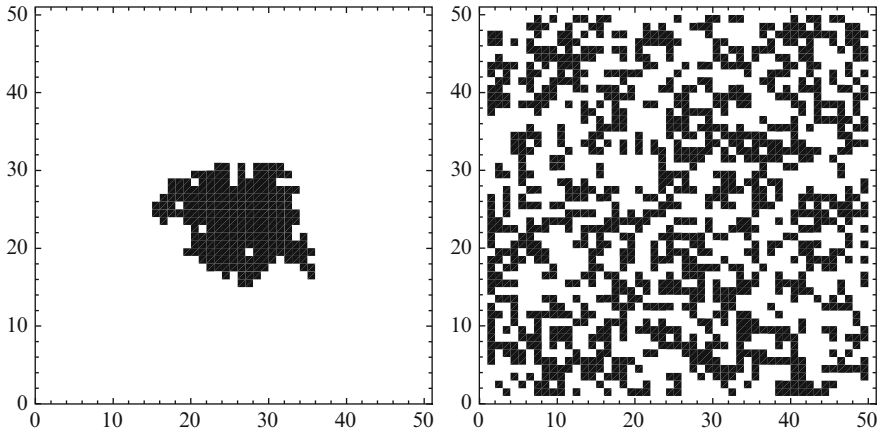

Fig. 6.6 The toy model 2: left – initial state ("primaeval forest") of the array, right – an example of the array state during stationary evolution stage of the model

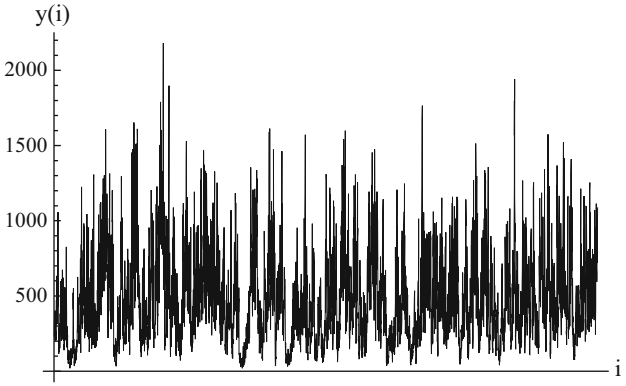

Fig. 6.7 Time series generated by the toy model 2 (oscillation of number of trees – black squares)

After each step including the two processes the number of black cells *y(i)* (the surface of forests) is calculated. The process becomes stationary (see the state of the array in Fig. 6.6 and the time series in Fig. 6.7) after an initial stage.

The time series is analyzed by the histogram procedure, and we obtain interesting forms of functions *a(y)* and *b(y)* (see Fig. 6.8), the fitted polynomials are as follows:

$$a(y) = 4255 - 7.95y + 0.053y^2 - 0.0001y^3 + 3.67 \cdot 10^{-8}y^4, \tag{6.4}$$

$$b(y) = 3145y + 7.098y^2. \tag{6.5}$$

The potential niche is presented in Fig. 6.9. Here, the drift force *a(y)* contains, apart of the influence of the array size, an average effect of the two competitive

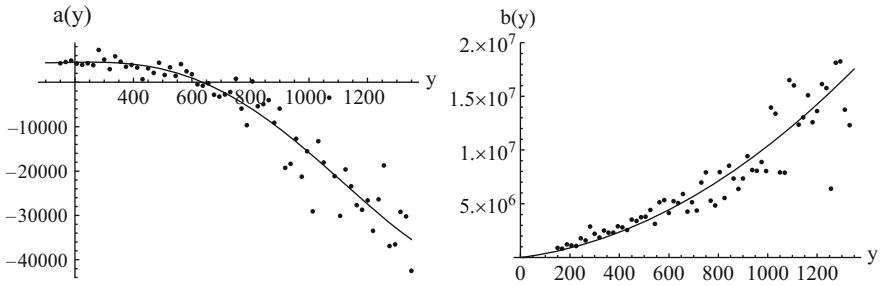

Fig. 6.8 Graphs of functions *a(y)* and *b(y)* for the toy model 2. Points – calculation from the time series, line – nonlinear fit: $a(y) = 4255 - 7.95y + 0.053y^2 - 0.0001y^3 + 3.67*10^{-8}y^4$, $b(y) = 3145y + 7.098y^2$

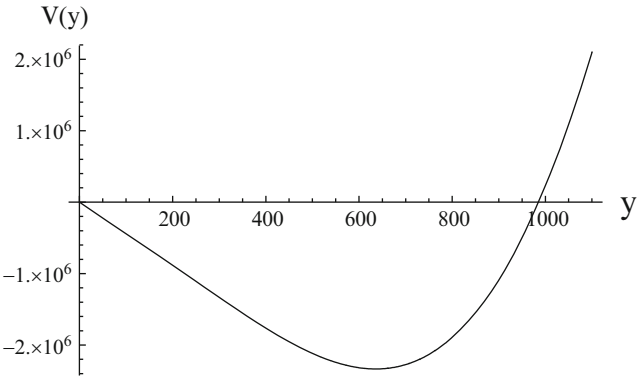

Fig. 6.9 Potential *V(y)* for the toy model 2

processes. The diffusion term is dependent on the state of array, *b(y)* is a square increasing function. The question is why random jumps, $\sqrt{b(y)}dW(t)$, are longer (in average) for a greater surface of forests. The appropriate construction of the toy model let us to give a simple answer: then r_1 and r_2 are chosen from wider ranges (current perimeter size and current number of trees are greater). It should be noted that the perimeter of percolation 2-D cluster is, in average, proportional to the size of the cluster [Stauffer and Aharony 1992].

3. Domino cellular automaton

We construct such a very simple 1-D toy model with avalanches which can be described by analytical equations (see Chapter 5.1 of the monograph). This feature will be useful in Section 6.4. The automaton rules are as follows: particles are added and lost from the 1-D grid (of size *N*) according to the procedure:

– at each step a particle is randomly added to one of the boxes,
– if it hits an empty box it becomes occupied,
– when it hits an occupied box the whole cluster (chain of neighbouring occupied boxes) is lost, i.e., the avalanche appears (see the time series in Fig. 6.10).

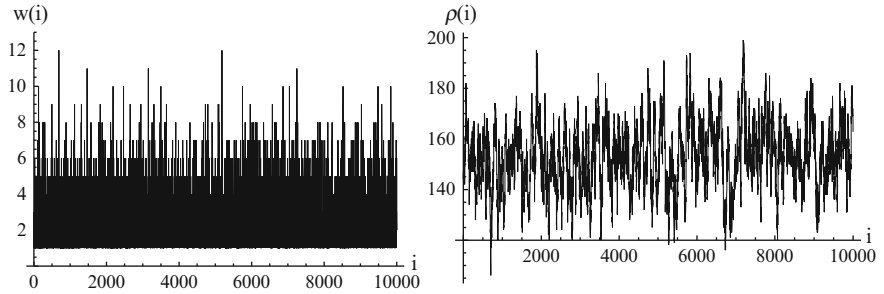

Fig. 6.10 The domino automaton: left – time series for avalanche sizes *w(i)*, right – time series for density *ρ(i)*

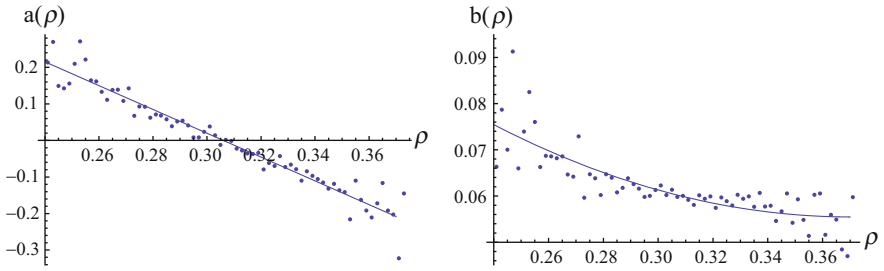

Fig. 6.11 Graphs of functions *a(y)* and *b(y)* for the domino automaton. Points – calculation from the time series, line – linear and nonlinear fit: $a(y) = 1 - 3.25y$, $b(y) = 0.22 - 0.87y + 1.17y^2$

However here, not avalanche sizes *w(i)*, but the density *ρ(i)* of occupied cells on the grid (calculated **after each avalanche**) is considered (see the time series in Fig. 6.10).

By using the histogram method we obtain adequate drift and diffusion terms (see Fig. 6.11). The drift function is a linear decreasing function as in the above-mentioned model of random replacing of black and white cells on 2-D array. The diffusion function *b(ρ)* is not a quadratic increasing function (as in the forest evolution toy model) but has a nonlinear decreasing shape.

Microscopic interpretation of these two functions is not simple. However, it can be shown that here the potential *V(ρ)* is not a result of the limitation of the array size (as in the above-mentioned random color replacing model), but arises from microscopic rules of the automaton. The left potential wall appears because for ρ smaller than ρ_{eq} creating of new occupied boxes is more probable than starting a big avalanche (so the effect of repulsive force, in direction towards the right, appears). Similarly, the right potential wall can be explained by the fact that for big ρ the probability of triggering an avalanche prevails over the tendency of increasing ρ (the repulsive force to the left).

The size of diffusion jumps $\sqrt{b(\rho)}dW(t)$ is dependent on the density ρ, but in the region $\rho_{eq} < \rho < 0.4$ the function *b(ρ)* is nearly constant. Greater jumps for $\rho < \rho_{eq}$

(the smaller the ρ the larger the jumps) mean that the randomness has a greater influence on evolution in this region. However, the effective jumps will be executed on the right (in average) because of prevailing influence of the potential left wall.

The analysis of the simple domino cellular automaton is a good initial point for investigation of the avalanche time series (Fig. 6.10). Unfortunately, microscopic interpretation of the avalanche behaviour is much more difficult because the avalanche size is a complicated function of the array state and we can not join the current avalanche with the previous one. Therefore, the choice of density ρ as an observable was more appropriate for a microscopic interpretation. Here we restrict our investigation of avalanches to extraction of the stationary probability and functions *a(y)* and *b(y)* from the time series.

The stationary probability (Fig. 6.12, top line) may be approximated by the exponential distribution (for $i > 1$). The function *a(y)* is a linear function (Fig. 6.12, top line) and the function *b(y)* is an increasing (for $y > 1$) nonlinear function which may be approximated by the polynomial $b(y) = 216 + 27.8y + 6y^2 + 6.2y^3$.

It is interesting to compare the results with that for the cellular automaton on the Bethe lattice and the Bak-Tang-Wiesenfield (BTW, see Bak et al. 1988) cellular automaton. For the three automata we observe similar behaviour (see Fig. 6.12): *a(y)* are linear decreasing functions, *b(y)* are nonlinear (square) increasing functions for larger y. The substantial difference is that for Bethe CA and BTW CA the stationary distribution function has an inverse-power (not exponential) form (in its central part).

6.3 Extracting microscopic information from *a(y)* and *b(y)*

In Section 6.2 we have shown that it is possible to construct such a toy model which gives required characteristics of drift and diffusion function in the (re)constructed (from the time series generated by the toy model) Ito equation. Here we will try to discuss the opposite problem: can we deduce information about the microscopic behaviour of the process from the forms of functions *a(y)* and *b(y)*? The problem is difficult, the knowledge of these functions (and of course the stationary distribution function and the transition distribution function) contains only averaged properties of the system.

We are going to extract some information from the geophysical time series (see Fig. 6.13): daily mean aerosol optical depths measured at wavelength 320 nm by the Brewer spectrometer in the period 1992-1996 at Belsk Geophysical Observatory (Poland) – summer seasons (Jarosławski et al. 2003).

By using the histogram method we obtain clouds of points (and fitted functions) which illustrate *p(y)*, *a(y)* and *b(y)* (see Figs. 6.13 and 6.14). We can divide the range of y on two limits. For $y < 0.4$, *b(y)* is nearly constant and *a(y)* is a decreasing linear function; this leads to the Gaussian stationary solution (see Table 1 in Czechowski and Rozmarynowska 2008). In the second region, for $y > 0.4$, *b(y)* becomes a square increasing function, therefore the exponential tail of the stationary distribution appears (Fig. 6.13). In the Gaussian regime there are additive

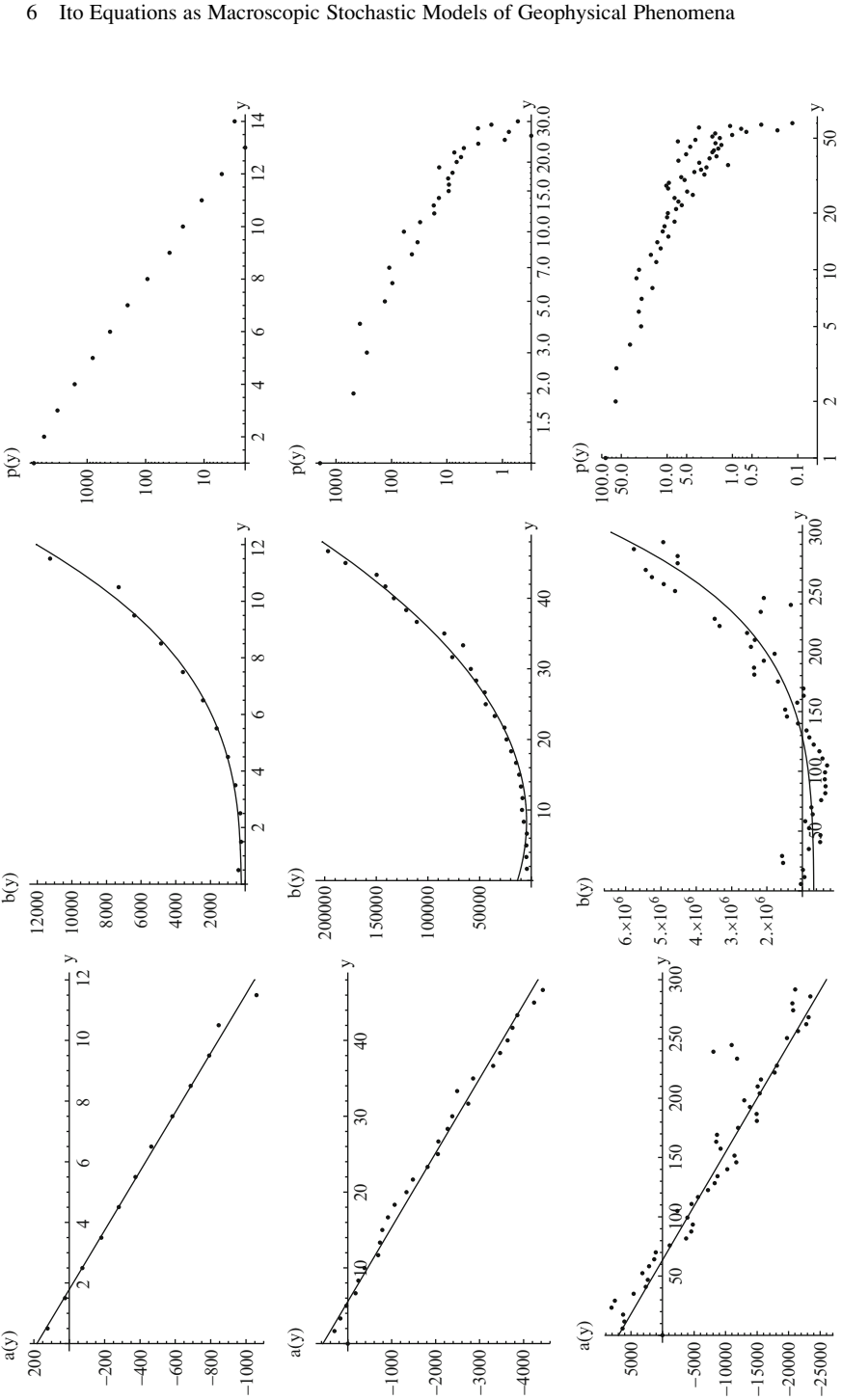

Fig. 6.12 Comparison of functions $a(y)$, $b(y)$ and $p(y)$ for avalanches for three cellular automata: top line – domino automaton, middle line – Bethe CA, bottom line – BTW CA. The top graph for $p(y)$ is in linear-log scale, two lower are in log-log scale

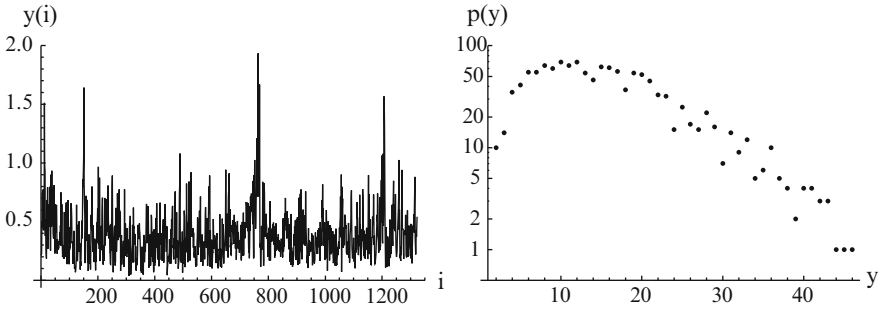

Fig. 6.13 Left - daily mean aerosol optical depths time series measured at wavelength 320 nm in period 1992–2006 at Belsk (only summer seasons: months April–September). Right - the stationary distribution function *p(y)* for daily mean aerosol optical depths time series

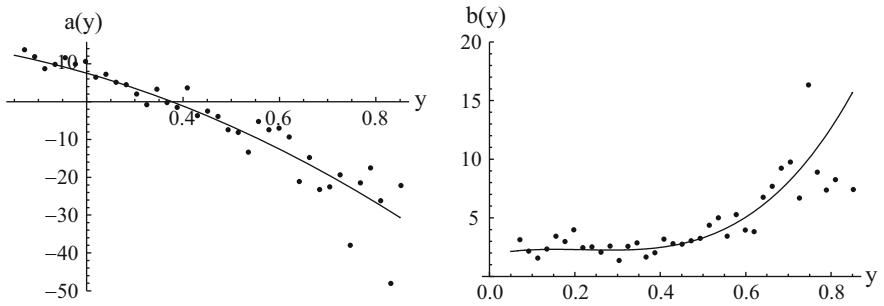

Fig. 6.14 Graphs of functions *a(y)* and *b(y)* for the aerosol optical depths. Points – calculation from the time series (Fig. 6.13), line – nonlinear fit: $a(y) = 13.5 - 23y - 34y^2$, $b(y) = 2.2 - 36.5(y - 0.1)^2 + 55.4y^3$

fluctuations and the process of daily mean aerosol optical depths change is the Ornstein-Uhlenbeck process. However, in the exponential regime a new mechanism appears, and there are multiplicative fluctuations, which are increasing with the current state *y*. Therefore, the process might be described by the modified domino cellular automaton (compare Fig. 6.14 with Fig. 6.12): avalanches are a manifestation of daily mean aerosol optical depths; the modification is that in the Gaussian regime probability of hit a cluster will not depend on the cluster size. The example shows that there are some prospects, but the topics needs further development in specific case studies.

6.4 Analytical derivation of *a(y)* and *b(y)*

In Sections 6.2 and 6.3 we have used the histogram method to construct Ito equations on the basis of time series. We have assumed silently that this macroscopic description is valid in these cases, i.e, that the processes might be approximated by the one-dimensional, Markov diffusion process. However, some of these

models (phenomena) have been complex systems with few or more degrees of freedom, so we are not sure if we are allowed to construct the Ito equation as a reliable macroscopic model. Of course, it is very difficult to solve this problem in general. However, it would be useful to derive analytically the Ito equation for a case of simple cellular automaton.

Just to this aim we introduced the domino model (Section 6.2 and Chapter 5.1 of this monograph). We assumed a quite natural convention in the model: what provokes us to investigate the lattice state are avalanches; therefore, we monitor avalanche sizes and the density ρ of occupied cells in the lattice after each avalanche. According to our convention the effective change of ρ is a result of growth of ρ in unit steps before an avalanche starts, and a drop of ρ in the avalanche.

Let us derive the probability *EG(k)* of effective gain (an increase by k boxes) of the number of occupied boxes calculated immediately after an avalanche:

$$EG(k) \equiv P\left(\rho_i + \frac{k}{N}, i+1 | \rho_i, i\right) = \sum_{s=k+1}^{\infty} (1-\rho)^s \cdot \rho \cdot w_{s-k}(\rho), \tag{6.6}$$

where *(1- ρ)*^{s} is the probability of hit one after the other of s empty boxes, ρ is the probability of hit of an occupied box in the next step, and $w_{s\text{-}k}(\rho)$ is the probability that this occupied box is a part of the cluster of size s-k.

Similarly, we can derive the probability of effective loss *EL(k)*:

$$EL(k) \equiv P\left(\rho_i - \frac{k}{N}, i+1 | \rho_i, i\right) = \sum_{s=k}^{\infty} (1-\rho)^{s-k} \cdot \rho \cdot w_s(\rho), \tag{6.7}$$

where the size of avalanche excels step gains before the avalanche. Due to the basic assumption in the model that a hit of any occupied box belonging to a cluster of size s triggers the avalanche of size s, we have

$$\rho \cdot w_s(\rho) = s \cdot n_s(\rho), \tag{6.8}$$

where $n_s(\rho)$ is the number of s-clusters per lattice site (i.e. divided by N).

Formulas for probabilities *EG(k)* and *EL(k)* allow us to calculate the transfer probability $P(\tilde{y}, t+\tau; y, t)$ needed in expressions for *a(y)* and *b(y)* (see Risken 1996):

$$a[y(t)] = \lim_{\tau \to 0} \int_{-\infty}^{\infty} \frac{1}{\tau} [\tilde{y}(t+\tau) - y] P(\tilde{y}, t+\tau | y, t) d\tilde{y}, \tag{6.9}$$

$$b[y(t)] = \lim_{\tau \to 0} \int_{-\infty}^{\infty} \frac{1}{\tau} [\tilde{y}(t+\tau) - y][\tilde{y}(t+\tau) - y] P(\tilde{y}, t+\tau | y, t) d\tilde{y}, \tag{6.10}$$

where $\tilde{y}(t+\tau)$ is the solution of the Ito equation after time τ (when the initial condition in time t is $\tilde{y}(t) = y(t)$) and $P(\tilde{y}, t+\tau | y, t)$ is the conditional distribution

function. The distribution function is approximated by using histograms of joint distribution function $P(\tilde{y}, t+\tau; y, t)$ and of stationary distribution function $P(y, t)$ according to the formula

$$P(\tilde{y}, t+\tau|y, t) = \frac{P(\tilde{y}, t+\tau; y, t)}{P(y, t)}. \tag{6.11}$$

Here we replace the integrals in (6.9) and (6.10) by sums and we omit limits. The time increment τ refers to the time step in time series. Therefore:

$$a(\rho) = \frac{u}{\tau}\left\langle \frac{k}{N} \right\rangle = \frac{u}{\tau}\sum_{k=1}^{\infty}\left[P\left(\rho_i + \frac{k}{N}, i+1|\rho_i, i\right) - P\left(\rho_i - \frac{k}{N}, i+1|\rho_i, i\right)\right]\frac{k}{N}, \tag{6.12}$$

$$\begin{aligned} b(\rho) &= \frac{u^2}{\tau}\left\langle \left(\frac{k}{N}\right)^2 \right\rangle \\ &= \frac{u^2}{\tau}\sum_{k=1}^{\infty}\left[P\left(\rho_i + \frac{k}{N}, i+1|\rho_i, i\right) + P\left(\rho_i - \frac{k}{N}, i+1|\rho_i, i\right)\right]\left(\frac{k}{N}\right)^2, \end{aligned} \tag{6.13}$$

where $u = 1/N$. However, in formulas (6.6) and (6.7) with (6.8) we need an evident expression for $n_s(\rho)$. If the automaton was as random as the 1-D percolation model, then $n_s(\rho)$ would have the form [Stauffer and Aharony 1992]:

$$n_s(\rho) = \rho^s \cdot (1-\rho)^2. \tag{6.14}$$

Then, we obtain the following analytical formulas:

$$P\left(\rho_i + \frac{k}{N}, i+1|\rho_i, i\right) = \frac{\rho(1-\rho)^{3-k}}{(1-\rho+\rho^2)^2} \tag{6.15}$$

for $k = 0, 1, 2, \ldots$, and

$$P\left(\rho_i - \frac{k}{N}, i+1|\rho_i, i\right) = \frac{\rho^k(1-\rho)^2(k+\rho-k\rho-\rho^2+k\rho^2)}{(1-\rho+\rho^2)^2} \tag{6.16}$$

for $k = 1, 2, \ldots$. They fulfill the normalization condition:

$$\sum_{k=1}^{\infty}[EG(k) + EL(k)] + EG(0) = 1. \tag{6.17}$$

Then, it is easy to calculate the functions $a(p)$ and $b(p)$:

$$a(\rho) = \frac{1-3\rho}{\rho(1-\rho)}. \tag{6.18}$$

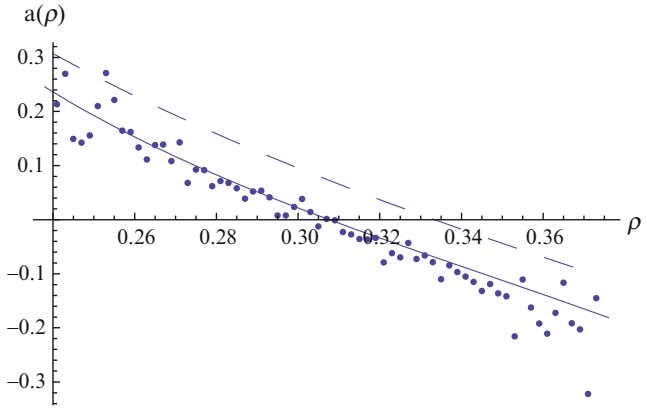

Fig. 6.15 Comparison of analytical formulas for *a(y)* with simulation for the domino automaton. Points – results from the time series, dashed line – percolation approximation (6.18), continuous line – calculation by using analytical recursive expressions (5.7), (5.8) and (5.9)

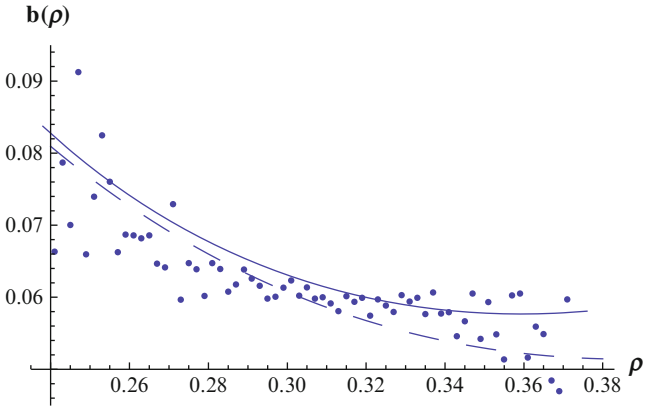

Fig. 6.16 Comparison of analytical formulas for *b(y)* with simulation for the domino automaton. Points – results from the time series, dashed line – percolation approximation (6.19), continuous line – calculation by using analytical recursive expressions (5.7), (5.8) and (5.9)

$$b(\rho) = \frac{2 - 9\rho + 12\rho^2 + \rho^3}{\rho^2(1-\rho)^2}. \tag{6.19}$$

A comparison with simulations (see Section 6.2) shows (see Figs. 6.15 and 6.16) that these functions behave in a similar way but they do not fit to simulation results: the function $a(\rho)$ is shifted upwards, the function $b(\rho)$ decreases too fast.

According to the analysis in Chapter 5.1 we know that we have adopted an improper formula for cluster distribution. Therefore, now we try to use analytical recursive expressions (5.7), (5.8) and (5.9) for $n_i(\rho)$ derived in that chapter. They are exact only in the equilibrium state, but for ρ away of ρ_{eq} there is a reasonable

correspondence between theoretical graphs and simulation data (see Fig. 6.17). Resulting graphs for $a(\rho)$ and $b(\rho)$ are presented in Figs. 6.15 and 6.16 (we do not write exact formulas here because of their great complexity). We observe much

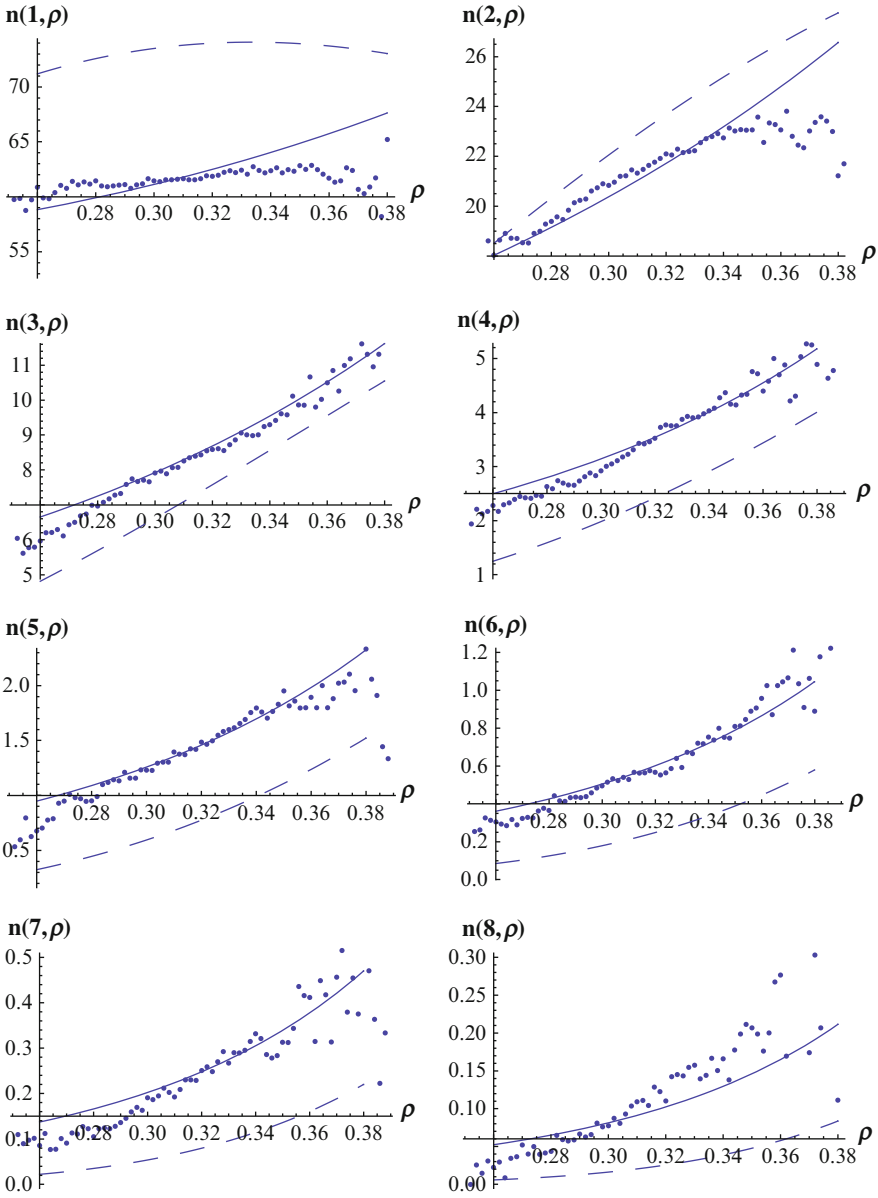

Fig. 6.17 Comparison of analytical formulas for $n(i, \rho)$ where i = 1, 2, . . . , 8, with simulation for the domino automaton. Points – results from simulations, dashed line – percolation approximation (6.14), continuous line – analytical recursive expressions (5.7), (5.8) and (5.9)

better conformability of these graphs (than functions given by the percolation approximation) with a cloud of points (illustrating functions $a(\rho)$ and $b(\rho)$) obtained from time series.

The derivation of the Ito equation for the cellular automaton shows how the complex nonlinear microscopic working of the model can be contained in the two functions $a(\rho)$ and $b(\rho)$ which represent macroscopic (averaged) aspects of the automaton. This result gives a hope that for some other complex systems the Ito models may become good approximate descriptions.

6.5 Stochastic control in Ito models

When we have the appropriate macroscopic stochastic model of the phenomena under investigation then we can study some interesting aspects, as for example the stochastic control or the synchronization. Here we analyze some possibilities of the stochastic control in order to reduce the probability of greater (more dangerous) events. We study the two examples.

1. The process is described by the following Ito equation:

$$dy(t) = \frac{1}{2}(1-2y)\Delta t + \sqrt{y^2}W(t) \tag{6.20}$$

for which (see Table 1 in Czechowski and Rozmarynowska 2008) the stationary solution has the inverse-gamma distribution function (long tail). We would like to introduce a small external force in order to shorten the long tail. The simplest method is to use the small additional white noise term:

$$dy(t) = \frac{1}{2}(1-2y)\Delta t + \sqrt{y^2}W(t) + \varepsilon W_1(t), \tag{6.21}$$

where we assume $\varepsilon = 0.1$. By using the histogram method to time series generated by the two Ito equations we calculate stationary distribution functions. Figure 6.18 shows that even such a simple random small term leads to the essential shortening of the distribution tail.

2. In the second example we try to use the y-dependent control term. The following Ito equation:

$$dy(t) = -\frac{1}{2}(y\log y - y)\Delta t + \sqrt{y^2}W(t) \tag{6.22}$$

has the log-normal stationary distribution (see Table 1 in Czechowski and Rozmarynowska 2008). Modified equation:

$$dy(t) = -\frac{1}{2}(y\log y - y)\Delta t + \sqrt{y^2}W(t) + \varepsilon\sqrt{y}W_1(t) \tag{6.23}$$

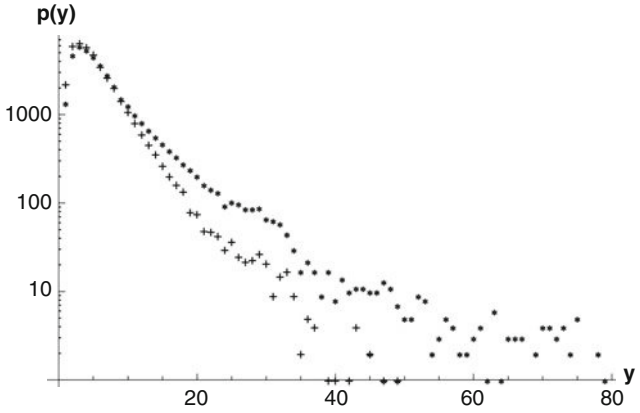

Fig. 6.18 Stationary distribution function p(y): "*" inverse-gamma solution of the equation (6.20), "+" solution of the equation (6.21) with a reduced tail

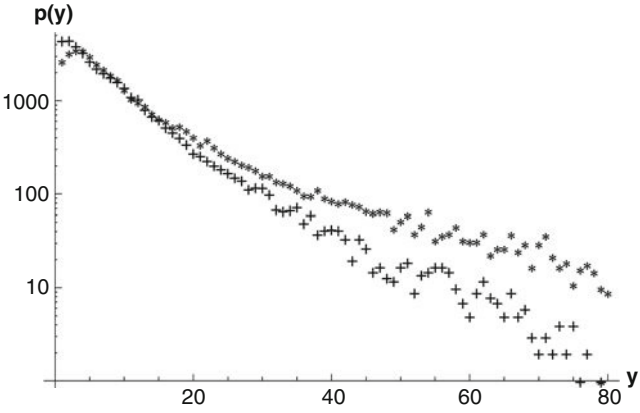

Fig. 6.19 Stationary distribution function p(y): "* " log-normal solution of the equation (6.22), "+" solution of the equation (6.23) with a reduced tail

gives the stationary solution with the reduced tail (see Fig. 6.19, $\varepsilon = 0.1$).

These simple cases show that Ito models and the histogram method are very handy for different uses. The synchronization between two correlated stochastic processes may be investigated by using the vector Ito equation.

6.6 Conclusions

There are two complementary methods of modeling of natural phenomena which in general are hidden but manifest themselves by some observable effects. The first consists creating a detailed deterministic microscopic model based on physical premises. In the second method, we construct the stochastic model describing

macroscopic (or averaged) behaviour of the system. This model uses mainly the information from time series of observable variables. This approach has advantages: what is important is not a detailed model but rather effects which we experience. They are results of collective or competitive interactions of system elements. Therefore, we are interested in external, macroscopic evolution; particularly in some regularities or statistical details which might help us in the prediction or the control.

In this paper we decided that promising stochastic macroscopic models of phenomena are the Ito equations. Therefore, we were checking whether the complex systems (toy models) could be described by the Ito equations and how microscopic working of the model creates the form of drift and diffusion terms. We showed also that, inversely, from the form of the Ito equation some microscopic details of the geophysical phenomenon can be deduced.

The histogram method of construction of Ito equation from time series is simple and effective – it always leads to clouds of points illustrating functions $a(y)$ and $b(y)$. However, the efficiency may be fallacious. It appears that sometimes the time series generated by the constructed Ito equation does not reflect characteristics of the initial time series. This must be caused not by the scattering resulting from too small number of data or from inaccurate fit of polynomials for $a(y)$ and $b(y)$, but rather by the fact that in this case the time series can not be approximated by a diffusion Markov process. For nonlinear processes it is difficult to deduce the Markov property, but it is more difficult to ascertain whether they are diffusion processes. Practically, we can only compare initial and generated time series – if they behave in a similar way, we can state that the time series under investigation may be approximated by the adequate diffusion Markov process.

However, in some simple examples one can try to derive analytically the Ito equation directly from equations or rules defining the model. We succeeded in achieving the purpose in the case of domino cellular automaton. Analytical derivation of the Ito equation for a simple cellular automaton advances the motivation for using the Ito equations in description of external, macroscopic effects generated by complex processes.

Ito equations have simple physical interpretation and compose handy models for studying some interesting aspects, as for example the stochastic control or the synchronization. The additional advantage of Ito models is their relevance to the Fokker-Planck equations which describe the evolution of distribution function of the process. In our opinion this topic deserves further detailed studies.

Acknowledgement The work was supported by INTAS 05-1000008-7889 and by Ministry of Science and Higher Education grant no. 30/W-INTAS/2007/0.

References

Bak P., Tang C., and K. Wiesenfeld, 1988, *Self-organized criticality*, Phys. Rev. A 38, 364-374.

Czechowski Z, 2002, *On linking of two approaches which lead to the power behaviour: The privilege concept and the non-linear models*, Acta Geophys. Pol., 50, 3, 321-335

Czechowski Z, 2003, *The privilege as the cause of power distributions in geophysics*, Geophys. J. Int., 154, 3, 754-766.

Czechowski Z, 2005, *The importance of the privilege in resource redistribution models for appearance of inverse - power solutions*, Physica A, 345, 1-2, 92-106.

Czechowski Z. and Rozmarynowska A, 2008, *The importance of the privilege for appearance of inverse-power solution in Ito equations*, Physica A, 387, 5403-5416.

Feller W., 1966, An Introduction to Probability Theory and its Applications, vol. I, J. Willey and Sons Inc., New York.

Jarosławski J, J.W. Krzyścin, S. Puchalski and P. Sobolewski, 2003, *On the optical thickness in the UV range: Analysis of the ground-based data taken at Belsk*, *Poland*, J. Geophys. Res., 108, 4722.

Oksendal B., 1998, Stochastic Differential Equations: An Introduction with Applications, Springer.

Risken H.V., 1996, The Fokker-Planck Equation, H. Haken, Springer-Verlang Berlin, Berlin.

Rozmarynowska A., 2009 *On the reconstruction of Ito models on the base of time series with long-tail distributions*, Acta Geophysica, 57, no 2, 311-329.

Siegert S., R. Friedrich and J. Peinke, 1998, *Analysis of data sets of stochastic systems*, Physics Letters A, 243, 275-280.

Stauffer D. and A. Aharony, 1992, Introduction to Percolation Theory, Tailor&Francis, London, Washington. DC.

Chapter 7
The Importance of Privilege for the Appearance of Long-Tail Distributions

Zbigniew Czechowski

7.1 Introduction

Many geophysical phenomena, because of their complexity, manifest non-regular and chaotic behaviour. It appears, however, that statistically some observational distributions and patterns reveal that their nature is not purely random (here we call a phenomenon to be purely random if it is characterized by the uniform, Poisson, exponential or Gaussian distribution function). The patterns have a fractal or multifractal structure and the distributions resemble long-tail inverse-power form. Particularly, the fractal excitament, since Mandelbrot's book (1982), caused a spreading interest of this subjest.

Widespread appearance of power distributions in nature and human activity raises self-evident questions about their reasons. Commonly, power distributions were related to the following four cases: phase-transitions, large interactive systems, nonlinearities which lead to chaotic behaviour, and formation of fractals. Applications of above-mentioned cases to geoscience and other branches of science are very wide. However, apart from recovering some analogies between phenomena in nature and the four cases, they did not explain causes for the appearance of inverse-power distributions. Using the designation 'inverse-power' we mean not only strictly inverse-power distributions but also those which resemble them over some ranges of scale. Still, the majority of observed distributions show the inverse-power behaviour for a limited range of scales only.

The aim of the chapter is to show that origins of inverse-power distributions in these phenomena may be enclosed into an unified description – by the privilege concept. Here, the privilege means the susceptibility of the state onto a change. The

Z. Czechowski
Institute of Geophysics, Polish Academy of Sciences, 01-452 Warszawa, Księcia Janusza 64, Poland
e-mail: zczech@igf.edu.pl

V. de Rubeis et al. (eds.), *Synchronization and Triggering: from Fracture to Earthquake Processes*, GeoPlanet: Earth and Planetary Sciences 1,
DOI 10.1007/978-3-642-12300-9_7,

particular example of the privilege was the idea of preferential attachment (new objects tend to attach to popular objects) introduced by Yule (1925) and explicated by Simon (1955). A development of the idea for the case of cities growth was given by Gabaix (1999). The privilege concept is intuitive. It can describe physical, biological, psychological, geometrical and even abstract mechanism. In spite of the lack of precise definition, the privilege concept illustrates the common feature of phenomena leading to long-tail distributions. For a given mathematical description the privilege is defined more precisely.

The Gutenberg-Richter law, Omori's law, the distribution of crack populations and fault distributions are examples of such self-similar organizations over a wide range of scales in seismology. It raises the question how deep the intrinsic fractal structure exists in nature. It may only be the output phenomena that show self-similarity, whereas the deep structure is purely random. On the other hand, if properties of physical intrinsic processes were purely random it should generate exponential (uniform, Poisson, Gaussian) distributions. However, nonlinearity of the process can be responsible for the transformation of distributions.

In this chapter we present results, pertaining to the privilege concept, chosen from our papers: Czechowski (1991, 1993, 1994, 1995, 1997, 1998, 2001, 2002, 2003, 2005), Czechowski and Rozmarynowska (2008). In Section 7.2 we show what properties of mathematical non-linear models (black box) are sufficient to lead to the transformation of random (exponential) distributions onto long-tail distributions. We find that quite a wide class of nonlinear functions (or equations) fulfills this requirement. This may explain the universality of long-tail distributions in nature. Section 7.3 introduces a simple model in which the privilege is taken into account. We analyze the influence of a type of privilege on the form of solutions. Due to the fact that the influence of the privilege on the output distribution depends on the initial/boundary conditions in the phenomenon, we explain this problem in Section 7.4. The correspondence of Ito equations with the privilege is discussed in Section 7.5. In Section 7.6 we shortly refer to the multiplicative processes and their relation to the privilege and the Ito equation. The theoretical approach presented in the mentioned sections is applied (in Section 7.7) to geophysical, physical and other problems in which long-tail distributions appear. Physical (geometrical, etc.) interpretations of the privilege are given.

7.2 Nonlinear Transformations

Geophysical phenomena as well as many others may be modeled as a kind of black box g which transforms input random variables x into the output random variable $y = g(x)$ that is of interest (is observed) in a given phenomenon. Unknown parameters or some aspects of intrinsic structure of the model g can be used as the input random variables. We assumed purely random (e.g., exponential) distribution functions for them.

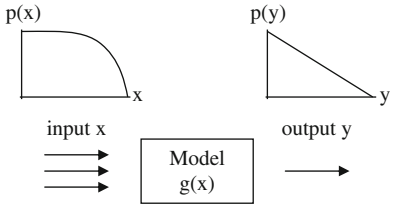

Fig. 7.1 Illustration of the black box model with the input governed by the exponential distribution and the output characterized by the long-tail distribution

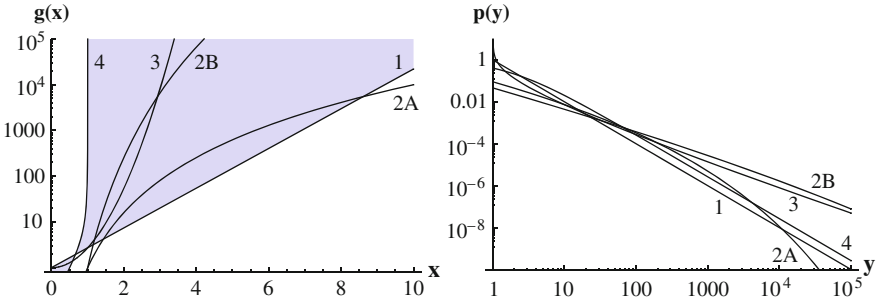

Fig. 7.2 Graphs of transformations $y=g(x)$ (left) and adequate distributions $p(y)$ (right) for cases (7.1) – (7.4). Here 2A and 2B correspond to the case (7.2) with $k = 4$ and $k = 8$ respectively

The influence of the non-linearity of the model g on the output behaviour is investigated. To be more exact, the kind of nonlinearity of a model that transforms an input random variable x with exponential (or uniform, normal) distribution into a variable y with a long-tail distribution (see Fig. 7.1) over a wide range of scales is analyzed. We follow our papers Czechowski (2001, 2002, 2008).

7.2.1 *Transformation* $\mathbf{y = g(x)}$ *of a random variable* $\mathbf{x}$

It was shown (Czechowski 2001) that the function $g(x) = a^a exp(ax)$, where $a = 1/(\alpha-1)$, transforms the input random variable x with exponential distribution function $p_X(x) = e^{-x}$ onto the output random variable y with the inverse-power distribution $p_Y(y) = y^{-\alpha}$. However, there also exists a wide class (shaded region in Fig. 7.2) of nonlinear, adequately fast increasing functions $g(x)$ which leads to power-like distributions. The class includes functions between power one, $g(x) = x^k$ for sufficiently large k, and those that increase very fast along a vertical asymptote. Figure 7.2 shows graphs for the four examples:

$$p_Y(y) = y^{-\alpha} \quad \text{for } y = g(x) = a^a \exp(ax), \tag{7.1}$$

$$p_Y(y) = \frac{1}{k} y^{\frac{1}{k}-1} \exp(-y^{\frac{1}{k}}) \quad \text{for } y = g(x) = x^k, \tag{7.2}$$

$$p_Y(y) = \frac{\exp(-\sqrt{\ln y}\,)}{2y\sqrt{\ln y}} \quad \text{for } y = g(x) = \exp(x^2), \tag{7.3}$$

$$p_Y(y) = \frac{\exp\left(\frac{y}{1+y}\right)}{(1+y)^2} \quad \text{for } y = g(x) = \frac{x}{1-x}. \tag{7.4}$$

This amazingly wide class of functions which transform purely random distributions into power-like output forms may lead to the explanation of the universality of long-tail distributions in nature.

7.2.2 *Transformations given by solutions of random differential equations*

The nonlinear transformation $y = g(x)$ (executed by the black box) may be given by a solution of random differential equation. We discuss some examples:

a) **Random initial problem:**

$$\frac{dy}{dt} = B(y), \qquad y(0) = x. \tag{7.5}$$

If $B(y) = ay^{\alpha}$ then for $\alpha > 1$ the solution $y(t,x) = \dfrac{x}{[1 - a(\alpha-1)x^{\alpha-1}t]^{\,1/\alpha-1}}$ increases to infinity along the vertical asymptote and the distribution function has an inverse-power form (for y big enough):

$$f(y,t) = \frac{1}{[1 + a(\alpha-1)y^{\alpha-1}t]^{\,\alpha/\alpha-1}} \exp\left(\frac{-y}{[1 + a(\alpha-1)y^{\alpha-1}t]^{\,1/\alpha-1}}\right). \tag{7.6}$$

The example corresponds to a simple (not time-dependent) case (7.4).

It should be noted that even for non-power form of $B(y)$, but such which increases faster than the linear function, the inverse-power solution is obtained; for example, if $B(y)=y\ log(y)$ then $y(t,x) = x^{exp(t)}$ and $f(y,t) = A(t)\exp[-y^{A(t)}]y^{A(t)-1}$ has the inverse-power $1/y$ tail for large t (where $A(t) = e^{-t}$).

b) **Random additive force *x***:

$$\frac{dy}{dt} = B(y) + x, \qquad y(0) = c \tag{7.7}$$

If $B(y)=ay^{\alpha}$ then for $\alpha=2$ the solution $y(t,x)=\frac{a\sqrt{x}+x\tan(\sqrt{x}t)}{\sqrt{x}-a\tan(\sqrt{x}t)}$ increases to infinity along the vertical asymptote and the adequate distribution function has an inverse-power form. The same behaviour is observed for other $\alpha>1$ (see Czechowski 2001).

c) **Random multiplicative force *x***:

$$\frac{dy}{dt}=xy(t),\qquad y(0)=c. \tag{7.8}$$

Here, the solution is exponential, $y(t,x)=a\exp(tx)$, and the distribution function (according to (1)) is the inverse-power one.

According to the Liouville theorem (see, e.g., Sobczyk 1991), the initial problem (7.5) corresponds to the Liouville equation:

$$\frac{\partial f(y,t)}{\partial t}+\frac{\partial[f(y,t)B(y)]}{\partial y}=0,\quad f(y,0)=e^{-y}. \tag{7.9}$$

The distribution function $f(y, t)$ of the solution $y(t, x)$ of eq. (7.5) satisfies the Liouville equation. This equation may be interpreted as the Fokker-Planck equation (see, e.g., Risken 1996):

$$\frac{\partial f(y,t)}{\partial t}+\frac{\partial[f(y,t)B(y)]}{\partial y}-\frac{1}{2}\frac{\partial^2[f(y,t)B(y)]}{\partial y^2}=0 \tag{7.10}$$

without the diffusion term.

7.3 The Master Equation and the Privilege Concept

The nonlinear transformation $y = g(x)$ may be the result of working of a very complex system for which it is very difficult to find the form of $g(.)$. However, if the process $y(t)$ is the Markov one, the transformation can be described by some Master equation.

The Master equation (see, e.g., Van Kampen 1987).

$$\frac{\partial f}{\partial t}=\int W(y;y')f(y',t)dy'-f(y,t)\int W(y';y)dy' \tag{7.11}$$

describes the evolution of the distribution function $f(y,t)$ of the Markov process $y(t)$. Here $W(y;y')dt$ is the probability of transfer from the state y' to the state y in time dt. The state vector y may contain many characteristic variables typical for the process under investigation. However, due to difficulties with constructing the

kernel *W(y;y')* and with a nontrivial analysis of the equation (7.11) only scalar or two-dimensional y is considered.

7.3.1 The Pure Birth Master equation

Let us assume that the evolution of the system is given by the Markov process with continuous time and with discrete state space. Then the **Master equation for the unistep process** (see, e.g., Van Kampen 1987) **with steps on right only** (pure birth process) is given by

$$\frac{dp_N(t)}{dt} = -B(N)p_N(t) + B(N-1)p_{N-1}(t) \tag{7.12}$$

where $N = 1, 2, \ldots$, denote states of the system, $p_N(t)$ is the probability that the system is at state N at time t, and $B(N)\Delta t$ is the probability of N changing to $N+1$ in $(t, t+\Delta t)$. The equation is of the gain/loss type; the second term on the right hand side describes gains (i.e., creating of the state N from the state N-1), the first term on the right hand side describes losses (i.e., transforming of the state N into the higher state). The function $B(N)$ can be used for describing the privilege, when **the privilege is the susceptibility of a given state onto a change**. For example, if $B(N_2) > B(N_1)$, then we acknowledge that the state N_2 (if $N_2 > N_1$) is **privileged**. There is no privilege when all states change with the same probability $B(N_i) = \text{const}$ for $i = 1, 2, \ldots$.

We showed (in Czechowski 2001, 2002) that the appropriate privilege of higher states (which means that $B(N)$ is sufficiently increasing function) may lead to the inverse-power form of the density $p_N(t)$. Analyzing solutions of (7.12) we take into account two cases: the initial problem, where we assume only the initial distribution $p_N(0) = \mathrm{e}^{-N}$, and the boundary problem of the source type, i.e., $p_1(t) = c = const$ for $t \geq 0$ (the number of states *1* is maintained constant all the time) and $p_N(0) = \mathrm{e}^{-N}$.

Let us discuss the initial problem. For constant function $B(N) = c$ and for linear function $B(N) = cN$, the solution is Poisson and geometrical (Fig. 7.3), respectively. Only when $B(N) \sim N^{\alpha}$ for $\alpha > 1$ the solution has a long-tail inverse-power distribution (Fig. 7.3) for a sufficiently long time t.

On the other hand, by introducing the boundary condition of the source type we obtain steady-state solutions. These are inverse-power functions (see Fig. 7.4) for $B(N) \sim N^{\alpha}$, where $\alpha > 0$. For example, for linear function $B(N) = N$ (and $p_1(t) = 1$ for $t \geq 0$ and $p_N(0) = \mathrm{e}^{-N}$ for $N > 1$), the solution has the form (Czechowski 2002):

$$p_N(t) = \frac{1}{N} + \sum_{k=2}^{N} (-1)^{k-1} \frac{(N-1)!}{(N-k)!} \left[\frac{1}{k(k-2)!} + \sum_{j=1}^{k-1} \frac{(-1)^j e^{-j}}{(k-1-j)!j!} \right] e^{-kt}. \tag{7.13}$$

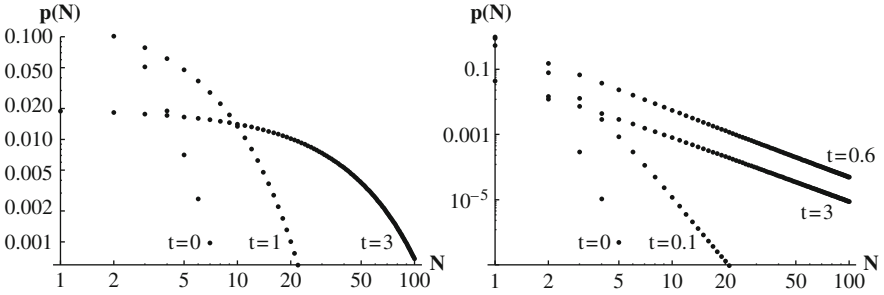

Fig. 7.3 Solutions $p(N, t)$ of eq. (7.12) with the exponential initial distribution $p(N, 0) = exp(-N)$, for some values of time, for two cases:
$B(N) = N$ (left), for each time the exponential distribution is obtained,
$B(N) = N^2$ (right), for $t = 0.6$ the power-like solution is obtained, for longer times solutions do not change the power exponents of theirs tails

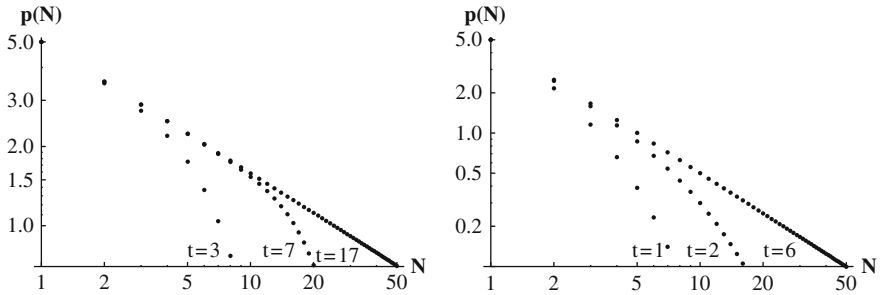

Fig. 7.4 Solutions $p(N, t)$ of eq. (7.12) with the boundary conditions: $p(1, t) = 5$, $p(N, 0) = e^{-N}$; for some values of time, for two cases:
$B(N) = N^{1/2}$ (left),
$B(N) = N$ (right), For a power form of $B(N) \sim N^{\alpha}$ with $\alpha > 0$ (privilege) an inverse-power form of solutions is observed for sufficiently long time, these are steady-state solutions

It tends asymptotically (for $t \to \infty$) to steady state inverse-power solution $p_N^s = N^{-1}$.

Therefore, it was concluded (in Czechowski 2001, 2002) that for the boundary condition even a very weak privilege given by $B(N) \sim N^{\alpha}$ with $0 < \alpha << 1$ leads to inverse-power solutions after sufficiently long time t.

The coagulation equation (Safronov 1972)

$$\frac{\partial f}{\partial t} = \frac{1}{2}\int_0^y B(y', y - y')f(y', t)f(y - y', t)dy' - f(y, t)\int_0^{\infty} B(y, y')f(y', t)dy \qquad (7.14)$$

may be treated as the macroscopic equation derived from the adequate Master equation. Here *f(y, t)* is the size distribution function (*y* is the size of the object) in time *t* and *B(y, y')* is the probability of fusion of two objects with sizes *y* and *y'*. This is a nonlinear equation but has the same loss/gain structure as the linear Master equation (7.11). It was shown (Czechowski 1993, 2003) that for a constant coagulation coefficient $B(y,y') = B$ (there is no privilege – small and large objects fuse with the same rate) the solution of (7.14) has the exponential form $f(y, t) = a(t)\ exp[b(t)y]$. On the other hand, for $B(y,y') = y+y'$ (then the probability of fusion for larger objects is greater that for smaller objects – the larger objects are **privileged**) the solution is inverse-power, $f(y,t) = c(t)\ y^{-3/2}$ for large *y* (see Safronov 1972).

7.3.2 The Fokker-Planck equation

The continuous version (discrete $N \rightarrow$ continuous *y*) of the master equation (7.12) is the Fokker-Planck equation (van Kampen 1987):

$$\frac{\partial f(y,t)}{\partial t} + \frac{\partial [f(y,t)B(y)]}{\partial y} - \frac{1}{2}\frac{\partial^2 [f(y,t)B(y)]}{\partial y^2} = 0 \tag{7.15}$$

It was shown (in Czechowski 2001, 2002) that the behaviour of solutions of the equation for the initial problem as well for the boundary conditions is analogous (see Fig. 7.5) to that in the discrete model (7.12). Because the Fokker-Planck equation describes processes with steps on the right and on the left, the conclusions concerning the privilege are valid in case of steps on both sides.

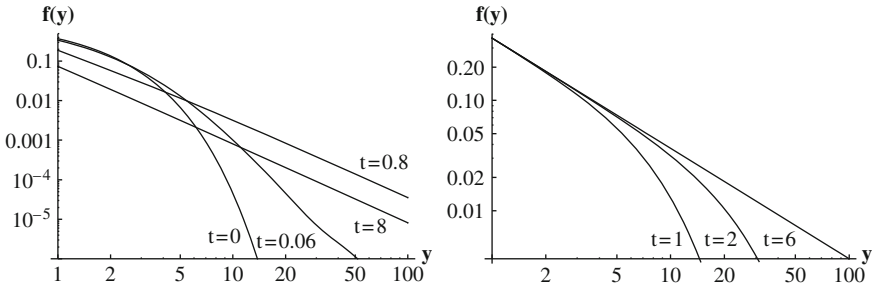

Fig. 7.5 Solutions *f(y, t)* of the Fokker-Planck eq. (7.15) with:
- the exponential initial distribution $f(y, 0) = exp(-y)$, and $B(y) = y^2$ (left),
- the boundary conditions: $f(1, t) = 1$, $f(y, 0) = exp(-y)$, and $B(y) = y$ (right). Compare with Figs. 7.3 and 7.4

7.4 The Role of Boundary Conditions

The goal of this section is to understand why the introduction of the boundary condition of the source type leads to inverse-power solutions even for a very weak privilege given by $B(y) \sim y^{\alpha}$, where $0 < \alpha \ll 1$.

The master equation (7.12) or the Fokker-Planck equation (7.15) was solved with the initial conditions or, additionally, with the boundary condition of the source type, i.e., we put $f(y_b, t) = \text{const}$ for $t \geq 0$. The same conditions could be assumed for the Liouville equation. However, the random equation (7.5), which corresponds to the Liouville equation, can be considered only as an initial problem.

At first we will show how to include the boundary condition into the random initial problem (7.5) (see Czechowski 2002). The linear case:

$$\frac{dy}{dt} = y + a, \qquad y(0) = x \tag{7.16}$$

has the solution

$$y(t) = a(e^t - 1) + xe^t. \tag{7.17}$$

The boundary condition $f(y_b, t) = c$ is assumed for $y = y_b$. The trajectory $y(t, x)$ cuts the line $y = y_b$ at the time

$$t = \log\left(\frac{y_b + a}{x + a}\right). \tag{7.18}$$

From the corresponding Liouville equation:

$$\frac{\partial f(y,t)}{\partial t} + \frac{\partial [f(y,t)B(y)]}{\partial y} = 0, \tag{7.19}$$

where $B(y) = y + a$, we obtain

$$\frac{d}{dt}\log f \equiv \left(\frac{\partial}{\partial t} + \dot{y}\frac{\partial}{\partial y}\right)\log f = -1 \tag{7.20}$$

along a trajectory (we used $B(y) = \mathrm{d}y/\mathrm{d}t$ and $\partial B/\partial y = 1$). Therefore, along the trajectory:

$$f(y,t) = e^{-t} f(y,0). \tag{7.21}$$

By inserting the boundary condition $f(y_b, t) = c$ on $y = y_b$ and the "time of cutting" from (7.18) we obtain the initial distribution function in $[0, y_b]$:

$$f(x,0) = c\frac{y_b + a}{x + a}. \tag{7.22}$$

This shows how the boundary condition $f(y_b, t)$ given on $y = y_b$ coverts itself onto the inverse-power initial condition $f(x, 0)$ on $x \in [0, y_b]$. However, for $x > y_b$ the initial distribution is exponential, i.e., $f(x, 0) = c \exp(-x + y_b)$.

According to Fig. 7.6 we see that the initial distribution from $[0, y_b]$ carried on by trajectories incoming from this sector has a greater and greater influence onto the distribution function for some fixed time $t' > 0$ because only these trajectories cut this line $t = t'$ (parallel to axis $0Y$) on a wider and wider range $y \in [0, y(t)]$, where $y(t) \to \infty$ for $t \to \infty$.

In the case of non-linear function $B(y)$ we can not calculate the differential along trajectory as in (7.20). Therefore, by transformation of variables $z = \psi(y)$ we put (7.19) in the form

$$\frac{\partial \tilde{f}(z,t)}{\partial t} + \frac{\partial [z\tilde{f}(z,t)]}{\partial z} = 0, \tag{7.23}$$

and follow eqs. (7.16) − (7.22). Then, we invert the transformation of variables in order to obtain the formula for the initial condition $f(x,0)$ on $0 \le x \le y_b$. For $B(y) = y^\alpha$ we obtain

$$f(x,0) = c\left(\frac{y_b}{x}\right)^\alpha. \tag{7.24}$$

We conclude (see Fig. 7.6) that the trajectories $t(y)$ incoming from $[0, y_b]$ start to dominate on a larger and larger range of y for sufficiently big t. For $\alpha < 1$ this time is very long. On the other hand, for $\alpha > 1$ we see that no trajectories incoming from (y_b, ∞) reach some fixed value of time $t = t'$ (see Fig. 7.6 for $\alpha = 2$). Of course, this is connected to a very fast growth of the function $y(t)$ along the asymptote (explosion).

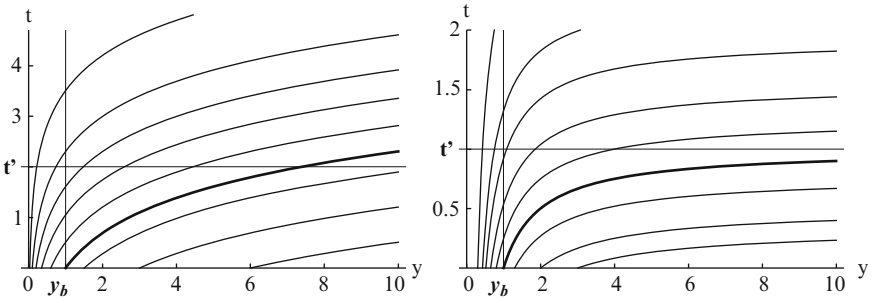

Fig. 7.6 Trajectories $y(t)$ for $B(y) = y^\alpha$, where: $\alpha = 1$ (left), $\alpha = 2$ (right). The boundary condition $f(y_b, t) = c$ is assumed for $y = y_b$. Trajectories, which cut that line convert this information backwards (to the axis OY) onto the inverse-power condition $f(y, 0) = c(y_b/y)^\alpha$, which is valid for $0 \le y \le y_b$. Note, that for $y_b > y$ the initial condition is exponential $f(y,0) = exp(-y)$. Thick line denotes the trajectory incoming from $y(0) = y_b$

In this way we have shown why introducing the constant boundary condition leads to inverse-power solutions even for a very weak privilege given by $B(y) \sim y^{\alpha}$ for $0 < \alpha \ll 1$. This boundary condition causes the existence of steady-state solutions which have the inverse-power form for the power privilege $B(y)$. The Fokker-Planck equation has the same steady state solutions, so these conclusions are valid also for equations with the diffusion term.

7.5 Ito Equations and the Privilege

The connection between the Ito equation and the Fokker-Planck equation may be found by using the Ito Formula (see e.g., Gardiner 1985). Then, the Ito equation, which corresponds to eq. (7.15), has the form

$$dy(t) = B(y)dt + \sqrt{B(y)}dW(t) \tag{7.25}$$

where $W(t)$ is the Wiener process. For the non-linear privilege $B(y) = y^2$ the solution $y(t)$ is (see Czechowski 2002)

$$y(t) = \frac{y(0)}{e^{W(t)-t/2}\left[1 - y(0)\int\limits_0^t e^{W(s)-s/2}ds\right]}. \tag{7.26}$$

The stochastic process $y(t)$ tends to ∞ in a finite time, i.e., it "explodes" if the denominator tends to 0. This is a similar behaviour as for the random initial problem (7.5) where there is no diffusion term.

In general, the Ito equation is defined by two different functions $a(y)$ and $b(y)$:

$$dy(t) = a(y)dt + \sqrt{b(y)}dW(t). \tag{7.27}$$

The equation is not related to the Master equation (7.15); therefore, we can not explain the privilege hidden in (7.27) by using (as in Section 7.3) the probability $B(.)$ of changing states. However, for some cases the Ito equation may correspond to the product of probabilities.

In order to show this we assume that A_i denotes succeeding states of the system and $P(A_i/A_{i-1})$ is the probability of transition from the state A_{i-1} to the state A_i. Therefore, if there is no privilege at all (each state evolve in the same way, i.e., $P(A_i/A_{i-1}) = p = const$, the probability $P(N)$ of achieving the state A_N by the system has the geometric distribution:

$$P(N) = \prod_{i=2}^{N} P(A_i|A_{i-1}) = p^N \tag{7.28}$$

However, by introducing the privilege in the form:

$$P(A_i|A_{i-1}) = \left(1 - \frac{1}{i}\right)^{\alpha}, \tag{7.29}$$

favouring higher states (the higher the state - the greater the probability of transfer to the next state), we obtain the inverse-power distribution $P(N) = N^{-\alpha}$.

In Czechowski and Rozmarynowska (2008) we showed that the discrete product of probabilities corresponds to the following continuous case:

$$\frac{dP(y)}{dy} = -q(y)P(y), \tag{7.30}$$

where the transfer probability is given by $1 - q(y) = 1 - \alpha/y$ and fits in predominant terms of expansion of (7.29) for large i. After differentiation in y, equation (7.30) has the form of the steady-state Fokker-Planck equation:

$$\frac{\partial}{\partial y}[a(y)p(y)] - \frac{1}{2}\frac{\partial^2}{\partial y^2}[b(y)p(y)] = 0, \tag{7.31}$$

where $a(y) = -\alpha/y$ and $b(y) = 2$. In this way we showed that the privilege described by the transfer probability (7.29) is hidden in the Ito equation of the form

$$dy = -\frac{\alpha}{y}dt + \sqrt{2}dW(t). \tag{7.32}$$

This conclusions can be widened (see Czechowski and Rozmarynowska 2008) onto other Ito equations

$$dy = -\frac{1}{2}(\beta - \alpha)y^{\beta-1}dt + \sqrt{y^{\beta}}dW(t). \tag{7.33}$$

which also lead to the steady-state inverse-power distribution $p_{st}(y) = y^{-\alpha}$. Then, the privilege for various α and β (i.e., for $\alpha > 1, 0 \leq \beta < 2$) may be explained by the transfer probability

$$P(A_i|A_{i-1}) = \left(1 - \frac{1}{i}\right)^{\gamma}, \tag{7.34}$$

where $\gamma = \dfrac{2 - 2\alpha}{2 - \beta} - 1$.

In cases of other Ito equations we can reduce them by the variable transformation to the form with the constant diffusion function $b(y) = 1$. Therefore, the privilege is described by the jump $y_k - y_{k-1} = a(y_{k-1})dt + dW(t)$. The stochastic component is

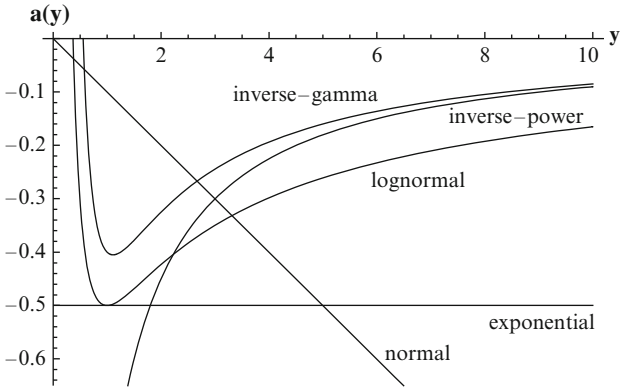

Fig. 7.7 Deterministic components *a(y)* of jumps generated by Ito equations which lead to: normal, exponential, lognormal inverse-gamma and inverse-power stationary solutions (see Table 1 in Czechowski 2008)

identical for different *a(.)*, so we investigate deterministic terms only. In Fig. 7.7 we compare such functions *a(y)* which lead (Czechowski and Rozmarynowska 2008) to the following distributions of stationary solutions of the Ito equation: normal, exponential, lognormal, inverse-gamma, and inverse-power. All the functions have negative values for a big enough y, which means that some positive quantity is subtracted from the stochastic jump *dW(t)*: the less is subtracted, the longer tail will appear. For three cases, which lead to lognormal, inverse-gamma and inverse-power distributions we observe the same behaviour: $|a(y)|$ decreases with increasing y. This describes the privilege: for greater y a smaller quantity is subtracted from the random jump (in jumps greater states y lose less). This is an alternative meaning of the privilege (by using jumps) presented in Section 7.3.

7.6 Multiplicative Processes and the Privilege

Multiplicative processes are defined by the law of proportionate effect

$$Y_k = F_k Y_{k-1} = F_k F_{k-1} \cdot \ldots \cdot F_1 Y_0, \tag{7.35}$$

where Y_0 and F_j are random variables. The simple law describes some kind of privilege; for higher states Y_j, greater growths are more possible (because they are proportional to the current state). This privilege leads to lognormal distribution (according to the Central Limit Theorem applied to logarithms of random variables); however, it is known that even small changes, by introducing the source (Sornette 1998), transport process (Manrubia and Zanette 1998) or boundary constraints (Kesten 1973) in the lognormal generative process, yield processes with inverse-power distributions. They produce steady-state solutions, and because the

growth process is the same ($Y_k = F_k Y_{k-1}$) at all scales, the final steady-state distribution process should be scale-invariant.

It should be noticed that the multiplicative process

$$Y_k = (N_k + 1)Y_{k-1} = Y_{k-1} + N_k Y_{k-1} \tag{7.36}$$

(where N_k is a normally distributed random variable) may be connected with a simple Ito equation

$$dy(t) = ydW(t). \tag{7.37}$$

It has the solution

$$y(t) = \exp\left[W(t) - \frac{t}{2}\right] y(0) \tag{7.38}$$

with the lognormal time-dependent distribution

$$p(y,t) = \frac{1}{y\sqrt{2\pi t}} \exp\left[-\frac{1}{2t}\left(\log y + \frac{t}{2}\right)^2\right], \tag{7.39}$$

which, however, has an inverse-power tail $y^{-3/2}$ for large t (see Czechowski and Rozmarynowska 2008). This case corresponds to the example (7.8) in Section 7.2 but here the input (i.e., N_k) has the normal distribution.

7.7 Applications

In this section we present some examples of applications of the considerations given above.

7.7.1 Transformation $\mathbf{y = g(x)}$

We start from an example of derivation of nonlinear transformation $y = g(x)$ for the case of crack propagation problem. The equation of motion of the crack tip was introduced by Kostrov (1966) (and Eshelby 1969, Freund 1972) and analysed by Husseini et al. (1975), Rybicki (1995) and Rybicki and Yamashita (1998). However, in Czechowski (2001) we applied the model for the case of stochastic stress drop field. In this way we obtained the nonlinear tranformation function $y = g(x_1, x_2, x_3)$, where y is the crack increment, and the vector $\boldsymbol{x}$ represents three characteristics of the stress drop field. Different sets of distribution functions for three input $\boldsymbol{x}$ components were taken into account, but even for three exponential distributions

the distribution $f(y)$ of output y had a long-tail form. If only one of x_i had the inverse-power distribution then $f(y)$ would more resemble the inverse-power form.

If we claim that the cause of inverse-power distribution is some privilege, then we should be able to show explicitly in different examples the form of the privilege and its physical bases.

7.7.2 Multiplication of probabilities

Looking for the privilege in such a purely random process like the random walk seems to be a nonsense. However, if we are interested in the time-to-the-origin problem, the distribution function of the time T has the inverse-power form $f(T) = T^{-3/2}$. In Czechowski and Rozmarynowska (2008) we resolved this problem to the product of probabilities (see Section 7.5) where

$$P(A_i|A_{i-1}) = 1 - \frac{3}{2i}. \tag{7.40}$$

Graphically we can interpret the process as the changing of paths (which start from the origin and end at the origin, not crossing *0*) in time-distance space. The privilege is connected with increasing number of possible paths for higher states.

Another example concerns the simple model of crack propagation by succeeding breaking of bonds (de Arcangelis 1990). If the probability of breaking each of k bonds is constant, the size distribution of cracks is the geometrical one. However, if it depends on the current crack size N and has the form (Heimpel 1996)

$$P(A_{N+1}|A_N) = 1 - \frac{1}{1 + (N/C)^{3/2}}, \tag{7.41}$$

the inverse-power distribution is obtained. The form (7.41) corresponds to the physical privilege that the probability of crack propagation is greater for longer cracks; the exponent *3/2* results from the fact that the number of asperities along the rupture contour is proportional to N and that the stress is proportional to $N^{1/2}$, according to the stress intensity factor.

7.7.3 The Master equation

Heimpel's model (1996) may be supplemented by the time evolution element. We constructed (Czechowski 2003) the model of sequentially breaking asperities on the fault surface. The model has a form of the Master equation (7.12) where $p_N(t)$ is the probability that the rupture area $N\Delta s$ is in state N at time t, and $B(N)dt$ is the

probability that the rupture grows by Δs in dt. Therefore, by using the Heimpel's formula (7.41) for $B(N)$ we showed that solutions evolve from the initial shape up to the power-like form.

The Master equation (7.12) is a handy model which was used (in Czechowski 2003) for explanation of long-tail distributions in percolation, simple cellular automata and in the growth of the Cantor set. It should be noted that the percolation processes are models of phase transitions, cellular automata are models of large interacting systems, and the Cantor set is a simple example of a fractal. These cases relate to known phenomena in which inverse-power distributions appear. In our previous papers (Czechowski 2002, 2003) we showed that in these three cases we can extract and explain the hidden privilege, and that we can include the privilege into the Master-like equation.

For example, the process of growth of the Cantor set may be described by the Master equation (7.12) with function $B(N) = N^{log2/log3}$, while $p_N(t)$ is a number of rods of lengths $N = 3^k$ which cover the fractal. The form of the privilege function $B(N)$ corresponds (Czechowski 2003) to the deterministic recipe for the fractal.

For the three cases of percolation we derived the following equation

$$\frac{dp_N(\rho)}{d\rho} = -B(N,\rho)p_N(\rho) + B(N-1,\rho)p_{N-1}(\rho) + C(N,\rho)p_{N-1}(\rho), \qquad (7.42)$$

where $p_N(t)$ is the probability of finding a cluster with size N (cluster size distribution) and ρ is the density of occupied sites on the lattice. Functions $B(N, \rho)$ and $C(N, \rho)$ depend on the dimensionality of the percolation problem. For 1-D lattice:

$$B(N,\rho) = \frac{2}{1-\rho} \quad \text{and} \quad C(N,\rho) = \frac{N(1-\rho)-2}{1-\rho}, \qquad (7.43)$$

for the percolation on the Bethe lattice:

$$B(N,\rho) = \frac{t(N)}{1-\rho} \quad \text{and} \quad C(N,\rho) \approx \frac{N[4(1-1/N)^{5/2}(1-\rho)^2 - 1] - 1}{1-\rho}, \qquad (7.44)$$

and for 2-D percolation:

$$B(N,\rho) = \frac{\bar{t}(N)}{1-\rho} \quad \text{and}$$
$$C(N,\rho) \approx \frac{N}{\rho}\left(1 - \frac{1}{N}\right)^{\tau} \exp[-(\rho_c - \rho)^w - \frac{N-1}{\rho}[1 - w\rho(\rho_c - \rho)^{w-1}], \qquad (7.45)$$

where $w = 91/36$ and $\tau = 187/91$ for $\rho \to \rho_c$ and $\tau \to 1$ for $\rho \to 0$.

We have shown that the percolation process can be described by the Master equation modified by the additional term $C(N, \rho)p_{N-1}(\rho)$. The function $B(N)$

describing the privilege is given by the perimeter $t(N)$ of the N-cluster. The longer perimeter really means a greater probability of growth of the N-cluster on one site, because each of $t(N)$ empty sites on the perimeter may become the occupied site when ρ increases to $\rho + d\rho$. The perimeter $t(N) = 2$ for 1-D percolation and $t(N) \sim N$ for the Bethe and 2-D percolation. Therefore, if we omit the term $C(N, \rho)\, p_{N-1}(\rho)$, we obtain (see Section 7.3) the Poisson distribution for 1-D percolation and the geometrical distribution for the Bethe and 2-D case. However, in the percolation process the N-clusters can be created not only by growth of the $(N-1)$-cluster on one site, but also by linking of neighbouring smaller clusters when a site on the intersection of their perimeters will become occupied. This process is included in the additional term $C(N, \rho)\, p_{N-1}(\rho)$. The function $C(N, \rho)$ has a similar behaviour for the three types of percolation: it is an increasing (approximately linear) function of N. This additional privilege leads to geometrical distribution (which has a longer tail than the Poisson distribution) for 1-D percolation and to the power-like distributions for the Bethe and 2-D percolation.

In the percolation theory, greater clusters are privileged because they have longer perimeters and, additionally, they have more ways of creating greater clusters in linking. The avalanches in cellular automata define some 'potential' dynamic clusters; the group of neighbouring boxes that will become unastable in the event, if one selected box becomes unstable. Therefore, we may treat such 'potential' clusters in a similar way to the percolation cluster and adequate privilege arguments should be valid (see Czechowski 2003).

It appears that a weak privilege $B(N) = N^{0.63093}$ is sufficient for creation of a fractal (Cantor set) because the boundary condition of the source type was taken into account in this case. On the other hand, only initial condition can be used for the percolation problem. Then, the linear privilege (for the Bethe lattice and 2-D lattice) is too weak to create inverse-power distributions (it leads to the geometrical distribution). We have shown that the inverse-power form of the number of N-clusters is connected with the fact that clusters are not isolated on the grid, so that larger clusters can form themselves by linking smaller clusters.

Another application of the continuous Master equation (7.11) to the crack problem was that of Petrov et al. (1970). They introduced a distribution function $f(q,t)$ of generalized coordinates q (the vector q can represents coordinates of the centre of the crack, dimensions, shape, orientation and other parameters of the crack). The standard form of the equation for $f(q,t)$ was used:

$$\frac{\partial f}{\partial t} = \int_{(0,q)} W(q', q_1; q) f(q', t) dq' - f(q,t) \int_{(0,\infty)} W(q, q_1; q') dq' + N(q,t) \quad (7.46)$$

where N describes the nucleation of crack q and $W(q', q_1; q)dqdt$ is the probability of the transition of the crack from the state q' into the state contained in $(q, q+dq)$, by joining a crack q_1 during the time interval dt. However, due to the complexity of these terms those authors used some assumptions: they considered a spatially homogeneous case of parallel disk-shaped cracks, so that $f(q, t) = f(r, t)$, where

r is the crack radius, and they assumed that nucleated cracks are unable to grow independently. Then, they obtained the reduced form of the kinetic equation:

$$\frac{\partial f(r,t)}{\partial t} = n(t)\omega(r) + n(t)\sigma \int_0^r \omega(r-r')f(r',t)dr' - n(t)\sigma f(r,t) \tag{7.47}$$

where the nucleation rate of microcracks is $n(t)$, their distribution function is $\omega(r)$ (i.e., $N(r,t) = n(t)\ \omega(r)$), and σ is the volume of the region of mutual instability in which two cracks are going to fuse. Equation (7.47) is a Volterra-type equation of the first kind. Applying to this equation Laplace transformations, Petrov et al. (1970) found the solution:

$$f(r,t) = \int_0^t n(t_0)e^{-\lambda}\left[\omega(r) + \frac{\lambda}{1!}\int_0^r \omega(r')\omega(r-r')dr' + \frac{\lambda^2}{2!}\int_0^r \omega(r')\int_0^{r-r'} \omega(r'')\omega(r-r'-r'')dr''dr' + \ldots\right]dt_0 \tag{7.48}$$

where

$$\lambda(t) = \sigma \int_{t_0}^t n(t')dt' \tag{7.49}$$

The results has a simple interpretation: the number of cracks of radius r is a superposition of microcracks resulting from the coalescence of various numbers of cracks into a single crack of a given radius. Their approach led to a very particular model of rupture: under the applied stress the microcracks nucleate but are unable to grow independently. The crack can grow only by joining the newly-nucleated cracks in its region of mutual instability.

Lomnitz-Adler (1985, 1988) used two components characterizing the state of the fault: stress σ and a surface a (i.e. 2-dimensional vector y in (7.11)). By using the percolation theory he derived the kernel $W(\sigma, a;\sigma', a')$ in the Master equation (7.11). Therefore, he obtained the Gutenberg-Richter formula with excess of the strongest (characteristics) events and a time-dependent seismicity.

The coagulation equation was used by Safronov (1972) to planetesimals evolution. The physical details for the form of $B(y, y') \sim y+y'$ for gravitational bodies (planetesimals) are presented in his book. However, it is evident that gravitational cross-section increases with growing body size. The example excellently joins the physical privilege (given by gravitational forces) with the coefficient $B(y, y')$ describing the rate of evolution of bodies.

The asymptotic solution of the coagulation equation (7.14) was used by Vityazev (1979) to derive theoretically the known empirical Gutenberg-Richter formula.

Another application of the coagulation equation in geophysics was the problem of crack fusion (Czechowski 1991, 1993, 1997). It seems that for brittle materials, such as rocks, the fusion cross-section may also be given by $B(y, y') \sim y+y'$, because larger cracks induce greater stresses around their tips. Therefore, the process of fusion of numerous microcracks leads to the inverse-power distribution of crack sizes. Experimental investigations (e.g. Mogi 1962; Scholz 1968; Hirata 1987) confirm this form of the distribution in rocks and ceramics. On the other hand, for ductile material, such as metals, the exponential form of the crack size distribution was observed (see Curran et al. 1987), which suggests a weaker influence of tip stresses on the crack fusion, probably due to the ductility.

The coagulation model was particularly fruitful in applications to the crack evolution problem. In Czechowski (1997) we used it to the macrocrack propagation model. A generalization of the kinetic model of crack fusion onto three component mixture of cracks (i.e., shear cracks, tensile cracks and shear-tensile cracks) was presented in Czechowski (1998). In our other papers (Czechowski 1991, 1993, 1994) we performed the discretization in the size space and reduced the coagulation equation to the set of differential equations for hierarchical crack populations of the Newman and Knopoff's (1983, 1990) type. Analysis of the behaviour of successive crack populations led us to explanation of physical basis of the time delay in the Newman and Knopoff model and, moreover, to the linear logarithmic time to fracture versus applied stress relationship (which was confirmed by experimental data for rock (Kranz el al., 1982).

7.7.4 Multiplicative processes

We showed in Czechowski (2005) that the normalization model of resources redistribution (introduced by Wilhelm and Hanggi, 2003) can be described by the multiplicative process. Moreover, we also showed that it leads to the inverse-power distribution (instead of the lognormal one) because logarithms of random variables do not fulfill assumptions of the Central Limit Theorem; their variances increase very fast to infinity with increasing state values. In this way the product of random variables converges to the random variable with logexponential (i.e. inverse-power) distribution. Here the privilege corresponds to the law of proportionate effect – the 'richer' gains more in this method of redistribution.

It is interesting to note that the process of redistribution can be treated as a transformation of random variables (like those presented in Section 7.2). Therefore, it was shown (Czechowski 2005) that the nonlinear transformation is of the type of the rational function (7.4) increasing very fast along an asymptote. This important conclusion joins the privilege approach, given by law of proportionate effect, with the nonlinear transformation $y = g(x)$.

7.7.5 *Ito equations*

Applications of the Ito (or Langevine, Fokker-Planck) equations were discussed in Chapter 6.1. Here are additional three examples.

For an analytical investigation of cellular automata (spring-block model) with long-range interactions, Klein et al. (1997, 2000) derived the Ito equation describing stresses connected with "superblocks" (clusters of cells linking by long-range interactions). They proved the existence of metastable states and adequate spinodals.

Other Ito equation was derived by Rundle et al. (1999) for slips in a given cell on the grid. The authors investigated solutions of the equation in the vicinity of a spinodal. They obtained structures, similar to percolation clusters, which were created by cells in which the slip took place.

In these two approaches the Ito equation was derived to demonstrate spinodals i.e., stability limits connected with strength thresholds on the fault. This is the Ito equation which describes the approaching of the system to the state of the lowest energy. For the spinodal case the effect of noise can be a strong enough to throw out the system of the metastable state. Therefore, the system drops to a new metastable state with lower energy, i.e., the first-order phase transition occurs.

In the third example (Matthews et al. 2002) the simple Ito equation for the Brownian motion was used to construct a probability model for rupture times on a recurrent earthquake source. The model was applied to long-term earthquake forecasts for the San Francisco Bay region and inland faults in Japan.

7.8 Conclusions

In the face of generality of long-tail distributions and fractal patterns, the question about their causes is very important. We have proposed a simple and physically clear explanation – by the privilege concept. This concept encloses into a unified description four phenomena in which inverse-power distributions were observed: phase transitions, low-dimensional chaos, large interactive systems and fractals. Due to the obvious complexity we have limited ourselves to simple cases (or models) of these phenomena: percolations, simple nonlinear transformations, cellular automata and the Cantor set. Next, by using the introduced mathematical models we have shown the physical nature of the privilege in some geophysical cases. For example, in the fault rupture problem the privilege is connected to the stress field around the crack tip. A beautiful and a modeling example of the physical privilege presents the model of planetesimal coagulation which explains the privilege by the law of gravitational attraction. It it worth noting that the privilege effect may be present even in such a purely random process as the random walk; we mean the time-to-the-origin problem.

In our considerations we applied a typical mathematical stochastic apparatus: the Master equation and the Ito (Fokker-Planck, Langevin) equation. These equations

can be very useful in modeling of seismic and other geophysical phenomena. The Ito equations were successfully advantaged in nonlinear modeling of stochastic processes which are represented by time series (see Chapter 6).

Both Chapter 6 and the present one, suggest that the macroscopic behaviour of many phenomena and some new macroscopic laws which are observed can be a result of complex internal interactions or synchronization of various physical fields. These processes may generate the adequate Ito equation on the macroscopic level.

Of course, for different mathematical models three different descriptions of the privilege had to be given: as the susceptibility of a given state onto a change (in Master, Fokker-Planck and coagulation equations), as the law of proportionate effect (in multiplicative processes), and by using jumps (in the Ito equation). However, they correspond to the same idea; in order for the long-tail distribution to appear, states can not evolve the same way, an additional mechanism which favours higher states is required.

We hope that the privilege concept brings some order to our knowledge about the macroscopic rules and patterns in nature.

Acknowledgement The work was supported by INTAS 05-1000008-7889 and by Ministry of Science and Higher Education grant no. 30/W-INTAS/2007/0.

References

de Arcangelis L., 1990, Randomness in breaking thresholds, [in] Statistical models for the fracture of disordered media, [eds] H. J. Herrmann and S. Roux, Elsevier Sci. Pubs. B. V. North-Holland, 229-260.

Curran D.R., Seaman L., and D.A. Shockey., 1987, Dymanic failure of Solids, Phys. Rept. 147, 253-338.

Czechowski Z., 1991, A kinetic model of crack fusion, Geophys. J. Int., 104, 419-422

Czechowski Z., 1993, A kinetic model of nucleation, propagation and fusion of cracks, J. Phys. Earth, 41, 127-137.

Czechowski Z., 1994, A kinetic model of the evolution of cracks, Publication of the Institute of Geophysics, Pol. Ac. Sci., A-22 (262), p. 1-65.

Czechowski Z., 1995, Dynamics of fracturing and cracks [in] „Theory of Earthquake Premonitory and Fracture Processes", R. Teisseyre [ed], PWN, Warszawa, 447-469

Czechowski Z., 1997, A kinetic model of macrocrack propagation, Acta Geophys. Pol. 45, no 3, 193-204

Czechowski Z., 1998, A generalized model of three component mixture of crack, Acta Geophys. Pol, 46, no 4, 375-388

Czechowski Z., 2000, A stochastic approach to the cracktip propagation model, Acta Geophys. Pol. 48, no.1, 57-68

Czechowski Z., 2001, Transformation of random distributions into power-like distributions due to non-linearities: application to geophysical phenomena, Geophys. J. Int., 144, 197-205.

Czechowski Z., 2002, On linking of two approaches which lead to the power behaviour: the privilege concept and the non-linear models, Acta Geophys. Pol., 50, no 3, 321-335.

Czechowski Z., 2003, The privilege as the cause of the power distributions in geophysics, Geophys. J. Int., 154, 754-766.

Czechowski Z., 2005, The importance of the privilege in resource redistribution models for appearance of inverse-power solutions, Physica A, 345, 92-106.

Czechowski Z. and Rozmarynowska A., 2008, The importance of the privilege for appearance of inverse-power solution in Ito equations, Physica A, 387, 5403-5416.
Eshelby J.D., 1969, The elastc field of a crack extending nonuniformly under general anti-plane loading, J. Mech. Sol., 17, 177-199.
Freund L. B., 1972, Energy flux into the Tipp of an extending crack in an elastic solid, J. Elast., 2, 341-349.
Gabaix X., 1999, Zipf's law for cities: an explanation, Quarterly Journal of Economics 114, 739-767.
Gardiner, C.W., 1985, Hanbook of Stochastic Methods for Physics, Chemistry and the Natural Sciences, Springer-Verlag, Berlin-Haidelberg.
Hirata T., Satoh T. and K. Ito, 1987, Fractal structure of spatial distribution of microfracturing in rock, Geophys. J. R. Astron. Soc., 90, 369-374.
Heimpel M., 1996, Earthquake size-frequency relations from an analytical stochastic rupture model, J. Geophys. Res., 101, 22435-22448.
Husseini M. I., Jovanovich D.B., Ranalli M.J. and L.B. Freund, 1975, The fracture energy of earthquakes, Geophys. J. R. Astr. Soc., 43, 367-385.
Kesten H., 1973, Random difference equations and renewal theory for products of random matrices, Acta Math. CXXXI, 207-248.
Klein W., J. B. Rundle, C. D. Ferguson, 1997, Scaling and nucleation in models of earthquakes faults, Physical Review Letters, 78, 3793-3796.
Klein W., M. Anghel, C. D. Ferguson, J. B. Rundle, J. S. Sa Martins, 2000, Statistical analysis of a model for earthquake faults with long-range stress transfer, [in] [in] GeoComplexity and the Physics of Earthquakes, [Eds] J. B. Rundle, D. L. Turcotte, W. Klein, American Geophysical Union, Washington, DC, 43-71.
Kostrov B.V., 1966, Unsteady propagation of longitudinal-shear cracks, J. Appl. Math. Mech., 30, 1241-1248.
Kranz R.L., Harris W.J. and N.L. Carter, 1982, Static fatigue of granite at 200 C, Geophys. Res. Letts., 9, 1-4.
Lomnitz-Adler J., 1985, The statistical dynamics of the earthquake process, Bull. Seismol. Soc. Am., 75, 441-454.
Lomnitz-Adler J., 1988, The theoretical seismicity of asperity models: an application to the coast of Oaxaca, Geophys. J., 95, 491-501.
Mandelbrot B.B., 1982, The Fractal Geometry of Nature, Freeman, San Francisco.
Manrubia, S.C., and D.H. Zanette., 1998, Intermittency model for urban development, Phys. Rev. E 58, 295-302.
Matthews M.V., Ellsworth W.L. and P.A. Reasenberg, 2002, A Brownian model for recurrent earthquakes, Bull. Seism. Soc. Am., 92, 6, 2233-2250.
Mogi K., 1962, Magnitude-frequency relation for elastc shocks accompanying fractures of various materials and some related problems in earthquakes, Bull. Earthq. Res. Inst. Univ. Tokyo, 40, 831-853.
Newman W.I. and L. Knopoff, 1983, A model of repetitive cycles of large earthquakes, Geophys. Res. Lett., 10, 305-308.
Newman W.I. and L. Knopoff, 1990, Scale invariance in brittle fracture and the dynamics of crack fusion, Int. J. Fracure, 43, 19-24.
Petrov V. A., V. I. Vladymirov, A. N.Orlov, 1970, A kinetic approach to fracture of solids. I. General Theory, Phys. Stat. Sol., 42, 197-206.
Risken H., 1996, The Fokker-Planck equation – Methods of solution and applications, Springer-Verlag, Berlin.
Rundle J. B., W. Klein, S. Gross, 1999, Physical basis for statistical patterns in complex earthquake populations: models predictions and tests, Pure appl. geophys., 155, 575-607.
Rybicki K.R., 1995, Fracture arrest on a vertical strike-slip fault in a layered medium, in „Theory of Earthquake Premonitory and Fracture Processes", R. Teisseyre [ed], PWN, Warszawa, 226-236.

Rybicki K.R. and T. Yamashita, 1998, Faulting in vertically inhomogeneous media and its geophysical implications, Geophys. Res. Lett., 25, 2893-2896.
Safronov V.S., 1972, Evolution of the Protoplanetary Cloud and Formation of the Earth and the Planets, IPST, Jerusalem.
Scholz C.H., 1968, Microfracturing and the inelastic deformation of rock in compression, J. Geophys. Res., 73, 1417-1454.
Simon H.A., 1955, On a class of skew distribution functions, Biometrika, 42, (3/4), 425-440.
Sobczyk K., 1991, Stochastic differential equations with applications to physics and engineering, Kluwer Academic Publishers.
Sornette D., 1998, Multiplicative processes and power laws, Phys. Rev. E 57, 4811-4813.
Vityazev A.V., 1979, Spectrum of energy of the elastic deformation during earthquakes (in Russian, unpublished).
Yule G., 1925, A mathematical theory of evolution based on the conclusions of dr. J.C. Willis, F.R. S., Phil. Trans. RS of London (B), 213, 21-87.
Van Kampen N.G., 1987, Stochastic processes in physics and chemistry, Elsevier Science Publishers, Amsterdam.
Wilhelm T. and P. Hanggi, 2003, Power-law distributions resulting from finite resources", Physica A, 329, 499-508.

Part II
Laboratory Experiments

Chapter 8
Triggering and Synchronization of Stick-Slip: Experiments on Spring-Slider System

T. Chelidze, T. Matcharashvili, O. Lursmanashvili, N. Varamashvili, N. Zhukova, and E. Meparidze

8.1 Introduction

Triggering and synchronization are the two faces of the same coin; both effects imply that the additional forcing causing triggering and synchronization is much smaller than the main driving force, which means that these phenomena are connected with nonlinear interactions of objects, namely, with initiation of instability in systems that are close to the critical state. In a seismic process, the main driving component is the tectonic stress; earthquakes are considered as dynamic instabilities generated in the process of friction (stick-slip) between faces of geological faults (Brace and Byerlee, 1966; Kanamori and Brodsky, 2004; Ben-Zion, 2008). The additional forcing is exerted by various external impacts: tides, reservoir exploitation, big explosions, magnetic storms, etc.

Experimentally, triggering is revealed by correlation of some single external impact and single seismic event with some delay; according to this definition, statistics of triggering events is relatively small. Synchronization, on the other hand, is defined as "the adjustment of rhythms due to an interaction" and this means that it manifests itself not in rear solitary acts but in systematic multiple process, which provides relatively rich statistics and allows applying rigorous methods of assessment of the strength of synchronization.

We can illustrate the essence of synchronization phenomenon by considering the relaxation or integrate-and-fire oscillator under periodic forcing (Fig. 8.1).

T. Chelidze (✉), T. Matcharashvili, O. Lursmanashvili, N. Varamashvili, N. Zhukova, and E. Meparidze
M. Nodia Institute of Geophysics, 1 Alexidze str., 0171 Tbilisi, Georgia
e-mail: tamaz.chelidze@gmail.com

V. de Rubeis et al. (eds.), *Synchronization and Triggering: from Fracture to Earthquake Processes*, GeoPlanet: Earth and Planetary Sciences 1,
DOI 10.1007/978-3-642-12300-9_8,

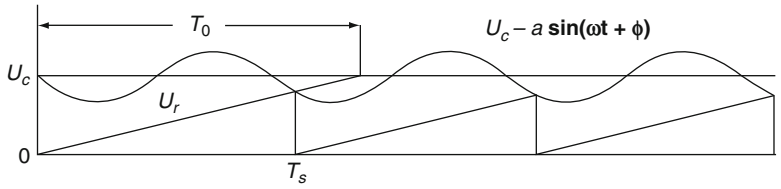

Fig. 8.1 Scheme of synchronization of relaxation oscillator by periodic forcing: T_0 is the period of non modified relaxation process and T_s is the same for a synchronized one, U_r is the current value of the voltage, U_c is the critical value of voltage for discharge of non synchronized generator and U_c is the same for a synchronized one

The examples are numerous, from biology to electricity and mechanics. Such oscillator exhibits interchange of the epochs of slow evolution, when accumulation of energy U_r takes place and the rapid phase, when, on reaching some critical threshold U_c, a fast discharge of accumulated energy occurs. The application of periodic forcing $a(\sin \omega t + \phi)$ affects the process, as now the critical threshold is $U_c + a(\sin \omega t + \phi)$. Accordingly, it changes the natural frequency T_0 of relaxation oscillator to some other value T_s, which now becomes a characteristic (synchronized) frequency of system.

8.2 Electromagnetic Triggering of Slip

Up to now, the problem of triggering and synchronization of seismic process is far from being resolved and relevant publications are controversial due to the complexity of natural processes (Beeler and Lockner, 2003; Scholz, 2003a; Grasso, 1998; Nikolaev A, 1994; Nikolaev V, 2003; Scholz, 2003; Kanamori and Brodsky, 2004; Ben-Zion, 2008). Understanding of main regularities can be obtained in controllable experiments. We carried out laboratory experiments on the slider-spring system with superimposed pulse or periodic electromagnetic (EM) forcing, which is weak in comparison with the main dragging force of the spring. The use of EM impact was prompted by experiments carried out in 1983-1988 by the Institute of High Temperatures of Russian Academy of Sciences (IHT RAS) at the Bishkek test area in Central Asia. After performing series of MHD soundings as well as "cold" discharges, initially aimed at finding resisitivity precursors of strong earthquakes in upper layers of the Earth crust, an unexpected effect of micro-seismicity activation by strong EM pulses has been discovered (Tarasov et al., 1999). We reproduced the effect in laboratory conditions and it turns out that EM forcing is a flexible tool for the study of triggering and synchronization phenomena in laboratory slider experiments (Chelidze et al., 2002; Chelidze and Lursmanashvili, 2003; Chelidze, Matcharashvili, 2003; Chelidze et al., 2005; Chelidze et al., 2006; Chelidze et al., 2007; Chelidze et al., 2008, Chelidze et al., 2009).

8.2.1 EM Triggering – Experimental Setup

The experimental setup has been designed in such a manner that the mechanical system could be easily driven to the critical state where the triggering of mechanical instability by some weak impact, such as electrical pulse, becomes more probable. The system (Fig. 8.2) consists of two pieces of rock; the upper piece can slip on the fixed supporting sample if a special frame tilts the latter one up to the critical angle α_c.

The electrical part consists of EM pulse generator and acoustic signals amplifier. The signal from the standard generator of 0.5–5 V amplitude is applied to the input of the amplifier and goes out from the output with the amplitude up to 1300 V. Up to 10 DC-pulses of this amplitude were applied to the sample. The duration of pulses was from 5 to 10 s; interval between pulses was also from 5 to 10 s. The high voltage source (discharger) was also used. Another amplifier was designed for registration of acoustic signals from the sensors which respond to the slip events. The amplifier's output voltage was sufficient for registration of acoustic signals by the sound card of PC. The scanning of the process was performed on the frequency 96 kHz, i.e., the sampling rate was 1/96 000 s.

Electrodes were applied in the following ways: (i) to the bottom of the supporting sample in a coplanar manner or to the sides of the supporting sample (the first mode); (ii) to the upper surface of the sliding sample and the bottom of the supporting one (the second mode). In the first case, the EM field is oriented roughly parallel to the slip surface and in the last case current lines are normal to it. In most cases, the supporting and the slipping blocks were prepared from basalt; these samples were saw-cut and roughly finished. The slipping block is 10 cm long, 10 cm wide and 2 cm thick. Other samples, such as granite, labradorite, and glass, which were better finished, were also tested. The height of surface protuberances was in the range of 0.1–0.2 mm for basalt samples and 0.05–0.1 mm for other ones.

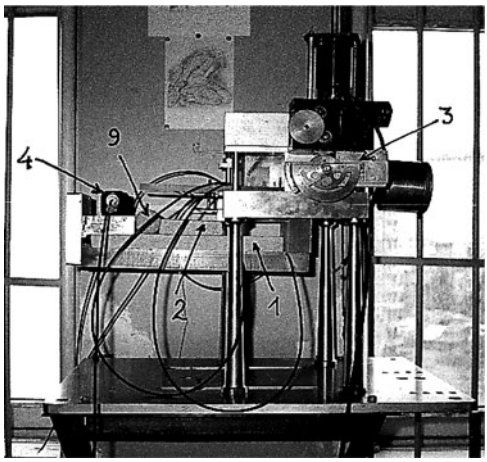

Fig. 8.2 Mechanical setup for slip initiation on the inclined surface: 1 – supporting (fixed) sample; 2 – slipping sample; 3 – slope regulating unit; 4 – acoustic emission sensor; 9 – shock absorber

The basalt samples were preferred because they do not contain significant quantity of piezoelectric minerals.

8.2.2 EM Triggering Experiments

The main objective of experiments was to find out whether EM-pulse could indeed displace the rock sample resting on the supporting sample at the slope of support, less than but close to the critical slip angle. The details of experiments are presented in (Chelidze et al., 2002; Chelidze et al., 2004).

Slip events were registered as acoustic bursts (Akay, 2002) by the sound card of PC.

It should be noted that although high voltage was applied to the outer surfaces of samples, the voltage in the gap between sliding surfaces was much less, of the order of 1 V.

8.2.3 Experimental Procedure and Case Stories

After finding the critical angle (Fig. 8.3), the slope of support was decreased by 0.1–2°. In this state, the upper sample was stable for many hours (2 days), which means that other sources of instability, such as building vibration by trucks, elevator, wind, etc, were not strong enough to initiate the slip. The critical angle for the rough surface varies from one test to another because it is impossible to reproduce exactly the arrangement of asperities between the support and the

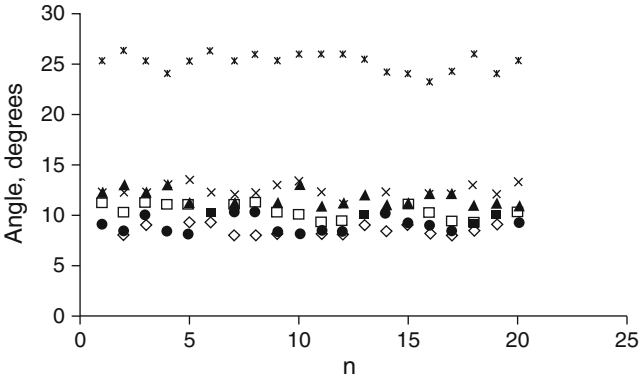

Fig. 8.3 The critical angle of slip (degrees) for various samples on the same supporting material versus number of experiment n. * – basalt, x – glass cylinder (diameter 14 cm, thickness 12 mm), □ – glass cylinder (diameter 7.5 cm, thickness 10 mm), ◇ – glass cylinder (diameter 2 cm, thickness 10 mm).

slipping blocks in different experiments. The scatter in values of critical angle for the same sample is of the order of $\pm 2.5^\circ$ so we can define only the average value of α_c (Fig. 8.3), which changes from one test to another. Because of the critical angle scatter, before the EM impact the sample was kept at the angle less than the (average) critical one for 10 minutes, and only after this exposure it was subjected to the EM-impacts also for 10 minutes.

That allows assessing correctly the statistics of EM-activation, as the probability of slip in the time intervals without EM-impact can be compared with that in the time intervals covering the whole EM-activation period. The activation period lasts several minutes and it includes also the gaps between pulses. A sequence of pulses applied in a single experiment and gaps between them will be related as a run. Practically the probability of slip without EM-impact at $\alpha < \alpha_c$ was zero: no slip was observed during any of 10 min. preliminary repose periods (500 min in total).

8.2.4 EM Triggering — The First Mode

We found that the application of EM-pulses in the first mode, i.e., to the coplanar electrodes at the bottom of support, initiates slip in approximately 40 cases from 600 runs (i.e., the slip initiation probability is around 0.07) either during pulse (i.e., in the active phase), or after it (i.e., in the passive phase). The last observation means that the polarization of the sample can be important for the slip initiation. As the delay of slip after switching off the pulse sometimes was considerable (seconds), our guess is that in this case polarization is related mainly to the accumulation of the bulk charge near electrode surfaces. This phenomenon (electrode polarization) is well known; it accompanies the application of high voltage to ionic conductors and its relaxation is slow.

A typical recording of acoustic emission generated by the slip event is shown in Fig. 8.4a and b for different time scales.

Besides the pulse generator, a second source of high voltage, namely the electrical discharger TESLA OPOCMO TVI 200, has been used for initiation of slip. In this case, the voltage applied was of the order of 10 kV. Again series of pulses were applied to the sample in the first mode and in this case the probability of slip initiation was much higher – around 0.2.

8.2.5 EM Triggering — The Second Mode

In the second mode, the electrodes were applied to the upper facet of the slipping block and to the bottom side of support, i.e., in this case the applied electrical field was oriented in the direction normal to the slip surface.

That means that when the EM is applied in the second mode, it increases the friction force (EM field hampers the slip) according to electrostriction rule (Tamm, 1956).

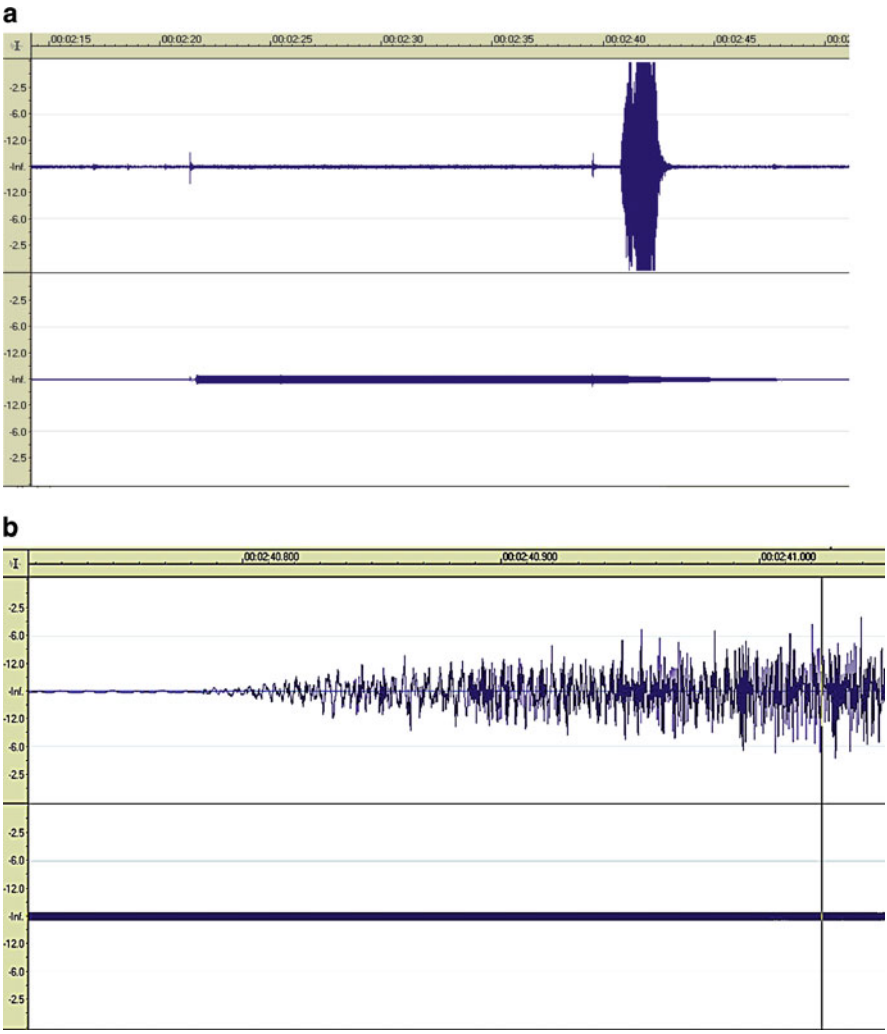

Fig. 8.4 (**a**) Recording of acoustic emission generated by the electromagnetically initiated slip of the basalt sample (upper trace). Lower trace shows EM pulse switching on (thick line) and switching off (thin line) periods. The slip was initiated just after the active period. y-axis shows amplitude of the signal in db, x is the time axis. (**b**) The initial part of the same recording with the stretched time axis

8.2.6 Finding Mechanical Equivalent of EM Impact

For assessment of mechanical equivalent of electrical impact, both direct and theoretical methods were used.

In the first case, the mechanical force initiating slip at the same angle $\alpha < \alpha_c$ that has been set in experiments with EM-impact, was measured by spring and torsion dynamometers (accuracy of ± 0.01 N and ± 0.005 N, respectively). Both methods gave comparable results. The force, equivalent to slip-initiating EM-impact, is of the order of 0.2 N. Another way to get mechanical equivalent is to calculate it from the general equation of balance of forces for a sample placed on the inclined plane:

$$F = mg(\mu \cos \alpha - \sin \alpha) \tag{8.1}$$

As long as μ is known (for basalt samples $\mu = 0.47$), slip-initiating force can be calculated for any angle. For example, if α_c equals 25°, at $\alpha = 24°50'$ the initiating force is 0.42 N. This value is of the same order as in direct experiments (0.2 N).

Thus, in the situation close to the critical one, even 0.2 N force can initiate the slip of a sample weighting 700 g.

Our guess is that the EM impact is equivalent to the above value, i.e., it promotes slip in the first mode and hampers it in the second mode by the additional force of the order of 0.2–0.4 N.

8.3 Analysis of Recorded Acoustic Waveforms

The results of experiments, namely, acoustic signals emitted during initiated slip, were recorded as *.wav files with 96 kHz sampling frequency at 8 bit resolution. The 3D patterns of original signals were obtained using program WaveLab (Figs. 8.6a, 8.7a in Chelidze et al., 2004). They show that some periodic components span the whole time axis. As they are present even before slip initiation, we guess that they are connected with weak vibrations due to computer and generator fans and other alias sources.

For filtering the background noise and further analysis of recordings, *.wav files were imported to the MatLab and their wavelet transform was performed. Mayer wavelet with a compact support in the frequency domain was used. Calculated wavelet coefficients were used for filtering of original signal. Namely, the wavelet components related to frequency range of noise, quite different from these of slip movement, were excluded. The de-noised signal reproduces the slip-generated wave package quite satisfactorily. Resulted de-noised data were analysed again using Wavelab, and filtered 3D images of frequency distribution in the time domain during slip were obtained (Figs. 8.6b and 8.7b in Chelidze et al., 2004b).

The consideration of the above images shows that the emitted signals are concentrated in 500–20,000 Hz frequency range and the manner of slip initiation (EM or mechanical) does not change significantly the wavelet and spectral patterns.

8.4 The Elementary Theory of EM Coupling with the Friction Force

In order to understand physics of EM-slip it is necessary to consider fundamentals of surface phenomena. Intermolecular and intersurface forces, responsible for adhesion and friction, can be loosely divided into three categories: (i) purely electrostatic, arising from the Coulomb interaction between charges; (ii) polarization forces arising from the dipole moments, induced by internal (bound charges, dipoles) or external electric field; (iii) quantum-mechanical forces, responsible for covalent bonding and steric interactions. All these forces can act simultaneously, resulting in some total adhesion (friction) force. For friction we have:

$$F_f = \mu F_n, \tag{8.2}$$

where μ the is friction coefficient and F_n is the normal component of force acting on the body (gravity, compression).

From the above classification it can be deduced that in principle as far as intersurface forces are of electromagnetic origin, external electrical field can affect the adhesion (friction) forces, changing μ and thus initiating slip of the body placed on the inclined plane. We can rewrite (8.2) in the following way:

$$F_f = \mu(F_n + F_p), \tag{8.3}$$

where μ is the friction coefficient and F_p is the increment (decrement) of normal component of force due to the application of EM field.

Of course, coupling of EM-impact with friction in a sample containing piezoelectric materials is a trivial phenomenon. However, the EM-activation of slip is clearly observed on samples that are practically free of piezoelectric minerals (basalts). That is why we exclude the piezoelectric effect as a principal mechanism of EM-slip.

The elementary theoretical model of EM coupling with friction can be formulated in the following way. It is well known that the application of EM field to a dielectric invokes some forces acting upon molecules of the body; the resultant force is called the electrostriction force F_p which is affecting the whole sample. The force is proportional to the gradient of the field intensity squared and it carries away the sample in the direction of the largest intensity. The tension tensor $\vec{T}_n$ operating on the element of dielectric's surface in EM field of intensity E on the assumption that the sample of dielectric constant ε is surrounded by the immobile dielectric medium in *ESU* system is (Tamm, 1956):

$$\vec{T}_{np} = \pm \frac{\varepsilon + \frac{\partial \varepsilon}{\partial \delta}\delta}{8\pi} E^2 \vec{n}, \tag{8.4}$$

where the sign (+) applies when the field $\vec{E}$ is parallel to the external normal $\vec{n}$ to the considered surface element, and the sign (−) when the field $\vec{E}$ is normal to $\vec{n}$.

We can imagine that the elastic strings are stretched along field lines (Tamm, 1956): in our case, they pull together the surfaces of sliding and supporting samples in the second mode or build the side thrust on each other according to (8.4). The latter case corresponds to the first mode and the former one to the second mode of EM-triggering.

The above equations can be simplified if the dielectric increment due to the striction force is negligible: $(\partial\varepsilon/\partial\delta \to 0)$. Introducing the area of dielectric's surface S and taking into account the above assumption, the electrostriction force is:

$$\vec{F}_p = \pm\frac{\varepsilon}{8\pi}E^2\vec{n} = \pm\frac{\varepsilon S}{8\pi}\left(\frac{\Delta V}{d}\right)^2\vec{n} \tag{8.5}$$

where ΔV is the applied voltage and d is the distance between electrodes; the sign depends on the mutual orientation of dielectric's surface and electrical field.

Substituting into (8.5) the values: $\Delta V = 1200$ Volt $= 4$ ESU, $\varepsilon = 5$; $S = 100$ cm^2 and $d = 5$ cm, which correspond to the capacitor, created by two electrodes we obtain:

$$\left|\vec{F}_p\right| = 0.5 \text{ dyne} = 5\ 10^{-6}\text{N}$$

That is much less than the experimental values of electromagnetic pull force, which is of order of 0.2 N. Here we have to note that the value of $(\Delta V/d)$, substituted in (8.5), is an average value for the whole system and on the contact between two blocks the gradient can be quite different. The matter is that the most part of the voltage drop occurs in the gap and the local gradient of EM field in the gap between samples can be much larger than for the whole system between electrodes. In order to assess the forces acting in the narrow gap between slipping and supporting samples, it is necessary to consider the gradient in the gap between the samples. The inner surfaces of slipping and supporting samples carry bound charges, due to the polarization of material, and thus create the local gradient of electrical field in the gap. The opening of the gap itself is varying; we can introduce some effective value of opening d_{eff}. Then, applying again the equation (8.6) to the "inner" capacitor, we obtain the electrostriction force F_{pi} acting on the gap surfaces as follows:

$$\vec{F}_{pi} = \pm\frac{\varepsilon_{eff} S}{8\pi}\left(\frac{\Delta V_{eff}}{d_{eff}}\right)^2\vec{n}, \tag{8.6}$$

where $\Delta V_{eff}/d_{eff}$ is the effective voltage gradient in the gap and ε_{eff} is the effective dielectric constant of the gap, which is between values of ε for the air and the sample: $1<\varepsilon<5$.

Assuming $\varepsilon_{eff} = 2.5$, $S = 100$ cm^2, we have to put in equation (8.6) the gradient $(\Delta V_{eff}/d_{eff)}) = 0.07$ V/cm in order to obtain the experimental values of slip-initiating electrostriction force, namely, $F_p \approx 0.2$ *N*.

Thus the expression (8.7) can be written, taking into account (8.6):

$$F_f = \mu\left(F_n + F_{pi}\right), \tag{8.7}$$

which is similar to the expression for the friction force, taking into account the pore pressure term (Sibson, 1994).

The above value of F_{pi} can be considered as an order of magnitude of electrostriction force that promotes the slip in the first mode and hampers it in the second mode, according to the expression (8.6) for the accepted set of parameters.

Both our experiments and theoretical considerations are related to the "dry" environment, namely, to the 60 ± 20% humidity of the atmosphere at a temperature of (20 ± 5)°C.

It is interesting to note that somehow similar effect of synchronization of acoustic vibrations (not stick-slip motion) in rock samples by the superimposed EM forcing has been observed by Chernyak (1978).

In the "humid" environment, when the rock's pore space is fully or partially saturated with water, additional factors should be taken into account: (i) the pore pressure increment (decrement) in the gaps, caused by the electrokinetic flow of fluid at the application of EM field; (ii) the change of surface fracture energy of cracks due to electroosmotic fluid inflow into the cracks of an undersaturated rocks due to the EM impact. Both these factors can facilitate fracture process in water-bearing rocks.

8.5 Synchronization of Stick-slip

8.5.1 Synchronization: Experimental Setup

Experimental setup in synchronization experiments represents a system of two horizontally oriented plates of roughly finished basalt (Fig. 8.5). A constant pulling force F_p of the order of 10 N was applied to the upper (sliding) plate; in addition, the same plate was subjected to periodic mechanical or electric perturbations with variable frequency and amplitude (from 0 to 1000 V), which was much weaker (of order of 1 N) compared to the pulling force; the electric field was normal to the sliding plane. Acoustic bursts accompanying slip events were registered by the sound card of PC. Details of the setup and technique are given in (Chelidze and Lursmanashvili, 2003).

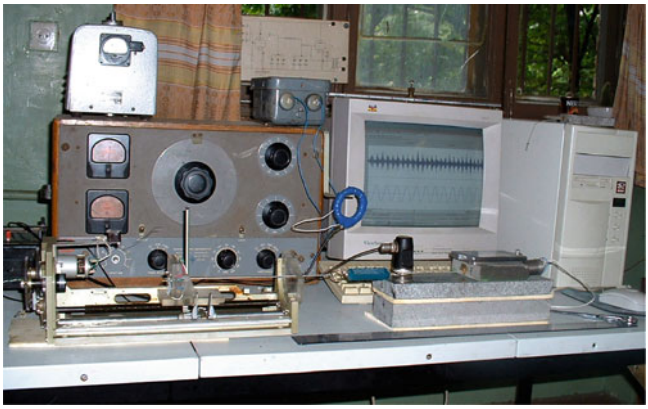

Fig. 8.5 Laboratory setup for synchronization experiments

8.5.2 Signal Processing: Separation of AE Wave Trains

The first step of AE data analysis consists in signal conditioning and wave trains separation. A relatively simple form of signal conditioning is calculation of its envelope by the Hilbert transform (Kurz et al., 2004). The Hilbert transform generating phase shift of $\pi/2$ is defined as:

$$\hat{R} = \frac{1}{\pi} \int_{-\infty}^{\infty} \frac{R(t)}{\omega - u} du = H\{R(t)\} \tag{8.8}$$

It is a causal transfer function which behaves like a filter of a real time dependent function *R(t)*.

Then the envelope time function *E(t)* can be calculated:

$$E(t) = \sqrt{R(t)^2 + \hat{R}(t)^2} \tag{8.9}$$

Squared and normalized envelope of the signal leads to suppression of noise of lower amplitude and to increase of the signal content of higher amplitude (Fig. 8.6).

Then, the envelope can be used to estimate the onset of the signal or for correct signal detection in general. Strictly speaking, in order to determine the onset time of AE signal, AIC (Akaike Information Criterion) function was calculated according to Maeda (1985). The minima of AIC function correspond to AE signal onsets; afterwards, the onsets can be correlated with forcing signal phase (Fig. 8.7).

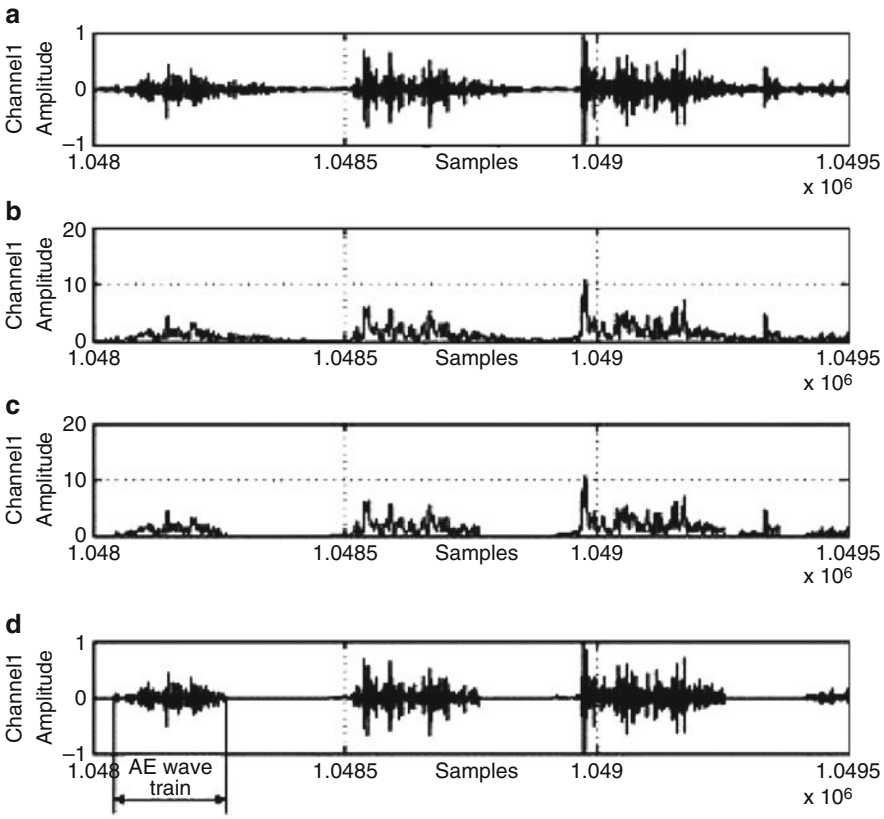

Fig. 8.6 Processing of the acoustic signal: (**a**) source (initial) signal; (**b**) Hilbert transform of the source signal; (**c**) filtered Hilbert-transformed signal using Standard Deviation criterion – only the part of signal of amplitude less than 3σ was eliminated; (**d**) the recording (a) filtered from the noise according to criterion (c)

Typical examples of filtered AE recordings during various regimes of stick-slip are presented in Fig. 8.8. The random sequence of AE, obtained for stiff springs, probably corresponds to macroscopically "stable" sliding, and quasi periodic sequences – to macroscopically "instable" process, characteristic for soft springs.

After such a processing, the catalogue of waiting times of acoustic bursts has been compiled.

Besides, the catalogue of "magnitudes" of AE was also compiled. The energy released by acoustic pulse (or the power of AE) was calculated as the plot area delineated by a singled acoustic burst recording.

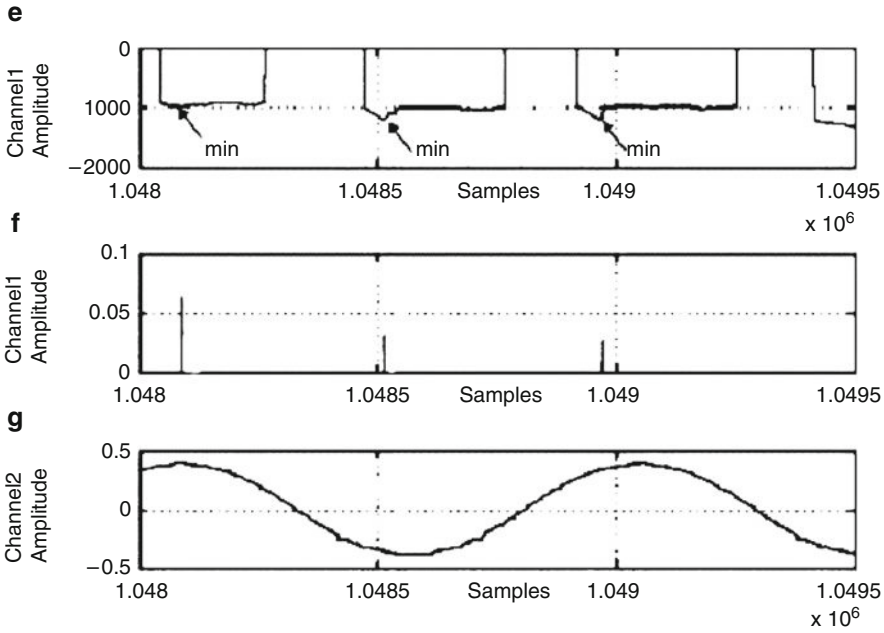

Fig. 8.7 The AIC (Akaike Information Criterion) function of AE signal: (**e**) the minima of AIC function are picked; (**f**) corresponding AE signal onsets are located; (**g**) onsets can be correlated with forcing signal phase

8.5.3 Synchronization: Results

In our experiments the following parameters were varied: (i) the stiffness of the spring, K_s; (ii) the frequency, f, of superimposed periodical perturbation; (iii) the amplitude of the excitation (applied voltage V_a); (iv) the direction of applied electrical field; (v) the velocity of drag, v_d; vi) the normal (nominal) stress σ_n.

The typical background behavior of the system with stiff spring during conventional stick-slip is presented in Fig. 8.9a. It is evident that in these conditions AE events do not manifest any visible periodicity at the time scale from several to hundred milliseconds. In case of soft spring, the friction movement is realized by quasi periodic slips (Fig. 8.9b).

Slip with superimposed periodic low-frequency EM field ($f \approx 60$ Hz) of varying intensity, oriented normally to the slip surface, is presented in Figs. 8.10a, b, c. The significant synchronization at this frequency occurs at $V_a \geq 500$ V. Under EM excitation the AE events (micro slips) occur twice per period (Fig. 8.10c). The maxima of AE coincide (approximately) with the extreme points of oscillation.

Synchronization was observed only at some definite values of the set of parameters (K_s, f, V_a). The "phase diagram" for variables f and V_a, or the so-called Arnold's tongue (see Pikovsky et al., 2003) is presented in Fig. 8.11.

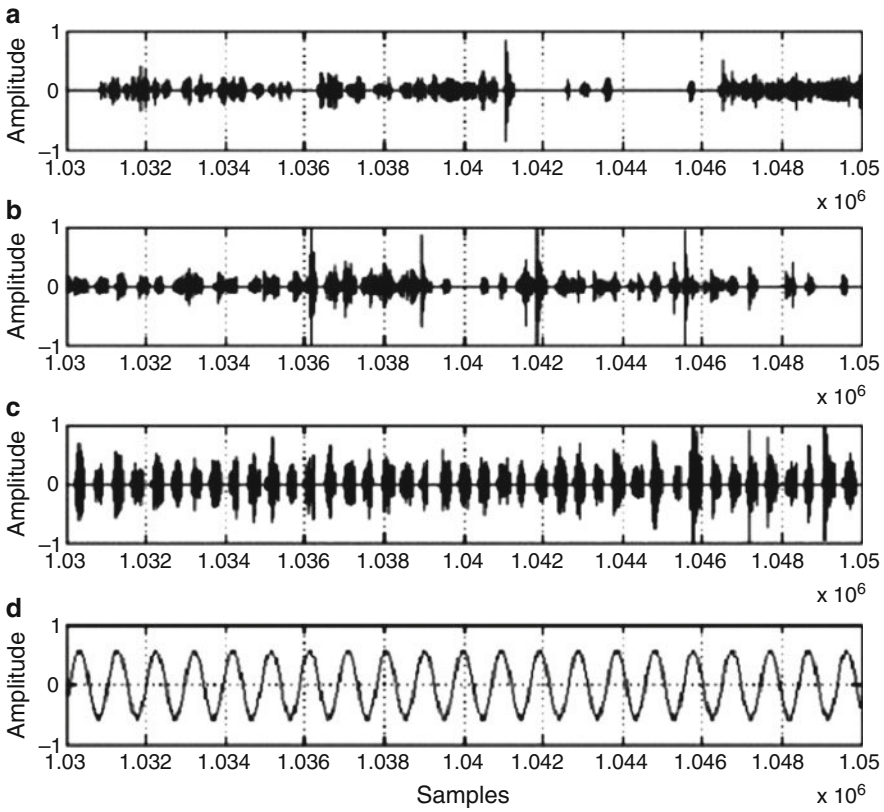

Fig. 8.8 Filtered AE recordings for various regimes of stick-slip: (**a**) and (**b**) – stiff springs; (**c**) – soft spring; (**d**) – forcing signal

It should be noted that the phenomenon of synchronization was observed only with the EM field directed normally to the slip surface. When the EM field was applied to the vertical sides of the slipping block, that is, roughly parallel to the slip plane, we were not able to observe the effect of synchronization. We conclude that the synchronization is related to "electromagnetic braking" of slip at passing the extreme values of sinusoidal EM forcing and a sudden slip after the accumulation of enough stress provided by spring pull.

Moistening of the slip surface by wetted blotting paper does not affect the "mechanical' synchronization, but practically kills the "electromagnetic" synchronization.

We observe transition (bifurcation) in stick-slip from 1:2 or period doubling synchronization, when two slip events occur per a period of EM forcing, to 1:1 synchronization, when one slip event occur per a period of forcing (Fig. 8.12) at simultaneous action of direct $V(0)$ and periodic $V(p)$ voltages; transition occur at $V(0) > V(p)$.

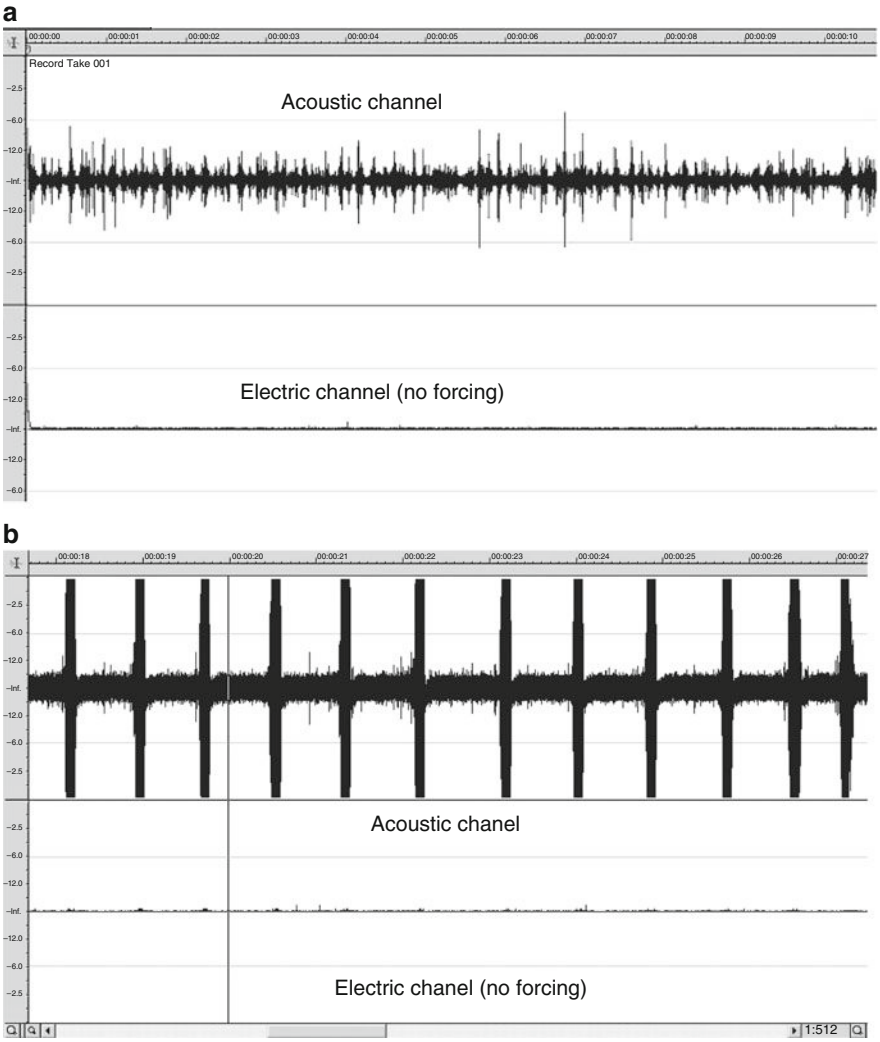

Fig. 8.9 Typical acoustic emission during slip without periodical impact: (**a**) stiff spring; practically random release of acoustic bursts. The stiffness of spring $K_s = 1000$ N/m; $\sigma_n = 2$ kPa.; the mean drag velocity $v_d = 2.5$ mm/s; dragging force $F_d = 3.5$ N; T = 20°C; humidity W = 40%; (**b**) soft spring; quasi periodic acoustic bursts (without external periodical forcing) with the mean waiting time 0.7 sec during natural slip; $v_d = 1.45$ mm/s; $F_d = 3$ N; $K_s = 125$ N/m; T = 20°C; W = 50%. Here and in Figs. 8.10a, b, c; 8.12; 8.15a, b; 8.26; 8.27a; 8.28a; 8.29a; and 8.30a, b, the amplitude of AE and synchronizing field is given in dB

Synchronization affects not only waiting times, but also the frequency-energy distribution: the amplitudes of bursts are much less scattered than in the absence of periodic forcing.

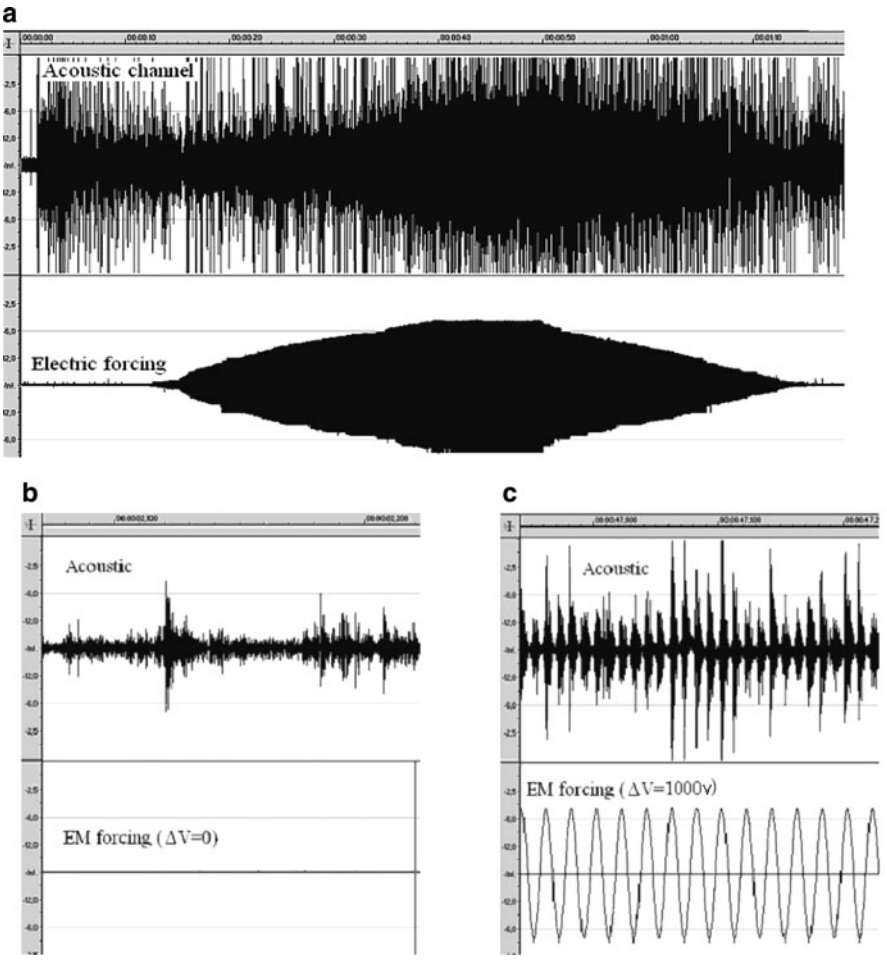

Fig. 8.10 (**a**) Acoustic emission during slip under periodical external voltage varying from zero to 1000 V; (**b**) the extended part of record with zero EM forcing; (**c**) the extended middle part of record under maximal EM forcing. Note complete phase synchronization – PS

We tried to plot (Fig. 8.13) the slopes of distribution of number of AE events versus reduced power of AE (that is, an analogue of Gutenberg-Richter plot) in sequential windows (time intervals) using data of experiment with different intensity of forcing (see Fig. 8.10 a).

The (negative) slope of the plot is maximal in the most synchronized part of AE record on Fig. 8.10a, due to increasing contribution from small events leading to appearance of plateau in the small energy section and decreasing of number of strong events (see Fig. 8.11 in Chelidze et al., 2005). This means that the energy is pumped from large events to some intermediate scale ones. As the contribution from very large events is limited, the plot in this interval looks like

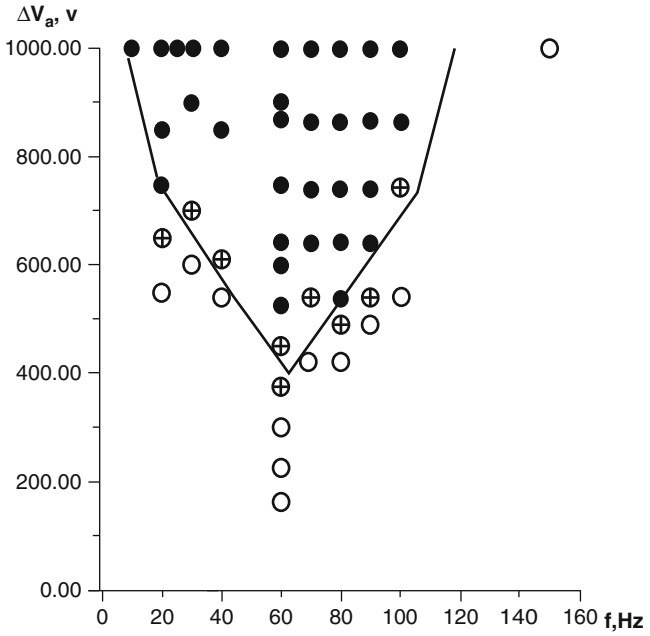

Fig. 8.11 Stick-slip synchronization area (Arnold's tongue) for various intensities (V_a) and frequencies (f) of the external EM forcing. Filled circles – perfect, circles with crosses – intermittent, and empty circles – absence of synchronization

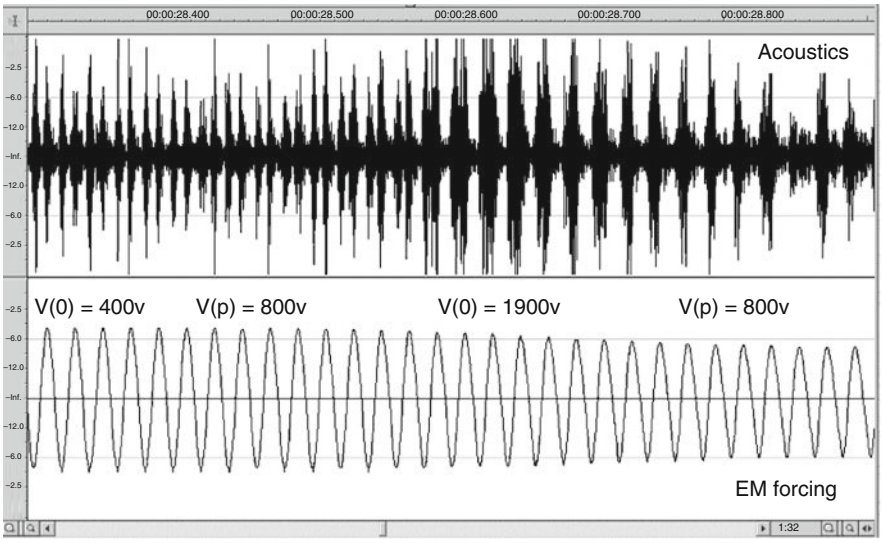

Fig. 8.12 Transition (bifurcation) in stick-slip from 1:2 synchronization (period doubling) to 1:1 synchronization at simultaneous action of direct V(0) and periodic V(p) voltages; transition occurs at $V(0) > V(p)$

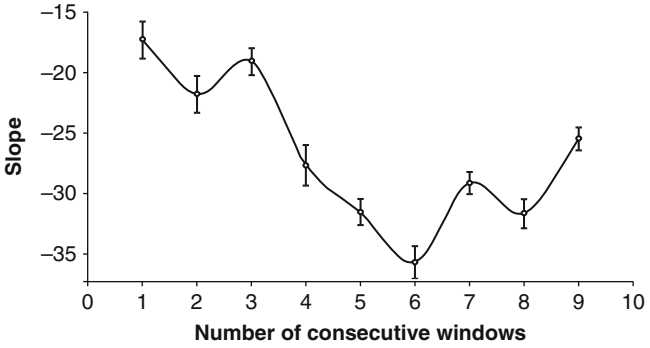

Fig. 8.13 Slopes of linear parts of magnitude-frequency (log cumulative value of number of AE events versus reduced power of acoustic emission) plots versus the serial number of 300 data-length sliding windows in the time series of AE. The data of experiment with different intensity of forcing (Fig. 8.10a) were used. The (negative) slope of the plot is maximal in the most synchronized part of AE record (Fig. 8.10c), due to increasing contribution from small events leading to appearance of plateau in the small energy section and decreasing number of strong events (Fig. 8.11 in Chelidze et al., 2005). The middle part of analyzed time series (window 6) was the most synchronized one

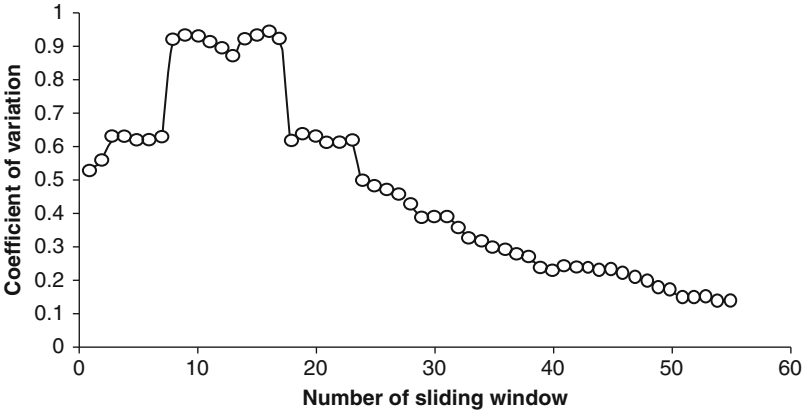

Fig. 8.14 Coefficient of variation of power of acoustic emission time series at increased external forcing for 500 data length sliding window with 50 data shift. Here only half of record (Fig. 8.10a) is used from the start of test to the maximal synchronization state

magnitude-frequency distribution for characteristic earthquake model; hence, the distribution of energies becomes less scattered due to increasing share of "characteristic" events.

A decrease of contribution of extreme events at synchronization is confirmed by calculation of the coefficient of variation CV (CV = standard deviation/mean). As shown in Fig. 8.14, the extent of the deviation from the mean value of released AE power calculated for consecutive sliding windows decreases at synchronization.

This means that synchronization limits the energy release associated with individual events (quantization effect). Sudden decrease or total cessation of synchronizing forcing is followed by acoustic burst of much larger energy than during the periodic forcing (Fig. 8.15a, b).

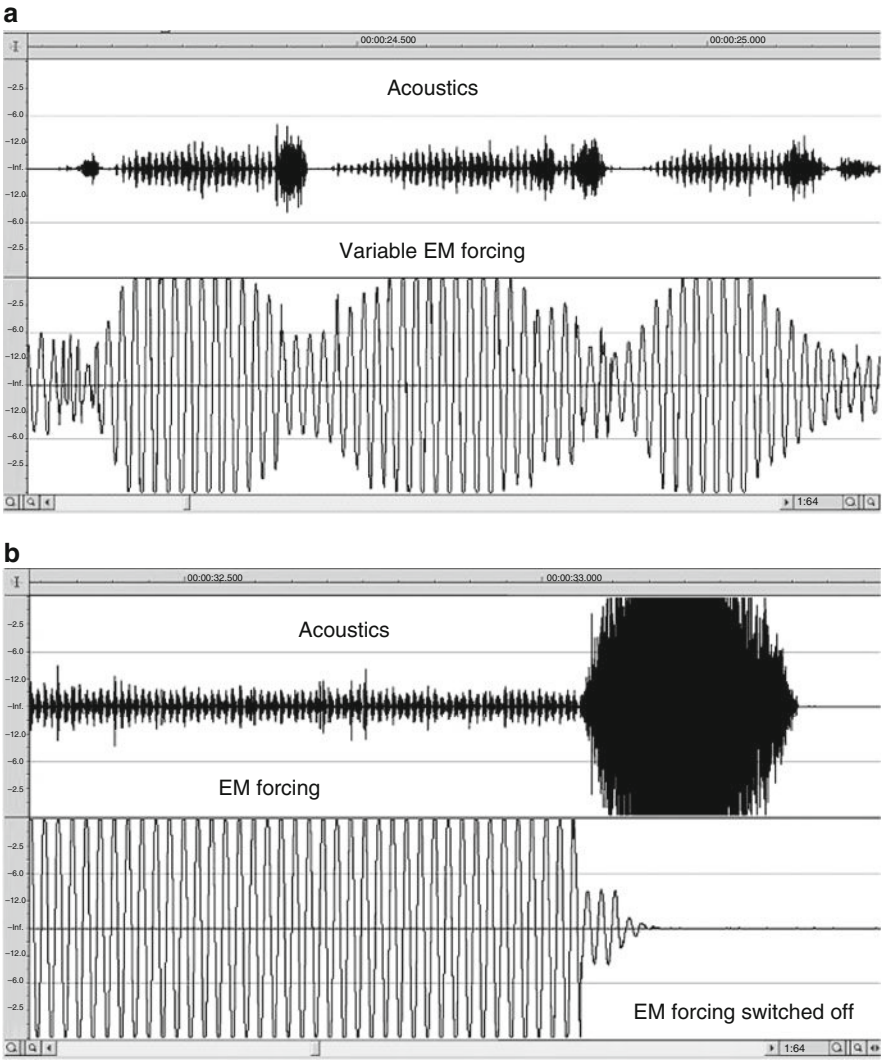

Fig. 8.15 Increased acoustic energy release after decreasing (**a**) or total cessation (**b**) of periodic EM forcing, which means that synchronization limits the energy release associated with a single event (quantization effect)

8.6 Synchronization: Quantitative Analysis

Several tools for quantitative analysis of the strength of synchronization (Ditto, 1990; Zbilut, 1992; Rosenblum et al., 1996; Rosenblum et al., 1998; Kantz, 1997; Quiroga et al., 2002; Pikovsky et al., 2003; see also Chapter 1) were tested on the recordings of stick-slip process, where the superimposed periodic EM field intensity was raised monotonously from zero to 1000 V and then decreased in the same way to zero (Fig. 8.10a).

In order to assess synchronization in the qualitative manner we used the easiest approach for estimating phases of acoustic signal: digitized waveforms were transformed to sharp spikes to have well pronounced markers. Then time series (catalogues) of time intervals between consecutive maximums (waiting times) ($\Delta t = t_i - t_{i-1}$) in wave trains for π periods of external sinusoid (Fig. 8.10c) were composed (the time scale in Figs. 8.16 – 8.20 corresponds to sequential values of t_i).

In order to achieve more reliable phase construction and precise synchronization testing, various tools of nonlinear dynamics (synchronization) theory described in Chapter 1 were applied to experimental data obtained under variable intensity of forcing; the results are shown in Figs. 8.13–8.14 and 8.16–8.20. All these approaches yield similar results.

In Fig. 8.17 we present the temporal evolution of phase difference $\Delta\phi$ obtained from Hilbert transform of waiting times time series. Well-defined horizontal part of $\Delta\phi$ versus t (Fig. 8.17) represents the time during which the acoustic emission becomes phase synchronized to the external sinusoidal forcing in the wide range of their amplitudes (from approximately 500 V to 1000 V). Clear phase synchronization is especially obvious in Fig. 8.17, as long as in the most synchronized part of the plot the phase difference variation $\Delta\phi$ does not exceed 10 radian (compare with the total increment $\Delta\phi$ of 1800 radian during the whole experiment).

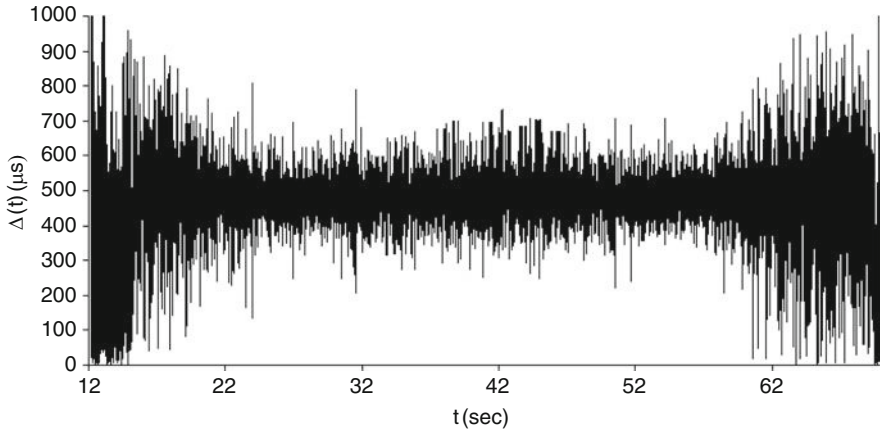

Fig. 8.16 Time series of waiting times between consecutive maximal amplitudes of acoustic signals in consecutive π-periods of external forcing for a whole record (compare with Fig. 8.10a)

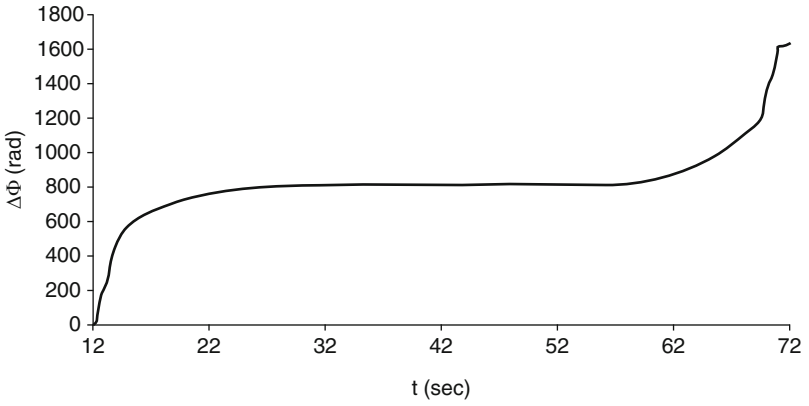

Fig. 8.17 Phase difference $\Delta\Phi$ between the sequence of maximums of acoustic emissions' bursts (AE catalogue) and external sinusoidal forcing for the whole record (Fig. 8.10a)

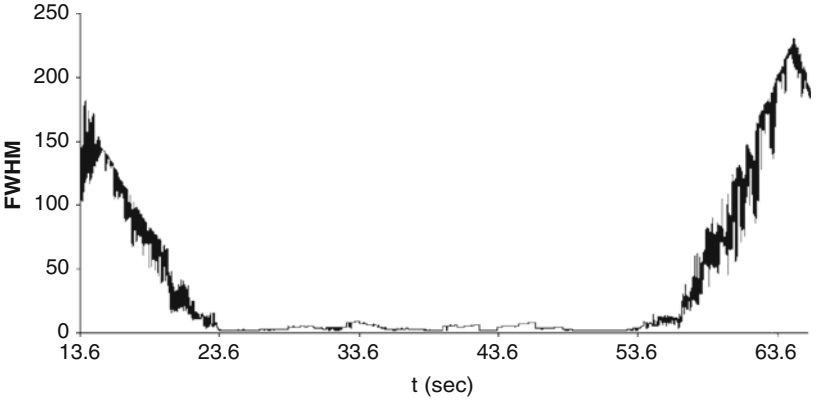

Fig. 8.18 Variation of the full width of probability density distribution of phase differences between the catalogue of acoustic events and periodic signal at a half maximum (FWHM), calculated for consecutive sliding windows, containing 500 events

It is known that the probability density distribution must be narrower for the synchronized signal compared to a non-synchronized one. As follows from Fig. 8.18, the full width at half maximum (FWHM) of probability density distribution of phase differences between AE pulses and sinusoidal forcing is indeed much narrower for the synchronized part of Fig. 8.10a.

Frequency locking, expressed as a minimum of the phase diffusion coefficient, is also a quantitative measure of the phase synchronization (see Fig. 8.19).

Moreover, clear decrease of Shannon entropy value S indicates that dynamics of acoustic emission becomes much more regular in the synchronized part of acoustic emission data set (Fig. 8.20).

One of interesting methods of revealing synchronization in relaxation-type processes is a "gap" technique (Lursmanashvili, 2001), which is described in detail

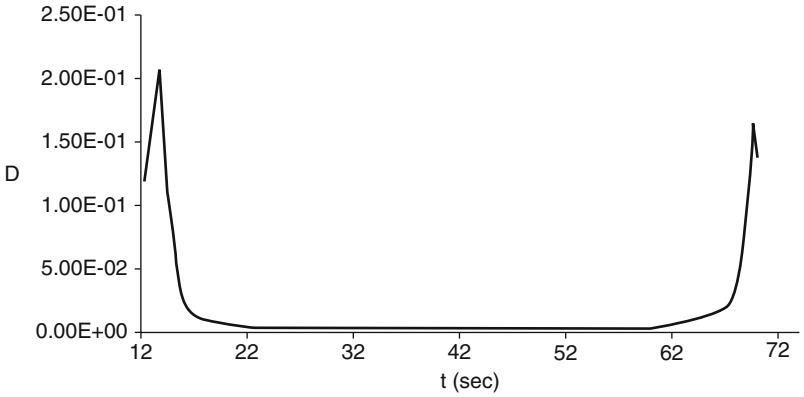

Fig. 8.19 Variation of phase diffusion coefficient *D* of phase differences, calculated for consecutive sliding windows, containing 500 events

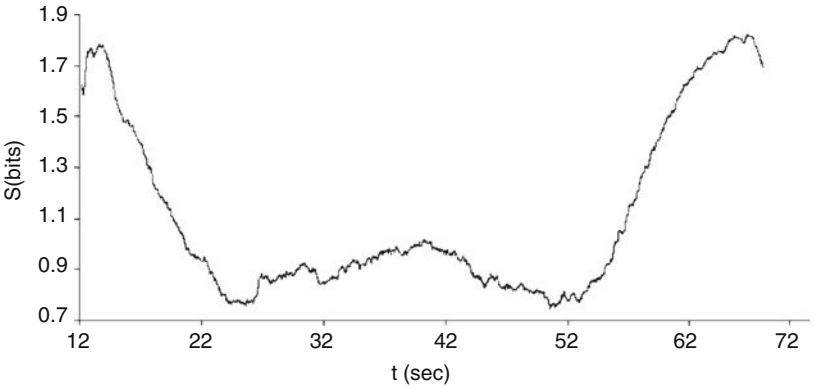

Fig. 8.20 Variation of Shannon entropy *S* of phase differences, calculated for consecutive sliding windows, containing 500 events

in Chapter 18 and which has an analogue in the analysis of radio technical systems (Blekhman, 1988). It is founded on the effect of concentration of slips (and associated seismic/acoustic events) in the definite phases of forcing period. Of course, this means that the occurrence of dynamic events in the remaining phases of forcing is less probable (prohibited). The width of the prohibited zone is larger for stronger synchronization. Of course, some intervals of silence can occur just randomly, but these intervals are relatively short and are distributed randomly relative to the forcing phase. These short gaps can be considered as a noise; the gaps due to synchronization are much wider. The method has been tested on the laboratory spring-slider model with mechanical forcing.

Consider stick-slip as a nearly periodic relaxation process, where the stress is accumulated for a long time in order to release it in a fast slip. As this last phase is very short, the duration of a whole cycle is practically equal to that of accumulation stage.

Assume that a periodic relaxation process with period τ is exposed to also periodic forcing of period T. Let us suppose that the forcing period is not known exactly, but some preliminary guess on the range of periods can be made. Is it possible to retrieve the unknown forcing period accurately from the observed modified relaxation process? So, the objective is to find exact forcing period from a given sequence of onsets of slips $d(j), j = 1,2,3, \ldots . m$. Here m is the total number of slips. We are looking for the forcing period inside the interval $[T_{min}; T_{max}]$ of a width $\Delta T = T_{max} - T_{min}$. We use a scanning window with the optimal length dT, which is much less than ΔT. The window length dT is calculated by the following empirical formula:

$$dT = T^2 min/50t, \tag{8.10}$$

where t is the duration of experiment. As a result we will have $n = \Delta T/\, dT$ (virtual) periods to test inside the chosen interval of periods ΔT. For the $T(i)$-th trial (virtual) forcing period we have:

$$T(i) = T_{min} + i \times\, dT, \quad i = 0, 1, 2, 3.....n \tag{8.11}$$

For revealing phase synchronization the times of slip occurrences $d(j)$ are divided by the corresponding period $T(i)$:

$$\mathrm{d(j)}/T(i); \quad j = 1, 2, 3... ....\mathrm{m}; \; i = 1, 2, 3... ....n. \tag{8.12}$$

Let us consider for each period $T(i)$ the remainder of the above division $F(j,i)$:

$$F(j, i) = remainder(d(j)/T(i)) \quad j = 1, 2, 3.....m; \quad i = 1, 2, 3.....n.$$

For revealing phase synchronization just the non integer part is essential as it characterizes the distribution of phases of "discharges" inside the trial forcing period. For convenience these values are normalized in the following way:

$$F^n(j, i) = F(j, i)T(i) \times 1000 \tag{8.13}$$

After such a normalization, the considered values of $F_n(j,i)$ do not depend on the absolute value of trial period $T(i)$ and are distributed inside the range [0;1000]. The normalized phases are arranged according to their ascending values and the largest free-of-slips interval between neighboring phases or the local maximal "gap" width $dF(j, i)^{loc}_{\max}$ is found for each trial period $T(i)$. As a result, two numerical sequences for $T(i)$ and $dF(j, i)^{loc}_{\max}$ are obtained. The graph of $dF(j, i)^{loc}_{\max}$ versus $T(i)$ actually forms a spectrum of local maxima of gaps widths for a chosen range of trial forcing

periods. The largest gap (or the absolute maximum in the set of local ones) returns the value of the sought forcing period.

The method has been tested on the laboratory spring-slider model with mechanical forcing. The results are shown in Figs. 8.21–8.23.

In these experiments the forcing frequency (30 Hz) was known beforehand and the objective was to retrieve it from the observed data as if it were unknown. So the known forcing frequency was used only for validation of the gap method. The amplitude of mechanical forcing was changed (namely, the excitation of mechanical vibrator was realized by application of voltages of 4, 5 and 6 V

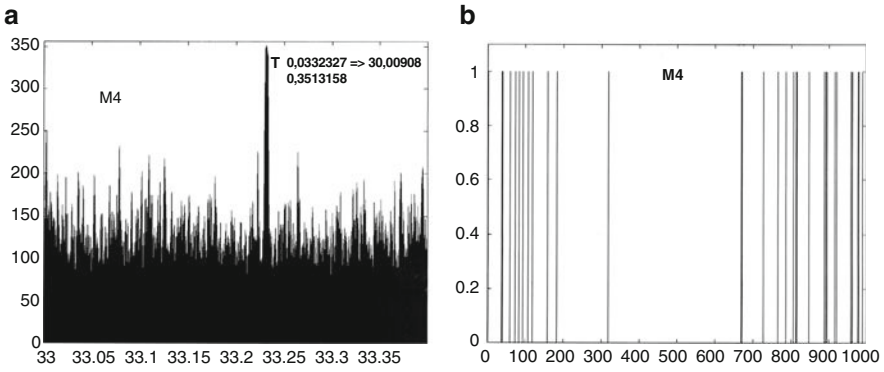

Fig. 8.21 (**a**) Recurrence spectrum of local maxima of gaps widths for a chosen range of trial forcing periods spectrum of slips for exciting voltage of 4 V: *Y*-axis — the local maxima of the gap widths $dF(j,i)^{loc}_{\max}$; *X*-axis — trial periods $T_i \cdot 1000$; (**b**) The distribution of slip moments inside the genuine forcing period T_{ig} divided in 1000 intervals

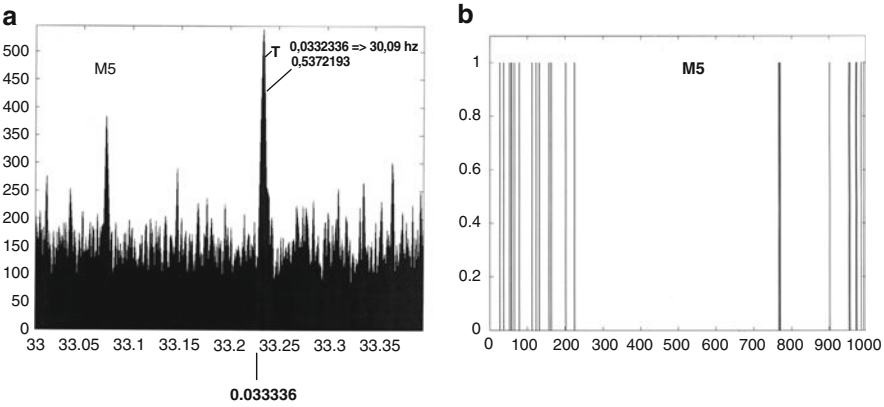

Fig. 8.22 (**a**) Recurrence spectrum of local maxima of gaps widths for a chosen range of trial forcing periods spectrum of slips for exciting voltage of 5 V: *Y*-axis – the local maxima of the gap widths $dF(j,i)^{loc}_{\max}$; *X*-axis – trial periods $T_i \cdot 1000$; (**b**) The distribution of slip moments inside the genuine forcing period T_{ig} divided in 1000 intervals

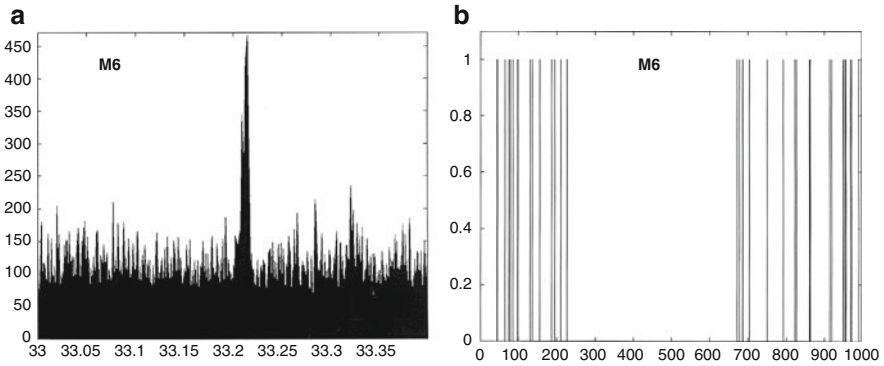

Fig. 8.23 (**a**) Recurrence spectrum of local maxima of gaps widths for a chosen range of trial forcing periods spectrum of slips for exciting voltage 6 V: *Y*-axis — the local maxima of the gap widths $dF(j,i)^{loc}_{\max}$; *X*-axis — trial periods $T_i \cdot 1000$; (**b**) The distribution of slip moments inside the genuine forcing period T_{ig} divided in 1000 intervals

respectively, in Figs. 8.21–8.23). Figs. 8.21a, 8.22a, 8.23a show the hidden periodicity of slips (in particular, recurrence spectra of local maxima $dF(j,i)^{loc}_{\max}$ for each trial period T_i) and Figs. 8.21b, 8.22b, 8.23b present gaps in distribution of slip moments inside the genuine (T_{ig}) period of forcing (returned from the value of absolute maximum of the gap width $dF(j,i)^{abs}_{\max}$, here 0.0332327 s), which is divided into 1000 intervals.

From the analysis of the gap spectra we can conclude that synchronization is present at the forcing frequency of 30 Hz and the genuine forcing period $T_{ig} = 1/\mathrm{f} = 0.0332327$ can be extracted with no less than 0.01 Hz accuracy. It is evident that the forcing frequency can be determined accurately from the observed synchronized slip recurrence spectra.

The above approach has been tested on the Catalogue of Caucasian earthquakes of M. Nodia Institute of Geophysics and some significant gaps related to tidal effects were revealed (Chapter 18).

We hope that the methods applied in the present work to the laboratory data can be used in future for detection and quantitative assessment of seismic process synchronization strength induced by a weak external impact, such as tides, reservoir loading, etc (Heaton, 1975; Nikolaev V. 2003; Grasso, 1998).

8.7 Phase Time Delay

The acoustic response lags behind the periodic forcing phase; the lag is inversely proportional to the forcing intensity (Fig. 8.24a, b, c, d). The delay is quite similar for both AE burst onsets and AE wave train maxima. The dependence of phase delay on the intensity of periodic or pulse-like forcing points to a nonlinear response of the system to a weak external impact.

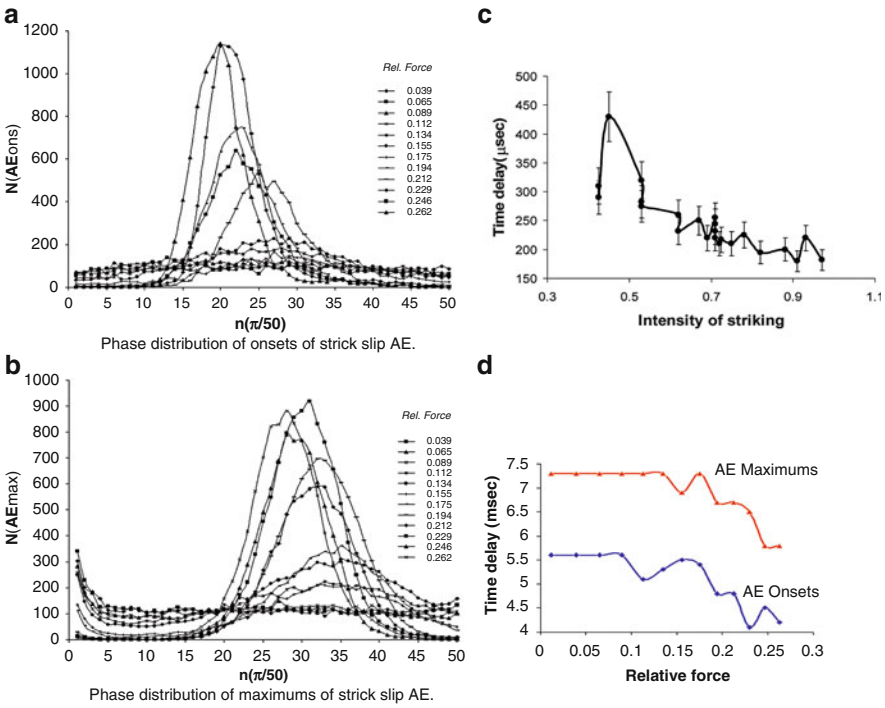

Fig. 8.24 AE phase delay relative to forcing phase: distributions of AE number versus delays for: (**a**) onsets and (**b**) maximums of acoustic signal at periodic EM forcing. (**c**) Time delays for slips triggered by mechanical strike. (**d**) Phase time delays at synchronization by periodic EM forcing for panels a and b

8.8 Synchronization by Mechanical Forcing

Of course, synchronization of stick-slip can be achieved by a weak mechanical forcing also. Such experiments are quite numerous as the phenomenon of stick-slip is ubiquitous in friction processes and it is considered as a negative factor, disturbing the stable displacement of contacting surfaces. In order to achieve smooth functioning of technical systems with friction, application of weak mechanical vibrations of relatively high frequency is studied mainly as a tool for stabilization of friction process (Bureau et al., 2000; Perfettini et al., 2001; Boissou et al., 1998). It has been found that at some intensity of mechanical forcing (but still much less than the main driving force) the stick-slip phenomenon is strongly reduced. At the same time, it is clear from analysis of recordings (Fig. 8.25) that what is considered as stabilization of friction is in fact the stick-slip of small amplitude synchronized with the (high) frequency of forcing. Thus, the stabilization of motion is achieved not by elimination of stick-slip, but by drastic decrease of amplitude of slips, which occur much more frequently than in motion without forcing.

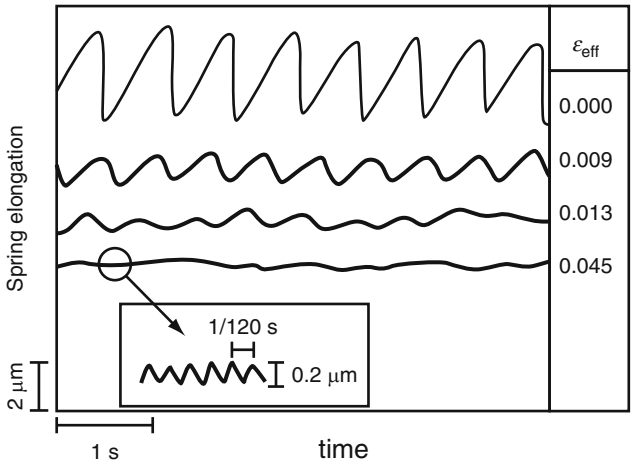

Fig. 8.25 Time evolution of the loading spring elongation for $v = 8$ μm/s and different modulation amplitudes ε_{eff} indicated at the right end of each trace. The bifurcation sequence from stick-slip to stable sliding is evident. The insert is a blow-up of the stable sliding trace showing the remaining oscillating response at the frequency of the load modulation $f = 120$ Hz, much higher than the stick-slip frequency (Bureau, 2000). It seems that what is considered as stabilization is indeed a synchronization of slips with quantization of slip amplitudes

The phenomenon can be considered as a "quantization" of slips, which has been observed also in our experiments with EM forcing (Fig. 8.15). Thus, a single dynamic instability (slip) of magnitude of the order of 3.5 μm in a non-modified friction process is released in the same time interval by 12 small-scale events of magnitude 0.2 μm in synchronized friction as result of quantization. In total, the cumulative slip rate of 12 small displacements was 2.4 μm/s, which is close to the one large slip rate of 3.5 μm/s.

It is unrealistic at present, but the quantization effect of periodic forcing can in principle be considered as a tool for reducing the magnitude of impending strong earthquake.

8.9 High Order Synchronization of Stick-Slip Process: Experiments on Spring-Slider System

In the previous chapters we considered relatively simple synchronization regimes. At the same time it is well known that when the processes of various timescales are coupled, there is a possibility of high order synchronization (HOS). Namely, if ω_n is the natural frequency of first (driven) oscillator, ω is that of the second (forcing) one and Ω is the resulting frequency of driven system under forcing, the system tends to synchronize at different integer ratios of ω/Ω. Such effects are observed, for

example, in biological systems, lasers, electronic relaxation generators, etc (Pikovsky et al., 2003; Kantz, Schreiber, 1997).

Our experiments were aimed to reveal HOS in the frictional system, namely in the stick-slip process of spring-slider setup, subjected to weak electromagnetic (EM) or mechanical forcing.

8.9.1 High Order Synchronization

In the paper the following definitions are used: ω_0 – natural frequency of autonomous oscillator (here spring-slider system); T_0 – corresponding natural period; and ω, T, and ϕ — forcing frequency, period and phase, respectively; Ω, T_{obs}, and ϕ_{obs} – frequency, period and phase, respectively, of autonomous oscillator observed after application of forcing.

There are several kinds of synchronization between oscillating system with natural frequency ω_0 and forcing frequency $\omega = 2\pi f$. We are looking for the phase synchronization (PS), when amplitudes are irregular and uncorrelated, but the frequencies ω and Ω are adjusted, i.e., there is a regular phase shift between ω and Ω.

High-order or (*n:m)* synchronization means that the observed and forcing frequencies satisfy the equation (Pikovsky et al. 2003):

$$n\ \omega = m, \quad \text{or} \quad nT_{obs} = mT_f, \tag{8.14}$$

where n and m are some integer numbers. In our case, ω is the EM or mechanical forcing frequency and Ω is the observed frequency of AE bursts under forcing. The ratio n/m is called the winding or rotation number ρ and is defined as:

$$\rho = \Omega/\omega = T_f/T_{obs}. \tag{8.15}$$

This condition of so-called high-order synchronization can also be incorporated in the general framework of the frequency-locking model, using equation (8.14) ; in this case the ratio *n:m* is the winding number: $\rho = n/m$. The phase-locking can be also expressed in terms of the oscillators' phases:

$$|n\phi - m\phi_{obs}| < const, \tag{8.16}$$

where ϕ is the phase of the forcing and Ω is that of the kicked oscillator.

8.9.2 HOS Synchronization by Electromagnetic Forcing

Figure 8.12 represents actually the example of high order ($n/m = 1{:}2$) synchronization. The experiment shows that the addition to the high frequency EM signal (40 Hz) of a strong enough component of the constant electric field invokes transition from 1:2 to 1:1 synchronization.

The same 1:1 regime can be obtained also upon application of relatively low frequency ($T_0 = 0.5$ s) signal (see the left part of Fig. 8.26). At still lower forcing frequencies, for example, $T_0 = 4.5$ s, the stick-slip process demonstrates swarm-like behavior: one EM forcing generates dozens of AE bursts (see the right part of Fig. 8.26).

Figure 8.27 represents the HOS of stick-slip at EM forcing by pulses of different duration. Both the onsets of swarms and these of the individual events within sequences (swarms) turn out to be very well organized.

The onsets of swarms have almost the same delay relative to the times of onsets of identical forcing (t_{if0}; $i = 1, 2 \ldots . k$, where i is the number of forcing pulse) and the events within swarms manifest regular phase difference. Besides, even small difference in the duration of the forcing pulses causes regular changes in the delays, number of AE bursts in the induced swarm and in phase differences. Characteristics of EM forcing and AE response are as follows. Short forcing pulses: $n{:}m = 1/3$; mean duration $t = 0.618$ s; mean delay $t_{if0} = 0.295$ s; the AE response consists of three consecutive bursts with mean phase differences of 0.258; 0.411; 0.537 s, and St. Dev. of 0.037; 0.048; 0.034, respectively. Long forcing pulses: $n{:}m = 1/4$ or $1/5$; mean duration $t = 0.82$ s; mean delay $t_{if0} = 0.358$ s; the AE response consists of four

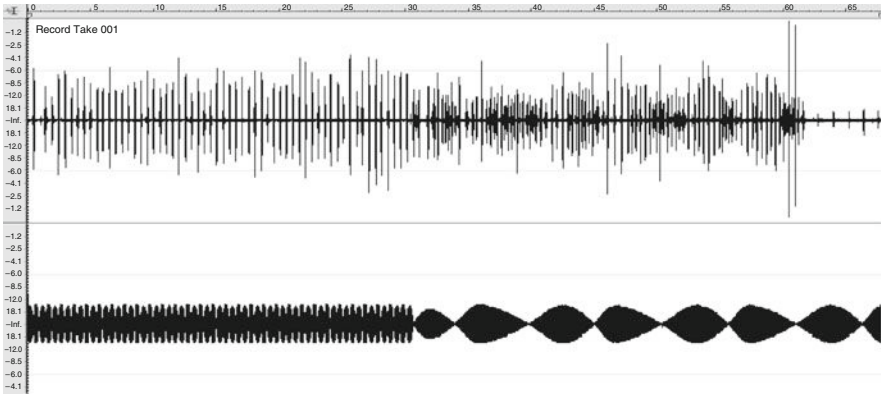

Fig. 8.26 Transition (bifurcation) in stick-slip from 1:1 synchronization to high order synchronization at increasing period of forcing from 0.5 s to 4.5 s (exp: Zura5). Note that in Figs. 8.26, 8.27a and 8.28a the forcing signal was filled by high frequency (HF) oscillations in order to visualize the low frequency forcing on the computer screen; the HF signal was applied only to computer and not to the rock plates

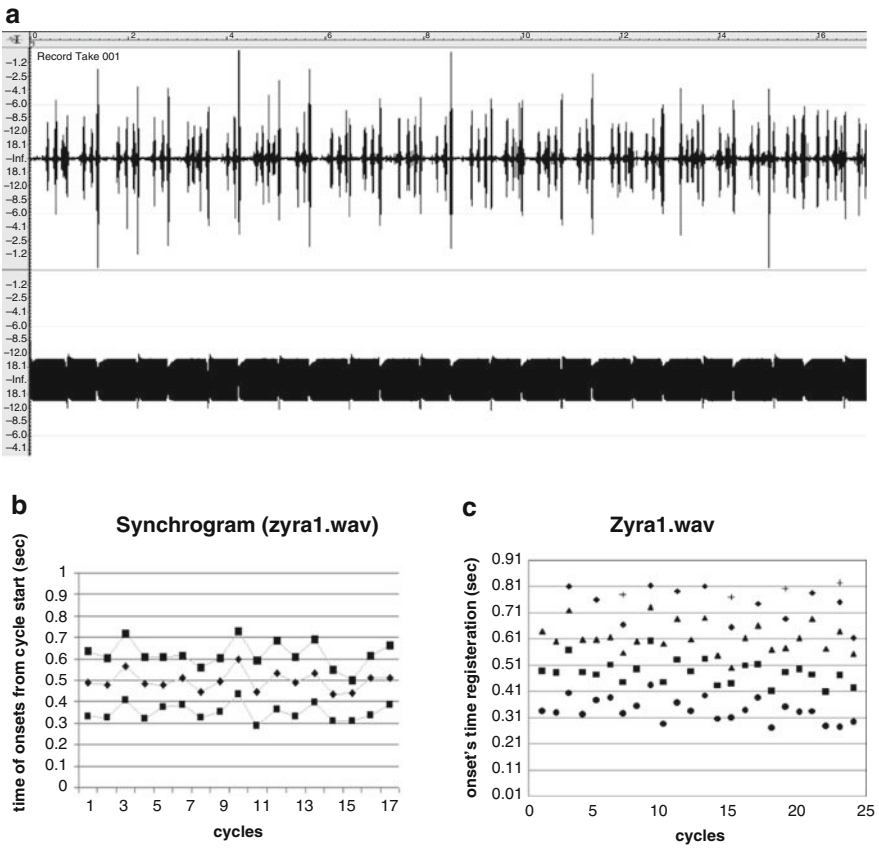

Fig. 8.27 High order synchronization: $n<m$ (exp. Zyra1). Note that the onsets of swarms and those of the individual events within sequences (swarms) turn out to be very well organized (see text). (**a**) High order synchronization: $n<m$; (**b**) synchrogram for short forcing pulses $n:m = 1/3$; (**c**) synchrogram for longer forcing pulses $n:m = 1/4$ or $1/5$. Note that the onsets of swarms and those of the individual events within sequences (swarms) turn out to be very well organized (see text)

consecutive pulses with mean phase differences of 0.268; 0.467; 0.601; 0.736, and St.Dev. of 0.046; 0.05; 0.07; 0.055; 0.046, respectively.

Figure 8.28 presents even more numerous AE swarms generated by longer EM pulses; in this case the swarms contain up to 40 AE events, so $n:m \approx 1/40$. Again, the AE bursts within the swarm are well organized. The first ten of bursts show almost constant phase shift relative to the EM forcing onsets. The following bursts demonstrate a regular small increase of the phase delay in sequential swarms.

So, it seems that the lower the frequency of forcing, the larger the number of triggered synchronized events in the forcing-generated AE swarms. Probably the same mechanism can lead to formation of seismic swarms.

Besides $n<m$ coupling, we observe also $n>m$ HOS (Fig. 8.29 a, b). Here the AE bursts occur rarely in comparison with EM forcing pulses. The forcing pulse

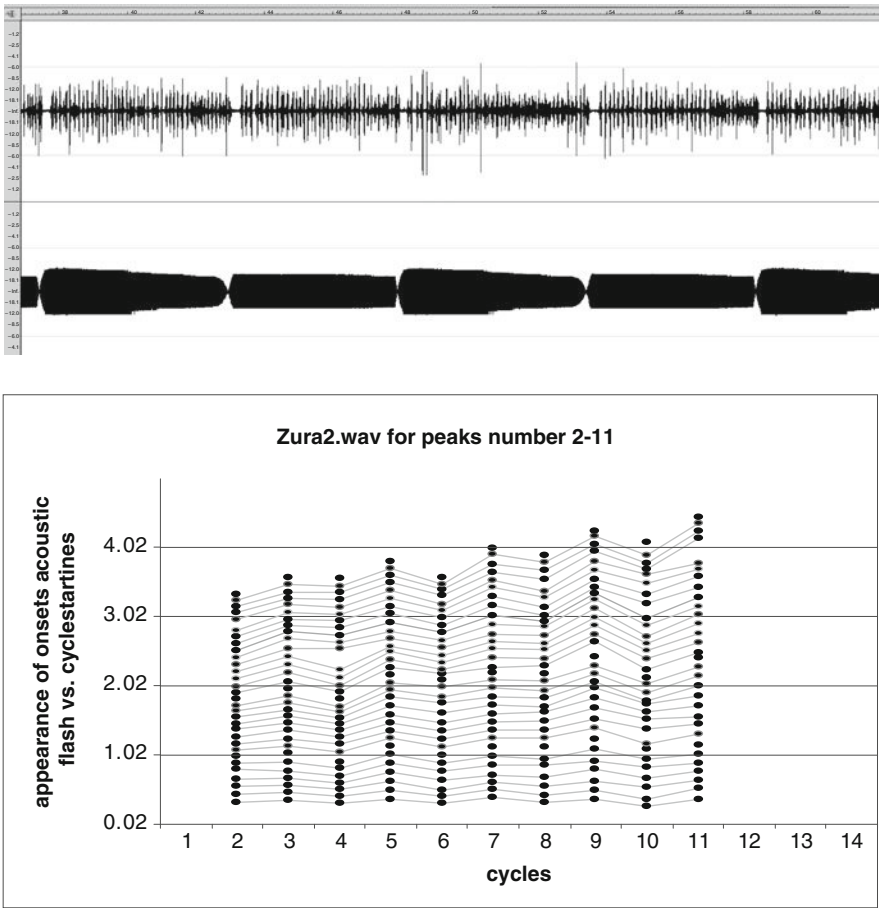

Fig. 8.28 High order synchronization: $n{:}m \approx 1/40$ (exp. Zura2); a) wav. file; b) stroboscopic diagram (synchrogram) for the first 31 AE bursts in the swarms number 2-11 generated by 11 forcing EM pulses; note the stripe structure of synchrogram, which shows that the phase shift between EM forcing and AE pulses is almost constant for the first 10 slips

(repetition) rate was $T_f = 1.8$ sec, AE delay relative to the pulse onset – 0.24 s. The observed AE period was $T_{obs} = 25$ s. Thus, in this case $n>m$, namely the winding number is 14:1. Fig. 8.29 b presents the AE distribution relative to the forcing period phase, which is very sharp though slips wait quite long (hundreds of forcing periods) to occur.

8.9.3 HOS by Mechanical Forcing

We also investigated synchronization of the same spring-slider system under weak periodic mechanical forcing (Chelidze et al., 2007; Varamashvili et al., 2008). The

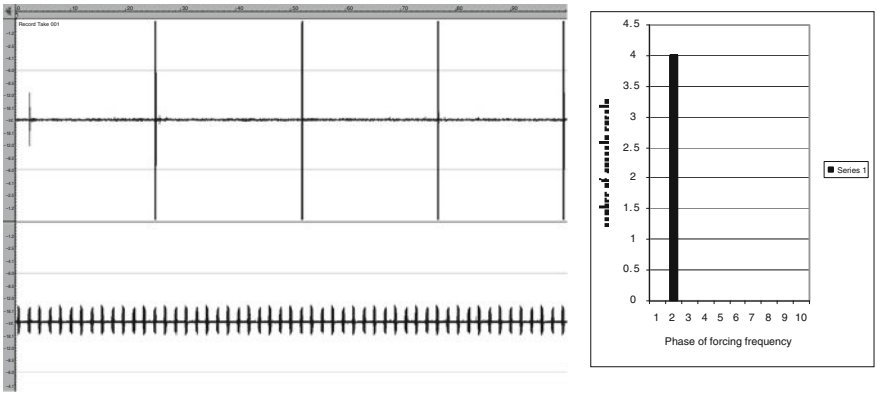

Fig. 8.29 High order EM synchronization: $n>m$; (exp.Sopo1). $T_f = 1.815$ s; delay time = 0.240 ms; $T_{ob} = 25$ s; $n\ \omega = m\ \Omega$; $14n \cong m$. (a) recording of AE at synchronization by EM pulses; (b). histogram of AE bursts distribution in phases of EM forcing

experiments were conducted for two modes of mechanical forcing: (i) the forcing is applied normal to the slip surface and (ii) forcing is applied parallel to the slip surface; for brevity we will refer to them as normal and tangential forcing, respectively. In the case of normally directed forcing we calculated the maximum value of mechanical forcing, which corresponds to the maximum measured voltage applied to mechanical vibrator (i.e., when the voltage applied to the vibrator equals 6.5 V). The mass of the oscillating element of the vibrator m is $\approx$ 20 g, so we obtain for oscillating element of the vibrator the natural frequency f: $f = \sqrt{k/m} = 5$ Hz, where k is the stiffness of the vibrator spring. Then $k = 25\ m = 0.5$ N/m.

The maximum deflection x_{max} of the oscillating element at the applied voltage 6.5 V equals $x_{max} \approx 4.10^{-3}m$, so the corresponding (maximal) intensity of forcing F_{max} is $F_{\max} = kx_{\max} \approx 2.10^{-3}$N.

At smaller voltages, the forcing is much weaker – our assessment for 1V is $\sim 5.10^{-4}N$. Thus, the forcing was always much less than the driving force $F = 4\ N$. Similar numbers were obtained for tangential mechanical forcing. The forcing frequencies were 30 Hz for the tangential and 20 Hz for the normal loading cases. In both cases, the forcing rate was larger than the dragging rate, which means that the synchronization of the process is possible.

Figure 8.30 a, b presents experimental records, when the mechanical forcing is in the range $(5.10^{-5} - 2.10^{-3})$ N, which corresponds to 4 V voltage applied to the vibrator.

Distributions of the AE burst onsets relative to the phase (in decimals) of mechanical forcing period for the normal forcing are presented in Fig. 8.31.

At low voltages (up to 1V) the onsets are more or less randomly distributed in the decimals of the forcing period. Voltage increase results in concentration of the offsets at a definite part of forcing period, namely in the first and the last decimals of forcing phase. Evidently, increasing of voltage applied to mechanical vibrator

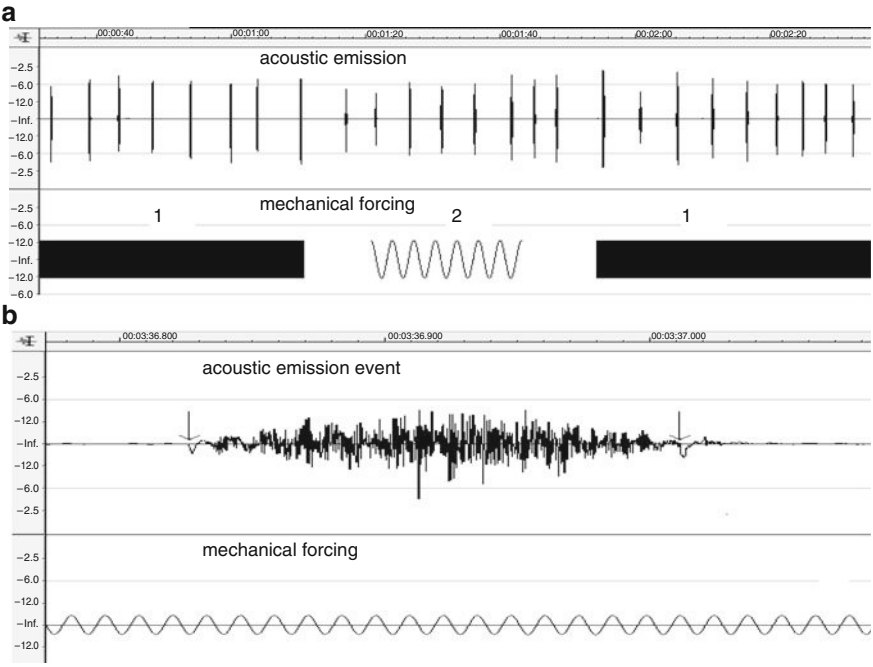

Fig. 8.30 (**a**) The full record of AE bursts (upper channel) and mechanical forcing (lower channel), sections 1 — total record of forcing, corresponding to the time scale, shown at the upper side of figure; section 2 — part of forcing record in the expanded form; here the time scale is disregarded in order to visualize the form of forcing signal during synchronized stick-slip. Mechanical forcing corresponds to vibration intensity generated by application of 4 V voltage to the vibrator; (**b**) A single acoustic pulse and corresponding tangential mechanical forcing on the expanded scale. The initial slow deviation from the background line is considered as the onset of the AE pulse and the start of slow terminal phase as a pulse termination; these moments are marked by arrows

promotes synchronization of AE offsets with external forcing. The same behavior is observed for tangential mechanical forcing (Fig. 8.32).

Thus at low voltages (up to 2 V) the onsets are more or less randomly distributed in the decimals of the forcing period (Figs. 8.31, 8.32). Voltage increase results in concentration of the offsets at a definite part of forcing period, namely in the first and the last decimals of forcing period for normal forcing; in the case of tangential forcing (Fig. 8.32) synchronization is most pronounced in the interval 0.25–0.5 of the forcing period and fills the gap observed for normal forcing (Fig. 8.31).

Alteration of the forcing frequency affects the phase distribution of AE. Figure 8.33 (the left column) shows the AE distribution for tangential forcing at frequency 80 Hz. It is evident that the maximum of AE shifts to other phases of forcing period compared to the distribution for 20 Hz.

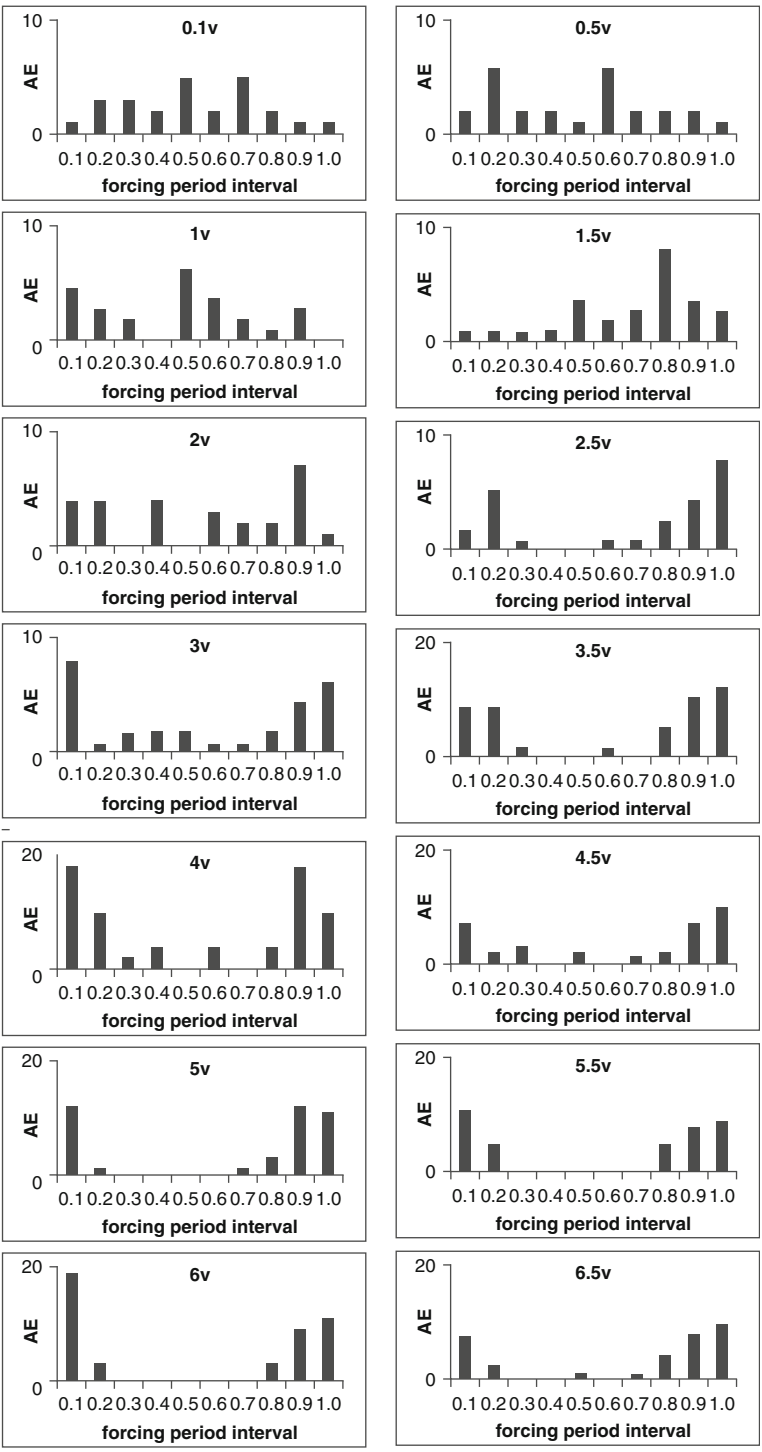

Fig. 8.31 Distribution of acoustic emission onsets relative to mechanical forcing period phases (in decimals) for different intensities of normal forcing. Forcing frequency – 20 Hz

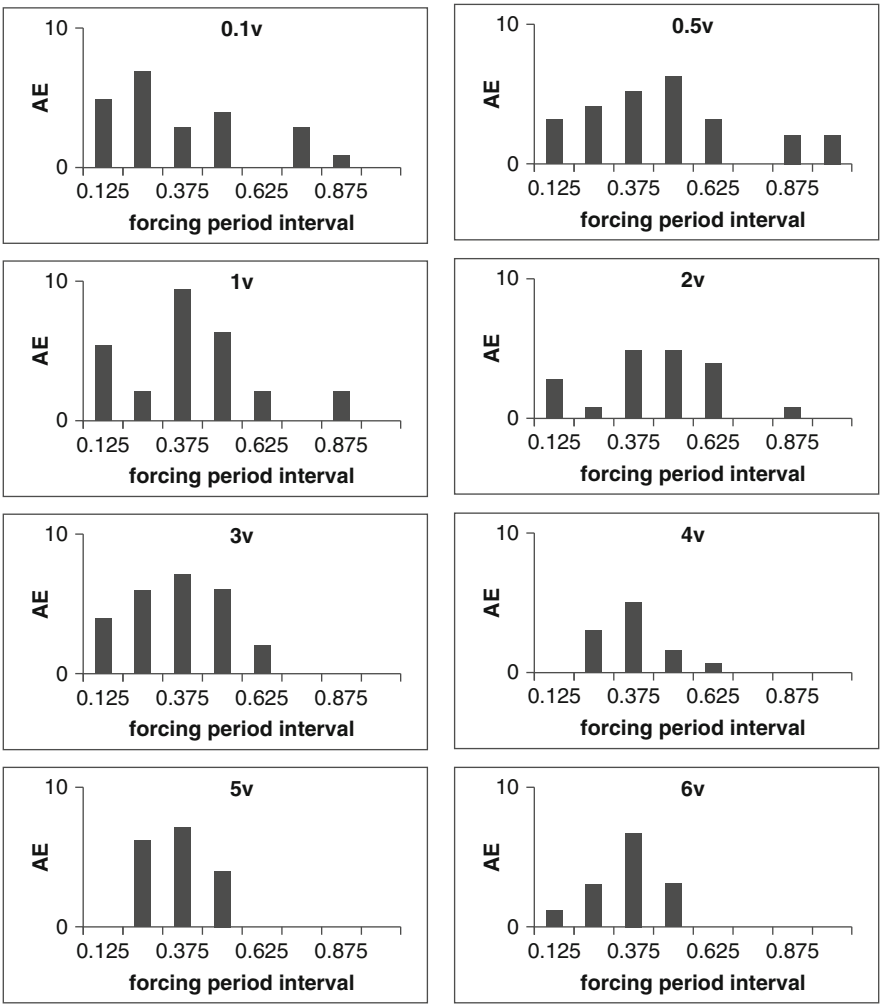

Fig. 8.32 Distribution of acoustic emission onsets number relative to the forcing period phase (in decimals) for different intensities of tangential forcing. Forcing frequency – 30 Hz

8.9.4 Synchronization of AE Signal Terminations

It was a surprise to discover that not only AE onsets can be synchronized by a weak mechanical forcing; Fig. 8.33 (right column) illustrates that the terminal parts of the signal also are synchronized by forcing with the same strength as the onsets.

We suppose that the forcing (here 80 Hz) can affect not only the phases of onsets but also the phases of terminations of AE bursts, but their influence is realized in quite different phases of forcing: presumably, the onsets are triggered by tangential

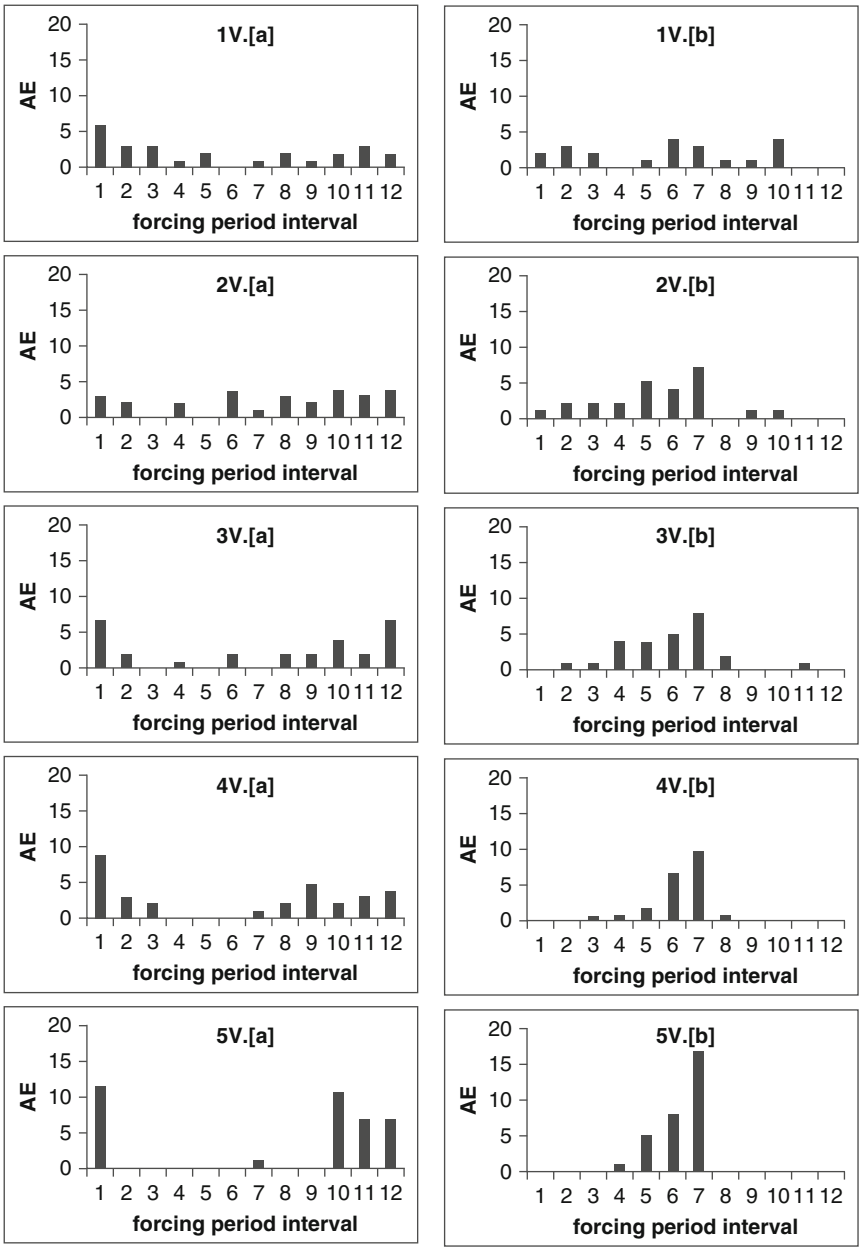

Fig. 8.33 Distribution of acoustic emission onsets (the left column) and terminations (the right column) relative to the (mechanical) forcing period phase (in twelfths of the forcing period) for different intensities of tangential forcing. Forcing frequency – 80 Hz

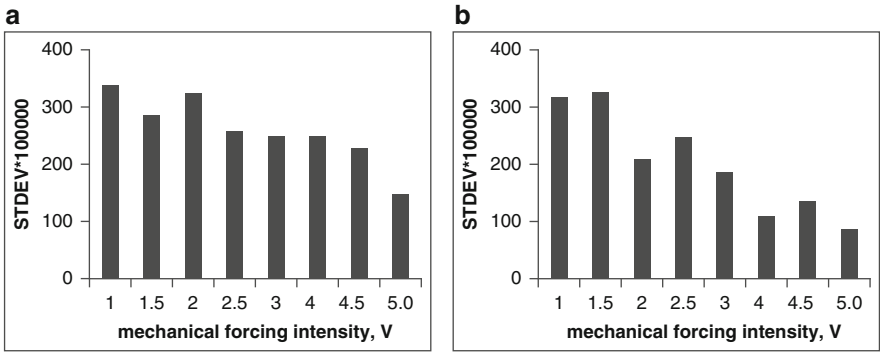

Fig. 8.34 Standard deviation of onsets (**a**) and terminations (**b**) distributions for different intensities of external applied voltages, which are proportional to intensity of (tangential) mechanical forcing

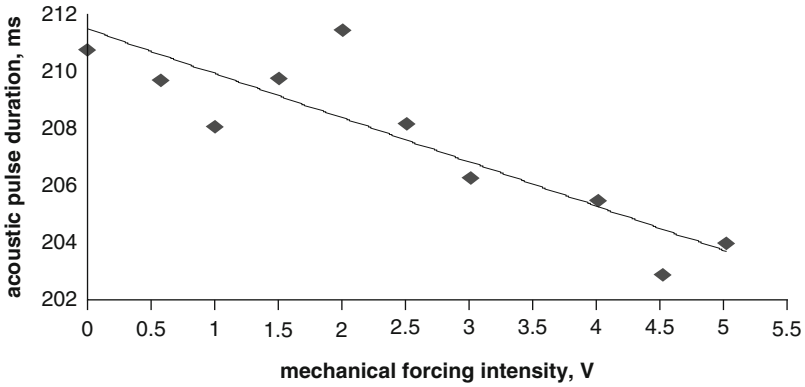

Fig. 8.35 Mean duration of stick-slip generated acoustic pulses for different intensity of normal mechanical forcing, with a trend line

forcing around the minimum area of forcing period and suppressed by forcing in the maximum area of forcing period.

The standard deviation of onset and termination times regularly decreases with increase of forcing intensity (Fig. 8.34).

Besides better synchronization of onsets and terminations, the increase in forcing intensity also brings on regular shortening of duration of AE bursts (Fig. 8.35).

It is evident that increasing voltage applied to the vibrator promotes synchronization of AE offsets with external forcing.

It is striking that the AE bursts are well synchronized though the waiting interval of bursts varies between 100-200 periods of forcing, i.e., to initiate the phase-synchronized slip event the forcing oscillator should pump the energy of hundreds of oscillations to the slider-spring system.

The important conclusion for the much discussed interaction between tidal deformation and EQ-s (Beeler, Lockner, 2003; Scholz, 2003) is that in order to

find it we should not only look for direct 1:1 correlation between events recurrence frequency and forcing, namely for the increase of seismicity exactly at the tide frequency (say, 12 h). The high order phase synchronization can occur at multiples of tide frequency like it was shown in laboratory experiments. It is important to note that HOS can be responsible for phase synchronization of AE or seismic events irrelative to the duration of their nucleation; of course, the optimal condition of synchronization (minimal forcing) should correspond to the forcing period, close to natural event nucleation time. Additional complication arises from the phenomenon of delay; the response can be shifted quite significantly for weak forcing. Thus, the question of tidal forcing of earthquakes should be reconsidered taking into account new experimental evidence.

8.10 EM Synchronization: Physical Mechanism of Period Doubling

It is well known that the slider-spring system displays the stick-slip behavior described by the nonlinear equations (Dietrich, 1979; Ruina, 1983; Rice et al., 2001; Becker, 2000): $\tau = \sigma_n[\mu_0 + \Theta + A\ln(v_d/v_c)]$; $\dot{\Theta} = (-v_d/d_c)[\Theta + B\ln(v_d/v_c)]$, where τ is the friction stress, σ_n is the normal stress, Θ is the surface state parameter, μ_0 is a nominal (constant) value of friction, d_c is the dimension of asperity, v_d is the slip speed, v_0 is the initial value of v_d and A and B are constants. Both theoretical solutions and experiments demonstrate a possibility of very different behavior of the system depending on the conditions of the test. For example, nonlinear analysis of a simple quasi-static slider-spring system with rate- and state-dependent friction shows chaotic dynamics behavior in the deterministic sense (Becker, 2000). In particular, at the critical value of spring stiffness, the friction stress may undergo oscillations close to periodical.

On the other hand, it has been shown (Ott et al., 1990; Bocaletti et al., 2000) that it is possible to control the behavior of chaotic systems using very small feedback impact. The matter is that the attractor of a chaotic system contains an infinite number of unstable periodic orbits. Given such an attractor, one can choose some of the low-period orbits (or steady states) embedded in the attractor and use a feedback perturbation of an accessible parameter P of the system in order to stabilize the chosen orbit and thus improve the performance of the system, for example, convert the chaotic behavior into periodic process. The extreme sensitivity of chaotic systems to external impact allows to control the dynamic state of the physical object by using a very small perturbation. Experimental control of chaos has been successfully realized first by Ditto et al. (1990) on the parametrically driven magnetoelastic ribbon and then by many others on mechanical, electronic, biological and chemical systems (see Ott et al., 1994).

An alternative mathematical formalism for explanation of control phenomenon is provided by synchronization theory (Blekhman, 1988; Lursmanashvili et al., 2001;

Pikovsky et al., 2003). The crux of this approach is the existence of some critical parameter in the system that causes its relaxation. Then small periodic impact can synchronize relaxation of the whole system with the period of impact, if some force regularly drives the system close to the critical state. Let us consider some relaxation process in which the intensity U_r (it can be related to voltage, stress, etc) builds up slowly to some critical value U_c; when $U_r = U_c$, the intensity drops instantly to some initial value. Then the application of synchronizing pulses of relatively small amplitude U_s and of very short duration may impose coherency of these drops with the timing of pulses, as now the condition of criticality is $U_r + U_s = U_c$ or, in the case of sinusoidal impact, $U_r + a\sin(\omega t + \varphi) = U_c$, where ω, a and φ are the angular frequency, phase and amplitude of periodic impact, respectively. This means that intensity drops occur, when the increasing value of U_r is equal to $U_c - a\sin(\omega t + \phi)$; for details see Chapter 18. It has been shown (Blekhman, 1988; Pikovsky et al., 2003) that synchronization may appear at even weak coupling between objects with significantly different characteristic frequencies that implies nonlinear interaction of objects.

What is the physical mechanism leading to synchronization? In case of mechanical excitation, synchronization is connected with mechanical triggering of microslips in the system that is close to critical state and thus reveals sensitive dependence on (small) external perturbation.

In the case of EM forcing, the driving mechanism of triggering is electrostriction (equations 8.5 and 8.6); synchronization occurs when the oscillating EM component of Coulomb stress is strong enough.

We suppose that EM synchronization is connected with polarization of surfaces of fixed and sliding samples. As the polarization forces arise at both polarities of applied periodic field, it seems reasonable to expect that the synchronization follows each reversal of EM field. As the mechanical instabilities synchronize with both positive and negative sections of sinusoid (the response is symmetric) we can postulate that the additional elastic strain, u, induced by forcing has a quadratic dependence on the intensity of electrical field $E = E_m \sin \omega t$:

$$u = kE^2 \tag{8.17}$$

which is the well known expression of electrostriction in solids (compare with expressions 8.3 and 8.4); here k is some proportionality constant depending on the forcing frequency and physical properties of rock (Chernyak, 1978).

If the electromagnetic forcing contains, besides the periodic component, also a constant one, that is:

$$E = E_c + E_m \sin \omega t, \tag{8.18}$$

then, after inserting (8.18) into (8.17), the elastic response becomes:

$$u = kl(E_m)^2 \left\{ 1 + 2(E_c/E_m)^2 + 4(E_c/E_m) \sin \omega t - \cos 2\omega t \right\}, \tag{8.19}$$

where $k1$ is proportionality constant, which depends on the forcing frequency, physical properties of rock and constant component intensity E_c. It is evident that the stick-slip response to forcing in the latter case depends on the value of ratio E_c/E_m. At $E_c/E_m << 1$ the $\cos 2\omega t$ term of (19) is dominant, which means that the slip events will occur with the double frequency of forcing, but at $E_c/E_m >> 1$ the slip regime is governed by the $\sin \omega t$ term, that is, only one slip event occurs per period of forcing. These conclusions are confirmed by experiments (Fig. 8.12).

8.11 Conclusions

The phase synchronization of stick-slip process induced by a weak electromagnetic or mechanical periodic forcing was analyzed. Stick-slip events were identified as acoustic emission (AE) bursts and recorded on the sound card of computer. The onsets of acoustic events were picked by special program using Akaike criterion. For quantitative measuring of synchronization strength, several modern tools of nonlinear dynamics were used (mean effective phase diffusion coefficient, Shannon entropy based characteristic phase synchronization measure *(γH-Sh)*, recurrence plots, and recurrence quantitative analysis RQA, namely, percent of determinism %DET, etc).

An application of varying frequencies and intensities of forcing allows to compile Arnold's tongue for EM forcing. We found that not only the onsets/maxima of a definite kind of AE signals are synchronized with forcing, but also AE wave train terminations.

The effect of high order synchronization of stick-slip events by weak electromagnetic or mechanical periodic forcing was discovered. There were two kinds of high order synchronization: (i) one or more AE bursts during one forcing period and (ii) one AE burst during many forcing periods.

It was found that the onset time of the synchronized slip events lags behind the forcing phase; the delay is smaller for stronger forcing.

The results obtained point to possibility of revealing some new fine details in the stick-slip process which can be very useful for refining the physical mechanism of frictional motion in general. These findings can also help to find new regularities in seismic time series.

Acknowledgements The authors express their gratitude to the Georgian National Science Foundation (Grant No GNSF/ST06/5-028) and INTAS foundation (Ref. *N* 05-100008-7889) for financial support.

References

Akay, A. 2002, Acoustics of Friction. J. Acoust. Soc. Am., **111**, 1525–1548.

Bak, P., C. Tang and K. Wiesenfeld. 1988. Self-organized criticality. Phys. Rev. A38, 364–374.

Becker, T.W. 2000. Deterministic Chaos in the Two State-variable Friction Sliders and the Effect of Elastic Interactions. In: Rundle, J.B, Turcotte, D.L. and Klein, W. (Eds.), Geocomplexity and the Physics of Earthquakes. American Geophysical Union, Washington, DC, pp.5–26.

Ben-Zion, Y., Collective Behavior of Earthquakes and Faults: Continuum-Discrete Transitions, Evolutionary Changes and Corresponding Dynamic Regimes, Rev. Geophysics, **46**, RG4006, doi:10.1029/2008RG000260, 2008.

Beeler, N.M. and D.A. Lockner. 2003. Why earthquakes correlate weakly with the solid Earth tides: Effects of periodic stress on the rate and probability of earthquake occurrence. Journal of Geophysical Research, **B108**, 2391–2405.

Benguigi, L. (1988). Simulation of dielectric failure by means of resistor-diode random lattices. Phys. Rev. B 38, 7211–7214.

Blekhman I.I., 1988. Synchronization in Science and Technology. ASME Press, New York.

Brace W. E., and I.D. Byerlee. 1966. Stick slip as a mechanism for earthquakes. Science, **153**, 990–992.

Bocaletti, S., Grebogi, C., Lay, Y.-C., Manchini, H., Maza, D. 2000. The Control of Chaos: Theory and Applications. Physics Reports. 329, 103–197.

Bouissou, S., Petit, J., Barquins, M. 1998. Experimental evidence of contact loss during stick-slip: possible implications for seismic behavior. Tectonophysics, **295**, 341–350.

Bureau, L., T. Baumberger and C. Caroli, 2000, Shear response of a frictional influence to a normal load modulation. Phys. Rev. E, **62**, 6810–6820.

Chelidze, T., N. Varamashvili, M. Devidze, Z. Chelidze, V. Chikhladze and T. Matcharashvili. 2002. Laboratory study of electromagnetic initiation of slip. Annals of Geophysics, **45**, 587–599

Chelidze, T., Lursmanashvili, O. 2003. Electromagnetic and mechanical control of slip: laboratory experiments with slider system. Nonlinear Processes in Geophysics, 20, 1–8.

Chelidze, T., T. Matcharashvili. 2003a. Electromagnetic control of earthquake dynamics? Computers&Geosciences, 29, 587–593.

Chelidze, T., A. Gvelesiani, N. Varamashvili, M. Devidze, V. Chikchladze, Z. Chelidze and M. Elashvili. 2004b. Electromagnetic initiation of slip: laboratory model. Acta Geophysica Polonica, **52**, 49–62

Chelidze, T., T. Matcharashvili, J. Gogiashvili, O. Lursmanashvili and M. Devidze. 2005. Phase synchronization of slip in laboratory slider system. Nonlinear Processes in Geophysics, **12**, 1–8

Chelidze, T., O. Lursmanashvili, T. Matcharashvili and M. Devidze. 2006. Triggering and synchronization of stick slip: waiting times and frequency-energy distribution Tectonophysics, **424**, 139–155

Chelidze T., and T. Matcharashvili. 2007. Complexity of seismic process, measuring and applications – A review, Tectonophysics, **431**, 49–61.

Chelidze, T. Matcharashvili, O. Lursmanashvili, N. Varamashvili. 2008. Acoustics of stick-slip deformation under external forcing: the model of seismic process synchronization. In: Advanced Topics in Geology and Seismology. D. Triantis, M. Jelenska, F. Vallianatos (Eds). University of Cambridge, WSEAS Press. pp:36–43.

T. Chelidze, O. Lursmanashvili, T. Matcharashvili, N.Varamashvili N. Zhukova, E. Mepharidze. 2009. High order synchronization of stick-slip process: experiments on spring-slider system. Nonlinear Dynamics, DOI 10.1007/s11071-009-9536-6

Chernyak, G. 1978. On the physical nature of seismoelectric effect in rocks. Izvestia Ac. Sci. USSR, Physics of Earth. N2, 108–112, (in Russian).

Dieterich, J.H. 1979. Modeling of rock friction 1. Experimental results and constitutive equations. Journal of Geophysical Research, **84B**, 2161–2168.

Ditto, W.L., Rauseo, S.N. and Spano, M.L. 1990. Experimental control of chaos. Phys. Rev. Lett., 65, 3211–3214.

Grasso, J-R and D. Sornette. 1998 Testing self-organized criticality by induced seismicity. Jour. Geoph.Res., 103, 29 965–29 987.

Heaton T. H. 1975. Tidal Triggering of earthquakes. Geoph.J. of the Royal Astr. Soc., 43, p. 307–326.

Kanamori, H., and E.E. Brodsky. 2004. The physics of earthquakes. Rep. Prog. Phys., **67**, 1429–1496.

Kantz, H., Schreiber T., 1997. Nonlinear time series analysis. Cambridge University Press, Cambridge.

Kurz, J., CU. Grosse, HW Reinhardtet. 2005. Strategies for reliable automatic onset time picking of acoustic emissions and of ultrasound signals in concrete, Ultrasonics, 43, 538–546

Lursmanashvili O. 2001. Role of exogenous factors in initiation of Caucasus Earthquakes Journal of the Georgian Geophysical Society, Issue (A), Physics of Solid Earth, v. 6, pp. 22–27.

Maeda, 1985. A method for reading and checking phase times in autoprocessing system of seismic wave data, J. Seismology Soc. Japan. 38, 365–379.

Marwan, M. 2003.Encounters with neighborhood, Ph.D Thesis.

Nikolaev, A.V. (Ed.). 1994. Induced Seismicity. Moscow, "Nauka", 220 p, (in Russian).

Nikolaev, V. A. 2003. Research of lithospheric stress state on the base of correlation of tidal forces and seismicity. Anakharsys, Moscow (in Russian).

Ott, E., Grebogi, C., Yorke, J.A. 1990. Controlling chaos. Phys.Rev.Lett., 64, 1196–1199.

Perfettini H., J. Schmittbuhl and J.R. Rice. 2001. Frictional response induced by time-dependent fluctuations of the normal loading. Journal of Geophysical Research, **106B**, 13455–13472

Pikovsky, A., Rosenblum, M.G., Kurths. J. 2003. Synchronization: Universal Concept in Nonlinear Science. Cambridge University Press, Cambridge.

Rice J. R., N. Lapusta and K. Ranjith. 2001. Rate and state dependent friction and the stability sliding between elastically deformable solids. Journal of the Mechanics and Physics of Solids, **49**, 1865–1898

Rosenblum, M.G., Pikovsky, A., Kurths. J. 1996. Phase synchronization of chaotic oscillators. Phys. Rev. Lett., 76, 1804–1808.

Rosenblum, M.G., Pikovsky, A., Kurths. J. 1997. Effect of phase synchronization in driven chaotic oscillators. IEEE Trans. CAS-I, 44. 874–881.

Ruina A. 1983. Slip instability and state variable friction laws. Journal of Geophysical Research, **88B**, 10359–10370

Quiroga, R., R Quian Quiroga, A Kraskov, T Kreuz, P Grassberger. 2002. Performance of different synchronization measures in real data, Phys.rev.E, **65**, 041903.

Scholz, C. (1990): The mechanics of earthquakes and faulting (Cambridge Univ. Press. Cambridge.1990)

Sobolev, G., A. Ponomarev, A.Avagimov, V. Zeigarnik. (2000): Initiating acoustic emission with electric actions. In Reports of ESC conference, Madrid.

Sobolev, G.A. and Ponomarev, A.V., 2003. Physics of Earthquakes and Precursors. Moscow, "Nauka", (in Russian).

Scholz C. H. 1998. Earthquakes and friction laws. Nature, **391**, 37–42

Scholz, C.H. 2003. Mechanics of Earthquakes and Faulting. Cambridge University Press, Cambridge.

Sibson R. 1994. Crustal stress, faulting and fluid flow. In: Deformation and Fluid Flow Geological Society, London, Special Publications; 1994; v. 78; p. 69–84

Tamm, I. 1956. Fundamentals of theory of electricity. Moscow (in Russian).

Tarasov, N., H. Tarasova, A. Avagimov and V. Zeigarnik (1999), The effect of high-power electromagnetic pulses on the seismicity of Central Asia and Kazakhstan. Volcanology and Seismology (Moscow), N4-5, 152–160 (in Russian).

Varamashvili, N., T. Chelidze, O. Lursmanashvili. 2008. Phase synchronization of slips by periodical (tangential and normal) mechanical forcing in the spring-slider model. Acta Geophysica, 56, 357–371.

Zbilut, J.P., Webber, C.L. Jr., 1992, Embeddings and delays as derived from quantification of recurrence plots. Physics Letters A, 171, 199–203

Chapter 9
Oscillating Load-Induced Acoustic Emission in Laboratory Experiment

A. Ponomarev, D. Lockner, S. Stroganova, S. Stanchits, and V. Smirnov

Abstract Spatial and temporal patterns of acoustic emission (AE) were studied. A pre-fractured cylinder of granite was loaded in a triaxial machine at 160 MPa confining pressure until stick-slip events occurred. The experiments were conducted at a constant strain rate of 10^{-7} s^{-1} that was modulated by small-amplitude sinusoidal oscillations with periods of 175 and 570 seconds. Amplitude of the oscillations was a few percent of the total load and was intended to simulate periodic loading observed in nature (e.g., earth tides or other sources). An ultrasonic acquisition system with 13 piezosensors recorded acoustic emissions that were generated during deformation of the sample. We observed a correlation between AE response and sinusoidal loading. The effect was more pronounced for higher frequency of the modulating force. A time-space spectral analysis for a "point" process was used to investigate details of the periodic AE components. The main result of the study was the correlation of oscillations of acoustic activity synchronized with the applied oscillating load. The intensity of the correlated AE activity was most pronounced in the "aftershock" sequences that followed large-amplitude AE events. We suggest that this is due to the higher strain-sensitivity of the failure area when the sample is in a transient, unstable mode. We also found that the synchronization of AE activity with the oscillating external load nearly disappeared in the period immediately after the stick-slip events and gradually recovered with further loading.

A. Ponomarev (✉) and S. Stroganova
Schmidt Institute of Physics of the Earth, Russian Academy of Sciences, Moscow, Russia
e-mail: avp@ifz.ru

D. Lockner
USGS, Menlo Park, CA, USA

S. Stanchits
GFZ, Potsdam, Germany

V. Smirnov
Schmidt Institute of Physics of the Earth, Russian Academy of Sciences, Moscow, Russia
Moscow State University, Moscow, Russia

V. de Rubeis et al. (eds.), *Synchronization and Triggering: from Fracture to Earthquake Processes*, GeoPlanet: Earth and Planetary Sciences 1,
DOI 10.1007/978-3-642-12300-9_9,

Cosmic and meteorological forces can produce periodic changes in the Earth's crust. This periodicity in terrestrial processes is observed over a wide range of time scales [Atlas. . ., 1998; 2002]. Seismicity, for example, contains periodic components as well as random activity, due to both natural and man-made sources [Gomberg et al., 1998]. Earth tides are a significant source of periodic stress and deformation of the crust and under favorable conditions can influence the occurrence of earthquakes [Cochran et al., 2004]. Sadovsky et al. [1981] have shown that micro-mechanical influence on deformed samples of different rock and artificial materials favors the transformation from brittle rupture to plastic deformation and thereby leads to release of elastic energy stored in the sample. Sobolev et al. [1996] have shown in laboratory experiments on granite blocks under biaxial loading that the addition of vibrational loads leads to a shortening of the time period between consecutive unstable motions like stick-slip. Under 50 MPa confining pressure, a strong correlation between the periodic forcing function and the occurrence of model earthquakes was found by using granite cylinders containing precut bare fault surfaces [Lockner and Beeler, 1999]. More recently, those researchers demonstrated on laboratory-scale experiments that seismicity should correlate strongly with the amplitude and frequency of small periodic stress of tidal magnitude if the period exceeds the duration of earthquake nucleation [Beeler and Lockner, 2003].

The objective of the current study was to analyze acoustic emission time series (considered an analogue of natural seismicity) generated in laboratory-scale experiments to reveal variations in the sensitivity between periodic loading and induced AE response. Unlike the preceding experiments, we used a pre-fractured Westerly granite core of 76.2 mm diameter and 190 mm height under confining pressure of 160 MPa (Fig. 9.1). The sample was loaded axially until stick-slip events occurred. The experiments were carried out under constant strain rate of 10^{-7} s^{-1}. The steady axial loading was modulated by sinusoidal oscillations of 175 and 570 second periods and with peak-to-peak amplitudes that were a few percent of the applied load. This loading pattern was intended to simulate periodic loading observed in nature (e.g., earth tides or other sources), although the stress variations are more than 3 orders of magnitude larger than tidal stress oscillations. As discussed in Lockner and Beeler [1999], correlations between tidal stresses and natural seismicity are expected to be much smaller than the correlations observed in this experiment. An ultrasonic acquisition system described in Lockner et al. [1991], included 13 piezosensors and recorded arrival time and amplitude information from induced AE events to provide a database for further analysis.

Loading history and variation of AE activity are shown in Fig. 9.2. The initial stage of the experiment (before 310,000 s) was loaded at constant strain rate without the addition of periodic forcing. In the range of 310,000-360,000 s, the constant loading rate was modulated by the addition of a small-amplitude sine-wave with a period of 175 s. In the range of 375,000 to 445,000s, the period of the modulating signal was 570 seconds. The amplitude of the periodic loading was approximately 20 MPa in both cases.

Artificial fault surfaces used in laboratory studies are typically formed by making an inclined saw cut that is surface ground to produce planar, well-mated

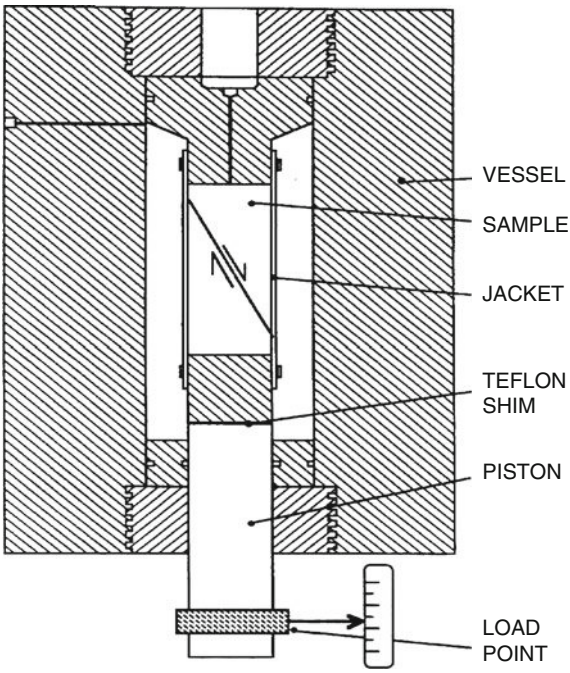

Fig. 9.1 Schematic diagram of the loading system (after Lockner and Beeler, 1999)

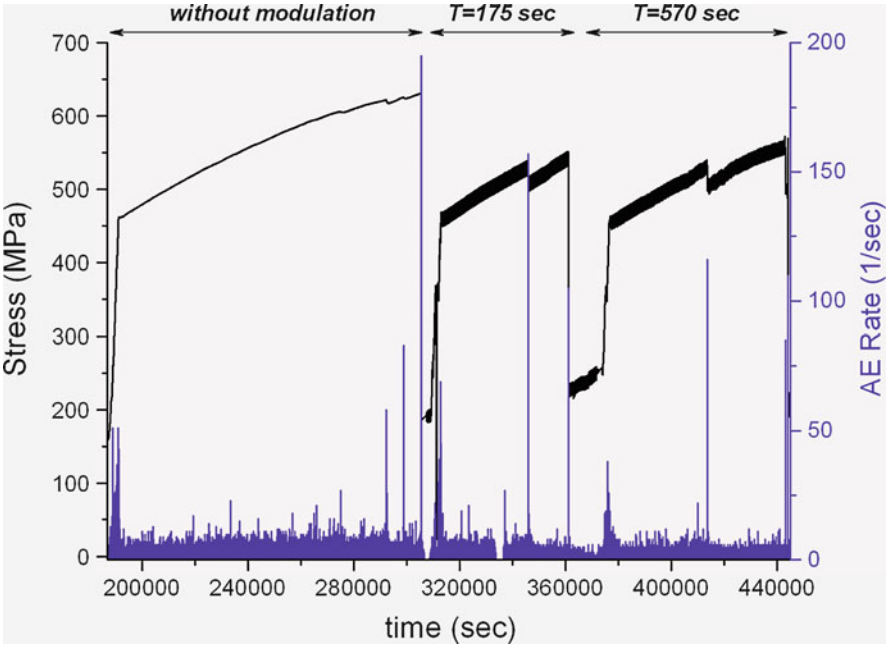

Fig. 9.2 Axial load and recorded AE rate are plotted as a function of time. Broad bands in axial stress between 500 and 600 MPa indicate amplitude of imposed sinusoidal stress oscillations

surfaces. A different technique was employed here to produce a more 'natural' fault surface. In a separate procedure, before the experiment, a fracture was propagated quasi-statically in an initially intact granite cylinder. An "AE feedback control" technique was used in which the load was adjusted to maintain constant acoustic activity [Lockner et al., 1991]. This loading style results in a narrow rupture zone with complex surface roughness and abundant gouge that is more like a natural fault than an artificial saw-cut surface. Locations of AE sources generated from initial loading to 200,000 s are plotted in Fig. 9.3. These events, that have location accuracy of approximately ±3mm, are the result of re-activation of the existing fault surface and provide an image of its shape. While AE activity is greater in the central portion of the fault, there is activity over the entire fault surface. This distributed activity indicates that during reloading of this pre-fractured sample, the entire fault surface is reactivated and although the two fault blocks are locked together by the applied normal stress (up to 260 MPa) a small amount of inelastic strain is continuously occurring. The AE activity plotted in Fig. 9.3a indicates that the lower portion of the fault has slight curvature and that the damage zone associated with the fault is more than 1 cm in width.

Dynamic stick-slip events involve rapid motion on the entire fault surface accompanied by a measurable stress drop and audible sound. Only a few such stick-slip events occurred during this experiment and all were followed by periods of increased AE activity. Variation in the relevant acoustic activity is shown in Fig. 9.4 for two stick-slip events with differential stress drops of approximately

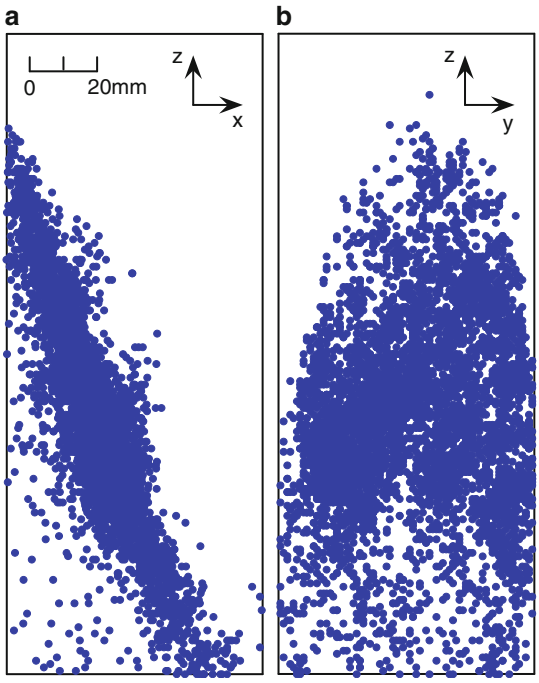

Fig. 9.3 Locations of AE events during initial loading (before running time of 200,000 s) of sample. **(a)** Sample viewed along strike of the pre-existing fault. **(b)** Sample view rotated 90° to fault strike. Lower portion of the fault has slight curvature. Width of the damage zone, as indicated by AE activity, is more than 1 cm. The broadly distributed AE activity indicates that the entire fault is undergoing inelastic strain as it is loaded

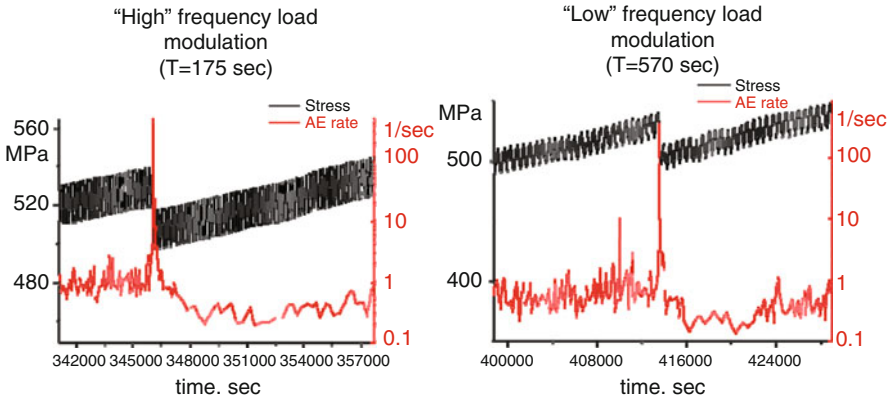

Fig. 9.4 Acoustic activity associated with stick-slip events. Steady loading rate results in an average AE rate of about 10 events per second. Rapid fluctuations in the AE rate prior to stick-slip events indicates the response to applied stress oscillations. Each stick-slip event produces a sudden increase in AE rate followed by a 1/time 'aftershock' decay and a 'stress shadow' where AE rate drops to about 30% of the previous rate. During the aftershock decay, the correlation between AE rate and stress oscillations is lost

20 MPa. In both examples shown in Fig. 9.4, AE activity preceding stick-slip was strongly correlated with the imposed stress oscillations. However, synchronization of acoustic emission nearly disappears following the stick-slip events and the associated stress drops. Then, after about 10,000 seconds, as the load rises, the correlation between AE rate and periodic loading rate is gradually re-established. Stress drops for the different stick-slip events were variable. The two events shown in Fig. 9.4 had stress drops of approximately 20 MPa or only about 4 percent of the applied differential stress. These stress drops were of the same magnitude as the applied stress modulations. Notice in Fig. 9.4 that the decrease in ambient stress level due to the stick-slip events resulted in an overall ½ decade decrease in AE rate during the aftershock sequence that reached a minimum after about 5000 s. This inverse-time transient decay in AE rate is the laboratory equivalent of an Omori aftershock decay sequence and represents the time period in which AE rate is insensitive to the imposed stress oscillations. Once the sample emerges from this region of lowered stress, the AE rate again begins to correlate with the imposed stress oscillations. This memory of past stress history is similar to the Kaiser effect discussed, for example, in Lockner (1993) in which the induced AE rate remains low until the previous maximum stress level is exceeded.

The change in correlation between stress oscillations and AE rate is shown more clearly in Fig. 9.5. In these plots, AE activity occurring within an extended time interval is binned according to time of occurrence relative to the peak in the stressing cycle. Fig. 9.5a shows that in a 10,000 s interval prior to the stick-slip event in Fig. 9.4a, AE activity has a strong correlation with and is in phase with the stress oscillations. The number of AE events associated with peak stress is nearly 3 times more than the number of events occurring near the stress minimum. Plotted

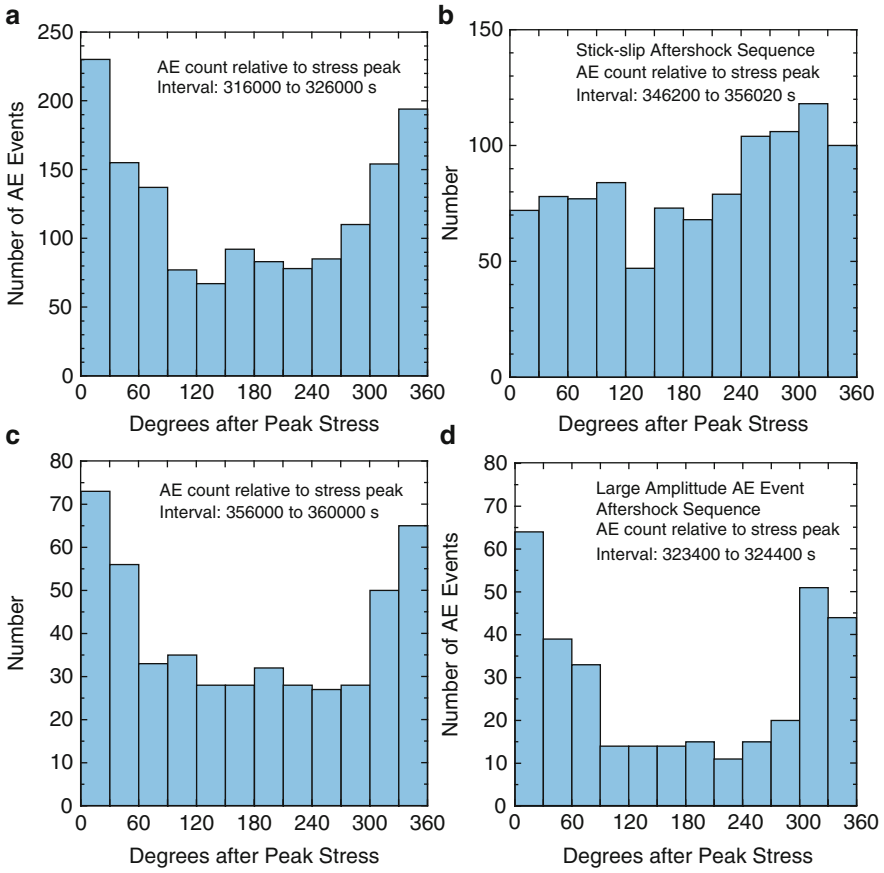

Fig. 9.5 AE activity plotted relative to the peak in each stressing cycle (T = 175 sec). Events for each sampling interval are grouped in 30° bins. **(a)** AE activity for 10,000 sec time interval before stick-slip event shown in Fig. 9.4a. Activity at peak stress is nearly 3 times as large as activity near stress minimum. **(b)** AE activity during 10,000 sec following stick-slip event showing a loss of correlation with stress cycling. **(c)** Activity during 4000 sec time interval following aftershock sequence of stick-slip event. In this interval, the correlation between stress and AE rate is re-established. **(d)** AE activity for 1000 sec aftershock sequence of a large amplitude AE event (see text). In this case, correlation of AE activity with stress oscillations is greater than for the background activity shown in Fig. 9.5a

in this way, Fig. 9.5a approximates the probability density function for AE events in this time interval. In contrast, Fig. 9.5b plots the AE activity during the 10,000 s following the stick-slip event. The correlation between stress and AE rate is essentially lost. However, in the next 4,000 s (Fig. 9.5c) the correlation between peak stress and peak AE rate is re-established.

Another interesting feature of induced acoustic emission is that AE synchronization with external loading becomes apparent following large amplitude AE events (events that are large enough to have their own aftershock sequences).

This is illustrated in Fig. 9.6. Similar to the aftershock sequence for stick-slip events, these large AE event aftershocks diminish with an inverse-time rate dependence. Unlike stick-slip aftershocks, however, aftershocks of large AE events show strong correlation with stressing cycles. This characteristic is further illustrated in Fig. 9.5d where the peak activity is more than 4 times the activity associated with the stress minimum.

We suggest that the appearance of strong synchronization between imposed stress oscillations and acoustic emission variations during laboratory-scale modeling is the result of increased strain-sensitivity of the fault and indicates that the fault has been driven into an unstable state. In Fig. 9.4, the stick-slip events involved slip of the entire fault surface and resulted in an overall reduced stress state as measured by

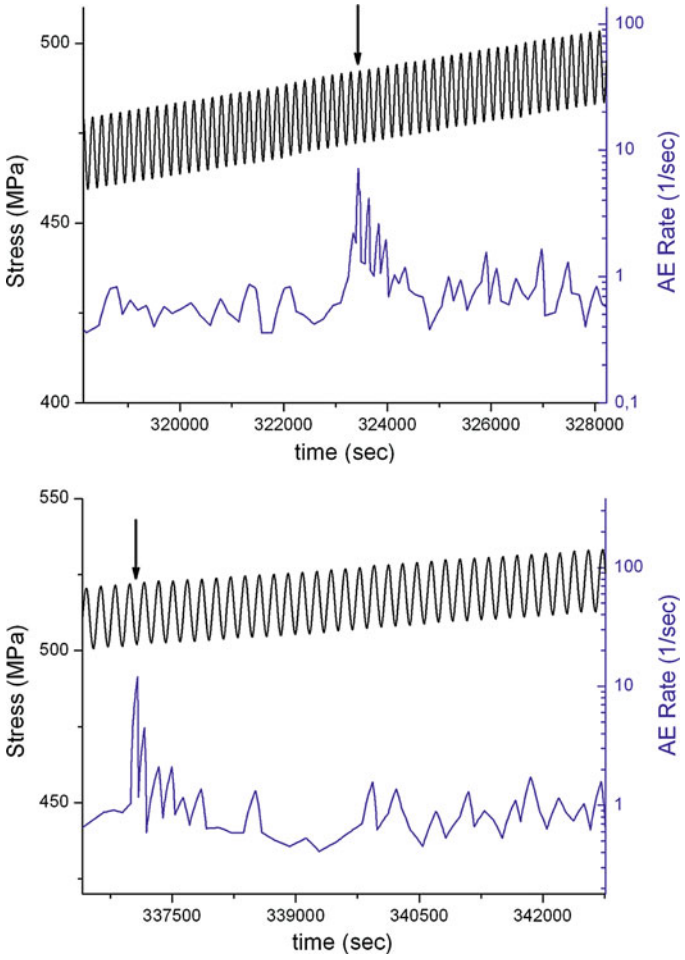

Fig. 9.6 Acoustic activity synchronizes with applied stress oscillations after large amplitude acoustic events that occur at times indicated by arrows. Interval of enhanced correlation is approximately 1000 sec

the applied axial load. This reduced stress state was characterized by a loss of correlation between AE rate and imposed stress oscillations. In contrast, in Fig. 9.6, while the AE events were large enough to produce their own aftershock sequences, they did not reduce the overall stress on the fault as measured by the total applied axial load. Instead, the drop in stress in the source region of the large AE events simply transferred stress to the remainder of the fault surface resulting in a transient increase in overall AE rate.

More than 65,000 AE events were recorded and located during this experiment. AE activity associated with the stick-slip event at 346,023 sec is plotted in Fig. 9.7. A very large amplitude AE event was recorded at the beginning of the aftershock sequence (plotted as the star in circle) and may indicate the nucleation site of the stick-slip event [Thompson et al., 2005]. Differences between locations of pre-stick-slip AE and aftershocks are small. Activity in regions 'A' and 'B' decreased while activity in 'C' increased. These changes may indicate evolution of highly stressed zones or asperities due to fault slip. Otherwise, the broad distribution of AE both before and after the stick-slip event indicates that the entire fault is stressed and undergoing inelastic deformation. Figure 9.8 shows locations of AE events before and after the large amplitude AE event described in Fig. 9.6a. The large event, indicated by the star, occurred near the center of the sample. Once again, there is little difference in location of preceding and immediately following the large amplitude AE event. Apparently, the occurrence of the large event resulted in a sudden increase in AE activity but not in a change in the spatial distribution of activity, implying a relatively uniform increase in stress over the entire fault surface.

$$\lambda(t) = \mu \cdot (1 + a \cdot \cos(\omega t + \varphi))$$

We employ a method described by Lyubushin et al. [1998] to extract the periodic component from the AE time series that represents a 'point' process. The model of acoustic intensity includes a Poisson process with a uniform purely random part with intensity μ (μ>0) and a periodic component (frequency ω, amplitude a ($0 \le a \le 1$) and phase φ). Thus the Poisson part of the intensity is modulated by a harmonic oscillation.

The log-likelihood function for the set of observations is defined as

$$\ln L(\mu, a, \varphi|\omega) = \sum_{t_i} \ln(\lambda(t_i)) - \int_0^T \lambda(s)ds$$

and the increment of the log-likelihood function becomes

$$\ln L(\mu_i, a, \varphi|\omega) = \sum_{t_i} \ln(1 + a\cos(\omega t_i + \varphi)) + N \cdot \ln(\mu_i, a, \varphi|\omega)) - N$$

$$\Delta \ln L(a, \varphi|\omega) = \sum_{t_i} \ln(1 + a\cos(\omega t_i + \varphi)) + N \cdot \ln(\mu_i, a, \varphi|\omega))$$

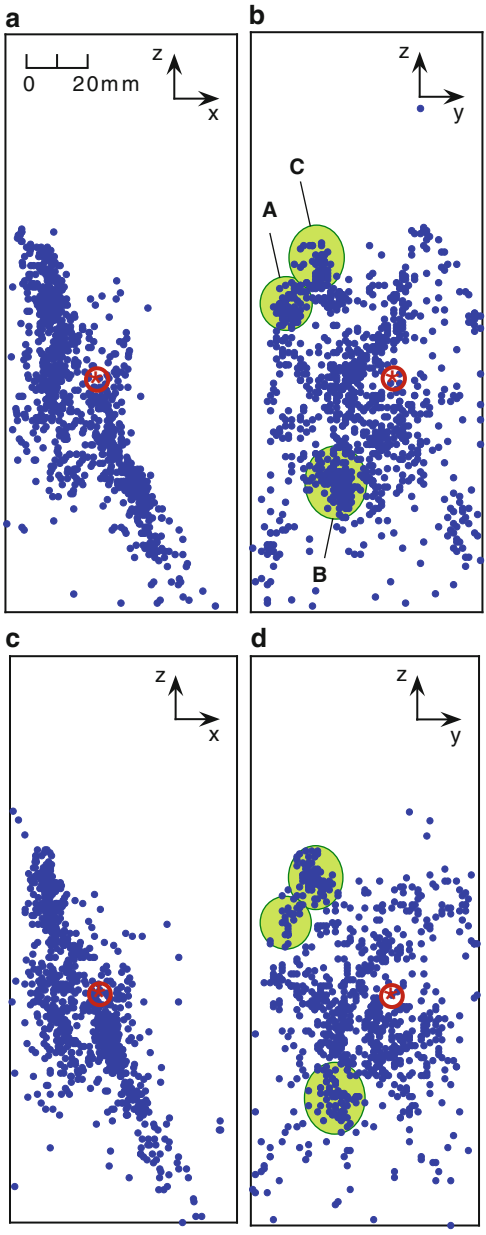

Fig. 9.7 Plots of AE activity associated with stick-slip event at 346,023 s running time. **(a)** and **(b)** show locations of events in 10,000 s interval before the stick-slip. **(c)** and **(d)** show aftershocks occurring for 10,000 s following the stick-slip. Star in circle indicates location of an off-scale amplitude AE event that coincides with the time of the stick-slip and may represent its nucleation site. Groups of events 'A', 'B', and 'C' show a change in relative activity from before to after the stick-slip and may reflect evolution of the fault surface due to co-seismic slip

The maximum of this function indicates which frequencies provide the greatest increase in the log-likelihood function when compared to a purely random model. Parameters a and ω can be estimated.

A time-frequency diagram of the AE response (log-likelihood increments) for the entire experiment is shown in Fig. 9.9. Horizontal red lines identify the portions

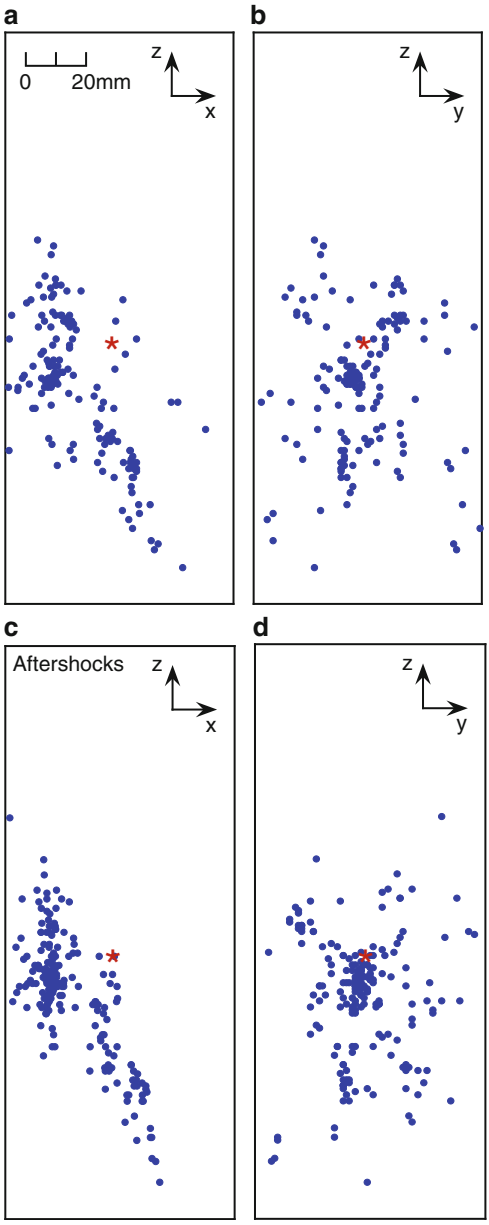

Fig. 9.8 Plots of AE activity associated with the large amplitude AE event described in Fig.6a at 323,377 sec running time. Location of this event is indicated by star. **(a)** and **(b)** Location of events occurring 2000 sec before the large AE. **(c)** and **(d)** Location of aftershock events occurring for 1000 sec following the large AE. Spatial distribution of AE events does not appear to be affected by the occurrence of the large event. Only the AE rate increased, suggesting that the large event redistributed stress relatively uniformly over the entire fault surface

of the experiment in which the AE response had periodicity of 175 s (logT = 2.24) and 570 s (logT = 2.75).

There is no periodic acoustic response during the initial stage of the experiment because no sinusoidal load is added to the constant loading rate. In general, a correlation between the sinusoidal loading and the AE response is observed over

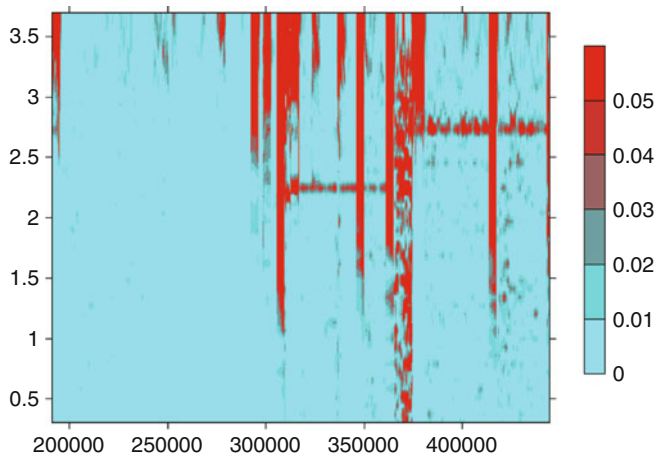

Fig. 9.9 Plot of the log-likelihood function for the entire experiment. Light-grey background indicates essentially random occurrence of AE activity. Dark regions indicate high values of log-likelihood function. Horizontal red bands during second half of the experiment indicate periods where AE activity correlates with the periodic stressing function. Vertical streaks are typically the result of rapid stress changes, including stick-slip events

the next part of the experiment. However, the magnitude of the response is not stable – sometimes it becomes very small and almost disappears. This effect is seen by a detailed examination of spectral-temporal diagrams (Fig. 9.10). Wide vertical stripes of the high values of the log-likelihood function are the result of an abrupt increase or decrease of acoustic activity due to rapid unloading of the sample, including stick-slip events.

From this preliminary analysis we can draw the following conclusions.

1) Prior to stick-slip events that represent dynamic failure of the entire fault surface, the AE rate correlates with the applied stress oscillations (periods of 175 s and 570 s). Omori-type aftershock sequences of these events lasted for a few thousand seconds. During these time intervals, AE activity did not correlate with the imposed stress oscillations. As AE activity increased due to reloading of the sample following the co-seismic stress drop and aftershock decay, AE rate again correlated with the imposed stress oscillations.
2) 'Significant' large-amplitude AE events were identified that produced Omori-type aftershock AE activity but did not involve slip of the entire fault surface or a drop in average stress. In this case, the aftershock activity showed an increased correlation with imposed oscillating stress.
3) These observations are consistent with a model in which AE activity becomes increasingly sensitive to stress perturbations as the stress level in the sample is raised and the fault is driven close to failure. If this is a general property of natural fault systems, it may be possible to identify instability and impending failure by the response of the fault to periodic stressing. It would seem reasonable to search for these effects during real aftershock series.

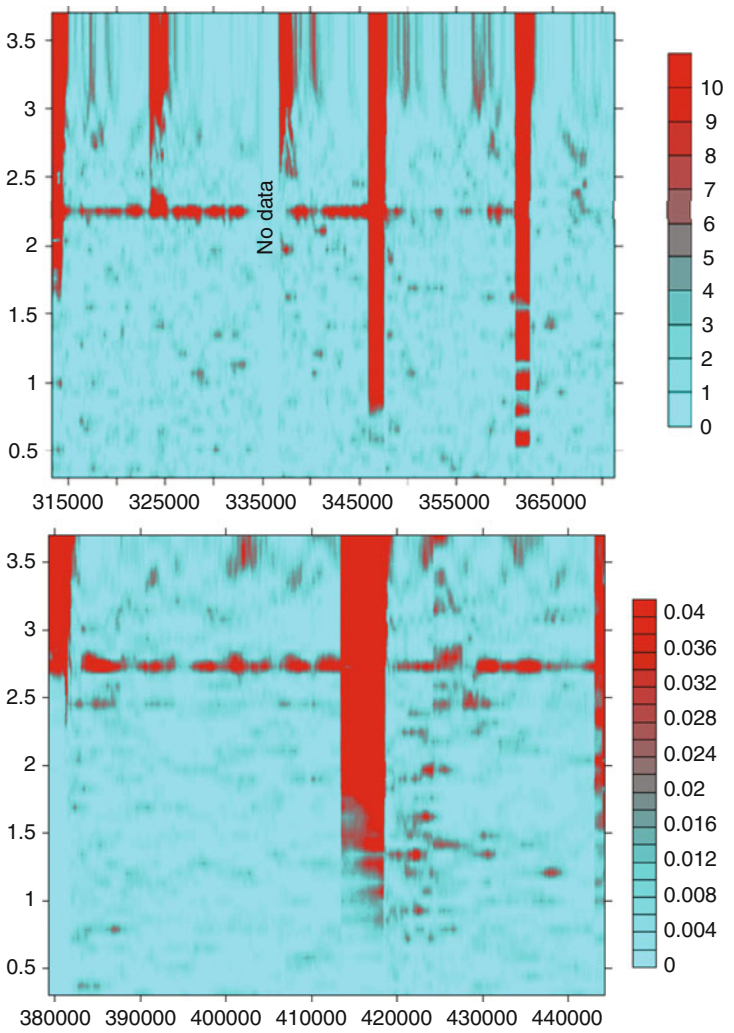

Fig. 9.10 Log-likelihood plots showing detailed segments of the experiment. Stick-slip events shown in Fig. 9.4 occur at 346,027 and 413,528 s running time and are followed by aftershock sequences with no distinct correlation to stress oscillations

References

Atlas of temporal variations of natural, antropogenic and social processes. V.2. M., Scientific World. 432 p., 1988 (in Russian).

Atlas of temporal variations in natural, antropogenic and social processes. V.3. M., Janus-K, 676 p., 2002 (in Russian).

Beeler, N. M., and D. A. Lockner. Why earthquakes correlate weakly with the solid Earth tides: Effects of periodic stress on the rate and probability of earthquake occurrence, J. Geophys. Res., 108(B8), 2391, doi:10.1029/2001JB001518, 2003.

Cochran, E. S, J. E. Vidale and S. Tanaka. Earth tides can trigger shallow thrust fault earthquakes, Science, 306, 1164–1166, 2004.

Gomberg, J., N. M. Beeler, M. L. Blanpied, and P. Bodin. Earthquake triggering by transient and static deformations, J. Geophys. Res., 103, 24411 –24426, 1998.

Lockner, D. A., and N. M. Beeler. Premonitory slip and tidal triggering of earthquakes, J. Geophys. Res., 104, 20133–20151, 1999.

Lockner, D. A.. The role of acoustic emission in the study of rock fracture, Int. J. Rock Mech. Min. Sci. Geomech. Abstr., 30, 883–899, 1993.

Lockner, D. A., J. D. Byerlee, V. Kuksenko, A. Ponomarev, and A. Sidorin. Quasi-static fault growth and shear fracture, Nature, 350, 39–42, 1991.

Lyubushin A.A., V.F.Pisarenko, V.V.Ruzich and V.Yu.Buddo. A New method for identifying seismicity periodicities – Volcanology and Seismology, vol.20, 1998, pp. 73–89.

Sadovsky M.A., Mirzoev K.N, Negmatullaev S.Kh., Salomov N.G. Influence of mechanical microoscillations on the feature of material plastic strain. Solid Earth, N 6, 1981, 32–42, 1981 (in Russian).

Sobolev G.A., Ponomarev A.V., Koltzov A.V. and Smirnov V.B. Simulation of triggering earthquakes in the laboratory. PAGEOPH, v.147, N 2, 1996, p.345–355.

Thompson, B. D., R. P. Young and D. A. Lockner, Observations of premonitory acoustic emission and slip nucleation during a stick slip experiment in smooth faulted Westerly granite, Geophys. Res. Lett., 32, doi:10.1029/2005GL022750, 2005.

Chapter 10
Acoustic Emission Dynamics Initiated by Fluid Infusion on Laboratory Scale

A. Ponomarev, G. Sobolev, and Yu. Maibuk

10.1 Introduction

The influence of water on the increase of seismic activity has been investigated in various seismotectonic environments, including the observations of the processes of reservoir filling [Gupta, 1992; Simpson et al., 1988; Mirzoyev et al., 1988; Sobolev, 1993]. The physical interpretation considered was mainly related to increase of pore pressure and the corresponding decrease of effective pressure according to modified Coulomb-Moore law [Brace, Martin, 1968]. This effect is the basis of the Dilatation-Diffusion (DD) model of the earthquake preparation [Scholz et al., 1973]. Quantitative estimates of the dependence of this effect on various values of lithostatic and hydrostatic pressure, temperature and rock permeability were made in [Miller et al., 1999]. A review of possible induced seismicity mechanisms can be found in the special issue of *Pure Appl. Geophys.* [Trifu (ed.), 2002]. The fractal properties of the water-induced seismicity are investigated in [Smirnov, 1994]. Connection of local seismic activity and small changes of water level in the reservoir (phase synchronization) were detected in [Peinke et al, 2006]. It should be noted that small changes in pore pressure also correlate with the variations of small earthquakes activity. It is shown that seismicity in the zone adjacent to lake Baikal depends on the seasonal variations of the water level in the lake, which change the pore pressure by several millibars [Djadkov, 1997]. This paper investigates the influence of relatively low water inflow on the acoustic emission in compressed samples.

A. Ponomarev (✉), G. Sobolev, and Y. Maibuk
Schmidt Institute of Physics of the Earth, Russian Academy of Sciences, Moscow, Russia
e-mail: avp@ifz.ru

V. de Rubeis et al. (eds.), *Synchronization and Triggering: from Fracture to Earthquake Processes*, GeoPlanet: Earth and Planetary Sciences 1,
DOI 10.1007/978-3-642-12300-9_10,

10.2 Experiment procedure

The biaxial compression experiments were conducted on samples consisting of basalt sand and cement. The detailed description can be found in [Sobolev, Ponomarev, 1997; Sobolev, Ponomarev, 2003]. The model has the form of an edge brick: base of 205 mm, thickness of 85 mm, side of 266 mm, the angle between the long side and base 25°. The model consisted of 3 equal-size layers parallel to the slanted sides. Two outer layers had higher durability than the central one: therefore, the inner layer was more prone to destruction. Basalt gravel with sizes from 2 to 20 mm was added to the inner layer. Initial values of P-wave velocities were 3.5 km/sec in the outer layers and 1.7 km/sec in the inner layer.

Experiments were conducted on a mechanical (lever) press which can maintain constant load over extended periods of time. The lateral load normal to the slanted sides, was kept constant for all experiments at the level of 4 tons. The vertical load F was increased stepwise by adding loads on the long arm of the lever. We call these actions the "mechanical load-ons". After each load step, the model was kept stable for 1-3 days, while the acoustic emission caused by the load-on decreased to the background levels.

Acoustic emission (AE) was collected by the 10-channel acquisition system A–Line32D (manufactured by "INTERUNIS", Russia). The dynamic range was 96 dB, sampling frequency was 5 MHz, and acoustic passband was 30-500 KHz. Besides AE, the vertical load and mechanical shortening of the model were measured and recorded every 10 seconds. The results presented here were obtained in the course of experiments with 2 identical models. During the final stage of the loading of the first model, when the vertical load exceeded 95%, water was infused into the model. The 5 mm diameter hole was drilled to a depth of 10 cm, the hole opening being located on the upper side. The hole was cased with a polyethylene tube except for the lowest 5 mm, so the water penetrated the model only in hole-bottom area. The 5 ml volumes of water which equaled to ~0.1% of the model volume were kept constant during the experiments. Figure 10.1a shows the view of the model in the press, Fig. 10.1b shows the plot of vertical load F during two consecutive infusions of water. Infusion of water caused significant increases of AE activity, thus we will call these actions "initiations" infusion.

10.3 Experiment results

10.3.1 Initiation #1

Figure 10.2 shows the AE dynamics in the lower (I) and in the upper (II) parts of the model. The initiation hole was located in the upper part. The starting point of the X-axis corresponds to the moment of mechanical load-on. At this moment, the load increased by 1.6% (up to 97% of the rupturing load). The water was infused into the

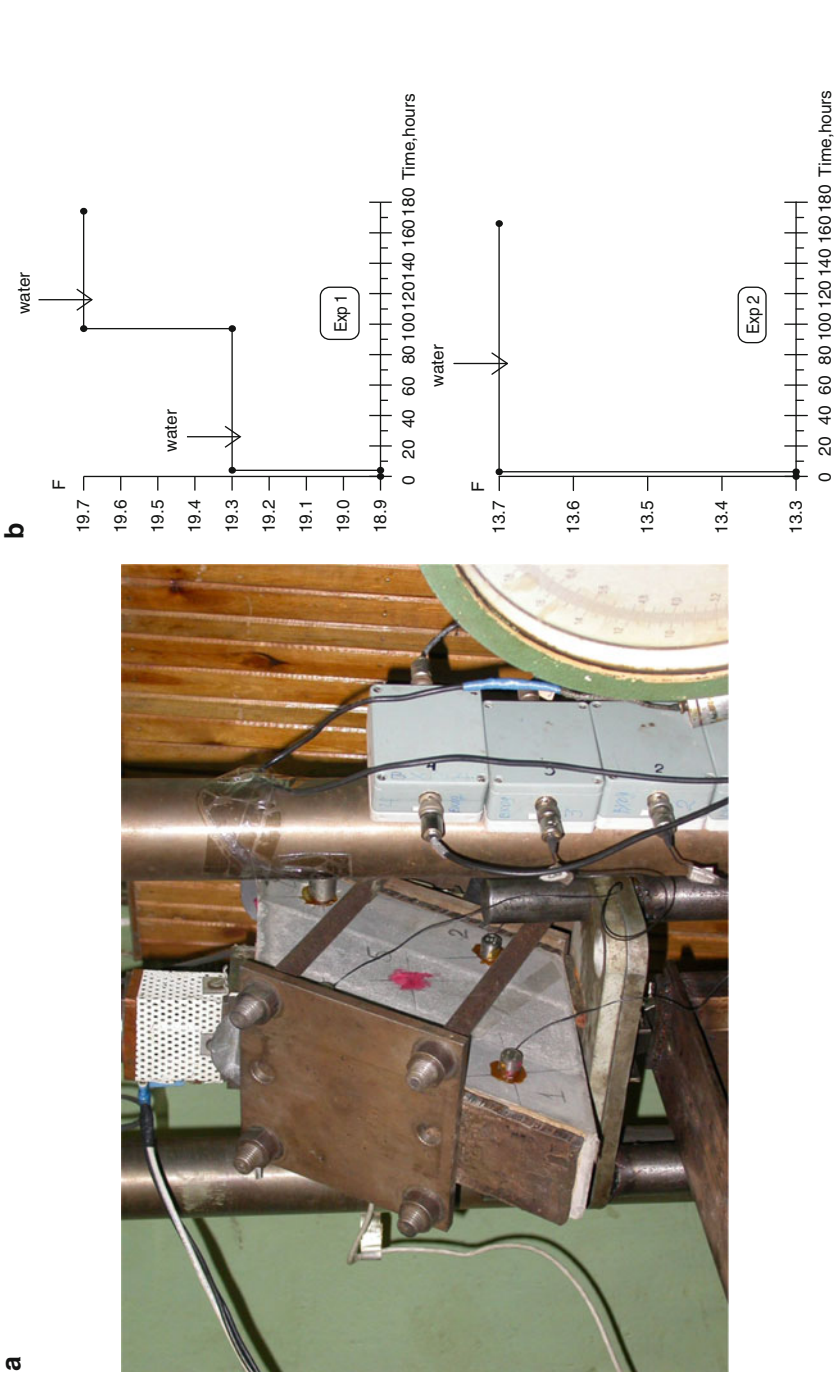

Fig. 10.1 General layout of the experiment with the model in the press (**a**) and the diagram of load F at the moments of water infusion (**b**). The arrows indicate the moments of water infusion during experiments with the 1st model (#1, #2) and with the 2nd model (#3)

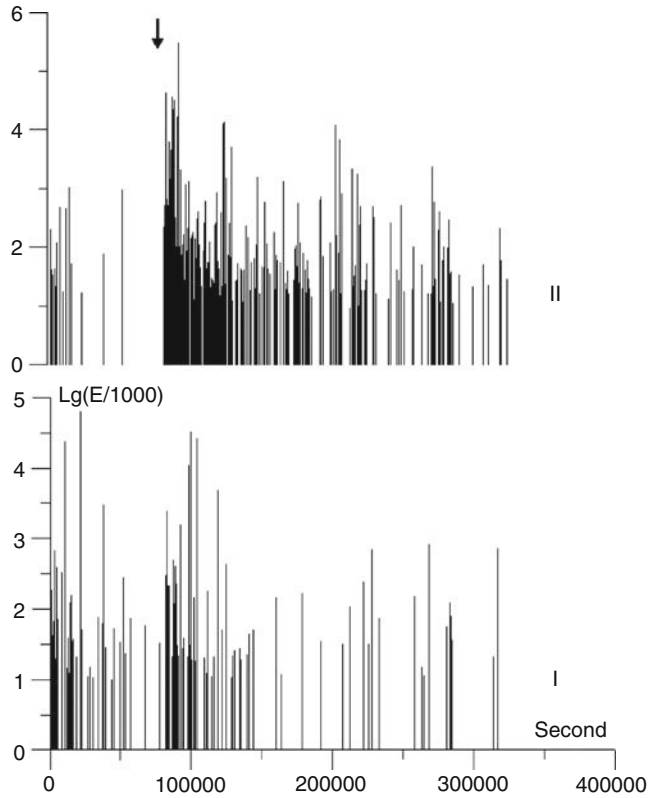

Fig. 10.2 The sequence of AE signals and their energy E in the zones I and II during the experiment with Initiation #1. The arrow indicates the start of water infusion

hole at 80828th second (marked by an arrow) and was absorbed by the model during 24 minutes (1440 seconds). Energy of AE events was estimated as the square of amplitude of signal from the sensor nearest to the hypocenter. Averaging of energy by all sensors reduced the computational stability due to the following two reasons. First, the number of sensors used for hypocenter location varied from 4 to 8. Second, with increasing distance between the sensor and the hypocenter, the frequency and amplitude of the signal changed significantly due to absorption and scattering of acoustic waves. A comparison of the upper and lower plots in Fig. 10.2 definitely shows a considerable increase of AE activity following the water infusion into the upper part of the model.

The epicenters of acoustic signals on the two faces of the model are shown in Fig. 10.3. The two lower diagrams correspond to the time span between the load-on F and the water infusion; the duration is 80827 seconds. The two upper diagrams correspond to the time span after water infusion (80828 sec. – 323768 sec. in Fig. 10.2, this is 67.48 hours). The following details must be noted: the intensity of signals increased significantly in the upper part (II), and also, whereas the

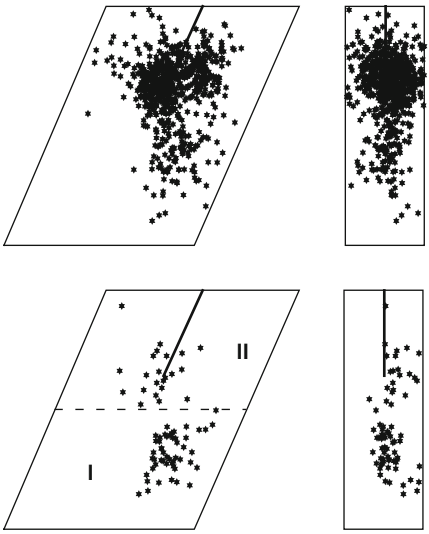

Fig. 10.3 Locations of the AE epicenters onto the front side and the perpendicular side during the experiment with Initiation #1; lower plot – before the infusion, upper plot – after the infusion. The dotted line separates the model into zones I and II. Solid straight lines show the hole projection onto the faces of the model

strongest acoustic events before water infusion happened in the lower part of the model, the strongest activity migrated to the upper part of the model following the water infusion (Fig. 10.2). The sources of acoustic signals were located inside the model, i.e., the internal cracking took place. Usually during the loading of specimens many cracks occur on the edges. In the current experiments, the internal cracking, which better corresponds to the processes of earthquake origination, was achieved due to lower durability of the inner layer of the model.

Now let us consider in greater detail the time interval immediately following the water infusion. First signals in zone II were detected just 19 seconds after infusion while in zone I scarce acoustic signals emitted only after 1308 s. In our previous paper [Sobolev, Ponomarev et al., 2006] it was discovered that penetration of water into the tip of an active crack causes an acoustic signal (crack extension) with the time delay of no more than 5 seconds. The data on the first interval in Fig. 10.2 shows that before the water infusion area I exhibited even greater acoustic activity than area II, i.e., there appeared to be more active cracks. Thus, the 1308 second delay can be interpreted as the time needed for water to come to the remote area. The low acoustic activity can be explained by the fact that, given the small amount of water injected (0.1% of the model volume), the water did not penetrate all active cracks in the area. At the same time the emergence of acoustic signals after 1308 seconds in the area I can be attributed to the influence of water. The indirect evidence of this can be found in the results of AE locations. The hypocenters of the signals on the upper plots in Fig. 10.3 are located in the upper part of this area (I), i.e., closer to the hole than it is the case before the water infusion (lower plots in Fig. 10.3).

The hypocenters of the first signals emerging in zone II immediately after the water infusion in the time span of the first hundreds of seconds are located at

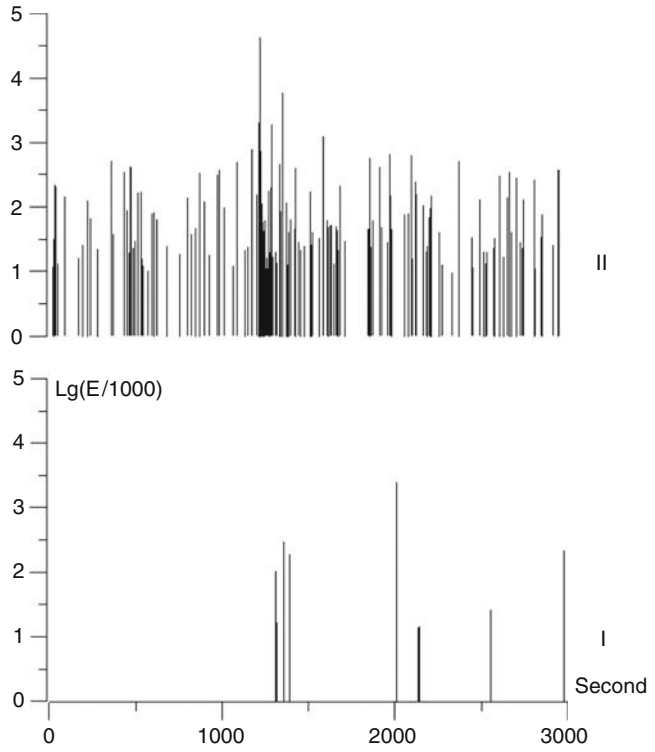

Fig. 10.4 Sequence of AE signals and their energies in the zones I and II after water infusion in the experiment with Initiation #1

30-50 mm distances from the hole. In Fig. 10.3 one can see a cluster group of high energy signals in the interval 1212–1225 seconds from the moment of water infusion. Their sources lie at 40-60 mm distances from the hole; the strongest signal (E = 4.63) occurred close to the middle of the group; its coordinates are x = 153 mm, y = 40 mm, z = 160 mm.

10.3.2 Initiation #2

The second infusion of water into the hole was conducted 4 days after the first one. The starting point of X-axis in Fig. 10.5 corresponds to the moment of load-on while F was increased by 2%. The total resulting load was equal to 20.1 tons, which is 0.5 tons above the level maintained during the Initiation #1. The moment of water infusion is marked by the arrow. Time interval between the moment of load-on and the moment of water infusion was 62760 seconds (17.43 hours). The water was

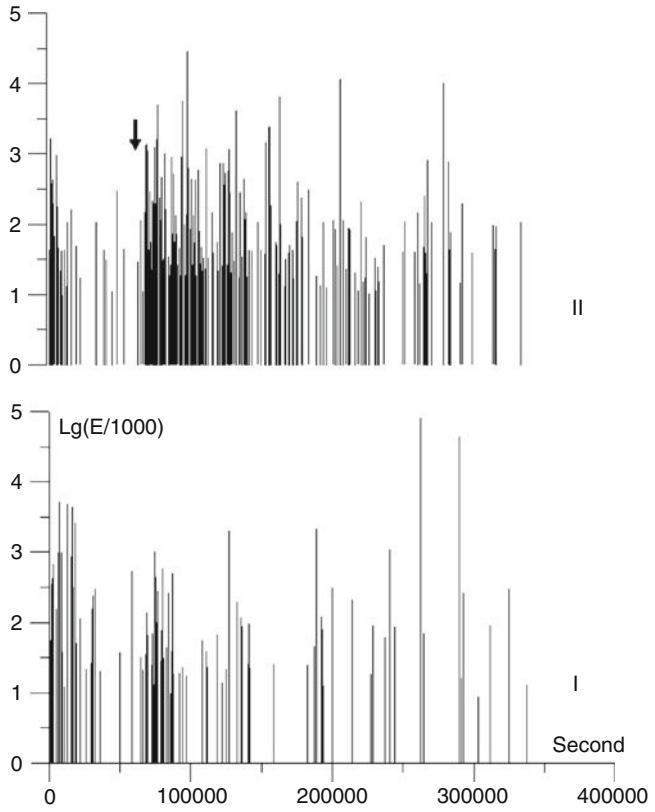

Fig. 10.5 The sequence of AE signals and their energy E in the zones I and II during the experiment with Initiation #2. The arrow indicates the start of water infusion

absorbed by the sample through the hole-bottom area after 38 minutes, which is 16 minutes longer than for the previous initiation. There can be two possible reasons for this effect. First, the moisture content of the model in the area adjacent to the hole-bottom was elevated compared to the initial one as a result of the previous initiation. Second, the number of active cracks where the water is actively absorbed could decrease as a result of the first initiation. Figure 10.5 shows that in the second initiation, just like it happened in the first one, the inflow of water resulted in the increase of AE activity.

The lower plots in Fig. 10.6 show the epicenters of the AE events occurring between the mechanical load-on and water infusion; the upper plots show the AE activity during 274610 seconds following the water infusion. Most events occurred in the area adjacent to the hole-bottom.

As one of significant differences between Initiations #1 and #2, we can mention the lower number of AE signals occurring in the upper area (II) after water infusion. So, during the same $\Delta T = 48$ hour interval, 548 AE signals occurred in Initiation

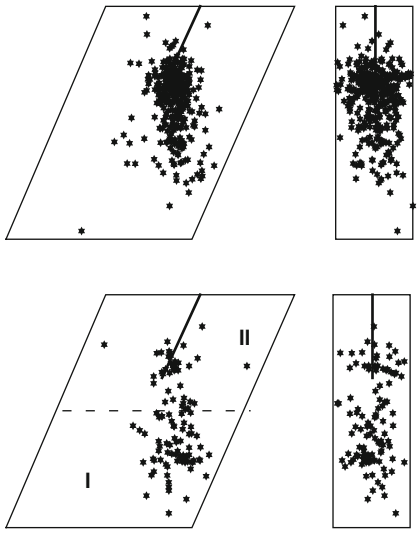

Fig. 10.6 Locations of the AE epicenters onto the front side (slanted) and the perpendicular side during the experiment with Initiation # 2; lower plot – before the infusion, upper plot – after the infusion. The dotted line separates the model into areas I and II. Solid straight lines show the hole projection onto the faces of the model

#1, whereas only 255 occurred in Initiation #2. At the same time, the AE activity in the remote area (I) was comparable in both Initiations.

The second notable difference is that in Initiation #2 the delays between the water infusion and the start of AE pulses were longer and practically identical in both parts of the model. This is shown in Fig. 10.7 where the events are plotted on a more detailed time scale following the moment of water infusion. One can see significant differences compared with Fig. 10.4. In the first case, the delays were 19 and 1308 seconds, in the second case being 2219 and 2000 seconds.

10.3.3 Initiation #3

It was interesting to find out whether the AE initiation effect would occur with the lower stresses applied to the model, and whether there is any difference in the manifestation of the effect. This was performed in experiment #2. The water was infused when the load F equaled 13.8 tons, i.e., the load was 70% of the critical instead of 97% in the previous experiment. The water infusion started 256683 seconds (71.3 hours) after the mechanical load-on by 3.4%. The water was absorbed slower than in Initiation #1 (2 hours versus 24 minutes). This difference is probably explained by the fact that the lower stress resulted in lower number of water-containing microcracks. Figure 10.8 shows the significant increase in AE activity around the hole location II; this area also exhibits the strongest events.

Figure 10.9 shows the epicenters of the AE events before water infusion (lower plots) and after infusion (upper plots). One can see the increased density of events

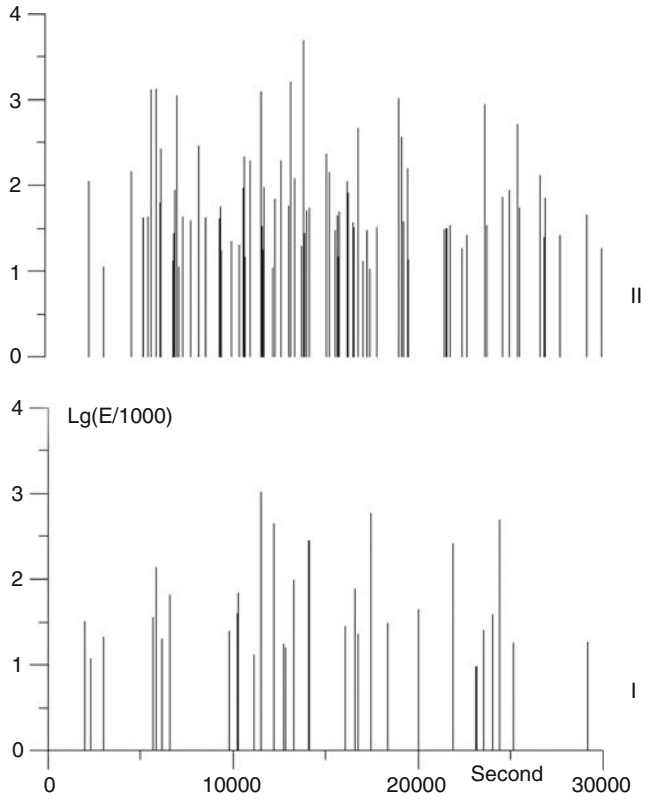

Fig. 10.7 Sequence of AE signals and their energies in the zones I and II after water infusion in the experiment with Initiation #2

around the hole location in area II after water infusion. Before the water infusion, the events occurred practically with the same density in the upper and lower parts of the model. The sources of AE signals were located inside the model, i.e., it was internal cracking again.

Figure 10.10 shows an expanded plot of the interval immediately following the water infusion; significant time delays of AE events relative to the moment of water infusion are observed in both areas. First AE signals in area II emerge after 1909 seconds (32 min.), in area I the delay is 4269 seconds (71 min.). Since the intensity of AE activity had been comparable in both areas prior to water infusion, it is reasonable to assume that the greater delay in area I is basically the delay of water arrival in the remote area. The lower AE activity compared to Initiation #1 is probably caused by smaller number of active microcracks accumulated inside the model by the moment of Initiation #3. Hypocenter locations of the first AE events emerging in area I after water infusion show that these hypocenters are located close to the upper limit of this area at 40-50 mm distances from the hole-bottom.

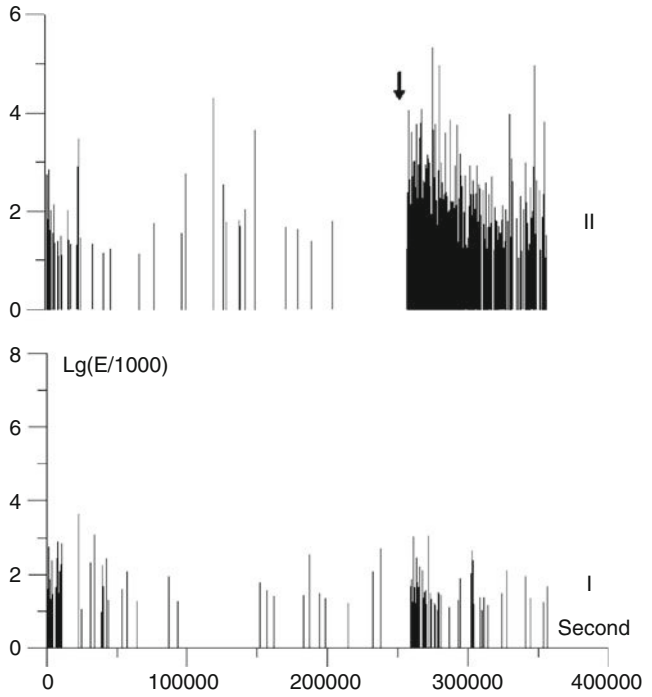

Fig. 10.8 The sequence of AE signals and their energy E in the areas I and II during the experiment with Initiation # 3. The arrow indicates the start of water infusion

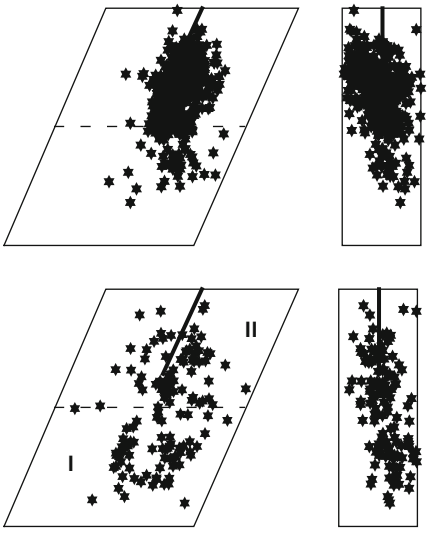

Fig. 10.9 Locations of the AE signal epicenters onto the front side (slanted) and the perpendicular side during the experiment with Initiation # 3; lower plot – before the infusion, upper plot – after the infusion. The dotted line separates the model into zones I and II. Solid straight lines show the hole projection onto the faces of the model

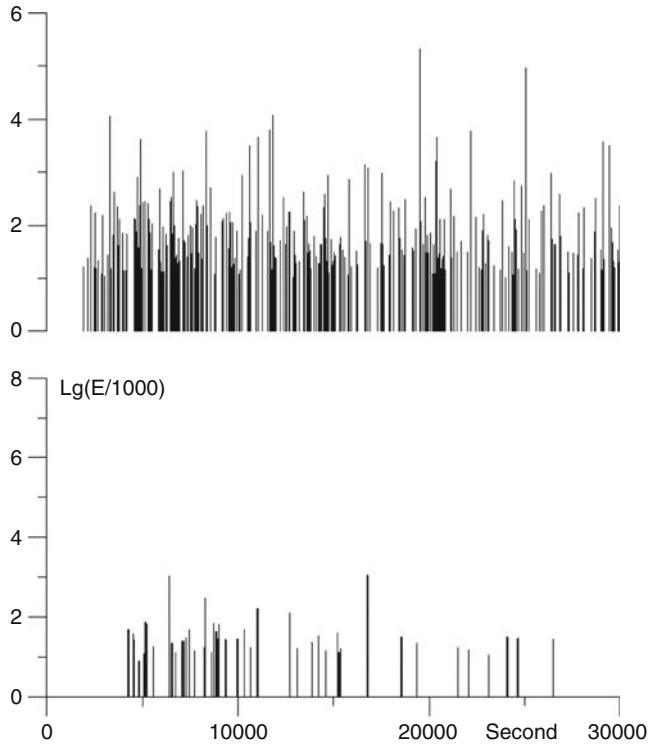

Fig. 10.10 Sequence of AE signals and their energies in the zones I and II after water infusion in the experiment with Initiation #3

10.4 Discussion

From Figs. 10.2, 10.5, and 10.8 it follows that the patterns of AE relaxation after mechanical load-ons and after water infusions are substantially different. In the first case, the high activity decreased significantly during several hundreds of seconds following the load-on. In the second case, the elevated activity was maintained at a high level during several thousands of seconds. Additionally, this elevated activity did emerge with a certain time delay relative to water infusion; see Figs. 10.4, 10.7, and 10.10.

Another aspect of this difference in AE patterns can be seen in Figs. 10.11 and 10.12. In these figures the rate of change of AE activity dN/dt is plotted for the cases of mechanical load (lower plots) and for water infusions during Initiations #1 and #3 (upper plots). The number of events was divided by the time interval dt, which was incremented logarithmically.

In both cases of AE excitation by a mechanical load-on, the relaxation process conforms to the Omori law (slanted lines in the lower plots).

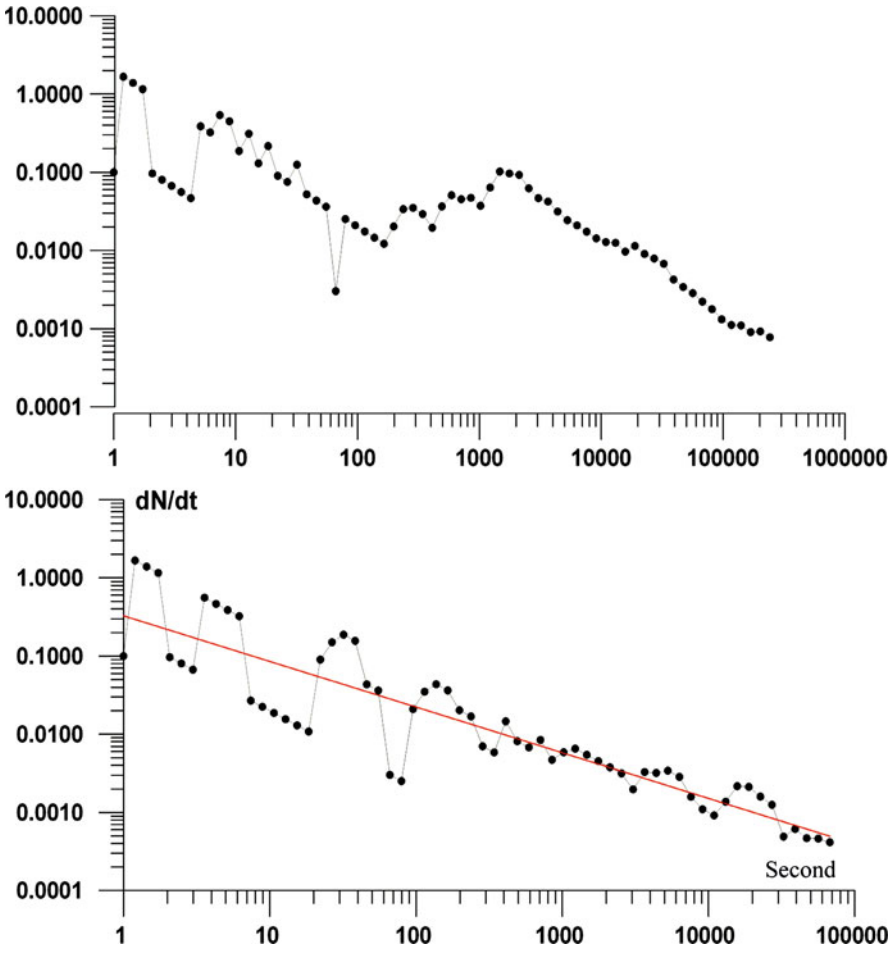

Fig. 10.11 Changes in the rate of AE activity dN/dt (per second) during the experiment with Initiation #1. The lower plot shows the reaction to mechanical load-on, the upper plot – the reaction to water infusion

$$dN/dt = C/(1+t)^{p} \tag{10.1}$$

In particular, the "log-log" plot (a) in Fig. 10.11 corresponds to the equation

$$dN/dt = 0.32/(1+t)^{0.58} \tag{10.2}$$

with the determination factor $R = 0.81$, whereas plot (a) in Fig 10.12 corresponds to the equation

$$dN/dt = 1.1/(1+t)^{0.66}; \quad R = 0.88 \tag{10.3}$$

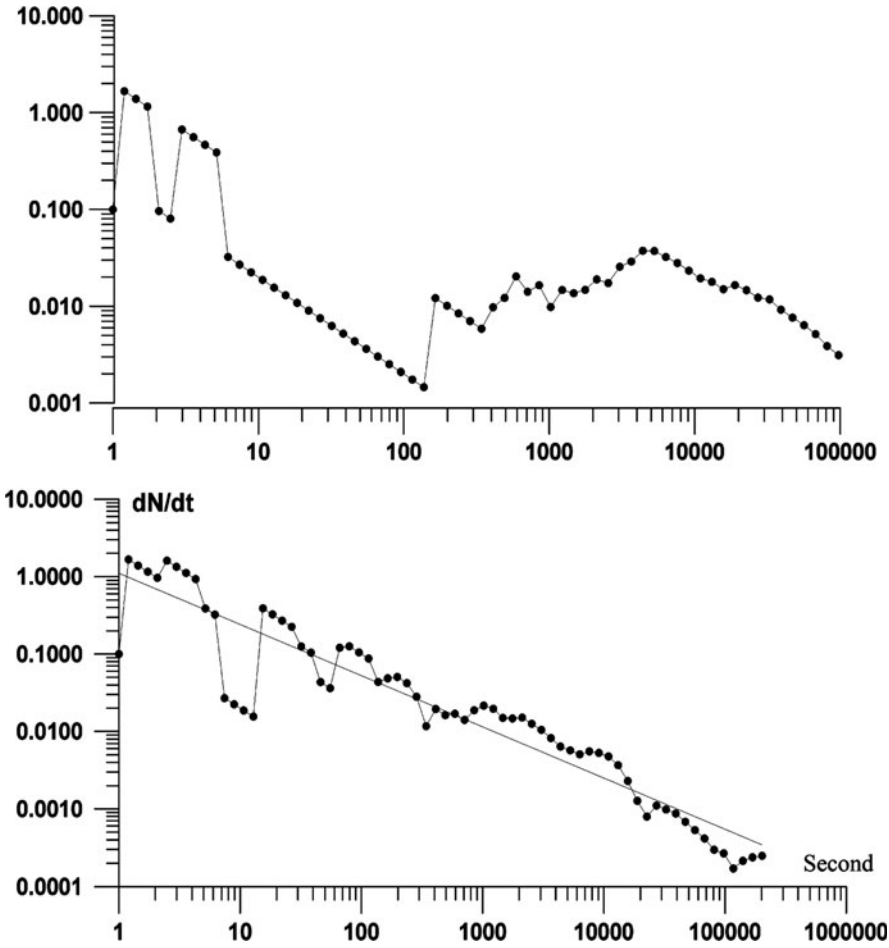

Fig. 10.12 Changes in the rate of AE activity dN/dt (per second) during the experiment with Initiation #3. The lower plot shows the reaction to mechanical load-on, the upper plot – the reaction to water infusion

As it was already noted, the AE activity after water infusion occurred with a certain time delay. Let us consider the process after the activity emergence — plots (b) in Figs. 10.11 and 10.12. In both cases, during Initiations #1 and #3 the AE activity decreased during the first 100 seconds after the emergence of the initial signals; this was followed by a gradual activity increase and subsequent decrease. This pattern cannot be described in terms of relaxation equation type (10.1). During Initiation #2 the dynamic pattern was basically similar; however, it was not processed statistically due to lower number of AE signals.

The decay in the activity within a short time interval, covering the first 100 s, is hardly connected with the process of water infusion, which lasted dozens of minutes. The physical sense of the decay in the acoustic activity is not clear so far.

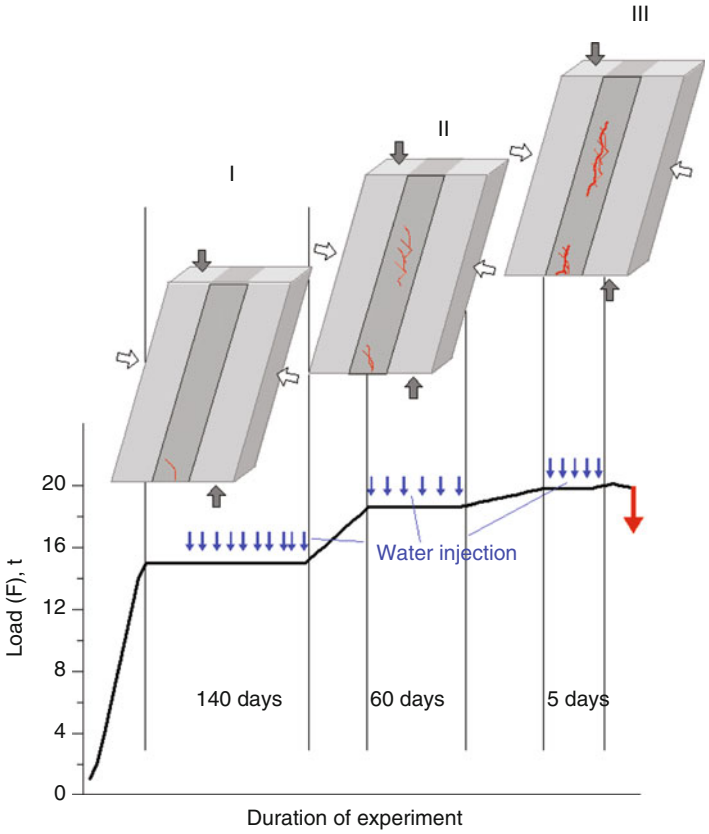

Fig. 10.13 Layout of the experiment for water infusion into the cracks at different stages of loading, I, II, and III, with the increasing load F on the model

In our previous paper [Sobolev, Ponomarev et al., 2006] the influence of water injected directly into the cracks visible on the surface on the AE activity was investigated; the model was similar in composition to the one described here. In Fig. 10.13 one can see the layout of that experiment which lasted for more than 7 months. As an example, Fig. 10.14 shows the dynamics of the AE response to the water infusion during stages I, II, III corresponding to increasing values of load F. It was determined that the patterns of gradual increase and subsequent decrease of AE activity can be described by the formula

$$dN/dt = (dN/dt)_0 \cdot \exp[\phi(t) - \Psi(t)] \tag{10.4}$$

where the terms in the exponent expression are time dependent. Variations in experimental data are accounted for by adjustment of factors a, k and V in the formula

$$dN/dt = a \cdot \exp[t^k - V/(1+t)^m] \tag{10.5}$$

The physical interpretation of these effects must take into account several concurrent processes. The increased rate of cracking can be caused by the decrease of durability of the moistened area, by an increase of brittleness, or by an increase of stresses. The effect of durability decrease in solids caused by absorption, chemisorptions, wetting and other physical-chemical processes was discovered for solids of various compositions (Rehbinder effect). This effect was discovered also for rocks [Rehbinder, Schukin, 1972; Traskin et al, 1989]. The effect is caused by a decrease of the free surface energy U on the liquid-solid surface. As determined by the spectral analysis, the chemical composition of the model includes: MgO, Al_2O_3, SiO_2, P_2O_5, K_2O, CaO, TiO_2, Cr_2O_3, MnO, FeO. The chemical composition of the water used in the experiments includes: HCO_3, Cl, SO_4, NO_3, NO_2, Na, Ca, Mg, NH_4.

Intensified destruction of brittle solids under the influence of surfactants absorbed on the surfaces of the cracks is quantitatively treated in [Kornev, 2003]. However, the manifestation of this effect must gradually decrease due to the limited number of cracks in metastable state, due to decrease of accumulated potential energy as a result of AE, and due to exhaustion of water which causes the AE activation.

We support the hypothesis that the number of cracks in metastable state is a significant, and possibly the crucial factor determining the AE dynamics after an external influence. The number of such cracks grows together with the growth of the applied loads and (or) with the increased duration of load application. This can be seen, for example, in the changes of curves plotted in Fig. 10.14. Along with the increase of the load F from stage I to stage III (Fig. 10.13), the AE reaction to the water infusion manifests itself as a general increase in activity and the occurrence of a maximum soon after the infusion. This effect was discovered in various experiments and is described in [Sobolev, Ponomarev et al., 2006]. With the low F values, the AE decrease starts even with the increasing load. With the high F values, the AE maximum occurs after the moment of reaching the maximum value of F and even after the moment when F starts decreasing. The plots in Fig. 10.14 can be adequately described by formula (10.5) under the assumption that the number of active cracks at the current moment t_i is decreased by the number of cracks which had already generated the acoustic signals and had thus become inactive (not stressed to subcritical level), i.e., calculations by formula (10.5) are amended by

$$dN/dt = dN/dt_{(i)} - dN/dt_{(i-1)} \tag{10.6}$$

The structure of formulae (10.4, 10.5) resembles the equation of the kinetic concept of the strength of solids [Zhurkov, 1984]. In the work [Stavrogin and Protosenya, 1985], on the basis of numerous experiments it was established that the creep of different rocks is described by the following equation

$$d\varepsilon/dt = \varepsilon_0 \cdot \exp[(\gamma\sigma - U_0)/KT] \tag{10.7}$$

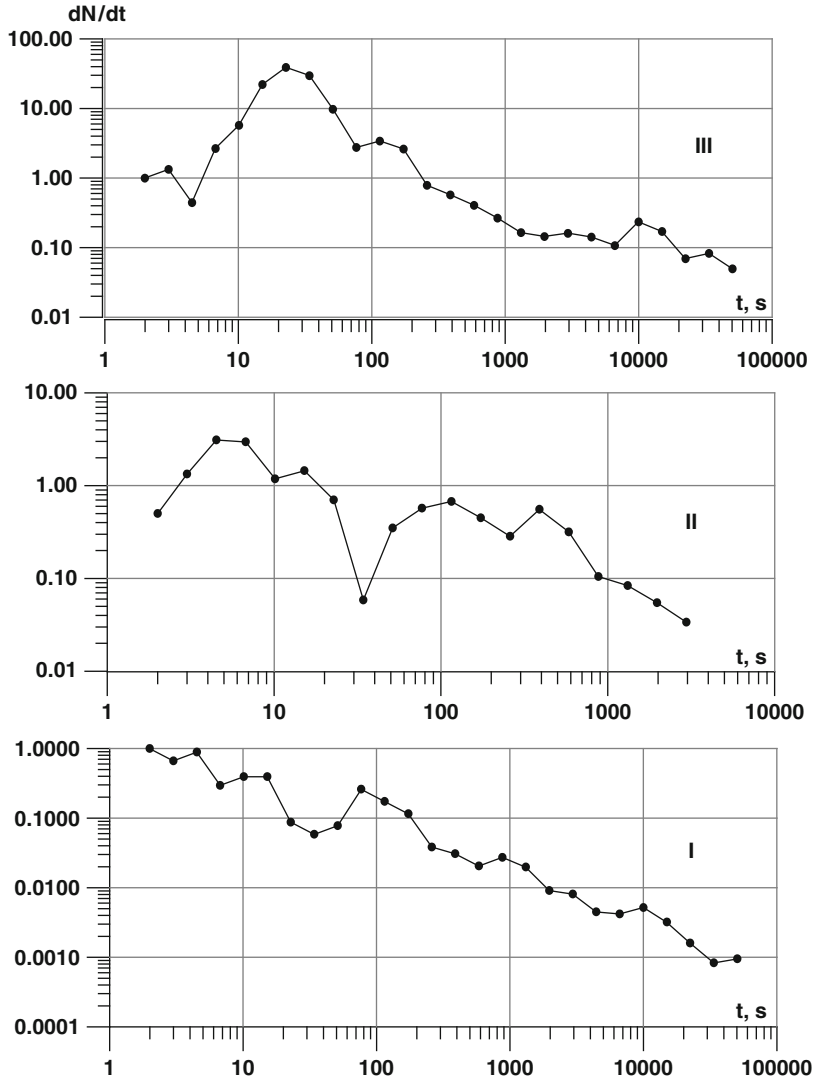

Fig. 10.14 Examples of differential changes of the number of AE events per unit time after water infusion during stages I, II, and III

where ε is the relative deformation, γ the parameter sensitive to structure, σ the applied stress, U_0 the activation energy, K the Boltzmann constant, and T is the absolute temperature.

The parameter ε_0 indicates the maximum possible rate of deformation, which coincides with the velocity of elastic waves. The authors of the work [Tamuzh and Kuksenko, 1978] showed that with a similar type of equation it is possible to describe the rate of destruction. In this case, the parameters of the equation contain

factors describing the gradual weakening in the undistorted bonds, and thus indicative of the increase in the effective stress.

Besides the formal similarity of formulas (10.4), (10.5), and (10.7), there must exist much more profound physical connections. The rate of crack formation in the brittle material (like our models) is roughly proportional to the rate of relative deformation: $dN/dt \sim d\varepsilon/dt$. In case of the initiation of AE by water infusion one can assume that $\gamma\sigma$ increases with time, for example due to the decreased friction along the crack faces and associated growth of stresses in the tips of these cracks. The U_0 value, giving the level of energy barriers, also does not stay constant due to changes in the material strength.

In Fig. 10.15 one can see examples of the use of equations (10.5), and (10.6) for modeling plots of the Fig. 10.14 type. The plotted curve 1 was calculated with the following parameters in (10.5): $a = 10$, $k = 0.005$, $V = 20$, $m = 1$. The low value of k should be noted – it means that the first term in the exponent in (10.4), (10.5), and (10.7) changes insignificantly with time. When $m = 1$, the second term in exponent changes according to the same law as in the Omori equation (10.1). Consequently,

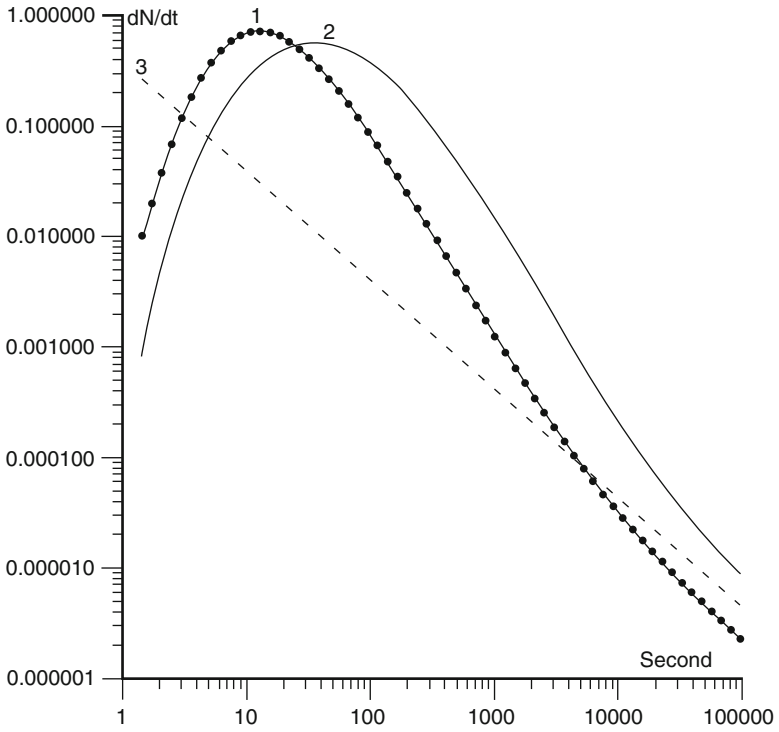

Fig. 10.15 Evaluation of AE dynamics according to formulas (10.5) and (10.6):
1 – parameters: $a = 10$, $k = 0.005$, $V = 20$, $m = 1$;
2 – same values of parameters, but the delay of water arrival to metastable cracks is accounted for;
3 – same values of parameters k and V, but $m = 10^{-6}$, $a = 10^{10}$

the growth or decrease of k results in the growth or decrease of the number of AE signals per unit time, but the time position of the maximum for plot 1 in Fig. 10.15 does not change. On the other hand, the growth or decrease of m results in the shift of the maximum along the time scale. Plot 3 corresponds to the value of $m = 10^{-6}$ with the values of k and V unchanged; the vertical scale is increased by a factor of 10^9. This plot can be described by the equation of type (10.1):

$$dN/dt = 0.38/(1+t)^{0.98}; \quad R = 0.99 \tag{10.8}$$

Comparing the plots (b) in Figs 10.11, 10.12, and 10.14 it follows that in the current experiment the AE reaction to the water infusion through the hole (Figs. 10.11, 10.12) is reached later than in the previous experiments when water was injected directly into the crack (Fig. 10.14). The probable reason is that water coming through the hole-bottom only gradually reaches the metastable cracks. Plot 2 in Fig. 10.15 shows the shifting and flattening of the maximum in case when calculations are done with the same values of a, k, V, m as for plot 1, but the certain velocity of water propagation after infusion is taken into account. If the calculations by formulas (10.5) – (10.6) are made under the assumption that the water will access the active cracks not immediately, but 10 seconds later, the maximum dN/dt time is shifted from 12.8 sec (plot 1) to 38.3 sec (plot 2). Slower water propagation explains big time delays in plots (b) in Figs 10.11 and 10.12. It should also be noted that after the local maxima, plots (b) in Figs. 10.11 and 10.12 can be quite adequately described by the relaxation equations of type (10.1). The values of parameters p are equal to 1.1 and 0.77, i.e., higher than the corresponding values in equations (10.2) and (10.3). This must be understood as a steeper decrease of AE rate after water initiation than after the mechanical load-on. The data obtained up to now seems insufficient to explain the reason of this disparity.

It should be understood that the kinetic approach described by the equations (10.4), (10.5), and (10.7) is probably not the only one possible. Real processes inside heterogeneous medium subject to external influences must include various nonlinear mechanisms. An adequate physical description must be based on additional experiments where the inner properties of media will be varied, as well as external influences.

The above experiments also provided the answer to the following question: does the shape of the seismograms and/or their spectra change after water infusion? To this end, several signals were selected which occurred practically at the same locations before and after water infusion. The search area was restricted by several centimeters around the bottom of the hole. Another requirement was approximate amplitudes of signals. With these quite rigid restrictions, several pairs of signals were selected.

Example of such signals can be seen in Fig. 10.16. The sources were located about 2 cm from the hole; the hypocenters were coincident within 1 cm. The lower oscillogram in Fig. 10.16 was recorded in the Initiation #1 before the water infusion; the upper one – 6 minutes after the water infusion; the amplitudes of the signals were practically identical. The structure of the oscillograms consists of 2 parts. In the first part, the high frequency oscillations can be seen during ~30

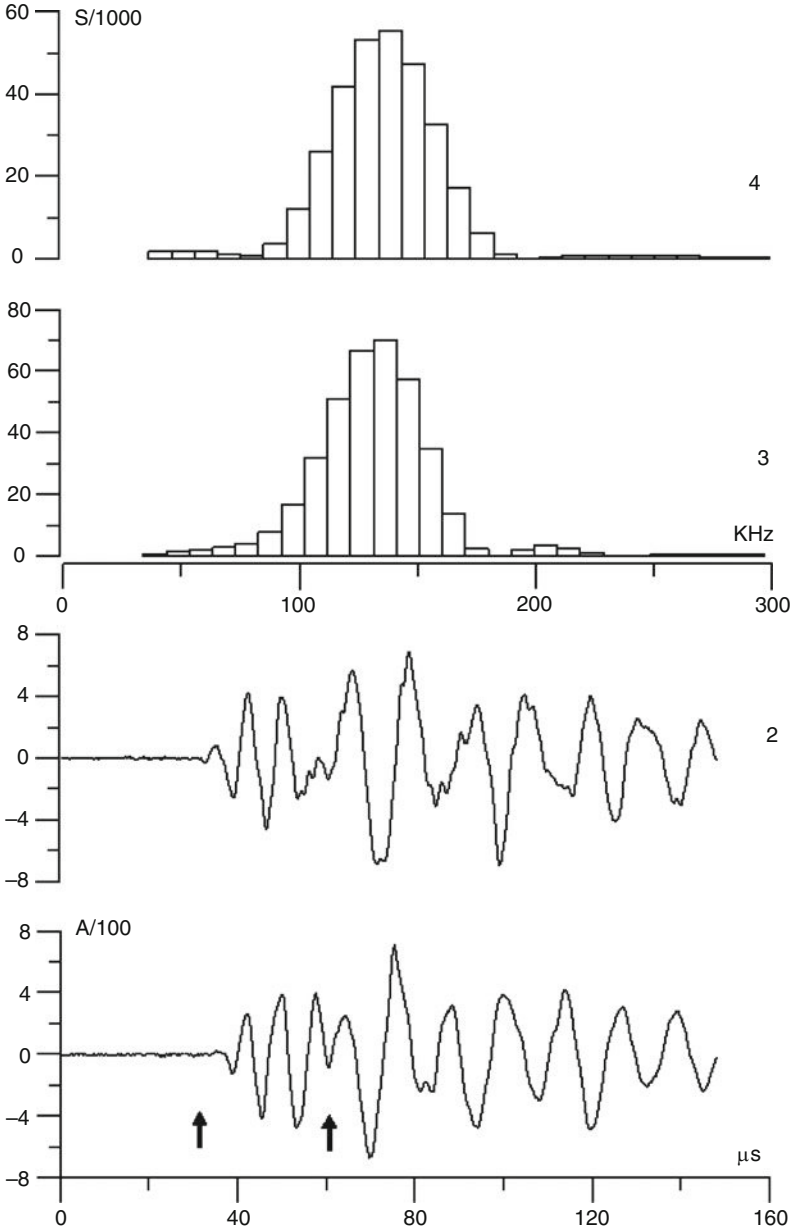

Fig. 10.16 Acoustic waveforms (1 and 2) and amplitude spectra for their initial parts (3 and 4) before water infusion (1 and 3) and after water infusion (2 and 4). Arrows show the time interval for spectra analysis

microseconds. Then these oscillations become lower-frequency ones. Having recorded and processed several hundreds of such signals, we came to the conclusion that the first part of the seismogram carries more information about the signal source and that information about the media is less pronounced in this part. The frequency composition is widely variable within 10^3–10^2 kHz, depending on the distance and azimuth between the source and the sensor. The second part basically reflects the oscillations of the sensor and adjacent parts of the model. The frequencies in this part of the signal were concentrated in the narrow 80–90 kHz range.

Two upper plots of Fig. 10.16 show the spectral densities calculated from the fist parts of the oscillograms; the intervals are indicated with arrows near plot 1; the spectral maxima are located near the ~130 kHz frequencies. The maxima for the second parts of oscillograms are equal to 86 kHz. Analysis of this pair and another pairs of signals did not yield any substantial differences in the waveforms or in the spectra of signals before and after the water infusion. This means that the influence of water did result in the decreased values of strength or in the increased values of local stresses, but dynamic "frictional sliding" occurred over the "dry" material, whose properties did not change significantly after the water infusion. It should be stressed that our experimental setup and conditions were substantially different from the majority of other experiments (laboratory as well as field ones) which are routinely conducted in the studies of hydrofractures. The effect of the pore pressure on the strength was insignificant, if present at all. The AE initiation in our case was due to the physical-chemical interaction of the solid and liquid interval for which the spectra were calculated. In the experiments described here AE signals with high energy always occurred after smaller events, aftershock activity was almost nonexistent, and the activity itself had a clustered dynamics. The latter feature is probably caused by the penetration of water into the areas of metastable cracks. The sizes of the AE emitting cracks can be indirectly estimated as follows. In the paper [Kuksenko, 1983] it was discovered that the length L of a crack developing with a constant velocity V is directly proportional to the pulse build-up τ of the AE signal thus emitted

$$\mathrm{L(mm)} = \mathrm{a}\cdot\mathrm{C(mm/\mu s)}\cdot\tau(\mu\mathrm{s}) \tag{10.9}$$

where a is some dimensionless factor close to 1. The pulse build-up of the majority of AE signals in Fig. 10.16, depending on the amplitude of the signal, was in the range 1-3 microseconds. Assuming the average velocity of crack development in the weakened area of the model C ~= 1 mm/microsecond, the crack sizes can be estimated at 1-3 mm.

10.5 Conclusions

The series of long-term experiments show that at a constant stress level the infusion of a relatively small volume of water (0.1% of the model) results in the activation of AE emission, which does not contradict the theory of the triggered mechanism of AE activation.

AE emissions of greater energy emerge after the initial smaller events; the sequence of different-energy events resembles the swarm which is observed in seismically active areas.

The AE activity emerges at different moments in different areas of the deformed model; this is caused by the different times of fluid inflow to the active cracks and by differences in local stresses.

There are no significant differences in the waveforms and in the spectral composition of AE signals recorded before and after the water infusion; this fact suggests the local decrease of material strength and/or the local increase of stresses near the metastable cracks.

The relaxation dynamics of AE processes after the load-ons and after initiation by water infusion is substantially different. In the first case it corresponds to the Omori law, whereas in the second case the AE activity has a clearly defined maximum.

Applying the kinetic approach to a medium with the finite number of metastable cracks allows to describe the AE dynamics caused by water infusion.

References

Brace WF., Martin RJ. A test of the law of effective stress for crystalline rocks of low porosity // Intern. J. Rock Mech. Mining. Sci. 1968, Vol. 5, p. 415–426.

Djadkov P.G. Induced Seismicity at the Lake Baikal: Principal Role of Load Rate. The 29-th General Assembly of the International Association of Seismology and Physics of the Earth's Interior, August 18-28, 1997, Thessaloniki, Greece, Abstracts, p. 359.

G.A. Sobolev, A.V. Ponomarev, A.V. Kol'tsov, A.A. Kruglov, V.A. Lutsky, and Yu.V. Tsyvinskaya. The effect of water injection on acoustic emission in a long-term experiment. Geology and Geophysics. 2006, Vol. 47, No. 5, pp. 608–621.

Gupta H.K., Reservoir-Induced Earthquakes, Elsevier, Amsterdam, 1992, p. 364).

Kornev V.M. The quantitative description of Rebinder effect (fragile and quasifragile materials) from retarding destruction to spontaneous dispersion. The physical mesomechanics, 2003, Vol. 6, No 3, p. 9–18, (in Russian).

Kuksenko V.S. et al. The estimation of dimensions of growing cracks and zones of unloading with parameters of acoustic signals. The mechanic of composite materials. 1983, No. 3, p. 536–543, (in Russian).

Miller S.A., Y. Ben-Zion, J. Burg. A three-dimensional fluid-controlled earthquake model: Behavior and implications. J.Geoph.Res., 1999, Vol. 104, No. B5, p. 10621–10638.

Mirzoev K.N., Negmatulaev SKh., D. Simpson &others. The induced seismicity in the region of the Nurek GES reservoir. Dushanbe, M. Donish, 1988, p. 402, (in Russian).

Peinke J., Matcharashvili T., Chelidze T., Gogiashvili J., Nawroth A., Lursmanashvili O., and Javakhishvili Z., "Influence of Periodic Variations in Water Level on Regional Seismic Activity Around a Large Reservoir:Field and Laboratory Model," Phys. Earth Planet. Inter., **156** (1–2), 130–142 (2006).

Rehbinder P.A., Shchukin E.D. The surface effects in solid materials during processes their deformation and failure. The successes of physical sciences. 1972, T. 108, p. 3–42, (in Russian).

Scholz C.H., Sykes L.R., Aggarwall Y.P. Earthquake prediction: A physical basis. Science. 1973. Vol. 181, p. 803–810.

Simpson, D., Leith, W., Scholz, C.: Two types of reservoir- induced seismicity. Bull. Seismol. Soc. Am. 78, 2025–2040, 1988.

Smirnov V.B., A.S. Cherepantsev, V.K.Mirzoev. The fractal properties of induced seismicity in the region of Nurek reservoir. The induced seismicity. M. Nauka, 1994, (in Russian).

Sobolev G.A., Ponomarev A.V. The method of detection of instability of the geological medium model. DAN, 1997, Vol. 356, No 4, p. 541–544, (in Russian).

Sobolev G.A., Ponomarev A.V. The physic of earthquakes and forerunners. M., Nauka, 2003, p. 270, (in Russian).

Sobolev G.A. Fundamental of Earthquake Prediction. Moscow. 1993, 313 p, (in Russian).

Stavrogin A. N. and Protosenya A. G. The Strength of Rocks and the Competence of Workings at Large Depths. Nedra, Moscow, 1985, pp. 1–272. (in Russian).

Tamuzh V. P. and Kuksenko V. S. Micromechanics of the Polymer Materials' Destruction. Zinatne, Riga, 1978, pp. 1–295. (in Russian).

Traskin V.U., Pertsev N.V., Kogan I.S. The influence of water on mechanic properties and disperse structure of rocks., In book The water in disperse systems. M. Khimia, 1989, p. 83–100, (in Russian).

Trifu, C.I. (ed.): The mechanism of induced seismicity, special volume. Pure Appl. Geophys. 159 (2002).

Zhurkov S.N. Kinetic concept of the strength of solids. Int. J. Fracture 1984, Vol. 26, No 4, p. 295–307.

Chapter 11
Acoustic Emission Spectra Classification from Rock Samples of Etna Basalt in Deformation-Decompression Laboratory Experiments

V. de Rubeis, S. Vinciguerra, P. Tosi, P. Sbarra, and P.M. Benson

Abstract Recent laboratory experiments on Etna basalt have permitted the generation of an extensive catalogue of acoustic emissions (AE) during two key experimental phases. Firstly, AE have been generated during triaxial compressional tests and formation of a complex fracture/damage zone. Secondly, rapid fluid decompression through the damage/shear zone after failure. We report new results from an advanced analysis method using AE spectrograms, allowing us to qualitatively identify high and low frequency events, essentially comparable to seismicity in volcanic areas. Our analysis, for the first time, quantitatively classifies 'families' of AE events belonging to the same experimental stage without prior knowledge. We then test the method using the AE catalogue for verification, which is not possible with field data.

The FFT spectra obtained from AE are subdivided into equal log intervals for which a local slope is calculated. Factor analysis has been then applied, in which we use a data matrix of columns representing the variables considered (frequency data averaged in bins) vs. rows indicating each AE data set. Factor analysis shows that the method is very effective and suitable for reducing data complexity, allowing distinct factors to be obtained.

We conclude that most of the data variance (information content) can be well represented by three factors only, each one representing a well defined frequency range. Through the factor scores it is possible to represent data in a lower dimension factor space. Classification is then possible by identifying clusters of AE belonging to the same experimental stage. This allows us to propose a deformation/decompression interpretation based solely on the AE frequency analysis and to identify a third type of AE related to fluid movements in the deformation stage.

V. de Rubeis (✉), S. Vinciguerra, P. Tosi, and P. Sbarra
Istituto Nazionale di Geofisica e Vulcanologia, Via di Vigna Murata, 605 00143, Roma, Italy
e-mail: valerio.derubeis@ingv.it

P.M. Benson
Rock & Ice Physics Laboratory (RIPL), Department of Earth Sciences, University College London, Gower Street, WC1E 6BT, London

V. de Rubeis et al. (eds.), *Synchronization and Triggering: from Fracture to Earthquake Processes*, GeoPlanet: Earth and Planetary Sciences 1,
DOI 10.1007/978-3-642-12300-9_11,

11.1 Introduction

An acoustic emission (AE) is defined as a transient elastic wave generated by the rapid release of energy within a material. In the Earth sciences, studies of AE and seismology show a significant overlap. Both approaches deal with the radiation of elastic waves, although at different scales and frequencies. Generally, AE recorded in the laboratory are generated by flaws at the grain size scale with source dimensions between micron and millimeter scale and frequency ranges between 100 kHz and 2 MHz [Lockner, 1993].

In the brittle regime, the damage evolution in a rock under load involves the growth of microcracks from stress concentrators such as voids, inclusions and grain contacts, resulting in both inelastic strain and acoustic emissions. The acoustic signals that are spontaneously generated from the microcracking provide information about the size, location and deformation mechanisms of the events as well as properties of the medium through which the acoustic wave travels (e.g. velocity, attenuation and scattering). Importantly, laboratory rock fracture and earthquake rupture are processes obeying similar statistics for source dimensions over more than eight orders of magnitude [e.g., Hanks, 1992; Zang et al., 1998].

The main goals of AE studies so far aimed to:

(a) Characterize individual AE events in terms of their frequency content, amplitudes and durations, so that they can be related to the micro-mechanisms that produce them. A temporal correlation between the onset of AE and dilation in samples under loading was found, showing that dilation was caused by pervasive microcracking, primarily oriented parallel to the maximum compressive principal stress [Brace, 1966; Scholz, 1968]. AE amplitudes and frequencies have been observed to increase before failure [Zang et al., 1998, and references therein]

(b) Locate the source of AE events in 3D in order to image the localization of failure processes. Insights have been provided into the nucleation phase of fracture, using AE source locations to map the temporal and spatial evolution of fracture. Two different processes operate, a process zone in front of the fault tip and a damage zone following the process zone (Lockner et al., 1992; Lei et al., 2000).

(c) Analyze the statistics of recorded events to gain insights into the deformation processes and their rates. The Gutenberg-Richter relationship between frequency and magnitude of earthquakes also applies to experimental rock failure [Meredith et al., 1990; Sammonds et al., 1992; Ponomarev et al., 1996; Lei et al., 2003]

(d) Study AE in the presence of fluid. The influence of fluid pressure on deformation has been investigated in drained conditions at constant pore pressure. A weakening effect of water in the brittle faulting and cataclastic flow regime has been found, because of reduction of both specific surface energy and friction coefficient [Baud and Meredith, 1997; Baud et al., 2000].

New directions are focussing on the fundamental similarity of the physical processes involved in generating different frequency content seismic signals, such as seismic tremor under the subduction zones in tectonic areas and volcanic tremor and long-period events in volcanic areas. To date, comparisons have been made to field scale seismicity by comparing the spectral character and frequency/size scaling of acoustic emissions [e.g., Burlini et al., 2007, 2008; Benson et al., 2008]. Frequency scaling offers the strongest argument to assess the equivalence of the physical processes between laboratory experiments and natural volcanic seismic signals. For example, experimental low frequency events and tremor have frequency of about 100 kHz for intrusion lengths ranging between few tens to 100 mm. In natural earthquakes, dominant frequencies around 1-2 Hz are associated with fracture lengths of some hundreds meters to 1 km. Considering that dominant frequencies of earthquakes scale inversely with source dimension [Aki and Richards, 1980], one may write $d_1 \times f_1 = d_2 \times f_2$, where d_1, d_2 and f_1, f_2 are the dimension and frequency of laboratory (subscript 1) and nature (subscript 2), respectively. Comparing laboratory data with typical frequency (1-2 Hz) and size (1 km) of low frequency earthquakes, we obtain $d_1/d_2 = 5 \times 10^6$ and $f_2/f_1 = 2.5\text{-}5 \times 10^6$, which indicates excellent agreement between laboratory information and natural cases [Burlini et al., 2007; 2009; Benson et al., 2008]. Here, we present a new and alternative analysis, aiming to quantitatively classify 'families' of AE through the analysis of spectral ratios and associated factors, without a-priori knowledge of the spatio-temporal evolution.

11.2 The data set

Samples of Etna basalt, Italy were deformed in using a triaxial cell installed at the University of Toronto (Fig. 11.1). Two experimental stages are performed, designed to separate the signals generated from deformation (stage 1) from those specific to fluid movement (stage 2), as described in Benson et al. (2008). Irrespective of the stage of experiment (deformation or decompression), events are located on or in close proximity to the fault (Benson et al., 2008). During the formation of the fault, waveforms show a distinctive, high frequency character (600-900 kHz), exhibiting a rapid onset (i.e., rapid acceleration) and relatively short duration (400 μs). These features are well known and understood from rock physics studies on brittle processes in rock fracture. During the decompression stage, however, waveforms exhibit a much lower frequency component (typically 80-100 kHz). The onsets of these waveforms are highly emergent, and with longer duration, of the order of ms. In the following analysis we refer to these characteristic signals as high frequency (HF) and low frequency (LF), respectively.

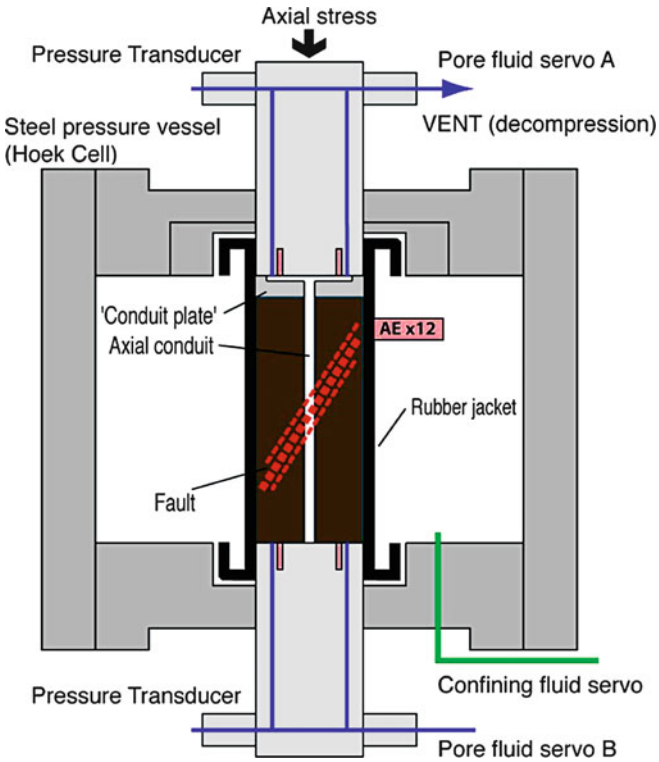

Fig. 11.1 Scheme of the experimental setup (after Benson et al., 2008). Note that, for clarity, the precise locations of the 16 AE sensors (12 lateral and 4 axial) have been omitted

11.3 Method

Input data consist of AE FFT spectra. The aim of the analysis is to statistically apply a classification method that is able to recognize different AE and their relation within each of the dynamic parts of the experiment. A key point is to classify the set of AE solely through spectral analysis, and then to test such classifications with other experimental information as the occurrence time, load history, AE spatial location, etc. We look for an AE classification showing a consistent interpretation. If the interpretation is in agreement with the other experiment variables not involved, then we interpret this to have yielded two methodological useful results: we receive an independent confirmation of the reliability of classification method, and can elucidate the dynamical process.

Our classification is based on the application of factor analysis [Davis, 2002, and reference therein]. It consists of a statistical multivariate approach useful to highlight relations among variables. Let us define the dataset as a matrix $[X]$, in which rows are the samples and columns are variables *(n x m)*. The statistical assumption

of the factor analysis is that the m variables, of the original dataset, derive from a smaller number of p independent factors *($p < m$)*. The principal component approach to factor analysis consists of the following steps:

- the original data matrix $[X]$is standardized in respect of the variables simply subtracting the mean and dividing each data by the standard deviation of the corresponding variable, thus obtaining $[X_{st}]$;
- a variance-covariance (correlation) matrix $[s^2]$ is extracted from $[X_{st}]$ (note that being extracted from standardized data, $[s^2]$ is a correlation matrix). It is symmetric and all diagonal elements are equal to unit;
- eigenvectors and eigenvalues are extracted from $[s^2]$; the eigenvectors define the matrix $[U]$, the square root of eigenvalues gives a diagonal matrix of singular values $[\lambda]$; the sum of the eigenvalues represents the total variance (information content) of data;
- eigenvectors are converted into factors using the relation: $[A^R] = [U] \cdot [\lambda]$, where $[A^R]$is an $(m \times m)$-sized matrix, each column representing a factor whose elements are referred to as factor loadings.

Due to the precise manner in which the factors are calculated, each factor loading is weighted proportionally to the square root of the amount of variance contributed by that variable to the factor. Looking at the proportion of variance accounted for by each factor, it is possible to select a smaller number of factors (p) accounting for most of the total variance in the dataset. The independence of all factors is guaranteed by orthogonal decomposition of the correlation matrix, given by the Eckart–Young theorem, through the extraction of eigenvalues and eigenvectors. Therefore, we can reduce the size of $[A^R]$ to $(m \times p)$.

The factor analysis results in factor scores $[\hat{S}^R]$, which represent the values of any single factor for every observation, as follows: $[\hat{S}^R] = [X_{st}] \cdot [A^R] \cdot ([A^R]^T \cdot [A^R])^{-1}$.

In this way it is possible to associate with each observation the value of a factor score related to each one of the p factors. Summarizing the benefits of factor analysis approach, we have a statistical tool able to reduce the complexity of a multi-variable data set into few factors, which retain the biggest amount of variance. The key to perform such a process is inside the idea that many original variables are redundant, having a certain degree of mutual correlation. Moreover, by the factor model application we can consider each original variable X_j as constituted by the composition of p factors f, following a specific loading a, plus a random variation ε. If we assume that p is less than the number of original variables we have reduced the complexity of the problems and separate a small amount of system information, which we consider random noise: $X_j = \sum_{r=1}^{p} a_{jr} f_r + \varepsilon_j$.

The specific application of factor analysis to AE spectra consists in the conversion of the data into a $[X]$ matrix: the logarithmic amplitude of each spectrum is standardized in order to remove any effect due to AE magnitude. The frequency range is then subdivided into equal log intervals and a mean amplitude for each interval is calculated. The columns of $[X]$ matrix thus represent the binned frequency variables. The rows are each AE as recorded during the loading experiment.

The assumption is that near frequencies may have the same behaviour, quantified by their mutual correlation. The unknown is the extent of the similar-correlated behaviour of contiguous frequencies. The method is to create frequencies variables of short intervals in order to remove noise. Then, by the application of factor analysis, the frequencies variables are grouped together as a function of their mutual correlation and true independent groups are extracted. They represent the true dimension of the process and give the basis for a useful data classification.

11.4 Results and discussion

The data matrix is constituted by 280 FFT spectra calculated on AE waveforms in the frequency range 29 KHz – 493 KHz. The logarithmic amplitude of each spectrum is standardized in order to remove any effect due to AE magnitude. The range is then subdivided into 10 equal log intervals and mean amplitude for each interval is calculated. Boundaries (in KHz) of each of the ten variables defined for the analysis are shown in Table 11.1.

Figure 11.2 shows the variance percentage expressed by each factor; the first 3 factors account of about 74% of total data variance: this value is satisfactory, ensuring a proper representation of the whole data set.

Figure 11.3 shows the factor loadings values for the three factors (the first, second, and third, respectively). Factor loadings express the correlation of each original variable – in this study the averaged frequency range – to each factor, which represents the new variable.

The first factor shows a positive correlation of the low frequency range, up to 70 kHz, while a negative correlation is found related to the highest frequency range (280-480 KHz). A moderate positive correlation occurs in the frequency interval 150-200 KHz (for the precise frequency interval see Table 11.1). The second factor shows also a positive correlation in the frequency range 60-120 KHz, while a negative correlation is found in the 200-370 KHz interval. Third factor is negatively

Table 11.1 Frequency boundaries of each of the ten variables defined for the factor analysis

Variable	Lower freq. limit (KHz)	Upper freq. limit (KHz)
1	29.52	39.13
2	39.13	51.85
3	51.85	68.72
4	68.72	91.07
5	91.07	120.69
6	120.69	159.95
7	159.95	211.97
8	211.97	280.91
9	280.91	372.27
10	372.27	493.35

correlated in the 90-200 KHz interval and positively in the highest frequencies interval 370-500 KHz.

These factors represent different groups of interrelated frequency ranges. Positive and negative correlations allow interpreting the relationship among the different frequencies. The first factor indicates that, when we have an AE where lower frequencies (up to 70 KHz) prevail, higher frequencies (280-480 KHz) tend to reduce, and vice versa. The second factor shows similar trends, but for the frequency range of 60-120 KHz and 200-370 KHz, respectively. Finally, the third factor mirrors the second, but correlations are shifted towards higher frequency ranges (90-200 KHz and 370-500 KHz).

Through the factor scores, it is hence possible to represent data in a lower dimension factor space and to see a similar behaviour of each AE associated in specific factor space portion or clustered. Since the first factor is the most informative (Fig. 11.2), we show two scatter diagrams representing original AE spectra as defined, respectively, by factors I-II and factors I-III (Fig. 11.4a, 11.4b).

In Fig. 11.4(a) and 11.4(b), all 280 AE samples are represented in the factor space. Each factor holds the frequency spectral content discussed above (Fig. 11.3). By construction, the factors are orthogonal, which means, they have no correlation: in fact, points are distributed with zero linear correlation between the two factors. In order to achieve a full understanding of the inter-factor relationship, we selected

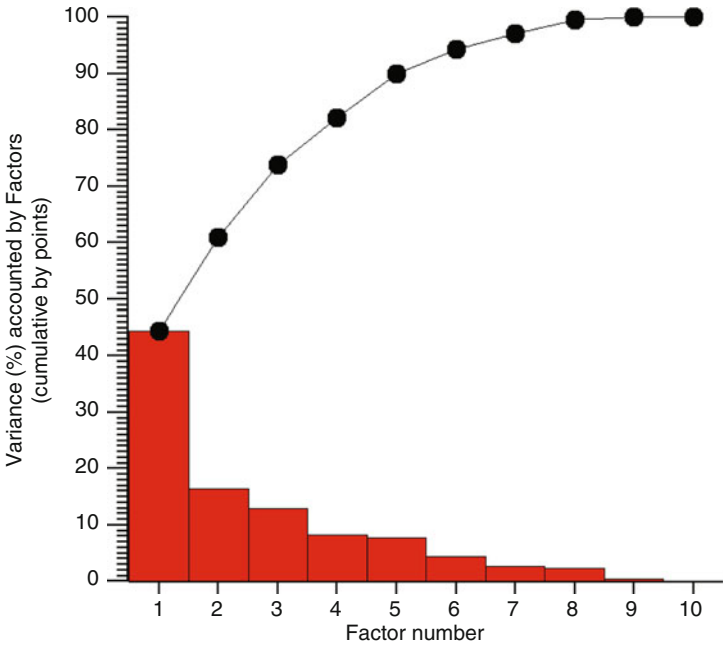

Fig. 11.2 Individual and cumulative variance of original data accounted by factors

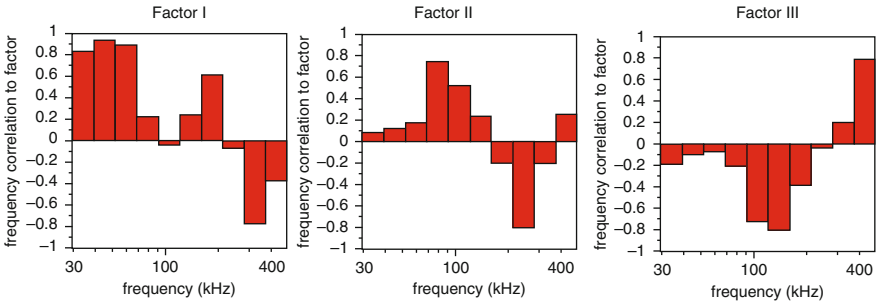

Fig. 11.3 Factor loadings values for the first three factors as extracted by factor analysis. See text for comments on ability of factors to represent original AE frequency bins

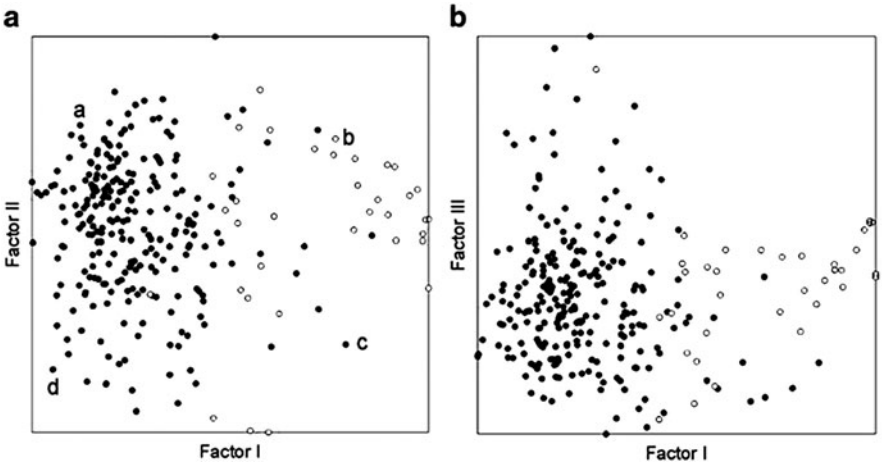

Fig. 11.4 All 280 FFT spectra represented on the factor space following factor I with factor II scores (4a) and factor I with factor III scores (4b). In dark are the AE spectra recorded during deformation phase, in open circles those recorded during rapid decompression of the pore fluid. Four spectra (a,b,c,d) are marked (4a) in order to interpret their factor space position under their spectral content. Compare with Figure 10.5 for complete interpretation

four binned spectra (a, b, c, d in Fig. 11.4a), which represent the end terms in the factor space, i.e., the frequency ranges analyzed.

In detail, AE spectra a-d and c-b have similar factor I values, while spectra a-b and c-d have similar factor II values. This similarity can be investigated by plotting the log of spectral amplitude vs. the frequency bins (Fig. 11.5). AE spectra a-d and AE spectra c-b show correspondent amplitudes (bins 1,2,3,7,9) in spectral frequencies represented by factor I. AE spectra a-d hold low amplitudes in frequency bins 1,2,3,7 (positive correlation) and high amplitudes in bin 9 (negative correlation). AE spectra c-b show an opposite behaviour. Analogous considerations apply for the factor II.

The factor analysis provides a quantitative tool to systematically discriminate AE events generated during deformation phase of the experiment (dark dots in Fig. 11.4) from those recorded during rapid decompression of the pore fluid

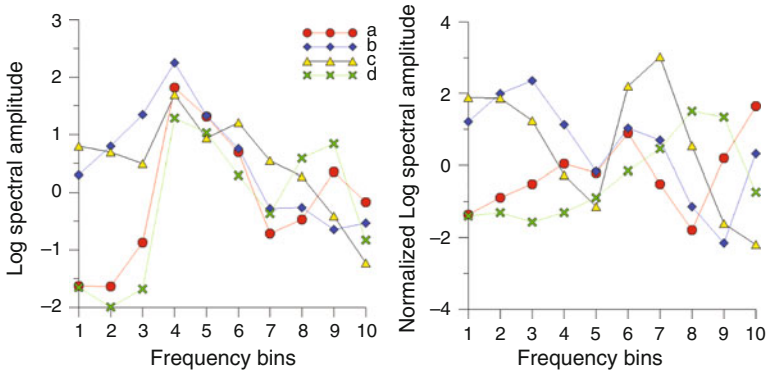

Fig. 11.5 Four binned log amplitude spectra from AE sample data (a,b,c,d samples as referred into Fig. 11.4a) as original values (left) and normalized values (right). Normalized spectra are represented to follow variables standardization applied to AE data matrix prior the extraction of eigenvalues and eigenvectors, as operated by factor analysis. See text for further details

(open dots in Fig. 11.4). High (HF) and low frequency (LF) events fill specific sectors in the factors space. In detail, the LF events reflect the pure origin of fluid driven events, due to the pore fluid flashing onto the damage/shear zone. No reactivation of cracks in terms of shearing/propagation of existing microfractures is triggered from the fluid propagation onto the fault plane, as no HF components are found from the factor analysis. HF shows a wider range of the amplitudes involved. This can be explained from the fact that the energy and size of HF events increases over time as micron to mm scale cracks are involved in the early stage of deformation, followed by cm scale faults formation at the failure.

The most intriguing observation is given from the position of several events generated during deformation phase (where HF events only were believed to occur) in the factor space domain of the LF events (dark dots in Fig. 11.4). This suggests that these events were generated from analogous mechanisms, which led to the formation of the LF, i.e., fluid migration onto the faults. We interpret this behaviour due to the fact that the cracks open and shear during loading. At the same time, pressurized fluids rapidly transit into the crack surfaces and generate same LF signals, similarly to those generated from pure fluid decompression in stage 2 (red dots in Fig. 11.4).

Taken together, this emphasizes that the factor analysis applied to a given AE data set can allow to highlight bulk AE patterns, that otherwise can not be easily seen by a pure visualization of single events.

11.5 Conclusions

We have statistically analysed AE spectra generated during deformation and failure of an Etna basalt sample (stage 1) and the subsequent rapid fluid decompression of the pore pressure (phase 2). A factor analysis has been applied to 280 FFT spectra

calculated on AE waveforms in the frequency range of 29 KHz - 493 KHz. The first 3 factors account of about 74% of total data variance. Through the factor values we reported data in a lower dimension factor space and we analysed the similar behaviour of each AE associated in a specific factor space portion or clustered.

The factor analysis provides a quantitative tool to systematically discriminate between HF and LF events generated during the two experimental stages (deformation and fluid movement), which essentially acts as to produce a higher proportion of HF and LF AE, respectively. Importantly, several events generated during the deformation phase occur in the factor space domain of the LF events. This suggests the existence of LF events forming during phase 1, due to the fluid migration into forming and propagating faults.

References

Aki, K., and Richards, P.G., 1980, Quantitative Seismology: Theory and Methods, Freeman & co., San Francisco (USA). 932 p.

Baud, P., and P. B. Meredith (1997), Damage accumulation during triaxial creep of Darley Dale sandstone from pore volumometry and acoustic emission, Int. J. Rock Mech. Min. Sci., 34, Pap. 024.

Baud, P., W. L. Zhu, and T.-F. Wong (2000), Failure mode and weakening effect of water on sandstone, J. Geophys. Res., 105, 16,371-16,389.

Benson, P. M., B. D. Thompson, P. G. Meredith, S. Vinciguerra, and R. P. Young (2007), Imaging slow failure in triaxially deformed Etna basalt using 3D acoustic-emission location and X-ray computed tomography, Geophys. Res. Lett., 34, L03303, doi:10.1029/2006GL028721.

Benson P. M., Vinciguerra, S. Meredith, P. G. and Young, R. P. (2008) Laboratory simulation of volcano seismicity, *Science*, 322, 249, doi: 10.1126/science.1161927.

Brace, W.F., Paulding, B.W., and Scholz, C. (1966), Dilatancy in the fracture of crystalline rocks, J. Geophys. Res. 71, 3939-3953.

Burlini L., Vinciguerra S., Di Toro G., De Natale G., Burg J.P., Seismicity preceding volcanic eruption: new experimental insight, Geology, 35,2,183-186; doi: 10.1130/G23195A, 2007

Burlini L., Di Toro G., Meredith P.G., Seismic tremor under the subduction zones: the rock-physics interpretation. GRL, VOL. 36, L08305, doi:10.1029/2009GL037735, 2009.

Davis, J.C. (2002). Statistics and Data Analysis in Geology, third edition, Wiley and Sons, Inc., New York.

Hanks, T.C., 1992, Small earthquakes, tectonic forces: Science, v. 256, p. 1430-1432.

Lei, X.-L., Kusunose, K., Rao, M.V., Nishizawa, O., and Satoh, T. (2000), Quasi-static fault growth and cracking in homogenous brittle rock under triaxial compression using acoustic emission monitoring, J. Geophys. Res. 105, 6127-6139.

Lei, X.-L., Kusunose, K., Satoh, T., and Nishizawa, O. (2003), The hierachical rupture process of a fault: An experimental study, Phys. Earth Planet. Inter. 137, 213-228.

Lockner, D. A., Byerlee, J. D., Kuksenko, V., Ponomarev, A., and Sidorin, A., Fault mechanics and transport properties of rocks (eds. Evans, B., and Wong, T-F) (Academic, London 1992).

Lockner D., The role of acoustic emission in the study of rock fracture, IJRM, 30, 7, 883-899, 1993.

Meredith, P.G., Main, I.G., and Jones, C., 1990, Temporal variations in seismicity during quasi-static and dynamic rock failure: Tectonophysics, v. 175, p. 249-268.

Ponomarev, A.V., Zavyalov, A.D., Smirnov, V.B., and Lockner, D.A., 1997, Physical modelling of the formation and evolution of seismically fault zones: Tectonophysics v. 277, p. 57-81.

Sammonds, P.R., Meredith, P.G., and Main I.G., 1992, Role of pore fluids in the generation of seismic precursors to shear fracture: Nature, v. 359, p. 228-230.

Scholz, C. H. (1968a), Microfracturing and the inelastic deformation of rock in compression, J. Geophys. Res. 73, 1417-1432.

Zang, A., C. F. Wagner, and G. Dresen (1996), Acoustic emission, microstructure, and damage model of dry and wet sandstone stressed to failure, J. Geophys. Res., 101, 17, 507-17, 521.

Chapter 12
Phase-Shifted Fields: Some Experimental Evidence

Roman Teisseyre, Tamaz Chelidze, and Krzysztof. P. Teisseyre

Abstract We present a comparison between some experimental results on the interaction and synchronization of mechanical and electric fields; such a synchronization may appear with the phase delay by $\pi/2$, as shown in recent theoretical results. The solutions related to such a phase-shifted synchronization between some fields follow from the Asymmetric Continuum Theory. This theory concerns not only the mechanical fields, strains and rotations, but also other physical fields entering into interaction with stresses.

12.1 Introduction

Some experiments have brought a light on mechanisms that lead to synchronization between different dynamic processes under various kinds of applied loads and additional external impulses. We present some examples related to the interaction and synchronization processes between the deformations and applied loads with the accompanied mechanical and electric field impacts. Our consideration is based on both the new theoretical approach to the asymmetric continuum and on the experimental evidence of such a synchronization, as given in some papers.

R. Teisseyre (✉) and K.P. Teisseyre
Institute of Geophysics, Polish Academy of Sciences, ul. Ksiecia Janusza 64, 01-452 Warszawa, Poland
e-mail: rt@igf.edu.pl

T. Chelidze
M. Nodia Institute of Geophysics, 1 Alexidze str., 0171 Tbilisi, Georgia
e-mail: tamaz.chelidze@gmail.com

V. de Rubeis et al. (eds.), *Synchronization and Triggering: from Fracture to Earthquake Processes*, GeoPlanet: Earth and Planetary Sciences 1,
DOI 10.1007/978-3-642-12300-9_12,

12.2 Synchronization and interaction: experimental evidence

Chelidze *et al*. (2006) presented the synchronization and triggering effects observed in samples subjected to a static basic load, close to a critical point (slip event experiments) and additionally to the weak mechanical or electric perturbations as an additional forcing.

These externally applied forces caused micro-slip episodes at the prepared surface, observed as acoustic emission bursts. The samples system consisted of two samples, stuck together with roughly polished neighboring surfaces; the gap between them was of microscopic size and the slips occurred on these stuck surfaces. The whole system serves as a simple model containing fracture zone or an active fault, at which repetitive episodes of slip take place.

The acoustic emission synchronized with applied oscillations:

a) of mechanical load
b) of externally applied voltage, but only in the case when the electric field direction was parallel to the gap between samples; perpendicularly applied electric field gave hampering effect on the slips

The experimental setup is described in Chelidze *et al*. this issue (Chapter 8, this issue). The acoustic emission (AE) and oscillating part of the externally applied forces were recorded using Sony Sound Forge software.

Further, we focus on the experimental series in which the electric field, parallel to the gap plane, acted as factor modifying response of the samples system to the static loads.

Most probably, acoustic emissions have originated in the gap zone. But it is obvious that processes in this zone were under control of the system of samples. Thus, some hidden structural adaptations of the samples to the experiment conditions permitted the observed repeated response to the stimuli. These adaptations should be of various scales, sub-molecular included. After an abrupt change of the conditions, the rise of the static part of externally applied electric field, the rhythm of acoustic emission changed immediately and then underwent some variations, in the time when a new pattern of repetitive acoustic bursts was gradually formed. In our opinion, such a result shows an adaptation of the samples to new condition.

Chelidze *et al*. (2006) state that synchronization limits the energy release at an individual event (burst). This was proven experimentally: “Sudden decrease or total cessation of synchronizing (electric) forcing is followed by acoustic burst of much larger energy than during periodic forcing”.

In the cited paper the authors observed the temporal evolution of phase difference between the maxima of acoustic emissions and external periodic forcing.

The applied electric field consisted of two components: the one oscillating from + 800V to –800V, and the constant one with initial constant voltage of 400V which has increased to 1900V in the middle of the experiment (about 28.6 s from the beginning). That is, it started to be bigger than the alternating field. This means that in the experiment’s first part, the voltage of external field oscillated between

+1200V and – 400V, and in the second part – between +2700V and +1100V. For these cases, the acoustic bursts were in different ways correlated to the oscillations of the external electric field.

In the first part of the experiment, the AE bursts coincided with all the extrema of the applied voltage; however, the entire burst started during the stage of the external field increase. We should be aware that in these experiments, both the stimulating impulses and the responses – acoustic emissions – did not oscillate in a sinusoidal way; the vertical scale in the reproduced display was a kind of decibel scale: the peaks were in fact more abrupt. Besides, a certain level of acoustic emission persisted in the considered experiments, obscuring beginnings and ends of the acoustic bursts. The response looks the same at "+" and "–" part of the stimulus curve; there is no visible hysteresis.

Further on, in the second part of the experiment with the increased static part of electric field, there occur changes in the rhythm of acoustic bursts. These changes, seen in Fig. 12.1, may be described as follows. The first very strong bursts consisting of two joint parts coincide with the nearest maxima of the oscillating field: one exactly, and the other with some phase shift, roughly $\pi/2$.

Subsequently, the AE bursts coinciding directly with the electric field maxima gradually decrease in time and finally there remains only an evident correlation of the bursts shifted in phase - by about $\pi/2$ - with the electric field maxima.

It is also worth to mention the observed synchronizations between the mechanical stimuli and the seismic noise, as described by Saltykov (2008); the observations, done in the region of Kamchatka and neighboring seas and islands, reveal the

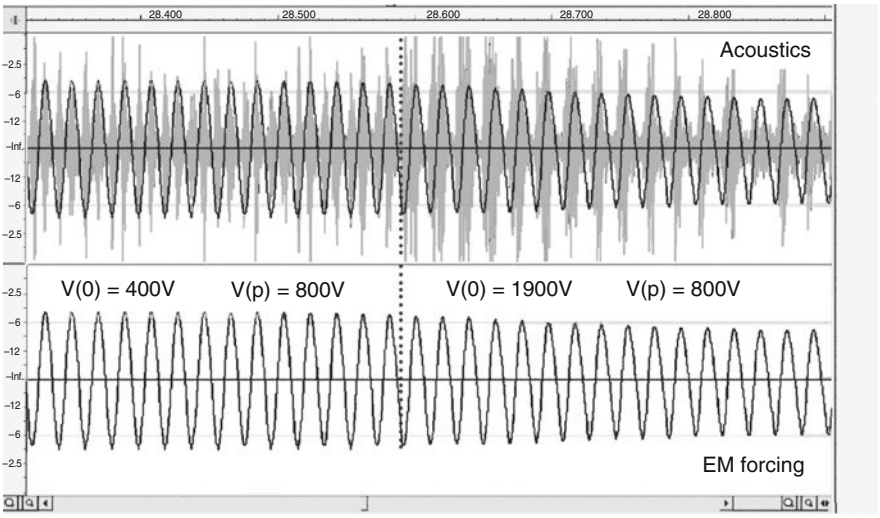

Fig. 12.1 Synchronization between the electric field oscillations and the acoustic bursts (after Chelidze et al., 2006 - modified); the curve of oscillating voltage V(p) is copied on the plot of acoustic emission (in grey), the vertical dotted line indicates a moment of increase of the static voltage

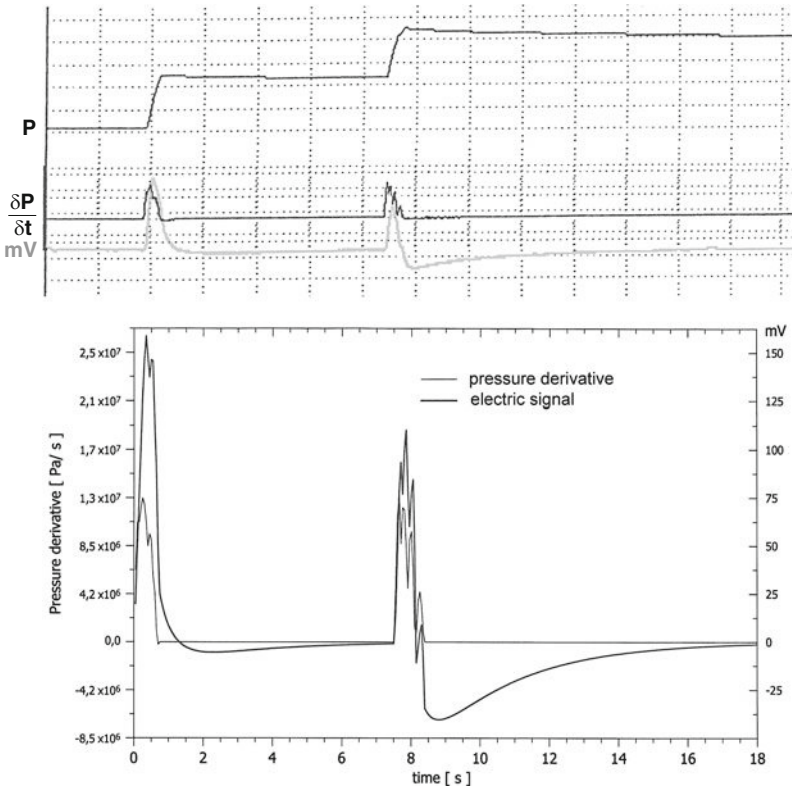

Fig.12.2 An example of correlation between the pressure applied to a limestone sample and excited electric polarization (upper part) and the numerical simulation results (lower part) (after Teisseyre, K.P., Hadjicontis, and Mavromatou, 2001)

synchronization of the envelope of high frequency microseismic noise to the Earth tidal O_1 waves. Such a synchronization appears before most of the large earthquakes in that area. Almost always, certain phase shift occurs – the envelope is delayed in relation to the Earth tides. This synchronization, of yet undisclosed mechanism, suits as an earthquake precursor in the region.

We should also note that Busse and Wang (1981) have found other interesting correlation effects; the two orthogonal acoustic waves shifted in phase by $\pi/2$, acting on a small disc (as compared to the acoustic wavelength) with its axis perpendicular to these waves produce a torque (acoustic torque). According to those authors, this effect is related probably to the particles of gas moving circularly over the disc (viscous effect rather than the Bernoulli pressure effect). This acoustic torque effect seems to present one more example of interactions of different fields.

Moreover, we analyze the experiments on anomalous piezoelectric effects conducted by V. Hadjicontis and C. Mavromatou (cf., Teisseyre et al., 2001) in which the appearance of electric polarizations was observed depending on the

rate of load variations. For these experiments, the materials were chosen which do not show electric polarization under constant load, that means, which are non-piezoeletric in a common meaning. On other hand, the electric response of one of these materials, the limestone, to load is found to be doubly anomalous – once, because it depends on the load changes and, moreover, it shows a kind of some reversal of the produced electric signal, a rebound release effect revealed by the negative electric bays (see Fig. 12.2). In various numerical simulations conducted to reproduce the experimental results, the main rules were as follows: each increase in load causes an increment in the excited voltage, and this added part immediately starts to decline (its decay has taken many steps of simulation).

The shape of the decaying part of the electric response to mechanical stimuli suggests the concurrence of two or three relaxation phenomena, that is, one quick process and one or two slow ones.

12.3 Theoretical interpretation of co-action and synchronization effects

First, we will refer to the results of experiments done by Chelidze et al. (2006), as discussed above. A general conclusion is that acoustic response occurs when electric field variation, superimposed on the present conditions of externally applied electric fields and mechanical stresses, cause a break of material bonds, thus producing an acoustic emission. Episodes of acoustic emission cluster in the acoustic emission burst. The experimenters observed temporal evolution of the phase difference between the extrema of external electric field and the bursts of acoustic emission.

As mentioned above, two modes of synchronization between the stick-slip events (acoustic bursts) and the periodic electric field, *V(periodic)*, were observed.

First, the doubling synchronization (1:2): each electric extreme amplitude synchronized with acoustic bursts, this is the case when the applied direct *V(0)* voltage is smaller than the periodic voltage, $V(0) < V(periodic)$.

Second, the direct synchronization (1:1): the electric maxima synchronized with acoustic bursts; it appears when the applied direct*V(0)* voltage is greater than the periodic voltage $V(0) > V(periodic)$.

For $V(0) < V(periodic)$ the micro-fracture processes appear when the resulting field reaches maximum, that is, for the maxima of the periodic voltage. The fracture processes appearing at these maxima of the periodic electric impulses become immediately observed as the acoustic emission, the acoustic bursts, caused by the breaks of bonds and released rotation motions. Induced by this fragmentation, the series of single shear couples form the rotation couples where each of the two perpendicular couples has opposite shears (the case quite opposite to the case of shear double couple). Thus, the resulting shear field in this fragmentation process appears almost compensated to minimum.

For *V(0) > V(periodic)*,when a constant electric field is high enough, we can expect that each electric impulse can break the material bonds, but the process runs due to the applied external shears; we may notice that first we observe the broad acoustic peaks partly synchronized with the impulses and after some stabilization there remain more narrow bursts occurring with the $\pi/2$ phase shift, as the related slip process, released in a kind of slip avalanche, becomes delayed in time. Thus, at first we probably deal with both the rotation and slip rebound processes, while after stabilization only slip avalanche releases remain in sites where molecular bonds are already broken.

Thus, the most important for our consideration on interaction between the electric periodic impulses and micro-fractures is the fact that the acoustic emissions (waiting time series) are observed in both synchronization modes. This means that the synchronization modes are retarded in phase by $\pi/2$ (similarly as the results of the Hilbert transform); we can underline an organization role of the electric impulses on the response of the samples to the experimental conditions. This is an important result for us, to be compared with the theoretical part describing the interaction and synchronization processes in the Asymmetric Continuum Theory (Teisseyre, 2009).

Worth mentioning are also some other effects that may appear when studying various experimental results with the induced electric signals; we refer here to the experimental results obtained by Hadjicontis and Mavromatou (1994 and 1995; cf., Teisseyre K.P, et al., 2001). Among other things, Hadjicontis and Mavromatou (1994) have studied the transient electric signals appearing before the failure of limestone or other rock samples. The samples were subjected to a uniaxial compression; it was found that the emitted electric signals, attributed to stress-induced polarization in rock samples, follow the variations of the first time derivatives of load; this means, there is a correlation between the time derivatives of the pressure load and the emitted signals of electric polarization.

Such immediate correlations between the time derivatives of the applied pressure (corresponding to a sinusoidal pressure load shifted by $\pi/2$) and the electric signals, as obtained by Hadjicontis' group are presented here according to Teisseyre K.P., et al. (2001), in Figs. 12.2 and 12.3.

The presented examples of interaction and synchronization processes between the deformation and electric fields or between the acoustic waves and electric oscillations reveal synchronization with a phase shift of $\pi/2$; we intend to interpret this phenomena on the basis of the Asymmetric Continuum Theory (Teisseyre, 2009) and possible interaction processes included in it (Teisseyre, Chapter 3, in this issue).

Our theory explains the co-action and synchronization processes between the displacement and rotation motions or, in another form, between the strains and rotations; the phase shift of $\pi/2$ appears as a possible consequence of one of the forms of the related solutions. Such processes are naturally explained by the release and rebound co-action of these deformation fields.

Synchronization between the strain or acoustic oscillations and the electric field appears to be more difficult for interpretation. However, according to the Theory, the rotations can produce some anti-symmetric stress counterpart (stress moments)

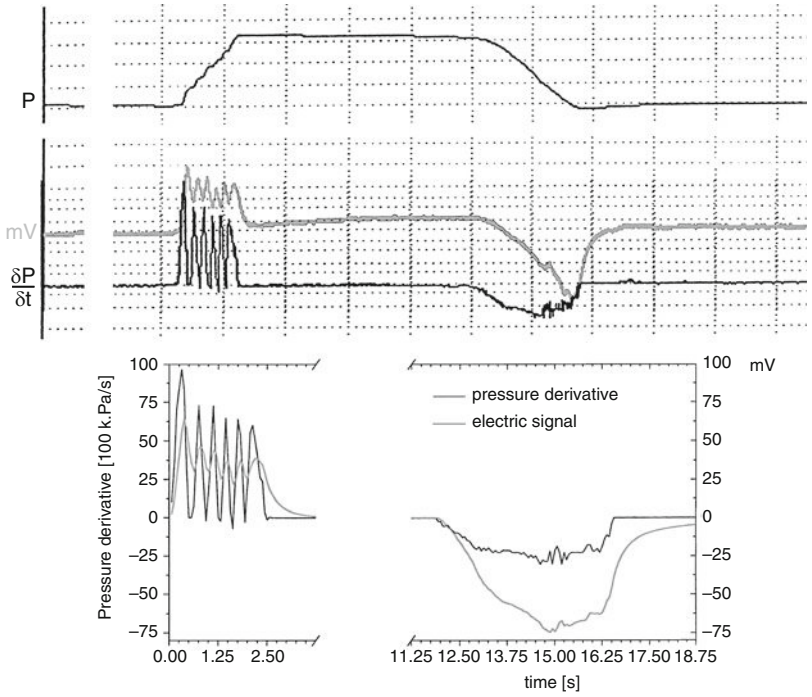

Fig. 12.3 Another example of correlation between the pressure applied to a limestone sample and excited electric polarization (upper part) and the numerical simulation results (lower part) (after Teisseyre, K.P., Hadjicontis, and Mavromatou, 2001)

and strains shifted in phase, as observed by the acoustic effects; such a chain follows from the synchronization of fields (cf., Teisseyre, Chapter 3, in this issue) and, further, can lead to the electric effects.

However, we can assume an intermediate action of the rotation field which can interfere and combine the strain or acoustic fields with an electric oscillation in more natural synchronization processes. In the proposed approach (cf., Teisseyre, Chapter 3, this issue) the electric and rotation fields can be directly synchronized under electric oscillations acting on rotations; the rotations will coerce strain or acoustic waves as is due to the appropriate synchronization solution. The reverse process is possible as well, and starts from strain impact, to be followed by rotations with a phase shift and an immediate electric response. The electromagnetic field stimulates rotation motions and acoustic emission; such a stimulation appears, among others, due to an increased mobility of the charge carriers. Therefore, the mechanical forcing and applied electromagnetic field lead to acoustic emission and spin motion. The latter releases the micro-displacements with the phase shift of $\pi/2$ and then the direct correspondence of phases appears after Hilbert transformation of the observed acoustic bursts.

12.3.1 Conclusions

We have presented a new interpretation of the synchronization processes with the shift of $\pi/2$. We have shown that in some experiments on the interaction and synchronization of the mechanical and electric fields there appears such a phase delay. In the very important experiments by Chelidze's group, these synchronizations appear in the plot shifted by the Hilbert transform to the waiting time series related to the acoustic emission. In the Theory presented in Chapter 3 (this issue), such a case corresponds to the expected phase shift between the synchronized spin and twist motions.

In searching for the interaction mechanism the interpretation we propose is such that the electric impacts cause the molecular bonds breaking and, at higher electric voltages, the rebound released micro-slips, which form an avalanche (triggering effect).

References

Busse F.H. and Wang T.G., 1981, Torque generated by orthogonal acoustic waves - Theory, J. Acoust. Soc. Am., 69 (6), 1634-1638.

Chelidze T., Lursmanashvili O., Matcharashvili T., Devidze M., 2006, Triggering and synchronization of stick slip: Waiting times and frequency-energy distribution, Tectonophysics, 424,139-155.

Hadjicontis, V., and Mavromatou, C., 1994, Transient electric signals prior to rock failure under uniaxial compression, Geophys. Res. Lett., **21**, 16, 1687-1690.

Hadjicontis, V., and Mavromatou, C., 1995, Electric signals recorded during uniaxial compression of rock samples: Their possible correlation with preseismic electric signals, Acta Geophys. Pol., **48**, 1, 49-61.

Saltykov, V.A., 2008, Tidal Effects in Seismoacoustic Noise: An Indicator of Medium Deflected Mode in Seismically Active Region, XX Session of the Russian Acoustic Society, Moscow, October 27-31, 2008

Teisseyre K.P, Hadjicontis, V., and Mavromatou, C., 2001, Anomalous piezoelectric effect: analysis of experimental data and numerical simulation, Acta Geophys. Polon., **49**, 4, 449-462.

Teisseyre R., Górski M., Teisseyre K.P., Fracture Processes: Spin and Twist-Shear Coincidence,111-122. In: Teisseyre R., Nagahama H., Majewski E. (eds), (2008) Physics of Asymmetric Continuum: Extreme and Fracture Processes, Springer, 111-122.

Teisseyre R., 2008, Introduction to asymmetric continuum: dislocations in solids and extreme phenomena in fluids, Acta Geophys., **56**, 2, 259-269.

Teisseyre R., 2009, Tutorial on New Developments in Physics of Rotation Motions, Bull. Seismol. Soc. Am., 99, No 2B, 1028-1039.

Teisseyre R. and Górski M., 2009, Fundamental Deformations in Asymmetric Continuum, Bull. Seismol. Soc. Am., 99, No 2B, 1132-1136.

Part III
Field Observations

Chapter 13
Periodical Oscillations of Microseisms before the Sumatra Earthquake of December 26, 2004

G. Sobolev and A. Lyubushin

13.1 Introduction

This work continues a series of papers published in *Izvestiya, Physics of the Solid Earth*, in 2003–2006 and devoted to the detection and study of periodic oscillations in the seismic flow and synchronization effects arising before strong earthquakes [Sobolev, 2003, 2004; Sobolev et al., 2005; Sobolev and Lyubushin, 2006; Lyubushin and Sobolev, 2006]. These studies were essentially based on the concepts of the dynamics of nonequilibrium media, including self-organization of the seismic process [Nicolis and Prigogine, 1977; Bak et al., 1989; Sornette and Sammis, 1995; Ott, 2002]. It is assumed that, in a metastable lithosphere immediately before an earthquake, natural periodic oscillations arise and/or oscillations from external sources are selectively amplified, with the microseismic field showing collective behavior.

Processing of 20-Hz records obtained at the Petropavlovsk IRIS station before the Kronotskii earthquake revealed waves at periods of a few tens of minutes in the microseismic flow (Fig. 13.1). These were observable during the last 2.5 days before the main shock after the onset of foreshock activation (the arrow F in Fig. 13.1) and after the two strongest ($M > 5$) foreshocks, Fa and Fb.

To analyze the periodic structure of microseisms, we examined the time series of seismic pulses exceeding a certain level. The time series were processed with a moving time window. Within each window, a low frequency trend was removed from the records by an orthogonal polynomial of a fairly high order. After the trend removal for a given window, we calculated a threshold equal to the product of the absolute median deviation (the median of the modulus of deviations from the median) and a certain coefficient (a parameter of the method), usually varying from 1 to 4. This parameter depends on the intensity of pulses in the signal and is

G. Sobolev (✉) and A. Lyubushin
Schmidt Institute of Physics of the Earth, Russian Academy of Sciences, Moscow, Russia
e-mail: sobolev@ifz.ru; lyubushin@yandex.ru

V. de Rubeis et al. (eds.), *Synchronization and Triggering: from Fracture to Earthquake Processes*, GeoPlanet: Earth and Planetary Sciences 1,
DOI 10.1007/978-3-642-12300-9_13,

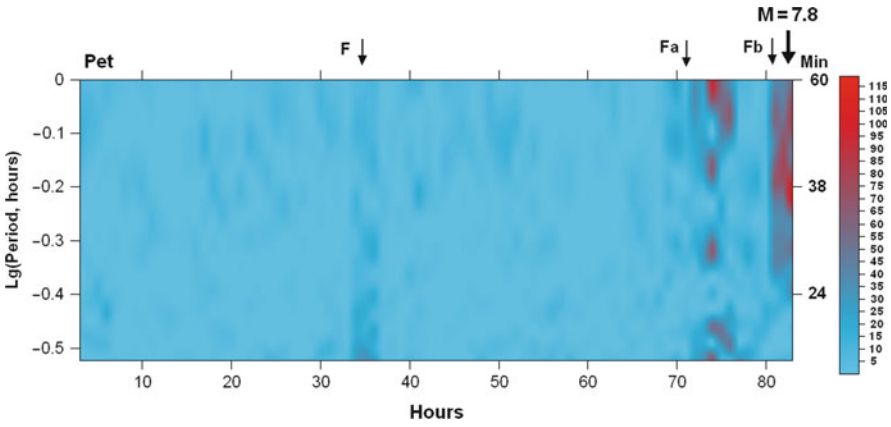

Fig. 13.1 Spectral–time diagram of the increment in the logarithmic function of likelihood $\Delta \ln L$ of microseisms at the Petropavlovsk (Pet) station. The vertical axes show the spectral period (on the right) in minutes and its logarithm (on the left). The large arrow indicates the time of the Kronotskii earthquake of December 5, 1997, with a magnitude of 7.8. The smaller arrows F, Fa, and Fb indicate the onset of foreshock activation and the two strongest foreshocks with $M > 5$

chosen experimentally. Next, we examined the sequence of the times of local maximums of the record that exceeded this threshold. Thus, the initial time series were reduced to a point process, a sequence of time moments. The latter are similar to the sequence of events in a seismic catalog. Further, we applied the method of the identification of periodic components in a sequence of events proposed in [Lyubushin et al., 1998]. We considered the model of the intensity of the event sequence (in the given case, the times of significant local maximums, i.e., pulsations of a microseismic time series), presumably containing the harmonic component

$$\lambda(t) = \mu \cdot (1 + a \cdot \cos(\omega t + \varphi)), \tag{13.1}$$

where the frequency ω, amplitude a, $0 \leq a \leq 1$, phase angle φ, $\varphi \in [0, 2\pi]$, and factor $\mu \geq 0$, (describing the Poisson part of the intensity) are model parameters. Thus, the Poisson part of the intensity is modeled by harmonic oscillations. If a richer intensity model (compared to that for a random flow of events) with a harmonic component of a given frequency ω is considered, the associated increment in the logarithmic function of likelihood is

$$\Delta \mathrm{In}L(a, \varphi|\omega) = \sum_{t_i} \ln(1 + a\cos(\omega t_i + \varphi)) + N\ln(\omega T/[\omega T + a(\sin(\omega T + \varphi) - \sin(\varphi))]) \tag{13.2}$$

Here t_i is the sequence of time moments of sufficiently large local maximums of the signal within the window, N is their number, and T is the window width.

Let

$$R(\omega) = \max_{a,\varphi} \Delta \ln L(a, \varphi|\omega), \quad 0 \leq a \leq 1, \ \varphi \in [0, 2\pi] \tag{13.3}$$

Function (13.3) can be regarded as a generalization of the spectrum for a sequence of events [Lyubushin et al., 1998]. The plot of this function illustrates how advantageous the periodic intensity model is in comparison with the purely random model. The maximum values of function (13.3) specify frequencies that are present in the flow of events. Let τ be the time of the right-hand end of the moving time window of a given width T_W. Expression (13.3) is actually a function of two arguments, $R(\omega, \tau|T_W)$, that can be visualized as 2-D maps or a 3-D relief on the plane of arguments (ω, τ). By using this frequency–time diagram, it is possible to examine the dynamics of the appearance and development of periodic components within the flow of events under study [Lyubushin, 2002; Sobolev, 2004]. It was established [Sobolev et al., 2005] that waves appeared only at the Petropavlovsk station, which was nearest to the Kronotskii earthquake epicenter (the epicentral distance $R \approx 310$ km), and were not identified in records of more remote stations (Yuzhno-Sakhalinsk, Yakutsk, and Obninsk). As the time of the Kronotskii earthquake approached, the number of predominant periods at the Petropavlovsk station decreased, so that the multimode spectrum was transformed into a unimodal spectrum, with shorter periods disappearing; 1 h before the earthquake, a period of 37 min was best expressed.

Another phenomenon recorded before the Kronotskii earthquake was the appearance of asymmetric pulses, a few minutes long [Sobolev et al., 2005]. They were observed as pulses of predominantly negative polarity that arose five days before the earthquake and three days before the onset of foreshock activation. This type of anomaly was typical only of the station nearest to the epicenter (Petropavlovsk).

13.2 Microseismic data

The Sumatra earthquake ($M > 9$), which caused a destructive tsunami, is one of the strongest events in the entire history of instrumental seismic observations. In this context, it was of interest to analyze whether this earthquake was preceded by short-term anomalous phenomena in the structure of microseisms similar to those detected before the Kronotskii earthquake. The RAS Geophysical Survey provided data from broadband IRIS stations located around the epicenter of the Sumatra earthquake (Fig. 13.2). The epicenter had the coordinates (3.32° N, 95.85° E), and the coseismic rupture trended mainly NNW for more than 1000 km.

The stations nearest to the epicenter, CHTO in the north and COCO in the south, were located at epicentral distances of 1770 and 1500 km, respectively. The CHTO and KMI stations were closest to the northern end of the rupture (1100 and 1750 km, respectively). Preliminary analysis of records of all stations sampled at a frequency

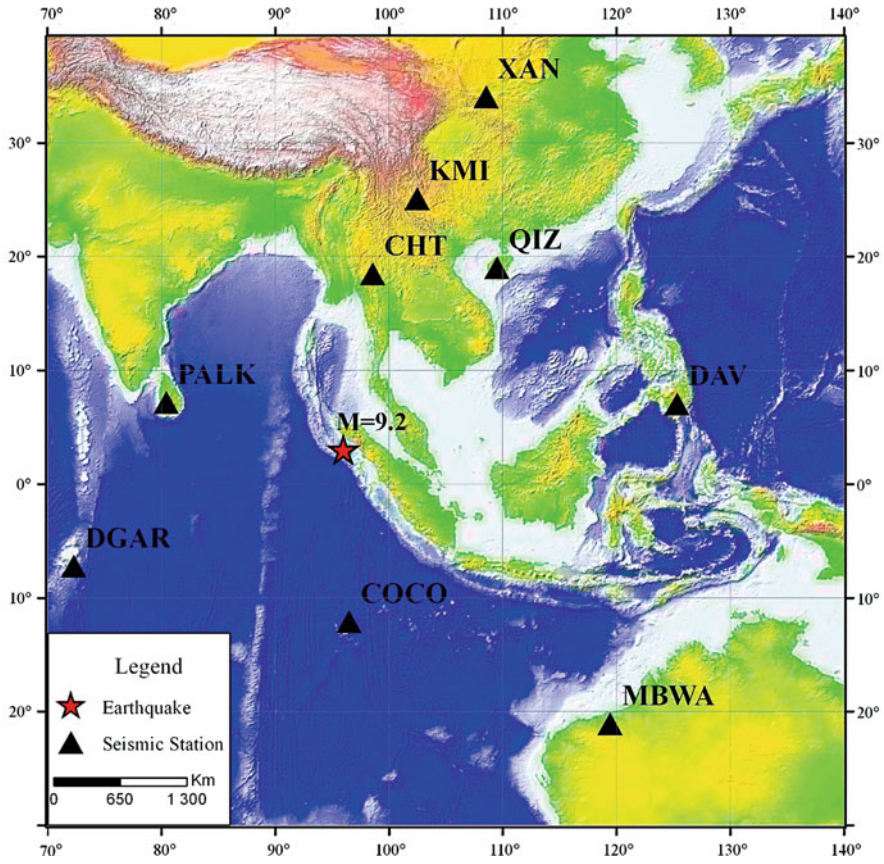

Fig. 13.2 Position of the IRIS stations whose records were analyzed before the Sumatra earthquake. The epicenter of the earthquake is shown by star

of 20 Hz showed that the MBWA station in Australia did not operate during the Sumatra earthquake, the records of the DGAR and PALK stations had defects and gaps, and the DAV and QIZ stations in the Pacific region showed a completely different structure of microseisms as compared with the stations in the Indian Ocean region. Therefore, our analysis was mainly based on data from the CHTO, KMI, XAN, COCO, and (in part) PALK stations. We used records of vertical components with the exception of the COCO station, where this component was not recorded, so that the COCO data on horizontal components were processed. The database used for these stations encompassed the interval of December 16–26, 2004 (the 350th to 360th days from the beginning of the year). Since the Sumatra earthquake occurred at 00:58:54 GMT on December 26, the records of December 26 were processed only up to the first arrival time.

An unusual circumstance was the fact that, 2.5 days prior to the Sumatra earthquake, another strong ($M = 7.9$) earthquake occurred in the southern

hemisphere; its epicenter had the coordinates (49.31° S, 161.35° E) and was located southwest of New Zealand (in the McQuary Ridge area). The vibrations generated by this earthquake were hundreds of times stronger than the microseism level at the aforementioned stations, and surface waves with periods of 300–500 s went around the Earth a few times.

Figure13.3 clearly shows a sequence of such signals, particularly at low noise stations KMI and CHTO. The interval between the successive signals going around

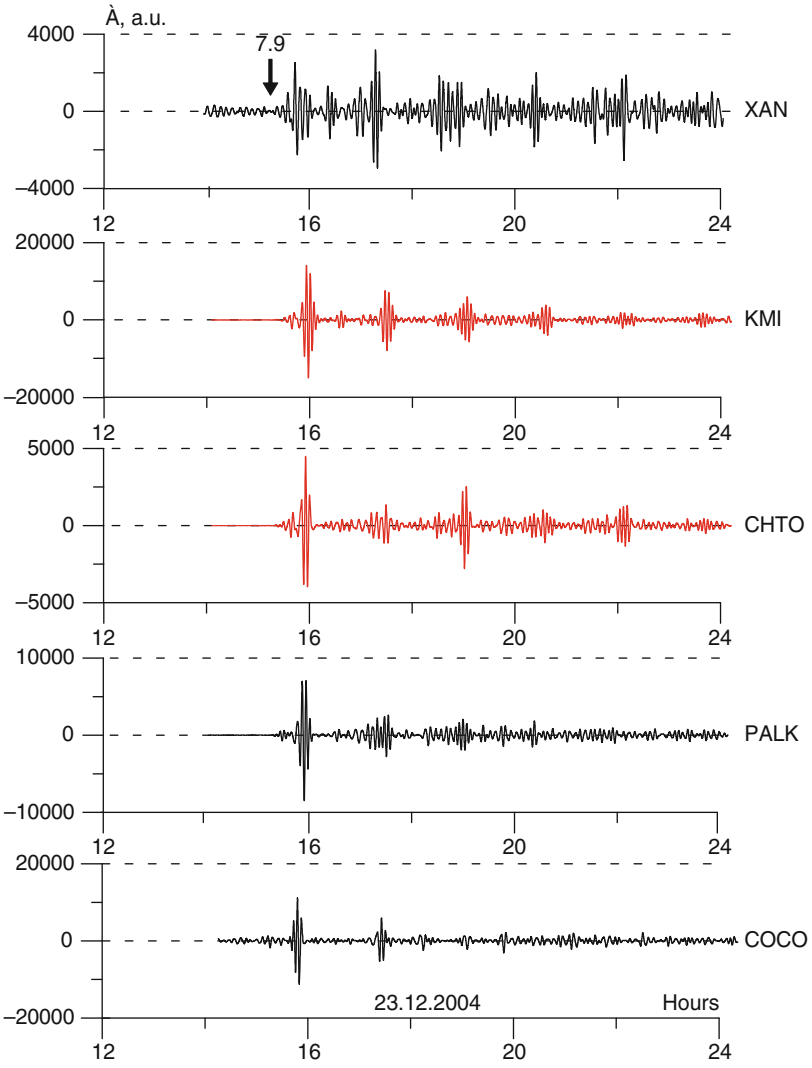

Fig. 13.3 Succession of seismic waves in the range of periods 256–512 min after the McQuary earthquake (marked by an arrow). The station codes are given to the right of the plots, and the station locations are shown in Fig. 13.2

the Earth in both NW and SE directions is 13 h. The records shown in the figure were obtained after aggregation of the signal to a 1-s period, trend removal by smoothing with Gaussian kernels and an averaging radius of 100 samples, and band-pass frequency filtering in the band 256–512 s. The distances from the McQuary earthquake epicenter to the aforementioned stations ranged from 7500 km for the nearest station (COCO) to 10100 km for the farthest station (PALK). Accordingly, the time delay before the arrival of surface waves was about 0.5 h (Fig. 13.3). Vibrations continued actually up to the time of the Sumatra earthquake. Figure 13.4 shows the 10-h record intervals immediately preceding the arrival of waves from this earthquake at the aforementioned stations. The records, from which high frequency components with periods less than 1 min were removed, are dominated by components with periods of 300–500 s but also contain waves with lower and higher frequencies.

13.3 Results

Comparison of wave amplitudes at the same stations shown in Figs. 13.3 and 13.4 reveals the following. Within the time interval of 2.5 days between the McQuary and Sumatra earthquakes, the amplitude of surface waves caused by the first earthquake decreased by a few thousand times at the CHTO, KMI, and PALK stations and only by a few tens of times at the COCO and XAN stations. Possibly, the difference is due to the distinctions in lithosphere quality factors along traces of waves traveling at different azimuths around the Earth. However, one may also assume that the more rapid (by two orders of magnitude) amplitude decrease along the traces of the CHTO, KMI, and PALK stations is caused by anomalously strong absorption of waves in the source area of the future Sumatra earthquake.

Following the aforementioned procedure for identifying hidden periodic oscillations, we checked whether this earthquake was preceded by periodic oscillations in the minute range of microseisms, as was the case before the Kronotskii earthquake. Figures 13.5 and 13.6 present results of the analysis of data from the KMI and CHTO stations. We calculated spectral–temporal plots of $\Delta \ln L(3)$ by processing records of these stations obtained in the period from December 15 to 26 (up to the Sumatra earthquake). The arrows in the figure indicate the times of the Sumatra ($M = 9.2$) and the preceding McQuary ($M = 7.9$) earthquakes. We examined the range of periods from 20 to 60 min with a 180-min window moving at a 60-min step. Prior to the calculations, the low frequency trend was removed by a third-order polynomial. For noise suppression, the calculations were performed only for waves whose amplitude exceeded the median value 1.5. Periodic oscillations arose after the McQuary earthquake and continued for about 24 h. Comparison with Fig. 13.1 reveals a similar effect observed after the foreshock of the Kronotskii earthquake. The records of the XAN, COCO, and PALK stations did not reveal any periodic oscillations. This may be due to a higher noise level, particularly at the XAN and COCO stations, which is evident from comparison of records in Fig. 13.3 with

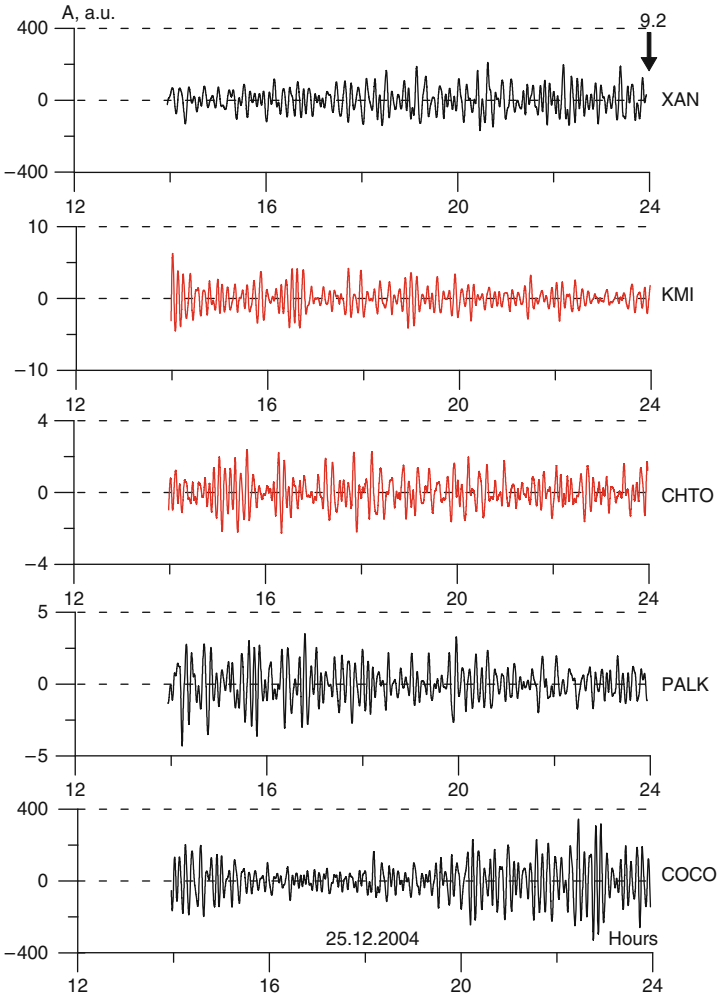

Fig. 13.4 Structure of seismic waves in the range of periods exceeding 1 min recorded 10 h before the Sumatra earthquake. The station codes are given to the right of the plots, and the station locations are shown in Fig. 13.2

amplitudes of surface waves from the McQuary earthquake. In the case of the Sumatra earthquake, we had a few stations located around the source area.

This provided the possibility of testing the hypothesis that the catastrophe was preceded by intensification of collective effects in a nonequilibrium medium, expressed in the synchronization of microseismic vibrations in the region surrounding the earthquake epicenter [Bak et al., 1989; Sornette and Sammis, 1995]. Unfortunately, a recording failure took place at the PALK station in the period between the McQuary and Sumatra earthquakes. Therefore, our analysis used data of only four stations: CHTO, KMI, XAN, and COCO. To analyze the effects of

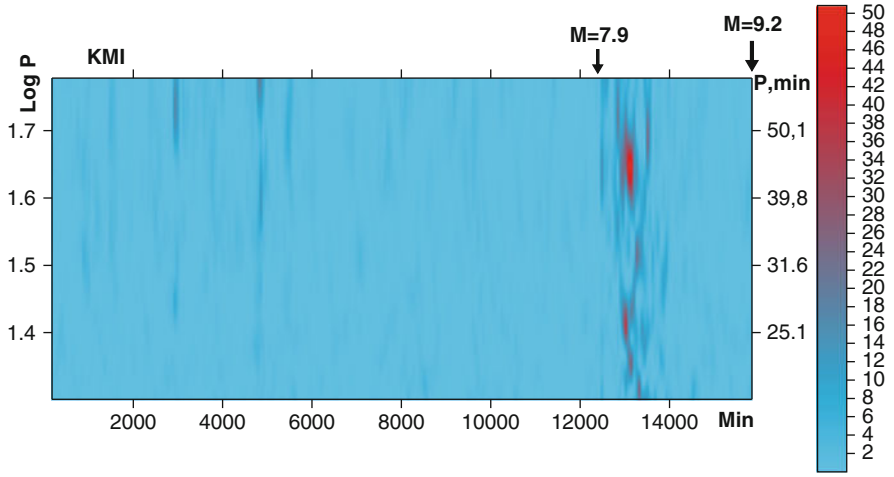

Fig. 13.5 Spectral–temporal diagram of the increment in the logarithmic function of likelihood $\Delta \ln L$ of microseisms recorded at the KMI station before the Sumatra earthquake ($M = 9.2$). The left arrow indicates the time of the McQuary earthquake ($M = 7.9$). The vertical axes show the spectral period (on the right) in minutes and its logarithm (on the left)

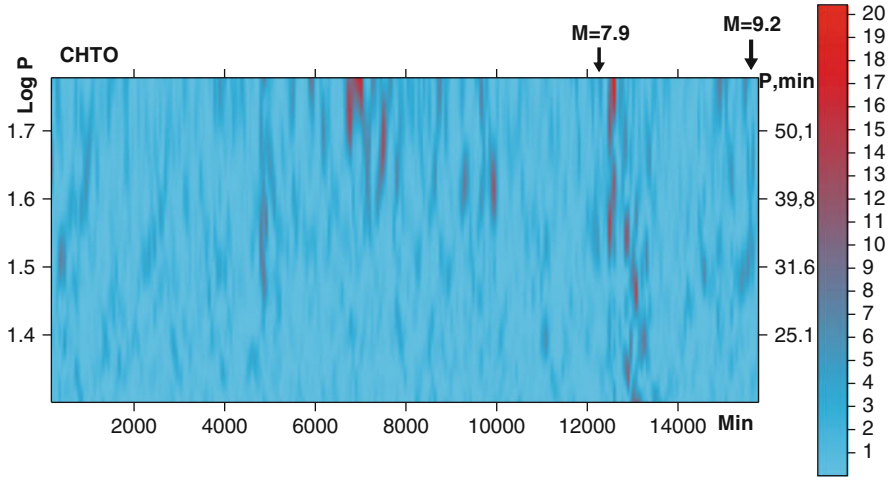

Fig. 13.6 Spectral–temporal diagram of the increment in the logarithmic function of likelihood $\Delta \ln L$ of microseisms recorded at the CHTO station before the Sumatra earthquake ($M = 9.2$). The left arrow indicates the time of the McQuary earthquake ($M = 7.9$). The vertical axes show the spectral period (on the right) in minutes and its logarithm (on the left)

collective behavior in microseismic vibrations at these four stations in the minute range of periods, the initial data sampled at a frequency of 20 Hz were first reduced to a 30-s sampling interval by calculating the averages over successive nonoverlapping intervals 600 samples long. The resulting time series were analyzed by two

approaches based on the calculation of robust wavelet and spectral measures of coherence in the moving time window. The use of different measures aimed to test the stability of the final synchronization effect with respect to different methods of representing the signals: their expansion in strongly nonstationary Haar wavelets and the classic Fourier expansion.

The robust wavelet measure of coherence is a modification of the approach to the analysis of multidimensional time series proposed in [Lyubushin, 2000; Lyubushin and Kopylova, 2004]. The scale-dependent measure of coherent behavior in a moving time window of a given width of N samples is constructed. The analysis is performed independently for each position of the time window (moved to the right by one sample). Before the wavelet decomposition of the analyzed time series fragments present in the current time window, the following sequence of operations is applied to each fragment: (i) the general linear trend within the time window is removed; (ii) a sample estimate of the standard deviation is obtained, and each value is divided by this estimate; (iii) the initial values are converted to the increments between adjacent time values; (iv) the window fragment is complemented with zeros to the full length of $M = \min\{2m : 2m \geq N\}$ samples. Operation (i) removes the strongest low frequency variations in signals, which cannot be statistically representative within the window. The division of each signal within the window by its standard deviation mutually adjusts different time series by reducing the total energy of their variations to the same value. Operation (iii) of the conversion to increments is standard in time series analysis and is intended to enhance the stationarity of sample sets within narrow time windows if low frequencies are predominant. Finally, the last operation (iv) is necessary for the subsequent application of the fast discrete wavelet transform.

Let $q \geq 3$ be the total number of simultaneously analyzed time series, and let τ be the position of the right-hand end of a moving time window N samples wide. We denote as $c_j^{(\beta,\tau)}(k)$ the coefficients of the discrete orthogonal wavelet transform [Mallat, 1998] of the jth time series fragment in the current time window with the position of the right-hand end τ at a detail level of the number β after preliminary operations (i)–(iv). We chose the Haar wavelet from the family of orthogonal wavelets as the most compact and suitable for the analysis of the most abrupt variations in signals. The index k successively enumerates the coefficients belonging to the level $\beta = 1, \ldots, m$. The number m is an exponent of two in the representation $M = 2^m$ such that it is the least number no smaller than the time window width N. At each detail level, the total number of coefficients is equal to $M_\beta = 2^{(m-\beta)}$. Each coefficient $c_j^{(\beta,\tau)}(k)$ reflects the signal behavior in the frequency band $[\Omega_{\min}^{(\beta)}, \Omega_{\max}^{(\beta)}] = [1/(2^{(\beta+1)}\Delta s),\ 1/(2^\beta \Delta s)]$, where Δs is the length of the sampling interval, in the neighborhood of the sample with the number $\tau_k^{(\beta)} = k \cdot 2^\beta,\ k = 1, \ldots, M_\beta$, measured from the position of the left end of the time window. The width of this neighborhood (the temporal "zone of responsibility" of the coefficient) is equal to 2^β. The wavelet transforms yield a set of coefficients $c_j^{(\beta,\tau)}(k),\ j = 1, \ldots, q,\ \beta = 1, \ldots, m,\ k = 1, \ldots, M_\beta = 2^{(m-\beta)}$. However, some of these coefficients can involve zero values complementing the data set via

preliminary operation (iv). Therefore, the real number of coefficients at the level β reflecting the signal behavior within the window is equal to $L_\beta = 2^{(m-\beta)} \cdot (N/M) = N \cdot 2^{-\beta}$.

Now we address a time series j_0 and construct the measure describing the relationship between this series and all other signals within the current time window. Naturally, this relationship depends on the scale of the variations in question and, therefore, should be sought at various levels of detail between wavelet expansion coefficients. The problem to be solved for this purpose is

$$\sum_{k=1}^{L_\beta} | \, c_{j_0}^{(\beta,\tau)}(k) - d_{j_0}^{(\beta,\tau)}(k|\gamma)| \;\; \to \min_{\gamma_j}, \quad d_{j_0}^{(\beta,\tau)}(k|\gamma) = \sum_{j=1,\, j\neq j_0}^{q} c_j^{(\beta,\tau)}(k) \cdot \gamma_j \qquad (13.4)$$

We should emphasize that the second sum in (13.4) is a linear combination of expansion coefficients of all time series except the chosen series j_0. Finding the vector γ from the solution of problem (13.4), we obtain certain values of $d_{j_0}^{(\beta,\tau)}(k)$. Now we can find the correlation coefficient between samples of the values of $c_{j_0}^{(\beta,\tau)}(k)$ and $d_{j_0}^{(\beta,\tau)}(k)$ for $k = 1, \ldots, L_\beta$; however, instead of the classic formula for calculating the sample value of the correlation coefficient, we use its robust modification [Huber, 1981], according to which the correlation coefficient between samples $x(k)$ and $y(k)$, $k = 1, \ldots, n$, can be calculated by the formula

$$\rho(x,y) = \frac{S(\overset{\frown}{Z}^2) - S(\overset{\smile}{Z}^2)}{S(\overset{\frown}{Z}^2) + S(\overset{\smile}{Z}^2)} \qquad (13.5)$$

where $\overset{\frown}{Z}(k) = a \cdot x(k) + b \cdot y(k)$, $\overset{\smile}{Z}(k) = a \cdot x(k) - b \cdot y(k)$, $a = 1/S(x)$, $b = 1/S(y)$, $S(x) = med|x - med(x)|$. Here, med(x) is the median of the sample x and, thereby, $S(x)$ is the absolute median deviation of the sample x. Substituting $x(k)$ for $c_{j_0}^{(\beta,\tau)}(k)$, $y(k)$ for $d_{j_0}^{(\beta,\tau)}(k)$, and n for L_β, we obtain the robust value we obtain the robust value $v_{j_0}(\beta,\tau)$ of the correlation coefficient describing the degree of connection of the process $j_0$with all other signals. If we replace in (13.4) the sum of the moduli of deviations by the sum of their squares, the problem can be reduced to the classic Hotelling problem of canonical correlations [Rao, 1965]. Therefore, the quantity $v_{j_0}(\beta,\tau)$ is here referred to as the robust canonical correlation of the time series j_0. The need to replace the classic scheme of the calculation of canonical correlations by its robust variant is dictated by the strong instability of the result of the classic calculations with respect to outliers in wavelet coefficients. The presence of such outliers is due to the well-known fact that the wavelet decomposition is capable of accumulating maximum information about the signal behavior in a relatively small number of wavelet coefficients. We should emphasize that the method is robust in two procedures: the solution of minimization problem (13.4) by the method of least moduli rather than by least squares and the calculation of the correlation coefficient by formula (13.5).

Note that the statistical significance of the estimated robust canonical correlations depends on the number of terms L_β in formula (13.4). Therefore, it is natural to introduce the parameter of statistical significance $L_{\min}$ as the minimum possible value of the number of wavelet coefficients L_β in formulas (13.4) and (13.5) that allows one to calculate correlations at the βth detail level. Thus, it is possible to determine the maximum possible detail level $\beta_{\max}$ defined by the formula $\beta_{\max} = \max\{\beta : L_\beta \geq L_{\min}\}$.

Since, with an increase in the number of the detail level, the number of wavelet coefficients involved in the estimation of $v_k(\beta, \tau)$ exponentially decreases, we reduce statistical fluctuations in estimates by introducing additional averaging over a certain number of coefficients obtained within preceding windows:

$$\bar{v}_k(\tau, \beta) = \sum_{s=1}^{m_\beta} v_k(\tau - s + 1, \beta)/m_\beta, \quad m_\beta = 2^\beta \tag{13.6}$$

The higher the detail level, the deeper the averaging (13.6) over the past time windows; this fact considerably decreases the dependence of the variance of statistical fluctuations in estimation (13.6) on the detail level number and makes this variance nearly the same for different values of β. According to formula (13.6), the effective width of the time window becomes scale-dependent and equal to $N_e^{(\beta)} = N + 2^\beta - 1$.

We define the robust wavelet measure of coherence by the formula

$$\kappa(\tau, \beta) = \prod_{k=1}^{q} |\bar{v}_k(\tau, \beta)| \tag{13.7}$$

The values of measure (7) range from 0 to 1. The larger the value of (13.7), the stronger the overall connection between all analyzed processes on scales corresponding to the number β. We should emphasize that the value of (13.7) is the product of q nonnegative values with moduli less than unity. Therefore, the greater the number q of the series analyzed, the lower the absolute values of $\kappa(\tau, \beta)$. As a consequence, the absolute values of statistic (13.7) can be compared only for the same number of series q. Most interesting are not the absolute values of measure (13.7) but its relative values for different values of τ. Thus, with a fixed Haar wavelet in use, the method has two free parameters: the window width N and the representativeness threshold $L_{\min}$.

The spectral measure of coherence was proposed in [Lyubushin, 1998] (see also [Lyubushin and Sobolev, 2006]) and is based on the use of canonical coherences, which extend the notion of the spectrum of coherence to the situation where, instead of a pair of scalar time series, it is necessary to investigate the relationship between two vector time series at various frequencies: an m-dimensional series $X(t)$ and an n-dimensional series $Y(t)$. The quantity $\mu_1^2(\omega)$, which is called the squared modulus of the first canonical coherence of the series $X(t)$ and $Y(t)$ and is used in this case

instead of the ordinary coherence spectrum, is calculated as the maximum eigenvalue of the matrix [Brillinger, 1975; Hannan, 1970]

$$U(\omega) = S_{xx}^{-1}(\omega) \cdot S_{xy}(\omega) \cdot S_{yy}^{-1}(\omega) \cdot S_{yx}(\omega). \tag{13.8}$$

Here, t is the discrete time enumerating successive samples; ω is the frequency; $S_{xx}(\omega)$ is the spectral $m \times m$ matrix of the time series $X(t)$; and $S_{xy}(\omega)$ is a cross-spectral rectangular $m \times n$, matrix, $S_{yx}(\omega) = S_{xy}^{H}(\omega)$, where the superscript H means Hermitian conjugation.

The component canonical coherences $v_i^2(\omega)$ of the q-dimensional time series $Z(t)$ $(q \geq 3)$are defined as the squared moduli of the first canonical coherence if the series $Y(t)$ in (13.8) is the ith scalar component of the q-dimensional series $Z(t)$ and the series $X(t)$ is the $(q–1)$-dimensional series consisting of the other components. Thus, the quantity $v_i^2(\omega)$ characterizes the correlation at the frequency $\omega \cdot \omega$ of variations in the ith component with variations in all of the other components. We define a frequency-dependent statistic $\lambda(\omega)$ characterizing the correlation at the frequency. ω between variations in all components of the vector series $Z(t)$:

$$\lambda(\omega) = \prod_{i=1}^{q} v_i(\omega) \tag{13.9}$$

Note that, by definition, the values of $\lambda(\omega)$ lie within the interval [0, 1] and the closer the value of $\lambda(\omega)$ to unity, the stronger the correlation between variations in the components of the multidimensional time series $Z(t)$ at the frequency ω. If $q = 2$, measure (13.9) is the ordinary squared modulus of the coherence spectrum. In order to estimate the temporal variability in the measure of interaction between the recorded processes, it is necessary to perform calculations in a moving time window of a given width. Let τ be the time coordinate of a window N samples wide. Calculating the spectral matrices for samples in the time window τ, we obtain the two-parameter function $\lambda(\tau, \omega)$, whose peaks define frequency bands and time intervals of enhanced collective behavior of the jointly analyzed processes.

To implement this algorithm, it is necessary to have in each time window the estimated spectral $q \times q$ matrix $S_{zz}(\tau, \omega)$. Below, we use the model of vector autoregression [Marple, 1987]:

$$Z(t) + \sum_{k=1}^{p} A_k \cdot Z(t-k) = e(t) \tag{13.10}$$

Here, A_k is the $q \times q$ matrix of autoregressive parameters; p is the order of autoregression; and $e(t)$ is the q-dimensional time series of the remainders of identification, which is assumed to be a series of independent Gaussian vectors with a zero mean and an unknown covariance matrix P. Model (13.10) is estimated after the preliminary operations of the elimination of the general linear trend,

transition to increments (in order to increase the stationarity within narrow time windows), and normalization of each scalar component to the unit variance. These operations are performed independently in each time window and for each scalar component of the multidimensional series. The spectral matrix is estimated by the formula

$$S_{zz}(\omega) = F^{-1}(\omega) \cdot P \cdot F^{-H}(\omega), \quad F(\omega) = I + \sum_{k=1}^{p} A_k \cdot \exp(-i\omega k) \qquad (13.11)$$

Estimation (13.11) has a good resolution in frequency for short samples. In the calculations, p was determined by the trial method as a minimum value such that the further increase does not lead to a significant change in the main features of the behavior of the dependence $\lambda(\tau, \omega)$. Everywhere below, we use the value $p = 3$. Thus, we see that the coherence measures $\kappa(\tau, \beta)$ and $\lambda(\tau, \omega)$ are constructed according to the same principle but differ significantly in the signal representation modes. Figures 13.7 and 13.8 plot estimates of these measures in a 12-h-wide moving time window (1440 30-s samples). The wavelet measure $\kappa(\tau, \beta)$ was estimated with the use of the Haar wavelet and the representativeness threshold equal to $L\min = 16$. In estimating the spectral measure $\lambda(\tau, \omega)$, the windows were shifted at a 1-h step (120 samples).

Analysis of the plots in Fig. 13.7 leads to the following conclusions. The wavelet measure of coherence $\kappa(\tau, \beta)$ drops after a seismic event; this is true of both the McQuary event preceding the Sumatra earthquake and the Sumatra earthquake itself. However, beginning from the 12 800-min time mark, the measure of coherence at all levels increases; at the fifth to sixth detail levels, this increase exhibits an obvious positive trend up to the time moment of the shock. At lower detail levels, the measure of coherence reaches peak values approximately 1000–1500 min before the earthquake. Moreover, with increasing detail level number, or "period," the peak of the coherence measure migrates toward the time moment of the shock; i.e., the migration tends to increase the period.

The frequency–time diagram for the spectral measure of coherence $\lambda(\tau, \omega)$ in Fig. 13.8 independently confirms this conclusion; moreover, as the spectral approach makes it possible to trace more smoothly the frequency migration of the coherence measure, Fig. 13.8 even more clearly displays the effect of the migration of the coherence measure from high to low frequencies. However, the approach using wavelet decomposition is more effective for "very low frequencies" (periods longer than 10 min, detail levels 5 and 6 in Fig. 13.7). Thus, the application of both methods of calculating the coherence revealed the scenario of synchronization, which consists in the migration of the fundamental period (or time scale in the wavelet analysis), characterized by maximum collective behavior, from short to long periods.

Further, we attempted to identify asymmetry in the pulsed microseismic oscillations recorded before the Sumatra earthquake at the aforementioned stations. By asymmetry, we mean unequal amplitudes of positive and negative oscillation

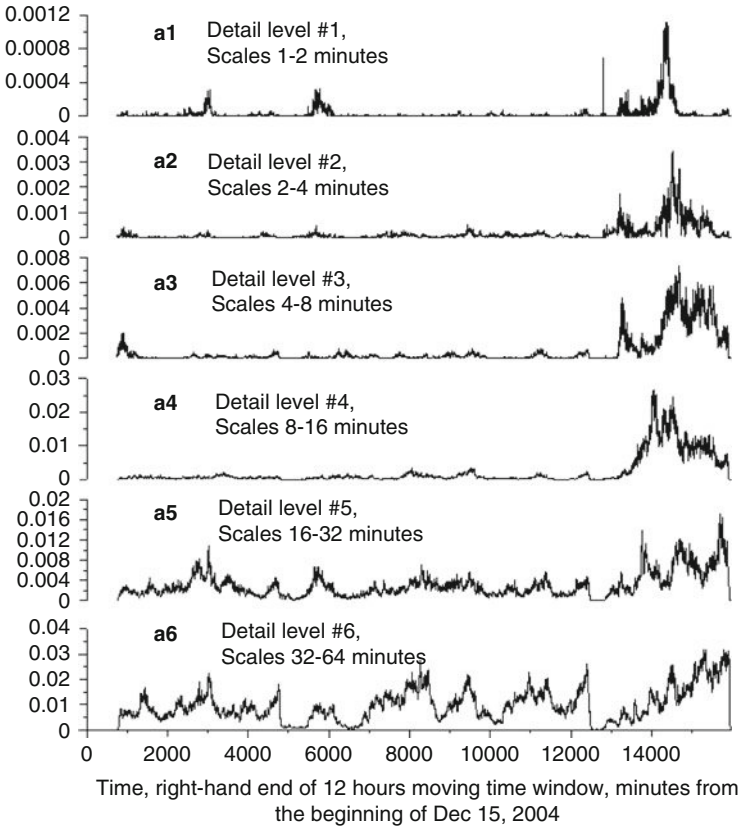

Fig. 13.7 Evolution of the robust wavelet measure of coherence $\kappa(\tau, \beta)$ calculated with a 12-h wide moving time window of 1440 samples from XAN, KMI, CHTO, and COCO records after transition to a 30-s sampling interval. The Haar wavelet was used with a representativeness threshold of $L\min = 16$. The series were preliminarily converted to increments. Plots (a1–a6) relate to detail levels 1–6, which correspond to time scales (periods, the parameter β) of 1–2, 2–4, 4–8, 8–16, 16–32, and 32–64 min. Time measured in minutes from the beginning of December 15, 2004, is plotted on the horizontal axis and corresponds to the right-hand end of the 12-h-wide moving time window τ of 1440 samples; the last time mark is 15975 min, i.e., 02:15 on December 26, 2004

phases, what was clearly expressed in the case of the Kronotskii earthquake [Sobolev et al., 2005]. For this purpose, a program of their automatic identification was developed (it was used in [Sobolev and Lyubushin, 2006]). Since the pulses of interest belong to the middle range of periods, it was necessary first to pass from the initial 0.05-s sampling interval to 1 s and then to eliminate low frequency (including tidal) effects on records and (after the transition to 1-s sampling) high frequency noise. These preliminary operations were effected through averaging and 20-fold downsampling of records, removal of the low frequency Gaussian trend with the scale parameter $H = 1000$ samples (seconds), and subsequent calculation of the

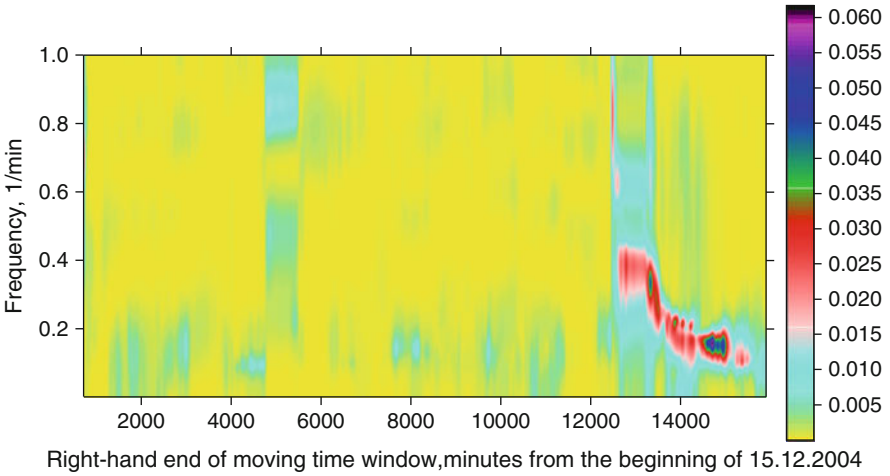

Fig. 13.8 Evolution of the spectral measure of coherent behavior $\lambda(\tau, \omega)$ calculated from XAN, KMI, CHTO, and COCO records after transition to 30-s sampling intervals. The estimation is made in a 12-h-wide moving time window for 1440 samples with a reciprocal shift of 120 samples (1 h) strictly before the arrival from the Sumatra earthquake (AR(3) model and transition to increments). The last time mark is 15900 min, or 01:00 on December 26, 2004

Gaussian trend with a scale parameter of 100 s. We should emphasize that the trend is first removed at $H = 1000$ s, after which deviations from the trend are removed at $H = 100$ s.

These preliminary operations yielded a signal with a sampling interval of 1 s whose power spectrum lay in the range of periods approximately from 200 to 2000 s. It was necessary to automatically identify high amplitude pulses in this signal. For this purpose, after the direct Haar wavelet transform [Mallat, 1998], we left only a small preset part $(1 - \alpha)$ of the wavelet coefficients with maximum moduli (the positive parameter $\alpha < 1$ can be referred to as the compression level), while the remaining coefficients were set to zero. Then, we performed the inverse wavelet transform, yielding a sequence of pulses of sufficiently high amplitudes that are usually separated by intervals of constant values previously filled with noise. This operation is known as denoising in wavelet analysis. The selection of the Haar wavelet for this operation is dictated by the simplicity of the subsequent automatic identification of rectangular pulses. The choice of the compression level determines the number of pulses being identified and the degree of denoising. Note that a signal processed in this way already contains a sufficiently large number of wavelet coefficients that are close or even equal to zero, simply because it was obtained by the preliminary operations of the trend identification and removal. In addition, the compression level obviously depends on the length of the data set because the larger the set, the greater the number of coefficients.

In the time interval from December 15 to 26, we processed 24 h long sampling sets (in all 86400 1-s samples) from all stations. The compression level was 0.9995, yielding about 30 pulses per day. We then calculated the number of pulses of

negative and positive polarities; the two calculation runs included, respectively, all pulses and the most significant pulses with amplitudes exceeding $1m$, where m is the median of their distribution. Since the majority of high amplitude vibrations with periods of 300–500 s were caused by the McQuary earthquake, the analysis was conducted both in the range 200–2000 s and, with the suppression of these waves, in the range 600–2000 s. In both cases and for all stations, we could not detect any significant asymmetry in the shape of the pulses. On the whole, as can be seen from Figs. 13.3 and 13.4, vibrations of positive and negative polarities are symmetric relative to the zero line.

13.4 Discussion

Before the Sumatra earthquake, we did not detect any asymmetry in microseismic amplitudes in the minute range of periods, as was observed before the Kronotskii and Neftegorsk events [Sobolev et al., 2005; Sobolev and Lyubushin, 2006]. We relate the asymmetry, expressed as the difference between amplitudes of positive and negative polarities, to the imperfect elasticity of rocks containing fractures. This is confirmed by laboratory experiments in which a sinusoidal signal is distorted during its propagation through a sample subjected to deformation [Sobolev and Ponomarev, 1997]. Phases of compressive and tensile stresses under these conditions cause different deformations due to the difference in the strain moduli under compression and extension. One should assume that either the lithospheric region near the stations surrounding the source of the Sumatra earthquake did not possess imperfect elasticity of this type or the epicentral distances (more than 1000 km) were too great for this effect to be reflected in records of the stations. However, as noted above, the attenuation of the surface waves produced by the McQuary earthquake increased during their repeated propagation near the CHTO, KMI, and COCO stations. A possible interpretation of the absence of wave asymmetry notwithstanding significant wave attenuation is that the latter is caused by an increase in the damping decrement due to an increase in the plasticity or water saturation in the source area of the forthcoming Sumatra earthquake. The difference between moduli under compression and extension conditions in plastic media is known to decrease with increasing plasticity of the consolidated medium subjected to deformation [Malinin, 1968].

As was noted in [Sobolev, 2004; Sobolev et al., 2005], foreshocks can provoke periodic oscillations near the epicentral area of a future strong earthquake. This phenomenon is a feature indicating an unstable state of the lithosphere. The analysis of the Sumatra earthquake confirmed, to an extent, this hypothesis, with the McQuary earthquake acting as a foreshock (Figs. 13.5, 13.6). This effect was also observed before the Kronotskii earthquake, which occurred 27 days after an earthquake in Tibet with $M = 7.7$. During 3.5 h after the latter, the Petropavlovsk station on Kamchatka recorded waves with periods of a few tens of minutes [Sobolev, 2004].

The second effect that was clearly observed before the Sumatra earthquake was a gradual decrease in the predominant periods of premonitory vibrations in the range from a few minutes to tens of minutes (Figs. 13.7, 13.8). Under the assumption of an intraterrestrial mechanism of these vibrations, they can be related to resonance effects in lithospheric blocks of increasingly larger scales and/or in lithospheric and deeper layers of the Earth. The analysis of microseismic amplitudes in the second range of periods showed that, at all of the aforementioned stations in the time interval from December 15 to 26, the microseismic level was virtually stationary, thereby ruling out the influence of atmospheric effects. This phenomenon was previously noted in the range of very long periods (of the order of one year) in the analysis of a seismic catalog and in a laboratory experiment involving deformation and failure of a sample [Sobolev, 2003]; apparently, this is a fundamental property of a nonequilibrium system approaching instability. In the case of the Sumatra earthquake, the instability could have been triggered by the McQuary earthquake, which caused propagation of deformation waves along the future Sumatra rupture [Nikolaevskii, 1996]. A theoretical substantiation of the decrease in the period of oscillatory processes in the same place of the lithosphere was proposed by Dubrovskii [1988], who proved the following theorem. If a system with a set of characteristic critical parameters is in an unstable equilibrium separating the steady- and unsteady-state ranges of parameters, then the steady-state system will produce waves whose frequency tends to zero if the system approaches the critical state of unstable equilibrium and the dimensions of wave disturbances are finite. Dubrovsky and Dieterich [1990] extended this approach to the case of deformation waves propagating along a fault (trapped waves), giving rise to instable slip of fault walls relative to each other. The development of this instability (an earthquake or creep) is preceded by a decrease in the frequency of these waves.

One cannot exclude the mechanism by which the waves under discussion originate as a result of selforganization of the source area. The appearance of rhythms is a common phenomenon in the evolution of nonequilibrium systems [Nicolis and Prigogine, 1977]. If waves in blocks of different sizes are described by nonlinear equations of the type (13.12) containing chaotic and periodic components, and K is the coupling coefficient (e.g., between stresses in the blocks), such systems will show the effects of phase synchronization and the frequency ω range of synchronization widens with an increase in K [Ott, 2002].

$$\mathrm{dx/dt} = \mathrm{F(x)} + \mathrm{K^{*}P}(\omega \mathrm{t}) \tag{13.12}$$

One may suppose that the degree of the mutual influence of blocks (or seismically active faults) increases as macroscopic instability (an earthquake) is approached. This is accompanied by enlargement of the geometric region of collective behavior, in agreement with the concept of self-organized seismic criticality [Bak et al., 1989; Sornette and Sammis, 1995]. In this case, the spectrum of vibrations can evolve into the lower frequency range. We realize that, to gain more substantiated ideas of the physical mechanisms responsible for the phenomena

discussed in this paper, additional (and not only seismological) investigations are required.

13.5 Conclusion

The analysis of records obtained at a few stations 60 h before the Sumatra earthquake revealed periodic vibrations in the range of periods from 20 to 60 min that arose after the McQuary earthquake and continued for about 24 hours. This phenomenon was previously observed after the foreshocks preceding the Kronotskii earthquake.

Synchronization of vibrations recorded at the stations began 53 h before the Sumatra earthquake and continued up to its onset time, with the predominantperiod gradually increasing from a few minutes to tens of minutes.

These phenomena are consistent with the hypothesis according to which the radius of correlation and collective effects in the microseismic field increases prior to an earthquake within the framework of the concepts of self-organized seismic criticality.

References

Bak P., S. Tang, and K. Winsenfeld, "Earthquakes As Self-Organized Critical Phenomenon," J. Geophys. Res. **94**, 15 635–15 637 (1989).

Brillinger D. R., Time Series. Data Analysis and Theory (Holt, Rinehart and Winston, New York, 1975).

Dubrovskii V.A., "Tectonic Waves and Contemporary Movements," in Lithosphere of Central and Eastern Europe: Geodynamics (Naukova Dumka, Kiev, 1988) [in Russian].

Dubrovskiy V.A. and J. Dieterich, "Wave Propagation along Faults and the Onset of Slip Instability," EOS **71**(17), 635–636 (1990).

Hannan E.J., Multiple Time Series (Wiley, New York, 1970).

Huber R.J., Robust Statistics (Wiley, New York, 1981).

Lyubushin A.A., "Analysis of Canonical Coherences in the Problems of Geophysical Monitoring," Fiz. Zemli, No. 1, 59–66 (1998) [Izvestiya, Phys. Solid Earth **34**, 52–58 (1998)].

Lyubushin A.A., "Wavelet-Aggregated Signal and Synchronous Peaked Fluctuations in Problems of Geophysical Monitoring and Earthquake Prediction," Fiz. Zemli, No. 3, 20–30 (2000) [Izvestiya, Phys. Solid Earth **36**, 204–213 (2000)].

Lyubushin A.A., "Periodicities and Rhythms of Global Seismicity in the 20th Century," in Joint Session"Rhythmicity and Cyclicity in Geology As Evidence for General Laws of Development" of the OGGGGN RAN Scientific Workshop "Theoretical Problems of Geology" and the X Workshop "System of the Planet Earth," February 7 and 8, 2002, Abstracts (OGGGGN RAN, Moscow, 2002), pp. 66–67 [in Russian].

Lyubushin A.A., V.F. Pisarenko, V.V. Ruzhich, and V. Yu. Buddo, "Extraction of Periodicities in the Seismic Regime," Vulkanol. Seismol., No. 1, 62–76 (1998).

Lyubushin A.A. and G.N. Kopylova, "Multidimensional Wavelet Analysis of Time Series of Electrotelluric Observations in Kamchatka," Fiz. Zemli, No. 2, 82–96 (2004) [Izvestiya, Phys. Solid Earth **40**, 163–176 (2004)].

Lyubushin A.A. and G.A. Sobolev, "Multifractal Measures of Synchronization of Microseismic Oscillations in aminute Range of Periods," Fiz. Zemli, No. 9 (2006) [Izvestiya, Phys. Solid Earth **42**, 734–744 (2006)].

Malinin N.N., Applied Theory of Plasticity and Creep (Mashinostroenie, 1968) [in Russian].

Mallat S., A Wavelet Tour of Signal Processing (Academic, San Diego, 1998).

Marple, Jr. S.L., Digital Spectral Analysis with Applications (Prentice-Hall, Englewood Cliffs, 1987).

Nicolis G. and I. Prigogine, Self-Organization in Non-Equilibrium Systems (Wiley, New York, 1977; Moscow, Mir, 1979) [in Russian].

Nikolaevskii V.N., Geomechanics and Fluid Dynamics (Nedra, Moscow, 1996) [in Russian].

Ott E., Chaos in Dynamic Systems (University Press, Cambridge, 2000).

Rao S.R., Linear Statistical Inference and Its Applications (Wiley, New York, 1965).

Sobolev G.A., "Microseismic Variations Prior to a Strong Earthquake," Fiz. Zemli, No. 6, 3–13 (2004) [Izvestiya, Phys. Solid Earth **40**, 455–464 (2004)].

Sobolev G.A. and A.V. Ponomarev, "The Vibratory Effect on the Fracture Process and Acoustic Regime in a Fault Zone Model," Vulkanol. Seismol., No. 6, 51–57 (1997).

Sobolev G.A., A.A. Lyubushin, and N.A. Zakrzhevskaya, "Synchronization of Microseismic Variations within a Minute Range of Periods," Fiz. Zemli, No. 8, 3–27 (2005) [Izvestiya, Phys. Solid Earth **41**, 599–621 (2005)].

Sobolev G.A. and A.A. Lyubushin, "Microseismic Impulses As Earthquake Precursors," Fiz. Zemli, No. 9 (2006)Izvestiya, Phys. Solid Earth **42**, 721–733 (2006)].

Sobolev G.A. and A.A. Lyubushin, "Microseismic Anomalies before the Sumatra Earthquake of December 26, 2004," Fiz. Zemli, No. 5, 3–16 (2007) [Izvestiya, Phys. Solid Earth 43, 341–353 (2007)].

Sornette D. and C.G. Sammis, "Complex Critical Exponents from Renormalization Group Theory of Earthquakes: Implications for Earthquake Predictions," J. Phys. I. France **5**, 607–619 (1995).

Chapter 14
Synchronizations of Microseismic Oscillations as the Indicators of the Instability of a Seismically Active Region

G.A. Sobolev, A.A. Lyubushin, and N.A. Zakrzhevskaya

14.1 Introduction

Nearly all models of earthquake preparation are known to indicate magnification of the collective component in the behavior of geophysical fields in the preparation zone as the moment the earthquake occurrence is approached. The geophysical monitoring is aimed at the detection of the so-called *synchronization signal* in variations of different geophysical parameters, as well as its duration and frequency range.

It is the synchronization and collective behavior of measured characteristics that are relevant to the problems of monitoring and preparation of an earthquake or other natural catastrophes. In this respect, certain methodological recommendations can be suggested which result from the most general regularities of the system behavior; we mean the regularities that draw a system nearer to a bifurcation, or catastrophe [Nicolis, Prigogine; 1989]. An increase in the fluctuation correlation radius in the bifurcation vicinity indicates that the system tends to be self-consistent throughout its volume, thereby preparing for the collective transition to a new state. In the statistical physics of fluids, such a behavior is known as "critical opalescence" or abnormal dispersion, and is considered as a universal signal of the approaching catastrophe.

To extract hidden synchronization effects we applied the method using the estimation of canonical coherences in a moving time window developed in [Lyubushin, 1998, 2007] for the detection of earthquake precursors from geophysical monitoring data. This method was applied in [Lyubushin et al., 2003, 2004] to the analysis of multivariate hydrological and oceanographic (water-level valued) time series. The method consists in the estimation of the frequency dependent measure of the coherent behavior of components of multivariate time series, and its essentials are outlined below.

G. Sobolev (✉), A.A.Lyubushin, and N.A. Zakrzhevskaya
Schmidt Institute of Physics of the Earth, Russian Academy of Sciences, 10 Bol'shaya Gruzinskaya, Moscow, Russia
e-mail: sobolev@ifz.ru; lyubushin@yandex.ru

V. de Rubeis et al. (eds.), *Synchronization and Triggering: from Fracture to Earthquake Processes*, GeoPlanet: Earth and Planetary Sciences 1,
DOI 10.1007/978-3-642-12300-9_14,

A complex structure of geophysical data and a high level of noises of different origin lead to the necessity of preprocessing time series and making a transition from initial data to some other parameters, which describes the most general properties of each time series. Here we take an argument providing maximum to multi-fractal singularity spectra of initial monitoring signals as such a parameter. In fractal analysis, this quantity is known as generalized Hurst exponent. The singularity spectra are estimated within moving time window of a certain length. Thus, there is a transfer from the analysis of variations of initial geophysical parameters to the analysis of generalized Hurst exponent variations. This preprocessing step turns to be rather efficient for detecting synchronization before strong earthquakes.

14.2 Initial data

We have taken broad-band vertical component seismic records with 20 Hz sampling rate from IRIS stations before 3 strong events: Kronotskii (Kamchatka Peninsula) $M = 7.7$ earthquake of December 5, 1997, [54.64°N, 162.55°E] and Hokkaido $M = 8.3$ earthquake of September 25, 2003 [41.81°N, 143.91°E]. The initial data were kindly provided by the Geophysical Service of the Russian Academy of Sciences.

For the case of Kronotskii earthquake we studied records of seismic stations in Petropavlovsk-Kamchatskii, (PET), Yuzhno-Sakhalinsk (YSS), Magadan (MAG), Yakutsk (YAK) and Obninsk (OBN), whose location is shown in Fig. 14.1.

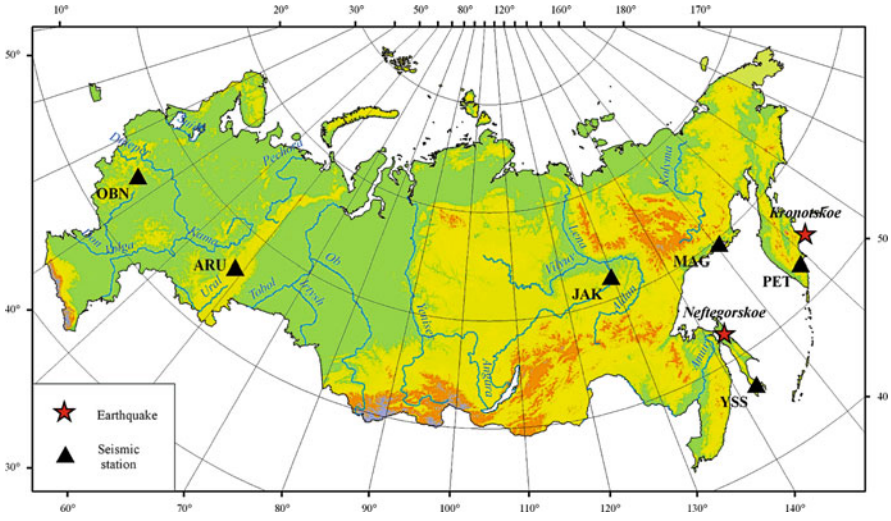

Fig. 14.1 Position of the IRIS stations whose records were analyzed before the Kronotski earthquakes. The epicenters of the earthquakes are shown by stars

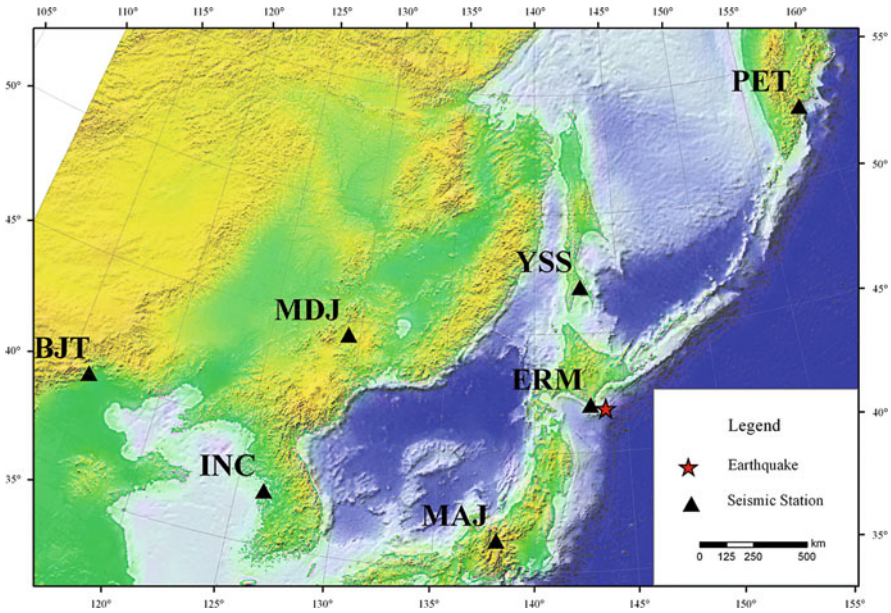

Fig. 14.2 Position of the IRIS stations whose records were analyzed before the Hokkaido earthquake. The epicenter of the earthquake is shown by star

For the case of Hokkaido earthquake we have taken data from stations ERM, MAJ, INC, MDJ, BJT, PET, YSS, which are shown in Fig. 14.2. All these stations are located at distances from 70 up to 7160 km from epicenters under different geological conditions.

The time intervals we have analyzed before earthquakes are the following:

– Kronotskii earthquake: November 05 – December 05 of 1997;
– Hokkaido earthquake: September 01 – 25 of 2003.

In previous studies [Sobolev et al., 2005; Sobolev, Lyubushin, 2006] we have found that the main precursory information is contained within low-frequency variations of microseismic background. Thus, for the transition to a minute range of periods, the initial records were averaged and downsampled 600 times, which gave time series with a sampling interval of 30 sec.

14.2.1 Brief description of the methods

14.2.1.1 Transforming to generalized Hurst exponent variations

Below we describe briefly the main points of estimating multi-fractal measure of coherence which is based on the analysis of generalized Hurst exponent

variations. More detailed description could be found in [Lyubushin, Sobolev, 2006; Lyubushin, 2007].

The analysis of fractal and multifractal properties of geophysical monitoring time series is a promising direction of data analysis in the physics of the solid Earth [Currenti et al., 2005; Telesca et al., 2005; Lyubushin, 2007]. This is due to the fact that the fractal analysis can effectively explore signals that, in terms of covariance and spectral theory, are no more than white noise or Brownian motion.

Let $X(t)$ be some signal. Let us define its variability measure $\mu(t,\delta)$ on the time interval $[t, t+\delta]$as the range:

$$\mu(t,\delta) = \max_{t\le s\le t+\delta} X(s) - \min_{t\le s\le t+\delta} X(s). \tag{14.1}$$

A Holder-Lipschitz exponent $h(t)$ for time moment t is defined as the limit:

$$h(t) = \lim_{\delta\to 0} \frac{\ln(\mu(t,\delta))}{\ln(\delta)} \tag{14.2}$$

i.e., in the vicinity of time moment t, variability measure $\mu(t,\delta)$ tends to zero when $\delta \to 0$according to the formula $\delta^{h(t)}$.

Singularity spectrum $F(\alpha)$ is defined [Feder, 1989] as a fractal dimensionality of the set of time moments t, for which $h(t) = \alpha$, i.e. having the same Holder-Lipschitz exponent α. Singularity spectrum exists for scale-invariant signals $X(t)$. Let us calculate a mean value of variability measure $\mu(t,\delta)$ at the power q:

$$M(\delta, q) = M\{(\mu(t,\delta))^q\}. \tag{14.3}$$

The random process $X(t)$ is scale-invariant if the value of $M(\delta, q)$ tends to zero when $\delta \to 0$ according to the formula $\delta^{\kappa(q)}$, i.e., the following limit exists:

$$\kappa(q) = \lim_{\delta\to 0} \frac{\ln M(\delta, q)}{\ln(\delta)}. \tag{14.4}$$

If the function $\kappa(q)$ is linear: $\kappa(q) = Hq$, where $H = const,\ 0 < H < 1$, then the process is called mono-fractal. For Brownian motion H=0.5. The process $X(t)$ is called multi-fractal if function $\kappa(q)$ is nonlinear.

If the spectrum $F(\alpha)$ is estimated in a moving window, its evolution can give information on the variation in the structure of chaotic pulsations of the series. In particular, the position and width of the support of the spectrum $F(\alpha)$, i.e., the values $\alpha_{\min},\ \alpha_{\max},\quad \Delta\alpha = \alpha_{\max} - \alpha_{\min}$, and $\alpha^*(F(\alpha^*) = \max_{\alpha} F(\alpha))$ are characteristics of the noise. The value α^* can be called a generalized Hurst exponent. In the case of a mono-fractal signal, the quantity $\Delta\alpha$ should vanish and $\alpha^* = H$. As regards the value of $F(\alpha^*)$, it is equal to the fractal dimension of points in the vicinity of which the scaling relation (4) holds true. Usually $F(\alpha^*) = 1$, but there exist windows for which $F(\alpha^*) < 1$.

To estimate the singularity spectrum $F(\alpha)$, we used Detrended Fluctuation Analysis (DFA) [Kantelhardt et al., 2002]. All details are described in [Lyubushin, Sobolev, 2006; Lyubushin, 2007].

14.2.1.2 Spectral measure of synchronization

Spectral measure of synchronization $\lambda(\tau,\omega)$ is defined as a product of absolute values of canonical coherences [Lyubushin, 1998, 2007]:

$$\lambda(\tau,\omega)=\prod_{j=1}^{q}|v_j(\tau,\omega)| \tag{14.5}$$

Here q is the dimensionality of multiple time series, ω the frequency, τ the right-hand end time coordinate of moving time window which is composed of a certain number of adjacent samples, $v_j(\tau,\omega)$ the canonical coherence of j-th scalar component which describes the strength of linear relations of this component with all other components of multiple time series. The value of $|v_j(\tau,\omega)|^2$ is a generalization of the usual squared coherence spectrum between 2 scalar time series for the case when the 2nd series is multidimensional but not scalar. The inequality $0 \le |v_j(\tau,\omega)| \le 1$ takes place and the closer the value of $|v_j(\tau,\omega)|$ to unity, the stronger the linear relation between variations of j-th scalar component at the frequency ω within time window with coordinate τ and analogous variations of all other scalar components. Thus, the value $0 \le \lambda(\tau,\omega) \le 1$ describes the effect of coherent (synchronous, collective) behavior of all scalar signals included in the considered multiple time series.

Note that, by definition, the quantity $\lambda(\tau,\omega)$ lies in the interval [0, 1], and the closer its value to unity, the stronger the coherence between variations of the components of the multivariate series at the frequency ω. We should emphasize that the comparison of absolute values of the statistic $\lambda(\tau,\omega)$ is possible only for the same number q of simultaneously processed time series because, by virtue of formula (5), with increasing q, the value of $\lambda(\tau,\omega)$ decreases as the product of q values smaller than unity. If $q=2$, measure (5) is the ordinary squared modulus of the coherence spectrum.

To implement this method it is necessary to have a spectral matrix estimate within each time window. To calculate spectral matrix we used a vector autoregression model of 3rd order [Marple, 1987].

14.3 Synchronization of microseismic oscillations within minute range of periods

Figure 14.3 presents variations of generalized Hurst exponent α^* estimated within moving time windows of the 12 h length (1440 samples with 30 s time interval) taken with mutual shift of 1 h (120 samples) for 5 seismic stations with positions

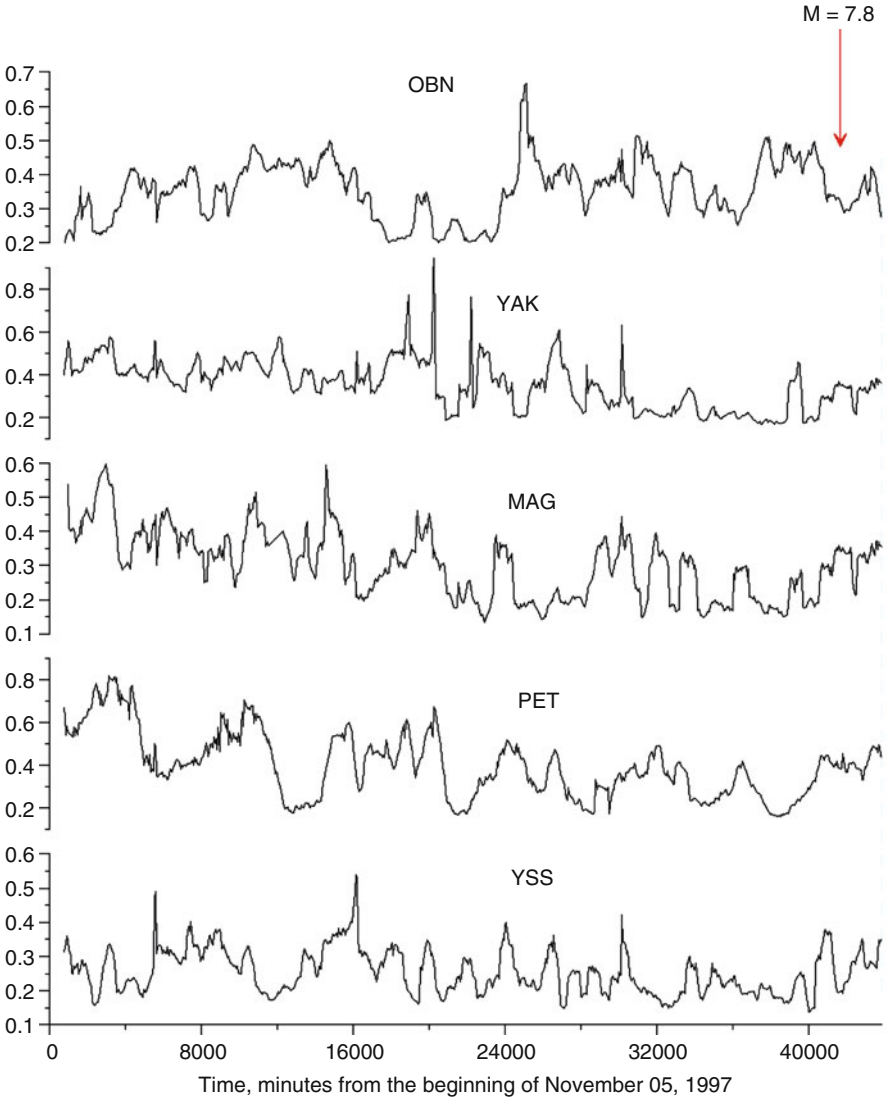

Fig. 14.3 Before the Kronotskii earthquake. Plots of the generalized Hurst exponent α^*realizing the maximum of the singularity spectrum of the micro-seismic background at all stations with the estimation in a moving 12 h wide time window with a shift of 1 h. The coordinate of the right-hand end of the moving time window is plotted on the time axis

presented in Fig. 14.1. Scale-depended trends following from tidal and temperature influences in DFA-technique were removed by local polynomials of 4^{th} order. We have taken an interval of 30 days length before the Kronotskii earthquake. A further analysis provides estimation of spectral measure of synchronization (5) for time series of α^*-variations (Fig. 14.3). The length of moving time window for obtaining

statistics $\lambda(\tau, \omega)$ was taken to be 109 samples. Because each α^*-value is obtained from time window of 12 h length with a shift of 1 h, this means that the length of time window for the measure (5) is (109-1)·1+12 = 120 h = 5 days.

Figure 14.4 presents time-frequency diagrams of statistics (5) for different combinations of stations. A main burst of coherence is concentrated within range of time marks 40000-42000 minutes, i.e., a few days before the earthquake. In the process of approaching of moving time window to the moment of the main shock the α^*-variations coherence decreased although still remained at the level which is

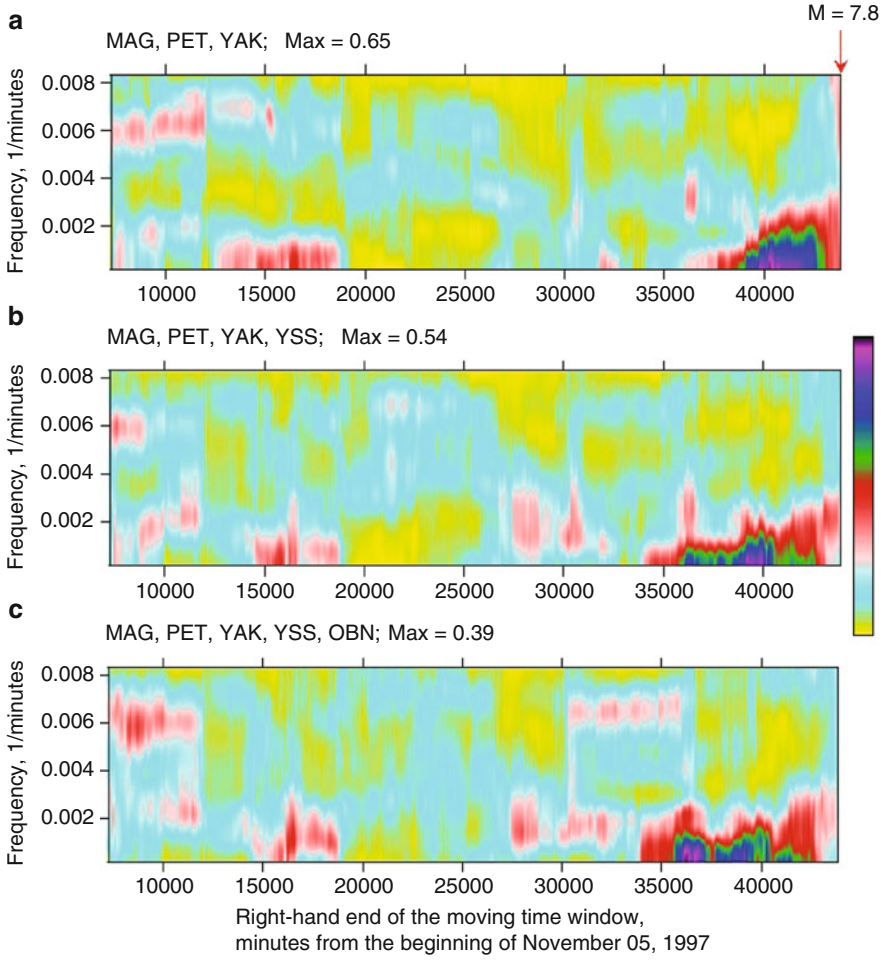

Fig. 14.4 Before the Kronotskii earthquake. Frequency–time diagrams of the evolution of the spectral measure of coherence of α^* variation spectral series with the estimation in the moving time window 109 samples (5 days) long for a successively increasing number of simultaneously analyzed stations. Maximum values of the coherence measure are shown in each diagram after the codes of the stations analyzed

higher than the background of statistical fluctuations. Time-frequency diagrams in Fig. 14.4 testify that the length of time span of "coherence spot" increases with increasing number of analyzed stations.

Series of diagrams $\lambda(\tau, \omega)$ were calculated to check the stability of the low frequency coherence pulsation in the vicinity of the time mark 40000 min by estimating the results of various combinations of three stations. Note that it is admissible to compare maximum values of the coherence measure because the number of simultaneously analyzed time series is the same. The highest peak of coherence (0.65) is observed for the MAG, PET, and YAK stations, at Kronotskii earthquake epicentral distances of 900, 350, and 2050 km, respectively; the peak is the lowest (0.32) for the OBN, ARU, and YAK stations, which are the farthest from the earthquake source (6800, 5900, and 2050 km, respectively). In all variants, the coherence measure experiences a pulsation in the neighborhood of the time mark 40000 corresponding to the observation interval November 29–December 3, 1997, i. e., three to seven days before the shock.

During data analysis before the Hokkaido earthquake, seismic records of stations ERM and MAJ were not used because ERM was not working the last 4 days before the shock, whereas MAJ was not working 7 days during time interval 2 weeks before the event. A similar analysis (with the same parameters as for Kronotskii earthquake data processing) combining multi-fractal singularity spectra estimates within moving time window of 12 h length with further application of spectral measure of synchronization to α^*-variations was applied. The main result of this analysis is

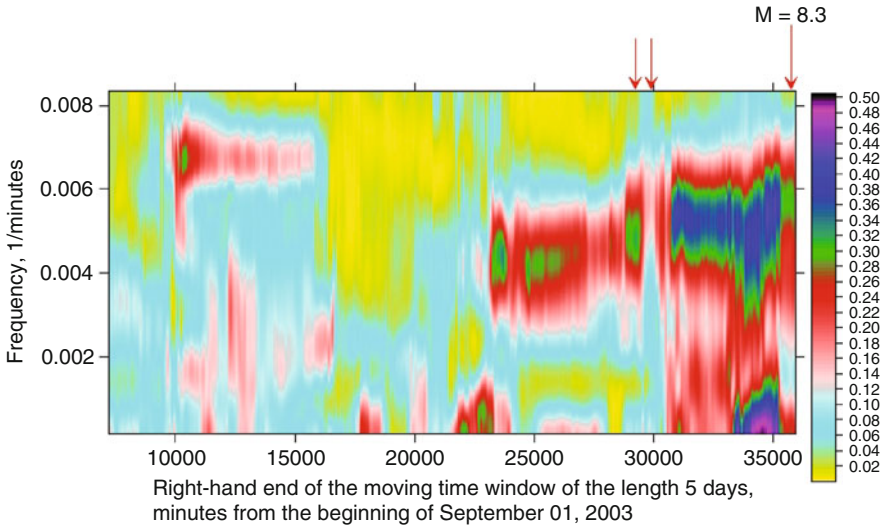

Fig. 14.5 Before the Hokkaido earthquake. Frequency–time diagrams of the evolution of the spectral measure of coherence of α^* variation spectral series with the estimation in the moving time window 109 samples (5 days) long for seismic stations YSS, MDJ, INC. Arrows indicate successive time moments of 2 remote earthquakes (M=6.6) and of Hokkaido earthquake (the last one)

that synchronization occurred 2 days before the Hokkaido event (interval 33000-35000 minutes from beginning of September 01, 2003). This synchronization covers range of periods from 3 h on. When different variants of 3 stations were tested, the strongest effect was observed for stations which are closest to the epicenter of future shock. Time-frequency diagram, $\lambda(\tau, \omega)$, for these stations (YSS, MDJ, INC) is presented in Fig. 14.5. The following 3 peculiarities of this diagram should be underlined: (1) synchronization at 3 h period (frequency ~ 0.005 min^{-1}) began 9 days before the event (time mark 23000 minutes); (2) the brightest synchronization within wide range of periods began 2 days before the shock (time marks 33000-35000 minutes); (3) the gap in synchronization scenario within interval 29000-31000 minutes of time marks is connected with 2 remote strong earthquakes (indicated by red arrows) with magnitude 6.6. The first one has epicenter [19.72°N, 95.46°E] and occurred on September 21 and the second one has epicenter [21.16°N, 71.67°W] and occurred 10 hours later, on September 22. The arrival of seismic waves from these earthquakes with different onset times to the analyzed stations disturbed the synchronization pattern.

14.4 Conclusion

Estimates of spectral measure for variations of either low-frequency (in minute range of periods) micro-seismic background oscillations or their generalized Hurst exponents detect synchronization effect on large areas, 2-5 days before strong earthquakes. This coherence effects between different stations manifest themselves on periods: for Kronotskii earthquakes – more than 6 hours, for Hokkaido – more than 3 hours, for Sumatra earthquake – within range 2-60 minutes. The coherence measure is increasing when it is calculated for the set of stations which are closer to the epicenter of future event.

References

Currenti G., C. del Negro, V. Lapenna, and L. Telesca (2005) Multifractality in local geomagnetic field at Etna volcano, Sicily (southern Italy) – Natural Hazards and Earth System Sciences, 5, 555–559, 2005

Feder J. (1989) Fractals. Plenum Press, New York, London

Kantelhardt J. W., Zschiegner S. A., Konscienly-Bunde E., Havlin S., Bunde A., and Stanley H. E. (2002) Multifractal detrended fluctuation analysis of nonstationary time series, Physica A, 316, 87–114, 2002.

Lyubushin A.A. (1998) Analysis of Canonical Coherences in the Problems of Geophysical Monitoring – Izvestiya, Physics of the Solid Earth, vol. 34, 1998, pp. 52-58. http://alexeylyubushin.narod/Canonical_Coherences_in_the_Problems_of_Geophysical_Monitoring.pdf

Lyubushin A.A., Pisarenko V.F., Bolgov M.V. and Rukavishnikova T.A. (2003) Study of General Effects of Rivers Runoff Variations – Russian Meteorology and Hydrology, 2003, No.7, pp. 59-68. http://alexeylyubushin.narod/Coherence_measures_of_rivers_runoff_time_series.pdf

Lyubushin A.A., Pisarenko V.F., Bolgov M.V., Rodkin M.V., and Rukavishnikova T.A. (2004) Synchronous Variations in the Caspian Sea Level from Coastal Observations in 1977–1991. – Atmospheric and Oceanic Physics, 2004, Vol. 40, No.6, pp. 737-746. http://alexeylyubushin.narod/Canonical_Coherences_of_Caspian_Sea_Level_Variations.pdf

Lyubushin A.A. and G.A. Sobolev (2006) Multifractal Measures of Synchronization of Microseismic Oscillations in a Minute Range of Periods – Izvestiya, Physics of the Solid Earth, vol.42, No.9, 2006, pp.734-744. http://alexeylyubushin.narod/Multifractal_Measures_of_Synchronization_of_Microseismic_Oscillations.pdf

Lyubushin A.A. (2007) Geophysical and ecological monitoring systems data analysis. Moscow, 'Nauka', 228 p. (in Russian). http://alexeylyubushin.narod/Geophysical_Monitoring_Systems_Data_Analysis_Book_Rus.pdf

Lyubushin A.A. and G.A. Sobolev (2007) Synchronization effects of microseismic background oscillations field before strong earthquakes – IUGG XXIV General Assembly "Earth: our changing planet", Perugia, Italy, July 02–13, 2007. Session SS005 "Earthquake Sources – Modeling and Prediction".

Marple S.L. (Jr.) (1987) Digital spectral analysis with applications. Prentice-Hall, Inc., Englewood Cliffs, New Jersey.

Nicolis G. and I. Prigogine (1989) Exploring Complexity. An introduction. W.H.Freeman and Company. New York, 1989.

Sobolev G.A. (2003) Evolution of Periodic Variations in the Seismic Intensity before Strong Earthquakes – Izvestiya, Phys. Solid Earth, 2003, vol.39, No.11, 2003, pp. 873–884.

Sobolev G.A. and A.A. Lyubushin (2006) Microseismic Impulses as Earthquake Precursors – Izvestiya, Physics of the Solid Earth, vol. 42, No.9, 2006, pp.721-733.

Sobolev G. A. and A. A. Lyubushin, "Microseismic Anomalies before the Sumatra Earthquake of December 26, 2004," Fiz. Zemli, No. 5, 3–16 (2007) [Izvestiya, Phys. Solid Earth 43, 341–353 (2007)].

Sobolev G. A., A. A. Lyubushin, and N. A. Zakrzhevskaya, "Asymmetric Impulses, Periodicities and Synchronization of Low-Frequency Microseisms," Vulkanol. Seismol., No. 2, 135–152 (2008).

Sobolev G.A. and A.A. Lyubushin (2007) Using Modern Seismological Data for Earthquake Precursors Detecting – Russian Journal of Earth Sciences, in press.

Telesca L., G. Colangelo, and V. Lapenna (2005) Multifractal variability in geoelectrical signals and correlations with seismicity: a study case in southern Italy – Natural Hazards and Earth System Sciences, 5, 673–677, 2005.

Chapter 15
Multifractal Parameters of Low-Frequency Microseisms

A. Lyubushin

15.1 Introduction

Low-frequency microseismic oscillations serve as an important source of information about processes proceeding in the crust, in spite of the fact that the main energy of these oscillations is caused by processes proceeding in the atmosphere and ocean, such as variations in the atmospheric pressure and the action of oceanic waves on the coast and shelf. The relation of low-frequency microseisms having periods of 5–500 s to the intensity of oceanic waves is comprehensively investigated in [Friedrich et al., 1998; Kobayashi and Nishida, 1998; Tanimoto et al., 1998; Tanimoto and Um, 1999; Ekstrom, 2001; Tanimoto, 2001; 2005; Berger et al., 2004; Kurrle and Widmer-Schnidrig, 2006; Stehly et al., 2006; Rhie and Romanowicz, 2004; 2006]. The reverse influence of low-frequency microseisms with still longer periods (from several tens to a few hundreds of minutes) on atmospheric pressure variations due to slow wave-like deformations of the lithosphere were investigated in [Lin'kov, 1987; Lin'kov et al., 1990; Petrova et al., 2007]. Actually, the Earth's crust is a medium propagating the energy from atmospheric and oceanic processes, and since the transmitting properties of the crust depend on its state, the statistical properties of microseisms reflect changes in lithospheric properties.

This basically simple idea of the use of low-frequency microseismic oscillations for monitoring the lithosphere, nevertheless, cannot be realized in a simple way. The main difficulty consists in a strong influence of numerous uncorrelated sources on the data. These sources are often diffusely distributed over the Earth's surface. Therefore, it is impossible in this case to investigate the transmitting properties of the lithosphere by controlling input actions and responses. Additionally, the division into "signal" and "noise" which is typical of the traditional methods used for data analysis, loses its

A. Lyubushin
Schmidt Institute of Physics of the Earth, Russian Academy of Sciences, 10 Bol'shaya Gruzinskaya, Moscow, Russia
e-mail: lyubushin@yandex.ru

V. de Rubeis et al. (eds.), *Synchronization and Triggering: from Fracture to Earthquake Processes*, GeoPlanet: Earth and Planetary Sciences 1,
DOI 10.1007/978-3-642-12300-9_15,

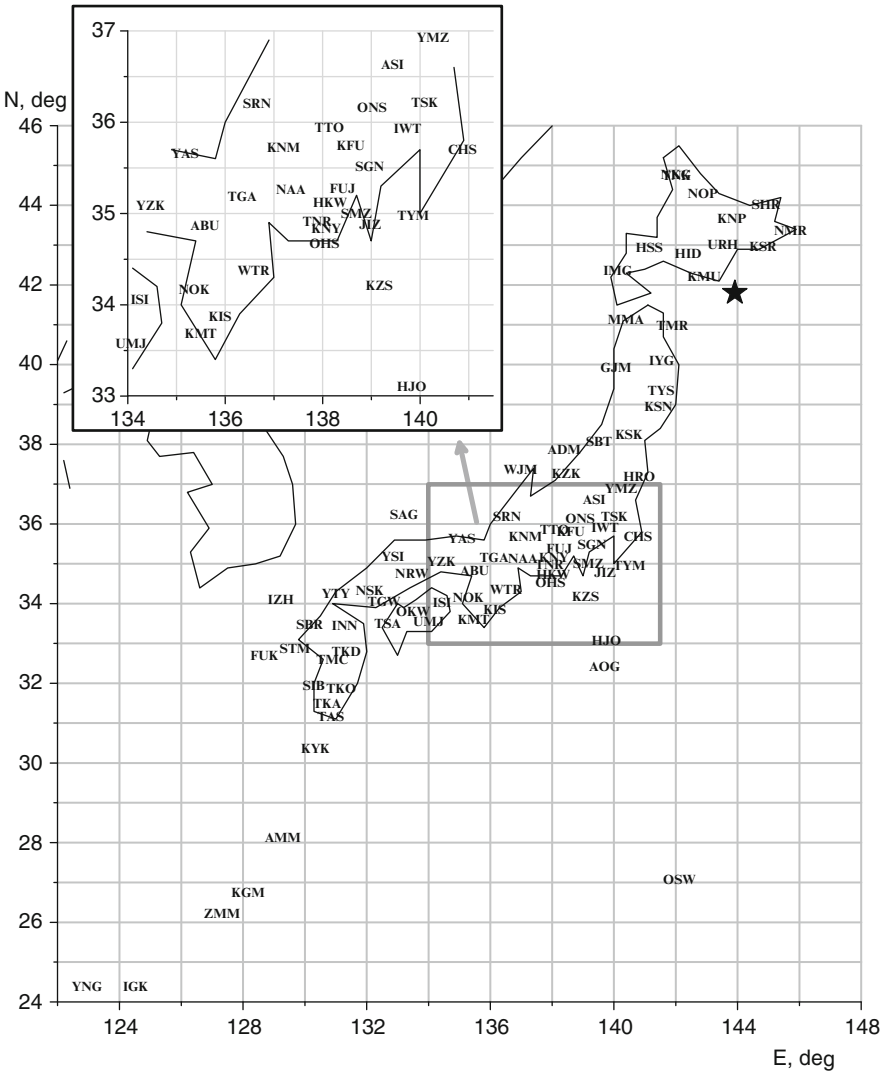

Fig. 15.1 Positions of 83 broadband seismic stations of the F-net network with their three-letter codes. The second letter of the code corresponds to the position of the station center. The inset in the upper left-hand corner shows the region of concentration of the stations in central Japan. The star marks the hypocenter of the September 25, 2003, earthquake (M = 8.3) off the Hokkaido coasts

sense when microseismic oscillations are processed. Only tidal variations in the amplitude of microseisms, as well as the arrivals and coda from the well-known strong earthquakes, can be related to "signals". For a long time, these signals have traditionally been used in geophysics. All other microseism variations relate to "noise".

If the terminology of orthogonal wavelet analysis is used, it will be quite sufficient to retain 1% of the maximum in module wavelet coefficients and nullify

all other coefficients in order to identify the signals listed above and remove noise [Lyubushin, 2008]. Evidently, such an approach is too wasteful, and the remaining 99% of information deserve more careful study. This raises the problem of investigating the statistical properties of low-frequency microseismic noise. Spectral analysis traditionally used in the geophysical practice for investigating noise is inapplicable in this case, because noise does not contain either monochromatic components or narrow-band signals. Therefore, in this paper, we use for analysis the apparatus of multifractal singularity spectra [Feder, 1988; Mandelbrot, 1982]. This method allows the most complete description of the noise structure. To analyze geophysical time series, the estimates of singularity spectra were used in [Kantelhardt et al., 2002; Currenti et al., 2005; Ramirez-Rojas et al., 2004; Ida et al., 2005; Telesca et al., 2005; Lyubushin and Sobolev, 2006; Lyubushin, 2007; 2008].

This paper continues the cycle of works on the analysis of low-frequency microseismic oscillations and the search for new precursors of strong earthquakes on their basis [Sobolev, 2004; Sobolev et al., 2005; 2008; Sobolev and Lyubushin, 2006; 2007; Lyubushin and Sobolev, 2006; Lyubushin, 2008]. The main feature of this work is the use of long-term observations of low frequency microseisms based on the information from 83 seismic stations of the F-net broadband network (Japan) over the period from the beginning of 1997 through June 2008. Such large data volume allowed us to investigate long-period trends of the evolution of singularity spectrum parameters averaged both over the stations of the entire network and over some subgroups of these stations.

15.2 Initial Data: F-net Network

Data of the F-net broadband seismic network are freely accessible on the internet at the address: http://www.hinet.bosai.go.jp/fnet. The positions of all 83 stations of the network are shown in Fig. 15.1. However, when the network started to function in 1997, it had only 17 stations. Subsequently, new stations were put into operation (especially large number of stations in 2001), but at the same time, some of the old stations (that had been in operation since 1997) were shut down. The data to be analyzed, i.e., vertical components with a time step of 1 s (LHZ records) contain intervals with gaps and incorrect data (such as constant zero values) due to malfunctions of measuring and recording instrumentation.

Data were loaded in the form of 2-month long time fragments. For each station, the loaded record began at 00:00:00 of the following day (month-day format): 01.01, 03.01, 05.01, 07.01, 09.01, and 11.01. If inside the 2-month fragment of data, the record began not from these standard initial time marks, such a record was rejected. Small gaps, no longer than 2 h, were filled in accordance with the signal behavior to the right and to the left from the gap in time intervals of the same length as the gap length. If the record contained longer gaps and malfunctions, we considered only the initial part of such a record (preceding the first long gap). Such a choice corresponds to the rules of functioning of the F-net database, according to which the user has the

right to load an indefinitely large amount of information, but in the form of discrete portions, whose volume must not exceed 50 MB.

As a result, we accumulated an array of seismic records divided into 2-month time fragments from the beginning of 1997 through June 2008. Each 2-month fragment contains records from different stations that do not have long gaps and begin synchronously. However, the lengths of these records can be different, depending on the presence of large gaps and long faulty interval. Nevertheless, for almost each 2-month fragment, there existed a fairly large number of stations ensuring a complete and continuous covering of the entire fragment length by their records. Additionally, records with a time step of 1 min were formed for each 2-month fragment of the initial 1-s data through the calculation of consecutive average values over 60 samples.

15.3 Parameters of the Singularity Spectrum of Low-frequency Microseisms

Below, we briefly describe the technical details of the used singularity spectrum estimates [Lyubushin and Sobolev, 2006; Lyubushin, 2007]. The elimination of scale-dependent trends by local polynomials is an important element of this estimate. Such a procedure makes it possible to get rid of some trends (in our case, tidal and temperature variations) and investigate only relatively high-frequency pulsations of a series, i.e., precisely the noise component.

Let $X(t)$ be a random process. Define the range $\mu_X(t,\delta) = \max\limits_{t\le s\le t+\delta} X(s) - \min\limits_{t\le s\le t+\delta} X(s)$ as the measure $\mu_X(t,\delta)$ of the behavior of the signal $X(t)$ in the interval $[t, t+\delta]$ and calculate the average modulus of such measures raised to the power q:

$$M(\delta, q) = M\{(\mu_X(t,\delta))^q\} \tag{15.1}$$

A random process is scale-invariant if $M(\delta,q) \sim |\delta|^{\kappa(q)}$, i.e., there exists the limit:

$$\kappa(q) = \lim_{\delta\to 0} \frac{\ln M(\delta,q)}{\ln|\delta|} \tag{15.2}$$

If the dependence $\kappa(q)$ is linear, $\kappa(q) = Hq$, where $H = const,\ 0 < H < 1$, then the process is monofractal [Taqqu, 1988].

For calculating the function $\kappa(q)$ from a finite sampling from the time series $X(t),\ t = 1,\ldots,N$, it is possible to apply the DFA method [Kantelhardt et al., 2002]. Let s be the number of samples associated with the varied scale δ_s: $\delta_s = s\cdot\Delta t$. We divide the sampling into nonoverlapping small intervals, s samples in length,

$$I_k^{(s)} = \{t:\ 1 + (k-1)\cdot s \le t \le k\cdot s,\quad k = 1, ..., [N/s]\} \tag{15.3}$$

and let

$$y_k^{(s)}(t) = X((k-1)s + t), \quad t = 1, \ldots, s \tag{15.4}$$

be the part of the time series $X(t)$ corresponding to the interval $I_k^{(s)}$. Let $p_k^{(s,m)}(t)$ be a polynomial of order m fitted by the least squares method to the signal $y_k^{(s)}(t)$. Consider deviations from the local trend

$$\Delta y_k^{(s,m)}(t) = y_k^{(s)}(t) - p_k^{(s,m)}(t), \quad t = 1, \ldots, s \tag{15.5}$$

and calculate the value

$$Z^{(m)}(q,s) = \left(\sum_{k=1}^{[N/s]} (\max_{1 \le t \le s} \Delta y_k^{(s,m)}(t) - \min_{1 \le t \le s} \Delta y_k^{(s,m)}(t))^q \Big/ [N/s] \right)^{1/q} \tag{15.6}$$

which will be regarded as an estimate for $(M(\delta_s, q))^{1/q}$. Now, we will define the function $h(q)$ as the coefficient of linear regression between the values $\ln(Z^{(m)}(q,s))$ and $\ln(s)$: $Z^{(m)}(q,s) \sim s^{h(q)}$. It is evident that $\kappa(q) = qh(q)$, and for a monofractal process $h(q) = H = const$.

After the determination of the function $h(q)$, the next step in the multifractal analysis [Feder, 1988] is the calculation of the singularity spectrum $F(\alpha)$, which is the fractal dimension of the time moments τ_α, which have the same value of the local Holder–Lipshitz exponent: $\lambda(t) = \lim_{\delta \to 0} \frac{\ln(\mu(t,\delta))}{\ln(\delta)}$, i.e., $\lambda(\tau_\alpha) = \alpha$. The standard approach consists in the calculation of the Gibbs statistical sum

$$W(q,s) = \sum_{k=1}^{[N/s]} (\max_{1 \le t \le s} \Delta y_k^{(s,m)}(t) - \min_{1 \le t \le s} \Delta y_k^{(s,m)}(t))^q \tag{15.7}$$

and the determination of the mass indicator $\tau(q)$ from the condition $W(q,s) \sim s^{\tau(q)}$, after which the spectrum $F(\alpha)$ is calculated by the formula

$$F(\alpha) = \max \{ \min_q (\alpha q - \tau(q)),\ 0 \} \tag{15.8}$$

Comparing (15.6) and (15.7), it is easy to see that $\tau(q) = \kappa(q) - 1 = qh(q) - 1$. Thus, $F(\alpha) = \max \{ \min_q (q(\alpha - h(q)) + 1,\ 0 \}$.

If the singularity spectrum $F(\alpha)$ is estimated in a moving time window; its evolution provides information about changes in the noise structure. In particular, the position and width of the support of the spectrum $F(\alpha)$, i.e., the values $\alpha_{\min},\ \alpha_{\max},\quad \Delta\alpha = \alpha_{\max} - \alpha_{\min}$, and α^* ($F(\alpha^*) = \max_\alpha F(\alpha)$) are the characteristics of noise. The quantity α^* is called the generalized Hurst exponent. For a monofractal signal, the value of $\Delta\alpha$ must be zero, and $\alpha^* = H$. Usually, $F(\alpha^*) = 1$, but

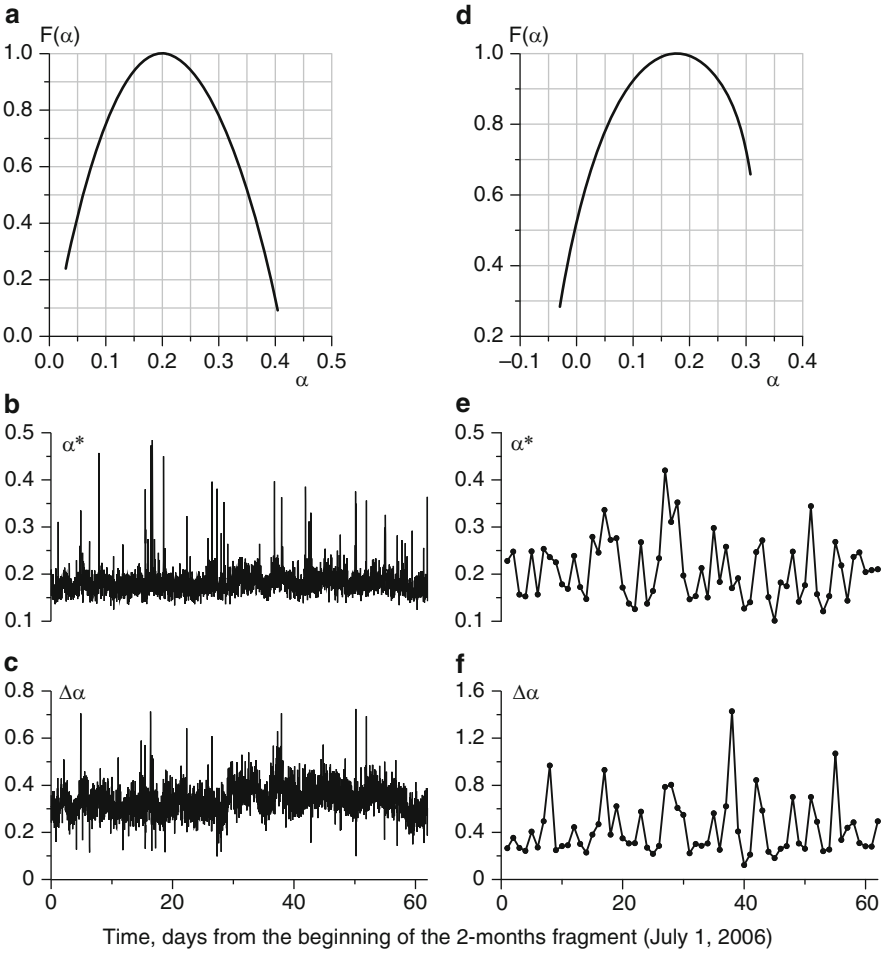

Fig. 15.2 Plots showing estimates for the singularity spectrum $F(\alpha)$ and variations in its parameters: the generalized Hurst exponent α^* and the singularity spectrum support width $\Delta\alpha$, at the KSK station for the 2-month fragment (July 1–August 31, 2006): (**a**), (**b**), and (**c**) for 1-s data in the consecutive intervals 30 min long (1800 samples); (**d**), (**e**), and (**f**) for 1-min data in the consecutive intervals 24 h long (1440 samples); (a) and (d) are presented for one of the intervals specified above

there exist windows for which $F(\alpha^*)<1$. In the general case, $F(\alpha^*)$ is equal to the fractal dimension of the multifractal measure support [Feder, 1988].

In the calculation of $\Delta\alpha$ and α^*, we were guided by the following considerations. The exponent q was varied within the interval $q \in [-Q,\ +Q]$, where Q is a certain sufficiently large number, for example, $Q = 10$. For each value of α within the interval $\alpha \in [A_{\min},\ A_{\max}]$, where $A_{\min} = \min\limits_{q\in[-Q,+Q]} \frac{d\tau(q)}{dq}$, and $A_{\max} = \max\limits_{q\in[-Q,+Q]} \frac{d\tau(q)}{dq}$, we calculated the value $\tilde{F}(\alpha) = \min\limits_{q\in[-Q,+Q]} (\alpha q - \tau(q))$. If the value of α is close to $A_{\min}$ then $\tilde{F}(\alpha)<0$, and this value is unsuitable as an estimate of the singularity

spectrum, which must be nonnegative. However, beginning from a certain α, the value $\tilde{F}(\alpha)$ becomes non-negative, and this condition defines the $\alpha_{\min}$ value. At a further α increase, the value $\tilde{F}(\alpha)$ increases, reaches its maximum when $\alpha = \alpha^*$ then begins to decrease, and finally attains a certain value $\alpha_{\max} < A_{\max}$, at which $\tilde{F}(\alpha)$ again becomes negative if $\alpha > \alpha_{\max}$. Thus, $F(\alpha) = \tilde{F}(\alpha)$ provided that $\tilde{F}(\alpha) \geq 0$, which determines the interval of the singularity spectrum support $\alpha \in [\alpha_{\min},\ \alpha_{\max}]$. The derivative $\frac{d\tau(q)}{dq}$ is calculated numerically from the values $\tau(q),\ q \in [-Q,\ +Q]$, and the accuracy of its calculation is of little significance, because this derivative is used for a rough determination of an a priori interval of possible exponents q.

Below, in the analysis of low-frequency microseisms, we used the estimates of singularity spectra in the following successive nonoverlapping time windows: for the initial 1-s data, in the window 30 min long (1800 samples), and for 1-min data, in the window 24 h long (1440 samples). In the first case, local trends were removed by fourth-order polynomials, and in the second case, by eighth-order polynomials. Additionally, for estimating the spectral measure of coherence between variations in the singularity spectra parameters for 1-min data, we used the moving time window 12 h long (720 samples) with the shift by 1 h (60 samples). In this case, scale-dependent trends were removed by local fourth-order polynomials.

Most of the attention will be concentrated on changes in two parameters of the singularity spectrum, namely, the generalized Hurst exponent α^* and the singularity spectrum support width $\Delta\alpha$. The quantity α^* characterizes the most typical and often met Holder–Lipshitz exponent, whereas $\Delta\alpha$ reflects the diversity of the random behavior of the signal, and, as will be discussed below, this quantity is a peculiar measure for the number of hidden degrees of freedom of a stochastic system.

15.4 Variations in the Singularity Spectrum Support Width

Figure 15.2 shows examples of the plots of estimates of the singularity spectrum $F(\alpha)$ in one of the windows for 1-s (Fig. 15.2a) and 1-min (Fig. 15.2d) data obtained at one of the stations of the network (KSK). In addition, the plots of variations in parameters α^* and $\Delta\alpha$ during the 2-month fragment (July 1–August 31, 2006) for 1-s (Figs. 15.2b, 15.2c) and 1-min (Figs. 15.2e, 15.2f) are given below each plot of $F(\alpha)$. The sharp outliers in Figs. 15.2b and 15.2c reflect the influence of arrivals from different close and remote earthquakes. These outliers are absent in Figs. 15.2e and 15.2f due to double averaging: first, in passing from the 1-s to 1-min time step, and then in passing from the window length 30 min to the window length 24 h.

Consider the set of estimates of parameter $\Delta\alpha$ for 1-s data (Fig. 15.2c). For each 30-min window in which these estimates were obtained, there exist a certain number of stations supporting these estimates by their data. The number of such stations changes from one 2-month fragment to another and inside each fragment. We will calculate for each 30-min window the median of $\Delta\alpha$ values over all stations, whose data are suitable for analysis. The median is a robust (stable with respect to the outliers) alternative to an ordinary average value.

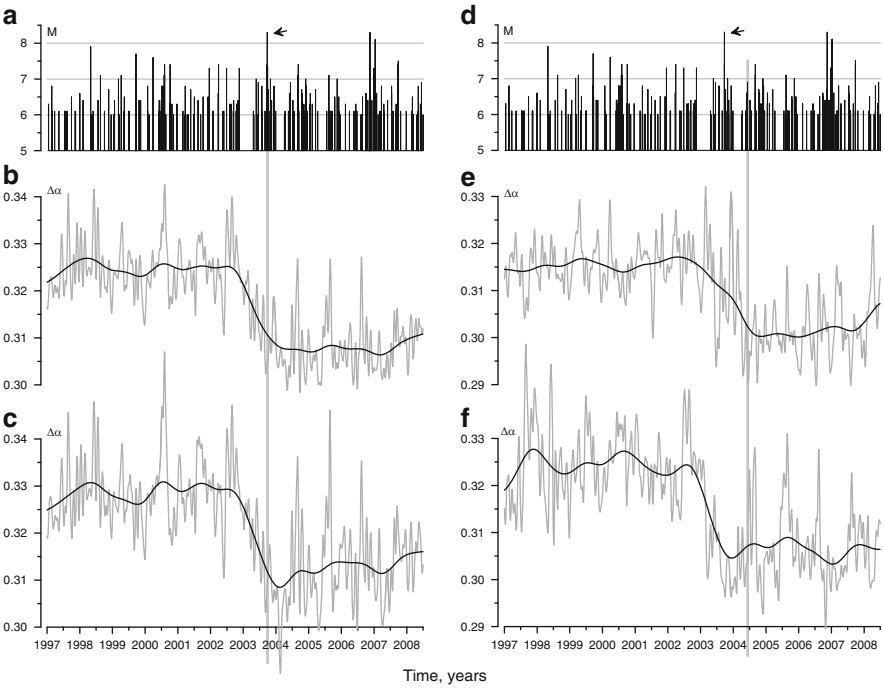

Fig. 15.3 (**a**), (**d**). Identical sequences of magnitudes ($M \geq 6$) of seismic events in the rectangular region between 20°–60° N and 120°–160° E. (**b**), (**c**), (**e**), and (**f**) Results of the Gaussian smoothing of variations in the median of the singularity spectrum support width $\Delta\alpha$ for 1-s data in the consecutive intervals 30 min long: gray lines show the smoothing with a radius of 13 days and the bold black lines, with a radius of 0.5 yr. The median is determined for: (**b**) all 83 stations of the network; (**c**) 41 central stations ($34° \leq 39°$ N); (**e**) 17 northern stations ($\geq 39°$ N); (**f**) 25 southern stations ($\leq 34°$ N). The vertical gray lines with the arrows mark the time moment of the Hokkaido earthquake of September 25, 2003 ($M = 8.3$)

The sequence of medians $\Delta\alpha$ over all stations will form one continuous time series, whose total duration is 11.5 yr and the time step is 30 min. This time series is a certain integral statistical characteristic of the field of the microseism. Let us consider the behavior of this series at different types of smoothing. Gaussian trends with definite optimal properties are chosen as the method of smoothing [Hardle, 1989]. The following quantity:

$$\bar{X}(t|H) = \int_{-\infty}^{+\infty} X(t + H\xi) \cdot \psi(\xi)\, d\xi \Big/ \int_{-\infty}^{+\infty} \psi(\xi)\, d\xi \cdot \psi(\xi) = \exp(-\xi^2) \qquad (15.9)$$

will be called the Gaussian trend $\bar{X}(t|H)$ of the signal $X(t)$ with the parameter (radius) of smoothing $H > 0$.

For time series with discrete times, quantity (15.9) can be efficiently calculated with the use of the fast Fourier transform. This method of averaging was applied to the investigation of microseisms in [Sobolev and Lyubushin, 2006; Lyubushin, 2007].

According to formula (15.9), the average value roughly relates to the interval with the center at the point t with the radius H.

Two values of the radius: $H = 13$ days and $H = 0.5$ yr, were used for smoothing the $\Delta\alpha$ medians. The results of smoothing the medians over all stations are presented in Fig. 15.3b: the plots of smoothing with the radii 13 days and 0.5 yr are shown by the gray and bold black lines, respectively. The synchronous sequence of magnitudes ($M \geq 6$) of seismic events in the rectangular region $20^\circ \leq 60^\circ$ N and $120^\circ \leq 160^\circ$ E is presented in Fig. 15.3a. In this figure, the vertical gray line with the arrow indicates the time moment of the Hokkaido earthquake of September 25, 2003 ($M = 8.3$).

An important feature of the behavior of the $\Delta\alpha$ value smoothed with $H = 0.5$ yr (Fig. 15.3b) is its considerable drop, which began early in 2003, half a year before the Hokkaido event. The average level of the parameter attained after this event did not return to its previous value. Additionally, one should pay attention to a clearly pronounced annual periodicity in variations of the value smoothed with the radius $H = 13$ days (gray line in Fig. 15.3b): an outburst of this value, as a rule, falls on July–August, which is especially clearly seen in 2000, 2002, and 2004–2006.

To check the stability of the result obtained, i.e., a decrease in the average value of $\Delta\alpha$, analogous estimates were calculated for some stations of the network: for 41 central stations with latitudes from 34° to 39° N (Fig. 15.3c); for 17 northern stations with latitudes $\geq 39^\circ$ N (Fig. 15.3e); and for 25 southern stations with latitudes $\leq 34^\circ$ N (Fig. 15.3f). Figure 15.3d is identical to Fig. 15.3a and is presented here for convenience of comparing Figs. 15.3e and 15.3f with the seismic regime.

It is seen from Figs. 15.3c, e, and f that the average value of $\Delta\alpha$ decreases independently of the set of stations, for which it is calculated. The annual periodicity at the smoothing with the radius $H = 13$ days (Figs. 15.3b, 15.3f) remains nearly the same as for all stations (Fig. 15.3b). Note also that after the Hokkaido earthquake, annual variations in $\Delta\alpha$ (Figs. 15.3b, c, f) became more clearly pronounced, whereas the annual periodicity is pronounced less clearly for the northern stations.

15.5 Variations in the Generalized Hurst Exponent

We will now consider the median of estimates for the generalized Hurst exponent α^* obtained from different stations for 1-min data (Fig. 15.2e). The median is calculated by the same method as in the preceding section, but instead of the 30-min window, the 24-h window (1440 minute samples) is used. As a result, we obtain the time series of the α^* medians, whose duration is 11.5 yr and the time step is 24 h. This series is smoothed according to formula (15.9) with the radius $H = 13$ days. The result is presented in Fig. 15.4. Just as in Fig. 15.3, Figs. 15.4a and d are also identical to each other and depict the sequence of magnitudes of strong events in the rectangular vicinity of Japan islands. Figures 15.4b, c, d, and f show the plots of smoothed values of the α^* median calculated, respectively, for all 83 stations of

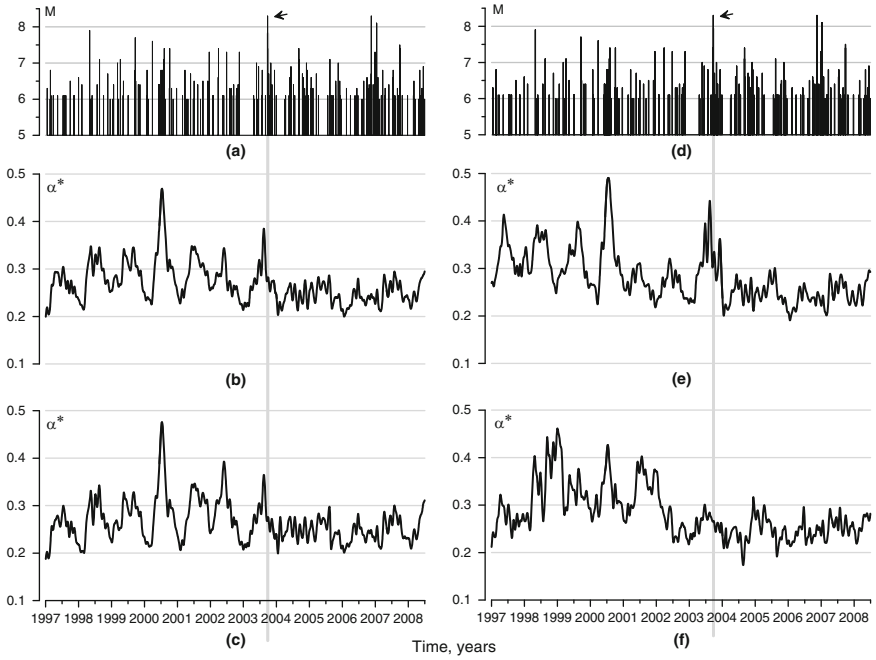

Fig. 15.4 (**a**), (**d**) Identical sequences of magnitudes ($M \geq 6$) of seismic events in the rectangular region between 20°–60° N and 120°–160° E. (**b**), (**c**), (**e**), and (**f**) Results of the Gaussian smoothing of variations in the median of the generalized Hurst exponent α^* for 1-min data in the consecutive intervals 24 h long with the radius of smoothing 13 days. The median is determined for: (**b**) all 83 stations of the network; (**c**) 41 central stations (34°–39° N); (**e**) 17 northern stations ($\geq$39°N); and (f) for 25 southern stations ($\leq$ 34° N). The vertical gray lines with the arrows mark the time moment of the Hokkaido earthquake of September 25, 2003, ($M = 8.3$)

the network, consisting of 41 central stations, 17 northern stations, and 25 southern stations.

The main feature of the plots presented in Fig. 15.4 is the behavior of the seasonal component of the variations. This component is clearly pronounced before the Hokkaido event (to a lesser degree for the southern stations (Fig. 15.4f)) but decreases afterwards.

15.6 Variations in the Products of Cluster Canonical Correlations

This and the next sections of the paper will be devoted to the investigation of measures of correlation and coherence between variations in both the support width $\Delta\alpha$ and the generalized Hurst exponent α^* estimated for 1-min data for different parts of the network. The choice of 1-min data for this purpose was dictated by the circumstance that, based on experience, the lower the frequency of the variations in

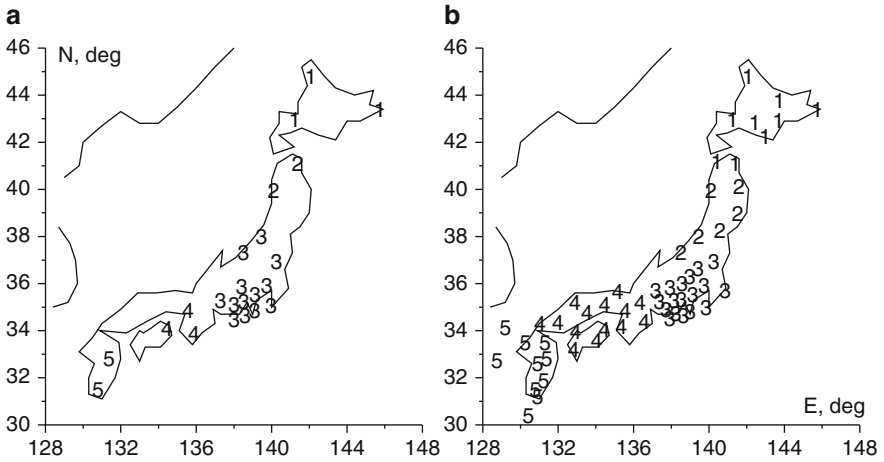

Fig. 15.5 Examples of the division of stations, according to their positions, into five clusters for two 2-month fragments: (**a**) for the fragment September 1– October 31, 1998, 23 stations; and (**b**) for the fragment July 1 – August 31, 2002, 57 stations. The stations belonging to the same cluster have identical numbers

singularity spectrum parameters, the greater the amount of coherence effects that are observed in them. The main correlations and coherences during the investigation of 1-s data are caused by a trivial presence of traces of arrivals from large and moderate earthquakes, which is of weak interest.

In our case, it is necessary to construct statistics that would more or less objectively reflect an increase or a decrease in the total correlation or coherence of the behavior of singularity spectrum parameters during the entire interval of observations (1997–2008), in spite of the fact that some stations ceased operation long before the end of the analyzed time interval, and some stations started to operate after its beginning. In addition, due to malfunctions of the instrumentation and recording systems, data from some or other station can be absent in the 2-month fragment under consideration, in spite of their presence in the preceding and subsequent fragments. The fragmentary character of the data from any station is a substantial methodological barrier for a direct application of multidimensional spectral coherence measures [Lyubushin, 1998; 2007; 2008; Lyubushin and Sobolev, 2006; Sobolev and Lyubushin, 2007] to the analysis of relations between the readings of different stations, because the synchronism and continuity of data are required for calculating the statistics of coherence.

However, the presence of a large number of stations allows us to overcome this difficulty by considering cluster measures of the multidimensional correlation and coherence. The essence of this approach is as follows: only the stations which possess continuously recorded data throughout the entire 2-month fragment are considered. Further, these stations are grouped to always form the same number of spatial clusters. Below, the number of clusters was assumed to be five, i.e., all stations with continuous records during the 2-month fragment under consideration

are always divided into five clusters in accordance with the spatial positions of the stations. The number of clusters (five) was chosen, because this number is not too large but sufficiently large for a more or less uniform covering of the seismically active territory under consideration (Japan's islands). The use of the same number of clusters for all 2-month fragments eliminates the influence of dimensionality on the values of the measures of correlation or coherence and allows their comparison with each other, regardless of the number of suitable stations in some or other 2-month fragment.

Figure 15.5 shows two examples of the automatic division of the network stations with continuous records for 2-month fragments into five clusters. The stations belonging to the same spatial cluster are designated by the same numeral (cluster number). Stations were automatically divided into five clusters by using the method of hierarchical clusterization with the "far neighbor" metric [Duda and Hart, 1973]. The use of this metric instead of the often used "nearest neighbor" metric makes it possible to obtain compact "rounded" clusters and avoid long "chain-like" clusters. The characteristic linear scale of the clusters obtained varied from 120 to 350 km.

When cluster measures are considered, solitary stations must be excluded from the analysis, because during the automatic division, they will always form individual clusters consisting of one element. In our case, there were six such stations located on the remote islands, and they could be excluded from the analysis through restricting the stations' latitude to not less than 30° N (Fig. 15.1).

After the division of stations into clusters, we calculated the average values of parameters $\Delta\alpha$ and α^* in each time window (equal in this case to 24 h) for the stations included in the same cluster. Thus, independently of the number of suitable stations in the 2-month fragment, after the clusterization, we always obtained two 5-dimensional time series of variations in the average cluster values of $\Delta\alpha$ and α^*. Such a method makes it possible, on the one hand, to take into account the contributions of stations located in different subregions of a seismically active region and, on the other hand, to compensate for the fragmentary character of data caused by instrumental malfunctions.

We should stress once more that both the positions of the cluster centers and the number of stations in each cluster vary, as a rule, from one 2-month fragment to another. Only two factors remain unchanged: (15.1) the number of the output average values of $\Delta\alpha$ and α^* is always equal to five, and (15.2) the clusters more or less uniformly cover the territory under investigation. These circumstances allow us to consider the multidimensional measures of the correlation or coherence between the components of the obtained 5-dimensional time series as an integral measure reflecting the general correlation of changes in the multifractal characteristics of the field of low-frequency microseismic noise.

In order to obtain a multidimensional measure of the correlation of the average values of $\Delta\alpha$ or α^* corresponding to a chosen 2-month fragment, we will use the Hotelling construction of canonical correlations [Hotelling, 1936; Rao, 1965]. Let $x_j(t),\ j = 1, \ldots, m$ be an m-dimensional time series, and $t = 1, ..., N$ be discrete time. In our case, $m = 5$, x_j are the average cluster values of $\Delta\alpha$ or α^*, and t is the

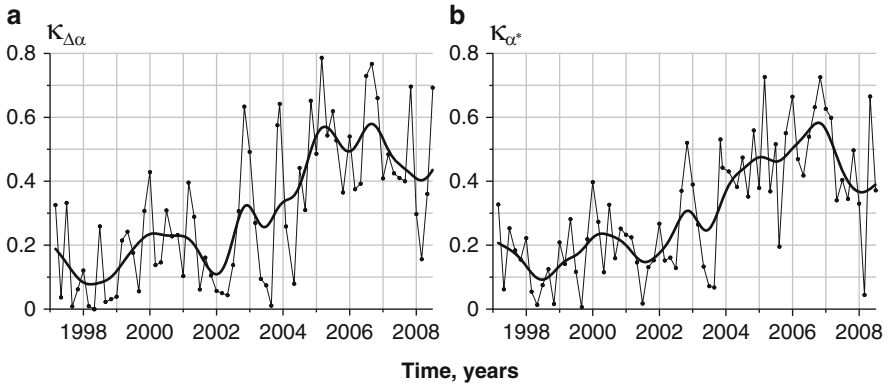

Fig. 15.6 Plots of variations in the product of moduli of canonical correlations (**a**) $\kappa_{\Delta\alpha}(\xi)$ and (**b**) $\kappa_{\alpha^*}(\xi)$ between the average values of the singularity spectrum support width $\Delta\alpha$ and the generalized Hurst exponent α^* calculated inside five spatial clusters of stations for 2-month fragments. The singularity spectra were calculated for 1-min data in the consecutive time intervals 24 h long. The bold lines are results of the Gaussian smoothing with the radius of averaging 0.5 yr

index numbering the consecutive days inside the 2-month fragment. Let us select the component with the number k and consider the regression model of the influence of all the other components on the selected component x_k

$$x_k(t) = y_k(t) + \varepsilon_k(t), \quad y_k(t) = \sum_{j=1,\, j\neq k}^{m} \gamma_j^{(k)} \cdot x_j(t) \tag{15.10}$$

The regression coefficients $\gamma_j^{(k)}$ will be found from the condition of the minimum of the sum of squared residuals $\sum_{t=1}^{N} \varepsilon_k^2(t)$ or the sum of moduli (robust variant) $\sum_{t=1}^{N} |\varepsilon_k(t)|$. After that, we will calculate the correlation coefficient μ_k between the selected component $x_k(t)$ and the obtained regression contribution $y_k(t)$. The quantity μ_k is the canonical correlation of the k-th component with respect to all other components. We perform these calculations successively for all $k = 1, \ldots, m$ and then determine the quantity

$$\kappa = \prod_{k=1}^{m} |\mu_k| \tag{15.11}$$

It is obvious that $0 \leq \kappa \leq 1$ and the closer the quantity (15.11) to unity, the stronger the mutual relation of the variations in the components of the multidimensional time series $x_j(t)$ to each other. Having calculated quantities (15.11) for the average cluster values of $\Delta\alpha$ and α^* for all 2-month fragments, we will obtain the two sequences, $\kappa_{\Delta\alpha}(\xi)$ and $\kappa_{\alpha^*}(\xi)$, where ξ is the time mark corresponding to the end of the 2-month fragment. The plots of these values are presented in Fig. 15.6 (thin lines with circles).

It is seen from these plots that, in spite of considerable fluctuations, the measure of correlation generally rises for both $\Delta\alpha$ and α^*. Let us smooth the dependences $\kappa_{\Delta\alpha}(\xi)$ and $\kappa_{\alpha^*}(\xi)$ by the Gaussian kernel according to formula (15.9) with the radius of averaging $H = 0.5$ yr. The results of the calculation of the Gaussian trends are presented in Fig. 15.6 as bold lines. A general tendency toward an increase in the measures of correlation after 2003 is seen. After the Hokkaido earthquake, the average values of correlation measures did not return to their level before 2003. Consequently, it can be inferred that the 2003 earthquake led to a prolonged increase in the average correlation of the fluctuations of the multifractal parameters of the field of low-frequency microseismic noise.

15.7 Variations in the Cluster Spectral Measure of Coherence

The measure of correlation (15.11) relates to the entire 2-month fragment under consideration and does not discriminate between variation frequencies. At the same time, the decomposition of this measure over different frequency bands and the stability of the correlation inside a 2-month fragment are of interest. To answer these questions, it is necessary to replace the product of the canonical correlations (15.11) by the spectral measure of coherence proposed in [Lyubushin, 1998], which was used, among other purposes, for the analysis of low-frequency microseisms [Lyubushin and Sobolev, 2006; Sobolev and Lyubushin, 2007; Sobolev et al., 2008; Lyubushin, 2008]. Numerous examples of the application of this measure not only in the physics of the solid Earth, but also in hydrology, meteorology, and climatic investigations are presented in [Lyubushin, 2007]. The same work contains all technical details of the calculations, which are omitted here.

The spectral measure of coherence $\lambda(\tau,\omega)$ is constructed as the module of the product of component-bycomponent canonical coherences

$$\lambda(\tau,\omega) = \prod_{j=1}^{m} |v_j(\tau,\omega)| \tag{15.12}$$

Here, $m \geq 2$ is the total number of jointly analyzed time series; ω is frequency; τ is the time coordinate of the right-hand end of the moving time window consisting of a definite number of neighboring samples; and $v_j(\tau,\omega)$ is the canonical coherence of the j-th scalar time series, which describes the strength of coupling of this series with all other series. The quantity $|v_j(\tau,\omega)|^2$ is the generalization of the ordinary squared spectrum of coherence between two signals for the case when the second signal is not scalar but vector. The inequality $0 \leq |v_j(\tau,\omega)| \leq 1$ is fulfilled, and the closer the value of $|v_j(\tau,\omega)|$ to unity, the stronger the linear relation of variations at the frequency ω in the time window with the coordinate τ of the j-th series to analogous variations in all other series. Accordingly, the quantity $0 \leq \lambda(\tau,\omega) \leq 1$, due to its construction, describes the effect of the cumulative coherent (synchronous, collective) behavior of all signals.

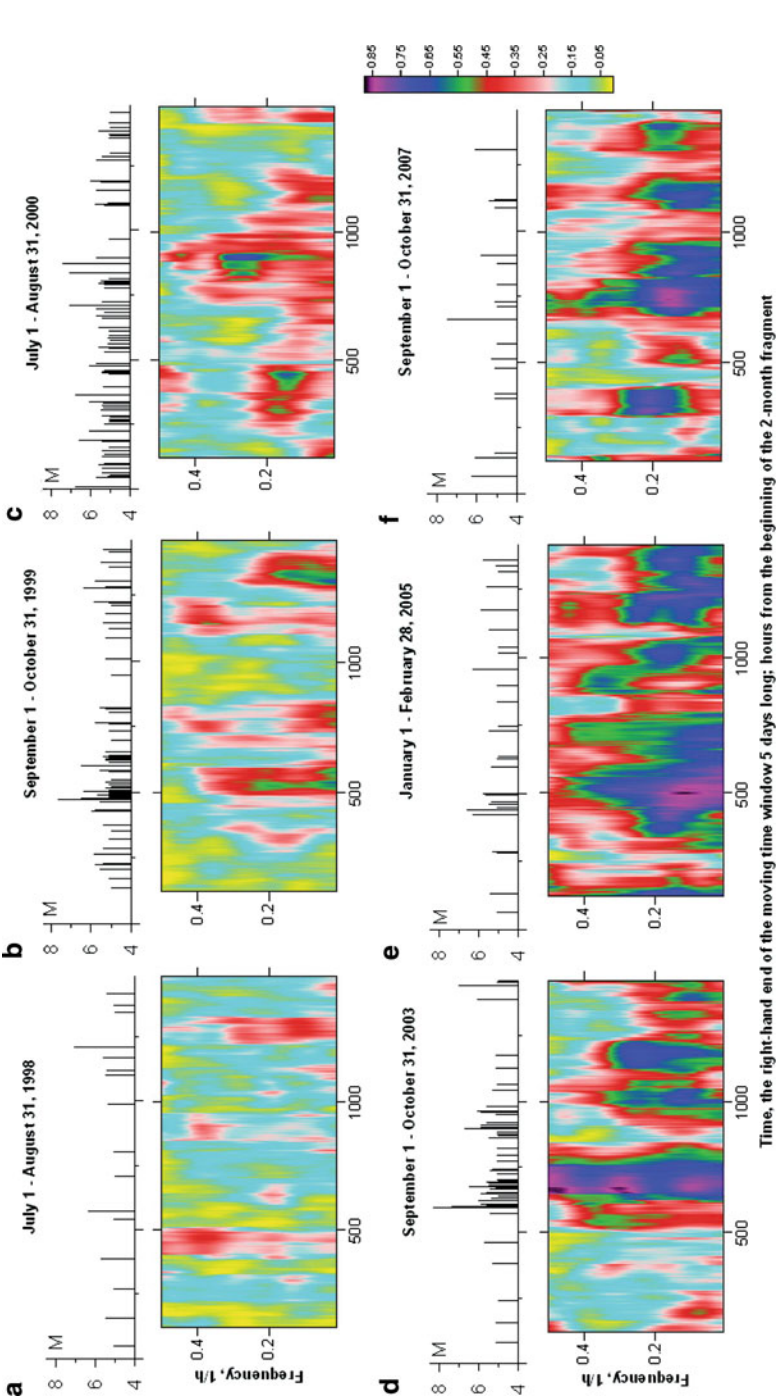

Fig. 15.7 Frequency–time diagrams of the evolution of the spectral measure of coherence between the average values of the generalized Hurst exponent α calculated inside five spatial clusters of stations for six different 2-month fragments. The measure of coherence was estimated in the moving time window 5 days long. The singularity spectra were calculated for 1-min data in the consecutive time intervals 12 h long with a shift of 1 h. The sequence of magnitudes ($M \geq 5$) of seismic events in the rectangular region between 20°–60° N and 120°–160° E is presented above each frequency–time diagram

Note that due to the construction of the quantity $\lambda(\tau, \omega)$, its values belong to the interval [0,1], and the closer the corresponding value to unity, the stronger the relation between variations in the components of the multidimensional time series at the frequency ω for the time window with the coordinate τ. It should be emphasized that the comparison of absolute values of the statistics $\lambda(\tau, \omega)$ is possible only for the same number m of simultaneously processed time series, because, due to formula (15.12), if m increases, $\lambda(\tau, \omega)$ decreases as the product of m values smaller than unity. In our case, stations are clusterized at a fixed number of clusters (five).

Since the spectral measure (15.12) was used for the analysis of the variability of the cumulative coherence inside 2-month fragments, singularity spectra were estimated for 1-min data in the moving time window 12 h long (720 samples) with a shift of 1 h (60 samples). Further, we again calculated the average cluster values of $\Delta\alpha$ and α^*, which thus formed five time series with a time step of 1 h (shift of the moving time window).

Below, we present the results of the application of the spectral measure (15.12) for the analysis of effects of the coherent behavior between the time series of variations in the average cluster values of α^*. The results for the support width $\Delta\alpha$ of the singularity spectrum are qualitatively analogous. To realize this method, it is necessary to have an estimate of the spectral matrix of the initial multidimensional series in each time window. Below, we prefer to use the model of vector autoregression [Marple (Jr.), 1987] of the 3rd order. To obtain the dependence $\lambda(\tau, \omega)$, the time window length was assumed to be 5 days. Since each value of α^* was obtained in the time window 12 h long, and the shift of these windows was 1 h, the time window length for estimating the spectral matrix will be 109 samples, because $(109 - 1) \cdot 1 + 12 = 120$ h $= 5$ days.

Six frequency–time diagrams of statistics (15.12) for different 2-month fragments are presented in Fig. 15.7. These diagrams are constructed on the same scale (unified color scale is shown on the right), depending on the position of the right-hand end of the moving time window 5 days long (time is indicated in hours from the beginning of the corresponding 2-month fragment). The sequences of magnitudes of the earthquakes with $M \geq 5$, which occurred in the rectangular vicinity of Japan's islands during the corresponding 2-month fragment, are shown above each frequency–time diagram. The 2-month fragment presented in Fig. 15.7d corresponds to the 2003 Hokkaido earthquake. A moderate coherence observed before the earthquake, was previously noted in [Sobolev et al., 2008; Lyubushin, 2008] from data of the IRIS broadband network. However, it should be noted that post-seismic outbursts of the coherence are stronger than the precursory ones.

In addition, the outbursts of statistics (15.12), which can hardly be related to the post-seismic or precursory coherence from some event, are seen in the frequency–time diagrams of Fig. 15.7 in comparison with the seismic regimes. Such coherence outbursts were noted in the work [Lyubushin, 2008], where the author suggested that a simple hypothesis stating that the coherence of the variations in parameters of the singularity spectrum of noise should be expected to increase before a strong earthquake is groundless. Indeed, meteorological or oceanic factors, including

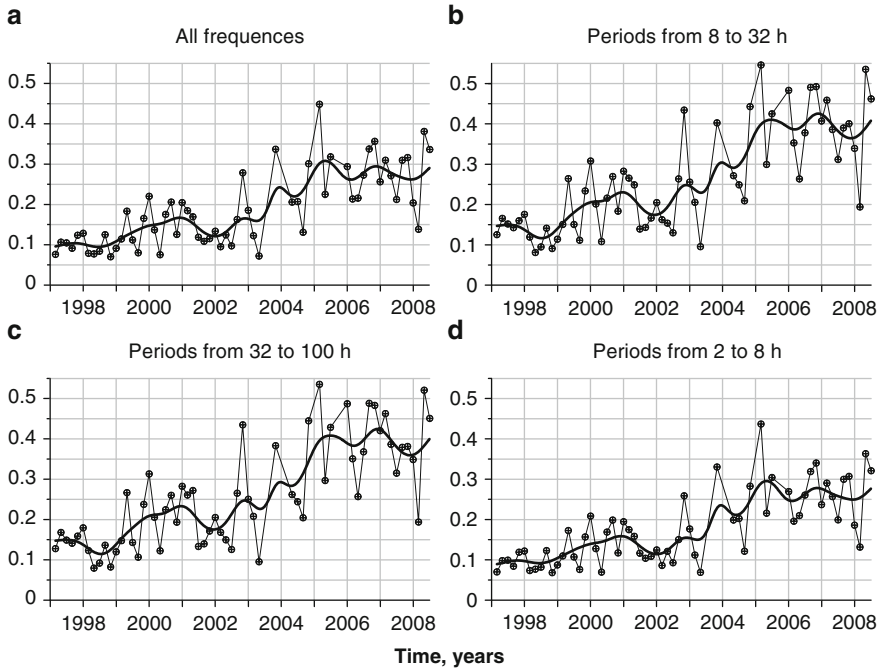

Fig. 15.8 Thin lines with circles are the plots of the spectral measure of coherence between the average cluster values of α^* for the consecutive 2-month fragments averaged over four different frequency bands restricted by their boundary periods (h). The bold lines are results of the Gaussian smoothing with the radius of averaging 0.5 yr. The singularity spectra were calculated for 1-min data in the consecutive time intervals 12 h long with a shift of 1 h

oceanic waves in very remote regions, equally can be coherence sources. The idea to investigate some scenarios of the behavior of outbursts of synchronization seems more promising [Lyubushin, 2003]. The trend of increasing the average measure of correlation presented in Fig. 15.3 is one such scenario. The use of spectral statistics (15.12) allows us to find out whether such trends are present in different frequency bands.

The values of statistics (15.12) for the sequence of 2-month fragments after its averaging over frequencies from certain frequency bands are presented in Fig. 15.8. Figure 15.8a corresponds to all frequencies; Fig. 15.8b to the band with boundary periods from 8 to 32 h (containing tidal harmonics); Fig. 15.8c to the low-frequency band with boundary periods of 32 and 100 h; and Fig. 15.8d to the high-frequency band with boundary periods of 2 and 8 h. The Gaussian trends with a radius of averaging of 0.5 yr are shown by the bold lines. It is seen that spectral measure (15.12), as well as the simple measure of correlation (15.11), yields qualitatively the same results for all frequency bands. The average coherence increases after 2003. Thus, changes in the state of the lithosphere after the Hokkaido earthquake of September 25, 2003, have resulted in a more correlated behavior of the multifractal

characteristics of the field of microseismic noise in response to actions on the Earth's crust, which was also observed previously, in the period from 1997–2003.

15.8 Conclusions

The analysis showed that after the Hokkaido earthquake of September 25, 2003 (M = 8.3), a considerable synchronization of the variations in the multifractal parameters of the low-frequency microseismic field took place and is retained to the present day. Thus, the 2003 Hokkaido earthquake, in its own way, is a crucial point in the behavior of microseisms, and this fact may testify in favor of the hypothesis that this event can be a foreshock of a still stronger earthquake.

The results presented in Figs. 15.3 and 15.4, even more clearly than the plots showing the behavior of the average measures of correlation and coherence in Figs. 15.6 and 15.8, indicate that the September 25, 2003 event is a kind of time marker separating the behavior of the field of microseisms into two modes. Additionally, Fig. 15.3 estimates the time of preparation of this event at 0.5 yr. The question arises as to how a decrease in the average value of $\Delta\alpha$ is related to an increase in the linear correlations between fluctuations of singularity spectrum parameters. In this sense, the quantity $\Delta\alpha$ reflects the degree of diversity of the random behavior of the signal, and therefore its decrease is an indirect indicator of the suppression (decrease) of certain degrees of freedom of the medium.

At the same time, it is possible to find more direct analogies with a decrease in the number of degrees of freedom reflecting in the $\Delta\alpha$ decrease. Singularity spectra for the sequence of recurrence times in the Poincare cross-section for systems of two coupled oscillators (Ressler and Lorenz oscillators) were numerically investigated in the works of [Pavlov et al., 2003; Ziganshin and Pavlov, 2005]. In the presence of a sufficiently strong coupling, these oscillators become synchronous. It turned out that the synchronization of oscillators substantially decreases the singularity spectrum support width $\Delta\alpha$. Consequently, the set of results presented as plots in Figs. 15.3, 15.6, and 15.8 indicate that the field of microseismic oscillations in Japan after the 2003 event became synchronous, and this state is retained to the present day.

Based on the well-known statement of the theory of catastrophes that the synchronization is one of the flags of an approaching catastrophe [Gilmore, 1981], it may be suggested that the Hokkaido event, notwithstanding its power (M = 8.3), could be only a foreshock of a still stronger earthquake forming in the region of Japan's islands.

As for the sharp decrease in seasonal variations of the parameter α^* for 1-min data after the September 25, 2003, earthquake, the interpretation of this result is not so transparent as for $\Delta\alpha$. We can only suggest that this decrease also reflects a blocking of some degrees of freedom of the medium, which were previously responsible for annual changes in the state of the lithosphere. On the other hand,

the situation for 1-s data on $\Delta\alpha$ is the opposite: after the September 25, 2003, event, the annual variations became more clearly pronounced.

References

Currenti G., C. del Negro, V. Lapenna, and L. Telesca, "Microfractality in Local Geodynamic Fields at Etna Volcano, Sisily (Southern Italy)," Natural Hazards and Earth System Sciences 5, 555–559 (2005).

Duda R.O. and P.E. Hart, Pattern Classi.cation and Scene Analysis (John Wiley and Sons, New York, London, Sydney, 1973; Mir, Moscow, 1976).

Ekstrom G., "Time Domain Analysis of Earth's Long-Period Seismic Radiation," J. Geophys. res. 106, N B11, 26483–26493 (2001).

Feder J., Fractals (Plenum Press, New York, 1988; Mir, Moscow, 1991).

Friederich A., F. Kruder, and K. Klinge, "Ocean-Generated Microseismic Noise Located with the Grafenberg Array," Journal of Seismology 2, No. 1, 47–64 (1998).

Gilmore R., Catastrophe Theory for Scientists and Engineers (John Wiley and Sons, New York, 1981; Mir, Moscow, 1984).

Hardle W., Applied Nonparametric Regression (Cambridge Univ. Press, Cambridge, New York, New Rochell, Melbourne, Sydney, 1989; Mir, Moscow, 1993).

Hotelling H., "Relations between Two Sets of Variates," Biometrika 28, 321–377 (1936).

Ida Y., M. Hayakawa, A. Adalev, and K. Gotoh, "Multifractal Analysis for the ULF Geomagnetic Data during the 1993 Guam Earthquake," Nonlinear Processes in Geophysics 12, 157–162 (2005).

Kantelhardt J.W., S.A. Zschiegner, E. Konsciently-Bunde, et al.,"Multifractal Detrended Fluctuation Analysis of Nonstationary Time Series," Physica A 316, 87– 114 (2002).

Kobayashi N. and K. Nishida, "Continuous Excitation of Planetary Free Oscillations by Atmospheric Disturbances," Nature 395, 357–360 (1998).

Kurrle D. and R. Widmer-Schnidrig, "Spatiotemporal Features of the Earth's Background Oscillations Observed in Central Europe," Geophys. Res. Lett. 33, L24304 (2006).

Lin'kov E.M., Seismic Phenomena (LGU, Leningrad, 1987) [in Russian].

Lin'kov E.M., L.N. Petrova, and K.S. Osipov, "Seismogravitational Pulsations of the Earth and Disturbances of the Atmosphere as Possible Precursors of Strong Earthquakes," Dokl. Akad. Nauk SSSR 313(5), 1095–1098 (1990).

Lyubushin A.A., "Analysis of Canonical Coherences in the Problem of Geophysical Monitoring," Fiz. Zemli, No. 1, 59–66 (1998) [Izvestiya, Phys. Solid Earth 34, 52–58 (1998)].

Lyubushin A.A., "Outbursts and Scenariosof Synchronization in Geophysical Observations," in Sketches of Geophysical Investigations. To the 75th Anniversary of the Schmidt United Institute of Physics of the Earth (OIFZ RAN, Moscow, 2003) pp. 130–134 [in Russian].

Lyubushin A.A. and G.A. Sobolev, "Multifractal Measures of Synchronization of Microseismic Oscillations in a Minute Range of Periods," Fiz. Zemli, No. 9, 18–28 (2006) [Izvestiya, Phys. Solid Earth 42, 734–744 (2006)].

Lyubushin A.A., Analysis of Data of Geophysical and Ecological Monitoring (Nauka, Moscow, 2007) [in Russian].

Lyubushin A.A., "Microseismic Noise in a Minute Range of Periods: Properties and Possible Prognostic Indicators," Fiz. Zemli, No. 4, 17–34 (2008) [Izvestiya, Phys. Solid Earth 43 (2008)].

Mandelbrot B.B., The Fractal Geometry of Nature (Freeman and Co., New York, 1982; Institute of Computer Investigations, Moscow, 2002).

Marple (Jr.) S.L., Digital Spectral Analysis with Applications (Prentice-Hall, Englewood Cliffs, New Jersey, 1987; Mir, Moscow, 1990).

Pavlov A.N., O.V. Sosnovtseva, and E. Mosekilde, "Scaling Features of Multimode Motions in Coupled Chaotic Oscillators," Chaos, Solitons and Fractals 16, 801–810 (2003).

Petrova L.N., "Seismogravitational Oscillations of the Earth from Observations by Spaced Vertical Pendulums in Eurasia," Fiz. Zemli, No. 4, 83–95 (2002) [Izvestiya, Phys. Solid Earth 38, 325–336 (2002)].

Petrova L.N., E.G. Orlov, and V.V. Karpinskii, "On the Dynamics and Structure of Earth's Oscillations in December 2004 from Seismic Gravimeter Observations in St. Petersburg," Fiz. Zemli, No. 2, 12–20 (2007) [Izvestiya, Phys. Solid Earth 43, 111–118 (2007)].

Rao C.R., Linear Statistical Inference and Its Applications (John Wiley and Sons, New York, London, Sydney, 1965; Nauka, Moscow, 1968).

Ramirez-Rojas A., A. Muñoz-Diosdado, C.G. Pavía-Miller, and F. Angulo-Brown, "Spectral an Multifractal Study of Electroseismic Time Series Associated to the Mw = 6.5 Earthquake of 24 October 1993 in Mexico," Natural Hazards and Earth System Sciences 4 703–709 (2004).

Rhie J. and B. Romanowicz, "Excitation Earth's Continuous Free Oscillations by Atmosphere–Ocean–Sea.oor Coupling," Nature 431, 552–554 (2004).

Rhie J. and B. Romanowicz, "A Study of the Relation between Ocean Storms and the Earth's hum-G3: Geochemistry, Geophysics, Geosystems," Electronic "Earth Sciences" 7(10.7) (2006); http://www.agu.org/ journals/gc/.

Sobolev G.A., "Microseismic Variations Prior to a Strong Earthquake," Fiz. Zemli, No. 6, 3–13 (2004) [Izvestiya, Phys. Solid Earth 40, 455–464 (2004)].

Sobolev G.A., A.A. Lyubushin, and N.A. Zakrzhevskaya, "Synchronization of Microseismic Variations within a minute Range of Periods," Fiz. Zemli, No. 8, 3–27 (2005) [Izvestiya, Phys. Solid Earth 42, 599–621 (2005)].

Sobolev G.A. and A.A. Lyubushin, "Microseismic Impulses As Earthquake Precursors," Fiz. Zemli, No. 9, 5–17 (2006) [Izvestiya, Phys. Solid Earth 42, 721–733 (2006)].

Sobolev G.A. and A. A. Lyubushin, "Microseismic Anomalies before the Sumatra Earthquake of December 26, 2004," Fiz. Zemli, No. 5, 3–16 (2007) [Izvestiya, Phys. Solid Earth 43, 341–353 (2007)].

Sobolev G.A., A.A. Lyubushin, and N.A. Zakrzhevskaya, "Asymmetric Impulses, Periodicities and Synchronization of Low-Frequency Microseisms," Vulkanol. Seismol., No. 2, 135–152 (2008).

Sobolev G.A., "Series of Asymmetric Impulses in a Minute Range of Microseisms As Indicators of a Metastable State of Seismically Active Zones," Fiz. Zemli, No. 4, 3–16 (2008) [Izvestiya, Phys. Solid Earth (2008)].

Stehly L., M. Campillo, and N. M. Shapiro, "A Study of the Seismic Noise from Its Long-Range Correlation Properties," J. Geophys. Res. 11, B10306 (2006).

Tanimoto T., J. Um, K. Nishida, and K. Kobayashi, "Earth's Continuous Oscillations Observed on Seismically Quiet Days," Geophys. Res. Lett. 25, 1553–1556 (1998).

Tanimoto T. and J. Um, "Cause of Continuous Oscillations of the Earth," J. Geophys. Res. 104 (28), 723–739 (1999).

Tanimoto T., "Continuous Free Oscillations: Atmosphere–Solid Earth Coupling–Annu. Rev.," Earth Planet. Sci. 29, 563–584 (2001).

Tanimoto T., "The Oceanic Excitation Hypothesis for the Continuous Oscillations of the Earth," Geophys. J. Int. 160, 276–288 (2005).

Telesca L., L. Colangelo, and V. Lapenna, "Multifractal Variability in Geoelectrical Signals and Correlations with Seismicity: a Study Case in Southern Italy," Natural Hazards and Earth System Sciences 5, 673–677 (2005).

Taqqu M.S., "Self-Similar Processes," in Encyclopedia of Statistical Sciences, Vol. 8, pp. 352–357 (John Wiley and Sons, New York, 1988).

Ziganshin A.R. and A.N. Pavlov, "Scaling Properties of Multimode Dynamics in Coupled Chaotic Oscillators— Physics and Control," in Proceedings. 2005 International Conference, pp. 180–183 (2005) [in Russian].

Chapter 16
Changes in Dynamics of Seismic Processes Around Enguri High Dam Reservoir Induced by Periodic Variation of Water Level

T. Matcharashvili, T. Chelidze, V. Abashidze, N. Zhukova, and E. Meparidze

Abstract The importance of elucidating the effects of small periodic influences on the behavior of complex systems is well acknowledged. In the present research, a possible impact of regular water level variations in large reservoir as an example of small external influence (comparing to tectonic forces) on the dynamics of local seismic activity was investigated.

In general, large reservoirs located in the seismically active zones are often considered as a factor which quantitatively and qualitatively influences the earthquakes generation. It was many times reported that during impoundment or immediately after it (namely from several months to several years), both the number and the magnitude of earthquakes around reservoir significantly increased. These changes in earthquake generation are named the reservoir induced seismicity (RIS). After several years of regular seasonal load/upload of the reservoir, the seismicity essentially decreases down to the level when lesser earthquakes occur with lower magnitudes. To explain this decrease, the authors of the present paper recently proposed a model of phase synchronization of local seismic activity by the periodic variation of the water level – the reservoir-induced synchronization of seismicity (RISS).

Generally speaking, RISS presumes a kind of control of local seismic activity by synchronizing small external periodic influence and hence an increase of the order in dynamics of regional seismic activity. To reveal these changes in dynamics of phase-synchronized seismic activity around a large reservoir, field seismic and water level variation data were analyzed in the present work. Data sets of laboratory stick-slip acoustic emission, under a weak influence imposed as a model of natural seismicity influenced by periodic water level variation, also were analyzed.

The evidence is presented showing that an increase of the order in dynamics of daily occurrence, as well as temporal and energy distribution of earthquakes took

T. Matcharashvili (✉), T. Chelidze, V. Abashidze, N. Zhukova, and E. Meparidze
M. Nodia Institute of Geophysics, 1 Alexidze str., 0171 Tbilisi, Georgia
e-mail: Matcharashvili@gtu.ge; tamaz.chelidze@gmail.com

V. de Rubeis et al. (eds.), *Synchronization and Triggering: from Fracture to Earthquake Processes*, GeoPlanet: Earth and Planetary Sciences 1,
DOI 10.1007/978-3-642-12300-9_16,

place around Enguri high dam water reservoir (Western Georgia) during the periodic variation of the water level in the lake.

It is shown that when the water level variation in a reservoir is close to periodic, monthly frequency of earthquake occurrence reveals two maximums: in spring and autumn. There is a clear asymmetry in the seismic response, possibly due to load/unload response ratio (LURR) effect; the maximal release of seismic energy is during loading, i.e., in the spring.

16.1 Introduction

It is known that the dynamics of natural systems may often be affected by a small external influence [Pikovsky et al., 2003; Postnov et al., 2003]. Phase synchronization is recognized as one of possible mechanisms when poorly correlated small interactions could lead to essential dynamical changes in systems behavior. Phase synchronization has been observed in many biological systems, numerical models and laboratory experiments [Matcharashvili et al., 2008; Nascimento et al., 2004; Pikovsky et al., 2003; Postnov et al., 2003]. At the same time, there are rare examples when the phase synchronization effects in complex environmental processes have been quantitatively evaluated using modern data analysis approaches.

In the present research we have investigated the character of dynamical changes in the local seismic activity around a large reservoir under quasi periodic forcing caused by water level variation during reservoir exploitation.

Generally, the scientific and practical importance of investigation of possible mechanisms related to the dynamics of influence of high dam water reservoirs on local earthquakes generation is well acknowledged [Simpson, 1986; Simpson et al., 1988; Smirnov, 1995; Talvani, 1997]. Since the mid of the past century, the RIS has been observed at many reservoirs located in seismically active areas. At the same time, many aspects of changes in seismic process induced by water reservoir remain subjects of intense scientific discussions and investigations [Assumpção, 2002; Smirnov, 2005].

Namely, we still lack knowledge on geological, hydrological, or physical features of relation between the observed increase of seismic activity and the impact of water in the lake. Presently this relation is explained by changes in the ambient stress condition due to the load (unload) of the water or, respectively, an increase of interstitial pore pressure in the rock matrix beneath the reservoir due to downward percolation of fluid. It is also supposed that the water reservoir-related changes in the seismicity of surrounding area (the so-called reservoir-induced seismicity – RIS), decrease after several years down to the level when even lesser earthquakes may occur with lower magnitudes comparing to the basic level of local seismic activity [Assumpção, 2002; Nascimento, 2004]. The problem of underlying dynamics of this decrease of seismic energy release following the initial RIS activity is not finally resolved.

In our previous researches based on the field and laboratory data, the evidence has been presented that the decrease of seismic energy release associated with RIS may be caused by the quasi periodic variation of the water level in a large reservoir [Matcharashvili, 2008; Peinke et al., 2006]. Based on the results of field (water level variation, seismic catalogues) and model laboratory (stick-slip acoustic emission) data analysis, it was shown that small (compared to tectonic strain) periodic influence on a complex seismic process may invoke phenomena which we call reservoir induced phase synchronization of seismicity (RISS).

In the present work we continued investigation of the character of dynamical changes in local seismic activity accompanying the above-mentioned synchronization with the periodic variation of water level. As far as the proposed RISS is regarded as a weakest form of synchrony – the phase synchronization [Nascimento et al., 2004], the investigation of dynamics of seismic process under a small periodic external influence acquires special importance in the light of the above-mentioned lack of appropriate researches for real natural and technical systems.

16.2 Data and Methods Used

The data sets used in the present research have been collected in 1973–1995 at one of the largest in Europe (272 m in height) Enguri high dam reservoir located in Western Georgia, Caucasus (42.030 N, 42.775 E) (Fig. 16.1). Strictly speaking, the data of daily water level variation in reservoir lake and daily number of

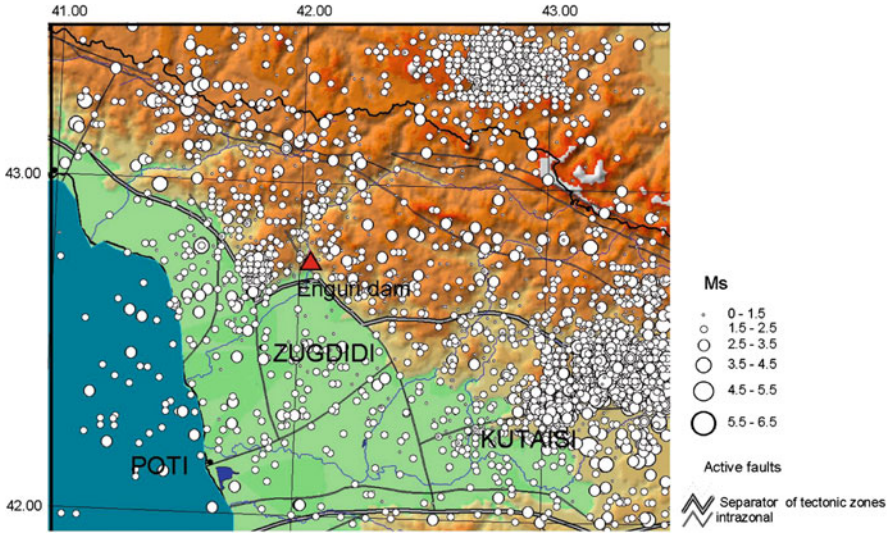

Fig. 16.1 Location of the Enguri high dam and patterns of local seismicity

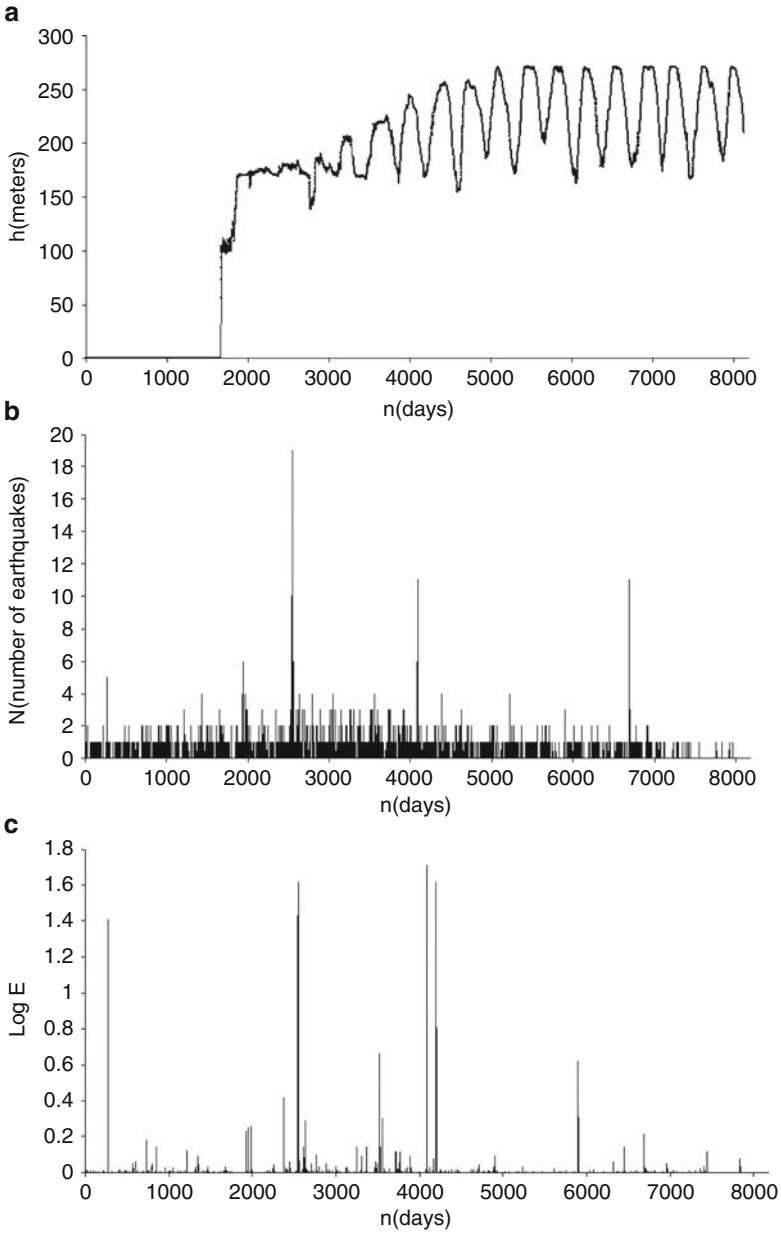

Fig. 16.2 (a) Record of the daily water level in the lake of Enguri dam from 1975 to 1993, (b) daily number of earthquakes, (c) Log of normalized daily released seismic energy

earthquakes that occurred in the above-mentioned period have been collected (Fig. 16.2 a and b). The size of the area around Enguri high dam, which can be considered as prone to reservoir influence, has been estimated based on the concept of energy release acceleration in the seismically critical regions. Namely, the minima of curvature parameter C (defined as C = (power-law fit RMS error)/(linear fit RMS error)) deduced from the Benioff strain $E(t) = \sum_{i=1}^{N(t)} E_i(t)^{1/2}$ [Bowman et al., 1998] was calculated. Here E_i is the energy of i-th event. Location of the Enguri high dam reservoir was assumed as a "virtual epicenter of impending strong earthquake" (for details see [Peinke et al., 2006], where it is shown that the radius of the area around Enguri high dam, sensitive to the reservoir influence, is about 90 km). Data sets of daily occurred number of earthquakes and released daily seismic energy consist of seismic events above representative magnitude threshold $M \geq 1.6$ within this 90 km area for 1973–1995. Besides these daily data, time series of sequences of magnitudes and time intervals between consecutive earthquakes (waiting times), unevenly sampled for the same time period and area, also were analyzed.

The sets of water level variation and seismic data used in the present study are available at the M. Nodia Institute of Geophysics (Tbilisi, Georgia).

Laboratory data of acoustic emission of stick-slip process have been collected on the specially developed laboratory setup represented by a system of two roughly finished basalt plates [Chelidze and Lurmanashvili, 2003; Chelidze et al., 2005]. To model small external influences on complex stick-slip (model of earthquake generation) the external faces of plates in our laboratory set up were subjected to periodic electric (48 Hz) perturbations (with amplitudes varying from 0 to 1000 V). The impact of this relatively small movement, normal to plate, was superimposed on the constant dragging force (normalized power of an external sinusoidal forcing is shown in Fig. 16.3 a). The waveforms of both acoustic emission and the sinusoidal EM field were digitized at 44 kHz. From the digitized waveforms of acoustic emission data sets, the time series (catalogs) of power of emitted acoustic energy were compiled (Fig. 16.3b). Specifically, the power of emitted during stick-slip acoustic energy was calculated as the area between the acoustic signal curve and the x-axis during the period of the superimposed external 48 Hz sinusoidal forcing divided by the time duration of these 2π periods. Additionally, sequences of time intervals between consecutive maximal amplitudes of acoustic signals (waiting times) were analyzed.

Besides the characteristics that were formerly described in [Peinke et al., 2006], the mean effective phase diffusion coefficient $D = \frac{d}{dt}\left[\langle \Delta\varphi^2 \rangle - \langle \Delta\varphi \rangle^2\right]$ was calculated as an additional statistical measure of the quality of synchronization between water level variation and seismicity, as well as between external periodic forcing and power of acoustic emission.

In order to investigate dynamical changes in analysed processes, Recurrence Quantitative Analysis (RQA) was used [Marwan et al., 2002; Marwan, 2003; Zbilut and Webber, 1992]. RQA is especially useful to overcome the difficulties often

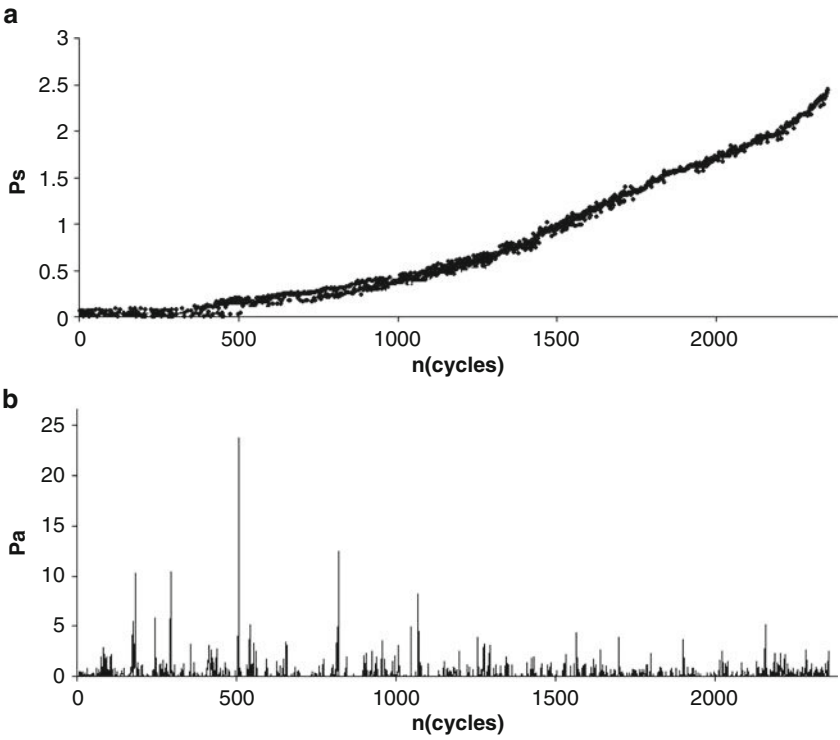

Fig. 16.3 Results of experiments on stick-slip, which is considered as a good laboratory model for seismicity, affected by weak external perturbations: (a) Normalized power of the external sinusoidal forcing, P_s, superimposed on the constant drag force; (b) normalized power of acoustic emission of stick-slip events, P_a

encountered while dealing with nonstationary and rather short real data sets. The recurrence plots (RP) are defined as:

$$R_{i,j} = \Theta(\varepsilon_i - \left\|\bar{x}_i - \vec{x}_j\right\|),$$

where ε_i is a cut-off distance. $\Theta(x)$ is the Heaviside function. A correct choice of cut-off distance ε is one of the main problems of RQA. It is desirable to have ε as small as possible, but the presence of noise always necessitates larger values. There are several suggestions how to set ε correctly [Iwanski and Bradley, 1998; Marwan et al., 2002; Marwan, 2003; Zbilut and Webber, 1992]. We selected the cut-off distance as 10% (for waiting times and daily number of earthquakes) and 20% (for magnitude sequence) of overall mean distance [Belaire-Franch et al., 2002; Marwan, 2003]. As a quantitative tool of complex dynamics analysis, RQA defines several measures mostly based on diagonally oriented lines in the recurrence plots: recurrence rate, determinism, maximal length of diagonal structures, entropy, trend, etc [Eckmann et al., 1987]. In the present work, the recurrence rate $RR(t)$ and

determinism $DET(t)$ — the measures based on an analysis of diagonally oriented lines in the recurrence plot have been calculated [Marwan et al., 2002; Marwan, 2003]. Generally, the recurrence rate $RR(t)$ is the ratio of all recurrent states (recurrence points) to all possible states and is therefore a probability of the recurrence of a certain state. The ratio of recurrence points forming diagonal structures to all recurrence points is called the determinism $DET(t)$. The larger values of $RR(t)$ and $DET(t)$ indicate the increase in regularity of the investigated dynamics.

16.3 Results and Discussions

The fact that water level variations in Enguri reservoir lead to distinctive changes in earthquake generation of local area is evident from Fig. 16.4. Almost uniform distribution of earthquakes occurrence before water level periodic variation was replaced by distribution with distinctive maximums in spring and autumn.

As it was mentioned in the previous section, several methods of quantitative indication of phase synchronization in field and laboratory data have been used. For example, the results of calculation of phase diffusion coefficient, D [Peinke et al., 2006], between water level periodic variation and seismic activity around reservoir are presented in Fig. 16.4. It follows from this figure that during the whole history of lake construction and exploitation, beginning from the territory flooding (n = 1668 in Fig. 16.2 a) and ending by regular regime (n $\approx$ 5000), D is indeed minimal for the time interval of periodic water level variation.

In the laboratory model of seismicity (acoustic emission accompanying stick-slip process), it was also shown that phase diffusion coefficient D strictly decreases

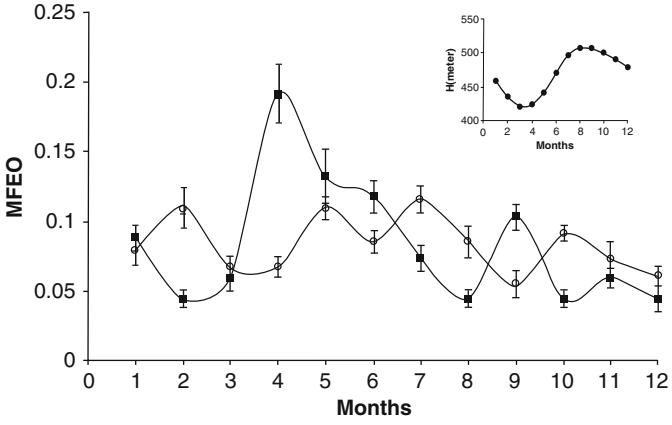

Fig. 16.4 Monthly frequency of earthquake occurrence before (open circles, thin line) and during water level periodic variation (dark squares, bold line)

when acoustic emission time series are phase synchronized (Fig. 16.6). The same conclusion follows from Fig. 16.7, showing essential increase of phase synchronization measure calculated for onsets and maximums of AE.

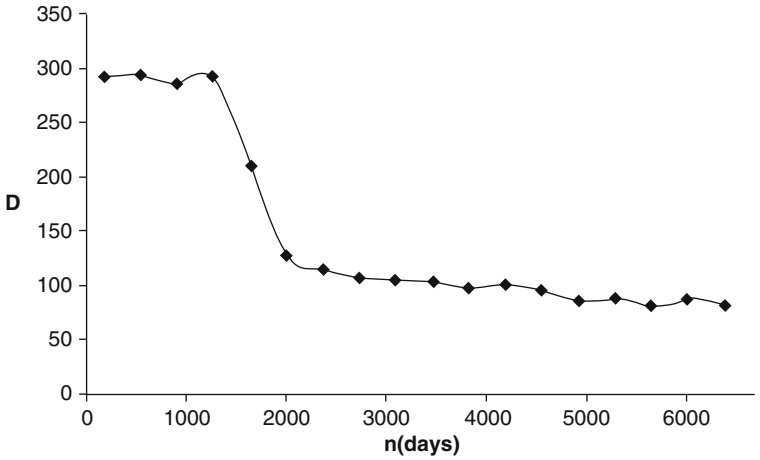

Fig. 16.5 Variation of phase diffusion coefficient of phase differences between daily released seismic energy and water level daily variations, calculated for consecutive sliding windows containing 365 events, shifted by 365 events (periodic forcing begins from n ≈ 5000)

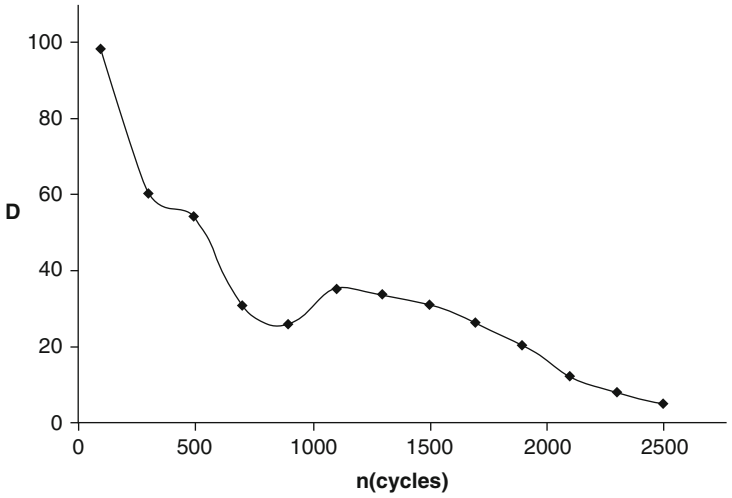

Fig. 16.6 Variation of phase diffusion coefficient of phase differences between power of external sinusoidal forcing, P_s, and power of acoustic emission of stick-slip events, P_a, calculated for consecutive sliding windows containing 200 events, shifted by 200 events (periodic forcing of large enough amplitude begins from $n \approx 2000$)

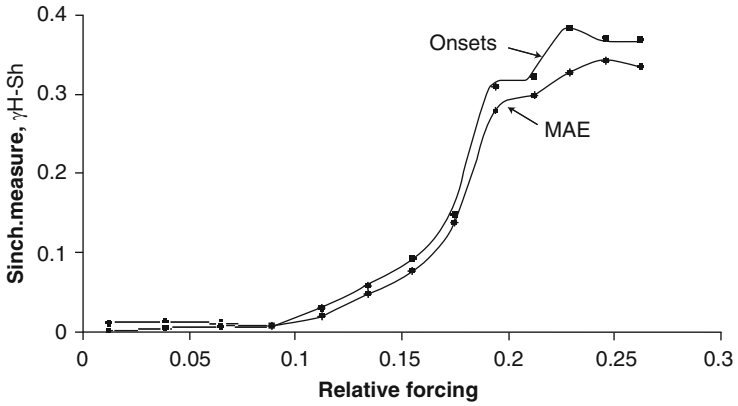

Fig. 16.7 Synchronization measure vs. relative force of external influence. Results for time series of onsets and maximums of stick slip AE (MAE) are shown

The decrease of seismic energy release shown in Fig. 16.2c which follows the period of RIS, may be explained by phase synchronization of seismic activity with quasi-periodic water level variation (it was mentioned above that we name this effect RISS). RISS observed at Enguri reservoir can be considered as an example of purposeful man-made influence on complex dynamics of seismic process.

To have more grounds for such a statement it should be mentioned that according to the present understanding the dynamics of earthquake-related processes in the earth crust is recognized as non random, having both low and/or high dimensional nonlinear structures [Iwanski and Bradley, 1998; Matcharashvili et al., 2000; Rundle et al., 2000; Smirnov, 2005]. One of the characteristic features of such processes in close-to-the-critical state is their high sensitivity to relatively weak external influences. This general property of complex systems acquires special significance for practically unpredictable seismic processes. Indeed, insofar as we are not able to govern initial conditions of lithospheric processes, even principal possibility of controlling dynamics of seismic process has immense scientific and practical importance (e.g., to modify the release of accumulated seismic energy via series of small or moderate earthquakes instead of one strong devastating event using the specific external impact). The way towards understanding such a control mechanism passes through investigation of dynamics of seismic processes, when a small external influence leads to phase synchronization.

It is known that nonlinear dynamical systems often respond to such external influences in a complicated way. One of possible responses is synchronization. Since Huygens, synchronization is understood as a phenomenon when coupled nonlinear systems become mutually adjusted. Presently, several types of synchronization are known, e.g., identical, generalized, phase synchronization, etc. [Calvo et al., 2004]. The phase synchronization between water level periodic variation and seismic activity, observed in our previous and present researches, is

recognized as the weakest form of synchrony when interacting nonlinear oscillators remain largely uncorrelated [Pazo et al., 2003; Rosenblum et al., 1996]. Generally, depending on the strength of coupling, interacting systems may have different dynamical features [Pazo et al., 2003]. It is most important that contrary to other forms of synchrony which lead to increase of order in the behavior of synchronized system, the phase synchronization does not require strong coupling between the processes involved. This in turn means that the presence of order and the character of changes in dynamics of phase synchronized system are not obvious.

This is why we aimed to investigate the character of dynamical changes in seismic process when phase synchronization with periodic variation of water level occurs. RQA, often used to detect changes in the dynamics of complex systems [Iwanski and Bradley, 1998], is the most convenient data analysis tool for this purpose. As follows from our RQA results, when the external influence on the earth crust caused by a water reservoir becomes periodic, the extent of regularity of earthquake daily distribution (evaluated as %REC and %DET) essentially increases (see Fig. 16.8 a, bold line). This result was tested by comparing with the surrogate data. Averaged results derived from RQA of 20 shuffled (asterisks) and phase randomized (triangles) surrogates (Fig. 16.8 a), assure that the above-mentioned increase of regularity in earthquakes distribution should not be an artefact. It is important to mention that an influence of increasing amount of water and its subsequent periodic variation essentially affects also the character of earthquakes magnitude and temporal distribution (see Fig. 16.8 b). The extent of order in earthquakes temporal (black columns) and magnitude (grey columns) distribution, calculated as value of %DET, substantially increases when the reservoir forcing becomes periodic. Results of %DET calculation of corresponding surrogates are always less than 50% to the original values (not shown here). It is interesting to mention that the dynamics of temporal and energetic distributions of earthquakes changes even under irregular variation of water level, though not so much as under periodic variation.

The above conclusions regarding the increase of the order in seismic process under the influence of periodic variation of water level using %DET measurements are confirmed by calculation of other RQA measures (%REC, Entropy, Laminarity).

As far as real field seismic data sets are short and incomplete, we carried out similar analysis on the acoustic emission data sets, obtained on laboratory spring-slider system under periodic electromagnetic (EM) forcing, which simulates the periodical loading by reservoir. Stick-slip experiments are considered as a model of a natural seismic process [Johansen et al., 1999; Rundle et al., 2000]. Time series of the emitted acoustic power during consecutive cycles (2π periods) of the external 48 Hz periodic forcing of stick-slip process were analyzed as well as time intervals between consecutive maximal amplitudes of acoustic signals (waiting times). As it is shown in Fig. 16.9 (circles), the extent of order increases both in energetic distribution as well as in temporal distribution of acoustic emission when synchronization is achieved (last windows in Fig. 16.8). The averaged

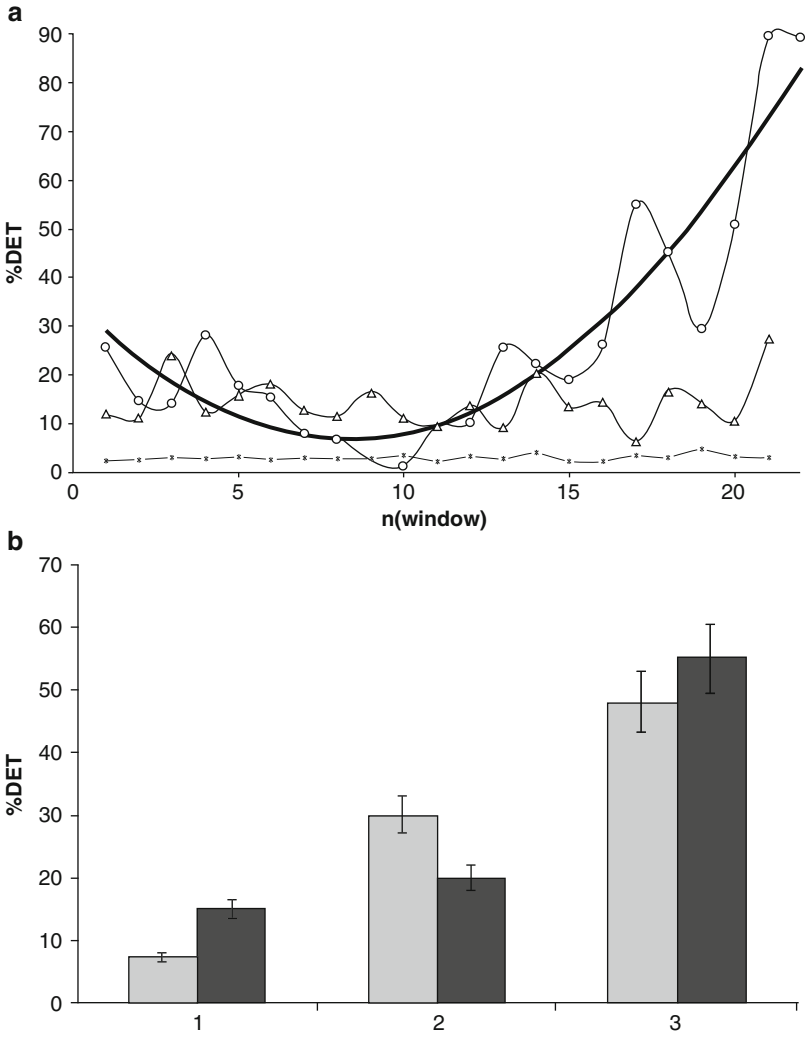

Fig. 16.8 (a) RQA %DET of daily number of earthquakes calculated for consecutive non overlapping one-year sliding windows (circles). Averaged results of RQA %DET for 20 shuffled (asterisks) and phase randomized (triangles) surrogates of daily number of earthquakes in consecutive one-year sliding windows; (b) RQA %DET of magnitude (black columns) and waiting time (grey columns) sequences: (1) before impoundment, (2) during flooding and reservoir filling, and (3) periodic change of water level in reservoir

results of 20 surrogates shown by triangles confirm the conclusion that the observed changes are indeed related to ordering in dynamics of acoustic emission under weak external forcing.

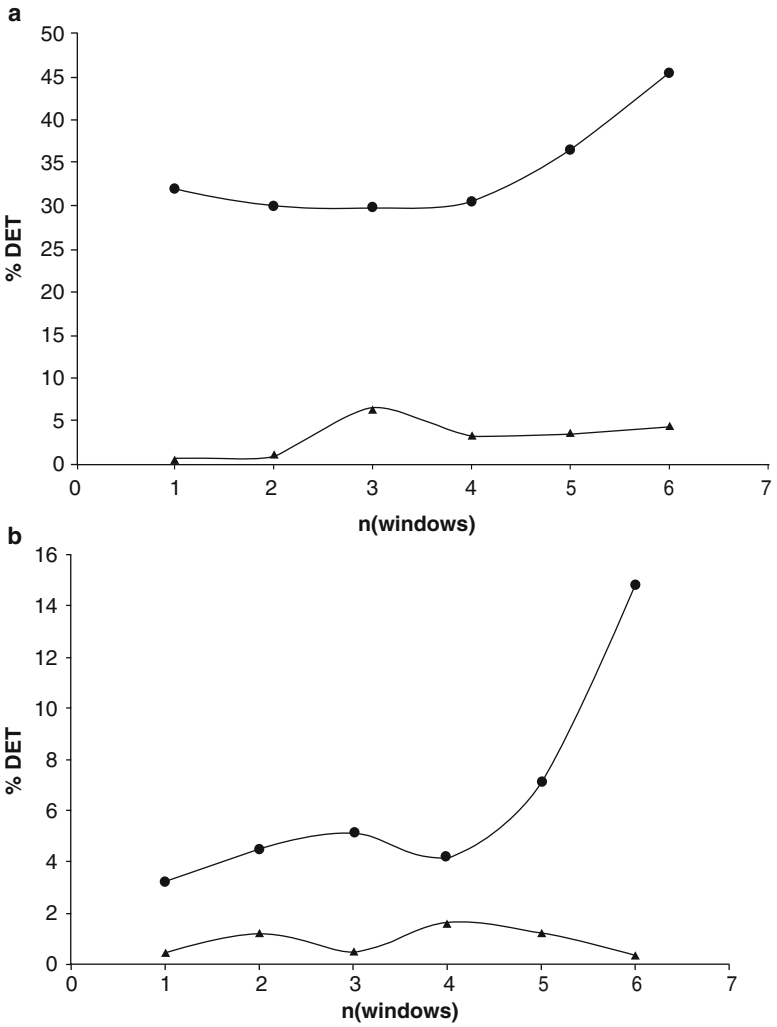

Fig. 16.9 RQA %DET calculated for consecutive non overlapping 400 data sliding windows of: (a) power of acoustic emission; (b) time intervals between consecutive maximal amplitudes of acoustic signals (waiting times). Averaged values for 20 shuffled time series are shown by triangles

16.4 Conclusions

The dynamics of seismic process during RISS has been investigated. Data sets of daily water level variation and released seismic energy as well as waiting time and magnitude sequences were analysed. As a model of natural seismicity, the

laboratory stick-slip acoustic emission data were also analysed. Methods of phase diffusion coefficient calculation and RQA were used.

Based on the results of investigation carried out both on field and experimental time series, we conclude that the order in dynamics of earthquakes' daily occurrence, as well as in earthquakes' temporal and energetic distributions increases when water level variations become periodic. Laboratory stick-slip acoustic emission data confirms the results of field data analysis.

Acknowledgements We acknowledge INTAS (#0748, 2002) for funding our experimental investigations.

References

Assumpção, M., Marza, V.I., Barros, L.V., Chimpliganond, C.N., Soares, J.E.P., Carvalho, J.M., Caixeta, D., Amorim, A., Cabral, E., 'Reservoir induced seismicity in Brazil', *Pure Applied Geophysics*, 159, 2002, 597–617.

Belaire-Franch, J., Contreras, J. D., Tordera-Lledo, L., 'Assessing nonlinear structures in real exchange rates using recurrence plot strategies', *Physica* D, 171, 2002, 249–264.

Bowman, D.D., Ouillon, G., Sammis, C. G., Sornette, A., Sornette, D., 'An observational test of the critical earthquake concept', *Journal of Geophysical Research*, 103, 1998, 24359-24372.

Calvo, O., Chialvo, D., Eguíluz, V., Mirasso, C., Toral. R., Anticipated synchronization: A metaphorical linear view, *Chaos*, 14, 2004, 7–13.

Chelidze, T., Lursmanashvili, O., 'Electromagnetic and mechanical control of slip: laboratory experiments with slider system', *Nonlinear Processes in Geophysics*, 20, 2003, 1–8.

Chelidze, T., Matcharashvili, T., Gogiashvili, J., Lursmanashvili, O., Devidze, M., 'Phase Synchronization of Slip in Laboratory Slider', *Nonlinear Processes in Geophysic*s, 12, 2005, 1–8.

Eckmann, J.P., Kamphorst S., Ruelle, D., Recurrence plots of dynamical systems. *Europhysics Letters*, 4 (9), 1987, 973–977.

Goltz C, *Fractal and chaotic properties of earthquakes*, Springer, Berlin, 1998.

Iwanski, J., Bradley, E., 'Recurrence plots of experimental data: To embed or not to embed?', *Chaos*, 8, 4, 1998, 861–871.

Johansen, A., Sornette, D., Acoustic Radiation Controls Dynamic Friction: Evidence from a Spring-Block Experiment', *Physical Review Letters*, 82, 1999, 5152–5155.

Marwan, N, Wessel, N., Meyerfeldt, U., Schirdewan, A., Kurths, J., Recurrence-plot-based-measures of complexity and their application to heart rate variability data. *Physical* Review E, 66, 2002, 026702.1-026702.8.

Marwan, M., Encounters with neighborhood, PhD Thesis, 2003.

Matcharashvili, T., Chelidze, T., Javakhishvili, Z., 'Nonlinear analysis of magnitude and interevent time interval sequences for earthquakes of Caucasian region', *Nonlinear Processes in Geophysics*, 2000, 7, 9–19.

Matcharashvili, T., Chelidze, T., Peinke, J., Increase of order in seismic processes around large reservoir induced by water level periodic variation, Nonlinear Dynamics, 399-407, 51, 3, 2008.

McAllister, R., Uchida, A., Meucci, A., Roy, R., 'Generalized synchronization of chaos: experiments on a two-mode microchip laser with optoelectronic feedback', *Physica D* 195, 2004, 244–262.

Nascimento, A, F., Cowie, P.A., Lunn, R, J., Pearce, G., 'Spatio-temporal evolution of induced seismicity at Açu reservoir, NE Brazil', *Geophysical Journal International*, 158, 2004, 1041–1052.

Pazo,D., Zaks, M.A., Kurths. J., Role of unstable periodic orbits in phase and lag synchronization between coupled chaotic oscillators, *Chaos*, 13, 2003, 309–318.

Peinke, J., Matcharashvili, T., Chelidze, T., Gogiashvili, J., Nawroth, A., Lursmanashvili, O., Javakhishvili, Z., 'Influence of Periodic Variations in Water Level on Regional Seismic Activity Around a Large Reservoir: Field and Laboratory Model', *Physics of the Earth and Planetary Interiors*, 156/1-2, 2006, 130–142.

Pikovsky, A., Rosenblum, M.G., Kurth. J., *Synchronization: Universal Concept in Nonlinear Science*, Cambridge University Press, Cambridge, 2003.

Postnov, D.E., Sosnovtseva, O.V., Mosekilde, E., Holstein-Rathlou, N.-H., 'Synchronization of Tubular Pressure Oscillations in Interacting Nephrons' *Chaos, Solitons and Fractals*, 15, 2, 2003, 343–369.

Rosenblum, M., Pikovsky, A., Kurth, J., 'Phase synchronization of chaotic oscillators, *Physics Review Letters'*, 76, 1996, 1804–1807.

Rundle, J., Turcotte, D., Klein, W., (eds),. *GeoComplexity and the Physics of Earthquakes*, American Geophysical Union, Washington, 2000.

Simpson, D. W., 'Triggered earthquakes', *Annual Reviews of the Earth and Planetary Sciences*. 14, 1986, 21–42.

Simpson, D., Leith, W., Scholz, C. 'Two types of reservoir-induced seismicity', *Bulletin of Seismological Society America*, 78, 1988, 2025–2040.

Smirnov, V.B., 'Fractal properties of seismicity of Caucasus', *J. of Earthq. Prediction Res.* 4, 1995, 31–45.

Talwani, P., 'On nature of reservoir-induced seismicity', *Pure and Applied Geophysics*, 150, 1997, 473-492.

Trifu, C.I. (ed)., The mechanism of induced seismicity, Special Volume, *Pure & Applied Geophysics*, 159, 2002.

Zbilut, J.P., Webber, C.L. Jr., Embeddings and delays as derived from quantification of recurrence plots. *Physics Letters A*, 171,1992, 199–203.

Chapter 17
Earthquakes' Signatures in Dynamics of Water Level Variations in Boreholes

T. Chelidze, T. Matcharashvili, and G. Melikadze

Abstract It is known that variations of water level represent an integral response of aquifer to different periodic as well as non-periodic forcing, including earthquake-related strain generation in the earth crust. Quantitative analysis of impacts of separate components in the observed integral dynamics remains one of the main geophysical problems. It is especially important for non-periodic processes related to the earthquake generation, taking into account their possible prognostic value. We can formulate the problem as a nonlinear analysis of hydrological anomalies "triggered" by both the earthquake preparation and post-seismic processes.

In the present study, the dynamical complexity of water level variations has been analyzed. The dependence of dynamics on the presence of periodic components in the data records (time series) under study was investigated. Modern tools of time series analysis such as complexity measure and singular value decomposition technique have been used. Values of Lempel-Ziv complexity of water level records before and after the Spitak and Racha earthquakes, both original and reconstructed by singular value decomposition, were analyzed. The main purpose was to study dynamical response of water level variation to increased seismic activity around boreholes. Spectral characteristics, Shannon entropy and mutual information of water level variation time series were calculated. It is shown that most of boreholes are responding to changes caused by seismic activity, but some are not. This can be explained by the complexity of geological and stress field structures. Sensitive boreholes reveal some general features, such as an increase of the order in water level variability in separate boreholes and a decrease of functional relationship between water level variations in pairs of different boreholes before a strong earthquake.

T. Chelidze (✉), T. Matcharashvili, and G. Melikadze
M. Nodia Institute of Geophysics, 1 Alexidze str, 0171 Tbilisi, Georgia
e-mail: tamaz.chelidze@gmail.com; matcharashvili@gtu.ge

V. de Rubeis et al. (eds.), *Synchronization and Triggering: from Fracture to Earthquake Processes*, GeoPlanet: Earth and Planetary Sciences 1,
DOI 10.1007/978-3-642-12300-9_17,

17.1 Introduction

Generally speaking, the water level (WL) variation in deep boreholes is caused by a number of different factors. One of the most important factors is a strain change in the upper Earth crust. In fact, deep boreholes represent some kind of sensitive volumetric strainmeters, where water level responds to the deformations of about 10^{-7} –10^{-8}. Hence, it is obvious that the process of water level variations will reflect also the integral response of aquifer to the earthquake-related strain redistribution in the Earth crust (Kumpel, 1992; Gavrilenko et al., 2000). The network of water regime boreholes existing in Georgia allows to create a spatial picture of the strain field and observe its evolution in the time domain. The retrospective analysis of materials shows that a characteristic annual course of levels of underground waters is disrupted in the period of strong earthquakes (Spitak, 1988; Racha, 1991; Java, 1991; and Barisakho, 1992). The area of compression is characterized by underground waters level increasing in comparison to the normal trend, and the area of dilatation – by its decrease (Melikadze and Ghlonti, 2000). Therefore, investigation of water level variations may provide additional understanding of the dynamics of processes related to earthquake preparation in the earth crust (Manga and Wang, 2009). Nevertheless, the problem of relationship between changes in dynamics of water level variation and strong earthquake preparation still remains practically unsolved (King et al., 1999).

In the present study we have investigated the dynamics of WL variation in the network of deep boreholes on the territory of Georgia. The aim of research was to clarify the character of influence of seismic processes on dynamics of water level variation. Taking into account practical problems and scientific discussions related to understanding of seismic processes, investigation of influence of seismic activity on the dynamics of water level variation is important both from scientific and practical points of view.

17.2 Methods of analysis

As the water level variation in deep boreholes is caused by a number of endogenous and exogenous factors, we prepared a special programme for defining the tectonic component; it calculates the theoretical signal composed of a sum of reduced values of atmospheric pressure, tidal variations and precipitation. In order to extract the geodynamical signal, correlation analysis between the real values of WL and the theoretical signal has been made (Gavrilenko et al., 2000; Melikadze and Ghlonti, 2000). The program gives a possibility to calibrate values of deformation in 10^{-8} range by comparison of geodynamic signals with tidal variations.

The WL variation data sets of deep boreholes in Georgia have been analyzed by modern methods of nonlinear dynamics. The network of underground water regime observations was set up in the Caucasus in 1985. Since that time, a network comprising

50 sub-artesian boreholes of different depths (ranging from 250 m down to 3500 m) has been functioning in the Caucasus. The Georgian network consists of 10 boreholes and covers the entire territory of Georgia. The present study is based on analysis of hourly water level variations time series of 6 boreholes, namely: Lisi (44.45 N, 21.45 E), Borjomi (43.27 N, 41.52 E), Akhalkalaqi (43.34 N, 41.22 E), Ajameti (42.49 N, 42.10 E), Marneuli (44.52 N, 41.26 E), and Kobuleti (41.48 N, 41.47 E) boreholes. Typical records of hourly water level variations are presented in Fig. 17.1. Depending on the availability and quality of data, time series of different length were analyzed. The longest one covers approximately two years (01.03.1990 through 29.02.1992) and the shortest one covers one month (11.10.1988 through 12.12.1988).

At first we calculated power spectrum as well as the power spectrum regression exponent (Allegrini et al., 1995; Feder, 1988) of water level time series. In order to evaluate the character of probability distribution, the Shannon entropy S:

$$S = -\sum_{i=1}^{N} P_i \log(P_i),$$

where P_i is the probability of an event to occur within box i, was calculated using different time-span sliding windows (Kantz and Schreiber, 1997; Schreiber, 2000). Then, in order to evaluate the strength of functional dependence between water level variations in different boreholes we used a measure of statistical independence between two variables, the averaged mutual information (Cover and Thomas, 1991; Kantz and Schreiber, 1997):

$$I(T) = \sum_{i=1}^{N} P(x(i), x(i+T)) \log_2 \left[\frac{P(x(i), x(i+T))}{P(x(i))P(x(i+T))} \right],$$

where $P(x(i))$ and $P(x(i+T))$ are, respectively, the probabilities of finding $x(i)$ and $x(i+T)$ measurements in time series, $P(x(i), x(i+T))$ is the joint probability of finding measurements $x(i)$ and $x(i+T)$ in time series, and T is the time lag.

In the present study we analyzed the integral dynamics of water level variability. Therefore we avoid any linear filtration or signal separation, only nonlinear noise reduction procedure (Kantz and Schreiber, 1997; Hegger et al., 1999) after zero mean and unite variance normalization have been carried out.

17.3 Results and discussion

As follows from our analysis, the response of WL variation of analyzed boreholes to the increased regional seismic activity varies from case to case. Indeed, it is shown in Fig. 17.1 that the water level change coinciding in time with strong Racha earthquake is essential for Lisi borehole. At the same time, during the same period, amplitudes of variation of water level in Akhalkalaki and Kobuleti boreholes are

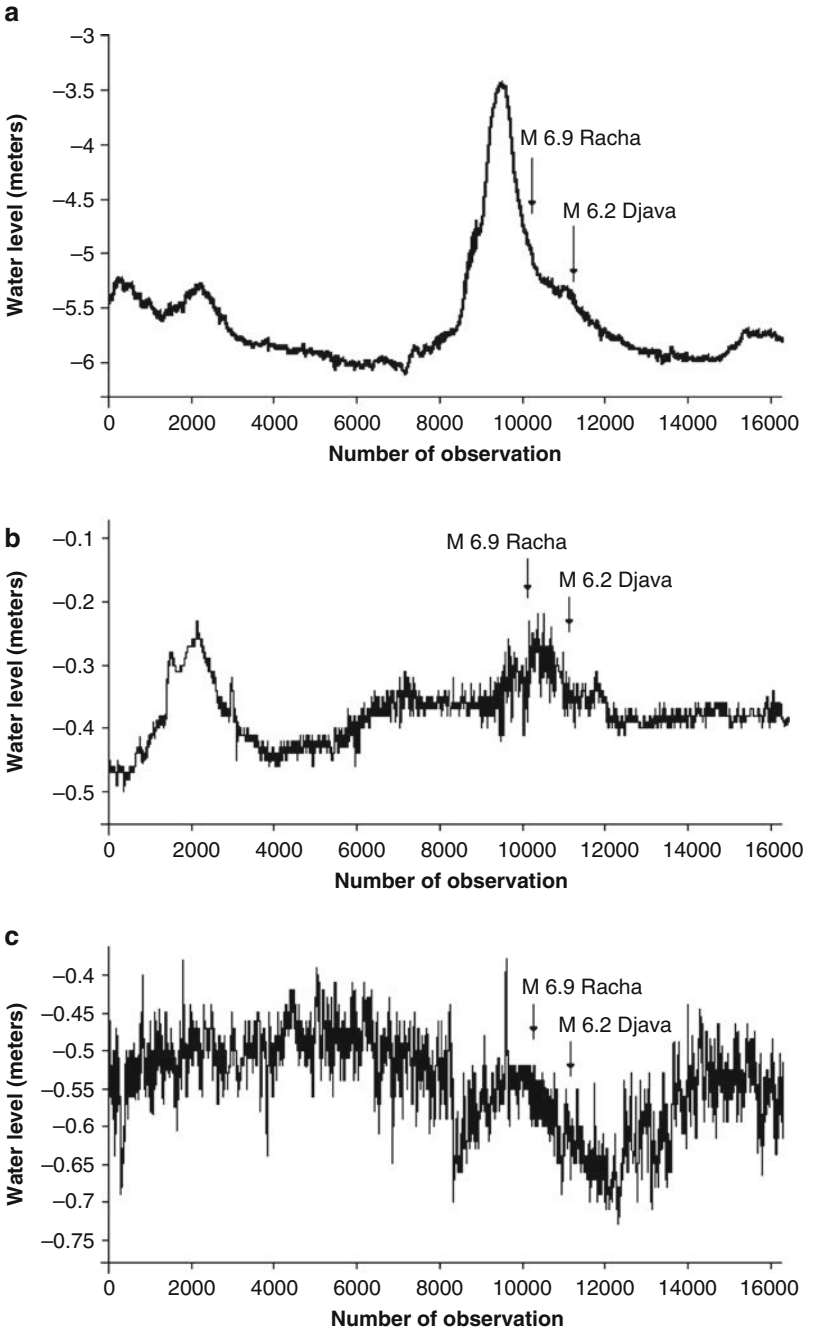

Fig. 17.1 Water level variation at (**a**) Lisi, (**b**) Akhalkalaki and (**c**) Kobuleti boreholes for the time period 01.03.1990−29.02.1992

rather small or even practically unchanged comparing to the Lisi borehole. This can be explained by the complex character of stress field in the region (Melikadze and Ghlonti, 2000).

Before the Spitak event, the infringement period of the background regime appeared in separate wells at different times and with different intensities: in Lisi from 25.11.88; in Borjomi from 28.11.88; in Lagodekhi from 28.11.88. First of all, the infringements are seen on boreholes located in northern part of the structure, in the zone of strongest compression, and later in the south. As a rule, the character of anomaly in the compression zone has a positive bay shape (Lisi, Borjomi, Lagodekhi, etc.), and in the stretching zone — the sawtooth or negative bay (Marneuli, etc.). The above-mentioned sequence of infringement occurrence can be caused by directional development of deformation processes.

The same is proved also by the materials of Racha earthquake (29.04.91) obtained from the boreholes network. The anomalies in hydro-geo-deformation field divide the Caucasus in two parts and have been precisely fixed before the event. The division between the zones passed along a deep tectonic fault of sub-meridian orientation. The zone of largest gradient specified the place of future disaster, coinciding with the point of junction of the fault.

Deformation processes covered the whole observed territory of the Caucasus. Despite the complicated geological structure of the territory and different strain-sensitivity of boreholes, the general tendency of changes is noticed in the underground waters regime. In boreholes located in the compression field, an abnormal rise of water level is observed (in Akalkalaki from 01.02 by +10 cm; in Marneuli from 15.04 by +25 cm; in Lisi from 02.04 by +2 m; in Borjomi from 02.04 by +1 m; in Lagodekhi from 03.04 by +50 cm; in Chargali from 10.04 by +30 cm). The greatest deformations are in the Lisi borehole. In boreholes located in the stretching area, the water level decreases: Kobuleti from 20.04 by −10 cm; Gali from 10.04 by −0,5 meters; and Adjameti from 10.04 by −30 cm.

In the stress field, the transitive zone between deformations of different signs extends along the above-marked deep fault and crosses the epicentral zone, where the dipole deformation structure is created. Its presence confirms the existing ideas about the strain distribution in the source area of earthquakes (Fig. 17.10).

In general, the water level variation dynamics before the Spitak earthquake is also characterized by increased extent of regularity expressed by decreased Shannon entropy value, though it is not so evident as for the Racha event; there are still local minima (Fig. 17.3). At the same time, contrary to the Racha earthquake, here, after the strong event, the dynamics of water level variability in most cases becomes much more disordered than before: the Shannon entropy increases.

During the Spitak earthquake preparation period, within several months, a strong stretching sub-latitude deformation was formed in the future epicenter area, and a compression area appeared to the north of it. The expanding zone of stretching, besides the territory of Armenia, covers a part of southern Georgia (boreholes Marneuli and Akhalkalaki) and western Azerbaijan (borehole Sheki).

Within three months, the decrease of water level on the borehole Akhalkalaki against the annual "background" reached 20 cm, that makes a half of the maximal amplitude of seasonal fluctuations. On the Marneuli borehole, the decrease was much larger (up to 50 cm), and almost the whole amplitude of seasonal fluctuation was leveled by tensile deformation. On the Sheki borehole, the difference was up to 30 cm. In the compression zone, there is located the Borjomi borehole, where during six months the difference of the level, in comparison to the average, makes +1.5 meters, and Lisi, where it is up to +1 meter. The Lagodechi borehole changes are of the same order. During some period of time, the intensity increases; at the critical point of deformation, the lunar-solar tidal variations disappear in the underground waters, and the impact of barometric pressure disappears too. At this time, the strong endogenous factors which influence the water bearing horizon muffle the exogenous ones.

The appearance of anomalies before the Spitak event was distributed in time: Lisi - from 25.11.88; Borjomi - from 28.11.88; Lagodechi - from 28.11.88; Sheki - from 4.12.88; Novkhvani - from 4.12.88; Shemakha - from 6.12.88. It is evident that the anomaly first of all manifests itself in the boreholes located in the northern part of the structure, in the strongest compression zone, and later on in the south. As a rule, the anomaly in the compression zone has a positive bay shape (Lisi, Borjomi, Lagodekhi, Novkhvani, Shemakha etc.) and in the stretching zone it looks like the sawtooth or negative deviation (Marneuli, Sheki etc.). Thus, there is some regular pattern of the anomalous field evolution (Fig. 17.11).

All the changes described above are obviously related to the seismic activity, because in most cases they concur with strong earthquakes. Such a relation is evident from an analysis of the longest water level variability time series available for us. In Fig. 17.4, Shannon entropy for time series containing 16300 readings (01.03.1990 through 29.02.1992) analyzed by two-week span sliding windows are presented. It is shown that the dynamics of water level variation undergoes clear changes both before and after strong earthquakes. As it is presented in Fig. 17.4 a, over about 9-5 month period of time before the strong Racha earthquake, water level variation in Lisi borehole becomes strongly ordered. The Shannon entropy value of water level variation noticeably decreases for this period clearly preceding the strong earthquake. At the same time, immediately before the earthquake (over 30-15 days period) the water level variation became maximally disordered; the entropy value has substantially increased.

Generally similar is the situation for the long time series of Akhalkalaki borehole (Fig. 17.4 b), where about 8 months before the Racha earthquake the water level variation for short time period has minimal (but higher than for the Lisi borehole and for a much shorter time period) value of Shannon entropy.

Immediately before the strong earthquake, the water level variation in Akhalkalaki borehole also became maximally disordered and is characterized by practically the same extent of Shannon entropy as for the Lisi borehole. At the same time, the water level variation in Kobuleti borehole does not show the features observed for the other two boreholes (Fig. 17.4 c), which can be explained by a relatively large epicentral distance (King et al., 1999).

Thus, in two out of the three long time series analyzed, the dynamics of water level variation becomes more irregular two-three weeks before a strong earthquake. At the same time, it is important to mention that some boreholes may by insensitive (King et al., 1999) to changes caused by regional seismic activity (see, e.g., the results for Kobuleti borehole in Fig. 17.4 c).

In spite of the observed differences in absolute values of amplitudes of water level in different boreholes, the dynamics of variation still reveals some interesting features which may be related to regional seismic activity. All the water level variation time series analyzed are characterized by a broadband power spectrum. By their exponents of power spectrum regression, the process of water level variation in 20.5-day duration time series (600 data), generally can be attributed to the coloured type of noise, both before and after strong earthquakes (see, e.g., Tables 17.1 and 17.2). The obtained values of power spectrum exponents are typical for processes where the low frequency events (taking place on long time-scales) dominate in the total variability compared to the high frequency component (Pimm and Redfearn, 1988). In this respect, as it follows from Tables 17.1 and 17.2, there are no significant differences in spectral characteristics of water level variations during or after strong earthquakes (excluding water level variation in Ajameti borehole for rhe Spitak and Borjomi borehole for the Racha earthquakes).

Thus, spectral characteristics of water level variability do not react on the level of regional seismic activity which significantly increased for the analyzed time period.

In spite of this integral insensitivity, we tried to clarify some details of the fine dynamical structure of process of interest on the shorter time scales. For this purpose, the Shannon entropy values of 10-day-span sliding windows of longer water level variation data sets (including time periods both before and after large earthquakes) have been calculated. In Fig. 17.2, it is shown that the dynamics of water level variability on 10-day time scale undergoes noticeable changes both before and after the Racha earthquake. The same is true for the aftershock of the

Table 17.1 Power spectrum regression exponents of water level variation before and after the Spitak earthquake

	Axalkalaki	Borjomi	Ajameti	Lisi
Before	-1.59 ± 0.08	-1.69 ± 0.09	-2.13 ± 0.02	-1.74 ± 0.08
After	-1.66 ± 0.08	-1.83 ± 0.03	-1.87 ± 0.07	-1.82 ± 0.03

Table 17.2 Power spectrum regression exponents of water level variation before and after the Racha earthquake

	Axalkalaki	Borjomi	Ajameti	Lisi
Before	-1.81 ± 0.09	-1.57 ± 0.08	-1.84 ± 0.05	-1.80 ± 0.01
After	-1.86 ± 0.07	-1.79 ± 0.05	-1.93 ± 0.08	-1.82 ± 0.03

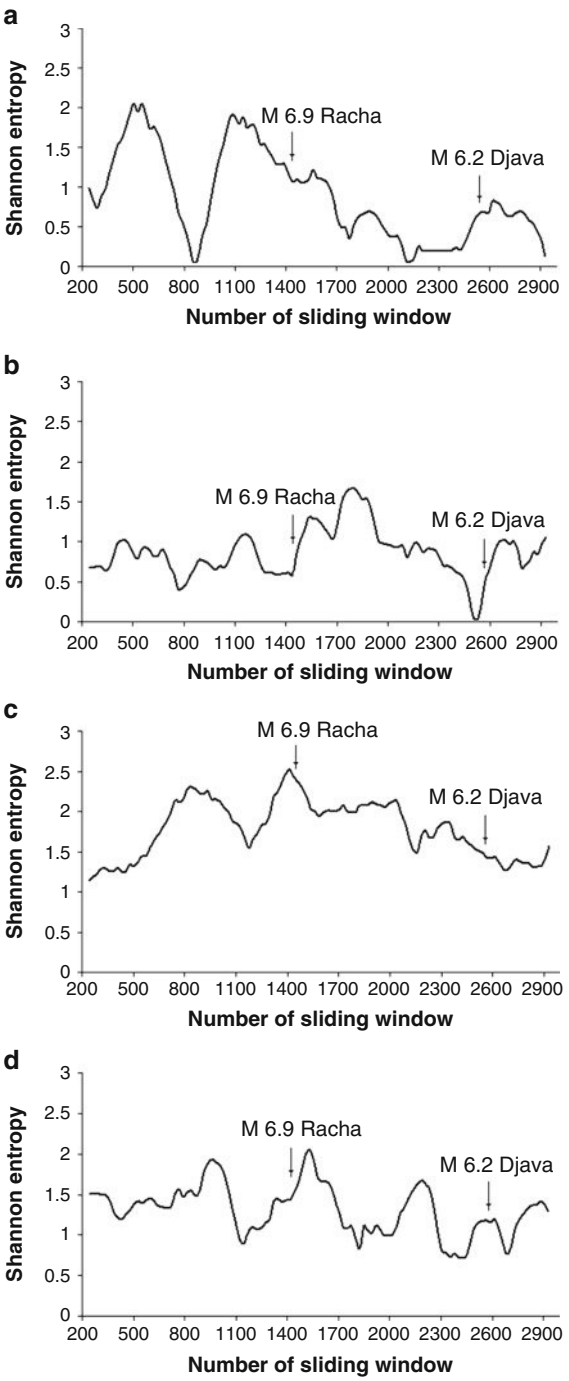

Fig. 17.2 Shannon entropy values of (**a**) Lisi, (**b**) Lagodekhi, (**c**) Akhalkalaki, and (**d**) Ajameti boreholes water level hourly records calculated for 240 data (10 day time span) sliding window at 24 hour step. Time of observation: 01.03.1991−30.06.1991

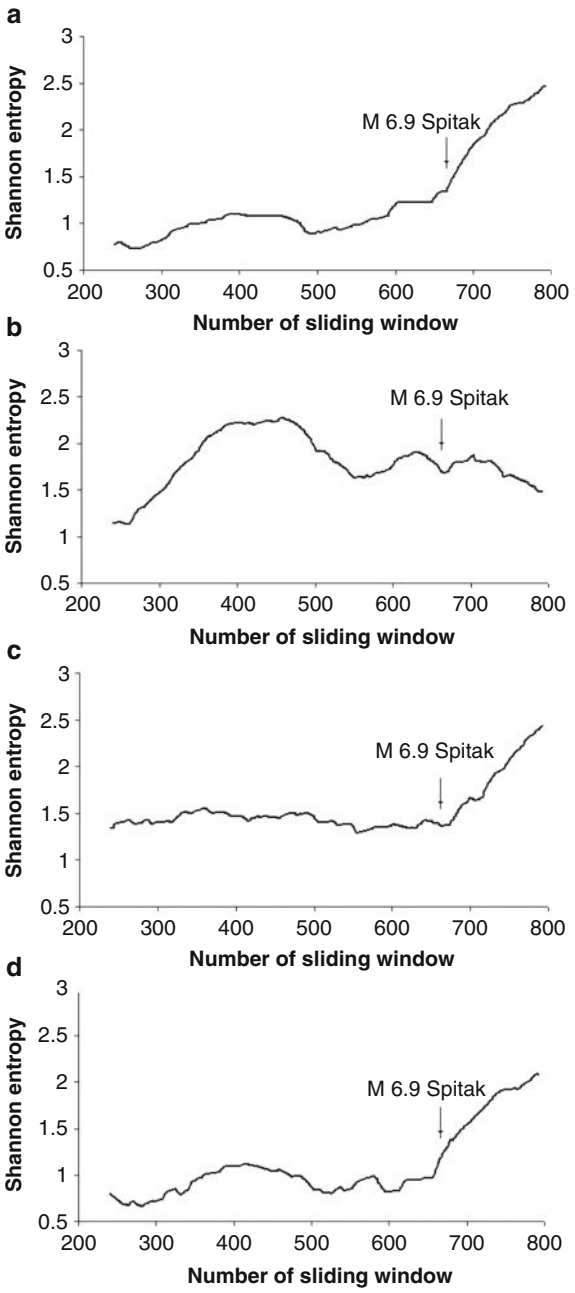

Fig. 17.3 Shannon entropy values of (**a**) Lisi, (**b**) Lagodekhi, (**c**) Borjomi, and (**d**) Marneuli boreholes water level hourly records calculated for 240 data (10 day time span) sliding window at 1 hour step. Time of observation: 11.10.1988−12.12.1988

Racha earthquake, M.6.2 Djava (15.06.1991) event. As shown in Fig. 17.2, in almost all the cases, the Shannon entropy of water level variability approaches their local extremes before the strong earthquake.

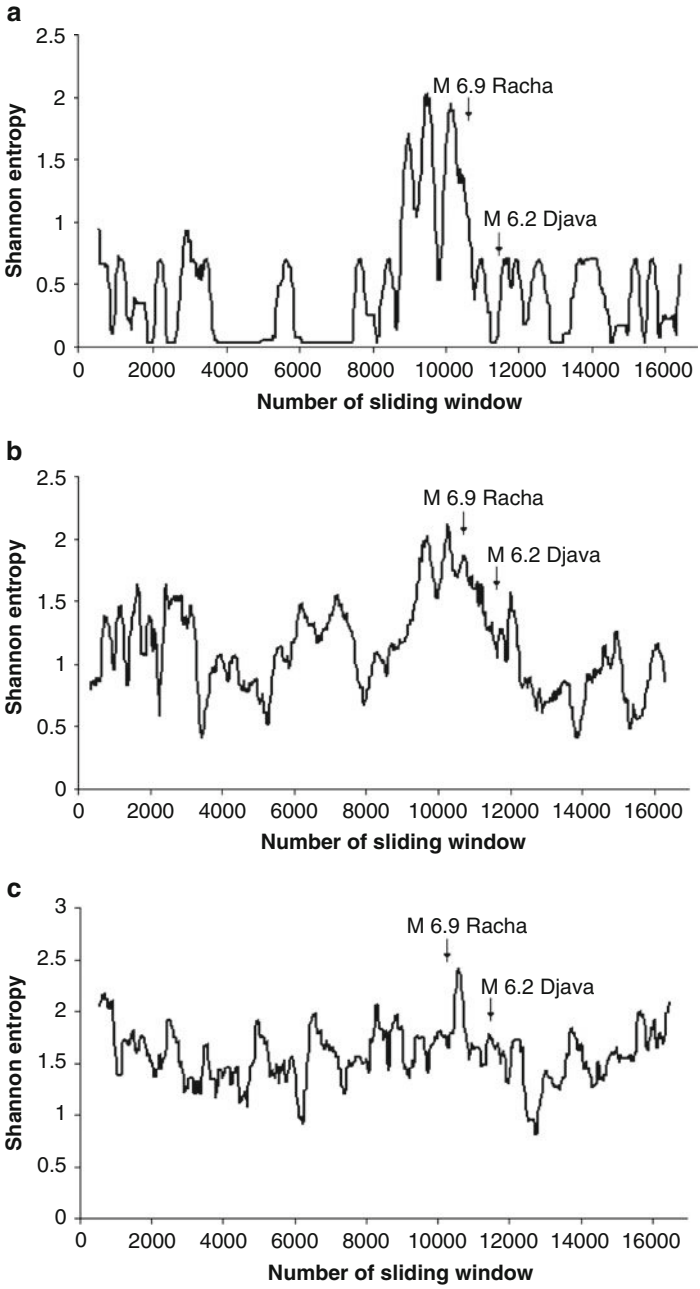

Fig. 17.4 Shannon entropy values of (**a**) Lisi, (**b**) Akhalkalaki and (**c**) Kobuleti boreholes water level hourly records calculated for 360 data (two-week time span) sliding window at 24 hour step. Time of observation: 01.03.1990−29.02.1992

It is also important to say that on the analyzed time scale and for the tested period of observation, the WL variation after the strong earthquake comes back to the background level.

As there are important similarities in dynamical responses of water level variations for different boreholes to regional seismic activity, we have investigated the strength of functional dependence between them. For this purpose, we calculated averaged mutual information, the well known measure of statistical independence between two variables (Cover and Thomas, 1991; Kantz and Schreiber, 1997). The mutual information value is the most suitable parameter for these purposes, because unlike the linear correlation function, it takes into account nonlinear correlations too (Hegger et al., 1999). It is shown in Fig. 17.5 that the strength of functional relationship between water level variability in pairs of boreholes before, during, as well as after strong earthquake undergoes noticeable changes. The water level variability in different boreholes is maximally de-correlated over about two-to-three weeks period before the Racha event (mutual information values have their minima). It is important that this strong earthquake as well as its aftershock is preceded by brief sharp changes in extent of interdependence of variability in boreholes.

In most cases, the above-mentioned sharp changes are characteristic for functional interdependence between water level variations in boreholes during seismic activity related to the Spitak earthquake (see Fig. 17.6). At the same time, the transition between functionally independent and dependent states are not as sharp and clear as for the Racha earthquakes. It is interesting that after the Spitak earthquake the dynamics of WL variation in different boreholes becomes more functionally dependent than before (values of mutual information increase).

The above-mentioned features of dynamics of water level variations are especially noticeable for the longest available time series. Indeed, as shown in Fig. 17.7 a and b, the dynamics of water level variability in Lisi borehole reveals a clear decrease in the extent of functional interdependence for several months before the strong earthquake. At the same time, as it was said above, some boreholes may be not sensitive to changes caused by seismic activity (King et al., 1999), e.g., water level variability in Akhalkalaki and Kobuleti boreholes does not reveal changes (Fig. 17.7 c), which can be explained by the character of regional stress field during seismic activity.

Before and during Racha and Spitak earthquakes it became possible to monitor spatial evolution of deformation processes and to define the anomalous zones relative to the background daily course of underground waters level (Figs. 17.10 and 17.11). This analysis bears information on the seismic event's approaching time. In the Racha earthquake, the compression zone anomalies are expressed by the suppression of tide effects, first of all in the boreholes located in the zone of the strongest gradient (Lisi - from 10.03. Chargali - from 05.04. Marneuli – from 08.04.) and further on boreholes located to the east, in the deformation zone with lesser gradient (from 15.04), and later on - to the east on the territory of Azerbaijan (Fig. 17.10).

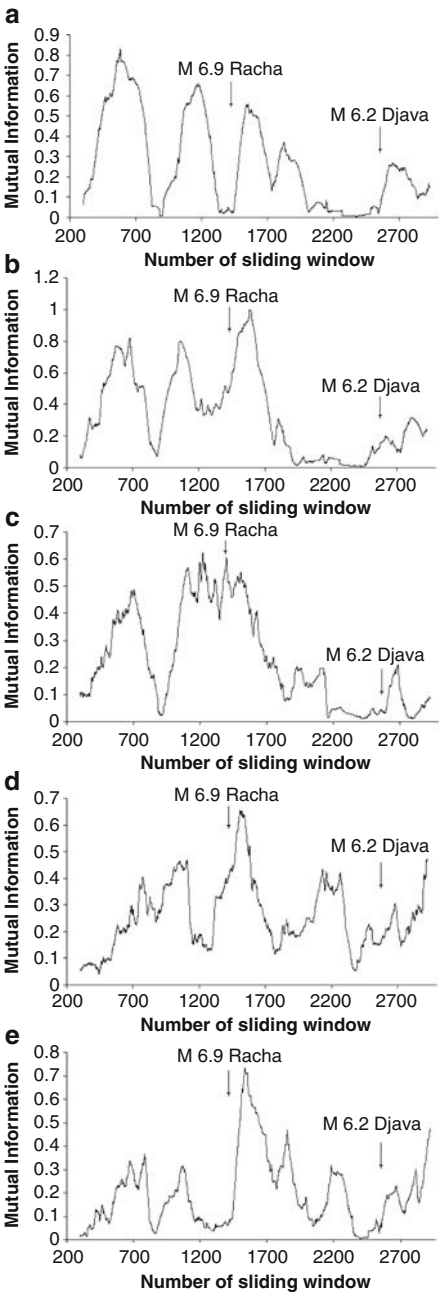

Fig. 17.5 Mutual Information values calculated for 300 data length sliding windows of water level time series of pairs of boreholes: (**a**) Lisi vs. Lagodekhi, (**b**) Lisi vs. Ajameti, (**c**) Lisi vs. Akhalkalaki, (**d**) Akhalkalaki vs. Ajameti, and (e) Ajameti vs. Lagodekhi. Time of observation: 01.03.1991−30.06.1991. Sliding window at 1 hour step

The majority of data confirms the abnormal behavior of WL in boreholes on the territory of the whole Caucasian region before and after strong earthquakes. The example of regional effect is the identical behavior of boreholes Lisi and Esentuki,

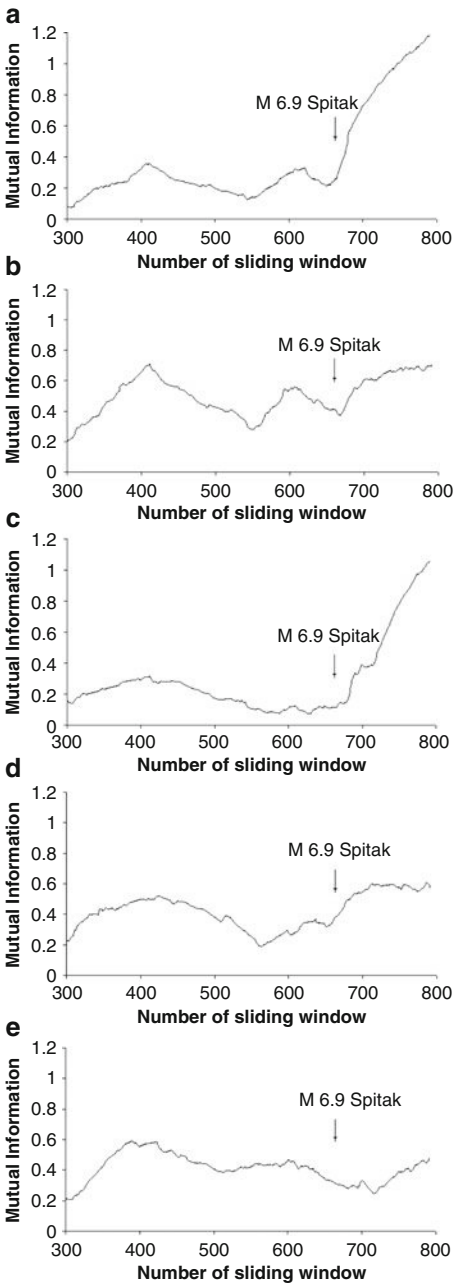

Fig. 17.6 Mutual Information values calculated for 300 data length sliding windows of water level time series of pairs of boreholes: (**a**) Lisi vs. Marneuli, (**b**) Lisi vs. Lagodekhi, (**c**) Lisi vs. Borjomi, (**c**) Lagodekhi vs. Marneuli, and (**d**) Borjomi vs. Lagodekhi. Time of observation: 11.10.1988−12.12.1988. Sliding window at 1 hour step

where compression processes adjusted the exogenous effects two months before the Racha event.

In a transitive zone (borehole Adjameti), the strong anomalies were not found. The presence of complex mosaic structure of deformation is a possible explanation

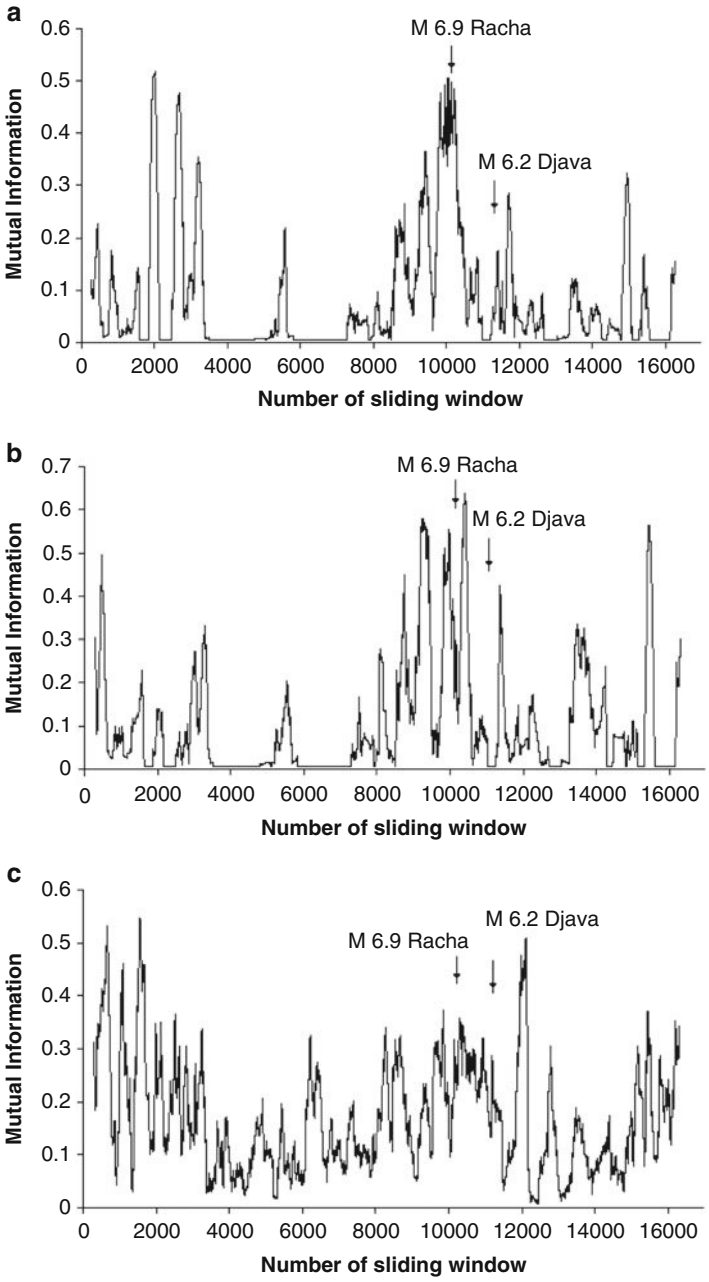

Fig. 17.7 Mutual Information values calculated for 300 data length sliding windows of water level time series of pairs of boreholes: (**a**) Lisi vs. Akhalkalaki, (**b**) Lisi vs. Kobuleti, and (**c**) Akhalkalaki vs. Kobuleti. Time of observation: 01.03.1990−29.02.1992. Sliding window at 1 hour step

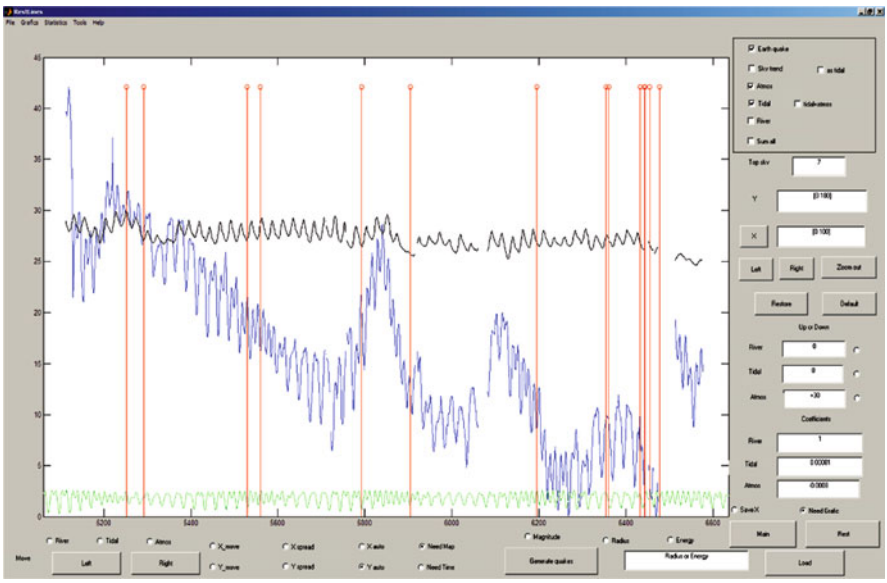

Fig. 17.8 Graph of a tidal (the bottom line), atmospheric pressure (the top line) and the underground water level (the middle line) variations in time. Vertical lines show earthquakes occurred in this period

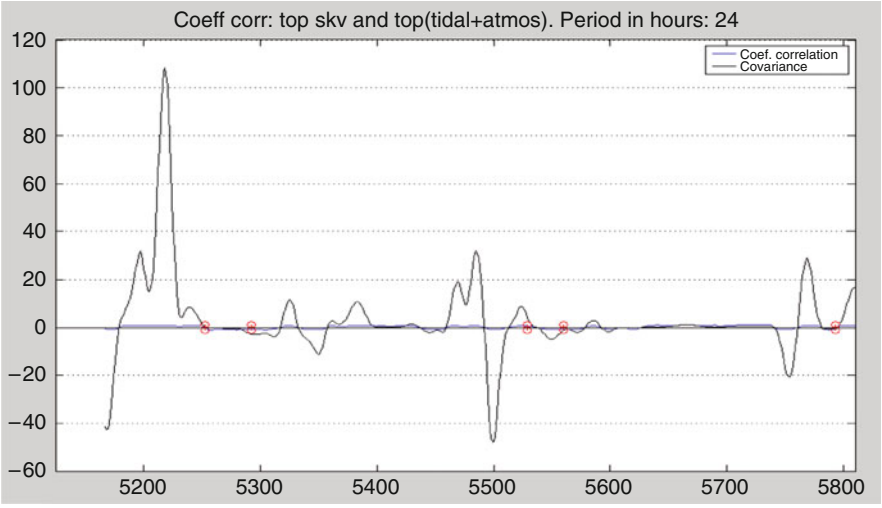

Fig. 17.9 Change of values of correlation coefficient between values of a water level and the sum of reduced values of atmospheric pressure and tidal variations

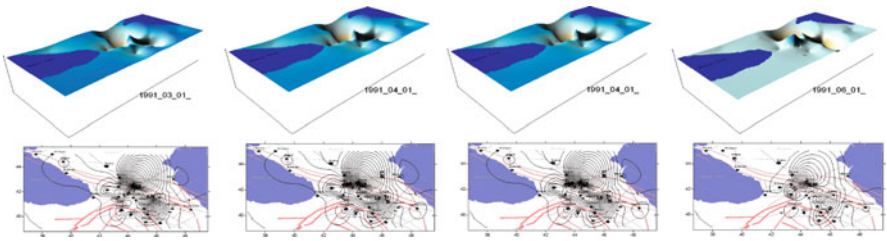

Fig. 17.10 3-D and 2-D models of evolution of stress field during preparation of the Racha earthquake of 29.04.1991 (red lines – main Caucasian faults)

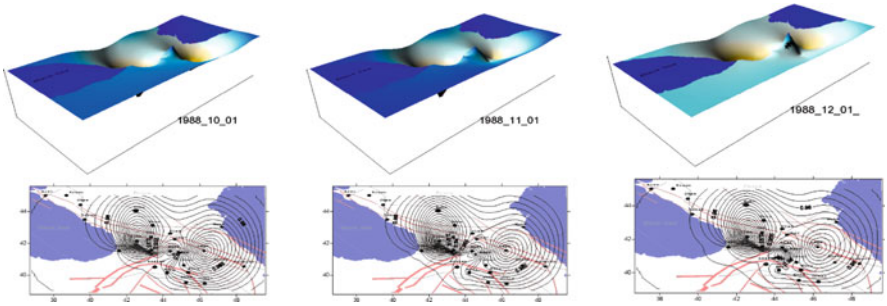

Fig. 17.11 3-D and 2-D models of evolution of stress field during preparation of the Spirak earthquake of 08.12.1988 (red lines – main Caucasian faults)

of the fact that anomaly at the borehole Oni is fixed only one month before the events - from 04.04.

In the stretching zone, the deviation from the background is marked as a weak distortion of the tide effect (borehole Adjameti from 4.04; Gali from 03.04; Sukhumi - 08.04). On boreholes Akalkalaki and Kobuleti, which are located far from the epicenter, the amplitudes of barometric fluctuation and tide effects have been gradually increasing since the beginning of March. According to the North-Caucasian data, a similar anomaly was marked on the borehole Light-blue Lakes. Such anomalies are caused by the amplification of aquifer's reaction to exogenous processes and easing of horizontal stress due to endogenous processes.

17.4 Conclusions

The dynamics of water level variability is strongly sensitive to the borehole and earthquake source location. Therefore, not all the boreholes react similarly to the

changes caused by tectonic/seismic activity in the analyzed region. In sensitive boreholes, dynamical changes both before as well as after strong earthquakes are evident. When approaching time of earthquake occurrence, in most of the observed cases, the water level variability becomes more and more regular comparing to the preceding, seismically quiet time period. At the same time, the regularity in water level variability is again distorted immediately prior to the earthquake occurrence.

In spite of observations of seismicity-related dynamical changes in water level variability, there are essential qualitative and quantitative differences in the dynamics of water level variability in separate boreholes, which supposedly are strongly dependent on geological and strain field peculiarities of the considered area.

References

Allegrini, P., Barbi, M., Grigolini, P., West, B.J. 1995. A Dynamical Mode the DNA Sequences. *Phys. Rev. E* 52, 5281

Cover, T. M., Thomas, J. A., 1991. Elements of Information Theory. J.W.S, NY 280 pp.

Feder, J. 1988. *Fractals* Plenum Press, New York

Gavrilenko. P., G. Melikadze., Chelidze, T., Gibert, D., Kumsiashvili, G. 2000. Permanent water level drop associated with Spitak earthquake: observations at Lisi borehole and modeling. Geophys. J. Int., 143, 83-98.

Hegger, R., Kantz, H., Shreiber, T., 1999. Practical implementation of nonlinear time series methods. The TISEAN package, Chaos. 9. P. 413-440.

Kantz, H; Schreiber T., 1997. Nonlinear time series analysis. C. U. P.Cambridge 350 pp.

King, C. Y., Azuma, S., Igarashi, G., Ohno, M., Saito, H., Wakita, H. 1999. Earthquake – related water-level changes at 16 closely clustered wells in Tono, central Japan, J. Geoph. Res. 104, B6, 13073-13082

Kumpel, H. 1994. Evidence for self-similarity in the harmonic development of earth tides, in: Kruhl, J.H. (Ed), Fractals and dynamic systems in geoscience, Springer, Berlin, 213-220.

Manga, M and Wang C.-Y. 2009. Earthquake Hydrology. In: Earthquake Seismology, H. Kanamori (Ed). Elsevier. P. 293-320.

Melikadze, G., Ghlonti, E. 2000. Some features of hydrogeodeformation field in Caucasus during strong earthquakes preparation period. Journal of Georgian Geophysical Society, issue A. Physics of Solid Earth, v. 5, 106-111.

Pimm, S., Redfearn, A. 1988. The variability of natural populations. *Nature*, **334**, 613-614.

Schreiber, T. 2000. Measuring Information Transfer. Phys. Rev. Lett., 85:461

Chapter 18
Detecting Quasi-Harmonic Factors Synchronizing Relaxation Processes: Application to Seismology

Otar Lursmanashvili, Tamar Paatashvili, and Lev Gheonjian

Abstract Investigations conducted during the last 20-30 years demonstrate some very deep, fundamental regularity in the statistics of earthquakes' time and space distribution that lead to the concept that the earthquake phenomenon is a system-defined complex of interacting events.

In the final stage of earthquake preparation, the epicentral area becomes sensitive to weak global disturbances such as tides, geophysical disturbances caused by solar activity, and variations of Earth rotation rate. One can consider the earthquake source as an analogue of nonlinear relaxation oscillator, storing the energy during dozens or hundreds of years. The "discharge", i.e., an earthquake, happens suddenly, when the stress on the fault reaches the critical value. Close to this limit, the epicentral area becomes sensitive even to weak external disturbances. The additional stresses caused by varying external factors contribute to premature "discharge" of relaxation oscillator, i.e., earthquake. In seismically active regions, varying external factors may operate as synchronizers of earthquake release moments.

Investigation of synchronizing effect of external factors in a certain region requires development of special methods, because the data of earthquakes are presented as unequally-spaced sequences of phenomena.

According to the synchronization theory of relaxation process, discharges (earthquakes) mainly happen when influencing external factor is in a certain phase. It is

O. Lursmanashvili (✉)
M. Nodia Institute of Geophysics of Georgia, 1 Alexidze str, Tbilisi 0171, Georgia
e-mail: Otar.lurs@gmail.com

T. Paatashvili
E. Kharadze National Astrophysical Observatory of Georgia, I. Chavchavadze State University, 32 Chavchavadze ave, Tbilisi 0179, Georgia

L. Gheonjian
M. Nodia Institute of Geophysics of Georgia, 1 Alexidze str, Tbilisi 0171, Georgia
E. Kharadze National Astrophysical Observatory of Georgia, I. Chavchavadze State University, 32 Chavchavadze ave, Tbilisi 0179, Georgia
e-mail: lev.gheonjian@yahoo.com

V. de Rubeis et al. (eds.), *Synchronization and Triggering: from Fracture to Earthquake Processes*, GeoPlanet: Earth and Planetary Sciences 1,
DOI 10.1007/978-3-642-12300-9_18,

possible to determine these moments by means of analysis of discharge recurrence and forms of distributions of event occurrence times' moments. The distribution corresponding to the period of an external synchronizing factor demonstrates a characteristic gap or modulation. All external influencing periodicities may be determined by an analysis of distributions for all virtual forcing periods and detection of typical characteristic forms.

A simple model describes the principles of the used approach. The stress $P(t) = P_o + b(t - t_0)$ increases monotonically and undergoes the influence of external small stress with amplitude, frequency and phase denoted by $a, \bar{\omega},$ and f, respectively. The resulting stress and the critical stress P_m, determining the discharge moment, which are connected by the equation $P_0 + b(t - t_0) + a\cos(\bar{\omega}t + f) = P_m$, will be obtained. The initial moment of energy integration process is unknown. If one examines a set of N different stress accumulation starting moments separated by a step ε, one will obtain N equations of type $b(t - t_0 + \varepsilon n) = P_m - P_0 - a\cos(\bar{\omega}t + f), n = 0, 1, 2, \ldots N$. The solutions of equations correspond to relaxation oscillator discharge moments for stress processes, started at different time moments. Solutions obviously reveal the "gaps", or time intervals when discharges are forbidden, and also demonstrate that the width of the gap depends on the stress growth velocity. The examination of the distribution of phases of discharges inside the period of external forcing shows that strong and slowly growing earthquakes triggered by a stable external forcing demonstrate wider gaps. Fast growth of stress gives birth to narrow gaps or modulation of distribution. An analysis of distributions for different forcing frequencies and appearance of gaps or modulation is the way for distinguishing different external synchronizing factors.

All of these considerations, and the validity of "gap" method for the discovery of external synchronizing factors, are tested and confirmed in model laboratory experiments on electromagnetic and mechanical control of slip, namely, laboratory experiments with spring-slider system.

In order to investigate the influence of external factors triggering earthquakes, the "gap" method was applied to Caucasus earthquakes. The results reveal a set of regularities for strong earthquakes (the earthquakes with $M > 6$ that occurred during the last 100 years). The spectrum of recurrence periods of earthquakes contains 19 components which have clear astronomical and geophysical meaning; spectral distribution of time series of such earthquakes indicates that release mechanism of tectonically prepared strong earthquakes correlates with different tidal effects - the positional relationship of Sun, Earth and the Moon and periodicities of their orbital movement.

18.1 Introduction

We consider the synchronization as the origin of frequency-phase dependence between physically slightly coupled periodic processes. Synchronization of oscillators is a ubiquitous phenomenon in many areas of science and engineering

(Blechman, 1971; Pikovsky et al., 2003). Synchronization phenomenon depends on the intrinsic mechanism of oscillation as well as on the nature of coupling; it has been thoroughly studied for a variety of oscillators.

Relaxation oscillators have properties quite different from that of non-relaxation ones. Relaxation oscillators need just a few or even one cycle to synchronize, and the synchronization is stable in the presence of nonuniformity of natural frequencies. Mathematical description of relaxation oscillator synchronisation process is simple, vivid, and was solved more than half a century ago in engineering (Gulyaev, 1939; Vitkevich, 1945; Meerovich and Zelichenko, 1954). One can consider the earthquake as an analogue of nonlinear relaxation oscillator, storing the energy during tens or hundred of years. The "discharge" of energy, or the earthquake event, happens suddenly, when tension in rocks exceeds friction resistance on the fault. We consider the synchronization of a series of earthquakes (as a series of relaxation processes) by an external quasi-harmonic factor, as the origin of dependence between time series of events and a well-expressed phase of external periodic processes. Close to breaking limit, earthquake epicentre becomes sensitive even to weak external disturbances. The additional tension caused by varying external factors contributes to earlier "discharge" of relaxation oscillator, i.e., release of earthquake. In seismically active regions, varying external factors operate as synchronizers of earthquake release moments. It should be mentioned that from the point of view of energetics, the earthquakes, represented as relaxation oscillators, contain a quite wide dynamic range. Within this range, different external factors may affect phenomena that belong to different energetic classes.

In seismology, the application of methods detecting quasi-harmonic factors which synchronize the relaxation processes is highly actual in view of earthquake prediction problem and contradictions in the results of the study of external factors. Such phenomena include tides, a set of geophysical disturbances caused by solar activity and variations of Earth rotation rate (tides, solar activity, as well as peculiarities of Earth orbital movement participate in this phenomenon). Some of researchers have found an external synchronizing influence (Allen, 1956; Hoffman, 1961; Tamrazian, 1968; Ryall et al., 1968; Heaton, 1975; Polumbo 1986; Dietrich, 1987; Weems and Perry, 1989; Grasso, 1992; Nikolaev, 1994; Tarasov et al., 1999; Lursmanashvili, 2001; Perfettini and Schmittbuhl, 2001; Custodio et al., 2002; Sobolev and Ponomarev, 2003; Scholz, 2003; Wang et al., 2004), others refuse it (Knopoff, 1964; Simpson, 1967; Shlien, 1972; Vidale et al., 1998; Beeler and Lockner, 2003).

Our objective is to comprehend rigorously the concept and routine methodology widely used in electrical engineering and apply it to the study of possible earthquake synchronization processes in the Caucasus region (Lursmanashvili, 1973; Lursmanashvili et al., 1987a, 1987b). This distribution is caused by the presence of migratory waves of plastic deformation. Recent investigations (Ulomov et al., 2006; Ulomov et al., 2007) confirm the importance of this factor of seismicity and also point to the process of preparation of strong earthquakes in the Caucasus.

There is strong reason for further development of the concept to study this region as an object of nonlinear dynamics (Matcharashvili, Chelidze, and Javakhishvili,

2000). Laboratory model experiments confirm the idea of applying the synchronization concept to seismicity (Chelidze and Lursmanashvili, 2003; Chelidze et al., 2005, 2006).

18.2 The model of relaxation oscillator synchronization

We present a simple model describing the principles of relaxation oscillator synchronization approach we used. Let the charge of oscillator, or stress in the epicentre of earthquake, $P(t)$, increase monotonically and undergo the influence of external small stress (or forcing) with amplitude, frequency and initial phase denoted a, $\bar{\omega} = 2\pi/T$, φ, respectively. T represents the period of external oscillating stress. The resulting stress may be represented as

$$P_c(t) = P(t) + a\sin(\bar{\omega}t + \varphi). \tag{18.1}$$

The discharge stage of oscillator cycle will start at the moment when the resulting stress will reach the breaking point of medium P_m, or

$$P_c(t) = P(t) + a\sin(\bar{\omega}t + \varphi) = P_m. \tag{18.2}$$

Assume that at the final stage of earthquake preparation, from the time moment $t = t_0$ and corresponding stress P_0, the stress increases linearly as

$$P(t) = b(t - t_0). \tag{18.3}$$

As a result of this assumption, we have the expression:

$$P_0 + b(t - t_0) + a\cos(\bar{\omega}t + \varphi) = P_m, \tag{18.4}$$

or the equation describing the relation between time-dependent linearly increasing stress and harmonically oscillating external stress:

$$b(t - t_0) = P_m - P_0 - a\cos(\bar{\omega}t + \varphi). \tag{18.5}$$

The initial moment of energy integration process is unknown. If we examine a set of N different start moments, separated by step ε, and, at least, covering the time interval equal to the period of external oscillating stress, we will obtain N equations

$$b(t - t_0 + \varepsilon n) = P_m - P_0 - a\cos(\bar{\omega}t + \varphi), \quad n = 0, 1, 2, \ldots N, \tag{18.6}$$

and solving them, we will be able to determine all possible time moments of discharges caused by external factor and positioned inside the time interval corresponding to the period of external factor. The distribution of these moments

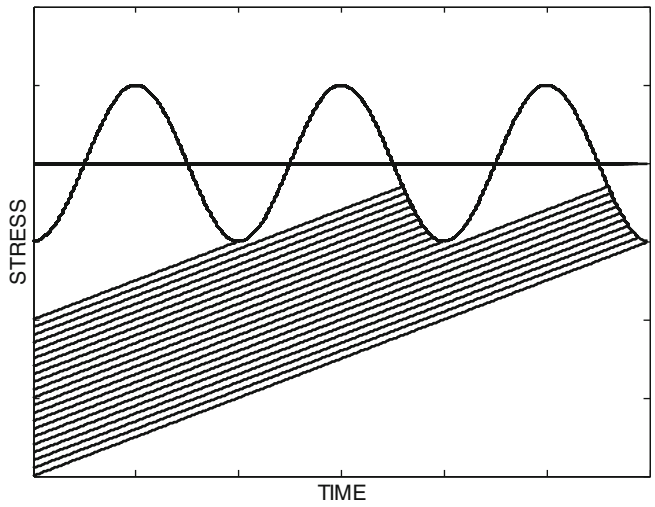

Fig. 18.1 The diagram demonstrating the principle of earthquakes synchronization by external forcing

inside the period corresponding to external oscillator time parameters, will represent the synchronizing properties of the phenomenon described by this model.

Figure 18.1 shows the external oscillating stress represented by the right side of equation (18.6), and the family of lines represented by the left side. They correspond to linearly increasing stress processes started at different time moments in the past and progressing inside the time period of external stress near the final stage of relaxation oscillator evolution. It is obvious that the curve and line intersection moments correspond to possible discharge moments, in our case – time moments of earthquakes. One can obviously see the time "gap", or a set of time moments when discharges are forbidden. It is also obvious that the width of the gap depends on the stress growth velocity. In general case, the widths is determined by the velocity relatively to external factor frequency. If one examines the distribution of earthquakes inside the period of external factor, it turns out that strong, slowly and long-time growing earthquakes triggered by a stable external factor, will demonstrate wider gaps. Fast growth causes narrow gaps or modulation of distribution. Therefore, an analysis of discharge time distributions inside the forcing periods for different frequencies and detection of gaps or modulation — is the way to the discovery of external synchronizing factors which trigger discharges.

Figure 18.2 demonstrates distribution of discharge time moments inside the period of forcing and the corresponding solutions of equations. Let us introduce normalized variable $\tau = t/T$ and examine the distribution of roots of equation (18.6). The equation will be transformed to a simple form

$$A(\tau + n/N) = C - \cos 2\pi\tau, \quad n = 0, 1, 2, \ldots N, \tag{18.7}$$

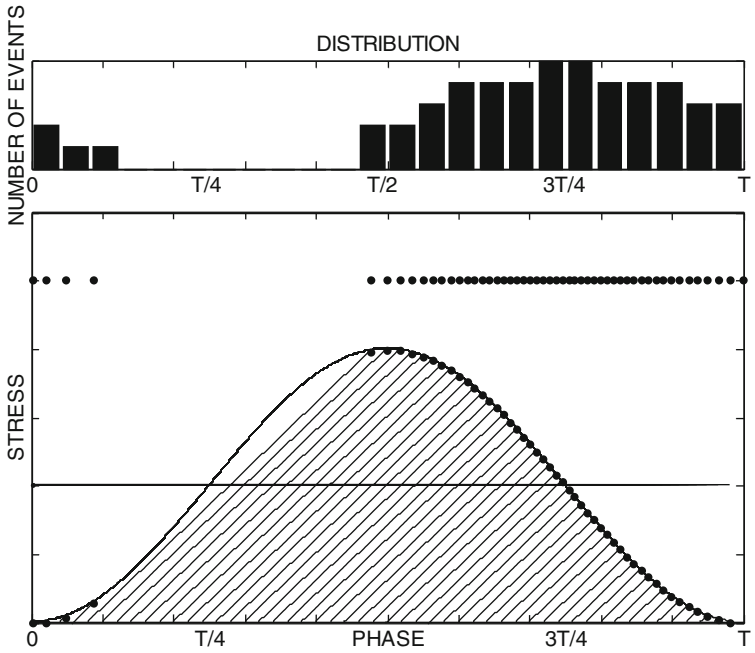

Fig. 18.2 Distribution of relaxation oscillator's discharge moments inside the forcing period T and the corresponding solutions of equations

where $A = b/a\bar{\omega}$ is the relative velocity of stress growth and $C = (P_m - P_0)/a$ is the constant determining the relative breaking point of relaxation oscillator. Parameter A determines the inclination of lines represented in Fig. 18.3. The figure illustrates four synchronization cases with different values of A. The corresponding distributions are presented in Fig. 18.4. The increase of A causes a decrease of the width of gap where oscillator discharges are forbidden and causes a change of the corresponding distribution form, but the information on synchronizing factor is retained even in the case when the gap vanishes.

The presented model shows the way to studying and discovering external factors synchronizing earthquakes. It is useful to examine the general diagnostic diagram, representing the roots of equation (18.7) for a set of values of parameter A. This diagram, shown in Fig. 18.5, demonstrates all the above-mentioned properties of synchronization. The increase of A causes deterioration of synchronization conditions. The gap area of the diagram – the root-free area – decreases to zero, and for $A > 1$ a discharge may occur for any value of phase. In this case, the information on external synchronizing factor remains in the roots' density variation and the minimum of density corresponds to the value of phase equal to $\pi/2$.

It should be mentioned that, in reality, any seismoactive region should be examined as a set of relaxation oscillators with different physical properties and being on different stages of evolution. The set of external harmonics, in reality

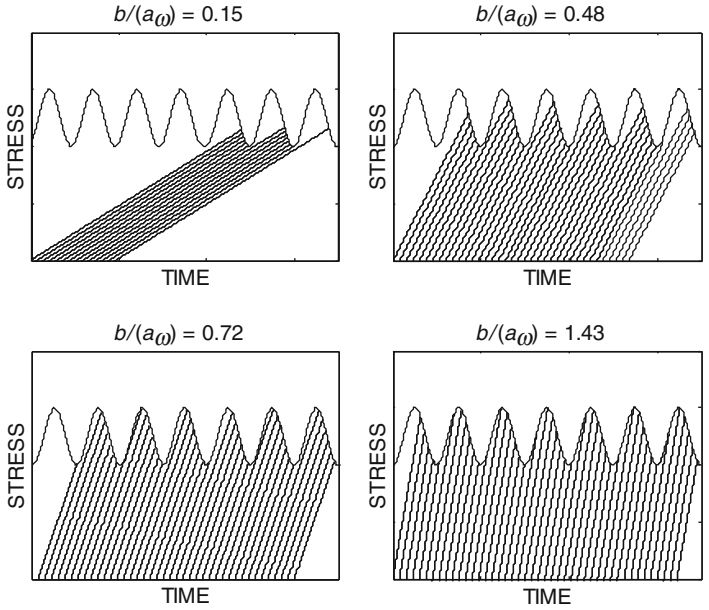

Fig. 18.3 Four relaxation oscillator synchronization cases with different values of relative velocity parameter *A*

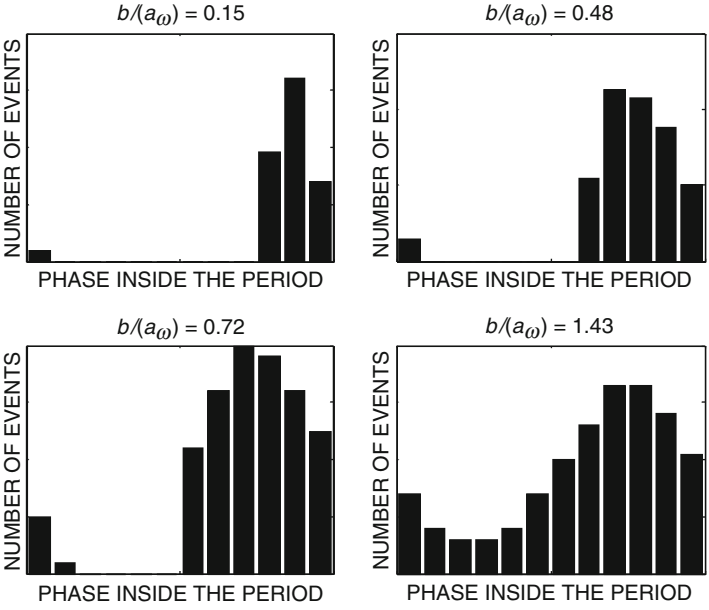

Fig. 18.4 Relaxation oscillator discharge time moment distribution inside the period of external synchronizing harmonic oscillator

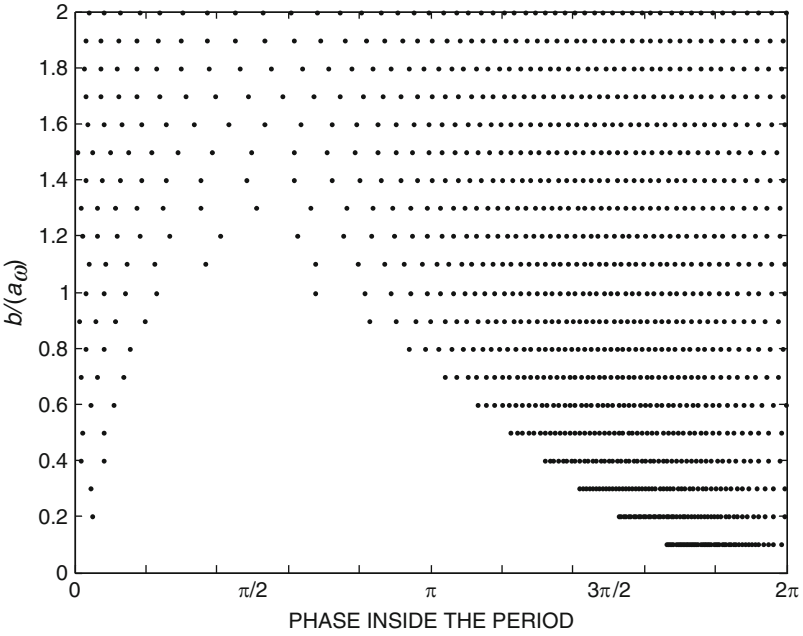

Fig. 18.5 Diagnostic diagram of relaxation oscillator synchronization. Note the forbidden area

quasi-harmonic synchronizers, is complicated too. The problem became very complicated and demands careful analysis and interpretation of data.

18.3 The compliance of synchronization model with statistical requirements of data processing

The study and detection of external synchronizing factors demands data discrimination and processing. The approach for the statistical estimation of the reliability of detected gaps in discharge time moment distributions, or their modulation, should be examined and proved as the necessary condition permitting to use the developed model.

Our case is typical for the application of approach which uses binomial distribution. Expression (18.8) determines the probability to obtain v equal results in the set of n probations:

$$P(v,n) = \frac{n!}{v!(n-v)!} p^v q^{n-v}. \tag{18.8}$$

where p is the probability to obtain the desired result in one probation, and $q = 1 - p$ is the probability to obtain undesirable result. If the relative gap width

inside the period is $\Delta T/T$, one can estimate the probabilities to hit in gap and outside the gap. The corresponding probabilities for one probation are $\Delta T/T$ and $1 - \Delta T/T$. If we examine the case of accidental gap existence, it means that for all n probations we obtain equal results for hitting in $1 - \Delta T/T$ width interval. This means that $n = v$ and expression (18.8) becomes simpler:

$$P(n) = (1 - \Delta T/T)^n. \tag{18.9}$$

For example, if $n = 30$ and $\Delta T/T$ is equal to 0.1, 0.2 and 0.3, the corresponding probabilities of accidental appearance of gaps are 0.04, 0.001 and 0.00002. In this way, the gap method proves reliability of developed synchronization. The appearance of wide enough gap reliably reveals the existence of external synchronizing factor.

Very fine tuning of virtual forcing frequency allows delineation of gaps in earthquake distribution and determines the probability of accidental appearance of a gap.

18.4 The study of strong earthquake synchronization

Investigations conducted during the last 20–30 years demonstrate some very deep, fundamental regularity in the statistics of time and space distribution of earthquakes that lead to the conclusion to study the earthquake phenomenon as a system-defined complex of connected and interacting events (Knopoff, 1996). The external synchronization influence phenomena come to light by the retro-statistical processing of earthquake catalogue.

The investigation of synchronizing effect of external factors in a certain region requires development of special methods, because catalogue data of earthquakes are presented as unequally-spaced sequences of phenomena. One of these methods, the "gap" method, has been examined above. From the point of view of energy, earthquake phenomena cover quite wide dynamic range. Within this range, different factors should affect phenomena that belong to different energetic classes. In order to investigate the influence of external factors, the gap method was applied to the catalogue of Caucasus earthquakes. The results pointed to a set of regularities for strong earthquakes — the earthquakes with $M > 6$ that occurred during last 100 years (Lursmanashvili, 2001; 1973; 1987). Thirty strong earthquakes became sensitive indicators of tectonic activity of the Caucasus. Investigations lead to the following conclusions that make it possible to apply the gap approach to analysis of seismic processes in the Caucasus: the Caucasus reveals strong regularities in recurrence of $M > 6$ earthquakes; the spectrum of recurrence of earthquakes contains 19 components, which have clear astronomical and geophysical sense; spectral distribution of time series of such earthquakes clearly indicated the fact that release mechanism of tectonically prepared strong earthquakes depends on tidal phenomena — on positional relationship of Sun, Earth and the Moon and

periodicities of their orbital movement. Table 18.1 presents the information on 9 components with clear astronomical sense (Lursmanashvili, 2001).

The parameter "Gap width" represents the estimate of the period significance. The sense of this parameter is described above. Spectral components of the set of 30 earthquakes with high precision manifest values of astronomical periods. The probability of accidental distribution of 30 time moments of earthquakes in such a way is practically zero.

As another evidence of tidal synchronization of earthquakes, we also present in Figs. 18.6 and 18.7 two distributions demonstrating distinct gaps corresponding to synchronization with long periods. The first is the distribution of angular distances of the Sun from Ascending Node on the celestial sphere for the time moments of 30 strong earthquakes, the second is the distribution of angular distances of the Sun from perigee on the celestial sphere for the time moments of the same earthquakes. They demonstrate the causal relationship of the Caucasus strong earthquakes with tides. The gap method reveals the 346-day period, which corresponds to astronomical Dragon Year — the period between two transits of the Sun across the node of Lunar orbit. Figure 18.6 demonstrates the distribution inside this period. Figure 18.7 demonstrates the distribution inside the revealed synchronization

Table 18.1 Spectral components of quasi-harmonic synchronizing factors

Information on Spectral Components				Comments
Period (days)	Gap width ($\Delta T/T\%$)	Astronomical sense	Frequency calculation formula	
27.303	34.2	Lunar sidereal month	*S*	Rotation frequency of: Moon – *s*, Perigee – *p*, Earth – *h*, Ascending Node – *N*
13.65	25.2	1/2 of Lunar sidereal month	*2s*	
27.5449	27.9	Lunar anomalistic month	*s-p*	
29.513	30.0	Lunar synodical month	*s-h*	
347.93	31.6	Eclipse year	*h+N*	
173.56	25.7	1/2 of eclipse year	*2(h+N)*	
411.18	30.2	Anomalistic year	*h-p*	
3177	21.5	Lunar orbit perigee revolution period	*P*	
1588.8	29.8	1/2 of Lunar orbit perigee revolution period	*2p*	

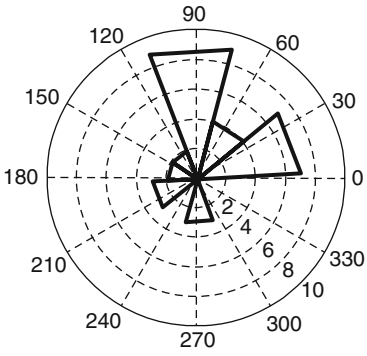

Fig. 18.6 The distribution of angular distances of the Sun from Ascending Node on the celestial sphere for strong earthquake time moments, reveals the 346 day period, which corresponds to astronomical Dragon Year — the period between two transits of the Sun across the node of Lunar orbit

period corresponding to 411 days. With this period, the Sun crosses the line of apsides of the Lunar orbit.

It is important to note that the spectrum of investigated phenomena gives a possibility to reconstruct time series well suited for prediction, i.e., gives possibilities to solve the inverse problem. With the help of time characteristics of revealed external factors, the time intervals when influence of exogenous factors increases (in other words the intervals of increased probability of release of prepared earthquakes) can be explicitly determined. During the last century, there were about 100 time intervals with high probability of strong earthquakes, and 32 strong events occurred in these intervals. We guess that in the remaining 68 cases epicentres were not prepared tectonically.

The spectral components obtained were used to synthesise the sequence of time moments with favourable conditions for earthquake triggering during the 19-th century. The time moments obtained coincide with all six strong earthquakes with $M \geq 6$.

The tidal factors presented in Table 18.1 influence the precession of the Earth rotation axis. Celestial mechanics also describes the very small contribution in precession caused by planets. Our analysis reveals a set of combination frequencies pointing possible planetary influence. Table 18.2 represents these frequencies. The

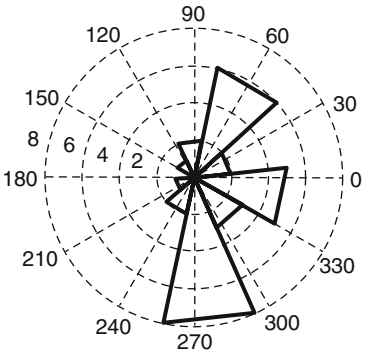

Fig. 18.7 The distribution of angular distances of the Sun from perigee on the celestial sphere for strong earthquake time moments, reveals synchronization period corresponding to 411 days. The Sun crosses the line of apsides of Lunar orbit with this period

Table 18.2 Combination frequencies of possible planetary synchronizing influence

Period (days)	Gap width ($\Delta T/T\%$)	Frequency calculation formula	Comments
39.58	24.9	*s-Me*	Rotation frequency of:
43.92	28.3	*2Me*	Moon – *s*,
44.41	27.1	*(s-h)-Me*	Earth – *h*,
175.14	30.1	*(Me-V)-(h-Ma)-(J-U)*	Mercury – *Me*
181.6	25.7	*(Me-V)-(hMa)-(J-St)*	Venus – *V*,
184.73	25.8	*(Me-V)-(h-Ma)-J*	Mars – *Ma*,
606.86	32.3	*(V-h)-(St-U)*	Jupiter – *J*,
635.38	29.8	*(V-h)-(J-St)*	Saturn – *St*
662.83	23.2	*(V-h)-(J-U)*	Uranus – *U*
674.43	20.0	*(V-h)-J*	

frequency calculation formulas are derived by the use of algorithm similar to that used by Melchior (1976) for decoding the spectrum of Luni-Solar tides. It seems, the fact of the sensitivity to this very small influence may be a reflection of complicated resonant phenomena in the Solar System (Grebennikov and Ryabov, 1978). The explanation and discussion of this result is beyond the objectives of this paper, but it possibly points out that the synchronisation mechanism is tightly connected with the variations in the Earth's rotation axis direction.

18.5 The study of synchronization of weak earthquakes

As pointed out in section 18.2, an increase of parameter A, determining the relative velocities of synchronization process, causes a decrease of the width of gap where the oscillator discharges are forbidden and causes a change of corresponding distribution form. The information on synchronizing factor persists in the corresponding histogram even in the case when the gap vanishes and may be used for the study of weak earthquakes synchronization. If one examines the values of possible external synchronizing periods with a sufficiently small step, it is possible to obtain the whole family of possible histograms. The study of their forms provides a possibility to discriminate histograms that are different from accidental and close to harmonic or pulse form. The difference from the accidental distribution may be determined by χ^2 criterion. The harmonic or pulse form may be modeled and fitted to the histogram by selection of its parameters and calculation of covariance as the measure of model and histogram similarity. The obtained phase and covariance values determine the amplitude and therefore all model parameters of the histogram representing the distribution inside the period of required external forcing.

This approach was tested by the use of Caucasus earthquakes data. We select the time interval from 1962 to 1987. During this period, the observational network of seismographs operated in Georgia was unified and equipped with homogeneous instrumental system. The objective was to study a possible tidal influence on weak earthquakes in the Caucasus region.

We selected two sets of events: 102 earthquakes with $M > 4.7$ and 62 earthquakes with $M > 5.0$. These sets are optimal for the study. There is sufficient amount of data and the energy growth velocity optimal for tidal influence study in the range of periods from 25 to 30 days. Four Lunar months – synodical, sidereal, anomalistic and draconic, with the corresponding periods of 29.53, 27.32, 27.55 and 27.21 days, represent the tide components in the selected period range.

The results of study are presented in Figs. 18.8 ($M > 4.7$) and 18.9 ($M > 5.0$). Upper diagrams represent the covariance obtained by sinusoidal and pulse forms and the middle one the amplitude of the same forms. The lower diagram represents modified estimation of the non-randomness obtained by χ^2 criterion. For non-random periods, the usual estimation gives values close to 1, and their perception is not convenient. We used the value of $1/P_{\chi^2}$ — a modification which helps to represent the result more distinctly. It points to the number of random distributions

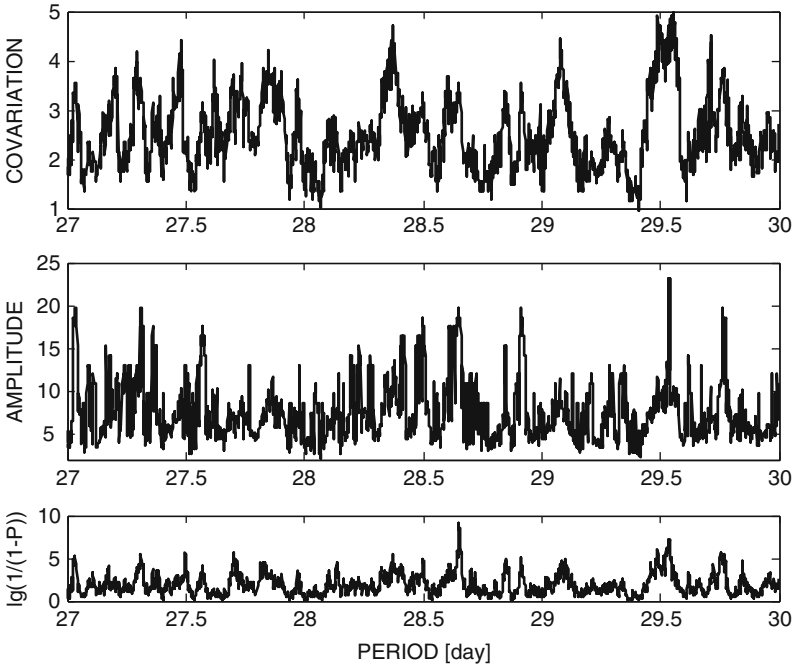

Fig. 18.8 Covariance obtained by sinusoidal and pulse forms, the amplitude of the same forms and modified estimation of the non-randomness obtained by χ^2 criterion for Caucasian earthquakes of magnitude $M > 4.7$

in which the given distribution may appear accidentally only once. The logarithmic scale of $1/P_{\chi^2}$ represents the result better. For example, for the 29.53 day period, we have the value of estimation parameter equal to 6. It means that in million accidental distributions, a distribution corresponding to the synodical tide period is obtained only once. This statistical approach provides the compliance of synchronization model with the statistical requirements of data processing for the case of gap absence.

Some gaps and the corresponding periods in covariance diagrams of Figs. 18.8 and 18.9 are not related to the tides. The increase of M and the estimation of the non-randomness obtained by χ^2 criterion separates the periods related to the tides. It is clear that the quakes of $M > 5.0$ represented in Fig. 18.9 better reveal the tidal synchronization.

The period of 29.53 corresponds to the period of Lunar phase recurrence, or to the period of highest tide recurrence, which is the sum of Lunar and Solar tidal waves. One can determine the phase of tide for which the frequency of earthquakes is maximal. The distribution of angular distances between the Moon and Sun, corresponding to earthquakes moments and expressed in celestial coordinates, is presented in Fig. 18.10. This distribution demonstrates the 2-5 day shift from the moment of a new moon.

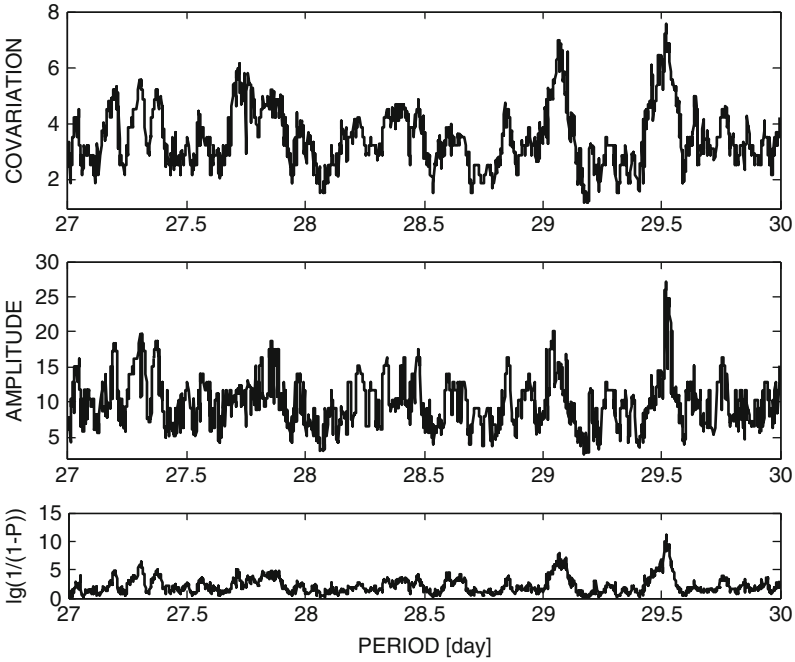

Fig. 18.9 Covariance obtained by sinusoidal and pulse forms, the amplitude of the same forms and modified estimation of the non-randomness obtained by χ^2 criterion for Caucasian earthquakes of magnitude $M > 5.0$. The increase of M separates the periods related to the tides and reveals the tidal synchronization better

Fig. 18.10 The distribution of angular distances between the Moon and Sun very distinctly reveals the earthquakes synchronization tidal period corresponding to 29.53 days

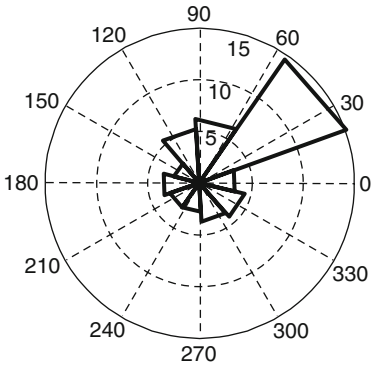

18.6 Synchronization in model laboratory experiments

All these considerations and the validity of "gap" method for the discovery of external synchronizing factors are tested in model laboratory experiments (Chelidze and Lursmanashvili, 2003, see also Chapter 8, this book). It is well

known that the slider-spring system displays stick-slip behavior. The goal of experiment was to prove the possibility of a nonlinear control of slip.

The approach and the model described in section 18.2 fully explain the synchronization phenomenon observed in stick-slip experiment. The core of this approach is using the existence of some critical parameter in the system that causes its relaxation. Then a small periodic impact can synchronize the relaxation of the whole system with the period of impact, if some force regularly drives the system close to the critical state.

The results obtained confirm in principle the possibility of controlling the regime of the natural seismicity, at least in the temporal domain, by relatively weak natural (magnetic storms, tides) excitations.

18.7 Discussion

The results described in sections 18.3 and 18.4, in particular the discovery of synchronization of Caucasus earthquakes caused by tides, testify to the tidal triggering and the effectiveness of the used method. In discussion of tidal triggering, we should point to all difficulties and remember that tidal impact in a point A with geographical latitude φ is determined by complicated gravitational potential $W(A)$, which represents the set of spherical harmonics corresponding to different types of tidal impact:

$$W(A) = \frac{3}{4} G\mu \frac{r^2}{c^2} \left(\left(\cos^2 \varphi \cos^2 \delta \cos 2H + \sin 2\varphi \sin 2\delta \cos H + 3\left(\sin^2 \varphi - \frac{1}{3}\right)\left(\sin^2 \delta - \frac{1}{3}\right)\right)\right), \tag{18.10}$$

where G is gravitational constant, μ the mass of tide-making body (the Moon or the Sun), r the distance from A to the center of the Earth, c the distance between the Earth and tidal body centers, and δ and H are the declination and hour angle. The first term describes semidiurnal sectorial tidal wave, the second the diurnal tesserial, and the third thelong period zonal wave.

The Lunar tide is approximately twice stronger than Solar. In any geographical point we have a complicated picture as the sum of two components with different values of δ and H. The tidal force projections on vertical and two horizontal directions may be calculated as:

$$\begin{aligned} F_V &= \frac{3}{2} G\mu M \frac{r}{c^3}\left(\cos^2\varphi\cos^2\delta\cos 2H + \sin 2\varphi \sin 2\delta \cos H + 3\left(\sin^2\varphi - \frac{1}{3}\right)\left(\sin^2\delta - \frac{1}{3}\right)\right) \\ F_{NS} &= -\frac{3}{4} G\mu M \frac{r}{c^3}\left(\sin 2\varphi \cos^2\delta \cos 2H - 2\sin 2\delta \cos 2\varphi \cos H - 3\sin 2\varphi\left(\sin^2\delta - \frac{1}{3}\right)\right) \\ F_{EW} &= \frac{3}{2} G\mu M \frac{r}{c^3}\left(\cos^2\delta\cos\varphi\sin 2H + \sin 2\delta \sin\varphi \sin H\right), \end{aligned} \tag{18.11}$$

where M is the mass of Earth.

Long-period tidal waves modulate short-period ones. The interaction of waves also complicates the tidal impact picture. There is one important consideration (Kartvelishvili & Kartvelishvili, 1996) concerning the time of maximal tidal impact on the seismic focus — the tidal impact depends on the mutual directions of tidal force and stress vector in the epicenter of the earthquake under preparation, and the time of tide maximum may differ from the time of maximal impact. Some epicenters may be less sensitive or even insensitive to tidal impact. The fact that we reveal tidal synchronization also points out that we have a regular tendency in distribution of earthquakes mechanisms.

If we consider only tidal forces, formula (18.5) may be written as:

$$b_i(t - t_0) = P_{mi} - P_{0i} - F_L(t)\cos\gamma_{iL} - F_S(t)\cos\gamma_{iS} \quad i = 1, 2, \ldots, N, \qquad (18.12)$$

where N is the number of developing sources, b_i the stress linear increase velocity in i-th epicenter, $P_{mi} - P_{0i} = C_i$ the stress necessary for this epicenter discharge and accumulated from the time moment t_0. $F_L(t)$ and $F_S(t)$ are the modules of Lunar and Solar tidal forces, and γ_{iL} and γ_{iS} determine mutual disposition of tidal and stress vectors.

As we have mentioned above, the epicenters with low stress accumulation velocity, low values of b_i coefficients in the system of equations (18.12), better "respond" to the external forcing.

The time moments of earthquakes and the corresponding values calculated for tidal components are known. The tidal impact on seismic region will be revealed at maximal values of tidal forces and their sum, and as better as close to each other are the directions of stressess responsible for earthquakes. For the Caucasus region, the maximal value of tidal force sum reveals the 29.53 day period for weak earthquakes.

18.8 Conclusions

It follows from this investigation that the analysis of earthquakes time series by the approach presented here, and determination of external synchronization impact, gives a possibility to estimate the background for long-term prediction of time intervals in which the probability of earthquake occurrence in the Caucasus region is relatively high. Similar investigations with the same approach for other seismic regions will be very useful for the creation of general picture of earth seismicity tidal response. Knowledge about spatial distribution of earthquakes in a given region should be also analysed for predicting probable location of earthquake initiation and monitoring of variations and abrupt disturbances of different geophysical quantities, required for making short-term prediction.

The investigation presented here has the objective to make a contribution to basic research on earthquake long-term and short-term prediction, valid for further practical application.

References

Allen M.W., The lunar triggering of earthquakes in southern California. Bull. Seism. Soc. Am. 1956. Vol.26. p. 147-157.

Becker, T. W., Deterministic Chaos in the Two State-variable Friction Sliders and the Effect of Elastic Interactions. Geocomplexity and the Physics of Earthquakes, edited by Rundle, J., Turcotte, D., and Klein, W., AGU, Washington, DC, 5–26, 2000.

Beeler, N. M. and Lockner, D. A.: Why earthquakes correlate weakly with the solid Earth tides: Effects of periodic stress on the rate and probability of earthquake occurrence, J. Geophys. Res., B108, 2391–2405, 2003.

Blechman I.I., *Synchronization of Dynamical Systems*, 1971. (Sinchronizatzia Dinamicheskich Sistem, Nauka, Moscow, in Russian.)

Bocaletti, S., Grebogi, C., Lay Y.-C.: The control of chaos; theory and applications, Physics Reports, 329, 103–197, 2000.

Chelidze, T. and Lursmanashvili, O.: Electromagnetic and mechanical control of slip: laboratory experiments with slider system, Nonlin. Proc. Geophys., 20, 1–8, 2003.

Chelidze, T., T. Matsharashvili, J. Gogiashvili, O. Lursmanashvili and M. Devidze (2005): Phase synchronization of slip in laboratory slider system, *Nonlinear Processes Geophys.*, **12**, pp. 163-170.

Chelidze, T., T. Matcharashvili, J. Gogiashvili, O. Lursmanashvili and M. Devidze (2006) Electromagnetic Synchronization of Slip. *Nonlinear Dynamics*, v 44, pp. 293-298.

Custodio, S., Fonseca, J., Faria, B., and d'Oreye, N.: Tidal modulation of volcanic tremor in Fogo Island, Cape Verde, Book of Abstracts, European Seismological Commission XXVIII Assembly, Genoa, 236, 2002.

Dieterich, J.: Nucleation and triggering of earthquake slip: Effect of periodic stresses, Tectonophysics, 144, 127–139, 1987.

Grasso, J.-R.: Mechanics of Seismic Instabilities Induced by the Recovery of Hydrocarbons, Pageoph, 139, 507–534, 1992.

Grebennikov E.A., Ryabov Y.A. Resonances and small denominators in celestial mechanics. 1978, Moscow, Nauka, 126 p.

Gulyaev V.P., On the synchronization of thyratron generator. Journal of Technical Physics, v 9, No.18, 1939.

Heaton T.N., Tidal triggering of earthquakes. Geoph. J. of the Royal Astr. Soc. 1975, vol.43. p. 307-326.

Hoffman R.B., Aftershock-energy release versus tidal effects, Hebgen Lake earthquakes, Montana. US.Geol.Survey Prpf. Paper 1961, 424-C. p. 267-270.

Kartvelishvili K., Kartvelishvili N. Tidal triggering of earthquakes. Journal of Georgian Geophysical Society. Issue(A), Solid Earth, v.2. 1996.

Knopoff L., Earth tides as triggering mechanism for earthquakes. Bull. Seism. Soc. Am., 1964. vol.54. p. 1865-1870.

Knopoff L. Earthquake prediction: The scientific Challenge. Proc.Nat. Acad. Sci. USA, vol 93, pp. 3719-3720, 1996.

Lursmanashvili, O.V., On periodicity of strong earthquakes in the Caucasus, Izv. AN SSSR, Fiz. Zemli, No. 2, in Russian, 1973.

Lursmanashvili, O.V., Gakhokidze L.D., Nikoladze, I.E., Ruda L.G., Results of calculations of the recurrence spectrum of earthquakes in the Caucasus, Soobshch. AN GSSR, 1926, No.1, in Russian, 1987a.

Lursmanashvili, O.V Gakhokidze L.D, Ruda L.G., Recurrence spectrum of strong earthquakes in some seismically active regions of the Eurasia, Soobshch. AN GSSR, 126, No.1, in Russian, 1987b.

Lursmanashvili O. Role of exogenous factors in initiation of Caucasus earthquakes. Journal of the Georgian Geophysical Society. Issue (A), Physics of Solid Earth, v. 6. 2001.

Matcharashvili, T., Chelidze, T., and Javakhishvil, Z.: Nonlinear analysis of magnitude and interevent time interval sequences for earthquakes of the Caucasian region, Nonlin. Proc. Geophys., v 7, pp. 9–19, 2000.

Meerovich L.A. and Zelichenko L.G., Impulse technique. Moscow, 600 p, 1954.

Melchior P., Physics and dynamics of planets, Mir, Moscow, in Russian, 1976.

Nikolaev, A. V. (Ed.): Induced Seismicity, Moscow, "Nauka", in Russian, 220, 1994.

Ott, E., Grebogi, C., and Yorke, J. A. Controlling chaos, Phys. Rev. Lett., 64, 1196–1199, 1990.

Perfettini, H. and Schmittbuhl, J.: Periodic loading on a creeping fault: Implications for tides, Geophys. Res. Lett., 28, 435–438, 2001.

Pikovsky, A., Rosenblum, M. G., and Kurth, J.: Synchronization: Universal Concept in Nonlinear Science, Cambridge University Press, Cambridge, 411, 2003

Polumbo A., Lunar and solar tidal components in the occurance of earthquakes in Italy. Geophys. J. Roy. Astron. Soc. 1986. Vol. 84. #1. p. 93-99.

Ryall A., Van Wormer J.D., Jones A.E., Trigering of microearthquakes by earth tides, and other features of the Truckee, California earthquake sequences of September, 1966. Bull. Seism. Soc. Am. 1968. 58. p. 215-248.

Scholz, C. H.: Good tidings, Nature, 425, 670–671, 2003.

Shlien S., Earthquake-tide correlation. Geoph. J. R. Astr. Soc. 1972. vol.28. p. 27-34.

Simpson J.F., Earth tides as a triggering mechanism for earthquakes. Earth. Planet. Sci. Lett., 1967. vol.2. p. 473.

Sobolev, G. A. and Ponomarev, A. V.: Physics of Earthquakes and Precursors, Moscow, "Nauka", in Russian, 270, 2003.

Tamrazian G.P., Principal regularities in the distribution of major earthquakes relative to solar and lunar tides and other cosmic sources. Icarus 9. 1968. p. 574-592.

Tarasov, N. G., Tarasova, N. V., Avagimov, A. A., and Zeigarnik, V. A.: The effect of high-power electromagnetic pulses on the seismicity of the central Asia and Kazakhstan, Vulkanologia I seismologia, in Russian, 4–5, 152–160, 1999

Ulomov, V., Danilova, T., Medvedeva, N., Polyakova, T. Seismogeodynamics of Lineament Structures in the Mountainous Regions Bordering the Scythian-Turan Plate. *Physics of the Solid Earth*, 2006, v 42, No 7, pp. 551-566.

Ulomov, V., Danilova, T., Medvedeva, N., Polyakova, T. Shumilina L.S. Assessment of Seismic Hazard in the North Caucasus. *Physics of the Solid Earth*, 2007, v 43, No 7, pp. 559-572.

Vidale, J., Agnew, D., Johnston, M., and Oppenheimer, D.: Absence of earthquake correlation with earth tides: an indication of high preseismic fault stress rate, J. Geophys. Res., 103, 24 567–24 572, 1998.

Vitkevich V.V., Geometrical theory of relaxation generator synchronization. Journal of Technical Physics, v 15, No 18, 1945.

Wang, Y., Mora, P., Yin, C., and Place, D.: Statistical tests of load/unload response ratio signals by lattice solid model, Pure Appl. Geophys., 161, 1829–1839, 2004.

Weems R. E., Perry W.H., Strong correlation of major earthquakes with solid-earth tides in part of the eastern United States. Geology. 1989. Vol.17. p. 661-664.

Chapter 19
Stacked Analysis of Earthquake Sequences: Statistical Space–Time Definition of Clustering and Omori Law Behavior

P. Tosi, V. De Rubeis, and P. Sbarra

Abstract The definition of the aftershocks sequence is still a debated topic. We propose here a study of the spatial and temporal variation of the earthquakes clustering and decay rate. We used five different seismic catalogues, characterized by specific spatial and magnitude ranges. They are respectively: the world catalogue for a global analysis, and Greek, Japanese, Californian and Italian regional catalogues in order to investigate different seismo-tectonic settings.

A stacking procedure has been applied to characterize a typical sequence behavior which allowed the evaluation of changes over time intervals (τ) and distances (r) from the mainshock. The resulting decay rate $p(r, \tau)$ has values comparable to the modified Omori law: $p(r, \tau) \simeq 1$ at small distances and inside specific time ranges. It is then possible to define sequences into a particular spatial range varying in time and reaching a maximum distance of 50-100 km. In a first time period (until 10-20 days), the slope p is small before reaching the typical sequence value ($p \simeq 1$). The slope of the first period increases with increasing threshold magnitude. This dynamics highlights the importance of looking at proper space-time limits when analyzing the seismic decay after the mainshock. Different decay domains have been evidenced: they depend on the threshold magnitude of the catalog and are characterized by smooth variations in space.

Catalogues have been analyzed under the fractal dimension aspect as related to the space and time clustering. Even in this case a pattern behavior of seismicity has been evidenced. After the occurrence of an event there is a space-time domain inside which the subsequent events are temporally related. Inside this domain the seismic sequences drive temporal occurrences. Concerning the space correlation dimension, results reveal the presence of a space clustering of hypocenters for distances greater than few tenth of km and for time intervals less than hundreds of days. At short distances, hypocenters are time clustered but there is no space

P. Tosi (✉), V. De Rubeis, and P. Sbarra
Istituto Nazionale di Geofisica e Vulcanologia, Roma, Italy
e-mail: patrizia.tosi@ingv.it

V. de Rubeis et al. (eds.), *Synchronization and Triggering: from Fracture to Earthquake Processes*, GeoPlanet: Earth and Planetary Sciences 1,
DOI 10.1007/978-3-642-12300-9_19,

clustering. This zone is probably due to the activity of seismicity on the seismic fault.

Relations between decay rate domains and clustering domains in space and time are evidenced and discussed.

19.1 Introduction

Earthquakes are the answer to tectonic load; stress is redistributed through the earthquakes, causing the aftershock sequence to develop in space and time. Triggering of earthquakes may act at several spatial and time scales. Short-range triggering (distance of the order of seismic fault size) is due to stress changes induced by the main-shock and related aftershocks in a recursive process.

Long-range triggering is a more difficult aspect to explain. Experimental evidences as well as physical explanations or synthetic earthquakes generation were proposed. They include analysis for geothermal sites, Coulomb-stress modifications, the application of declustering algorithms, multiple stress transfer, cellular automata behavior and the consideration that the crust is in a critical state [Tosi et al, 2008; Hill et al., 1993; Husen et al., 2004; Brodsky et al., 2000; Godano et al., 1999; King et al., 1994; Stein et al., 1994; Stein, 1999, Melini et al., 2002; Marzocchi et al., 2003; Ziv, 2006; Bak and Tang, 1989]. Other authors have attempted to find space-time relations of seismicity in order to study long-range relations for both global and regional catalogues.

Influence ranges of the order of 100 km from mainshocks were recognized [e.g., Gasperini and Mulargia, 1989; Reasenberg, 1999]. For highest magnitude earthquakes of the last century, Lomnitz (1996) found a very long-range correlation. Marsan et al. (2000) investigated space-time relations of scale-invariance of seismicity. They pointed out that space and time should not be considered separately, but rather the spatial correlation structure is evolving in time. They considered migration of aftershocks away from the mainshock in a form of a sub-diffusive process.

Several questions arise from the complexity of results and interpretations. Should the long range triggering be considered rare and peculiar to specific situations? Is the sequence extension in space constant, with the same parameters of the Omori law? Is a sequence the result of multiple overlapping Omori functions with shifted starting time, produced by remarkable aftershocks, as suggested in Ogata et al. (2003)? Does aftershock duration scale with the mainshock size? Ziv (2006) posed the question and found no correlation with magnitude of mainshock. What is the origin of c Omori parameter? Is it physical or due to catalogue incompleteness? What is the role of static and dynamic stress triggering?

To address these questions it is important to consider the spatial and temporal aspects of the seismic process simultaneously, in a combined way. In this work we apply a method of analysis [Tosi et al., 2008], suitable to point processes and based

on space-time correlations among earthquakes. Like the previously cited authors, we do not separate seismicity into main and aftershocks.

19.1.1 Data

A set of seismic catalogues has been chosen, covering different space and time ranges. Although there is strong scale invariance in seismic activities, geophysical constrains are present, like crustal thickness and the dimension of plate boundaries, as well as instrumental limits, like time length of dense seismic station networks, completeness of recordings etc.

In total, five different seismic catalogues have been analyzed. They have been firstly investigated on their completeness. A reliable method to assess completeness magnitude threshold is based on the application of the Gutenberg-Richter (GR) law to magnitude distribution. It is given by: $\log N = a - bM$, where N is the cumulative number of events with magnitude bigger or equal to M, a and b are constants. Coefficient a is related to the seismic activity level, while b is a quite robust parameter with values near 1. Assuming the validity of this law, a clear anomaly of the distribution at lower magnitudes may indicate a lack of completeness in the selected time range. After cutting earthquakes below the threshold magnitude and for a depth greater than 50 km, the resulting catalogues are here summarized (Figure 19.1).

- Global CMT catalogue (Centroid Moment Tensor, Harvard). It covers a time span from January 1980 to December 2004, threshold magnitude of completeness is 5.5 and maximum recorded magnitude is 9.5. The number of events is 13268.
- Greece catalogue (Geophysical Laboratory, University of Thessaloniki). It covers a time span from January 1964 to September 2007, threshold magnitude of completeness is 4.5 and maximum recorded magnitude is 7.5. The number of events is 5865.
- Japan catalogue (selection of USGS NEIC catalogue). It covers a time span from January 1980 to October 2008, threshold magnitude of completeness is 4.5 and maximum recorded magnitude is 8.3. The number of events is 6698.
- South California catalogue (Southern California Earthquake Center, relocated by Shearer et al., 2005). It covers a time span from January 1984 to December 2002, threshold magnitude of completeness is 2.0, but for this analysis we cut the catalogue at 2.5. Maximum recorded magnitude is 7.3. The number of events is 23576.
- Italy catalogue (INGV CSI 1981-2002 and ISIDE 2002-2009). It covers a time span from January 1988 to May 2009, threshold magnitude of completeness is 2.0, but for this analysis we cut the catalogue at 2.5. Maximum recorded magnitude is 5.8. The number of events is 11860.

These catalogues represent seismic activity over very different tectonic settings and spatial scales. The global catalogue reflects the activity of the whole planet,

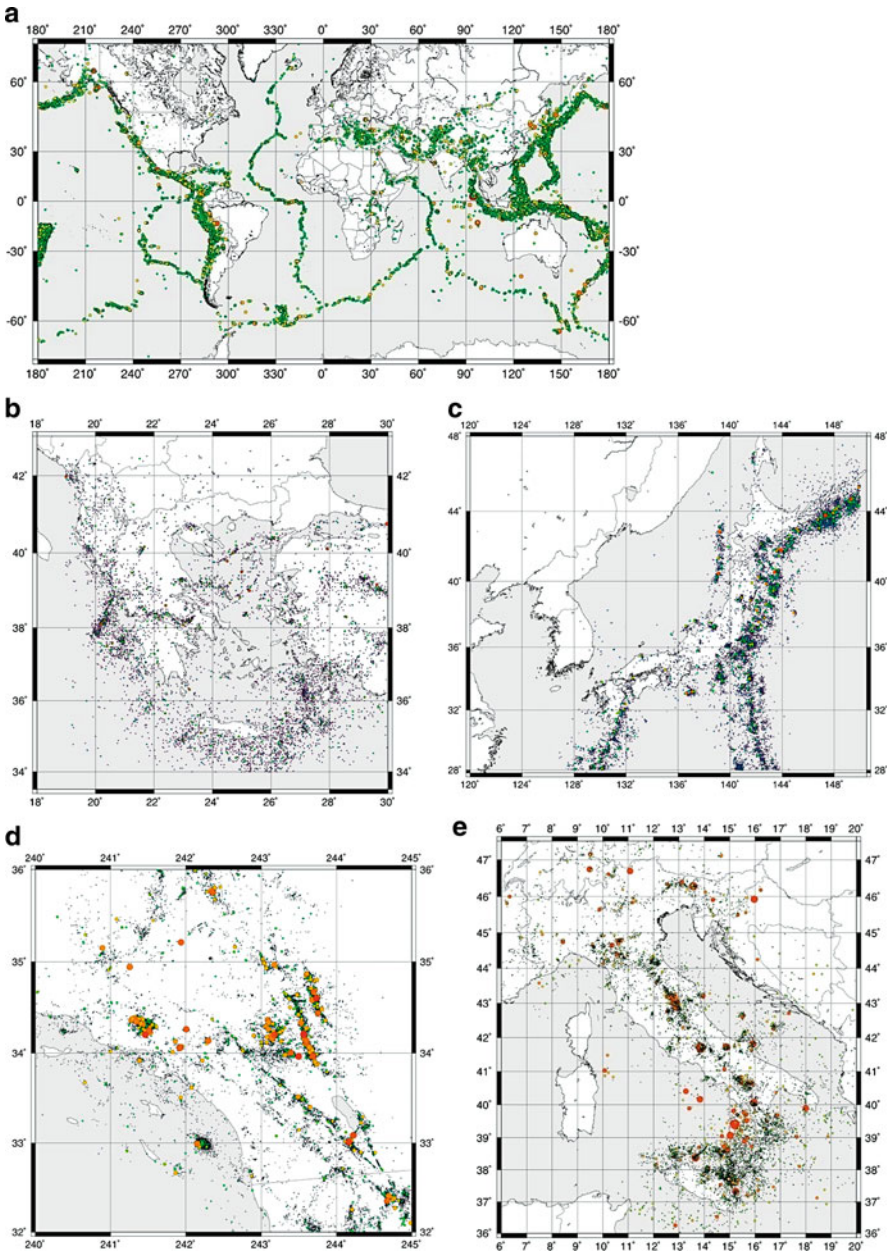

Fig. 19.1 Seismic catalogues used to analyze earthquake data. They are respectively:
a) Global CMT (Centroid Moment Tensor, Harvard). January 1980 - December 2004, 13268 events. b) Greece (Geophysical Laboratory, University of Thessaloniki). January 1964 – September 2007, 5865 events. c) Japan (selection of USGS NEIC catalogue). January 1980 – October 2008, 6698 events. d) South California (Southern California Earthquake Center, relocated by Shearer et al., (2005) January 1984 – December 2002, 23576 events. e) Italy (INGV CSI 1981-2002 and ISIDE 2002-2009), January 1988 – May 2009, 11860 events

focusing to the highest magnitudes events. This catalogue is suitable to study the activities related to high energy stress-strain relation due to global plate tectonics. South California catalogue is a good example of regional transcurrent tectonics seismic activity. Moreover, this catalogue derives from a good seismic network, showing a very low completeness magnitude threshold. Among the other regional catalogues, we chose the Italian region, which presents a seismic activity of medium magnitudes, coming from heterogeneous tectonic settings, recorded by a good seismic network too. Greece and Japan catalogues list medium-high magnitudes events; dominating tectonics is plate subduction.

19.2 Space–Time Fractal Dimensions of Seismicity

The above-described catalogues have been analyzed under their space and time clustering properties through the fractal dimension analysis. We apply the correlation integral method, defined as:

$$C(l) = \frac{2}{N(N-1)} \sum_{i=1}^{N-1} \sum_{j=i+1}^{N} \Theta\left(l - \left\|\mathbf{x}_i - \mathbf{x}_j\right\|\right),$$

where l is the metric of the space considered, N is the total number of elements, $\mathbf{x}$ is the coordinate vector and Θ is the Heaviside step function. If $C(l)$ scales like a power law, $C(l) \propto l^D$, the correlation dimension D can be defined by

$$d(l) = \frac{\delta \log C(l)}{\delta \log l}, \quad D = \lim_{l \to 0} d(l).$$

Experimentally, the self-similarity can best be found by plotting the local slope d of $\log C(l)$ versus $\log l$. From this we can extend the correlation integral to a combined space-time approach. It is defined as:

$$C_c(r,\tau) = \frac{2}{N(N-1)} \sum_{i=1}^{N-1} \sum_{j=i+1}^{N} \left(\Theta\left(r - \left\|\mathbf{x}_i - \mathbf{x}_j\right\|\right) \cdot \Theta\left(\tau - \left\|t_i - t_j\right\|\right)\right),$$

where the metrics of space and time are considered simultaneously (Tosi *et al.*, 2008).

Similarly to correlation dimension we define the time correlation dimension D_t and its local slope d_t as:

$$d_t(r,\tau) = \frac{\partial \log C_c(r,\tau)}{\partial \log \tau}, \quad D_t(\tau) = \lim_{\tau \to 0} d_t(r,\tau),$$

and the space correlation dimension D_s with its local slope d_s as:

$$d_s(r,\tau) = \frac{\partial \log C_c(r,\tau)}{\partial \log r}, \quad D_s(r) = \lim_{r\to 0} d_s(r,\tau).$$

The results show a statistical property of the different seismic catalogues that can be interpreted as an average behavior of seismic events following each earthquake.

Figure 19.2 shows the local slope of time correlation dimension for all considered catalogues. The overall pattern is quite similar for all catalogues. The light grey domain, corresponding to low d_t values, identifies time clustering. This means that, after the occurrence of each event, there is a space-time domain inside which the subsequent events, probably belonging to the seismic sequence, have temporally clustered occurrences. The light grey domain has the greatest spatial extension at 10 days for the global catalogue, while for regional one it reaches its maximum at

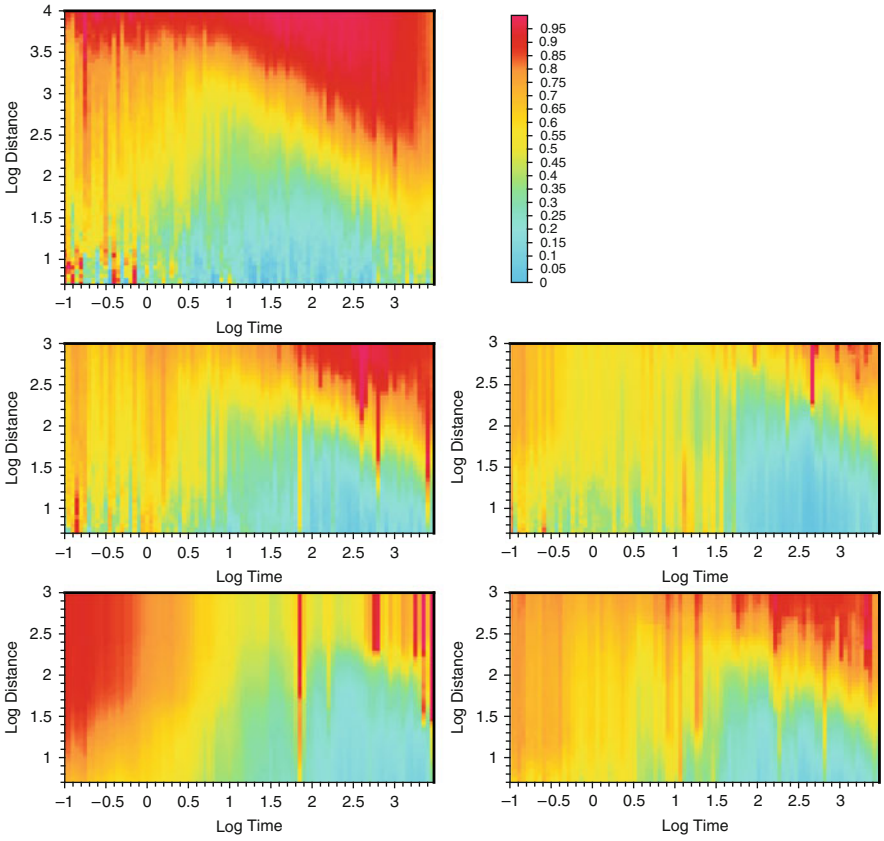

Fig. 19.2 Local slope d_t of time correlation dimension D_t for all considered catalogues (catalogues correspond to the same position as Fig. 19.1). Time correlation dimension ranges from 0 to 1 as indicated on the graduated bar

around one month. During the days after this time, the clustering domain spatially shrinks, but it is still present after more than 8 years (less for global CMT catalogue). Dark grey to black domains identify a relatively high time correlation dimension. At distances and time interval corresponding to this domain, the earthquakes occurrence approaches a random process, denoting the disappearance of the sequence or the overlapping of a sufficient number of independent sequences. This happens for large distances and long time intervals as expected, but even shortly after the reference earthquake (less than 10 days).

Comparing the analyzed catalogues, we note the different extension of the clustering domain, reaching distances ranging at its maximum 130 km (for Italy) to 500 km (for global catalogue). To test the effect of different magnitude threshold we cut the Italian catalogue minimum magnitude to 2, 2.5, 3, and 3.5, respectively. The comparison of time correlation dimension is shown in Figure 19.3. From the figure it is evident how the clustering domain reaches longer distances as magnitude threshold increases, even if this effect is partially blurred by the increase of noise, due to the reduced number of data. On the other hand, catalogues of Greece and Japan were analyzed with the same threshold ($m = 4.5$); catalogues of California and Italy have the threshold at $m = 2.5$. For this reason the explanation of the difference between members of each couple (sharing the same magnitude threshold) could be linked to the strongest earthquake recorded in each catalogue, that is: $m = 9.5$ for global CMT, $m = 7.5$ for Greece, $m = 8.3$ for Japan, $m = 7.3$ for South California and $m = 5.8$ for Italy.

Concerning the space correlation dimension d_s (Figure 19.4), results reveal in each catalogue the presence of a space clustering of hypocenters for distances

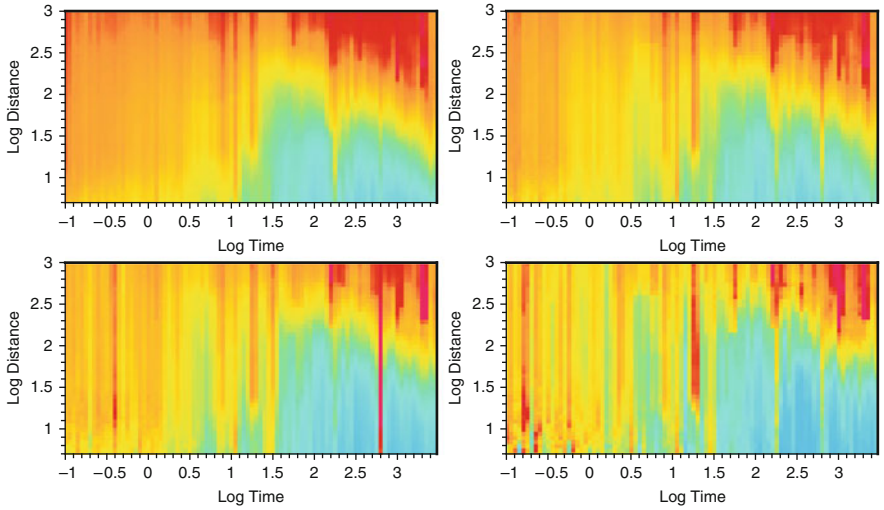

Fig. 19.3 Effects of different magnitudes threshold in local slope d_t of time fractal dimension for the Italian catalogue. Minimum magnitudes are respectively (from top left to down right, as reading succession) $m > 2.0$, $m > 2.5$, $m > 3.0$, and $m > 3.5$

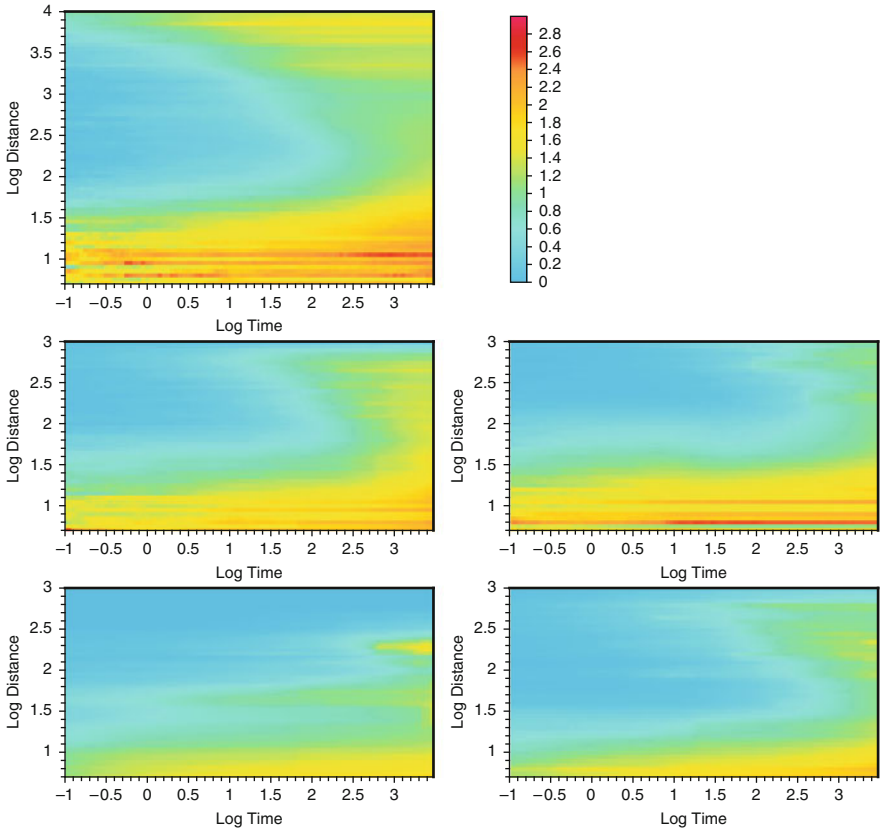

Fig. 19.4 Local slope d_s of space correlation dimension D_s for all considered catalogues (catalogues correspond to the same position as Fig. 19.1). Space correlation dimension ranges from 0 to 3 as indicated on the graduated bar

greater than few tenth of km and for time intervals less than hundreds of days. For longer time intervals, the disappearance of spatial clustering reveals the seismic structures related to preexisting tectonic settings, such as plate boundaries for bigger scales examples; after a sufficiently long time evolution, seismicity will tend to fill these seismic structures up to dimensions of thousands of kilometers. At short distances, d_s values mark clearly the presence of a zone, around each source, where hypocenters are not space clustered, but they tend to fill the space. The pairs of events, belonging to this domain, are characterized by time clustering, as showed before, for time intervals longer than 10 days. There is no clear demarcation of this near-source domain, but when fixing the limit of clustering at as example $d_s = 1.5$, it appears that the area with high correlation dimension is evolving with time. The separation line defines a radius, slowly growing in time, within which seismic events are spatially more uniformly distributed. This finding is in agreement with the accepted migration of aftershocks away from a mainshock [Tosi et al., 2008].

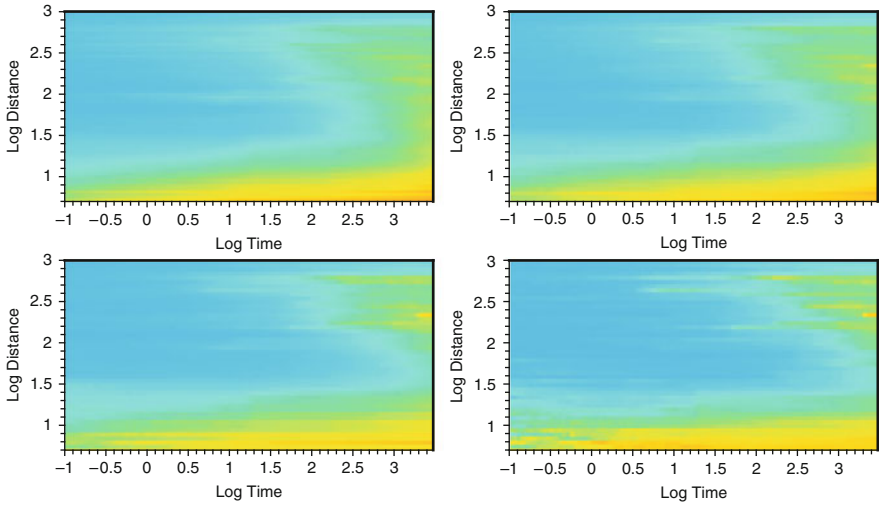

Fig. 19.5 Effects of different magnitudes threshold in local slope d_s of space fractal dimension for the Italian catalogue. Minimum magnitudes are respectively (from top left to down right, as reading succession) $m > 2.0$, $m > 2.5$, $m > 3.0$, and $m > 3.5$

Even in this case the overall pattern is very similar for the various catalogues, but the mean extension of the near source domain varies from 8 km (California and Italy), 16 (Greece and Japan) to 40 km (global CMT). It is interesting to note that the analysis of Italian catalogue at increasing magnitude threshold (Figure 19.5) does not produce significant differences in the pattern. Only the increase of noise is evident. Even maximum earthquake magnitude does not seem to drive d_s pattern. Probably the variation of the near-source extension is due to tectonic setting, as Japanese, Greek and global seismicity are dominated by big thrust earthquakes, whereas Italian and Californian have more direct and strike-slip faults.

19.3 Omori law analysis

This analysis is focused on time decay of seismic activity. Traditionally this analysis is dedicated to the study of seismic sequence produced by a mainshock [Omori, 1894]. Later Utsu (1961) defined the empirical, so-called modified Omori law (MOL):

$$n(t) = \frac{k}{(c+t)^p},$$

where $n(t)$ is the number of earthquakes per day, t is time from the mainshock, k reflects the seismic productivity and c is the "time offset" parameter; p modifies the decay rate and typically falls in the range 0.7–1.5.

The common approach is to take a big event as a mainshock. After having defined a suitable area, comprising generally the seismogenic fault, all related events following the mainshock are grouped inside a proper time unit (generally one day) and counted.

We are interested in analyzing space-time relations of earthquakes triggered by the main event. Assuming that every event can be a mainshock of its own sequence, we count all succeeding events as a function of both time and space distances. This space-time count is repeated for all N events and the result is a stacked generalized count:

$$n(r,\tau) = \frac{1}{NS\Delta\tau} \cdot \sum_{i=1}^{N-1} \sum_{j=i+1}^{N} (\Theta(R_1) \cdot \Theta(R_2) \cdot \Theta(\mathrm{T}_1) \cdot \Theta(\mathrm{T}_2)),$$

where r and τ represent, respectively, space and time distances from parent events. S is the area normalization coefficient:

$$S = \pi\left(\left(r + \frac{\Delta r}{2}\right)^2 - \left(r - \frac{\Delta r}{2}\right)^2\right),$$

Δr and $\Delta\tau$ represent the size of, respectively, space and time windows for the events counting. R_1, R_2, T_1 and T_2 are given by

$$R_1 = \left(r + \frac{\Delta r}{2}\right) - \left\|\mathbf{x}_i - \mathbf{x}_j\right\|,$$

$$R_2 = \left\|\mathbf{x}_i - \mathbf{x}_j\right\| - \left(r - \frac{\Delta r}{2}\right),$$

$$\mathrm{T}_1 = \left(\tau + \frac{\Delta\tau}{2}\right) - \left\|t_i - t_j\right\|,$$

$$\mathrm{T}_2 = \left\|t_i - t_j\right\| - \left(\tau - \frac{\Delta\tau}{2}\right)$$

and Θ is the Heaviside step function.

It is worth to note that, taking into account different spatial distances, the number of event pairs at bigger distances is simply increased according to the geometrical expansion of the area embedding the events. To account for this effect, the number of succeeding events is given normalized by the area of the circular annulus at a given distance.

The result of the Omori count is given at three distance ranges, same for all analyzed catalogues. Specifically, these ranges are: 3–10 km, 10–32 km and 32–100 km. In Figure 19.6, the results are displayed, respectively, for all five catalogues.

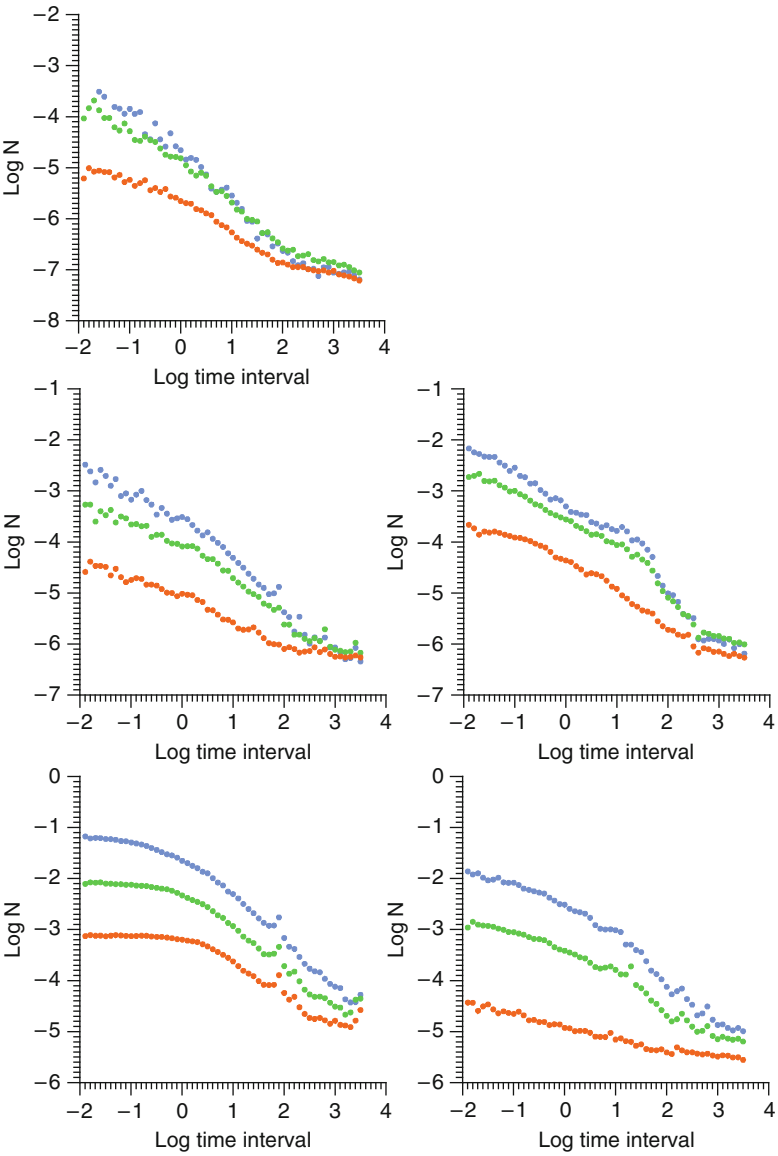

Fig. 19.6 Log-log plot of the number of events for time (day) and space (km^2) unit (stacked Omori count) at three distance ranges, for all analyzed catalogues (refer to Fig. 19.1). Distance ranges are: 3–10 km (upper curves), 10–32 km (middle curves) and 32–100 km (lower curves)

As expected, the closest range shows a quite similar behavior to the standard Omori count, as made from a single main event. This feature has two specific meanings: (a) the standard Omori count reflects the number of events decay at small distances from the epicenter, as defined by the size of the seismic fault; (b) the

stacked generalized count is in agreement with the standard Omori law in terms of c and p parameters.

The behaviour of the stacked Omori counts, for each catalogue, can be influenced by specific factors like: number of events, range of magnitudes present into the catalogue (defined as $m_{max} - m_{min}$), minimum magnitude of catalogue, tectonic settings of seismic area.

We can note common features in all five catalogues.

- A first part (times from parent shock occurrence until 1-10 days) in which the decay rate is very low. This feature is usually modelled with the presence of the c constant into the MOL. The California catalogue shows it in the clearest fashion. This is due to the very low minimum completeness magnitude limit, reflected by the highest number of events per unit area (slightly less than 10^{-1} events/km^2 for the closest range). This first portion is present in all catalogues for all distance ranges (sole exception is represented by 32-100 km range (crosses) for the Italian catalogue).
- A medium part of power law decay typical of the Omori law and represented by the exponent p. Time validity of this behavior is from 1 to 100 days for world and Greek catalogues; from 1 to 300 days for Californian, Italian and Japanese catalogues. Values of p constant are into the interval $0.87 < p < 1.36$ for closest range, $0.76 < p < 1.12$ for intermediate range and $0.24 < p < 0.68$ for longest distant range.
- A last part where the decay is very low and normalized number of events is the lowest and quite similar for all three spatial ranges.
- The behavior of two spatial ranges closest to the mainshock is similar, while the farthest range is quite different: this feature applies to all five catalogues.

Spatial ranges discrimination of Omori analysis gives a further element to establish the length of a sequence: in fact a sequence lasts until the rate decay of events is present. Moreover, we can assume that a sequence lasts until there is a marked difference of number of events per unit area at different distance ranges. This is due to the fact that the presence of aftershocks is higher close to the mainshock. In all five analyzed catalogues we can note that the difference of number of events per unit area is biggest at times closest to mainshock occurrence, and this difference tends to reduce in time. In fact, aftershocks are more concentrated near and at closest times to the mainshock. In time, the Omori law behavior appears to be linked to spatial distances from the mainshock and it is followed by a change of rate right before the end of the sequence.

An interesting result comes out from the comparison with the analysis of temporal fractal dimension as a function of space and time. The temporal clustering caused by an event lasts for longer time in respect to the end of the Omori power law (see Figure 19.2). This suggests a different definition of a seismic sequence, in dependence on the analyzed aspects: time, space and occurrence rate. In fact, while the rate decay pertains to the seismic activity increase due to sequence triggering, the temporal clustering takes account of occurrences disposition in the time axis. The low time fractal dimension indicates time clustering of events. When the

seismic sequence is characterized by an increased seismic activity, it is easily recognizable. On the other side, time clustering in periods of normal or slightly high background activity may indicate that the influence of the mainshock is still present. This influence probably reflects the persisting of triggering by parent events: the seismic activity, although at background rates, is not random, as it is still driven by main-aftershocks relations embedded inside background activity. Time clustering is due to clusters of events and voids caused by seismic shadows, as frequently observed at long time scales [Marsan, 2006].

19.4 Conclusions

Seismic sequences have been traditionally defined in relation with the mainshock, hence enclosing the succeeding events at limited spatial ranges. In general, all events located in the seismic main fault have been considered related to the mainshock. Such a definition allowed the early discovery of the decay law by Omori [Omori 1894, Utsu 1961], which is a simple and interesting statistical definition of a sequence. In this work we have proposed an extension of the definition of a sequence by the introduction of space-time constrains for the analysis of decay rate and clustering. To allow for such space-time analysis we have operated a stacking procedure: it consisted in considering every event as a mainshock and merging all subsequent seismic events in a stacked sequence. Davis and Frohlich (1991) with Nyffenegger and Frohlich (1998) already applied the stacking approach. We have used and analyzed five different seismic catalogues characterized by various space and magnitude ranges, spanning from a global catalogue to regional ones.

Stacked approach, in the constitution and analysis of sequences, allowed a more stable statistical analysis, as required by the added spatial distinction. Results are in agreement with the standard Omori p values but more articulated. In fact, the slope of the decay rate is small in the first time period after the mainshock (first 10–20 days) before the typical Omori values are reached. The behavior is influenced by spatial distance: the p values are smaller when the distance from parent shock increases. After a period of hundreds of days, the typical Omori p values disappear in favor of little or no decay. This happens in conjunction with the disappearence of differences as a function of distance. We interpret this as a closing of the typical sequence period.

The space-time fractal dimension was analyzed as a mean behavior, maintaining the same approach of stacking. After the occurrence of an event, there is, for all investigated catalogues, a space-time domain inside which earthquakes are time clustered, denoting close relationships among the events. Strong space clustering is present but only at distances bigger than seismic faults size, otherwise space fractal dimension is around 1.5, in agreement with fault fractal dimension. The time clustering domain denotes that in a particular space-time range after the occurrence of seismic events, earthquakes are not random.

Interestingly, sequences maintain time clustering longer than the sequence end indicated by the stacked Omori law result. The time clustering evidences that the influence of the parent shock is still present even if seismicity is at a background rate. This method could thus be used to detect seismic shadows after the end of the sequence.

The space-time analysis of seismic sequences, allowed by stacking of seismicity and considering every event as a mainshock, shows a more detailed analysis of seismicity under triggering effects: the results are in agreement with standard analysis of sequences and add a deeper insight into the topic. Influence area of seismic activity, related to a mainshock, is dynamically sized, giving further constrains to sequence modeling.

Acknowledgements The study was supported by INTAS Project Nr: 05-1000008-7889, by EU FP6 NEST Pathfinder programme TRIGS under contract NEST-2005-PATH-COM-043386 and by the DPC (Dipartimento della Protezione Civile) S1 2007-2009 Project.

References

Bak, P. & Tang C., 1989. Earthquakes as a self-organized critical phenomenon, J. Geophys. Res., 94, 15635-15637.

Brodsky, E. E., Karakostas, V. & Kanamori, H., 2000. A new observation of dynamically triggered regional seismicity: earthquakes in Greece following the August, 1999 Izmit, Turkey earthquake, Geophys. Res. Lett., 27, 2741–2744.

Davis S.C. & Frohlich C., 1991. Single-Link Cluster Analysis of Earthquake Aftershocks: Decay Laws and Regional Variations, J. Geophys. Res., 96, 6335-6350.

Gasperini, P. & Mulargia, F., 1989. A statistical analysis of seismicity in Italy: The clustering properties, Bull. Seismol. Soc. Am., 79, 973-988.

Godano, C., Tosi, P., De Rubeis, V. & Augliera, P., 1999. Scaling properties of the spatio-temporal distribution of earthquakes: a multifractal approach applied to a Californian catalogue, Geophys. J. Int., 136, 99-108.

Hill, D.P., Reasenberg, P.A., Michael, A., Arabaz, W.J., Beroza, G., Brumbaugh, D., Brune, J.N., Castro, R., Davis, S., dePolo, D., Ellsworth, W.L., Gomberg, J., Harmsen, S., House, L., Jackson, S.M., Johnston, M.J.S., Jones, L., Keller, R., Malone, S., Muaguia, L., Nava, S., Pechmaann, J.C., Sanford, A., Simpson, R.W., Smith, R.B., Stark, M., Stickney, M., Vidal, A., Walter, S., Wong, V. & Zollweg, J., 1993. Seismicity remotely triggered by the magnitude 7.3 Landers, California, earthquake, Science, 260, 1617-1623.

Husen, S., Wiemer, S. & Smith, R.B., 2004. Remotely Triggered Seismicity in the Yellowstone National Park Region by the 2002 Mw 7.9 Denali Fault Earthquake, Alaska, Bull. Seismol. Soc. Am., 94, 6B, 317-331.

King, G.C.P., Stein, R.S. & Lin, J., 1994. Static stress changes and the triggering of earthquakes, Bull. Seismol. Soc. Am., 84, 935-953.

Lomnitz, C., 1996. Search of a worldwide catalog for earthquakes triggered at intermediate distances, Bull. Seismol. Soc. Am., 86, 293-298.

Marsan, D., Bean, C.J., Steacy, S. & McCloskey, J., 2000. Observation of diffusion processes in earthquake populations and implications for the predictability of seismicity systems, J. Geophys. Res., 105, 28081-28094.

Marsan, D, 2006. Can coseismic stress variability suppress seismicity shadows? Insights from a rate-and-state friction model, Jou. Geoph. Res., 111, B06305.

Marzocchi, W., Selva, J., Piersanti, A. & Boschi, E., 2003. On the long-term interaction among earthquakes: Some insight from a model simulation, J. Geophys. Res., 108, 2538-2550.
Melini, D., Casarotti, E., Piersanti, A. & Boschi, E., 2002. New insights on long distance fault interaction, Earth and Planetary Science Letters, 204, 363-372.
Omori, F., 1894. On the after-shocks of earthquakes, J. Coll. Sci., Imp. Univ. Tokyo 7 (1894), 111–200.
Nyffenegger, P & Frohlich, C, 1998. Recommendations for Determining p Values for Aftershock Sequences and Catalogs, Bull. Seismol. Soc. Am., 88, 1144-1154.
Ogata, Y., L. M. Jones, and S. Toda, 2003. When and where the aftershock activity was depressed: Contrasting decay patterns of the proximate large earthquakes in southern California, J. Geophys. Res., 108(B6), 2318.
Omori, F. 1894. On the aftershocks of earthquakes, Journal of the College of Science, Imperial University of Tokyo, vol. 7, 111–200.
Reasenberg, P.A., 1999. Foreshock occurrence before large earthquakes, J. Geophys. Res., 104, 4755-4768.
Shearer, P., E. Hauksson, and G. Lin, 2005. Southern California hypocenter relocation with waveform cross-correlation, Part 2: Results using source-specific station terms and cluster analysis, Bull. Seismol. Soc. Am. 95, 904-915.
Stein, R. S., King, G.C.P. & Lin, J., 1994. Stress triggering of the 1994 M = 6.7 Northridge, California, earthquake by its predecessors, Science, 265, 1432-1435.
Stein, R. S., 1999. The role of stress transfer in earthquake occurrence, Nature, 402, 605-609.
Stein, R. S., King, G.C.P. & Lin, J., 1994. Stress triggering of the 1994 M = 6.7 Northridge, California, earthquake by its predecessors, Science, 265, 1432-1435.
Tosi, P., De Rubeis, V., Loreto, V. & Pietronero, L., 2008. Space–time correlation of earthquakes Geoph. Jou. Int. 173, 3, 932-941.
Utsu T., 1961. A statistical study on the occurrence of aftershocks, Geophys. Mag. 30 (1961), 521–605.
Ziv, A., 2006. What Controls the Spatial Distribution of Remote Aftershocks?, Bull. Seismol. Soc. Am., 96, 6, 2231-2241.

Chapter 20
Dynamical Changes Induced by Strong Electromagnetic Discharges in Earthquakes' Waiting Time Distribution at the Bishkek Test Area (Central Asia)

T. Chelidze, V. de Rubeis, T. Matcharashvili, and P. Tosi

Abstract From 1 August 1983 to 28 March 1990 at the Bishkek electromagnetic (EM) test site (Northern Tien Shan and Chu Valley area, Central Asia), strong currents, up to 2.5 kA, were released at a 4.5 km long electrical (grounded) dipole by discharge of MHD or large batteries. This area is seismically active and a catalogue with about 14100 events from 1975 to 1996 has been analyzed. The seismic catalogue was divided into three parts: the first, 1975–1983, with no EM experiments; the second, 1983–1988, during EM experiments; and the third part, 1988–1996, after the experiments. Qualitative and quantitative time series non linear analysis was applied to waiting times of earthquakes to the above three sub-catalogue periods. Qualitative and quantitative methods used include iterated function systems (IFS), Lempel-Ziv algorithmic complexity measure (LZC), correlation integral calculation, recurrence quantification analysis (RQA), and Tsallis entropy calculation. General features of temporal distribution of earthquakes around the test area reveal properties of dynamics close to low dimensional non-linearity. Strong EM discharges lead to the increase of extent of regularity in earthquakes' temporal distribution. After cessation of EM experiments, the earthquakes' temporal distribution becomes much more random than before the experiments. To avoid non-valid conclusions, several tests were applied to our data set: differentiation of the time series was applied to check the results that were not affected by non-stationarity, followed by surrogate data approach in order to reject the hypothesis that dynamics belongs to the colored noise type. Small earthquakes, below the completeness threshold, were added to the analysis in order to check the robustness of the results.

T. Chelidze (✉) and T. Matcharashvili
M. Nodia Institute of Geophysics, Georgian Ac. Sci. Tbilisi, Georgia
e-mail: tamaz.chelidze@gmail.com; matcharashvili@gtu.ge
V. de Rubeis and P. Tosi
Istituto Nazionale di Geofisica e Vulcanologia.Roma Italy
e-mail: valerio.derubeis@ingv.it

V. de Rubeis et al. (eds.), *Synchronization and Triggering: from Fracture to Earthquake Processes*, GeoPlanet: Earth and Planetary Sciences 1,
DOI 10.1007/978-3-642-12300-9_20,

20.1 Introduction

The dynamics of seismic process is far from being clearly understood and modeled; under a multidisciplinary approach during last years, several aspects have arisen showing that seismicity is certainly not a pure random process. Magnitude, waiting time and spatial distribution of earthquakes present features of self-similarity or fractal character, as evidenced by several authors [Turcotte, 1997; De Rubeis *et al.*, 1993]. On the other hand, seismicity cannot be deterministically explained although efforts to show its quasi periodic character have been numerous. A direct consequence of this situation is the almost complete impossibility to precisely predict earthquakes [Main, 1999; Geller *et al.*, 1997].

In the last years, nonlinear dynamics has offered several tools to analyze and characterize the seismicity. These qualitative and quantitative tools may help to distinguish between a purely random process and a complicate process driven by a finite, limited set of rules. The enormous gap between "simple" linear deterministic models and random, complicate and strongly unpredictable processes seems to be filled with these new analytical tools. The aim is to render tractable, in a certain way, phenomena and data, otherwise not clearly depicted.

In the present work, the influence of strong EM discharges on earthquakes temporal distribution has been investigated.

Experiments on triggering effect of MHD (magnetohydrodynamic) soundings on the microseismic activity of the region have been performed in 1975–1996 by IVTAN (Institute of High Temperatures of Russian Academy of Sciences) in the Central Asia test area [Tarasov, 1997; Tarasov et al., 1999; Jones, 2001]. During these experiments, deep electrical sounding of the crust was carried out at the Bishkek test site in the years 1983 to 1989. The source of electrical energy was MHD generator, and the load was an electrical dipole of 0.4 Ohm resistance with electrodes located at a distance of 4.5 km from each other. When the generator was fired, the load current was 0.28–2.8 kA, the sounding pulses had durations of 1.7 to 12.1 s, and the energy generated was mostly in the range of 1.2–23.1 MJ [Volykhin et al., 1993].

Evidences of some relationships between EM discharges and seismic activity have been pointed out under a statistical aspect and in a time range of days after EM experiments [Tarasov, 1997]. Here the general dynamical aspect is considered. A good seismic catalogue of the area has been available well before, during and well after this period. A simple causal relationship between the two processes is not clearly evident. Relations appear to be present but the data noise is also relevant. It is useful to investigate if the seismic dynamics, in periods before, during and after EM experiments is influenced by the introduction of strong electric current into the ground.

20.2 Methods

Investigation was performed according to general scheme of time series nonlinear analysis [Abarbanel et al. 1993; Sprott and Rowlands, 1995; Kantz and Schreiber, 1997; Goltz, 1998; Hegger and Kantz, 1999]. In general, data analysis can be

performed firstly under a more qualitative and visual approach and successively a more quantitative methodology can be applied.

Qualitative approach includes a visual inspection of the reconstructed phase space. Namely, p-dimensional phase space from the scalar time sequences was reconstructed by the method of time delay [Packard et. al, 1980, Takens, 1981]. According to Takens theorem, it is possible to catch the essential dynamical properties of a system by a reconstruction of its phase space by only one variable. Two- and three-dimensional phase space portraits, encapsulating the essential dynamical properties of the analyzed complex process, were used as qualitative tests. Other qualitative tools have also been used, such as Iterated Function Systems (IFS) [Jeffrey, 1992] and Recurrence Plots (RP) [Eckman et al. 1987].

Generally, the recurrence analysis is a graphical method designed to locate hidden recurring patterns and structure in time series. The recurring pattern (RP) is defined as:

$$R_{i,j} = \Theta(\varepsilon_i - \left\|\bar{x}_i - \vec{x}_j\right\|), \tag{20.1}$$

where ε_i is a cut-off distance (often $\varepsilon = 0{\cdot}1\sigma$,with σ the standard deviation), and $\Theta(x)$ is the Heaviside function. According to Eckman et al. (1987), the values one and zero in this matrix are commonly visualized as black and white. The black points indicate the recurrences of the investigated dynamical system revealing their hidden regular and clustering properties. By definition, RP has black main diagonal (line of identity) formed by distances in matrix compared to each other. In order to understand RP it should be stressed that it visualizes distance matrix which represents autocorrelation in the series at all possible time (distance) scales. As far as distances are computed for all possible pairs, elements near the diagonal on the RP plots correspond to short range correlation, whereas the long range correlations are revealed by the points distant from the diagonal. Hence, if the analyzed dynamics (time series) is deterministic (ordered, regular), then the recurrence plot shows short line segments parallel to the main diagonal.

Qualitative patterns of unknown dynamics presented as fine structure of RP are often too difficult to be considered in detail. Therefore, one uses a modern quantitative method of analysis of complex dynamics for RP approach (Recurrence Quantitative Analysis or RQA) [Zbilut and Webber, 1992]. RQA is especially useful to overcome the difficulties often encountered dealing with nonstationary and rather short real data sets. As a quantitative tool of complex dynamics analysis, RQA defines several measures mostly based on diagonally oriented lines in the recurrence plots: recurrence rate, determinism, maximal length of diagonal structures, entropy, trend etc. In the present work, recurrence rate $RR(t)$ and determinism $DET(t)$ measures, based on an analysis of diagonal oriented lines in the recurrence plot, have been calculated [Weber and Zbilut, 1994; Marwan et al., 2002].

Generally speaking, the recurrence rate $RR(t)$ is the ratio of all recurrent states (recurrence points) to all possible states and is therefore the probability of the recurrence of a certain state. Stochastic behavior causes very short diagonals, whereas deterministic behavior causes longer diagonals.

The ratio of recurrence points forming diagonal structures to all recurrence points is called the determinism, $DET(t)$. $DET(t)$ is the proportion of recurrence points forming long diagonal structures consisting of all recurrence points. Again, stochastic and heavily fluctuating data cause none or only short diagonals, whereas deterministic systems cause longer diagonals.

An Iterated Function System (IFS) is an iteration of Hutchinson operator for every finite set of functions in some space which maps a set of points to another set of points. If Hutchinson operator is repeatedly applied to a compact set, in the limit it will render the unique attractor of the IFS [Peitgen et al., 1992]. For the purpose of time series analysis, IFS attractors can be used as a qualitative measure of self similarity of analysed dynamics (the greater the order in time series, the more regular the structures in the IFS attractor). We use the IFS as an additional qualitative tool for detection of hidden structure in the analysed time series [Sprott and Rowlands, 1995].

These tests enable to accomplish first qualitative visual inspection of unknown dynamics and helps to uncover general properties of analyzed process. Qualitative analysis allows revealing possible existence of specific attractors, e.g., strange ones which point to the deterministic chaotic behavior.

Among others, for quantitative analysis of earthquakes dynamics, correlation integral calculation of the reconstructed phase space of temporal distribution has been performed [Abarbanel et al., 1993; Kantz and Schreiber, 1997; Hegger and Kantz, 1999]. This approach is based on the idea of correlation sum. Correlation sum $C(r)$ of set of points in the vector space is defined as the fraction of all possible pairs of points which are closer to each other than a given distance r. The basic formula useful for practical application is

$$C(r) = \frac{2}{N(N-1)} \sum_{i=1}^{N} \sum_{j=i+1}^{N} \Theta(r - \|x_i - x_j\|), \tag{20.2}$$

where $\Theta(x)$ is the Heaviside step function, $\Theta(x) = 0$ if $x < 0$ and $\Theta(x) = 1$ if $x \geq 0$, $\|x_i - x_j\|$ is the Euclidian norm, $i = j$ being excluded. For fractal systems, if the time series are long enough and r is small, the $C(r) \propto r^{v}$relationship is correct. Commonly, such a dependence is correct only for the restricted range of r values, called the scaling region. Correlation dimension v or d_2 is defined as

$$v = d_2 = \lim_{r \to 0} \frac{\log C(r)}{\log(r)}. \tag{20.3}$$

In practice, d_2 value is found from the slopes of $\log C(r)$ versus $\log r$ curves for different phase space dimensions. The correlation dimension of unknown process is the saturation value of d_2, which does not change by increasing the phase space dimension.

In order to reduce possible spurious conclusions about considered dynamics, noise reduction and surrogate testing methodologies were used [Kantz and Schreiber,1997; Hegger and Kantz, 1999].

The entropy calculation according to Tsallis [1988, 1998] has also been used as a measure of the complexity in earthquakes time distribution

$$S_q = k\frac{1}{q-1}(1 - \sum_{i=1}^{w} p_i^q), \tag{20.4}$$

where p_i are the probabilities of the separate configurations (W) and q is intrinsic parameter with a value greater than zero which demonstrates the correlation between subsystems.

Besides, as an additional quantitative test for relatively short time series, Lempel-Ziv's algorithmic complexity measure (LZC) was calculated [Lempel and Ziv, 1976]. The LZC is based on the transformation of the original one-dimensional time series into a finite symbol sequence and is defined as $C_{LZ} = \lim_{N\to\infty} \sup \frac{L(n)}{N}$, where N is the length of original time series, and $L(N) \sim N_w(N)(\log_b N_W(N) + 1)$ is the total length of encoded sequence, with $N_w(N) \leq N$ being the total number of code words. Being one of the tools for nonlinear analysis of time series, LZC is especially suitable for relatively short real data sets because it is not so demanding as concerns the time series length as other methods [Zhang and Thakor, 1999; Matcharashvili and Janiashvili, 2001].

20.3 Data and Analysis

In the present study nonlinear analysis has been performed on about 14100 time intervals (in seconds) between earthquakes contained in the IVTAN catalogue (1975–1996). In the original catalogue, the energy of the events was expressed as energy class, which we converted to magnitude using the following relation:

$$m = \frac{E-4}{1.8} \tag{20.5}$$

where m is magnitude and E is the energy class.

Completeness of the catalogue was investigated first by considering the realization of the Gutenberg-Richter relationship at low magnitudes: departure from a straight line was interpreted as a lack of completeness at low magnitudes. As a result, the catalogue was considered complete, under the sole magnitude aspect, for $m \geq 1.7$. The Gutenberg-Richter b-value was found to be equal to 0.83 with a reasonably good fit. Earthquakes with magnitude higher than 6 seem to show behavior typical of characteristic events.

A second test was oriented to check the time completeness. As is well known, a catalogue's completeness changes with time, usually as a result of improving seismic-network performance (e.g., by increasing the number of stations), leading to greater magnitude sensitivity. The completeness analysis was performed by employing the method of Mulargia *et al*. (1987). The method consists in separating

all events into magnitude classes and plotting separately the cumulative number of events versus time. Assuming that during the considered time interval the seismicity had a constant rate, the flat behavior in the beginning of the time period may be due to a lack of data; this is normal for low-magnitude ranges.

Only for magnitudes higher than 2.0 our catalogue is complete over the entire time period (number of earthquakes $n = 5297$). If a lower magnitude limit is desired, the time period from year 1980 is more appropriate (Fig. 20.1). As a result of the analysis performed, a relatively complete catalogue was obtained with a lower magnitude threshold of 1.7 from the year 1980.

For the present study, the catalogue has been analyzed under the time aspect, specifically on inter-event (waiting) times. The catalogue subset of waiting times was used according to the completeness analysis, i.e., the whole time span and $m>2.0$. Successively, in order to confirm the results and to test their robustness, all data used were selected by the same procedure.

20.4 Results and discussion

In Fig. 20.2, the results of qualitative analysis of waiting times sequences above the mentioned threshold are presented. The results of IFS clumpiness test presented in Fig. 20.2 a, c, e, [Jeffrey, 1992; Sprott and Rowlands, 1995] and the recurrence plot analysis in Fig. 20.2 b, d, f [Zbilut and Webber, 1992] reveal that after the beginning of the experiments some structure in plots is visible, which points to the increased amount of functional interdependence in earthquake temporal distribution.

As to the quantitative approach, the variation of correlation dimension vs. dimension of phase space where the reconstructed dynamics is embedded (embedding dimension) is presented in Fig. 20.3. The integral time series (5297 time intervals) for the whole period of observation (1975-1996) containing time intervals sequences between all events above the threshold reveals clear low correlation dimension ($d_2 = 1.22 \pm 0.43$) (asterisks). Shorter time series were also considered. Namely, 1760 waiting times data before (1975-1983), 1953 waiting times during MHD experiments (1983-1988) and 1584 waiting times of the period after experiments (1988-1992). Time series before and especially during MHD experiments also have low correlation dimension ($d_2 < 5$). Namely, $d_2 = 3.83 \pm 0.80$ before and $d_2 = 1.04 \pm 0.35$ during experiments. On the other hand, in opposite to what was mentioned above, after cessation of experiments (Fig. 20.3, triangles) correlation dimension of waiting times sequences noticeably increases ($d_2 > 5.0$), exceeding low dimensional threshold ($d_2 = 5.0$). This means that after termination of experiments the extent of regularity or extent of determinism in process of earthquake temporal distribution decreases. The considered process becomes much more random both qualitatively (Fig. 20.2. e, f) and quantitatively (Fig. 20.3, triangles). For clarity, results for random number sequence are also shown in Fig. 20.3 (diamonds).

The found low correlation dimension of waiting interval time series is in good accordance with the previously published results for the Caucasus [Matcharashvili,

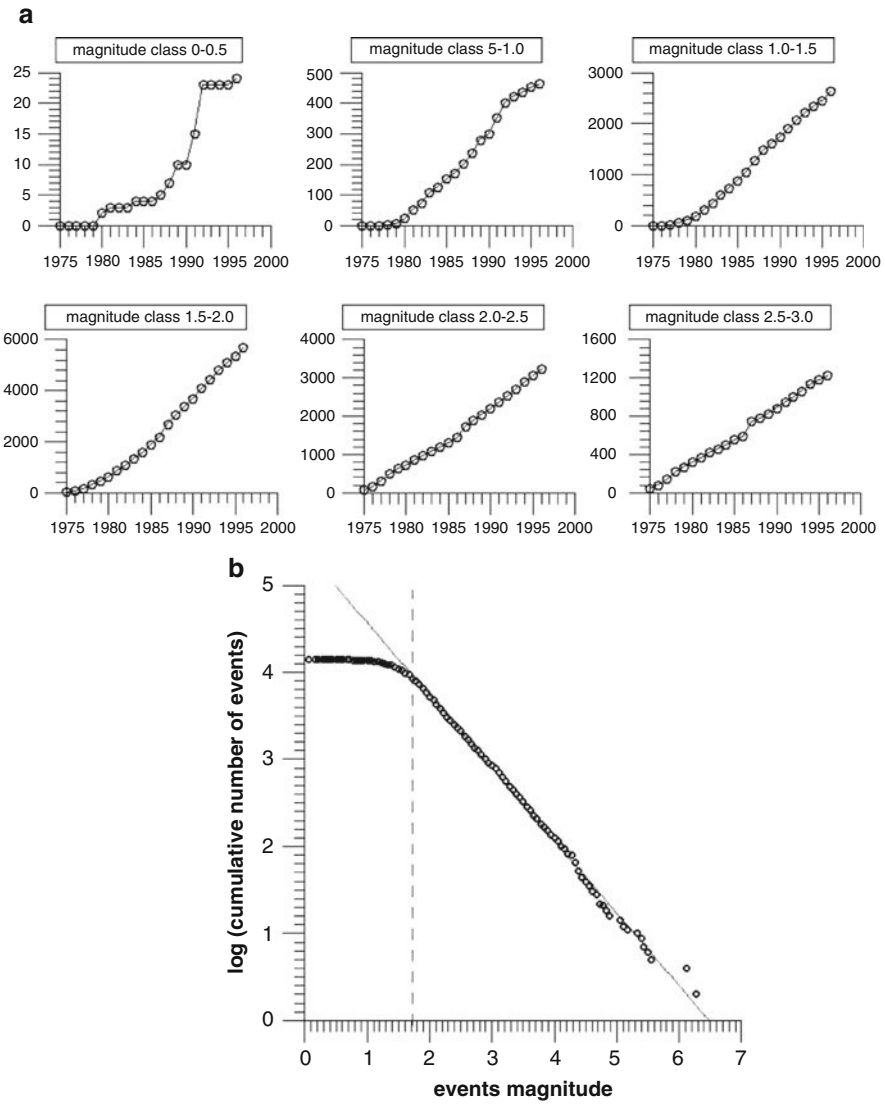

Fig. 20.1 **(a)** Cumulative number of events versus time for magnitude class step = 0.5. Note that cumulative number of events is rescaled among magnitude classes. **(b)** Log cumulative number of earthquake versus magnitude (Gutenberg-Richter relation); values of regression fit the equation $Y = -0.83 \times X + 5.40$. Coefficient of determination, R-squared = 0.995

et al., 2000] as well as with the results of Goltz [1998] for other seismoactive regions.

This result together with qualitative analysis results shown in Fig. 20.2, provide evidence that after the beginning of EM discharges the temporal distribution of

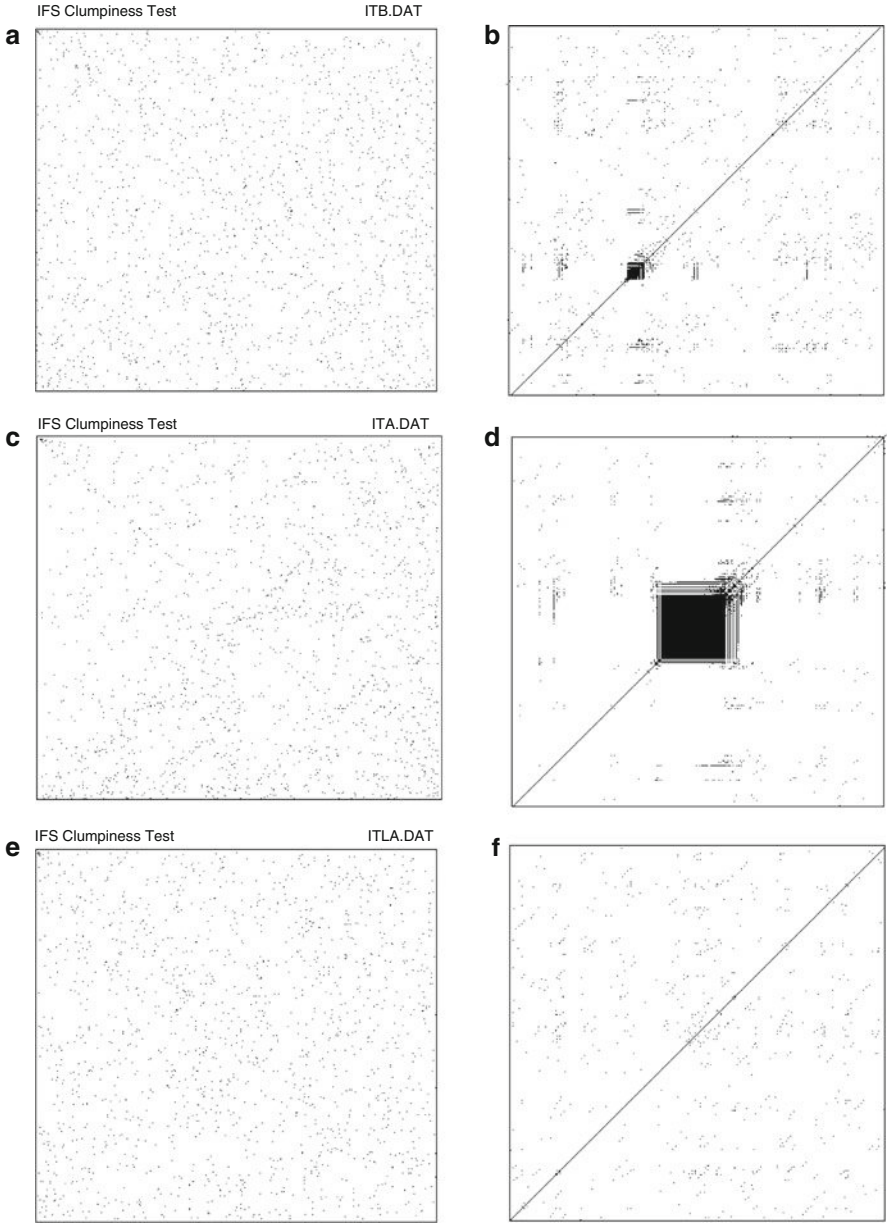

Fig. 20.2 Qualitative analysis of temporal distribution of earthquakes (complete catalogue, $M \geq 1.7$) before the beginning of EM experiments (1975-1983), during experiments (1983-1988) and after accomplishing of experiments (1988-1992). IFS-clumpiness test for inter-event time interval sequences: **(a)** before experiments, **(c)** during experiments, **(e)** after experiments. Recurrence plots analysis of waiting times sequences: **(b)** before experiments, **(d)** during experiments, **(f)** after experiments. Note diagonal lines in IFS plot and compact structure in RP during experiments

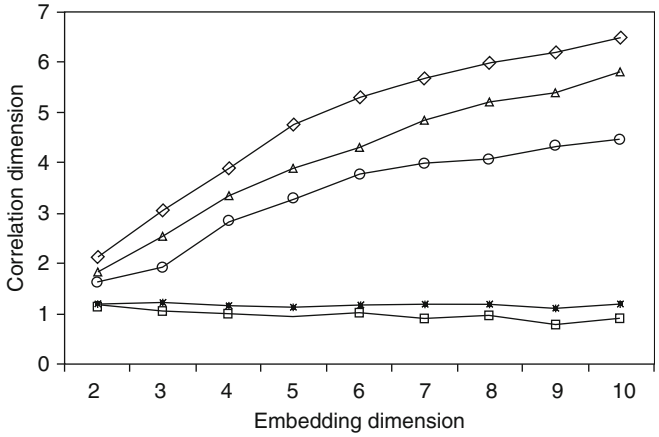

Fig. 20.3 Correlation dimension versus embedding dimension of waiting times sequences (complete catalogue): (a) asterisks–integral time series (1975-1996), (b) circles–before the beginning of experiment (1975-1983), (c) squares–during experiments (1983-1988), (d) triangles–after experiments (1988-1992), (e) diamonds correspond to random number sequence

earthquakes around IVTAN test area becomes more regular, or events of corresponding time series become functionally much more interdependent.

At the same time, the absence of typical phase space structure (not shown here), IFS and recurrence plot attractors (Fig. 20.2) do not allow to consider the process as deterministically chaotic.

In order to reduce effects of possible noises, we analyzed waiting time series after noise reduction procedure [Shreiber, 1993; Kantz and Schreiber, 1997]. Namely, we used methodology of nonlinear noise reduction (which in fact is phase space nonlinear filtering) instead of common linear filtering procedures. The latter, as it is well known, may lead to destroying the original nonlinear structure of analyzed complex processes [Hegger and Kantz, 1999; Schreiber, 2000]. Nonlinear noise reduction relies on the exploration of reconstructed phase space of considered dynamical process instead of frequency information of linear filters [Hegger and Kantz, 1999; Schreiber, 1993; Kantz and Schreiber, 1997].

Correlation dimension vs. embedding space dimension of noise-reduced time series is presented in Fig. 20.4. As follows from the obtained results, correlation dimensions are not essentially affected by unavoidable noises. Therefore, the results assure that the differences found in d_2-phase space dimension (P) dependence before, during, and after experiments (Fig. 20.3) are indeed related to dynamical changes in temporal distribution of earthquakes after the beginning of MHD discharges experiments.

When describing unknown dynamics of waiting times fluctuation, differentiation of original time series can be useful to avoid improper conclusions related to the effects of trends or non-stationarity in data sets, even when those are not clearly visible (as in the case of considered time series) [Goltz, 1998]. As it is shown in Fig. 20.5, differentiation of our time series, according to Goltz [1998], does not lead

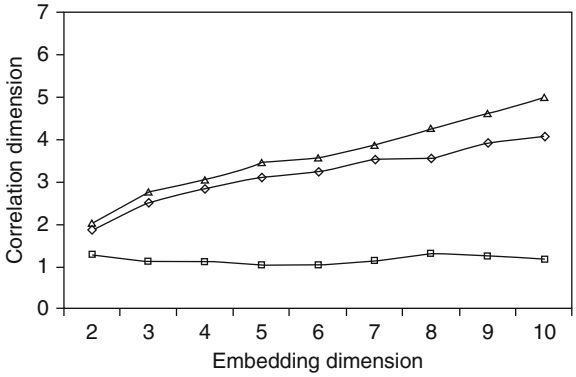

Fig. 20.4 Correlation dimension versus embedding dimension of waiting times sequences (complete catalogue) after noise reduction: (a) diamonds–before experiments, (b) squares–during experiments, (c) triangles–after experiments

Fig. 20.5 Correlation dimension versus embedding dimension of differenced waiting times sequences (complete catalogue). (a) diamonds–before experiments, (b) squares–during experiments, (c) triangles–after experiments

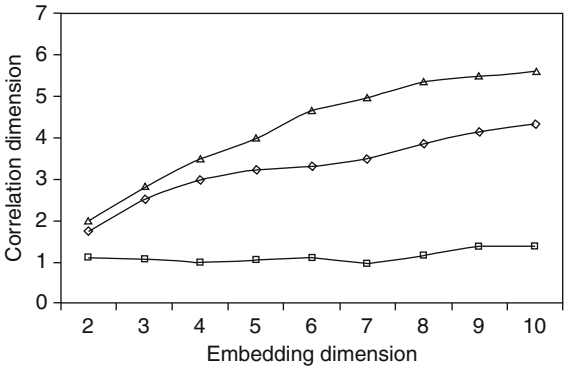

to significant changes of the obtained results (see Fig. 20.3). So our results could not be affected by trends or non-stationarity in the data sets used.

Analysis of differenced time series may be important also in the sense of inherent dynamical structure testing [Prichard et al., 1994]. Namely, the test is based on the finding that estimated nonlinear measure (correlation dimension in our case) for the differentiated series is larger than that estimated for original data, if the structure of their dynamics is caused by a linear stochasticity. At the same time, for chaotic (low dimensional) processes these measures are the same. From this point of view, the analysis of differentiated time series before detailed surrogate testing provides first additional evidence that variation of waiting times has inherent nonlinear structure indeed, and that their dynamical properties are not caused by linear relationships between data. Indeed, curves of Figs. 20.3 and 20.5 are characterized by comparable values of correlation dimension.

Moreover, in order to have a basis for more reasonable rejection of spurious conclusions caused by possible linear correlations in considered data sets, we have

used the surrogate data approach to test the null hypothesis that our time series are generated by a linear stochastic process [Theiler et al., 1992; Rapp et al., 1993, 1994; Kantz and Schreiber, 1997]. In other words, we would like to reject reliably the possibility that the revealed dynamics belongs to the colored noise type. Namely, Random Phase (RP) and Gaussian Scaled Random Phase (GSRP) surrogate sets for waiting times series were used [Matcharashvili et al., 2000]. The RP surrogate sets are obtained by destroying the nonlinear structure through randomization of phases of Fourier transform of original time series and then performing a backward transformation. The GSRP surrogate sets were generated in a three-step procedure. At first, a Gaussian set of random numbers was generated, which has the same rank structure as the original time series. After this phase, randomized surrogates of these Gaussian sets were constructed. Finally, the rank structure of original time series was reordered according to the rank structure of the phase randomized Gaussian set (Theiler, 1992).

In Fig. 20.6, the results are shown of surrogate testing of waiting time sequences before (a) and during (b) experiments, using d_2 as a discriminating metric. For each of our data sequences, we have generated 75 of RP and GSRP surrogates. There are several ways to measure difference between the discriminating metric measure of

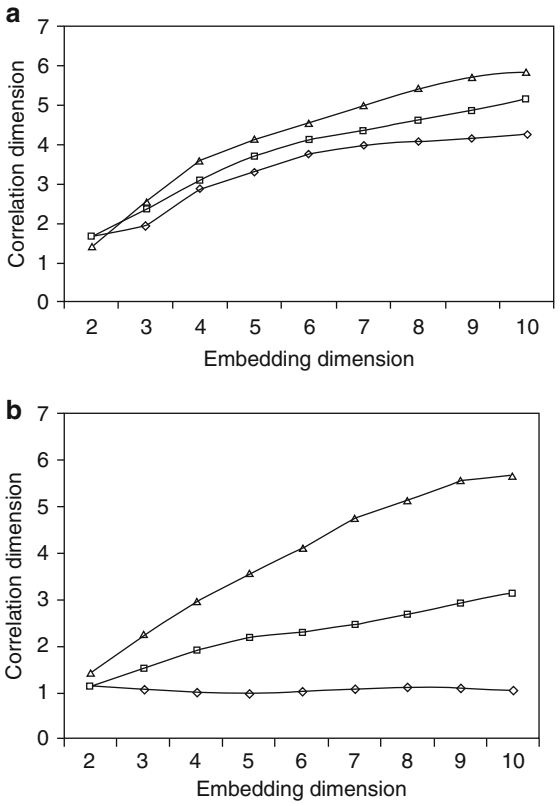

Fig. 20.6 Correlation dimension versus embedding dimension of original (diamonds) and surrogate (squares–GSRP, triangles–RP) waiting time sequences: (**a**) before the beginning of experiments, (**b**) during experiments

original (given by M_{orig}) and surrogate (given by M_{surr}) time series [Rapp, 1994]. Investigators often use the significance criterion $S=|\langle M_{surr} \rangle - M_{orig}|/\sigma_{surr}$, where σ_{surr} is the standard deviation of M_{surr} [Theiler, et al, 1992].

The significance criterion S, according to Theiler et al. [1992], for analyzed time series before experiments is significant: 22.4 ± 0.2 for RP and 5.1 ± 0.7 for GSRP surrogates. Consequently, after the beginning of experiments the null hypothesis that the original time series is a linearly correlated noise was rejected with significant value of S criterion: 39.7 ± 0.8 for RP and 6.0 ± 0.5 for GSRP surrogates.

These results can be considered as a strong enough evidence to prove that the analyzed time series are not a linear stochastic noise and that the corresponding processes of earthquakes' temporal distribution before and especially during experiments are characterized by inherent low-dimensional nonlinear structure.

According to the IVTAN catalogue, each considered time period contains one large ($M \approx 6.1$–6.3) earthquake. Therefore, in order to refine whether the above results are caused by special properties of a separate large earthquake or reflect total changes in dynamics caused by EM discharges, we have analyzed waiting time sequences (above the appropriate threshold) after each largest event. Namely, 1000 consecutive waiting time intervals after 03.24.78 $M = 6.1$ ($K = 15.0$), 01.24.87 $M = 6.3$ ($K = 15.3$) and 798 time intervals after 12.30.93 $M = 6.1$ ($K = 15.0$) events were analyzed. It is important to note that each of these relatively short time series is localized in the corresponding time periods named "before", "during" and "after" experiments.

It becomes clear from the results of IFS-clumpiness and RQA analysis (Fig. 20.7) that qualitatively this situation is like that shown in Fig. 20.2, i.e., after the beginning of experiments the dynamics becomes more regular and after accomplishing of experiments the dynamics is most random-like.

Quantitatively, it is shown in Fig. 20.8 that these short time series generally reveal that after the experiments the dynamics has also become more random than before. Some differences are noticeable in saturation values of correlation dimension (in Fig. 20.8) before (circles, $d_2 = 3.1 \pm 0.4$) and during (squares, $d_2 = 2.1 \pm 0.7$) experiments. The latter may be caused by the fact that the data length was too limited for proper nonlinear analysis of these time series (untypical shape of the curve at high embedding dimensions) as well as by artificially increased fraction of aftershocks in short time series, which contains only the events after the largest earthquake.

In any case, our main conclusion about low-dimensional dynamical structure of earthquake temporal distribution during experiments and increasing randomness after termination remains valid even for periods of separate large earthquakes.

The above conclusion about the increase of regularity in earthquakes temporal distribution after beginning of experiments is to some degree also confirmed by results of Lempel and Ziv's algorithmic complexity (C_{LZ}) measure calculation [Lempel and Ziv, 1976]. Indeed, C_{LZ} is larger when the necessary code words are longer, i.e., when regular patterns of analyzed time series are minor.

Indeed, measured values of Lempel-Ziv's complexity before, during, and after experiments for original time series above the threshold are $C_{LZ} = 0.99 \pm 0.07$; $C_{LZ} = 0.87 \pm 0.05$; $C_{LZ} = 1.00 \pm 0.08$, respectively.

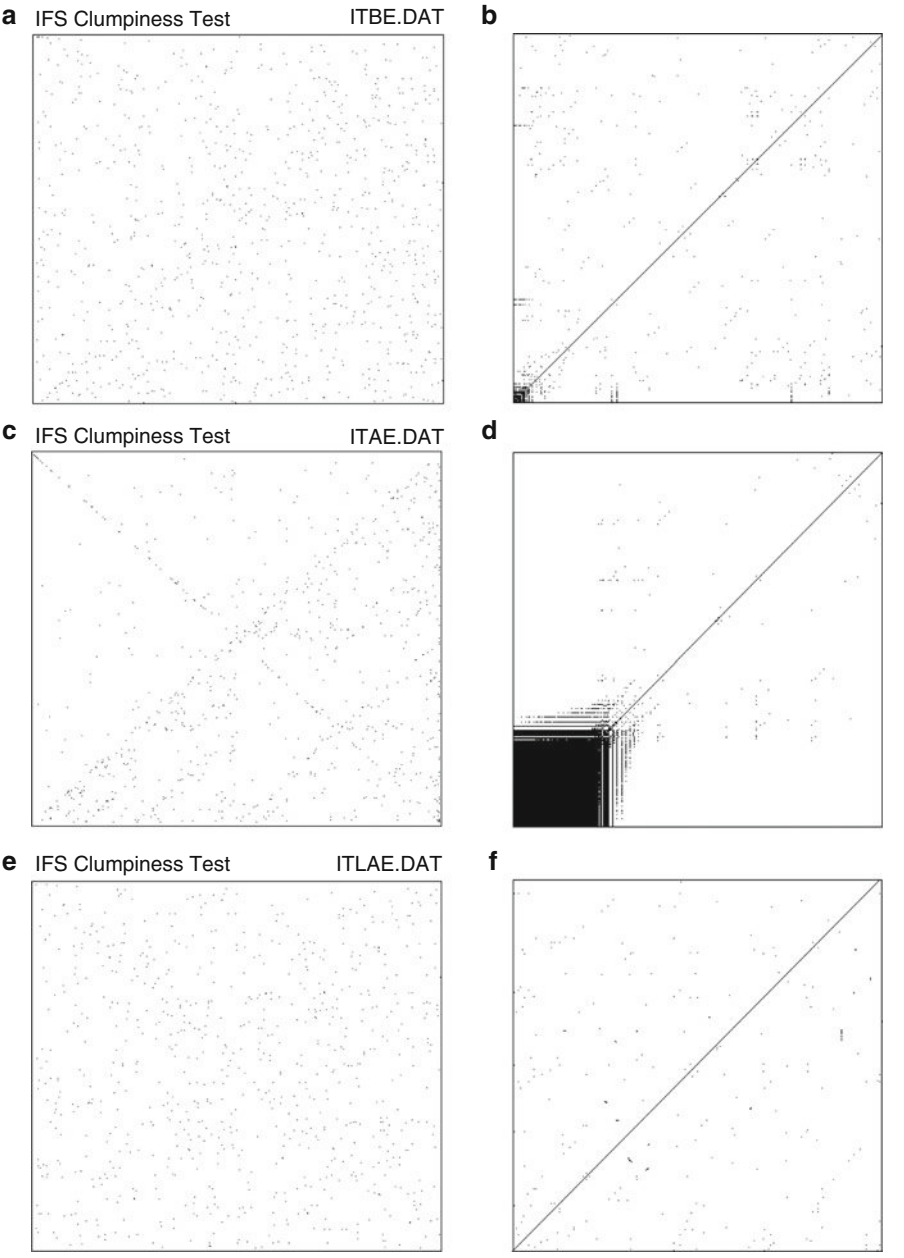

Fig. 20.7 Qualitative analysis of 1000 data waiting times sequences (complete catalogue), after largest events before the beginning of EM experiments (1975-1983), during experiments (1983-1988) and after accomplishing of experiments (1988-1992). IFS-clumpiness test for inter-event time interval sequences: (**a**) before experiments, (**c**) during experiments, (**e**) after experiments. Recurrence plots analysis of waiting times sequences: (**b**) before experiments, (**d**) during experiments, (**f**) after experiments

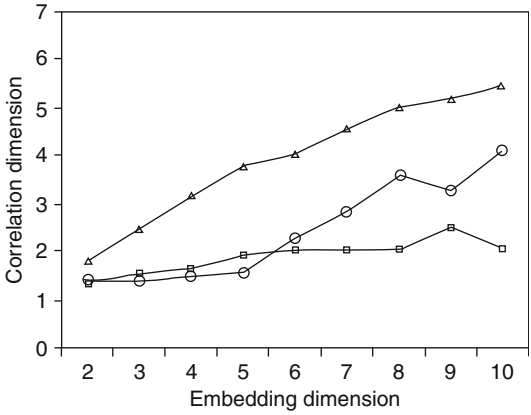

Fig. 20.8 Correlation dimension versus embedding dimension of 1000 data waiting times sequences (complete catalogue) after largest events:
(a) circles–time period before beginning of experiments (1975-1983),
(b) squares–time period during experiments (1983-1988), (c) triangles–time period after accomplishing of experiments (1988-1992).

The same conclusion follows also from quantitative RQA results; namely $RR(t) = 9.6$, $DET(t) = 3.9$ before the experiments, $RR(t) = 25$, $DET(t) = 18$ during, and $RR(t) = 3$, $DET(t) = 1.5$ after the experiments.

The increasing order in earthquake temporal distribution under the influence of EM is confirmed for short time interval sequences above the threshold after the largest earthquakes. Indeed, Lempel-Ziv's complexity measure values were: $C_{LZ} = 0.98 \pm 0.08$; $C_{LZ} = 0.74 \pm 0.05$; $C_{LZ} = 1.00 \pm 0.09$ before, during, and after MHD runs, respectively (note that $C_{LZ} = 0.04$ for periodic and $C_{LZ} = 1$ for random processes). Also, the increasing order in temporal distribution is documented by RQA results for the above-mentioned short time series; namely $RR(t) = 9.8$, $DET(t) = 6.5$ before the experiments, $RR(t) = 19.5$, $DET(t) = 49.3$ during, and $RR(t) = 7.1$, $DET(t) = 1.6$ after the experiments.

In other words, for the situation where the shape of d_2 (Fig. 20.8) is not informative for finding changes in dynamics, possibly due to too short time series, Lempel- Ziv and RQA analysis reveals the increase of regularity. The conclusion from Tsallis entropy calculation is the same. As it is shown in Fig. 20.10, normalized to the averaged S value calculated for randomized data sets, the entropy decreases for time series 2, i.e., the extent of regularity in the earthquake temporal distribution increased during MHD runs.

On the basis of results of previous research it is known that small earthquakes play a very important role in general dynamics of earthquake temporal distribution [Matcharashvili et al., 2000]. Therefore, we have additionally carried out an analysis of time series containing all the waiting time sequences available from the whole catalogue, including those between small earthquakes below the magnitude threshold. This test is also valid for checking the robustness of results in case of adding a new, not necessarily complete set of data to our original set. The total number of events in the whole catalogue increased up to 14100, while in the complete catalogue for the three above-mentioned periods (before, during and after MHD experiments) there were about 4000 data in each one.

The results of IFS and recurrence plots tests of these time series are shown in Fig. 20.9. Noticeable qualitative differences in waiting time distribution dynamics during, as well as after accomplishment of experiments is obvious.

The results of correlation dimension calculation for these time series are presented in Fig. 20.11. Practically, there are no differences from results obtained for the case with $m > 2.0$ (Fig. 20.3). Namely, according to Fig. 20.11, integral time series (14100 time intervals) for the whole period of observation (1975–1996) reveals a clear low correlation dimension ($d_2 = 2.40 \pm 0.71$) (diamonds). Time series before the beginning of experiment (squares) is characterized by correlation dimension $d_2 = 3.50 \pm 0.63$ which still is below the accepted low dimensional threshold ($d_2 = 5.0$). During experiments (Fig. 20.11, triangles), the correlation dimension of time interval sequence decreases noticeably ($d_2 = 1.71 \pm 0.09$) as compared to the situation before. After termination of experiments, the correlation dimension of waiting time interval sequences increases noticably ($d_2 > 5.0$), exceeding low dimensional threshold ($d_2 = 5.0$). As in the case of complete catalogue, this means that after termination of experiments the extent of determinism in process of earthquake temporal distribution decreases. The considered process becomes much more random, both qualitatively (Fig. 20.9. c, f), and quantitatively (Fig. 20.11 circles).

Both the complete and whole catalogues of waiting time sequences reveal low-dimensional nonlinear structure in temporal distribution of earthquakes before and especially during experiments, which was confirmed by 70 surrogate testing analyses (Fig. 20.12). The significance criterion S for analyzed time series before the experiments gives: 32.3 ± 0.2 for RP and 5.3 ± 0.6 for GSRP surrogates; consequently, after the beginning of experiments the null hypothesis that the original time series is a linearly correlated noise was rejected with significant value of S criterion: 46.2 ± 0.5 for RP and 6.5 ± 0.7 for GSRP surrogates.

The correlation dimension vs. embedding space dimension of noise-reduced time series of the whole catalogue is presented in Fig. 20.13. It is clear from this picture that calculated values of correlation dimension are not affected by noises as for the complete catalogue. The results show that the differences found in the d_2-phase space dimension (P) relationship before and during experiments in both catalogues are indeed caused by dynamical changes in temporal distribution of earthquakes during EM experiments.

We also analyzed waiting time sequences after each largest ($M \approx 6.1$–6.3) event for the whole catalogue, namely, 1000 consecutive waiting time sequences after 03.24.78 $M = 6.1$ ($K = 15.0$), 01.24.87 $M = 6.3$ ($K = 15.3$) and 12.30.93 $M = 6.1$ ($K = 15.0$) events. As it is shown in Fig. 20.14, these short time series generally reveal dynamical characteristics similar to those of the time series obtained from the complete catalogue. The differences which are noticeable in saturation values of correlation dimension before (circles, $d_2 = 2.0 \pm 1.1$ in Fig. 20.14) and during (squares, $d_2 = 3.2 \pm 0.8$, Fig. 20.14) experiments may be caused both by the shortness of these time series or by the influence of increased fraction of aftershocks.

Thus, conclusions concerning the influence of hot and cold EM runs on general characteristics of the dynamics of earthquakes' temporal distribution remain valid for small earthquakes too.

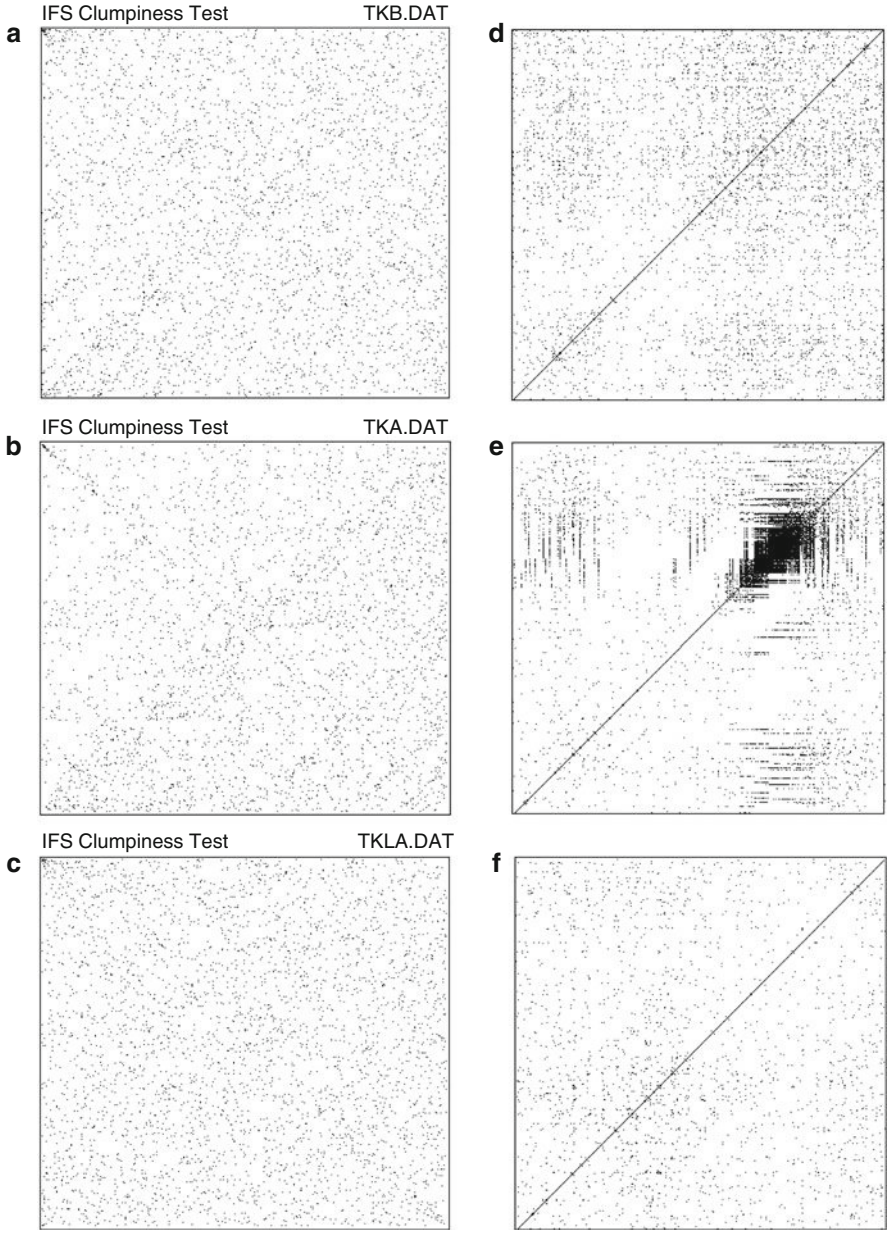

Fig. 20.9 Qualitative analysis of temporal distribution of earthquakes including small events (whole catalogue, all events) before the beginning of EM experiments (1975-1983), during experiments (1983-1988) and after accomplishing of experiments (1988-1992). IFS-clumpiness test for waiting times sequences: (**a**) before experiments, (**c**) during experiments, (**e**) after experiments. Recurrence plots analysis of inter-event time interval sequences: (**b**) before experiments, (**d**) during experiments, (**f**) after experiments

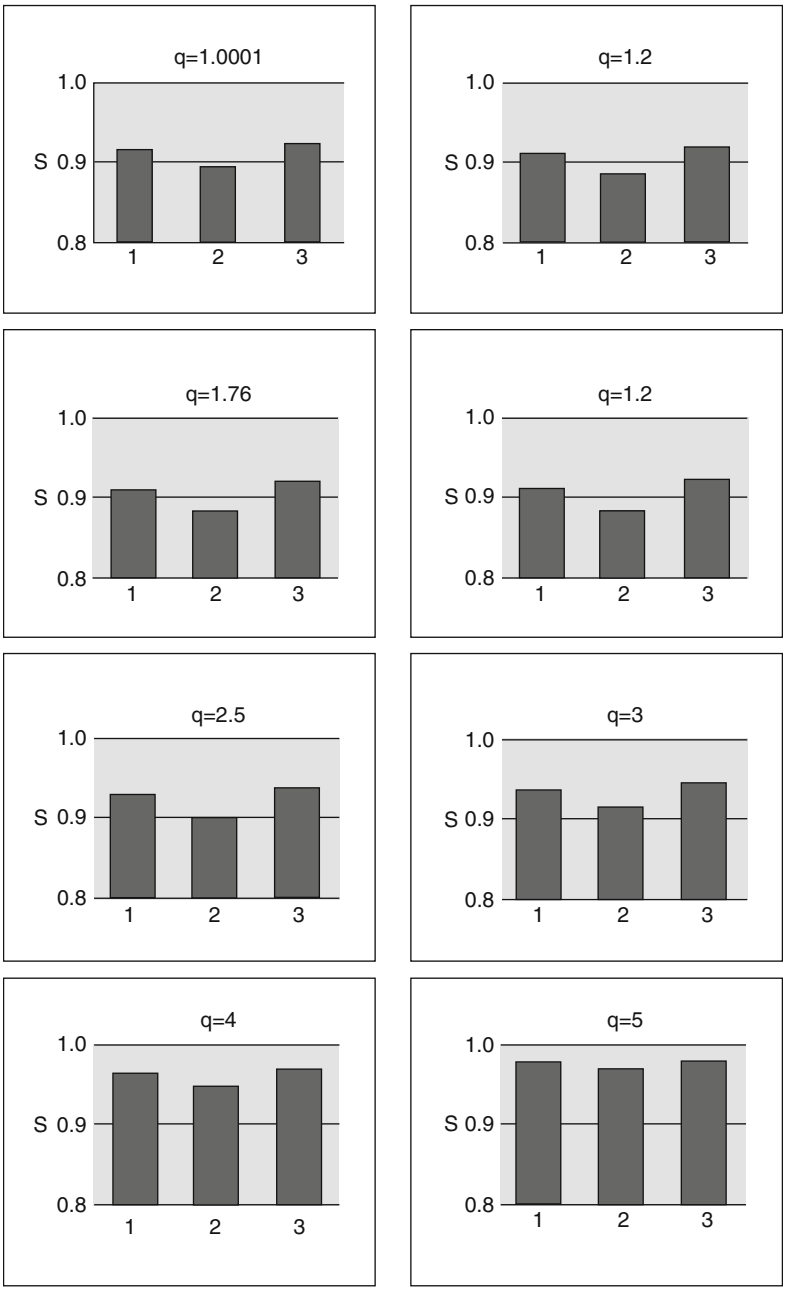

Fig. 20.10 The Tsallis entropies calculated for 3 windows (1–before, 2–during and 3–after MHD runs) for various entropic indexes q

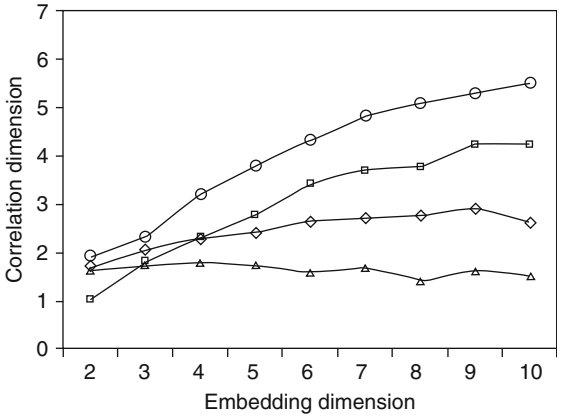

Fig. 20.11 Correlation dimension versus embedding dimension of waiting times sequences of the whole catalogue:
(a) diamonds–integral time series (1975-1996),
(b) squares–before the beginning of experiment (1975-1983),
(c) triangles–during experiments (1983-1988),
(d) circles–after experiments (1988-1992)

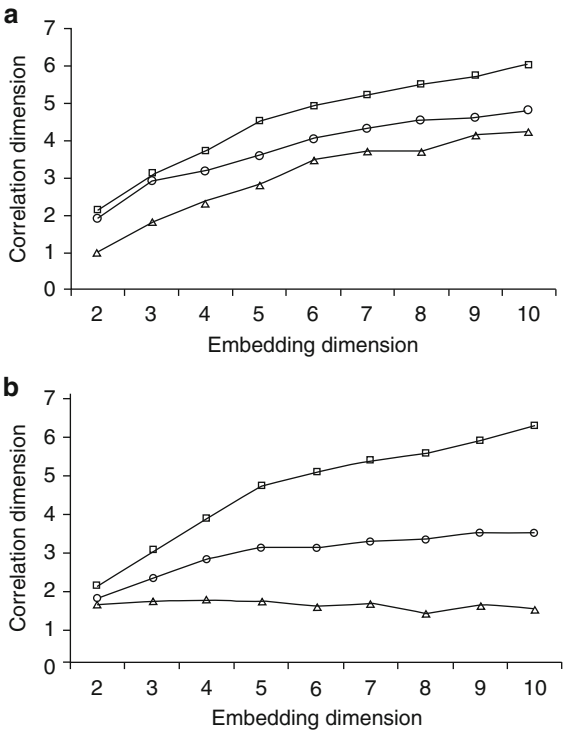

Fig. 20.12 Correlation dimension versus embedding dimension of original waiting time sequences of whole catalogue (triangles) and their surrogates (circles–GSRP, squares–RP): (**a**) before the beginning of experiments, (**b**) during experiments

It is interesting to note that on the laboratory scale the effect of triggering and synchronization of acoustic emission during a slip imposed by strong EM field is well documented in numerous experiments [Chelidze et al, 2002; Chelidze and Lursmanashvili 2003; Chelidze et al, 2005].

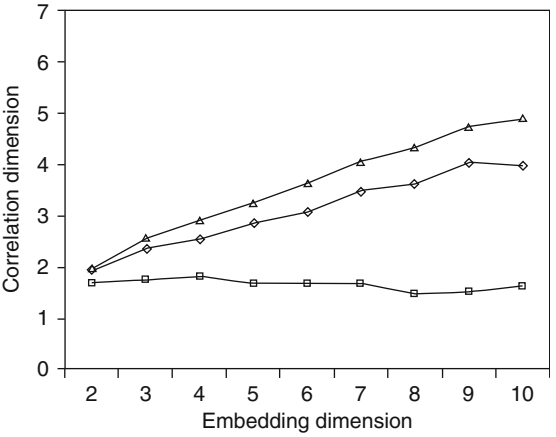

Fig. 20.13 Correlation dimension versus embedding dimension of inter-event time interval sequences of whole catalogue after noise reduction:
(a) diamonds–before experiments,
(b) squares–during experiments.
(c) triangles–after experiments

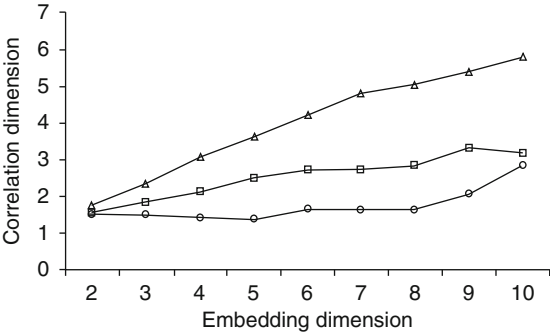

Fig. 20.14 Correlation dimension versus embedding dimension of 1000 data waiting times sequences of the whole catalogue after largest events: (a) circles–time period before the beginning of experiments (1975-1983), (b) squares–time period during experiments (1983-1988), (c) triangles–time period after accomplishing of experiments (1988-1992)

20.5 Conclusion

The question whether electromagnetic experiments on a specific site can influence the dynamics of a seismic region is complex. A complete answer to it, if any could be given, would involve a repeated set of analyses for different seismic regions over a long period of time with and without EM experiments. A theoretical explanation showing the cause-and-effect relationships between the two phenomena is also fundamental. This paper has addressed the question under statistical aspect involving nonlinear dynamics methods. These methods have been chosen because there are not trivial, simple and direct relations between the two phenomena: this means that relations are of complicated nature. Moreover, seismicity is very probably a critical process with a *per se* complicate evolution: under given conditions, possible relations must not be direct and simple. With nonlinear methods, the time evolution of seismicity has been investigated looking at relations with EM experiments. Waiting times constitute the aspect analyzed. The whole time period has been divided into three parts, the middle being the one when EM experiments took place.

The phase space attractor, reconstructed with delay time technique, shows low correlation dimension values for the whole time period; this indicates, at least, the presence of few seismicity-driving processes. The same analysis on the three sub-catalogues confirms the result, with the exception for the period after the EM experiments: strong EM discharges lead to the increase of extent of regularity in earthquakes temporal distribution, while after the EM influence ceases, the earthquakes' temporal distribution becomes much more random than before the experiments. This is the main result of the analysis and it has been confirmed by changing the conditions of the analysis itself. Non-linear noise reduced time series has confirmed such results, as also surrogate testing did. The middle period contains a large seismic event (January 24, 1987 $M = 6.3$ derived from energy class $K = 15.3$); this event has certainly a well-identified aftershocks activity and this can be a strong factor influencing the time dynamics. The root question is: is this event with its related sequence responsible of the change of the dynamics of analyzed data? If the answer would be yes we are forced to answer immediately the new question: is this earthquake related to the EM experiments? But it must be noted that inside the other two periods there are also important events of comparable magnitudes and the analysis has been conducted on the three sequences of catalogue after each strong event separately. General confirmation of results has been shown. Same results have been revealed with the use of the whole catalogue, regardless of the completeness criteria.

This analysis is certainly not exhaustive: the seismic catalogue covers a broad area and all complete data were used, with no distinction for space location of seismic events. The energy aspect has not been fully considered: all events were considered equal, regardless of their magnitude. These are strong simplifications and the results must be considered under these constrains. However, the results appear to be consistent: EM experiments influence seismic time dynamics to some extent, increasing the regularity of waiting times. After the EM experiments, seismic waiting times have increased their random character to a level higher than before experiments.

References

Abarbanel, H. D., Brown, R., Sidorovich, J. J., Tsimring, L. Sh., The analysis of observed chaotic data in physical systems, Rev. Mod. Phys. 65, 4, 1331-1392, 1993.

Chelidze T., N. Varamashvili, M. Devidze, Z. Chelidze, V. Chikladze, T. Matcharashvili. Laboratory study of electromagnetic initiation of slip, Annals of Geophysics, vol. 45, 587–598, 2002.

Chelidze T. and O. Lursmanashvili, Electromagnetic and mechanical control of slip: laboratory experiments with slider system, Nonlinear Processes in Geophysics. V. 20, 1–8, 2003.

Chelidze T., T. Matcharashvili, J. Gogiashvili, O. Lursmanashvili, M. Devidze. Phase synchronization of slip in laboratory slider system. Nonlinear Processes in Geophysics. 12, 1-8, 2005.

De Rubeis V., Dimitriu P., Papadimitriou E. and Tosi P. Recurrent patterns in the spatial behaviour of Italian seismicity revealed by the fractal approach, Geoph. Res. Lett. 20, 1911-1914, 1993.

Eckmann, J.P., Kamphorst S., Ruelle, D., Recurrence plots of dynamical systems. Europhysics Letters, 4 (9), 973-977, 1987.

Geller, R.J., Jackson, D.D., Kagan, Y.Y., and Mulargia, F., Earthquakes cannot be predicted, Sciences, 275, 1616-1617, 1997.

Goltz C, Fractal and chaotic properties of earthquakes, Springer, Berlin, 1998.

Hegger, R., Kantz, H., Practical implementation of nonlinear time series methods: the TISEAN package. Chaos, 9, 413-440, 1999.

Jeffrey, J.H., Chaos game vizualization of sequences, Comput. and Graphics, 1992, 16, 1, 25–33.

Jones, N., The quake machine. New Scientist. June 30, 34-37. 2001.

Kantz, H., Schreiber, T., Nonlinear time series analysis, Cambridge University Press, 1997.

Lempel, A., Ziv, J., On the complexity of finite sequences, IEEE Trans. Infor. Theory, IT-22, 75-81, 1976.

Main, I., *et. al*., Is the reliable prediction of individual earthquakes a realistic scientific goal?, in Nature Debates, http://www.nature.com/nature/debates/earthquake/equake_frameset.html, 1999.

Marwan, N, Wessel, N., Meyerfeldt, U., Schirdewan, A., Kurths, J., Recurrence-plot-based measures of complexity and their application to heart rate variability data. Physical Review E, 66, 026702.1-026702.8, 2002.

Matcharashvili, T., Chelidze, T., Javakhishvili, Z., Nonlinear analysis of magnitude and waiting time interval sequences for earthquakes of Caucasian region, Nonlinear Processes in Geophysics, 2000, 7, 9-19.

Matcharashvili, T., Janiashvili, M., Investigation of variability of indexes of myocardial contractility by complexity measure in patients with arterial hypertension. Sulis, W., Trofimova, I., (Eds), Nonlinear dynamics in life and social sciences. IOS Press, Amsterdam, 2001, 204-214.

Mulargia F., Gasperini P. and Tinti S.. Contour mapping of Italian seismicity. Tectonophysics 142, 203-216, 1987.

Packard, N.H., Crutchfield, J.P., Farmer, J.D., Shaw, R.S., Geometry from a time series.Phys. Rev. Lett. 45, 712-716, 1980.

Peitgen, H.O., Jurgens, H., Saupe, D., Chaos and fractals: New Frontiers of Science, Springer, NY, 1992.

Prichard, D., Theiler, J., Generating surrogate data time series with several simultaneously measured variables, Phys. Rev. Lett. 1994, 73, 7, 951-1018.

Rapp, P.E., Albano, A.M., Schmah, T.I, Farwell, L. A., Filtered noise can mimic low-dimensional chaotic attractors. Phys. Rev. E., 1993, 47, 4, 2289–2297.

Rapp, P.E., Albano, A.M., Zimmerman, I. D., Jumenez-Montero, M.A., Phase-randomized surrogates can produce spurious identification of non-random structure, Phys. Lett. A., 1994, 192, 1, 27–33.

Schreiber, T., Extremely simple nonlinear noise-reduction method, Phys. Rev. E, 1993, 47, 4, 2401–2404.

Schreiber, T., Schmitz, A., Surrogate time series, Physica D, 142, 346-352, 2000.

Sprott, J. C., Rowlands, G., Chaos data analyzer; the professional version. AIP, NY, 1995.

Takens, F., Detecting strange attractors in turbulence. in: Dynamical Systems and Turbulence, Warwick 1980, D.A. Rand and L.S. Young, eds Vol.898 of Springer Lecture Notes in Mathematics, 366-381, Springer- Berliner, 1981.

Tarasov, N.T. Crustal seismicity variation under electric action. Transactions (Doklady) of the Russian Academy of Sciences, 353A (3), 445-448, 1997.

Tarasov, N.G., Tarasova, N. V., Avagimov, A.A., Zeigarnik, V.A., The effect of high-powerelectromagnetic pulses on the seismicity of the central Asia and Kazakhstan, Vulkanologia iseismologia. 4-5, 152-160, 1999 (in Russian).

Theiler, J., Eubank, S., Longtin, A., Galdrikian, B., Farmer, J.D., Testing for nonlinearity in time series: the method of surrogate data, Physica D, 1992, 58, 77–94.

Tsallis, C., Possible generalization of Boltzmann-Gibbs statistics, J. Stat. Phys., 1988, 52, 479–487.

Tsallis, C., Generalized entropy-based criterion for consistent testing, Phys. Rev. E., 1998, 58, 1442–1445.

Turcotte. D.L., Fractals and Chaos in Geology and Geophysics, Cambridge University Press, Second Edition, 1997.
Volykhin, A.M., Bragin, V.D., Zubovich, A.P., Geodynamic Processes in Geophysical Fields, Moscow: Nauka, 1993.
Webber, C.L., Jr. and Zbilut, J.P., Dynamical assessment of physiological systems and states using recurrence plot strategies. Journal of Applied Physiology 76: 965-973, 1994.
Zbilut, J.P., Webber, C.L. Jr., Embeddings and delays as derived from quantification of recurrence plots. Physics Letters A, 171: 199-203, 1992.
Zhang, X., Thakor, N.V., Detecting Ventricular Tachicardia and Fibrillation by Complexity Measure. IEEE Trans. on Biomed. Eng. 46, 5. 548-555, 1999.

Index